UAB
Universitat Autònoma de Barcelona

Multiscale modelling to understand the influence of green infrastructure on temperature and atmospheric carbon capture

Ricard Segura Barrero

ADVERTIMENT. L'accés als continguts d'aquesta tesi queda condicionat a l'acceptació de les condicions d'ús establertes per la següent llicència Creative Commons:  https://creativecommons.org/licenses/?lang=ca

ADVERTENCIA. El acceso a los contenidos de esta tesis queda condicionado a la aceptación de las condiciones de uso establecidas por la siguiente licencia Creative Commons:  https://creativecommons.org/licenses/?lang=es

WARNING. The access to the contents of this doctoral thesis it is limited to the acceptance of the use conditions set by the following Creative Commons license:  https://creativecommons.org/licenses/?lang=en

UNIVERSITAT AUTÒNOMA DE BARCELONA (UAB)
INSTITUT DE CIÈNCIA I TECNOLOGIA AMBIENTALS (ICTA-UAB)

Programa de doctorat en Ciència i Tecnologia Ambientals

Ph. D. thesis

Multiscale modelling to understand the influence of green infrastructure on temperature and atmospheric carbon capture

Ricard Segura Barrero

Directors:
Dr. Gara Villalba Méndez (UAB)
Dr. Alba Badia i Moragas (UAB)
Dr. Alberto Martilli (CIEMAT)
Academic Tutor:
Dr. Gara Villalba Méndez (UAB)

Bellaterra, March 2024

Ich sih die liehte Heide
in gruner varwe stan
dar suln wir alle gehen
die Sumerzeit enpahen.

I see the sunstruck forest,
In green it stands complete.
There soon we are all going,
The summertime to meet.
- Carmina Burana

Acknowledgements

Per començar, voldria agrair tota la confiança, esforç, dedicació i paciència dels meus supervisors cap a la meva persona i aquesta tesis que difícilment hagués sigut possible sense ells. A la Gara, li voldria expressar la meva admiració en la seva dedicació a la ciència i tot el que ha aconseguit amb el grup de recerca. A l'Alba, voldria agrair-li que sempre hagi sapigut dir-me les paraules més tranquilitzadores en els meus moments de major estrès. A Alberto, me gustaría agradecerle su interés por mi trabajo y mi persona, pese a la distancia y las agendas tan apretadas. No hagués pogut tenir millors directors que vosaltres.

Voldria agrair també a tots els meus companys i companyes del grup de recerca URBAG i Sostenipra. Sense ells aquests més de 4 anys de tesis haguessin estat molt menys divertits. Moltes gràcies a tota la gent de l'ICTA i la UAB que s'han preocupat per mi i m'han dedicat un moment per molestar-los amb la meva tesis.

I would like to thank the dedication and effort to all the coauthors of the publications that I led, especially Joan Gilabert, Scott Krayenhoff, Carme Estruch, Sergi Ventura, Thomas Lauvaux, Jinghui Lian, Philippe Ciais, Hassan Bazzi, Ezzeddine Abbessi and Johannes Langemeyer.

I would like to thank my colleagues from the LSCE, especially to Philippe Ciais and Jinghui Lian for welcoming me in France, and integrating me in the group. Thanks for the unlimited help!

Nada de lo que soy ni seré, sería posible sin mi familia. Su apoyo ha sido fundamental para poder alcanzar esto. Mi amor más grande a mis padres, hermanos y mi abuela. Estoy seguro que mis abuelos Concha, José y José estarían muy orgullosos.

El meu agraïment a tots els meus amics i amigues, per acompanyar-me i recolzar-me durant aquests 4 anys tan intensos de la meva vida.

Per acabar, i no per això menys important, voldria agrair-li a l'única persona que ha estat pràcticament cada dia amb mi des que vaig començar aquesta aventura i encara tinc la sort que m'acompanyi. Alba sense tú això hagués estat inimaginable. Aquest treball també té molt de tú. De la teva paciència, la teva estima i dedicació. Espero poder començar moltes aventures més al teu costat. Ets la millor!

Summary (English version)

Green infrastructures (GI) refer to natural and semi-natural areas strategically designed and managed to enhance biodiversity and provide diverse ecosystem services. The implementation and expansion of GI stands as a nature-based solution for mitigating and adapting urban areas to climate change. This multifunctional approach contributes to the regulation of environmental impacts at various spatial scales, thereby promoting human well-being. In urban areas, GI, as street trees and urban parks, reduce urban temperatures and human thermal stress due to mechanisms of transpiration and shading. At the regional scale, natural ecosystems contribute significantly to climate change mitigation by capturing and retaining atmospheric carbon dioxide, thus counteracting partially anthropogenic emissions of this greenhouse gas.

Despite these benefits, the increasing frequency and severity of extreme climate events, such as heat waves and droughts amidst of changing climates, pose significant challenges to ecosystem functioning. These events can compromise the ability of GI to deliver essential ecosystem services at both urban and regional scales. The concurrent occurrence of heat waves and droughts profoundly impacts ecosystem-atmosphere carbon dioxide fluxes. Additionally, droughts hamper leaf transpiration, diminishing the cooling capacity of urban GI.

Moreover, the impacts of extreme climate events are highly dependent on the land cover type, producing different responses on natural vegetation and croplands. This is relevant as the implementation of peri-urban agriculture (peri-UA) is gaining high attention, due to its multifunctional role. Despite irrigated agriculture can provide with regional temperature reductions during the dry season potentially alleviating the effects of heat wave events on nearby urban areas, other trade-offs associated with peri-UA must not be disregarded, as the high water requirements, the emissions of greenhouse gases from the use of mineral fertilizers, and the displacement of natural vegetation that provide other crucial ecosystem services.

This thesis seeks to determine the capacity of GI to provide local temperature regulation, reduce human thermal stress, and capture atmospheric carbon dioxide, especially under the influence of heat waves and droughts. This study spans three spatial scales: street/neighbourhood, city, and regional scales. The innovative aspect of this research lies in enhancing, optimizing, combining, and implementing diverse numerical models in a multiscale approach in three distinct case studies- the Eixample district of Barcelona, the Metropolitan Area of Barcelona (AMB), and south-western Europe. This thesis is structured to answer the following research questions:

At street and neighbourhood scale:
RQ1. How do street trees impact air-cooling and radiation exchange within a highly-compact city?
RQ2. How do street trees impact outdoor thermal stress during heat waves in a highly-compact city?
At city scale:
RQ3. What is the role of urban GI in local temperature regulation in a coastal Mediterranean city?
RQ4. Can the expansion of peri-UA have measurable effects on local temperature regulation and atmospheric carbon capture?
At regional scale:
RQ5. What is the impact of heat and drought events on the biogenic carbon capture of ecosystems in the south-western European region?

Temperature and thermal stress effect of street trees
At the street and neighbourhood scales, using the Eixample district as case study, the impact of street trees on air temperatures and human thermal stress was analysed using a micrometeorological measurement campaign and the Building Effect and Parameterization with Trees model (BEP-Tree), which accounts for the effects of trees and buildings on neighbourhood-scale meteorology. The model described a reduction in shortwave radiation from trees due to shading, an increase in downwelling longwave radiation from trees, and, to some extent, the decrease in midday road surface temperatures. Observational data revealed that street trees can modify midday air temperatures by up to 1.3 ºC, dependent on tree density and local meteorological conditions. An extended modelling analysis, incorporating a summer month and a heat wave, indicated that the air-cooling effect of street trees varies significantly with soil moisture. Under moist conditions, trees can reduce midday/afternoon temperatures by 0.7 ± 0.4 ºC, while in dry soil conditions, they might increase temperatures slightly.

Furthermore, this thesis emphasizes the similar contribution of tree transpiration and shading in reducing human thermal stress. Street trees reduce the Universal Thermal Climate Index (UTCI), a bioclimatic index describing human body thermal comfort, by 0.9 – 1.2 ºC under optimal conditions, and by 0.5 – 0.8 ºC during dry conditions. The thermal stress effect is more significant during the first days of the heat wave due to enhanced tree transpiration, decreasing UTCI by 1.2 – 1.5 ºC under moist soils, and by 0.7 – 0.9 ºC under dry soils. Contrary to air-cooling, tree shade, which is assumed to be constant regardless of soil moisture, maintains a reduction of the human thermal stress under dry soil conditions, representing a 50-60 % of the potential reduction with moist soil conditions. This underscores the joint role of tree shade and the soil water availability, not only for preserving tree health and foliage, but also for maximizing their microclimatic benefits for urban residents.

Urban GI on temperature regulation and carbon capture: the case of peri-UA
This dissertation investigated the impact of urban GI on temperature regulation during heat

waves in the AMB, using high-resolution Weather Research and Forecasting (WRF) model simulations. This model is coupled with the Building Effect Parameterization and the Building Energy Model (BEP-BEM) to better represent the impact of urban areas on regional meteorology. The study found a linear relationship between urban areas near-surface temperatures and their impervious surface plan area fraction, with a stronger relation found at night (-0.18 ± 0.01 ºC for every 10 % of the area converted from impervious to pervious surface). Results indicate a lower potential of GI at the metropolitan scale to regulate daytime temperatures compared to smaller scales (street and neighbourhood). Although, this analysis does not account for the effect of different types of GI, vegetation irrigation, or the impact on various urban morphologies.

To address these limitations, this thesis presents a methodological approach to assess the trade-offs between ecosystem services in the food-water-climate nexus arising from the implementation of GI at the urban scale. This method is tested on the expansion of peri-UA in the AMB. This approach combines georeferenced urban metabolism models for food provision and GI irrigation requirements, with the local atmosphere and biogenic carbon balance simulation using regional atmospheric and biosphere models. The results show that increasing peri-UA enchances local food production (up to +85.8 %) but also raises irrigation water needs (up to +43.5 %). While it contribute to local temperature reduction with midday/afternoon near-surface temperature decreases up to 0.7 ºC, its positive impact on air-cooling is limited geographically and highly linked with irrigation. Moreover, peri-UA expansion disrupt the regional carbon balance, reducing atmospheric carbon capture by up to 18.5 %. This study emphasizes the need to assess not only the direct impacts of local crop production on the atmospheric carbon capture, including land-use changes, but also indirect effects such as those from replaced imported products and other agricultural emissions. This comprehensive approach is essential for designing equitable nature-based solutions that consider both local and global environmental impacts.

The impact of heat and drought events on biogenic carbon capture in south-western Europe

This thesis examined the effects of heat and drought events on biogenic carbon capture in south-western European ecosystems from 2001 to 2022. Utilizing a modified Vegetation Photosynthesis and Respiration Model (VPRM) for its application in the region, the study analysed long-term carbon flux trends, climatic influences on carbon flux anomalies, and intra-annual variations during extreme heat and drought events. An increase in both photosynthesis and respiration fluxes was found, attributed to longer growing seasons from warmer temperatures. However, their similar trends resulted in only a modest rise in the net carbon sink of 0.80 g C m^{-2} $year^{-2}$, particularly in high-altitude forests. This suggests a delicate balance between carbon capture and release that could be disrupted by ongoing warming and drying trends. The significant impact of summer heat and drought events also increase the variability of the net carbon exchange, posing a threat to the stability of the growing net carbon sink.

Soil water availability emerged as a critical climatic factor affecting carbon flux variability, particularly in non-Alpine regions. The study also established a connection between climate dryness and the impact of drought on photosynthesis and respiration carbon flux variabilities, with

the most pronounced control on Mediterranean climate ecosystems. However, the highest non-linearities between the response of the photosynthesis and respiration to droughts, implying a higher influence on the net carbon sink, are found in temperate humid regions, which are the highest net carbon sinks in the region. These results underscore the vulnerability of the south-western Europe's carbon sink capacity to drought occurrences. Exceptional heat and drought events in 2003, 2005, and 2022 significantly reduced net carbon capture in the region, by 34.1 %, 22.8 %, and 26.9 % respectively, in some cases turning ecosystems from carbon sinks to sources due to a greater decrease in photosynthesis compared to respiration. The ecosystems in the south-western European region present complex response to heat and drought events, which raise concerns about their ability to offset anthropogenic carbon dioxide emissions if the frequency and intensity of such events continue to increase.

Resum (Catalan version)

Les infraestructures verdes (IV) es refereixen a les zones naturals i seminaturals dissenyades i gestionades estratègicament per millorar la biodiversitat i proporcionar diversos serveis ecosistèmics. La implementació i expansió de les IV constitueix una solució basada en la natura capaç de mitigar el canvi climàtic i adaptar les zones urbanes a aquest. Aquest enfoc multifuncional contribueix a la regulació dels impactes ambientals en diverses escales espacials, promovent el benestar humà. En les zones urbanes, la IV, com els arbres dels carrers i els parcs urbans, redueixen les temperatures i l'estrès tèrmic percebut gràcies als mecanismes de transpiració i ombreig. A escala regional, els ecosistemes naturals contribueixen significativament a mitigar el canvi climàtic en capturar i retenir el diòxid de carboni atmosfèric, contrarestant parcialment les emissions antropogèniques d'aquest gas d'efecte hivernacle.

Malgrat aquests beneficis, la creixent freqüència i intensitat dels fenòmens climàtics extrems, com les onades de calor i les sequeres en mig del canvi climàtic, plantegen reptes significatius pel funcionament dels ecosistemes. Aquests fenòmens poden comprometre la capacitat de la IV per prestar serveis ecosistèmics essencials tant a l'escala urbana com regional. La ocurrència simultània d'onades de calor i sequeres afecta profundament els fluxos de diòxid de carboni entre l'atmosfera i els ecosistemes. A més, les sequeres dificulten la capacitat de transpiració de les fulles, disminuint el refredament de la IV urbana.

D'altra banda, els efectes dels fenòmens climàtics extrems depenen en gran mesura del tipus de cobertura del sòl, i produeixen respostes diferents en la vegetació natural i els cultius. Això és rellevant ja que la implementació de l'agricultura peri-urbana (peri-UA) està guanyant gran atenció, degut al seu paper multifuncional. Malgrat que l'agricultura de regadiu pot proporcionar reduccions de temperatura a escala regional durant l'estació seca, alleujant potencialment els efectes de les onades de calor en zones urbanes properes, no s'han de menystenir altres contrapartides associades a l'agricultura peri-urbana, com les elevades necessitats d'aigua, les emissions de gasos d'efecte hivernacle derivades de l'ús de fertilitzants minerals i el desplaçament de la vegetació natural que proporciona altres serveis ecosistèmics crucials.

Aquesta tesi pretén determinar la capacitat de la IV per proporcionar una regulació local de la temperatura, reduir l'estrès tèrmic percebut pels humans, i capturar diòxid de carboni atmosfèric, especialment sota la influència d'onades de calor i sequeres. L'estudi abasta tres escales espacials: carrer/barri, ciutat i regió. L'aspecte innovador d'aquesta recerca rau en la millora, optim-

ització, combinació i implementació de diversos models numèrics en un enfocament multiescalar en tres casos d'estudi diferents: el districte de l'Eixample de Barcelona, l'Àrea Metroopolitana de Barcelona (AMB) i el sud-oest d'Europa. Aquesta tesi està estructurada per respondre a les següents preguntes de recerca:

A escala de carrer i de barri:
Pregunta 1. Com afecten els arbres del carrer al refredament de l'aire i a l'intercanvi de radiació en una ciutat molt compacta?
Pregunta 2. Com influeixen els arbres en l'estrès tèrmic exterior durant les onades de calor en una ciutat molt compacta?
A escala de ciutat:
Pregunta 3. Quin és el paper de la IV urbana en la regulació de la temperatura local en una ciutat costera mediterrània?
Pregunta 4. Pot l'expansió de la peri-UA tenir efectes mesurables en la regulació de la temperatura local i la captura de carboni atmosfèric?
A escala regional:
Pregunta 5. Quin és l'impacte dels episodis de calor i sequera en la captura de carboni biogènic dels ecosistemes del sud-oest d'Europa?

Efecte en la temperatura i l'estrès tèrmic dels arbres dels carrers
A escala de carrer i de barri, utilitzant el districte de l'Eixample com a cas d'estudi, l'impacte en la temperatura de l'aire i l'estrès tèrmic dels arbres dels carrers va ser analitzat a partir d'una campanya de mesures micrometeorològiques i utilitzant el model Building Effect and Parameterization with Trees (BEP-Tree), que té en compte els efectes dels arbres i els edificis en la meteorologia a escala de barri. El model descriu una reducció de la radiació d'ona curta degut a l'efecte de l'ombra dels arbres, un augment de la radiació d'ona llarga descendent degut a la presència dels arbres, i en certa mesura, la disminució de les temperatures en la superfície de l'asfalt al migdia. Les dades d'observació revelen que els arbres dels carrers poden modificar la temperatura de l'aire al migdia fins a 1.3 ºC, depenent de la densitat d'arbres i de les condicions meteorològiques locals. Una anàlisi més extensa amb el model BEP-Tree, cobrint un mes d'estiu amb una onada de calor, mostra que l'efecte de refredament de l'aire dels arbres varia significativament amb la humitat del sòl. En condicions de sòl humit, els arbres poden disminuir les temperatures des del migdia fins a la tarda en 0.7 ± 0.4 ºC, mentre que en condicions de sòl sec poden augmentar lleugerament les temperatures.

A més, aquesta tesi fa èmfasi en la contribució similar de la transpiració i l'ombra dels arbres en la reducció de l'estrès tèrmic humà. Els arbres dels carrers redueixen l'Índex Tèrmic Climàtic Universal (UTCI), un índex bioclimàtic que descriu el confort tèrmic del cos humà, en 0.9 – 1.2 ºC en condicions de sòl humit, i entre 0.5 – 0.8 ºC en condicions de sòl sec. L'efecte en l'estrès tèrmic és més significatiu durant els primers dies de l'onada de calor degut a l'augment de la transpiració dels arbres, disminuint l'UTCI en 1.2 – 1.5 ºC amb sòls humits, i en 0.7 – 0.9 ºC amb sòls secs. Al contrari que el refredament de l'aire, l'ombra dels arbres, que es suposa constant independentment de la humitat del sòl, manté una reducció de l'estrès tèrmic humà en

condicions de sòl sec, la qual cosa representa un 50-60 % de la reducció potencial en condicions de sòl humit. Això subratlla el paper conjunt de l'ombra dels arbres i la disponibilitat d'aigua en el sòl, no només per preservar la salut i el fullatge dels arbres, sinó també per maximitzar els seus beneficis microclimàtics per als vianants.

La IV urbana en la regulació de la temperatura i la captura de carboni: el cas de la peri-UA

L'impacte de la IV urbana en la regulació de la temperatura s'ha investigat durant les onades de calor a l'AMB, utilitzant simulacions d'alta resolució amb el model Weather Research and Forecasting (WRF). Aquest model està acoblat amb el model Building Effect Parameterization and the Building Energy Model (BEP-BEM) per representar millor l'impacte de les zones urbanes i edificis en la meteorologia regional. L'estudi va trobar una relació lineal entre les temperatures properes a la superfície de les zones urbanes i la fracció urbana, amb una relació més estreta durant la nit (-0.18 ± 0.01 ºC per cada 10 % de la superfície convertida d'impermeable a permeable). Els resultats indiquen un menor potencial de la IV a escala metropolitana per regular les temperatures diürnes en comparació amb escales més petites (carrer i barri). Tot i així, aquest anàlisi no té en compte l'efecte de diferents tipus de IV, el reg de la vegetació ni l'impacte en diferents morfologies urbanes.

Per abordar aquestes limitacions, aquesta tesi presenta un enfocament metodològic per avaluar les compensacions entre els serveis ecosistèmics en el nexe aliments-aigua-clima derivades de l'aplicació de la IV a escala urbana. Aquest mètode es posa a prova amb l'expansió de la peri-UA a l'AMB. Aquest enfocament combina models georeferenciats del metabolisme urbà per estimar la producció d'aliments i les necessitats de reg de la IV, amb la simulació de l'atmosfera local i el balanç de carboni biogènic mitjançant models regionals atmosfèrics i de la biosfera. Els resultats mostren que l'augment de la peri-UA incrementa la producció local d'aliments (fins a un +85.8 %) però al mateix temps augmenta en les necessitats de reg (fins a un +43.5 %). Encara que contribueix a la reducció de la temperatura local amb descensos de temperatura de fins a 0.7 ºC durant el migdia/tarda, el seu impacte positiu en el refredament de l'aire és limitat geogràficament i està molt lligat al reg. A més, l'expansió de la peri-UA altera el balanç regional de carboni, reduint la captura de carboni atmosfèric fins a un 18.5 %. Aquest estudi fa èmfasi en la necessitat d'avaluar no només els efectes directes de la producció local de cultius en la captura de carboni, inclosos els canvis en l'ús del sòl, sinó també els efectes indirectes, com els derivats de la substitució de productes importats i altres emissions agrícoles. Aquest enfocament integral és essencial per dissenyar solucions equitatives basades en la naturalesa que tinguin en compte tant l'impacte ambiental local com el global.

L'impacte d'episodis de calor i sequeres en la captura de carboni biogènic dels ecosistemes del sud-oest d'Europa

Aquesta tesi examina els efectes dels episodis de calor i sequeres en la captura de carboni dels ecosistemes del sud-oest d'Europa de 2001 a 2022. Utilitzant un model de la biosfera adaptat a la seva aplicació en la regió, el model Vegetation Photosynthesis and Respiration Model (VPRM), l'estudi va analitzar les tendències dels fluxos de carboni a llarg termini, les influències

climàtiques en les anomalies dels fluxos de carboni i les variacions intra-anuals durant episodis extrems de calor i sequera. L'estudi revela un augment dels fluxos de fotosíntesi i respiració, atribuït a la prolongació dels períodes de creixement de la vegetació degut a les temperatures més càlides. No obstant això, les tendències similars entre els dos fluxos produeixen una compensació, donant lloc a un augment modest de l'embornal net de carboni de 0.80 $m^{-2}\,any^{-2}$, especialment en els boscos de muntanya. Això suggereix un delicat equilibri entre l'augment en la captura i l'alliberament de carboni dels ecosistemes que podria veure's alterat per les tendències actuals d'escalfament de l'aire i dessecament del sòl. Els episodis de calor i sequeres també tenen un impacte en la variabilitat interanual de l'intercanvi net de carboni, la qual cosa suposa una amenaça per a l'estabilitat del creixement de l'embornal net de carboni.

La disponibilitat d'aigua en el sòl es revela com un factor climàtic crític que afecta a la variabilitat del flux de carboni, sobretot en zones no alpines. L'estudi també estableix una connexió entre la sequedat climàtica i l'impacte de la sequera en la variabilitat dels fluxos de carboni fotosintètic i respiratori, amb una influència major en els ecosistemes de clima mediterrani. No obstant això, les majors no-linealitats entre la resposta de la fotosíntesi i la respiració a les sequeres, implicant una influència major en l'embornal net de carboni, es troben en les regions humides temperades, que representen els majors embornals net de carboni de la regió. Aquests resultats posen en relleu la vulnerabilitat de l'embornal net de carboni en el sud-oest d'Europa als episodis de sequera. Els episodis excepcionals de calor i sequera de 2003, 2005 i 2022 van reduir significativament la captura neta de carboni a la regió, en un 34.1 %, 22.8 % i 26.9 % respectivament, i en alguns casos provocant que els ecosistemes passessin de ser embornals de carboni a fonts degut a una major disminució de la fotosíntesi en comparació amb la respiració. Els ecosistemes de la regió occidental d'Europa presenten una resposta complexa als episodis de calor i sequera, el que fa témer per la seva capacitat per compensar les emissions antropogèniques de diòxid de carboni si la freqüència i intensitat d'aquests episodis continua augmentant.

Resumen (Spanish version)

Las infraestructuras verdes (IV) hacen referencia a las zonas naturales y seminaturales diseñadas y gestionadas estratégicamente para mejorar la biodiversidad y proporcionar diversos servicios ecosistémicos. La implementación y expansión de las IV constituye una solución basada en la naturaleza capaz de mitigar el cambio climático y adaptar las zonas urbanas a él. Este enfoque multifuncional contribuye a la regulación de los impactos ambientales en varias escalas espaciales, promoviendo el bienestar humano. En las zonas urbana, la IV, como los árboles de las calles y los parques urbanos, reducen las temperaturas y el estrés térmico percibido gracias a los mecanismos de transpiración y sombreado. A escala regional, los ecosistemas naturales contribuyen significativamente a mitigar el cambio climático al capturar y retener el dióxido de carbono atmosférico, contrarrestando parcialmente las emisiones antropogénicas de este gas de efecto invernadero.

A pesar de estos beneficios, la creciente frecuencia e intensidad de los fenómenos climáticos extremos, como las olas de calor y las sequías en medio del cambio climático, plantean retos significativos para el funcionamiento de los ecosistemas. Estos fenómenos pueden comprometer la capacidad de la IV para prestar servicios ecosistémicos esenciales tanto a escala urbana como regional. La ocurrencia simultánea de olas de calor y sequías afecta profundamente a los flujos de dióxido de carbono entre la atmósfera y los ecosistemas. Además, las sequías dificultan la capacidad de transpiración de las hojas, disminuyendo el enfriamiento de la IV urbana.

Por otra parte, los efectos de los fenómenos climáticos extremos dependen en gran medida del tipo de cobertura del suelo, y producen respuestas diferentes en la vegetación natural y en los cultivos. Esto es relevante ya que la implementación de la agricultura periurbana (peri-UA) está ganando gran atención, debido a su papel multifuncional. A pesar de que la agricultura de regadío puede proporcionar reducciones de temperatura a escala regional durante la estación seca, aliviando potencialmente los efectos de las olas de calor en zonas urbanas cercanas, no deben despreciarse otras contrapartidas asociadas a la agricultura periurbana, como las elevadas necesidades de agua, las emisiones de gases de efecto invernadero derivadas del uso de fertilizantes minerales y el desplazamiento de la vegetación natural que proporciona otros servicios ecosistémicos cruciales.

Esta tesis pretende determinar la capacidad de la IV para proporcionar una regulación local de la temperatura, reducir el estrés térmico percibido por los humanos, y capturar dióxido de car-

bono atmosférico, especialmente bajo la influencia de olas de calor y sequías. El estudio abarca tres escalas espaciales: calle/barrio, ciudad y región. El aspecto innovador de esta investigación radica en la mejora, optimización, combinación e implementación de diversos modelos numéricos en un enfoque multiescalar en tres casos de estudio distintos: el distrito del Eixample de Barcelona, el Área Metropolitana de Barcelona (AMB) y el suroeste de Europa. Esta tesis está estructurada para responder a las siguientes preguntas de investigación:

A escala de calle y de barrio:
Pregunta 1. ¿Cómo afectan los árboles al enfriamiento del aire y al intercambio de radiación en una ciudad muy compacta?
Pregunta 2. ¿Cómo influyen los árboles en el estrés térmico exterior durante las olas de calor en una ciudad muy compacta?
A escala de ciudad:
Pregunta 3. ¿Cuál es el papel de la IV urbana en la regulación de la temperatura local en una ciudad costera mediterránea?
Pregunta 4. ¿Puede la expansión de la peri-UA tener efectos medibles en la regulación de la temperatura local y la captura de carbono atmosférico?
A escala regional:
Pregunta 5. ¿Cuál es el impacto de los episodios de calor y sequía en la captura de carbono biogénico de los ecosistemas del suroeste de Europa?

Efecto en la temperatura y el estrés térmico de los árboles de las calles
A escala de calle y de barrio, utilizando el distrito del Eixample como caso de estudio, el impacto en la temperatura del aire y el estrés térmico de los árboles de las calles fue analizado a partir de una campaña de medidas micrometeorológicas y usando el modelo Building Effect and Parameterization with Trees (BEP-Tree), que tiene en cuenta los efectos de los árboles y los edificios en la meteorología a escala de barrio. El modelo describe una reducción de la radiación de onda corta debido al efecto de la sombra de los árboles, un aumento de la radiación de onda larga descendente debido a la presencia de los árboles, y en cierta medida, la disminución de las temperaturas de la superficie del suelo al mediodía. Los datos de observación revelan que los árboles de las calles pueden modificar la temperatura del aire al mediodía hasta en 1.3 ºC, dependiendo de la densidad de árboles y de las condiciones meteorológicas locales. Un análisis más extenso con el modelo BEP-Tree, abarcando un mes de verano con una ola de calor, muestra que el efecto de enfriamiento del aire de los árboles varía significativamente con la humedad del suelo. En condiciones de suelo húmedo, los árboles pueden disminuir las temperaturas des del mediodía hasta la tarde en 0.7 ± 0.4 ºC, mientras que, en condiciones de suelo seco, pueden aumentar ligeramente las temperaturas.

Además, esta tesis hace hincapié en la contribución similar de la transpiración y el sombreado de los árboles en la reducción del estrés térmico humano. Los árboles de las calles reducen el Índice Térmico Climático Universal (UTCI), un índice bioclimático que describe el confort térmico del cuerpo humano, en 0.9 – 1.2 ºC en condiciones de suelo húmedo, y entre 0.5 – 0.8 ºC en condiciones de suelo seco. El efecto en el estrés térmico es más significativo durante los primeros días

de la ola de calor debido al aumento de la transpiración de los árboles, disminuyendo el UTCI en 1.2 – 1.5 ºC con suelos húmedos, y en 0.7 – 0.9 ºC con suelos secos. Al contrario que el enfriamiento del aire, la sombra de los árboles, que se supone constante independientemente de la humedad del suelo, mantiene una reducción del estrés térmico humano en condiciones de suelo seco, lo que representa un 50-60 % de la reducción potencial en condiciones de suelo húmedo. Esto subraya el papel conjunto de la sombra de los árboles y la disponibilidad de agua en el suelo, no sólo para preservar la salud y el follaje de los árboles, sino también para maximizar sus beneficios microclimáticos para los viandantes.

La IV urbana en la regulación de la temperatura y la captura de carbono: el caso de la peri-UA

El impacto de la IV urbana en la regulación de la temperatura se ha investigado durante las olas de calor en el AMB, utilizando simulaciones de alta resolución con el modelo Weather Research and Forecasting (WRF). Este modelo está acoplado con el modelo Building Effect Parameterization and the Building Energy Model (BEP-BEM) para representar mejor el impacto de las zonas urbanas y edificios en la meteorología regional. El estudio encontró una relación lineal entre las temperaturas cercanas a la superfície de las zonas urbanas y la fracción urbana, con una relación más estrecha por la noche (-0.18 ± 0.01 ºC por cada 10 % de la superficie convertida de impermeable a permeable). Los resultados indican un menor potencial de la IV a escala metropolitana para regular las temperaturas diurnas en comparación con escalas más pequeñas (calle y barrio). Sin embargo, este análisis no tiene en cuenta el efecto de distintos tipos de IV, el riego de la vegetación ni el impacto en distintas morfologías urbanas.

Para dirigir estas limitaciones, esta tesis presenta un enfoque metodológico para evaluar las compensaciones entre los servicios ecosistémicos en el nexo alimentos-agua-clima derivadas de la aplicación de la IV a escala urbana. Este método es puesto a prueba con la expansión de la peri-UA en el AMB. Este enfoque combina modelos georreferenciados del metabolismo urbano para estimar la producción de alimentos y las necesidades de riego de la IV, con la simulación de la atmósfera local y el balance de carbono biogénico mediante modelos regionales atmosféricos y de la biosfera. Los resultados muestran que el aumento de la peri-UA aumenta la producción local de alimentos (hasta un +85.8 %) pero a su vez aumenta en las necesidades de riego (hasta un +43.5 %). Aunque contribuye a la reducción de la temperatura local con descensos de temperatura de hasta 0.7 ºC durante el mediodía/tarde, su impacto positivo en el enfriamiento del aire es limitado geográficamente y está muy ligado al riego. Además, la expansión de la peri-UA altera el balance regional de carbono, reduciendo la captura de carbono atmosférico hasta en un 18.5 %. Este estudio hace énfasis en la necesidad de evaluar no sólo los efectos directos de la producción local de cultivos en la captura de carbono, incluidos los cambios en el uso del suelo, sino también los efectos indirectos, como los derivados de la sustitución de productos importados y otras emisiones agrícolas. Este enfoque integral es esencial para diseñar soluciones equitativas basadas en la naturaleza que tengan en cuenta tanto el impacto ambiental local como el global.

El impacto de episodios de calor y sequías en la captura de carbono biogénico de los eco-

sistemas del suroeste de Europa
Esta tesis examina los efectos de los episodios de calor y sequías en la captura de carbono en los ecosistemas del suroeste de Europa de 2001 a 2022. Utilizando un modelo de la biosfera adaptado a su aplicación en la región, el modelo Vegetation Photosynthesis and Respiration Model (VPRM), el estudio analizó las tendencias de los flujos de carbono a largo plazo, las influencias climáticas en las anomalías de los flujos de carbono y las variaciones intra-anuales durante episodios extremos de calor y sequía. El estudio revela un aumento de los flujos de fotosíntesis y la respiración, atribuible a la prolongación de los periodos de crecimiento de la vegetación debido a las temperaturas más cálidas. Sin embargo, las tendencias similares entre los dos flujos produce una compensación, dando lugar a un aumento modesto del sumidero neto de carbono 0.80 g C m^{-2} $año^{-2}$, especialmente en los bosques de montaña. Esto sugiere un delicado equilibrio entre el aumento en la captura y la liberación de carbono de los ecosistemas que podría verse alterado por las tendencias actuales de calentamiento y desecación del suelo. Los episodios de calor y sequías también tienen un impacto en la variabilidad interanual del intercambio neto de carbono, lo que supone una amenaza para la estabilidad del crecimiento del sumidero de carbono.

La disponibilidad de agua en el suelo se revela como un factor climático crítico que afecta a la variabilidad del flujo de carbono, sobre todo en zonas no alpinas. El estudio también establece una conexión entre la sequedad climática y el impacto de la sequía en la variabilidad de los flujos de carbono fotosintético y respiratorio, con una influencia mayor en los ecosistemas de clima mediterráneo. Sin embargo, las mayores no linealidades entre la respuesta de la fotosíntesis y la respiración a las sequías, implicando una influencia mayor en el sumidero neto de carbono, se hallan en las regiones húmedas templadas, que representan los mayores sumideros de carbono neto de la región. Estos resultados ponen en relieve la vulnerabilidad del sumidero neto de carbono en el suroeste de Europa a los episodios de sequía. Los episodios excepcionales de calor y sequía de 2003, 2005 y 2022 redujeron significativamente la captura neta de carbono en la región, en un 34.1 %, 22.8 % y 26.9 %, respectivamente, y en algunos casos provocando que los ecosistemas pasaran de ser sumideros de carbono a fuentes debido a una mayor disminución de la fotosíntesis en comparación con la respiración. Los ecosistemas de la región occidental de Europa presentan una respuesta compleja a los episodios de calor y sequía, lo que hace temer por su capacidad para compensar las emisiones antropogénicas de dióxido de carbono si la frecuencia e intensidad de tales episodios sigue aumentando.

Disemination and training

These are the research publications derived from the work on this tesis and related participations:

- **Segura, R.**, Badia, A., Ventura, S., Gilabert, J., Martilli, A., & Villalba, G. (2021). Sensitivity study of PBL schemes and soil initialization using the WRF-BEP-BEM model over a Mediterranean coastal city. Urban Climate, 39, 100982. (doi.org/10.1016/j.uclim.2021.100982)
- **Segura, R.**, Krayenhoff, E. S., Martilli, A., Badia, A., Estruch, C., Ventura, S., & Villalba, G. (2022). How do street trees affect urban temperatures and radiation exchange? Observations and numerical evaluation in a highly compact city. Urban Climate, 46, 101288. (doi.org/10.1016/j.uclim.2022.101288)
- Gilabert, J., Ventura, S., **Segura, R.**, Martilli, A., Badia, A., Llasat, C., Corbera, J., & Villalba, G. (2021). Abating heat waves in a coastal Mediterranean city: What can cool roofs and vegetation contribute? Urban Climate, 37, 100863. (doi.org/10.1016/j.uclim.2021.100863)
- Badia, A., Langemeyer, J., Codina, X., Gilabert, J., Guilera, N., Vidal, V., **Segura, R.**, Vives, M., & Villalba, G. (2021). A take-home message from COVID-19 on urban air pollution reduction through mobility limitations and teleworking. npj Urban Sustainability, 1, 35. (doi.org/10.1038/s42949-021-00037-7)
- Badia, A., Vidal, V., Ventura, S., Curcoll, R., **Segura, R.**, & Villalba, G. (2023). Modelling the impacts of emission changes on O_3 sensitivity, atmospheric oxidation capacity, and pollution transport over the Catalonia region. Atmospheric Chemistry and Physics, 23, 10751-10774. (doi.org/10.5194/acp-23-10751-2023)
- Estruch, C., Belviso, S., Badia, A., Vidal, V., Curcoll, R., Udina, M., Grossi, C., Morguí, J.-A., **Segura, R.**, Ventura, S., Sola, Y., & Villalba, G. (2023). Exploring the influence of land use on the urban carbonyl sulfide budget: A case study of the Metropolitan Area of Barcelona. Journal of Geophysical Research: Atmospheres, 128(24). (doi.org/10.1029/2023JD039497)
- Bazzi, H., Ciais, P., Abbessi, E., Makowski, D., Santaren, D., Ceschia, E., Brut, A., Tallec, T., Buchmann, N., Maier, R., Acosta, M., Loubet, B., Buysse, P., Léonard, J., Bornet, F., Fayad, I., Lian, J., Baghadadi, N., **Segura Barrero, R.**, Brümmer, C., Schmidt, M., Heinesch, B., Mauder, M., Gruenwald, T. (2024). Assimilating Sentinel-2 data in a modified vegetation photosynthesis and respiration model (VPRM) to improve the simulation of croplands CO_2 fluxes in Europe. International Journal of Applied Earth Observation and Geoinformation, 127, 103666. (doi.org/10.1016/j.jag.2024.103666)

- Camacho-Caballero, D., Langemeyer, J., **Segura-Barrero, R.**, Ventura, S., Mendoza Beltran, A., & Villalba, G. (2024). Assessing nature-based solutions in the face of urban vulnerabilities: A multi-criteria decision approach. Sustainable Cities and Society, 103, 105257. (doi.org/10.1016/j.scs.2024.105257)

The results of this thesis have been presented in international conferences:

- **Segura, R.**, Gilabert, J., Ventura, S., Badia, A., Martilli, A., & Villalba, G.: Sensitivity study of PBL schemes and urban morphology parameters using the WRF-BEP-BEM model over a Mediterranean coastal city, EGU General Assembly 2021, online, 19-30 Apr 2021, EGU21-1121. (doi.org/10.5194/egusphere-egu21-1121)

- **Segura, R.**, Krayenhoff, S., Martilli, A., Badia, A., Estruch, C., Ventura, S., & Villalba, G.: Observational and numerical evaluation of the pedestrian-level microclimatic effect of street trees in a highly-compact city, EGU General Assembly 2022, Vienna, Austria, 23-27 May 20222, EGU22-9195. (doi.org/10.5194/egusphere-egu22-9195)

- **Segura, R.**, Estruch, C., Badia, A., Ventura, S., Krayenhoff, E.S., & Villalba, G.: Evaluating the impact of urban parks on the thermal comfort during a heat wave episode in a Mediterranean city, EGU General Assembly 2023, Vienna, Austria, 23-28 Apr 2023, EGU23-1367. (doi.org/10.5194/egusphere-egu23-1367)

- **Segura, R.**, Lauvaux, T., Lian, J., Ciais, P., Badia, A., Ventura, S., Bazzi, H., Abbessi, E., Fu, Z., & Villalba, G.: How extreme heat and drought events affect the Mediterranean biogenic CO_2 atmospheric concentration?, European WRF-Chem Workshop 2023, Lecce, Italy, 9-11 May 2023.

- **Segura, R.**, Langemeyer, J., Badia, A., Ventura, S., Vila-Traver, J., & Villalba, G.: The food-water-climate nexus of green infrastructure: Examining ecosystem services trade-offs of peri-urban agriculture, EGU General Assembly 2024, Vienna, Austria, 14-19 April 2024, EGU24-11400. ()

Publications under preparation:

- **Segura, R.**, Lauvaux, T., Lian, J., Ciais, P., Badia, A., Ventura, S., Bazzi, H., Fu, Z., Abbessi, E., & Villalba, G. Heat and drought events alter biogenic capacity to balance CO2 budget in south-western Europe, submitted to Global Biogeochemical Cycles.

- **Segura, R.**, Langemeyer, J., Badia, A., Ventura, S., Vila-Traver, J., & Villalba, G.: The food-water-climate nexus of green infrastructure: Examining ecosystem services trade-offs of peri-urban agriculture, submitted to Science of The Total Environment.

- **Segura, R.**, Martilli, A., Krayenhoff, S., Badia, A., & Villalba, G. The impacts of street trees on outdoor thermal stress during a heat wave in a highly- compact city, will be submitted to Urban Climate.

Moreover, the author of this thesis did a research stay of 3 months at the Laboratoire des Sciences du Climat et de l'Environnement in France, under the supervision of Dr. Philippe Ciais and Dr. Thomas Lauvaux.

The author has also collaborated as a Master thesis supervisor:

- "Optimization and evaluation of the Vegetation Photosynthesis and Respiration Model (VPRM) parameters for coniferous forests in Northern Europe" by Martha Domhoefer. Supervisors: Villalba, G., & **Segura, R.**. Academic year: 2021-2022.

The author has also imparted scientific seminars:

- **Course "Saps que respires?" in Bojos per la Ciència** about air quality and CO_2 emissions to high school students. Fundació Catalunya la Pedrera. 25/02/2023 and 13/04/2024.
- **Seminar in the Master of Modelling for Science and Engineering** about CO_2 emissions. 03/12/2019 and 24/01/2022.
- **Presentation in the URBAG Stake-holders participatory process, Metropolitan Science-Practitioners Exchange "Eixos Verds a l'Àrea Metropolitana de Barcelona. Co-creació d'una infrastructura verda resilient, sostenible i multifuncional"** 06/05/2021.

Contents

List of Tables **29**

List of Figures **31**

List of Symbols **35**

List of Acronyms **39**

1 Introduction and objective of the thesis **43**
1.1 Objective of the thesis 43
1.2 Introduction 45
1.2.1 Green infrastructure and ecosystem services to address global and local challenges 46
1.2.2 Urban green infrastructure for temperature regulation and other services 46
1.2.3 Atmospheric models to understand the influence of urban green infrastructure 48
1.2.4 Impact of heat and drought events on the carbon capture capacity of regional green infrastructure 51
1.3 Research gaps and research questions 52
1.3.1 How do street trees impact microscale air-cooling and radiation exchange within a highly compact city? 53
1.3.2 How do street trees impact outdoor thermal stress during heat waves in a highly-compact city? 53
1.3.3 What is the role of urban green infrastructure in local temperature regulation in a coastal Mediterranean city? 54
1.3.4 Can the expansion of peri-urban agriculture have measurable effects on local temperature regulation and atmospheric carbon capture? 55
1.3.5 What is the impact of heat and drought events on the biogenic carbon capture of ecosystems in the south-western European region? 55
1.4 Chapters description 58

2 How do street trees affect urban temperatures and radiation exchange? Observations and numerical evaluation in a highly compact city **59**
2.1 Introduction 60

2.2 Methodology . . . 62
2.2.1 BEP-Tree model . . . 62
2.2.2 Study area . . . 64
2.2.3 Observed data . . . 66
2.2.4 Model evaluation . . . 67
2.3 Results . . . 69
2.3.1 Sensitivity analysis to the wind parameterization . . . 69
2.3.2 Surface radiation downwards . . . 72
2.3.3 Road surface and air temperatures . . . 73
2.3.4 Relative humidity and specific humidity . . . 75
2.4 Discussion . . . 77
2.4.1 Sensitivity analysis to the wind parameterization . . . 77
2.4.2 Comparison of observations and BEP-Tree simulations . . . 78
2.5 Summary and Conclusions . . . 83

3 The impacts of street trees on outdoor thermal stress during a heat wave in a highly-compact city 87
3.1 Introduction . . . 88
3.2 Methodology . . . 90
3.2.1 BEP-Tree model . . . 90
3.2.2 Study area and period of study . . . 94
3.2.3 Model simulations . . . 95
3.3 Results . . . 96
3.3.1 Road surface and air temperatures . . . 96
3.3.2 Relative humidity and specific humidity . . . 98
3.3.3 Mean radiant temperature . . . 99
3.3.4 Universal Thermal Climate Index . . . 102
3.4 Discussion . . . 104
3.4.1 The impact of street trees on human thermal stress . . . 104
3.4.2 The impact of heat waves on human thermal stress reduction from street trees . . . 106
3.5 Conclusions . . . 108

4 Sensitivity study of PBL schemes and soil initialization using the WRF-BEP-BEM model over a Mediterranean coastal city 111
4.1 Introduction . . . 112
4.2 Methodology . . . 114
4.2.1 Region of interest and case study . . . 114
4.2.2 WRF implementation . . . 116
4.2.3 Sensitivity studies . . . 119
4.2.4 Observed data . . . 124
4.3 Results and discussion . . . 125
4.3.1 Evaluation of the reference simulation . . . 125
4.3.2 Sensitivity to the initialization of soil properties . . . 128

4.3.3 Senstivity to urban morphology parameters . . . 131
4.3.4 Sensitivity to PBL scheme . . . 133
4.3.5 Sensitivity of the UBL to urbanization . . . 138
4.3.6 Relation between near-surface temperatures and urban fraction . . . 141
4.4 Conclusions . . . 143

5 The food-water-climate nexus of green infrastructure: Examining ecosystem services trade-offs of peri-urban agriculture 147
5.1 Introduction . . . 148
5.2 Case Study . . . 150
5.2.1 Peri-UA scenario development . . . 150
5.3 Methodology . . . 152
5.3.1 Local food provision . . . 152
5.3.2 Irrigation water use . . . 152
5.3.3 Temperature regulation . . . 153
5.3.4 Biogenic carbon balance . . . 154
5.4 Results . . . 155
5.4.1 Spatial comparison of the food-water-climate nexus ecosystem services 155
5.4.2 Seasonal variability in ecosystem services . . . 161
5.4.3 Temporal variability within a hot summer month . . . 164
5.5 Discussion . . . 166
5.5.1 Methodological considerations . . . 167
5.5.2 Ecosystem services trade-offs in the food-water-climate nexus . . . 169
5.5.3 Policy and planning NBS in the context of resilience and environmental justice . . . 172
5.6 Conclusions . . . 173

6 Improving the Vegetation Photosynthesis and Respiration Model for the Southwestern European ecosystems 175
6.1 Introduction . . . 176
6.2 Methodology . . . 178
6.2.1 VPRM parameterization . . . 178
6.2.2 Eddy-Covariance flux tower data . . . 180
6.2.3 Optimisation of the VPRM parameters . . . 182
6.2.4 VPRM at regional scale . . . 184
6.2.5 WRF-Chem model . . . 184
6.2.6 $\mathbf{CO_2}$ atmospheric observations . . . 186
6.3 Results . . . 187
6.3.1 VPRM Performance in front of flux tower data . . . 187
6.3.2 VPRM performance in front of atmospheric $\mathbf{CO_2}$ concentrations observations . . . 192
6.3.3 VPRM ability to represent the 2017 Drought Impact . . . 197
6.4 Discussion . . . 199
6.4.1 Evaluation using flux tower data . . . 199

6.4.2 Evaluation using atmospheric CO_2 concentrations observations 201
6.4.3 Heat and drought impact on the VPRM carbon fluxes 202
6.5 Conclusions 203

7 Heat and drought events alter biogenic capacity to balance CO_2 budget in south-western Europe 205
7.1 Introduction 205
7.2 Materials and methods 208
7.2.1 Study area 208
7.2.2 VPRM model 208
7.2.3 Climate and remotely sensed data 209
7.2.4 Statistical analysis 210
7.3 Results 211
7.3.1 Trends of south-western Europe biogenic carbon fluxes 211
7.3.2 Interannual variability of the biogenic carbon fluxes 214
7.3.3 Intra-annual variability of the biogenic carbon fluxes 219
7.4 Discussion 221
7.4.1 Long-term trends of the biogenic carbon fluxes 221
7.4.2 Heat and drought events control the interannual variability of the fluxes 222
7.4.3 Warm spring do not compensate the decreasing effect of droughts on CO_2 fluxes 224
7.4.4 VPRM modifications improve the response of the fluxes to heat and drought 225
7.5 Conclusions 226

8 Conclusions and further research 229
8.1 Conclusions 229
8.2 Future research 233
8.2.1 Street and neighbourhood scales 234
8.2.2 Metropolitan scale 235
8.2.3 Regional scale 236

Bibliography 239

Appendix 281
A Supporting information for Chapter 2 281
A.1 Measurement set up 281
A.2 Manual segmentation of fisheye lens photographs 282
A.3 Urban canopy parameters 283
A.4 Sensitivity analysis to the potential temperature forcing 283
A.5 Comparison of the surface energy fluxes between the default and the new turbulent wind speed parameterization 285
A.6 Comparison of specific humidity between BEP-Tree and observations . 286
B Supporting information for Chapter 3 287

C Supporting information for Chapter 4 . . . 292
C.1 Synoptic analysis and the study case: heat wave July 2015 . . . 292
C.2 High Resolution Land Data Assimilation System simulations . . . 297
C.3 Urban canopy parameters . . . 299
C.4 Metadata of weather stations and validation statistics . . . 301
C.5 Additional Results . . . 303
C.6 Relation between near-surface temperatures and urban fraction . . . 309
D Supporting information for Chapter 5 . . . 310
D.1 Land-use/Land-cover maps development . . . 310
D.2 Agriculture irrigation water use estimation . . . 311
D.3 Additional WRF modifications . . . 311
D.4 Evaluation of the reference scenario and sensitivity to the PBL scheme 312
D.5 Additional VPRM modifications . . . 316
D.6 Evaluation of the reference scenario for the year-long WRF simulation 317
D.7 Additional results . . . 320
E Supporting information for Chapter 6 . . . 326
F Supporting information for Chapter 7 . . . 332

List of Tables

1.1 Main objective, research questions, subobjectives and outline of this Ph.D. thesis. 57

2.1 Mean view factors measured from upper-hemisphere fisheye photos and computed by the BEP-Tree model for the two streets. 67

4.1 WRF Model characteristics and experiment configurations. 117
4.2 Simulations design for the different WRF-BEP-BEM model sensitivities performed in this study. The reference simulation (BL-UM) is highlighted in bold. 119

5.1 Peri-UA surface and food provision in the land-use planning scenarios in the AMB. 156

6.1 WRF-Chem model physics parameterizations schemes. 186
6.2 Atmospheric stations selected in this study. 187

List of Figures

1.1 Conceptual diagram of the relationships between climate change, ecosystems, and human adaptation strategies. 44
1.2 Case studies of this Ph.D. thesis: south-western Europe, the Metropolitan Area of Barcelona, and the Eixample District in Barcelona. 44
1.3 Scheme of the urban boundary layer (UBL) and the vertical layers it includes and spatial scales. 50

2.1 (a) Administrative boundaries of Barcelona city; (b) detail of the region of study in the Eixample neighborhood with the two studied streets: Sparsely_treed (blue) and Densely_treed (green). 65
2.2 Comparison of the modelled road surface temperatures and air temperatures between the default BEP-Tree, the BEP-Tree with the buoyancy driven wind speed and observations. 71
2.3 Comparison of the vertical profiles of potential temperature and turbulent kinetic energy modelled with the default BEP-Tree and the BEP-Tree with the buoyancy driven wind speed. 71
2.4 Comparison of the modelled shortwave and longwave radiation downwards by BEP-Tree and the observations in Densely_treed and Sparsely_treed. 73
2.5 Comparison of the modelled road surface temperatures and air temperatures by BEP-Tree and the observations in Densely_treed and Sparsely_treed. 75
2.6 Comparison of the modelled specific and relative air humidities by BEP-Tree and the observations in Densely_treed and Sparsely_treed. 77
2.7 Windrose in percentage (%) of the two days of campaign during the central hours of the day measured at the Raval meteorological station. The streets studied are oriented from NW to SE. 81

3.1 Schematic diagram of the methodology used for the creation of the UTCI distribution. 92
3.2 BEP-Tree modelled diurnal cycles and midday/mid-afternoon averages in the study period of the canyon-averaged road surface temperatures, and air temperatures for the Sparse trees and Dense trees neighborhoods with moist soil and dry soil. 97

3.3 BEP-Tree modelled vertically averaged tree latent heat flux (a) for the Sparse trees and Dense trees neighborhoods with moist soil and dry soil, and (b) $F2$ coefficient of the soil moisture impact on stomatal conductance. 98
3.4 BEP-Tree modelled diurnal cycles and midday/mid-afternoon (between 9-15 UTC, 11-17 LT) averages in the study period of the air specific humidity , and relative humidity for the Sparse trees and Dense trees neighborhoods with moist soil and dry soil. 99
3.5 BEP-Tree modelled diurnal cycles of the mean radiant temperature (a) in the locations outside tree crown projections and moist soil, (b) the locations outside tree crown projections and dry soils, (c) the locations under tree crowns and moist soils, and (d) the locations under tree crowns and dry soils for the Sparse trees and Dense trees neighborhoods. 101
3.6 BEP-Tree modelled midday/mid-afternoon averages in the study period of the T_{MRT} (a) in the locations outside tree crown projections and moist soil, (b) the locations outside tree crown projections and dry soils, (c) the locations under tree crowns and moist soils, and (d) the locations under tree crowns and dry soils for the Sparse trees and Dense trees neighborhoods. 102
3.7 Average diurnal cycles for the UTCI for the comparison between Sparse trees and Dense trees neighbourhoods (a) under moist soil, (b) under dry soils, for the 10^{th}, 50^{th}, and 90^{th} percentiles. 103
3.8 Average midday/mid-afternoon (between 9-15 UTC, 11-17 LT) UTCI for the comparison between Sparse trees and Dense trees neighbourhoods (a) under moist soil, (b) under dry soils, (c) difference between Sparse trees and Dense trees with moist soil, (d) difference with dry soil, for the 10^{th}, 50^{th}, and 90^{th} percentiles. 104

4.1 (a) Domains of the WRF model for this study with 9, 3 and 1km grid size for d01, d02 and d03, respectively. (b) Detail of the domain 3 with a terrain height map and the political boundaries of the AMB and Barcelona city. 116
4.2 a) Land-use classification for the innermost domain d03, from the interpolation of LCZ and CLC with the red box defining the borders of the ROI; b) Histogram of land-use classes inside the ROI. 118
4.3 Comparison of WRF model initialization at 00 UTC on 24 June 2015 in the first soil layer for a) soil temperature with HRLDAS; b) soil temperature with ERA5; c) difference in soil temperature; d) soil moisture with HRLDAS; e) soil moisture with ERA5; f) difference in soil moisture. 121
4.4 Comparison of WRF model initialization at 00 UTC on 24 June 2015 in the second soil layer for the a) soil temperature with HRLDAS; b) soil temperature with ERA5; c) difference in soil temperature ; d) soil moisture with HRLDAS; e) soil moisture with ERA5; f) difference in soil moisture. 121
4.5 Temperature analysis for the performance of WRF simulations. Root mean square error, Mean bias and correlation coefficient at daytime and night-time for each simulation and LULC group of stations. 126

4.6 Wind speed analysis for the performance of WRF simulations. Root mean square error, Mean bias and correlation coefficient at daytime and night-time for each simulation and LULC group of stations. 127
4.7 Model comparison of T_{2m} and 10 m wind vectors averaged at daytime and night-time, for (a, d) BL-UM-HRL; (b, e) BL-UM; (c, f) difference BL-UM-HRL – BL-UM. 129
4.8 Model comparison of T_{2m} and 10 m wind vectors averaged at daytime and night-time, for (a, d) BL-noUM; (b, e) BL-UM; (c, f) difference BL-noUM – BL-UM. 132
4.9 Model comparison of T_{2m} and 10 m wind vectors averaged at daytime and night-time, for (a, d) MYJ-UM; (b, e) BL-UM; (c, f) difference MYJ-UM – BL-UM. 134
4.10 Time series of diagnosed PBL height at the radiosounding site by BL-UM and MYJ-UM simulations and the computed PBL height from radiosounding observations represented with black dots. 136
4.11 Comparison of vertical profiles of WRF model simulated potential temperature and wind speed and radiosonde observations from the launches at 12 UTC at the days 4 July 2015 (a, d), 5 July 2015 (b, e) and 6 July 2015 (c, f). 138
4.12 Vertical cross-section of potential temperature overlaid by wind vectors on 4 July 2015, for (a) BL-UM during day, (b) BL-crop during day , (c) BL-UM during night, (d) BL-crop during night. 140
4.13 Relation between urban fractions (λ_u) and the simulated mean 2 m temperatures (T_{2m}) in the daytime (a) and night-time (b) during the period of study. 142

5.1 (a) LULC maps at 100 m resolution within the D04 domain for scenarios S0, S1, S2 and S3. (b) Histogram showing the total land-use extent in the AMB land-cover type. (c) Changes in land-cover extent compared to S0. 151
5.2 (a) Domains of the WRF model for this study with 9 km, 3 km, 1 km and 333.3 m grid size for D01, D02, D03 and D04, respectively. (b) Detail of the domain 4 with an elevation map and the political boundaries of the AMB and the city of Barcelona. 153
5.3 Comparison of the ecosystem services indicators for the current scenario for the year 2015. (a) Food provision; (b) Irrigation water use; (c) Summer daily evapotranspiration; (d) Summer midday/afternoon air temperature; (e) Net ecosystem productivity; and (f) Carbon stocks. 157
5.4 Comparison between the LULC scenarios for (a) total food provision in 2015; (b) total irrigation water use in 2015; (c) median summer midday/afternoon air temperature; (d) Net ecosystem productivity in 2015; and (e) Carbon stocks for the AMB. 158
5.5 Comparison of the ecosystem services indicators differences between the LULC scenarios S1, S2 and S3 and the current scenario for the year 2015. 160

5.6 (a) Monthly irrigation amounts over the Metropolitan Area of Barcelona over the year 2015 for the four LULC scenarios; (b) Average monthly temperatures and monthly precipitation for the city of Barcelona over the year 2015, and the climatic mean (1980-2010) for the monthly temperatures and precipitation. . . 162
5.7 (a) Monthly total net ecosystem productivity by the AMB GI for the four LULC scenarios in the year 2015. (b) Difference of the net ecosystem productivity with respect to the scenario S0. 164
5.8 Time-series of the ecosystem services indicators simulated during the study period between June 25 and July 24, 2015 for the four LULC scenarios (a, c, e) and the difference with respect to S0 (b, d, f), for: (a,b) Daily evapotranspiration; (c, d) midday and mid-afternoon average temperature; (e, f) net ecosystem productivity. 166

6.1 Land cover classification and eddy-covariance flux towers. 181
6.2 WRF-Chem domain and the location of the Drought 2018 dataset atmospheric CO_2 stations. 185
6.3 Heatmap of RMSE for VPRM versions. 188
6.4 Heatmap of r^2 for VPRM versions. 188
6.5 Decomposed mean squared deviation comparison. 189
6.6 Seasonal cycles of monthly fluxes. 191
6.7 Time-series of mid-afternoon CO_2 concentrations. 193
6.8 Time-series of mid-afternoon decomposed CO_2 concentrations for OHP. 194
6.9 Spatial distribution of monthly aggregated NEE. 195
6.10 Heatmap of RSME and r^2 for modelled CO_2 concentrations. 197
6.11 Weekly GEE and CO_2 during the year 2017. 199

7.1 Biogeographical regions. 208
7.2 Longterm carbon flux trends. 212
7.3 Long-term carbon flux trends by PFT. 213
7.4 Time-series of annual anomalies over the study area. 214
7.5 Interannual drivers of carbon flux anomalies. 216
7.6 Correlogram between SPEI and GEE anomalies. 218
7.7 Correlogram between SPEI and NEE anomalies. 219
7.8 Intra-annual impact of heat and droughts. 221

List of Symbols

C_d Volumetric specific heat of dry soil.

C_p Latent heat of vaporization.

C_s Volumetric specific heat.

C_w Volumetric specific heat of water.

D_η Soil moisture diffusivity.

E_0 Activation energy parameter for the sensitivity of R_{ECO} to air temperature.

F_4 Soil moisture coefficient for the stomatal conductance.

K_η Hydraulic conductivity of soil.

K_f Hydraulic conductivity of soil at saturation.

K_i Directional shortwave radiation flux.

K_{bs} Foliage extinction coefficient.

LAI_{can} Street-canyon average leaf area index.

LAI_{tree} Tree crown space-average leaf area index.

$LSWI_{max}$ Maximum daily LSWI in the growing season.

L_D Leaf area density.

L_i Directional longwave radiation flux.

PAR Photosynthetically active radiation.

PAR_0 Half-saturation photosynthetically active radiation factor.

P_{scale} Phenology stress scaling factor.

R_0 Abiotic ecosystem respiration.

SH Sensible heat flux.

SM_{scale} Soil moisture stress scaling factor.

SW Downwelling short-wave radiation.

SW_0 Half-saturation shortwave radiation factor.

T Air temperature.

T_{2m} 2 m air temperature.

T_{low} Low temperature threshold.

T_{max} Maximum air temperature for photosynthesis.

T_{min} Minimum air temperature for photosynthesis.

T_{opt} Optimum air temperature for photosynthesis.

T_{scale} Temperature stress scaling factor.

U_{70} Wind speed at 70 m height.

U_s Wind speed.

W_{scale} Soil water stress scaling factor.

Δs 2-D ray step size.

Ω Foliage clumping factor.

Ψ_η Soil moisture potential.

Ψ_f Soil moisture potential at saturation.

α Linear sensitivity of respiration to air temperature factor.

α_k Adjustment parameter to the potential temperature.

β Baseline respiration.

η Soil moisture content/fraction.

η^* Soil moisture threshold.

η_f Soil moisture at saturation.

γ Response of ecosystem respiration to null θ.

λ Light-use efficiency factor.

λ_s Thermal diffusivity.

λ_u Urban fraction.

λ_{SW} Light-use efficiency factor for shortwave radiation.

$\lambda_{v,can}$ Fraction of plan area coverage of tree crowns inside the street canyon.

WS_{10m} 10 m wind speed.

λ_p Building-to-plan area fraction.

ρ_a Density of liquid water.

σ Stefan-Boltzmann constant.

θ Potential temperature.

θ_0 Reference potential temperature.

θ_v Virtual potential temperature.

φ Plant functional type plan area fraction.

a_L Coefficient of absorption of longwave radiation flux of human body.

a_k Coefficient of absorption of shortwave radiation flux of human body.

f_i Ratio of 3-D to 2-D distance travelled by the ray.

g Gravity acceleration.

$g_{vs,max}$ Maximum stomatal conductance.

g_{vs} Stomatal conductance.

k_1 Sensitivity of ecosystem respiration to GEE.

k_2 Sensitivity of ecosystem respiration to soil moisture.

q Sensitivity of the soil moisture stress factor.

r Correlation coefficient.

$w^\star$ Buoyancy driven turbulent wind velocity.

ws Mean wind speed.

z_0 Roughness length.

z_d Zero-plane displacement height.

z_m Mean building height.

List of Acronyms

CH_4 Methane.

CO_2 Carbon Dioxide.

NH_3 Ammonia.

R_{ECO} Ecosystem Respiration.

T_{MRT} Mean Radiant Temperature.

A/C Air conditioning.

AA Agricultural areas.

AMB Metropolitan Area of Barcelona.

BEM Building Energy Model.

BEP Building Effect and Parameterization.

BEP-Tree Building Effect Parameterization with Trees.

BouLac Bougeault-Lacarrere.

BVF Building View Factor.

CAMS Copernicus Atmosphere Monitoring Service.

CLC Corine Land Cover.

CRO Cropland.

CRO_S Summer croplands.

CRO_W Winter croplands.

DF Deciduous Forest.

EF Evergreen Forest.

EVI Enhanced Vegetation Index.

F&SNA Forest and seminatural areas.

FAO Food and Agriculture Organization.

FCOVER Green vegetation cover.

GEE Gross Ecosystem Exchange.

GHG Greenhouse Gas.

GI Green Infrastructure.

GOSIF Global Orbiting Carbon Observatory-2 SIF product.

GRA Grassland.

GREENFRAC Green vegetation fraction.

H/W Building height to street width ratio.

HRLDAS High-Resolution Land Data Assimilation System.

HW Heat Wave.

ICGC Catalan Institute of Geography and Cartography.

ICOS Integrated Carbon Observation System.

LAI Leaf Area Index.

LCS Lack of Correlations.

LCZ Local Climate Zone.

LES Large-Eddy Simulations.

LSWI Land Surface Water Index.

LT Local Time.

LULC Land-use/land-cover.

MB Mean Bias.

MF Mixed Forest.

MSD Mean Squared Deviation.

MYJ Mellor-Yamada-Janjic.

NAVUA Non-agricultural vegetated urban areas.

NBS Nature-Based Solutions.

NEE Net Ecosystem Exchange.

PBL Planetary Boundary Layer.

peri-UA Peri-urban Agriculture.

PET Potential Evapotranspiration.

PFT Plant Functional Types.

RMSE Root-Mean-Square Error.

ROI Region of Interest.

SAV Mediterranean Savanna.

SB Squared Bias.

SDSD Squared Differnce between Standard Deviations.

SHDFAC Vegetation plan area fraction.

SHR Shrubland.

SIF Sun-induced Clorophyll Fluorescence.

SM2 Soil Moisture between 7 to 28 cm depth.

SMC Catalan Meteorological Service.

SPEI Standard Precipitation Evaporation Index.

SSRD Surface Solar Radiation Downwards.

SVF Sky View Factor.

SYNMAP Synergetic Land Cover Product.

T2M 2 m Air Temperature.

TKE Turbulent Kinetic Energy.

UBL Urban Boudary Layer.

UCL Urban Canopy Layer.

UCM Urban Canopy Model.

UF&NVUA Urban fabric and non-vegetated urban areas.

UHI Urban Heat Island.

UTC Universal Time Coordinated.

UTCI Universal Thermal Climate Index.

VPRM Vegetation Photosynthesis and Respiration Model.

VVF Vegetation View Factor.

WB Water bodies.

WRF Weather Research and Forecasting.

WRF-Chem Weather Research and Forecasting with Chemistry.

WUDAPT World Urban Database and Access Portal Tools.

Chapter 1

Introduction and objective of the thesis

1.1 Objective of the thesis

The main objective of this Ph.D. thesis is to determine the capacity of the green infrastructures to provide temperature regulation and atmospheric carbon capture under the influence of heat and drought at the street/neighbourhood, city, and regional scales (see Figure 1.1). Green infrastructure implementation in urban areas has been proposed as a nature-based solution for the adaptation of these areas to the impacts of climate change effects as the increase of heat waves, while also contributing to the mitigation of the climate change by their capacity to capture atmospheric carbon. Green infrastrutucture implementation draws upon knowledge of ecosystem services, which represent the direct and indirect benefits for human population derived from ecosystems (i.e. green infrastructures), such as temperature regulation and atmospheric carbon capture. However, the impacts of climate change as heat waves and droughts puts pressure on the ecosystems, compromising their capacity to provide these ecosystem services.

This thesis focuses on three case studies corresponding to different spatial levels: the Eixample district of Barcelona at the street and neighbourhood scales, the city of Barcelona and its metropolitan region at the city and metropolitan region scales, and south-western Europe at the regional scales (see Figure 1.2). By investigating the capacity of green infrastructure to regulate local temperature and capture atmospheric carbon and understanding how are affected by heat and drought events at these specific scales, this research seeks to contribute valuable insights that can inform more sustainable and resilient urban planning and ecosystem management practices in the face of a changing climate in the Mediterranean context.

This Ph.D. thesis is embedded in the European Research Council (ERC) Consolidator project: Integrated System Analysis of Urban Vegetation and Agriculture (818002-URBAG). The project URBAG aims to determine to what extent green infrastructures can be effective in contributing to make cities more resilient to climate change and more sustainable in terms of water management, food production, air quality, human well-being, and biodiversity. This project aims to develop an integrated, spatially resolved framework for quantifying food-water-energy interactions and quantitative analysis and simulation of green infrastructure.

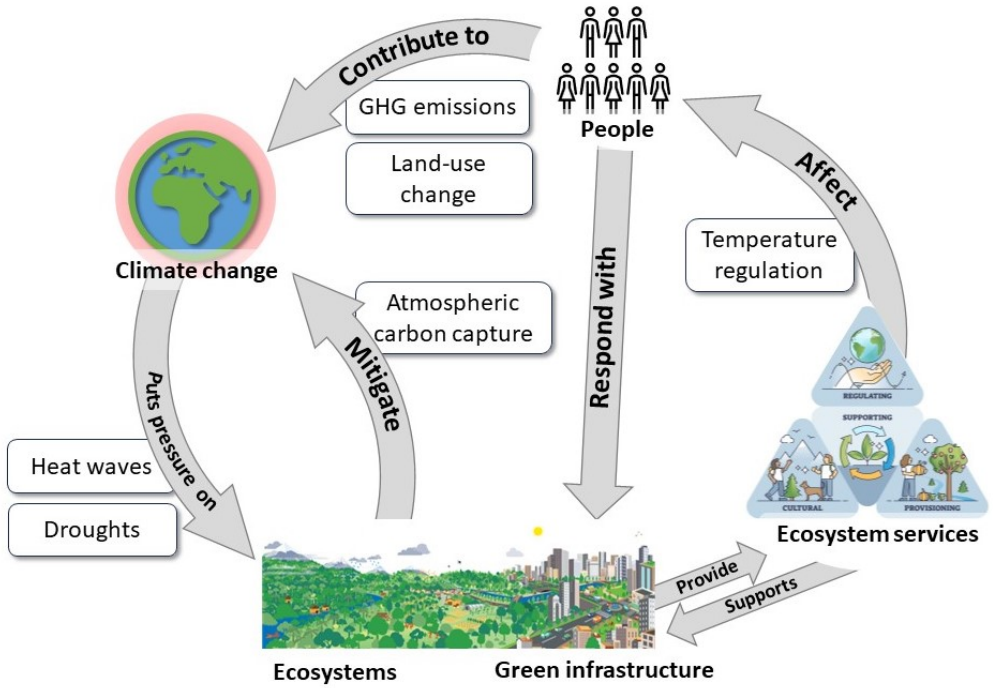


Figure 1.1: Diagram of the relationships between climate change, ecosystems, and green infrastructure.

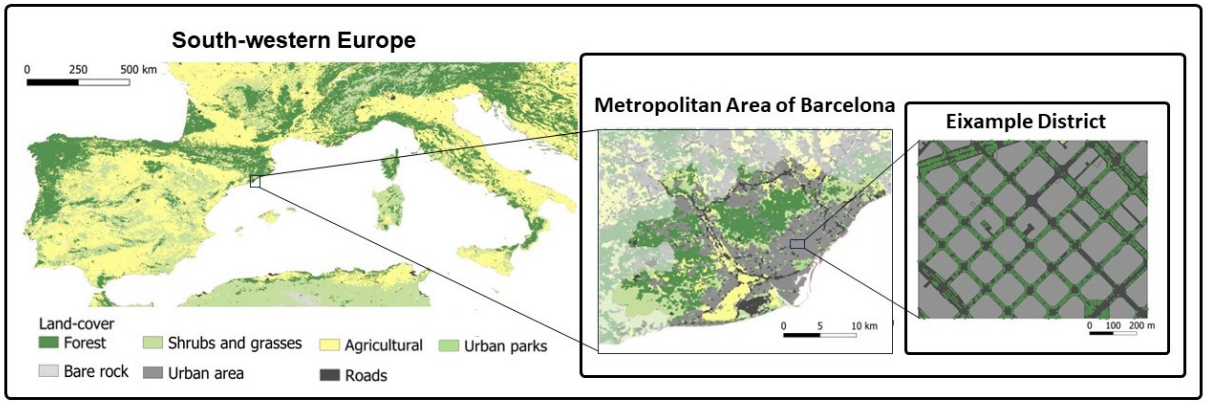


Figure 1.2: Case studies of this Ph.D. thesis: south-western Europe, the Metropolitan Area of Barcelona, and the Eixample District in Barcelona.

1.2 Introduction

Global climate change and the increasing urbanization pose significant challenges in our strive to achieve the Sustainable Development Goals of the United Nations 2030 Agenda (United Nations, 2019). These challenges are far from being independent but are interconnected. Human-induced global climate change, stemming from activities like greenhouse gas emissions and land use changes, poses risks for both urban areas and the natural environment (Calvin et al., 2023). The rise in global atmospheric and sea temperatures contributes to more frequent and intense extreme events, such as heat waves (HWs), droughts, heavy precipitation, and rising sea levels (IPCC, 2014). Simultaneously, the global urban population is growing, with over half currently residing in urban areas (55 %), projected to increase to 68 % by mid-century (United Nations, 2019). Much of this growth occurs in vulnerable regions, like low-altitude coastal cities and arid regions (Balk et al., 2013; Danan et al., 2015). Additionally, urban and suburban areas are primarily shaped by human activities, significantly contributing to pollutant and greenhouse gas emissions. The combustion of fossil fuels for transportation, energy production, and other human-driven activities leads to high emissions. Urban areas are major contributors to the increase of atmospheric greenhouse gas concentrations, accounting for 71-76 % of global carbon dioxide (CO_2) emissions and 67-76 % of global energy use (IPCC, 2015). Local and regional governments should prioritise achieving more resilient, sustainable, and healthy cities and their metropolitan regions, as it is englobed in the 11th objective of the Sustainable Development Goals of the United Nations, to minimize the impacts of climate change.

In this context, nature-based solutions (NBS) are key strategies for addressing these challenges and refer to "actions to protect, sustainably manage, and restore natural and modified ecosystems that address societal challenges effectively and adaptively, simultaneously benefiting people and nature" according to the United Nations (United Nations Environment Programme, 2022). This concept aligns with the broader framework of green infrastructure (GI) (Langemeyer and Baró, 2021), which entails a network of natural and semi-natural areas strategically designed and managed to enhance biodiversity and to provide a wide range of ecosystem services (European Commission, 2013). The NBS-GI network comprises elements such as urban parks, forests, shrublands, street trees, green roofs, agricultural areas, green corridors, and wetlands (Naumann et al., 2011), emphasizing on the quality and quantity of green spaces, their multifunctional role, and their interconnexions. The next sections will address the ecosystem services provided by these green infrastructures and how these services can be addressed to deal with environmental challenges at different spatial scales, emphasizing in the regulation of temperature and other ecosystem services at the urban scale. A brief description of atmospheric models is provided, which are used to simulate the effect of green infrastructure on the ecosystem services. While subsection 1.2.4. is dedicated to describing the effect of heat and drought on green infrastructure at the various spatial scales.

1.2.1 Green infrastructure and ecosystem services to address global and local challenges

Ecosystem services are defined as the direct and indirect contributions of ecosystems to human well-being and have an impact on our survival and quality of life (TEEB, 2011). Ecosystem services fall into four major categories (Millenium Ecosystem Assessment, 2005): provisioning services (extractable benefits from nature); regulating services (moderation of natural phenomena); cultural services (non-material contributions to human development); and supporting services (sustaining ecosystem process like photosynthesis, soil formation, nutrient, and water cycles). Effective planning and management of NBS-GI require a holistic, multiscale approach, considering synergies and trade-offs among different ecosystem services and the relevant territorial scales (Cortinovis and Geneletti, 2018; Baró and Maestre-Andrés, 2022).

NBS-GI has been suggested as a key strategy in the mitigation and adaptation of urban areas to climate change (Demuzere et al., 2014; EEA, 2015), while also being able to deal with some of the environmental hazards associated with urban areas itself (Marando et al., 2022). Moreover, it has been assessed its benefits in improving public health, promoting social cohesion, and providing with other beneficial services (Baró et al., 2019). However, land planification should not only consider the benefits of the ecosystem services derived from the NBS-GI planned to face the impacts of climate change and the increased urbanization, but also protect the ecosystems of the effects of a changing climate, minimizing the impacts on the environment from land-use changes and preserving the provision of important ecosystem services (Reidmiller et al., 2018). For this purpose, it is important to understand the effect of NBS-GI on climate, the spatial and temporal variations of the provision of ecosystem services and the impact of climate change on the ecosystems and their capacity to provide of ecosystem services. These aspects must be analysed at spatial scales relevant to the scope of the ecosystem services and NBS-GI strategies. The European Environment Agency (EEA, 2011) makes a distinction between GI on an urban scale and on a landscape scale (regional, national, or continental), involving distinct land elements and governed by specific managements procedures tailored to their respective scopes.

1.2.2 Urban green infrastructure for temperature regulation and other services

Urban green infrastructure consists of green spaces, corridors, urban parks, tree canopies, green roofs, and green walls, among other infrastructure, whose spatial scale ranges from street to city-wide scale and whose ecosystem services have a direct impact on city dwellers, providing of a great opportunity to contribute to human well-being. One of the most important services provided by urban GI is the regulation of local temperatures, as urban GI has been identified as potential solution to adapt cities to the impacts of increasing heat events and to mitigate health risks related urban heat (Demuzere et al., 2014).

Historically, urban climate studies focused on the urban heat island (UHI) phenomenon (Oke, 1982; Moreno-garcia, 1994; Arnfield, 2003), where cities exhibit higher temperature than their rural surroundings, particularly during calm-wind days and nights. UHI effect is attributed to the

high heat retention and absorption of construction materials, the geometry of the urban canyons, the reduced evapotranspiration due to a lack of vegetation, and heat emissions from human activities (Oke, 1982; Grimmond, 2007). Moreover, climate change supposes an additional challenge to the abatement of heat in urban areas as global warming is projected to widen temperature disparities between urban and rural areas (McCarthy et al., 2010; IPCC, 2014), rendering urban populations more susceptible to heat stress and related heat diseases (Ingole et al., 2020). Non-linear interactions between HWs and UHIs intensify heat stress (Li and Bou-Zeid, 2013), posing challenges for energy, water systems, and resilience of urban infrastructures and ecosystems (Hunt and Watkiss, 2011). For example, elevated temperatures have significant indirect consequences, such as heightened energy consumption due to increased air conditioning (A/C) usage, thereby exacerbating the retention of heat in the canyons (Tan et al., 2010).

The implementation of urban GI can help cities adapt to combined UHI and HWs effects (Demuzere et al., 2014). The literature extensively examines how urban GI regulates urban temperatures (Bowler et al., 2010; Oliveira et al., 2011; Zhang et al., 2013; Krayenhoff et al., 2021), evidencing the associated reduction of air and surface temperatures at different scales in the city (Oke, 1989; Shiflett et al., 2017). At city and neighbourhood scale, extensive vegetated areas alter energy exchange between the surface and the atmosphere due to the evapotranspiration, resulting in cooled air around the vegetation and a thermal reduction in the adjacent urban areas (Grimmond and Oke, 1991; Grimmond et al., 1996). On a microscale, trees offer shade to nearby built surfaces and pedestrians, altering the biometeorological conditions they encounter and enhancing thermal comfort (Coutts et al., 2016; Middel and Krayenhoff, 2019). The cooling effect of urban green spaces on the urban temperatures have been well studied (Fallmann et al., 2013; Demuzere et al., 2014; Feyisa et al., 2014; Yu et al., 2018) for different vegetation types, park sizes, city climates and urban morphologies (Bowler et al., 2010; Gago et al., 2013). Urban parks reduce on average air temperatures during the day by 0.94 °C (95 % CI = 0.71–1.16) based on a meta-analysis of 16 observational studies (Bowler et al., 2010). The provision of temperature regulation effect depends also on multiple characteristics and structural properties of the urban ecosystems itself. For instance, urban trees have a higher importance in the provision of evapotranspiration and shade than other kinds of vegetation, such as shrubs and herbaceous plants (Baró and Maestre-Andrés, 2022). For this reason, possible trade-offs arise when different types of ecosystem services, especially of different ecosystem services categories (provisioning, regulating, cultural and supporting ecosystem services), are contemplated and seek as part of the NBS-GI strategies.

For instance, peri-urban agriculture (peri-UA) is a strategy aiming to provide locally grown crops, offering a multifunctional NBS to promote circular economies, social cohesion, biodiversity preservation, and reduced environmental impacts within the food supply chain (Piorr et al., 2018). Local food production can also deal with some other issues that the food industry suffers nowadays such as food quality, transparency, traceability, security, regional production, organic and ecologic production, sovereignty, short food supply chains, between others (Piorr et al., 2018). Notably, irrigated peri-UA has been found to reduce regional temperatures during the dry season by 4-8 °C compared to urban environments and natural dry vegetation, effectively

creating a cooling effect for urban areas (Kueppers and Snyder, 2012). However, the development of peri-UA often displaces other natural land uses that provide crucial ecosystem services, including biodiversity conservation, carbon sequestration and other supporting services (Tilman, 1999). Agricultural practices, including the use of mineral fertilizers and biomass burning, contribute negatively to net greenhouse gas emissions in agricultural areas (Power, 2010), while higher temperature and conventional agricultural practices reduce soil organic carbon in agricultural land (Aguilera et al., 2018). Overall, the impact of increasing peri-UA on net carbon capture remains uncertain. Similarly, the irrigation demands of peri-UA need a stronger attention. Peri-UA can lead to significant water usage, potentially impacting the water balance in dry regions, especially under future drier climates such as the Mediterranean region (Gao and Giorgi, 2008; Giorgi and Lionello, 2008).

Local, metropolitan, and regional administrations are increasingly incorporating ecosystem services, as temperature regulation, into urban planning and policies, especially in the designing and implementation of GI, to support the decision making and produce more sustainable land-use decisions (Cortinovis and Geneletti, 2018). The city of Barcelona and its metropolitan area exemplify this, with various administrative entities promoting green infrastructure in their policies and urban planning. Barcelona's city hall, for instance, implemented the Nature Plan 2021-2030, focused on developing a GI capable of providing ecosystem services, naturalizing the city, and connecting it with the surrounding territory. Additionally, the local government's Climate Plan 2018-2030 emphasizes adaptation and mitigation efforts against climate change. On the metropolitan scale, the Metropolitan Urban Master Plan by the Metropolitan Area of Barcelona (AMB) aims to enhance ecological connectivity, naturalize the territory, and improve urban metabolism, minimizing environmental impacts and enhancing ecosystem services provided by the GI, as well as contemplating and increase in the peri-UA (Padró et al., 2020). Designing and implementing GI strategies aimed to adapt cities to heat events and mitigate climate change requires tools with robust scientific evidence. This entails atmospheric models capable of fine spatial resolutions, representing surface energy flux partitioning, evolution of rural and urban boundary layers, and temporal and spatial distribution of near-surface temperatures across entire metropolitan areas.

1.2.3 Atmospheric models to understand the influence of urban green infrastructure

The urban atmosphere is influenced by meteorological features occurring at different spatial scales, from mesoscale phenomena like sea-land breezes to local features at city, neighbourhood, and street levels, such as turbulent eddies (Santiago and Martilli, 2010). Vertically, the urban atmosphere is divided into layers across different spatial scales (see Figure 1.3). At the mesoscale (Figure 1.3a), the planetary boundary layer (PBL) is the atmospheric layer in direct contact with the Earth's surface, influenced by surface heating and roughness (Oke et al., 2017). In large urban areas, the part of the atmosphere with a direct influence of the city is called urban boundary layer (UBL). Downwind at the urban-rural border, the city's effects create an urban

plume in the PBL, transporting air pollutants hundreds of kilometres downwind. The surface layer, encompassing the lowest 10 % of the PBL, is marked by a highly heterogeneous flow due to surface friction. On a local scale (Figure 1.3b), the surface layer comprises two sublayers: the inertial sublayer, reflecting integrated effects of neighbourhoods, presenting high spatial homogeneity over homogenous neighbourhoods; and the roughness sublayer, resulting in high horizontal and vertical variations of the momentum, heat, and moisture. The roughness sublayer typically extends from the ground to 1.5-3 times the height of urban elements. At the microscale (Figure 1.3c), the lowest part of the roughness sublayer is the urban canopy layer (UCL) (Oke, 1976), spanning from the ground to the mean height of building/trees, where most human activities occur.

In order to integrate urban phenomena occurring at local and larger scales, atmospheric regional models such as the Weather Research and Forecasting (WRF) model (Skamarock et al., 2021), working at mesoscale, have been coupled with Urban Canopy Models (UCM), that represent the effect of buildings and streets at local scale (Kusaka et al., 2001; Martilli et al., 2002; Salamanca and Martilli, 2010). UCMs help to represent the surface heterogeneities in urban environments induced by the urban morphology. The Building Effect and Parameterization (BEP) and Building Energy Model (BEM) (Martilli et al., 2002; Martilli, 2003; Salamanca and Martilli, 2010; Brousse et al., 2016; Ribeiro et al., 2021) is a multi-layer scheme that not only considers the effect of buildings on the vertical distribution of heat, momentum and turbulence fluxes, but also takes into account radiative effects (trapping or shadow effects), energy consumption of buildings and anthropogenic heat released by A/C systems. Recently, the modelling capabilities of BEP-BEM have increased due to the incorporation of highly resolved urban land-use classifications (Gilabert et al., 2021b) and the improvement of the urban canopy parameters from considering high-resolution urban morphology data (Zonato et al., 2020; Segura et al., 2021).

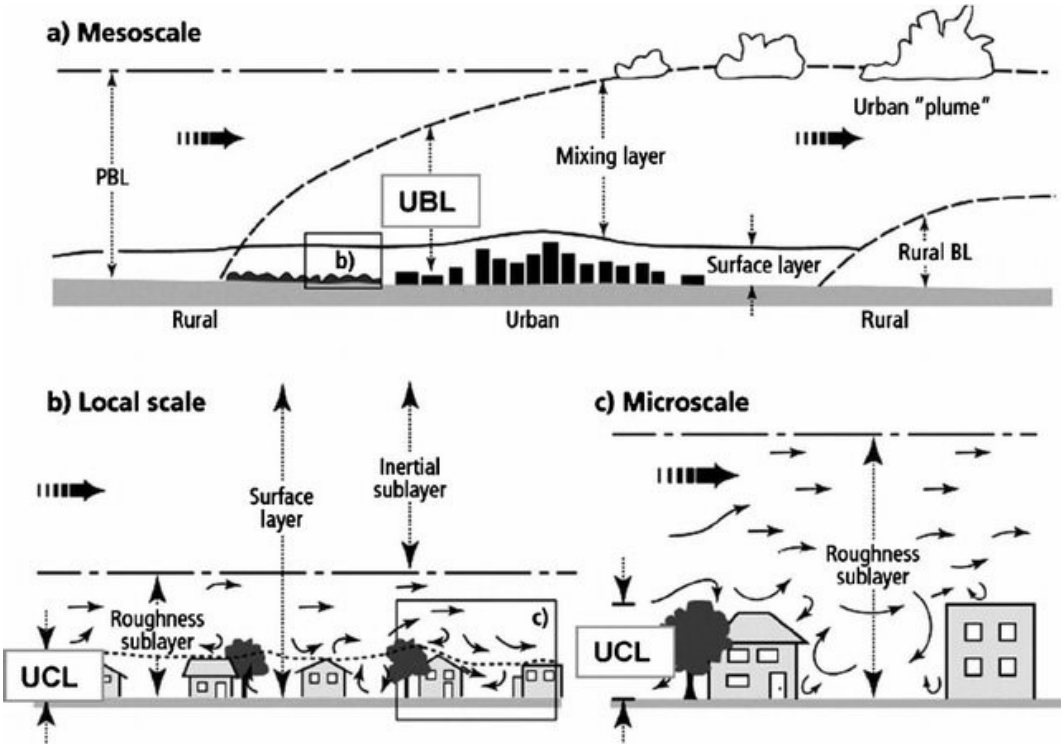


Figure 1.3: Scheme of the urban boundary layer (UBL) and the vertical layers it includes and spatial scales. UCL: Urban canopy layer; PBL: Planetary boundary layer (PBL). Figure obtained from (Gosling et al., 2014).

In the last two decades, several efforts have been made to understand the dynamics of the urban atmosphere and to study the implementation of different heat mitigation strategies involving increasing the albedo of building roofs (cool roofs) (Akbari et al., 2001; Campra, 2011; Li et al., 2014; Yang et al., 2015; Li and Norford, 2016; Gilabert et al., 2021b), greening roof tops (green roofs) (Imran et al., 2018; Li et al., 2014; Sharma et al., 2016; Zonato et al., 2021), increasing urban green spaces (Papangelis et al., 2012; Fallmann et al., 2013; Demuzere et al., 2014; Feyisa et al., 2014; Jacobs et al., 2018; Yu et al., 2018; Gilabert et al., 2021b), street trees (Krayenhoff et al., 2020), increasing urban irrigation (Gilabert et al., 2021b), and reducing anthropogenic heat releases from vehicles and air conditioning systems (Xu et al., 2018; Zhou et al., 2022). Li et al. (2014) studied the cooling capabilities of green roofs strategies over the Baltimore-Washington metropolitan areas (United States of America) during a heat wave episode using WRF with the Princeton Urban Canopy Model and found that the cooling capacity of green roofs is limited by the soil moisture, being a key variable in the performance of the green roof. Jacobs et al. (2018) studied the impact of incrementing green areas of Melbourne (Australia) from 27 % to 40 %, and found nighttime temperature reductions of 1.5 ºC. While Papangelis et al. (2012) found that increasing the green vegetation fraction from 27 % to 50 % in the city of Athens (Greece), can reduce the nighttime temperatures by 1.98 ºC, but no impact was observed during the day. Li et al. (2019) used a linear regression between simulated two-meter temperatures and urban fractions (defined as the fraction of the impervious surface area to the total plan area) using WRF

coupled to an UCM for the city of Berlin, for determining the UHI intensity of Berlin based on a set of validated urban fraction linear functions. These studies reveal the capabilities of urban atmosphere modelling to understand the physical mechanisms behind the implementation of NBS-GI strategies along to the impact of vegetation on the urban air temperature.

1.2.4 Impact of heat and drought events on the carbon capture capacity of regional green infrastructure

At the regional, national, or continental scale, green infrastructure provides of other more relevant ecosystem services as the provision of food, wood and biomass for energy and other materials, flood control, water pollutants filtration, control of soil erosion rates, global climate regulation through the atmospheric carbon sequestration and storage, the protection of biodiversity and other crucial supporting ecosystems services (García et al., 2020). For instance, global and regional terrestrial ecosystems play an important role limiting climate change due to their contribution in the global carbon cycle and their capacity to sequester CO_2.

Carbon dioxide is recognized as the most predominant anthropogenic greenhouse gas, given its elevated atmospheric concentration, resulting from various sources. These include (a) natural exchanges through biogeochemical interactions with organic molecules in the biosphere and hydrosphere (commonly referred as net ecosystem exchange – NEE), (b) substantial anthropogenic emissions from the combustion of fossil carbon and cement production, and (c) alterations in land use such as deforestation (Munassar et al., 2022). The primary absorption of atmospheric CO_2 occurs through terrestrial carbon capture by photosynthesis or gross ecosystem exchange (GEE) and is estimated to account for approximately one-third of anthropogenic emissions, attributed to the increased uptake of photosynthetic CO_2 in recent decades (Cai and Prentice, 2020; Friedlingstein et al., 2020). Consequently, the natural removal of atmospheric greenhouse gases by ecosystems plays a pivotal role in achieving the goals of the Paris Agreement, which aims to fulfil a balance between anthropogenic greenhouse gases emissions and natural sinks by mid-century to limit the increase in global average temperatures below 2 ºC above preindustrial levels (UNFCCC, 2015).

Understanding the terrestrial net carbon exchange is needed for assessing biosphere-atmosphere interactions (Feng et al., 2021). NEE is influenced by climatic conditions, varying at a wide range of timescales, from hourly, seasonally to interannual. Recognizing the dependence of NEE on climatic conditions and the effect of climatic disturbances is vital for predicting the evolution of the carbon balance in future climate scenarios and understanding the interactions between ecosystems and atmosphere (von Buttlar et al., 2018). In this context, the increasing occurrence of extreme climate events are profoundly impacting the terrestrial carbon balance, altering vegetation dynamics, and influencing the net carbon uptake from ecosystems (Ciais et al., 2005; Reichstein et al., 2013; Baldocchi et al., 2016; Keenan et al., 2016).

Among extreme climate events, heat waves and droughts have major effects on the ecosystems

functioning and carbon balance (von Buttlar et al., 2018), due to land-atmosphere feedbacks (Fischer et al., 2007; Fischer and Schär, 2010). For instance, droughts produce a closure of leaf stomas in plants, reducing the vegetation transpiration and the evaporative cooling, as well as the photosynthesis, and promoting the increase of air temperatures (Reichstein et al., 2013). At the regional scale, the coupling between soil moisture and air temperatures promotes the formation of heatwaves under drought conditions (Seneviratne et al., 2006). The low soil water availability usually causes an increase in the vapor-pressure deficit (atmospheric dryness) between the leaf and the atmosphere that leads to a stomatal closure to avoid a failure in the hydraulic system of the plant (Reichstein et al., 2013). Hydraulic failure is considered as a primary cause of tree mortality during droughts, which is accompanied commonly by starvation of carbohydrate reserves (Rita et al., 2020) and other lagged and delayed effects, as higher risk of fires, higher risk of plague and diseases. Regarding the carbon balance, the combination of concurring heat waves and droughts lead to stronger impacts in the NEE compared to the single-factor extreme events alone (von Buttlar et al., 2018). However, the impact of extreme events is highly dependent in the intensity and duration of the event (von Buttlar et al., 2018), as well as the ecosystem, vegetation species and climate (Reichstein et al., 2013; Qu et al., 2024).

Recent studies have focused on Southern Europe, one of the key regions impacted by climate change (Giorgi and Lionello, 2008), as the warming and drying projected trends compound for increasing the frequency and intensity of heat and drought events (Fischer and Schär, 2010; Molina et al., 2020). Over the last two decades, observable impacts have confirmed these climatic trends (Barriopedro et al., 2011; Vicente-Serrano et al., 2014), which pose significant risks to the integrity of the GI, both crops and natural ecosystems. Although the Mediterranean climate is typically characterized by long dry summers (Gilabert et al., 2015), the resilience of its forests to dryness (Gazol et al., 2018) reaches its limits when long drought episodes combine with heat waves start to affect the vegetation leading to a reduction of the NEE. Therefore, long drought episodes combined with heat waves not only implies a challenge for water security, but also for food security and the value of forest ecosystem services. It is crucial to comprehend the impact of heat and drought events on the south-western European carbon balance considering the perspective of more frequent and intense events in the region (Cook et al., 2022) and the pressing efforts to understand the interactions between ecosystems and climate (Friedlingstein et al., 2020).

1.3 Research gaps and research questions

Based on the current state-of-the-art addressing the capacity of urban and regional GI to provide of regulating ecosystem services, five research gaps have been identified:

1.3.1 How do street trees impact microscale air-cooling and radiation exchange within a highly compact city?

At street level scale, street trees are a key factor in the evolution of the local climate inside the street canyon and can play a key role in the greening strategies of high-compact cities (limited horizontal extension but high building density) due to the low capability of these cities to integrate large urban NBS-GI measures (Baró et al., 2019). Although numerous observational and numerical studies have focused on investigating the cooling effects of trees in urban parks (Shashua-Bar and Hoffman, 2000; Bowler et al., 2010; Lin and Lin, 2010; Oliveira et al., 2011), less research has been centred over the neighbourhood-scale cooling impact of street trees (Coutts et al., 2016; Krayenhoff et al., 2020; Segura et al., 2022). Coutts et al. (2016) observed daytime air temperature reductions of 0.2 to 0.6 ºC in a shallow street with dense tree canopy compared to another street with more sparse tree presence in Melbourne (Australia). Due to the increased necessity of assessing the impacts of street trees in pedestrian level climate, the effect of street trees on local climate has been recently included in UCM, which represent the radiation exchange, energy balance, hydrodynamic or hydrologic processes related with street trees.

The Building Effect Parameterization with Trees (BEP-Tree; (Krayenhoff et al., 2020)) is a multi-layer UCM that accounts for the integrated effects of streets trees on the neighbourhood-scale climate, in terms of radiation exchange, energy balance, wind drag, turbulence and pedestrian level climate. The model has been thoroughly evaluated in Krayenhoff et al. (2020), via comparison against measurement datasets of different trees in urban areas in three cities (Vancouver and London in Canada, and Salt Lake City in USA), spanning from street to neighbourhood scale. However, these three sets of measurements correspond to open low-rise residential neighbourhoods, characterized by a low density of impervious area and a low building height to street width ratio (H/W). Therefore, **BEP-Tree model evaluation is still lacking for more compact areas with high building height to street width rations, and bigger building-to-plan area fractions, where the impacts of street trees on pedestrian climate can affect a higher population density**.

1.3.2 How do street trees impact outdoor thermal stress during heat waves in a highly-compact city?

Several studies explore the impact of street trees on the human thermal stress at the microscale (Shashua-Bar and Hoffman, 2000; Coutts et al., 2016; Huang et al., 2020; Jia and Wang, 2021; Miao et al., 2023). The magnitude of daytime cooling effect of street trees depend on shading amount, street canyon geometry, and local meteorological conditions (Coutts et al., 2016). Street trees are highly effective in reducing daytime thermo-physiological heat stress indices for the city of Melbourne (Australia) (Coutts et al., 2016), such as the Universal Thermal Climate Index (UTCI) (Jendritzky et al., 2012), due to the reduction of mean radiant temperature (T_{MRT}) from shading. T_{MRT} is a crucial factor in estimating thermos-physiological heat stress indices (Middel and Krayenhoff, 2019) as it determines the effect of shortwave and longwave radiation exposure on the human body (Jia and Wang, 2021).

However, uncertainty surrounds the capacity of street trees to cool air and reduce human thermal stress during extreme heat events, which can impact physiological processes such as the stomatal conductance of leaves (Marchin et al., 2022), and structural components of trees (Qu et al., 2024). While heat stress may increase water evapotranspiration from tree leaves and soil under no water limitations (Drake et al., 2018), heat events are often accompanied by droughts. Droughts restrict soil water availability, limiting transpiration and prompting the closure of leaves' stomata to prevent further soil water depletion and reduce the risk of "hydraulic failure" in plants (McDowell et al., 2008).

BEP-Tree does not compute the T_{MRT} impeding its applicability to understand the impact of street trees on the human thermal stress and the variability of thermal stress within streets. Moreover, BEP-Tree does not include the hydrology of permeable urban soil and omits the impacts of soil water availability on tree transpiration (Krayenhoff et al., 2020), limiting the capabilities of the model to study the impact of heat waves on the air-cooling capacity of street trees specially in arid and semi-arid regions as the Mediterranean region during drought. The assessment of the cooling capacity and the reduction of the human thermal stress of street trees during extreme heat events requires of a UCM that properly integrates the effects of street trees at the pedestrian level climate, considering soil water availability impacts on the tree transpiration, and that computes the T_{MRT}, to derive heat stress indices.

1.3.3 What is the role of urban green infrastructure in local temperature regulation in a coastal Mediterranean city?

At the city and metropolitan region scales, the study of the adaption capabilities of NBS-GI strategies to face extreme heat events and to mitigate local heat requires of a deep understanding of the behaviour of the urban boundary layer, particularly during extreme heat events. In this context, numerical models as the WRF coupled with BEP-BEM play a key role, both as scientific tools to help researchers understand how different physical mechanisms shape UBL evolution, and as practical tools to aid urban planners and policy makers in evaluating the efficiencies of different mitigation strategies (Chen et al., 2011). However, atmospheric models have a range of different options in terms of their physical parameterizations, initializations, etc., that often need to be adapted to each case study. For instance, coastal Mediterranean cities are highly vulnerable regions to the effects of climate change as there are expected to experience an increasing frequency of longer lasting and more severe heat waves (Ballester et al., 2009), while the physical mechanisms responsible for the development of the UBL over this kind of cities have not been fully understood. **Different aspects and configurations in the WRF-BEP-BEM model that are very relevant to coastal Mediterranean cities have not been studied yet for this type of cities, as it is the case of the soil moisture and temperature initialization, the urban morphology parameters, and the planetary boundary layer scheme**. This analysis can be a basis to improve our scientific understanding of the physical mechanism responsible for the development of the UBLs of coastal cities, as well as to derive information that can be

used to design heat mitigation strategies.

1.3.4 Can the expansion of peri-urban agriculture have measurable effects on local temperature regulation and atmospheric carbon capture?

Between the different NBS-GI strategies proposed, peri-urban agriculture is gaining high attention as its multifunctional role provides solution for multiple economic, social, and environmental issues (Piorr et al., 2018). Different studies have shown the strong capacity of regional (Kueppers and Snyder, 2012) and global (Sacks et al., 2009) irrigated agriculture to regulate near-surface climate especially over dry climate regions. However, peri-UA strategies are not usually contemplated within the atmospheric modelling studies at urban or metropolitan region scale, aiming to examine the efficacy of different UHI and heat mitigation strategies. Additionally, the increase of irrigation demands provoked by the peri-UA strategies can potentially severely impact the water balance in dry regions such as the Mediterranean region. Moreover, the implementation of peri-UA often displaces the natural land uses, which can have an impact on the global carbon balance of the region, as natural areas as forests usually have a higher net carbon sequestration capacity than crops. Natural areas can be more adapted to the impacts of extreme climate events as droughts and water scarcity (Bastos et al., 2020; Ermitão et al., 2021). Forests regions present a higher resistance to droughts and heat events than croplands (Ermitão et al., 2021). This is especially relevant when considering the biosphere carbon balance of dry regions such as the Mediterranean basin. In this context, the implementation of peri-UA can have a considerable impact on the food-water-climate nexus, depending on the local climate of the metropolitan region, geography, and management practices (Power, 2010). **The study of peri-UA strategies and the associated land-use changes must explore spatial and temporal interdependencies and trade-offs in the elements of the food-water-climate-nexus**.

1.3.5 What is the impact of heat and drought events on the biogenic carbon capture of ecosystems in the south-western European region?

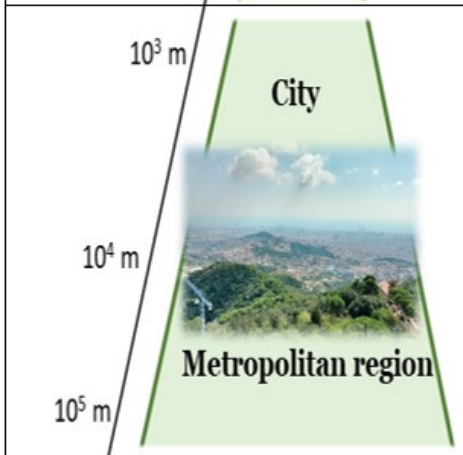
At European scale, the contribution of the regional GI and ecosystems to the carbon capture has been well assessed based on a combination of biosphere models and atmospheric and fluxes CO_2 observations (2022). However, while the impact of heat and drought events on the carbon balance has been well studied for Central and Northern Europe (Ciais et al., 2005; Bastos et al., 2020; Ramonet et al., 2020), a specific analysis of south-western Europe is lacking, especially for the Mediterranean region. **In this region different studies have investigated the role of water and heat stress on the vegetation photosynthesis** (Maselli et al., 2009; Gilabert et al., 2015; Gouveia et al., 2017; Ermitão et al., 2021; Martínez et al., 2022), **but the assessment of the net biosphere carbon balance remains highly uncertain given complex dependencies from heat and drought episodes on the ecosystem respiration**. The south-western Europe complex carbon balance presents unique challenges, notably the scarcity of long-term observational records of CO_2 concentrations and fluxes in the region. Additionally, soil water availability and vapor pressure deficit are the main factors driving interannual variability of photosynthesis (Gilabert

et al., 2015), but the timing of drought on heat events are also important factors in the vegetation response (Jin et al., 2023). However, biogeochemical models usually fail at capturing the plants carbon response to extreme variations in soil moisture, which is a key driver of the impact of droughts on the GEE in arid and semi-arid environments (Stocker et al., 2018, 2019).

Remote sensing data-driven biosphere models, which estimate the ecosystem CO_2 fluxes based on meteorological drivers and satellite sensed vegetation indices, usually estimate the water stress effect on GEE using satellite sensed water indices or using the vapor pressure deficit (atmospheric dryness) without considering soil moisture as a model input (Stocker et al., 2018, 2019; Fu et al., 2022). Although satellite sensed indices can capture some extent the effect of droughts on GEE (Maselli et al., 2009), these metrics tend to underestimate the magnitude of GEE reductions observed under dry conditions (Stocker et al., 2019). For instance, the Vegetation Photosynthesis and Respiration Model (VPRM) (Mahadevan et al., 2008) does not consider soil moisture as a driver variable, which limits its applicability to study the impact of drought events on the carbon fluxes (Mahadevan et al., 2008). However, different studies have shown the potential of enhancing the VPRM model capabilities thanks to model parameters optimisation (Dayalu et al., 2018) or by modifying the respiration equation (Gourdji et al., 2022), resulting in similar or even better model performances compared to more complex biosphere models.

The main objective of this thesis can be derived into eight specific subobjectives addressing the five research questions that are detailed in Table 1.1.

Table 1.1: Main objective, research questions, subobjectives and outline of this Ph.D. thesis.

Main objective: determine the capacity of the green infrastructures to provide temperature regulation and atmospheric carbon capture under the influence of heat and drought at the street/neighbourhood, city, and regional scales.			
Spatial scale	**Research questions**	**Subobjectives**	**Thesis chapter**
	RQ1. How do street trees impact microscale air-cooling and radiation exchange within a highly compact city?	SO1. Evaluate and improve the ability of the Building Effect Parameterization with Trees (BEP-Tree) to reproduce the local and microclimatic conditions inside the street canyons in a highly-compact city. SO2. Combine data from an observational campaign and numerical results to assess the microscale air cooling and radiation exchange effects of street trees inside highly-compact cities.	2
	RQ2. How do street trees impact outdoor thermal stress during heat waves in a highly-compact city?	SO3. Determine the microscale air cooling capacity and the human thermal stress reduction of street trees during a heat wave event over a highly-compact city using BEP-Tree.	3
	RQ3. What is the role of urban green infrastructure in local temperature regulation in a coastal Mediterranean city?	SO4. Test the sensitivity of the mesoscale meteorological Weather Research and Forecasting (WRF) model with the Building Effect Parameterization and the Building Energy Model (BEP-BEM) to the most relevant model configurations using the Metropolitan area of Barcelona as case study. SO5. Determine the impact of the city of Barcelona on the urban boundary layer development and the impact of vegetation on the urban air temperature.	4
	RQ4. Can the expansion of peri-urban agriculture have measurable effects on local temperature regulation and atmospheric carbon capture?	SO6. Explore the impacts of nature-based solutions in the form of green infrastructure planning strategies aiming to expand urban and peri-urban agriculture in the changes and trade-offs across local food provision, freshwater use, local climate regulation, and global climate change mitigation.	5
	RQ5. What is the impact of heat and drought events on the biogenic carbon uptake of ecosystems in the south-western European region?	SO7. Evaluate and improve a biosphere model (i.e. VPRM) to represent the impact of heat and drought events on the biogenic carbon fluxes of the ecosystems of south-western Europe.	6
		SO8. Determine the effect of heat and drought events on the temporal variability of the net biogenic carbon fluxes over south-western Europe.	7

1.4 Chapters description

Chapter 2 evaluates the BEP-Tree model by comparing numerical results with micrometeorological observations from two different streets in the Eixample District with varying tree density. Chapter 3 employs an improved BEP-Tree model, with a mean radiant temperature and soil moisture parameterizations, to investigate microscale air temperature and human thermal stress during a heat wave episode in the same streets described in Chapter 2.

In Chapter 4, a sensitivity study of the planetary boundary layer schemes and soil initialization within the WRF-BEP-BEM model in the Metropolitan Area of Barcelona is presented. This chapter also includes an analysis of the impact of the city of Barcelona on the development of the urban boundary layer and the influence of vegetation on urban air temperature. Chapter 5 explores the impacts of nature-based solutions, specifically green infrastructure planning strategies for expanding peri-urban agriculture. This exploration, utilizing WRF-BEP-BEM model and VPRM, includes an assessment of the impact of heat waves on urban green infrastructure in terms of air-cooling capacity and atmospheric carbon exchange.

Chapter 6 compares the performance of the default and a modified versions of the VPRM model against flux tower measurements and atmospheric CO_2 concentration observations in the south-western European region. In Chapter 7, the modified VPRM model is used to assess the long-term trends and interannual variability of net biogenic carbon fluxes from 2001 to 2022 over south-western Europe, determining the impact of heat and drought events on the temporal variability of these fluxes.

The concluding Chapter 8 summarizes the main findings and conclusions of this Ph.D. thesis, where the ongoing research studies and some recommendations for future research are detailed.

This thesis is organized into eight comprehensive chapters, each incorporating excerpts or complete journal publications, or articles submitted for publication as indicated in the respective introductory paragraph to each chapter (with corresponding publication details provided in each case). For chapters encompassing findings derived from this thesis (Chapter 2 to Chapter 7), a short introduction and conclusions accompany the presentation paragraphs. The numerical models used in this thesis, along with model improvements and configurations applied to the study cases are further explained in the Methods and material section of each corresponding Chapter.

Chapter 2

How do street trees affect urban temperatures and radiation exchange? Observations and numerical evaluation in a highly compact city

The work of this chapter has been published in:

Segura, R., Krayenhoff, E. S., Martilli, A., Badia, A., Estruch, C., Ventura, S., & Villalba, G. (2022). How do street trees affect urban temperatures and radiation exchange? Observations and numerical evaluation in a highly compact city. Urban Climate, 46, 101288. (doi.org/10.1016/j.uclim.2022.101288)

Abstract: Street trees are an important driver of street microclimate through shading and transpirative cooling, which are key mechanisms for improving thermal comfort in urban areas. Urban canopy models (UCM) with integrated trees are useful tools because they represent the impacts of street trees on neighborhood-scale climate, resolving the interactions between buildings, trees and the atmosphere. In this study, we present the results of a measurement campaign where vehicle transects were completed along two similar parallel streets of Barcelona with different tree densities, recording upward and downward radiation fluxes, air temperature and humidity at street level. These observations are used to evaluate and improve the multi-layer UCM Building Effect Parameterization with Trees (BEP-Tree). Prior simulations of the model revealed insufficient heat exchange between the canyon surfaces and the air at the lowest vertical levels inside the deep canyons, which we solve by including turbulent buoyancy driven wind velocity in the model. Air temperatures are 1.3 ℃ higher on average in the street with sparser trees when wind direction is perpendicular to the streets. The BEP-Tree simulations demonstrate good agreement with the observations in terms of temperature and radiation, and capture the diurnal evolution of temperature and radiation between the two streets.

2.1 Introduction

Climatic conditions in urban areas are likely to worsen in the near future if unaddressed, due to risks deriving from climate change, such as heat extreme events (Revi et al., 2014), and the added climatic stresses present in urban areas (Oke, 1982; Oke et al., 2017; Arnfield, 2003). The increasing urbanization and densification of cities is also an added challenge that urban planners and local governments must manage in order to preserve the city's environmental sustainability. The implementation of urban green infrastructure in urban planning strategies can help adapt cities to changing climates, improve public health, promote social cohesion, and provide with other beneficial services (Demuzere et al., 2014; Baró et al., 2019).

The moderating effect of urban vegetation on urban temperatures has been well assessed in the literature (Bowler et al., 2010; Oliveira et al., 2011; Zhang et al., 2013; Krayenhoff et al., 2021), evidencing the associated reductions of air and surface temperatures at different scales in the city (Oke, 1989; Shiflett et al., 2017). At local and neighborhood scale, large vegetated patches modify the surface energy balance through the evapotranspiration process, cooling the air around the vegetation and providing a thermal reduction of the surrounding urban areas (Grimmond and Oke, 1991; Grimmond et al., 1996). At microscale, trees provide shade to the surrounding built surfaces and to the pedestrians, modifying the biometeorological conditions experienced by them and improving thermal comfort (Coutts et al., 2016; Middel and Krayenhoff, 2019).

In particular, street trees are a key factor in the evolution of the local climate inside the street canyon, altering the radiation, momentum and convective heat exchange between the buildings and the atmosphere (Oke, 1989; Krayenhoff et al., 2020). Street trees can play an important role in the greening of high-compact cities (limited horizontal extension but high building density), due to the low capability of these cities to integrate large urban green infrastructure measures (Baró et al., 2019). The extent to which street trees can improve air temperatures and increase the resilience of these areas to heat events depends on different aspects that influence the magnitude of cooling, such as the canyon geometry and sun-orientation, the local meteorological conditions, the geographic setting of the city, the amount of tree canopy covering the canyon floor and distribution, tree typology, the water availability for trees and the tree health condition (Gillner et al., 2015b; Coutts et al., 2016; Salmond et al., 2016; Krayenhoff et al., 2020).

Although numerous observational and numerical studies have focused on investigating the cooling effects of trees in urban parks (Shashua-Bar and Hoffman, 2000; Bowler et al., 2010; Lin and Lin, 2010; Oliveira et al., 2011; Papangelis et al., 2012), less research has been centred over the neighborhood-scale cooling impact of street trees (Coutts et al., 2016; Krayenhoff et al., 2020). Johansson and Emmanuel (2006) found that the most comfortable air conditions were found in deep canyons, especially if tree shade is present, compared to open and wide streets, for a humid and hot city in southeast Asia. Coutts et al. (2016) observed daytime air temperature reductions of 0.2 to 0.6 ºC in a shallow street with dense tree canopy compared to another street with more sparse tree presence in Melbourne, Australia. They also observed that the cooling impact of trees was lower in a deep canyon with similar tree density because the shading effect of trees

was exceeded by the shading effect of the tall buildings. Moreover, street trees may increase nocturnal air temperatures under the canopies, due to the reduced sky view factor (SVF), which inhibits the cooling of canyon surfaces due to longwave radiation release (Bowler et al., 2010). This effect can exacerbate possible health issues during heat events due to the uncomfortable temperatures at night (Salmond et al., 2016).

Due to the increased necessity of assessing the impacts of street trees in pedestrian level climate and to avoid the dependence on costly observation campaigns, the effect of street trees on local climate has been recently included in diverse neighborhood-scale urban canopy models (Lee and Park, 2007; Lee, 2011; Ryu et al., 2016; Krayenhoff et al., 2020; Meili et al., 2020). These models are able to represent the radiation exchange, energy balance, hydrodynamic or hydrological processes related with street trees, or a combination of these processes. These models can be alternatively coupled with regional climate models to assess the cooling potential of street trees at city scale and to further improve the capabilities of these models for urban climate applications (Mussetti et al., 2020). The Building Effect Parameterization with Trees (BEP-Tree; Krayenhoff et al. (2020)) is a multi-layer urban canopy model (UCM) that accounts for the integrated effects of streets trees on the neighborhood-scale climate, in terms of radiation exchange, energy balance, wind drag, turbulence and pedestrian level climate. The model has been thoroughly evaluated in Krayenhoff et al. (2020), via comparison against measurement datasets of different treed urban neighborhoods in three cities (Vancouver and London in Canada, and Salt Lake City in USA), spanning from microscale to neighborhood scale. However, these three sets of measurements correspond to open lowrise residential neighborhoods, characterized by a low density of impervious area and a low building height to street width ratio (H/W). Therefore, model evaluation is still lacking for more compact areas with H/W greater than one, and bigger building-to-plan area fractions (λ_p), where the impacts of street trees on pedestrian climate can affect a higher population density.

In this context, there is much interest in the assessment of the effects of street trees on local climates in highly-compact cities, where the high density of urban dwellers and intense traffic activities require urban planners to focus on urban design for improved thermal regulation. The main objectives of this research are:

1. Evaluate and improve the ability of a neighborhood-scale urban canopy model that integrates the effect of trees inside the canyon (i.e. BEP-Tree) to reproduce the local and microclimatic conditions inside the street canyons in a highly-compact city.

2. Combine data from an observational campaign and numerical results to assess the microscale air cooling and radiation exchange effects of street trees inside highly-compact cities.

To achieve these objectives, we perform a micrometeorological measurement campaign in the city of Barcelona (Spain) for two cloud-free summer days. Vehicle transects were completed along two parallel streets with different tree densities but similar street geometry, recording upward and downward radiation fluxes, air temperature and humidity. These data are used to

evaluate the ability of the BEP-Tree model to reproduce the micrometeorology of this scenario. Finally, the meteorological simulations and the experimental data are used to evaluate the combined impacts of vegetation and buildings on urban canopy layer climate.

2.2 Methodology

2.2.1 BEP-Tree model

The standard BEP-Tree model description

The BEP-Tree model integrates the effects of street trees in the urban canopy layer within the Building Effect Parameterization (BEP) (Martilli et al., 2002). The BEP model is a multi-layer urban canopy scheme that accounts for the impact of buildings on airflow and computes the surface energy exchange between urban vertical and horizontal surfaces (building walls and roofs and street ground) and the atmosphere. This scheme derives neighborhood-scale averaged fluxes and local climate conditions at different vertical levels within the canopy to serve as surface boundary conditions in mesoscale atmospheric models. BEP parameterizes the impact of a regular arrangements of buildings on wind, turbulent kinetic energy, potential temperature, and specific humidity. The scheme computes the effect of urban geometry on the longwave (thermal radiation) and shortwave (solar radiation) radiation fluxes, considering the effect of reflections, shadowing and radiation trapping to derive the urban surface temperature evolution.

In the BEP-Tree model, BEP model is modified to include a one-dimensional vertical turbulent diffusion model (Santiago and Martilli, 2010), as well as an entirely new radiation scheme (Krayenhoff et al., 2014). This modification allows it to perform offline 1-D simulations uncoupled from a mesoscale atmospheric model. It only requires an atmospheric forcing at the top boundary of a vertical column, usually two-three times the mean building height. Street trees are not explicitly resolved, but the interaction with the incoming and outgoing radiation inside the canyons is parameterized based on a leaf area vertical density profile and a street canyon-average foliage clumping factor. The multi-layer approach of the model allows the representation of vertical distribution of building heights probabilities and leaf area density profiles, representing trees between and above buildings.

The built and leaf surface energy balances are derived in order to generate sink and sources of temperature and humidity to the vertical diffusion equations in the one-dimensional model. The multi-layer radiation model of BEP-Tree uses ray-tracing to determine the direct shortwave exposure of all urban canyon elements at each time step (Krayenhoff et al., 2014). Furthermore, view factors between all built and foliage elements are computed once at the start of the simulation using a Monte-Carlo ray tracing approach and then the model solves all longwave and diffuse shortwave exchange at each model timestep using a radiosity approach. Vegetation intercepts shortwave and longwave radiation according to the Beer-Lambert-Bouguer law:

$$\Delta V_i(iz) = r_i[1 - exp(-K_{bs}\Omega L_D(iz)\Delta s f_i)] \tag{2.1}$$

Where $\Delta V_i(iz)$ is the reduction of ray intensity due to the tree foliage at vertical layer iz (Wm^{-2}), r_i is the initial intensity of the ray (Wm^{-2}), K_{bs} is the foliage extinction coefficient, Ω is a foliage clumping factor, $L_D(iz)$ is the leaf area density at vertical level iz, Δs is the 2-D ray step size (m) and f_i is the ratio of 3-D (actual) to 2-D (model) distance travelled by the ray (depends on the canyon orientation to the sun) (Krayenhoff et al., 2014). The clumping factor is used to model the heterogeneous distribution of tree crowns in the canyon. The clumping factor ranges between 0 and 1, being 1 when foliage is randomly distributed within the canyon. For canyon spaces and tree crown scale clumping it is approximated as follows:

$$\Omega = \frac{-1}{0.5LAI_{can}} ln(1 - \lambda_{v,can}(1 - exp(-0.5LAI_{tree}))) \tag{2.2}$$

Where LAI_{can} and LAI_{tree} are street-canyon average and tree crown space-average leaf area indices, and $\lambda_{v,can}$ is the fraction of plan area coverage of tree crowns inside the street canyon (Krayenhoff et al., 2020).

BEP-Tree also includes a parameterization of building and tree effects on airflow inside the urban canopy layer (Martilli et al., 2002; Santiago and Martilli, 2010; Krayenhoff et al., 2015, 2020). BEP-Tree considers the sink effect for momentum of both building and foliage elements, due to the inclusion of form drag in the horizontal momentum conservation equation proposed in Santiago and Martilli (2010). Correspondingly, BEP-Tree also includes terms of enhanced turbulent kinetic energy due to wake production generated by the buildings and foliage drag. Moreover, turbulent length scales were updated based on the comparison of Large-Eddy Simulations (LES) and wind tunnel measurements (Nazarian et al., 2020) to account for building effects on the flow.

The required inputs of the model are meteorological forcing at the top level (within the inertial sublayer, roughly 2-3 times the mean building height) and geometric, radiative and thermal variables of the canyon including the vegetation. The forcing can be provided from an observation tower placed over the maximum roughness element in the urban area or from a mesoscale model. The geometric variables of the canyon are building height distribution and width, street width, thermal and radiative parameters of the building materials, the leaf area density vertical profile and the clumping factor. Further details about the model equations and parameterizations can be found in Krayenhoff et al. (2014, 2015, 2020).

A new buoyancy driven wind velocity parameterization

Our preliminary simulations using the BEP-Tree model for this highly-compact case indicated that the model had some limitations in terms of representing wind speed inside deep, narrow canyons during the central hours of the day with strong surface heating, as shown in Section 2.3.1. These initial BEP-Tree simulations had small sensible heat transfer from building walls and street to the canopy air that we interpret as caused by an underestimation of wind speed

in the lower levels of the street canyon. Moreover, reduced turbulent mixing inside the canyon and anomalously high surface and air temperatures in the lower levels of the canyon were also found (see Section 2.3.1). This may be caused by the modified drag coefficients and turbulent length scales in the model, which were updated based on LES simulations (Nazarian et al., 2020). Nazarian et al. (2020) investigated the turbulent flow around idealized urban configurations with aligned and staggered cube arrays with different packing densities (λ_p = 0.0625 – 0.44) and height-to-width ratios (H/W < 1.0). The studied geometrical conditions with the LES simulations do not fully cover the geometric conditions of highly-compact cities, with packing densities over 0.5 and height-to-width ratios exceeding 1. Moreover, LES simulations were performed under neutral conditions, which clearly differ from the unstable canyon conditions observed during hot summer days in temperate cities, with a high amount of solar radiation absorbed by the urban surfaces. Additionally, Nazarian et al. (2020) also concluded that spatially averaged kinetic energy was still underestimated in the lowest levels closest to the ground in highly-compact configurations in UCM simulations with the updated length scales.

For this reason, we have hypothesized that vertical air movements in the canyon are largely caused by buoyancy effects with characteristic length scales equal to the depth of the deep urban canopy which are not captured by the local formulation of the dynamics in the model. Therefore, a buoyancy driven turbulent wind velocity is defined to increase the aerodynamic conductance within the urban canyon, similar to the free convection velocity (w^*) term proposed by Lemonsu et al. (2004) to represent the urban canopy layer in the dense city of Marseille, France. This buoyancy driven wind velocity has been derived with dimensional analysis using the building height z_m, the buoyancy parameter g/θ_0, where g is the gravity acceleration and θ_0 corresponds to a reference potential temperature which has been defined to 300 K, and the difference in potential temperature between the lowest model level, θ_1 (0.5 m), and θ_m the potential temperature at the building height level, as follows:

$$w^* = \sqrt{\frac{z_m * g * (\theta_1 - \theta_m)}{\theta_0}} \tag{2.3}$$

This equation is used for unstable conditions ($\theta_1 > \theta_m$), while for neutral or stable conditions the non-local production of buoyancy generated turbulence is expected to be zero ($w^* = 0$). A sensitivity analysis of the impact of this new parameterization is shown in section 3.1.

2.2.2 Study area

The city of Barcelona

The city of Barcelona is situated in the northeast coast of the Iberian Peninsula, in the western Euro-Mediterranean region. The city coastline is oriented from southwest to northeast, and the city is bounded at the northwest by the mountainous region of the Collserola Natural Park (almost 500 m of altitude), and at the northeast and southwest by two rivers (Figure 2.1a). The city covers an extension of 101.4 km^2 from which 17.0 km^2 belongs to the Collserola Natural

Park and 11.7 km^2 are urban green areas (Barcelona City Council Statistical Yearbook, 2021). Barcelona has a population of 1.66 million inhabitants, with an average density of 163 inhabitants ha^{-1} and maximum values over 400 inhabitants ha^{-1} in some neighborhoods in the city centre. The city of Barcelona is characterized principally by two urban geometries: the first one is represented by the Eixample district (7.5 km^2) with regular block patterns, wide avenues and two street orientations (perpendicular and parallel to the coast); and the second one represented by the old neighborhoods of Gràcia, Raval and Gòtic (1.3 km^2, 1.1 km^2 and 0.8 km^2) with narrow streets and unregular patterns. The Eixample district is the most populated (269 341 inhabitants in 2021) and densest district in the city of Barcelona with 361 inhabitants ha^{-1}; and has the lowest coverage of urban greenness per inhabitant with 2.0 m^2 ha^{-1}.

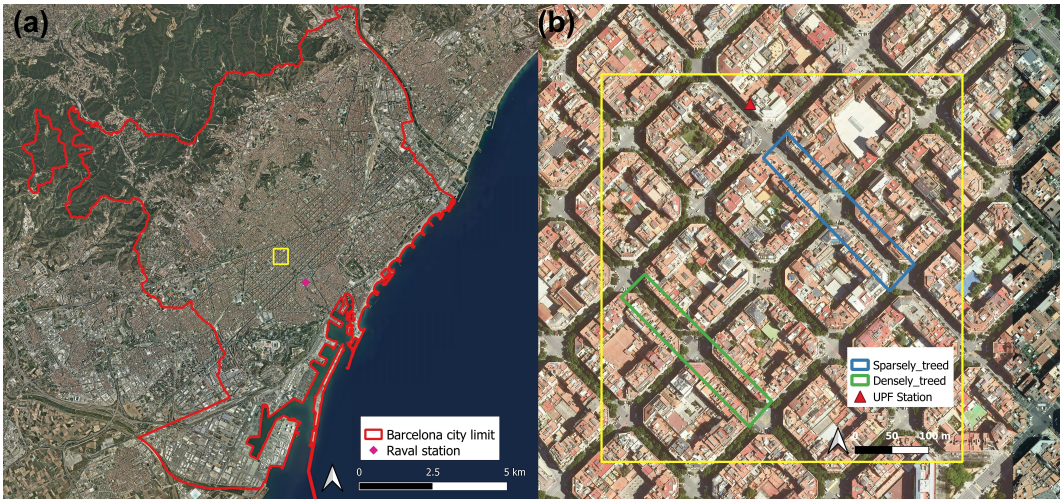


Figure 2.1: (a) Administrative boundaries of Barcelona city; (b) detail of the region of study in the Eixample neighborhood with the two studied streets: Sparsely_treed (blue) and Densely_treed (green). The Raval station is marked with a pink diamond and the UPF station is marked with a red triangle.

Despite the high compactness and density of the city and the low number of green urban areas per inhabitant (7.0 m^2/inhabitant on average in the entire city), Barcelona has a large number of street trees (157,636 trees), with 95 trees per 1000 inhabitants, which is well above the average range of other European cities (50-80 trees per 1000 inhabitants) (Pauleit et al., 2002; Baró et al., 2019). Moreover, the municipal government has a complete inventory of all the street trees and palm trees updated every 4 months, including information such as geographic coordinates, species name and other structural and health condition variables (available in https://opendata-ajuntament.barcelona.cat/data/ca/dataset/arbrat-viari).

The experiment site

Two parallel streets inside the District of the Eixample are studied due to the high compactness of the buildings and the regularity of the block pattern (Figure 2.1b). The regular form of the

urban canopy in the two horizontal directions facilitates that the observed values resemble the neighborhood-scale average for street of this orientation. The two streets are oriented perpendicular to the coast (from NW to SE) and have different tree covers and tree species: the Balmes street (Sparsely_treed) exhibits a sparse and short tree cover with a low tree canopy fraction in the urban canyon (16 % tree canopy cover within the urban canyon area), while the Aribau street (Densely_treed) exhibits a dense and tall tree cover (65 % tree canopy fraction in the urban canyon). The street trees in Sparsely_treed are composed of Tilia x euchlora which have a mean height of 5.8 m and the shade only partially covers the sidewalks. On the contrary, the trees in Densely_treed are composed of Celtis australis and Platanus x hispanica which have a mean height of 10.8 m, and the shade completely covers the full width of the urban canyon.

The streets are separated by a distance of 270 m. The street width of the two canyons is obtained from Google Earth and airborne photos. The width of both streets is 20 m, with the middle 10 m of the street section composed of 4 traffic lanes and 5 m at each side devoted for pedestrian sidewalks. There is considerable traffic on both streets during daytime, especially at peak hours in the morning and afternoon. Average building heights are gathered from LiDAR data and a digital surface model with 2 m resolution, available at the Institute Cartographic and Geological of Catalonia (ICGC, 2019). Average building heights are 30.6 m and 29.0 m, for Sparsely_treed and Densely_treed streets, respectively. This yields a height-to-width ratio of 1.53 and 1.45. The building plan to area fraction (λ_p) is similar for the streets with a value of 0.82.

2.2.3 Observed data

Vehicle transects around the two parallel streets were performed during two consecutive summer days, 28-29 July 2021. The vehicle was equipped with a net radiometer Hukseflux NR01 suspended at 1.5 m height over the back of the car, composed of two pyrgeometers measuring longwave radiation fluxes, and two pyranometers measuring shortwave radiation fluxes, in both the upwelling and downwelling vertical directions. Moreover, the vehicle was equipped with a Kestrel 4500 pocket weather tracker that recorded meteorological variables such as air temperature, relative humidity, and pressure, as well as a GPS device to track the coordinates of the sample points. A picture of the measurement set up can be seen in Figure A.1 in Appendix A. The measurements from the net radiometer were recorded with a data logger Campbell Scientific CR1000 every 10 s. The meteorological measurements were also recorded at each 10 s but independently by the Kestrel device. The transects started at each exact hour o'clock and consisted of two laps around the two streets stopping between 13 and 24 times in each one of the two outermost traffic lanes, leaving the two middle traffic lanes free so that the traffic would not be disturbed. Each measurement stop lasted between 25 and 30 s to fulfil the response time of the radiometers (18 s for the 95 % confidence interval). In total, each transect around the two streets took between 30 to 40 minutes to be completed, depending on the traffic. All the data of the different stops in each track and street is averaged and is assigned to the average time of all the stops in the same track and street. The hourly transects started at the 04 UTC (06 local time, local time is obtained adding two hours) of the 28 July 2021 until the 23 UTC of the same day, and from the 3 UTC of the 29 July 2021 to the 23 UTC of the same day. The radiometer

measurements on the 29 July at the 12 UTC were not recorded due to a mechanical problem. The measurements span from before dawn until past midnight in order to study the different stability regimes of the urban canopy layer and the cooling process of the surfaces and atmosphere during the evening. The high presence of traffic until even midnight (22 UTC), generates an additional contribution of anthropogenic heating that can be expected to generate some discrepancy between the modelled and observed air temperatures (since it is not included in BEP-Tree) and affects the urban canopy layer stability.

To complete the characterization of the two streets, upper hemisphere fisheye photos were taken at 1.1 m height and randomly distributed along the street axis but at the same traffic lanes of the vehicle transects to derive the sky view factor (SVF), the vegetation view factor (VVF) and the building view factor (BVF) perceived by the up-facing radiometer. A total of 12 photos for each street (between the two outermost traffic lanes) were taken using a Canon EOS 5D Mark III and a Canon EF 8-15mm f/4L Fisheye USM lens. The photos were manually segmented using a photo editor program and then, the view factors were obtained using the software RayMan 1.2 (Matzarakis et al., 2010). An example of the photographs manual segmentation can be seen in Figure A.2 in Appendix A. The mean values of the measured view factors and the ones estimated by the BEP-Tree model can be seen in Table 2.1. As we can see from the table, the view factors calculation of the BEP-Tree model using the Monte-Carlo ray tracing approach can reproduce the actual values observed with the photos for the Sparsely_treed street, while it overestimates the SVF for Densely_treed, in detriment of the BVF. However, BEP-Tree view factors are for the street average, while the observed view factors are taken from the outer vehicle lane only (i.e., not a representative sample across the width of the street), so a small discrepancy is expected.

Table 2.1: Mean view factors measured from upper-hemisphere fisheye photos and computed by the BEP-Tree model for the two streets.The values in parentheses correspond to the standard deviation. SVF, VVF and BVF stand for sky view factor, vegetation view factor and building view factor.

Street	Measured			BEP-Tree		
	SVF	VVF	BVF	SVF	VVF	BVF
Sparsely_treed	0.26 (0.03)	0.19 (0.08)	(0.55 (0.07)	0.248	0.139	0.613
Densely_treed	0.05 (0.03)	0.47 (0.05)	0.48 (0.03)	0.117	0.508	0.374

2.2.4 Model evaluation

BEP-Tree urban surface parameters

Two simulations spanning from the 28 July 2021 at 00 UTC to the 30 July 2021 at 00 UTC were conducted with BEP-Tree to model the two street canyons. The vertical resolution in the model is 1 m, the maximum vertical level with buildings is 35 m for the Sparsely_treed simulation and 30 m for the Densely_treed station, and the model's upper boundary is at 70 m, approximately two times the height of the highest building, which correspond just above the top of the roughness sublayer, within the inertial sublayer (Oke et al., 2017). While inside the roughness sublayer the flow is modified by the protruding elements below, varying in the horizontal and

vertical directions, in the above layer, the inertial sublayer, the flow responds to the integral effect of the urban neighborhood below. In our case, the urban morphological properties are homogenous in the horizontal, so the inertial sublayer can be considered homogenous horizontally and only vary vertically.

The model has been configured to represent just one street direction (135º) to better represent the conditions inside the two urban canyons. The urban surface thermal properties have been defined based on the most common construction materials of the study area. The street is composed of asphalt and concrete, while the building walls are primarily brick and roofs are clay tiles. The material properties have been defined based on typical values of reference tables (Oke et al., 2017). The rest of the properties have been defined based on the urban parameters of local climate zone 2 in Ribeiro et al. (2021). The leaf area per tree canopy is assessed from the measured canopy height and crown width, computed from the LiDAR data and airborne photos of the canyon, respectively, and the parameterization of Nowak (1996). The street-canyon average leaf area can be approximated to be $LAI_{tree} * \lambda_{v,can}$. The leaf density profile is derived based on the vertical distribution of total leaf area from Lalic and Mihailovic (2004). The urban canopy parameters and vegetation parameters used in the model for the two streets simulations can be seen in Table A.1 in Appendix A.

Meteorological forcing

The meteorological forcing of the model at its top boundary is obtained partially from fixed meteorological station observations placed over a building rooftop of the Universitat Pompeu Fabra (see Figure 2.1b) in the Sparsely_treed street. This station (at 1.5 m over the rooftop, 26.5 m over the street ground level) records downwelling shortwave and longwave radiation fluxes, and other meteorological data (air temperature, pressure, humidity). Due to the low height of the building with the station compared to the tallest buildings in the surrounding area, and the low mast height, only the radiometer measurements, specific humidity, and pressure (with a height correction to the forcing height) are used for the forcing. The rest of the meteorological variables, wind components and potential temperature are obtained from a meteorological station from the Meteorological Service of Catalonia, in the Raval neighborhood (see Figure 2.1a), at 2.0 km from the study area. This station, placed over a building rooftop at 21 m over the street ground level, records 10 m (above roof top) wind speed and direction and 2 m (above roof top) air temperature. Wind speed was corrected to represent the roughness values of the study area neighborhood using the approach of Wieringa (1986), and then the components were rotated to the same directions as the street orientation (45º and 135º). The Wieringa approach consists of applying a logarithmic height profile to the observed wind speed (U_s) to obtain the mesowind (the wind at the top of the roughness sublayer, U_{70}) based on this equation:

$$U_{70} = U_s \frac{ln\left(\frac{70-z_d}{Z_0}\right)}{ln\left(\frac{z_s-z_d}{z_0}\right)} \tag{2.4}$$

Where z_s is the observation height above street level, z_d is the zero-plane displacement height

at the measuring point (2/3 * z_m, where z_m is the mean building height), and z_0 is the roughness length at the measuring point (0.1 *z_m) (Grimmond and Oke, 1999).

In the case of potential temperature at the forcing height, the potential temperature measured by the Raval Station is corrected to 70 m applying a correction based on the height. According to previous mesoscale atmospheric simulations conducted with the Weather Research and Forecasting model (WRF) for the study area (Segura et al., 2021), we have determined a coefficient of reduction between the measuring height and the forcing height. This variation is mainly affecting the daytime potential temperature since the nighttime vertical profiles are close to neutral. Then, the potential temperature is corrected based on this approximation:

$$\theta_{70}(ih) = \theta_0 + \alpha_k(ih) * (\theta_s(ih) - \theta_0) \tag{2.5}$$

Where $\theta_{70}(ih)$ is the estimated potential temperature at 70 m and time of the day ih, θ_s is the measured potential temperature at time of the day ih, θ_0 is a reference potential temperature defining the lowest value at night (295.5 K), and α_k is the adjustment parameter that depends on the time of the day. The adjustment parameter has been obtained averaging between different days the reduction potential observed in WRF simulations for the grid cell that contains the Raval station, being 0.8 during daytime (6-19 UTC) and 1.0 during nighttime (20 UTC – 5 UTC). This methodology can introduce uncertainty in the BEP-Tree model to derive the air temperature inside the urban canyon, which is discussed in Appendix A.4.

2.3 Results

2.3.1 Sensitivity analysis to the wind parameterization

To determine the effects produced by the buoyancy-driven wind velocity described in the Section 2.2.1 a sensitivity analysis is performed to compare the temporal evolution of air and surface temperature, along to the vertical profiles of potential temperature inside the canyon. In the case of the default BEP-Tree model, the mean wind speed of a vertical layer inside the canyon, based on the mean horizontal components ($ws(iz) = \sqrt{u^2 + v^2}$), is used to derive the aerodynamic heat conductance between the building, ground or leaf surfaces and the air, as explained in Krayenhoff et al. (2020). In the case of the new parameterization, the wind speed used for computing the aerodynamic conductance at each time step is the maximum value between ws and w^* (see Equation 2.3), which represents the buoyancy effect on turbulent vertical wind velocity. In this sensitivity analysis, we compare the BEP-Tree simulations using the default air exchange parameterization (BT def.) and the simulations with the new thermal turbulent wind speed (BT w^*).

When the vertical thermally driven turbulent wind speed is not considered in the model (BT def.), a considerable increase of the road surface temperature is seen in the simulations (Figure 2.2a), reaching maximum daytime road temperatures up to 9.6 ºC and 7.0 ºC higher than

the simulations with the new parameterization for Sparsely_treed and Densely_treed streets, respectively. The low mean wind speed considered by the default BEP-Tree model in the lowest levels of the urban canyon (below 0.1 $\mathrm{m\,s^{-1}}$) produces a low turbulent sensible heat flux between the surface and the first air level (see Figure A.4 in Appendix A), increasing the surface temperature. In this case, the model simulates a higher temperature range between the daytime and nighttime surface temperatures, overestimating the maximum surface temperatures (up to 7.0 ºC for Sparsely_treed and up to 9.7 ºC for Densely_treed) and underestimating the minimum nighttime temperatures, for the two streets (down to -1.8 ºC for Sparsely_treed and -1.0 ºC for Densely_treed). However, the BT def. simulations seems to capture better the road temperature differences between the two streets at midday (7.4 ºC at 11 UTC) with respect to the BT w^* simulations (4.4 ºC) when they are compared to the observations (9.7 ºC). Even though, the inclusion of the thermally driven turbulent wind speed in the model improves the simulation of the road surface temperature diurnal range for the two streets, leaving only a small negative bias in the case of the Sparsely_treed simulation (-2.8 ºC).

The inclusion of the thermally driven turbulent wind speed parameterization reduces the simulated maximum air temperatures (up to 6.7 ºC compared to BT def.) for the two streets despite the enhancement of the sensible heat flux from the ground and walls (Figure 2.2b). The enhanced aerodynamic conductance between artificial canyon surfaces and air produces an increment in the turbulent kinetic energy of the entire column, especially during the middle hours of the day, which distributes the added heat from walls and ground to the entire urban canopy via turbulent motions (see Figure 2.3b). As with the surface temperature, the air temperature simulated with BT def. presents a higher diurnal range, with much higher maximum values at noon, and similar values at nighttime than the simulations with BT w^*. Moreover, BT def. presents a higher cooling rate during the evening and night compared to the simulations with the added thermally driven wind speed and observations, which present almost steady nighttime air temperatures in the two streets. The reduction of the nighttime cooling rate with the new parameterization comes from representing more neutral conditions inside the urban canopy layer compared to the default version of the model (see Figure 2.3a) which presents unstable profiles at nighttime.

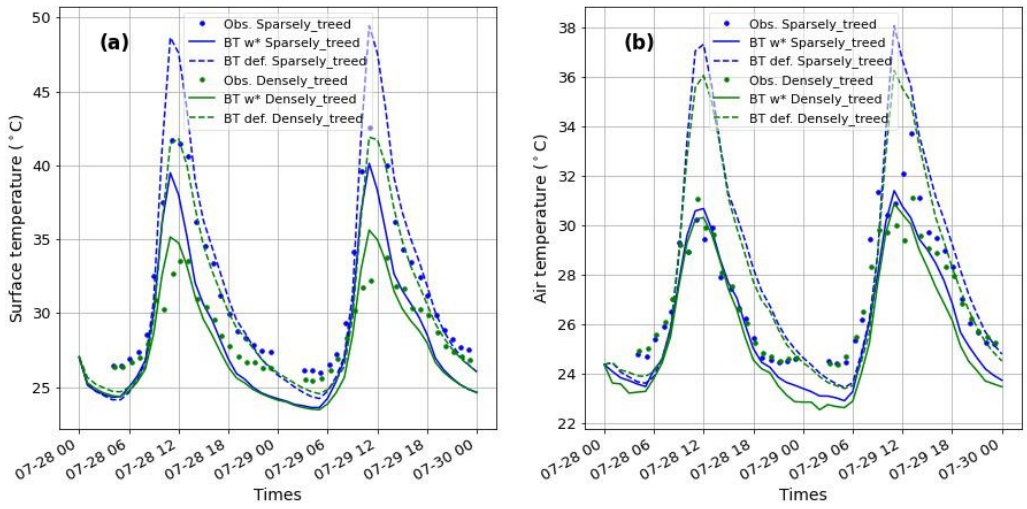


Figure 2.2: Modelled with the default BEP-Tree model (BT def., dashed lines), the BEP-Tree with the buoyancy driven wind speed (BT w^*, straight lines) and observed (Obs., circles) canyon averaged road surface temperature (a) and air temperature (at 1.5 m height from the ground) (b) for Sparsely_treed (blue) and Densely_treed (green) streets in Barcelona.

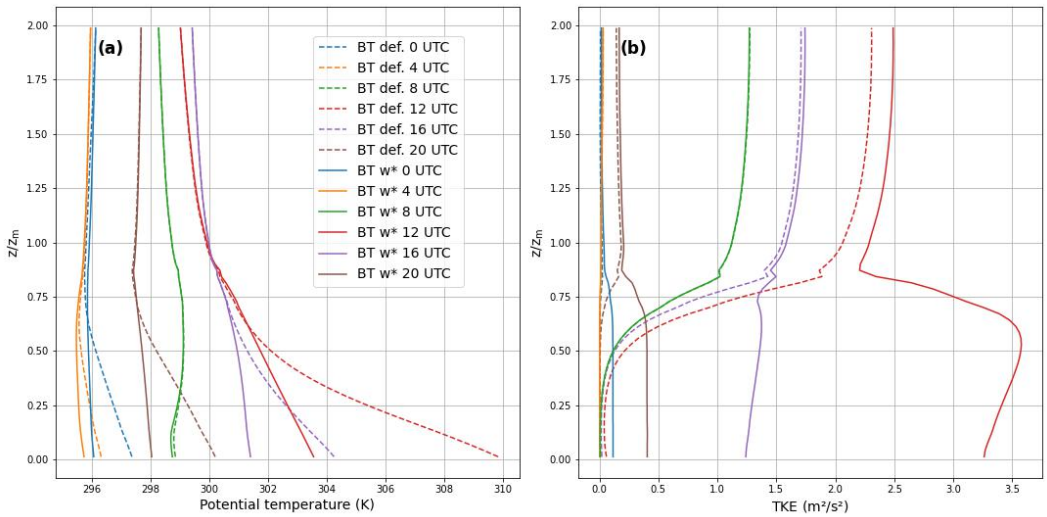


Figure 2.3: Vertical profiles of potential temperature (a), and turbulent kinetic energy (b), at 0, 4, 8, 12 16 and 20 UTC for the default BEP-Tree (BT def., dashed lines) and the new BEP-Tree with the thermally driven turbulent wind speed parameterization (BT w^*, straight lines) for the Sparsely_treed street. z_m refers to the maximum building height.

From now on, only the results of the BEP-Tree model with the new buoyancy driven turbulent wind speed parameterization (BT w^*) are compared with the observations, and we are referring

to BT.

2.3.2 Surface radiation downwards

The difference in tree cover density between the two street canyons produces an observed maximum street-level shortwave radiation difference of 550 ± 309 $\mathrm{W\,m^{-2}}$ at midday (Figure 2.4b). As it was expected, the maximum differences in the shortwave radiation fluxes are observed during the central hours of the day (between 9 – 13 UTC), being over 150 $\mathrm{W\,m^{-2}}$ higher for the Sparsely_treed street. During this period, the sun is at its cenital position and sun beams can reach the street ground without obstruction from the canyon buildings. The temporal profiles of the surface shortwave radiation downwards for the two streets follow a similar profile between the two days of the campaign, in agreement with the fact that there were no clouds during the measurement period. The small differences observed in the temporal profiles between the two days are produced by the spatial variability of the random measurement samples.

BEP-Tree presents similar profiles of the surface shortwave radiation downwards for the two streets compared to the observations (Figure 2.4a). BEP-Tree estimates a lower shortwave radiation incident to the ground for Sparsely_treed during midday than the measurements (down to -200 $\mathrm{W\,m^{-2}}$), especially during the second day. While the model estimates higher incident shortwave radiation at ground level during midday for the Densely_treed case (up to 170 $\mathrm{W\,m^{-2}}$) than the measurements. This causes that the modelled differences seen between the two streets are not as high as the ones observed, reaching the downwelling shortwave radiation almost 300 $\mathrm{W\,m^{-2}}$ lower for the Densely_treed case.

In the case of the longwave radiation, the measurements exhibit a difference of incoming radiation at street-level of 22 ± 6 $\mathrm{W\,m^{-2}}$ higher for the Densely_treed street with respect to Sparsely_treed (Figure 2.4d). This difference is kept almost constant during the diurnal cycle between 15 and 30 $\mathrm{W\,m^{-2}}$, except during the afternoon hours of the first day (between 17 and 20 UTC), where the difference dropped below 15 $\mathrm{W\,m^{-2}}$. Over all the hourly transects, the Densely_treed street presented a higher downwelling longwave radiation at street-level than the Sparsely_treed.

On the other hand, the modelled longwave radiations at ground level presented much smaller differences between the two streets during the campaign period (Figure 2.4d). The hourly differences vary between -5 and 10 $\mathrm{W\,m^{-2}}$. This discrepancy is produced by the larger longwave radiations estimated for the Sparsely_treed case, compared to the observation, which are between 5 and 35 $\mathrm{W\,m^{-2}}$ higher, especially during midday and early afternoon (10-15 UTC). In the case of the Densely_treed street, BEP-Tree estimates lower values during the evening and night than the observations (down to -16 $\mathrm{W\,m^{-2}}$), but higher values during midday (up to 10 $\mathrm{W\,m^{-2}}$). This causes that the model exhibits negative differences between Densely_treed and Sparsely_treed longwave radiation downwards during the afternoon (between 14-18 UTC), in disagreement with the observations, where the differences are always positive.

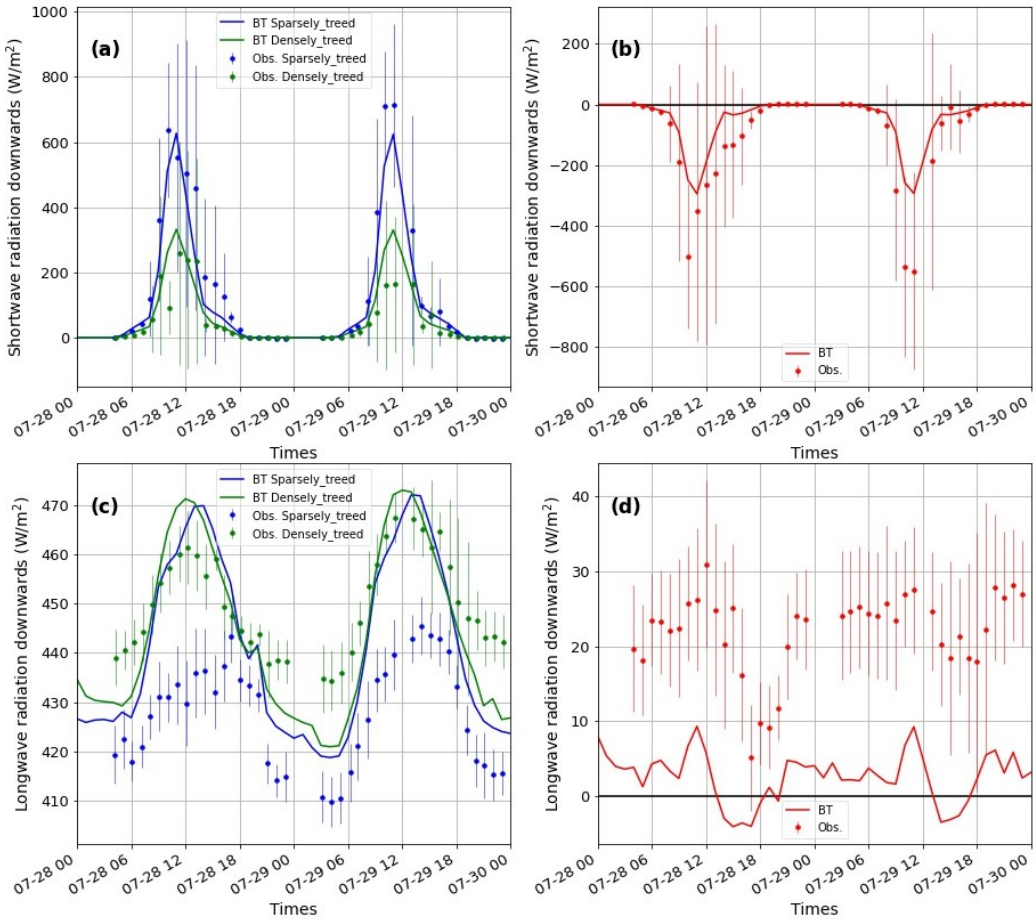


Figure 2.4: Modelled by BEP-Tree (BT, lines) and observed (Obs., circles) canyon averaged surface shortwave radiation downwards (a), difference in shortwave radiation downwards between Densely_treed and Sparsely_treed (b), surface longwave radiation downwards (c), difference in longwave radiation downwards between Densely_tree and Sparsely_treed (d) for Sparsely_treed (blue) and Densely_treed (green) streets in Barcelona, and their difference (Densely_treed – Sparsely_treed, red). Measurement error bars correspond to the standard deviation between all the stops.

2.3.3 Road surface and air temperatures

Road surface temperatures are cooler in Densely_treed than in Sparsely_treed during the whole study period (Figure 2.5b), showing maximum differences of 10.1 ± 2.9 ºC during midday. Maximum observed road surface temperatures reach up to 42.5 ± 1.9 ºC and 33.8 ± 2.8 ºC for Sparsely_treed and Densely_treed, respectively. Even during the night, Sparsely_treed exhibits higher surface temperatures than Densely_treed, 1 ºC on average during night measurements.

BEP-Tree simulations can capture the daytime effect of trees on the ground surface temperature, showing higher surface temperatures in Sparsely_treed compared to Densely_treed. Even though, the differences between streets are not as wide as in the case of the observations. The maximum difference between streets estimated by the model is 4.4 ºC. This low difference of the surface temperature difference between the two streets at midday is related to a lower estimation of the temperatures for the Sparsely_treed street (down to -5.4 ºC) and a higher estimation for Densely_treed (up to 3.4 ºC). The model estimates lower mid-afternoon and nighttime road surface temperatures for the two streets (around 2.5 - 3 ºC lower for Sparsely_treed and 2 ºC lower for Densely_treed) compared to the observations. Moreover, the model is not able to capture the nighttime temperature difference generated by the tree presence, showing identical nighttime surface temperatures between the two streets (differences below 0.3 ºC).

The observations of averaged air temperatures in the two streets present a different evolution of the variables for the two days of the campaign (Figure 2.5c). In the case of the 28 of July, the two streets show a similar evolution of the air temperature, reaching maximum values of 31.1 ± 0.4 ºC for Densely_treed and 30.2 ± 0.9 ºC for Sparsely_treed at 11 UTC. On the contrary, for the 29 of July, the street with lower tree cover density considered higher averaged air temperatures with maximum values of 33.7 ± 1.7 ºC compared to the maximum temperatures of Densely_treed of 31.1 ± 0.7 ºC. The average difference in air temperature between the two streets during midday and afternoon of the second day (from 8 UTC to 17 UTC) is 1.3 ºC. At nighttime, there is not an observable air temperature difference between the two streets.

BEP-Tree simulations can represent the daytime evolution of the air temperature in the two streets, although an underestimation of the air temperature is observed during the nighttime (Figure 2.5c). The model represents lower nighttime air temperatures for the two streets compared to the observations, by 1.8 ºC for Sparsely_treed and 1.5 ºC for Densely_treed. Model simulations represent higher daytime temperatures for Sparsely_treed compared to Densely_treed for the two days of study. This contrasts with the results of the measurements, where Densely_treed exhibits generally slightly higher air temperatures (up to 0.7 ± 0.8 ºC) during day 28 of July, while it presents lower temperatures during midday and afternoon of 29 of July (down to -2.8 ± 1.7 ºC). Contrasting with the observations, the higher differences between the streets are simulated during mid-afternoon (15 – 17 UTC) with maximum differences of up to 1.0 ºC, compared with the observations which the maximum differences are seen at midday of the second day (11 – 14 UTC).

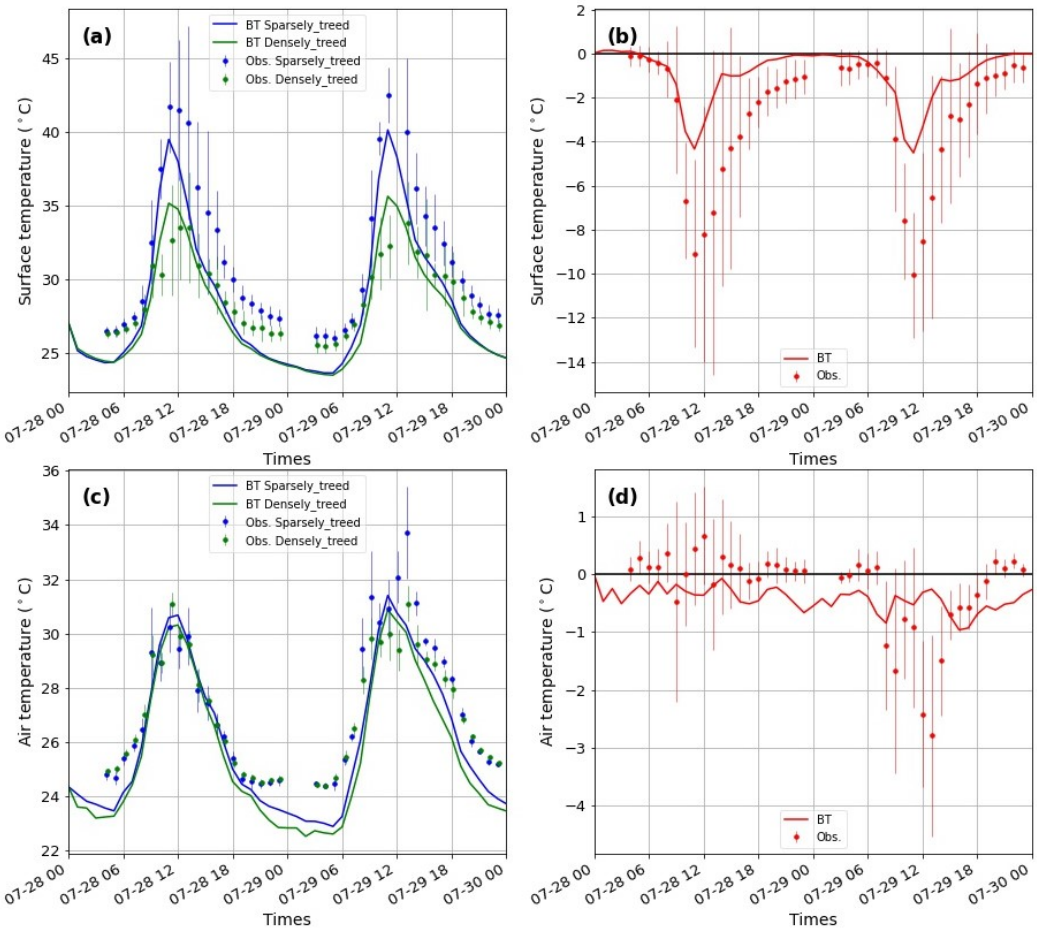


Figure 2.5: Modelled by BEP-Tree (BT, lines) and observed (Obs., circles) canyon averaged road surface temperatures (a), difference in road surface temperatures between Densely_treed and Sparsely_treed (b), air temperature (at 1.5 m height from the ground) (c) difference in air temperatures between Densely_treed and Sparsely_treed (d) for Sparsely_treed (blue) and Densely_treed (green) streets in Barcelona, and their difference (Densely_treed – Sparsely_treed, red). Measurement error bars correspond to the standard deviation between all the stops.

2.3.4 Relative humidity and specific humidity

Our observations do not show a significant difference in specific humidity between the two streets (Figure 2.6a). The observed differences between Densely_treed and Sparsely_treed are kept between 0.2 and -0.5 $g\,km^{-1}$. In the case of the relative humidity, a slight increase of 6.2 ± 3.0 % in Densely_treed with respect to Sparsely_treed is observed at noon of the 29 of July (Figure 2.6b), corresponding to the decrease of temperatures by the street trees observed in Fig-

ure 2.5d.

On the contrary, BEP-Tree simulations present a difference in specific humidity between the two streets. This difference is principally appreciable during the daytime, with the simulation with higher tree cover reaching up to 2.5 $g\,km^{-1}$ more than for Sparsely_treed. This higher difference modelled by BEP-Tree compared to the difference seen in the observations is produced by a higher estimation of the specific humidity in the Densely_treed street. The model is closely representing the evolution of the specific humidity for the Sparsely_treed street with a consistent positive difference, caused by the similar temporal profile between the observations and the specific humidity forcing conditions in the forcing level (see Figure A.5 in Appendix A). In the case of the relative humidity, the model is overestimating the differences between the two streets (up to 14 % difference between Densely_treed and Sparsely_treed), probably related to the differences seen in the specific humidity during the day, and of the specific humidity and temperature during the night (Figure 2.5d).

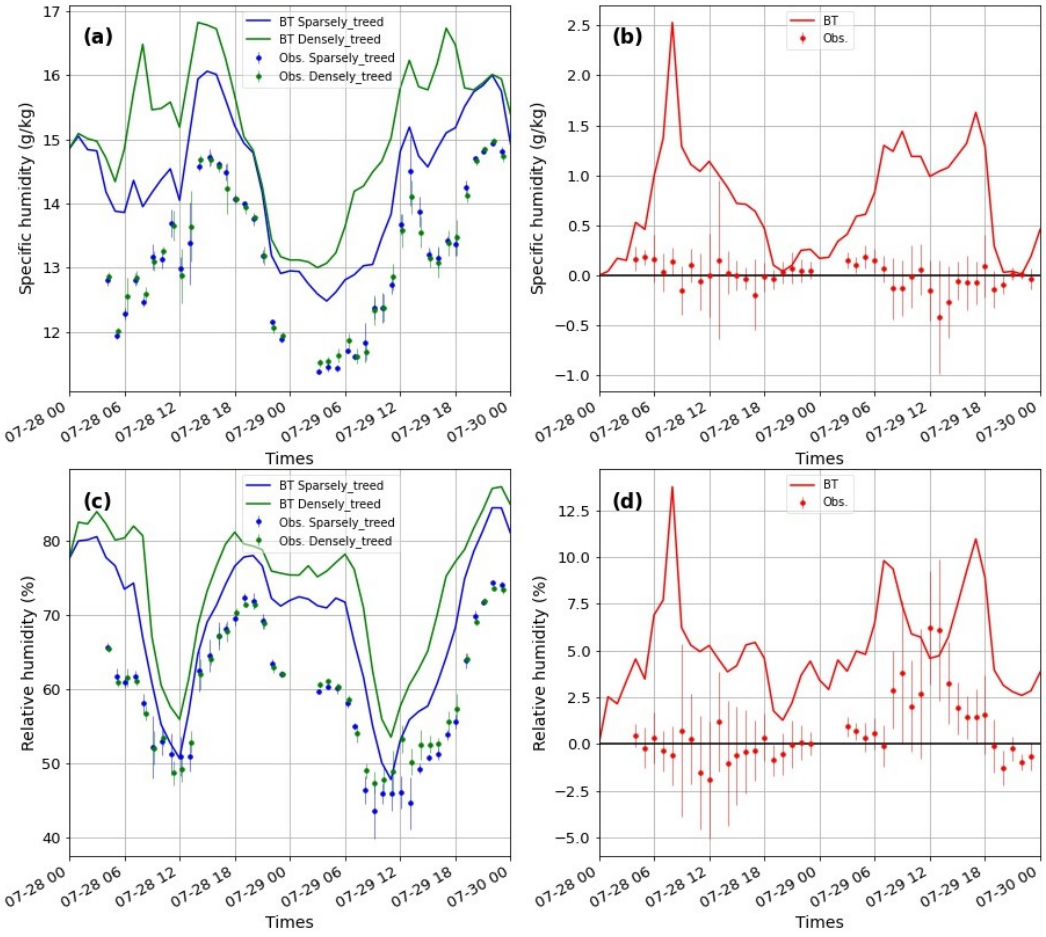


Figure 2.6: Modelled by BEP-Tree (BT, lines) and observed (Obs., circles) canyon averaged 1.5 m above ground specific humidity (a), difference in specific humidity between Densely_treed and Sparsely_treed (b), relative humidity (c), difference in relative humidity for Sparsely_treed (blue) and Densely_treed (green) streets in Barcelona. Measurement error bars correspond to the standard deviation between all the stops.

2.4 Discussion

2.4.1 Sensitivity analysis to the wind parameterization

Based on the results of the sensitivity analysis, the new parameterization improves the performance of the model in the representation of street-averaged surface temperatures, decreasing the maximum overestimation during midday (from 7.0 ºC to 5.4 ºC for Sparsely_treed, and from up to 9.7 ºC to 3.4 ºC for Densely_treed), and decreasing the cooling rate during the night.

Moreover, the buoyancy driven wind velocity parameterization decreases the overestimation of midday air temperatures (from 7.9 ºC to -3.4 ºC for Sparsely_treed, and from up to 6.3 ºC to 1.1 ºC for Densely_treed), although underestimating for Sparsely_treed, along to a decrease in the air cooling rate at night, as it is observed from the measurements. It also results in an increment of the TKE inside the canyon. We do not have experimental evidence to assess if this increment is realistic or not, and it is beyond the scope of the present study. To check it, a detailed field campaign should be organized with sonic anemometers located at different heights within the canyon, or a Large Eddy Simulation in non-neutral conditions with surface heat forcing similar the one observed in this case, and the same canyon aspect ratio should be performed.

2.4.2 Comparison of observations and BEP-Tree simulations

Radiation fluxes

The main mechanism that induces local thermal cooling from street trees derives from the shading of ground surfaces, especially artificial materials such as asphalt and concrete which have high heat retention, and the corresponding redirection of sensible heat into latent heat via transpiration. The random location of the stops made by the measurement vehicle in the two traffic lanes of each street provides sufficient sampling to capture the spatial variability of building and tree shade, which increases the standard deviation of the measurements observed from the pyranometer. BEP-Tree is able to capture the daily evolution of ground incident shortwave radiation, while it estimates a lower reduction from the interception by the tree canopies in each street than the observations. BEP-Tree estimates a lower downwelling shortwave radiation at ground level at Sparsely_treed street than the observations during midday (down to -200 $\mathrm{W\,m^{-2}}$), while BEP-Tree considers a higher downwelling shortwave radiation for Densely_treed (up to 170 $\mathrm{W\,m^{-2}}$). This lower simulated radiation in Sparsely_treed could be related to the spatial discrepancy between the measurements and the simulations. The measurements were taken in the middle of the street where a higher amount of sunlight is reaching the surface, away from the tree cover, which is mostly covering the sidewalks near the walls. This contrasts with the results of the model, which considers the street average surface radiation downwards, including the street sections with shading from tree cover. The higher simulated values than the observations in Densely_treed could be explained because BEP-Tree model is overestimating the SVF for this street in detriment of a lower BVF as seen in Table 2.1. This causes that the difference in SVF between the two streets is lower in the model, which produces lower differences in the modelled shortwave radiation downwards. Or it could simply be the result of the observations being taken under the densest part of the tree foliage, while BEP-Tree assumes that the foliage is equally likely to be located above any part of the street.

Despite the interception of direct shortwave radiation that can improve the biometeorological conditions of the pedestrian-level climate, street trees can make the perceived thermal comfort by pedestrians somewhat worse, especially at night, due to the higher emission of longwave radiation from the relatively warm tree leaves compared to the relatively colder sky that the vegetation obscures. The reduction of the SVF by street trees means that a higher proportion of

the longwave radiation released by the warm street ground and walls is absorbed and reemitted back to the ground by the vegetation. This effect can be seen in the measurements (Figure 2.4d) in which exhibit a difference of incoming longwave radiation at street level of 22 ± 6 $\mathrm{W\,m^{-2}}$ higher for the Densely_treed street with respect to Sparsely_treed. The BEP-Tree model predicts a small increase of incident longwave radiation to the street during midday and nighttime as a result of tree foliage blocking the relatively cool sky (however, in the afternoon it also blocks hot walls, causing reduced street level incoming longwave). The fact that the model is simulating the downward longwave radiation to the whole canyon ground, while the measurements only capture the radiation incident to the central portion of the canyon, leads to the model seeing a higher portion of the building walls than the measurements. This discrepancy affects principally the comparison between the model and the measurements in Sparsely_treed, which has lower tree cover, because the model computes a higher BVF for this street (0.613) compared to Densely_treed (0.374). Moreover, the model calculates a lower BVF for Densely_treed and a larger SVF than the one observed, which reduces even more the downwards longwave radiation from this street. This effect principally occurs during afternoon, due to the higher difference in temperature between the building walls and the sky or trees, likely causing that Sparsely_treed presents higher downwelling longwave radiation than Densely_treed in the model.

Road surface and air temperatures

Street trees produce a decrease in road surface temperatures due to the shading, while they can increase surface temperatures by the higher incident longwave radiation and the reduced street-level wind flow from the larger roughness elements, which lowers the heat flux transfer from ground to the air (Coutts et al., 2016; Krayenhoff et al., 2020). From the measurements it can be seen that street trees decrease road surface temperatures (Figure 2.5a), showing maximum differences of 10.1 ± 2.9 ºC during midday. Even during the night, the Sparsely_treed street surface exhibited higher temperatures than Densely_treed, likely indicating that the reduction of the thermal load accumulated in the asphalt from the tree shading was greater than the longwave and wind drag effects induced by trees that serve to increase street surface temperatures. BEP-Tree simulations can capture the daytime effect of trees on the ground surface temperature, showing higher surface temperatures in Sparsely_treed of up to 4.5 ºC. This underestimation of the surface temperature difference between the two streets at midday can be related to the differences seen in the shortwave radiation downwards between the observations and BEP-Tree (Figure 2.4b), which are in part related to the difference between point observations and the spatially-averaged model results. The model underestimates the mid-afternoon and nighttime road surface temperatures for the two streets. Moreover, the model is not able to capture the nighttime temperature difference generated by the tree presence, showing identical nighttime surface temperatures between the two streets. The SVF differences between the two streets are not as large in the 'spatially-averaged' model compared to the 'point' observations (see Table 2.1), which can reduce the difference in the radiative cooling of the canyon surfaces.

Air temperatures can be affected at neighborhood scales by street trees due to the reduction of ground and wall surface temperatures and the corresponding reduction of sensible heat transmit-

ted from the shaded surface to the air. Nevertheless, the effects of street trees can be suppressed by the local meteorological conditions. For example, periods of high wind speed can produce lower effects of trees on the air temperatures if the wind blows in the same direction of the street due to the advection of the cooling effects downstream (Oke, 1989). The observations of averaged air temperatures in the two streets present a different evolution of the variables for the two days of the campaign (Figure 2.5c). The differences observed between the two days could be related to the local wind direction. On the 28 of July, the wind flows principally from the coast coming from ESE (Figure 2.7), which is almost in the same direction as the street orientation. In this situation, wind flow can be channeled through the street canyons, advecting air masses from upwind locations of the city and suppressing the possible effects of streets trees on the air temperature. This can likely explain the low observed difference in air temperature between the two streets during this day (0.7 ± 0.8 ºC higher for Densely_treed). On the contrary, the wind flow mainly from SW and SSW on the second day of campaign (Figure 2.7), perpendicular to the street orientation. This causes less ventilation inside the deepest part of the canyons and the air exchange between the urban canopy layer and the free atmosphere above roof level was probably reduced (Oke et al., 2017). In this situation, the cooling effect of street trees shading on the ground is likely enhanced due to the reduced wind speed near the ground (Lin and Lin, 2010). This could explain the high temperature differences observed for this day (up to 2.8 ± 1.7 ºC higher for Sparsely_treed). However, even though the cooling effect of street trees is likely maximized during this wind direction, the dispersion of air pollution can be severely worsened during these situations, due to the stagnation of air pollutants inside the street canyon (Oke et al., 2017), especially if street trees are present, because they serve to further disconnect the wind flow above the canyon from that under the tree canopy (Janhäll, 2015; Jin et al., 2014).

The results have shown that BEP-Tree can represent the daytime evolution of the air temperature in the two streets, although an underestimation of the air temperature is observed during the nighttime (Figure 2.5c). This underestimation of nighttime temperatures could be in part explained by the emission of anthropogenic heat sources inside the canyon, not considered by the model. The high presence of traffic inside the two canyons during the day until after sunset, combined with the release to the canyon air of residual heat from building air conditioning systems can be a non-negligible factor in the evolution of the air temperature inside the urban canopy layer, especially in deep and narrow canyons (Huang et al., 2020) and during nighttime when mixing is reduced. Another possible explanation could be an underrepresentation of the heat storage in the street ground by the model which limits the amount of heat released at nighttime. The heat storage depends on the inner temperatures of the building and ground surfaces, as well as the material properties, which are highly uncertain and difficult to measure.

Model simulations represent higher daytime temperatures for the Sparsely_treed site compared to the Densely_treed site for the two days of study. BEP-Tree is unable to detect the differences in air temperature of the two days of study due to the different wind regime inside the urban canyons. BEP-Tree does not explicitly resolve the effect of above roof wind direction inside the streets canyons because it is designed to compute the neighborhood average urban canopy layer behavior, considering the average variables between the two street orientations. In this

case, since the simulations only consider one street orientation, we can account for the effects of street orientation on the solar radiation, but not the effects of above roof wind direction and neighborhood-city scale wind circulations. Future studies should focus on determining the impact of above-roof wind direction on the urban canopy layer, in order to estimate how this factor affects the air cooling of street trees.

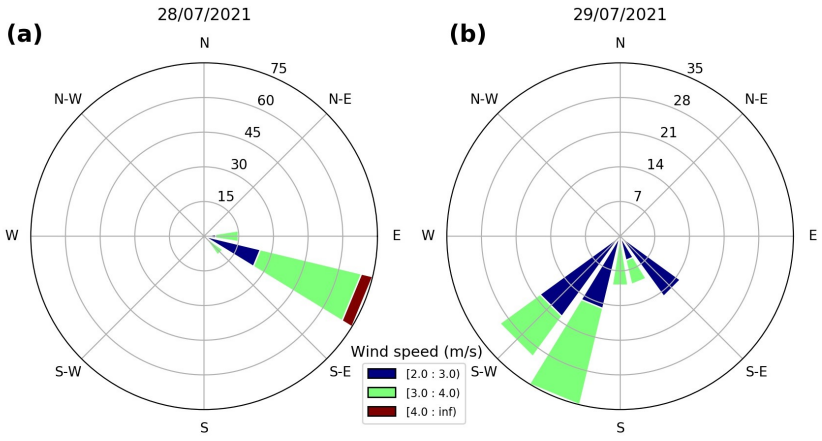


Figure 2.7: Windrose in percentage (%) of the two days of campaign during the central hours of the day (8 UTC - 17 UTC) measured at the Raval meteorological station. The streets studied are oriented from NW to SE.

Relative humidity and specific humidity

Street trees can produce a reduction of air temperature through transpiration, which is the transformation of sensible heat into latent heat, releasing water vapor into the air (Bowler et al., 2010). This process produces an increment of the relative humidity and specific humidity in the canyon. However, our observations do not show a significant difference in specific humidity between the two streets (Figure 2.6a). This could be explained by three reasons. The first one is that the meteorological device used in the measurements requires a longer time to reach the equilibrium conditions with the surrounding air in the case of relative humidity compared to air temperature and radiation fluxes. This can result in an inability of the device to determine the difference in the two streets if the time to complete an entire track is shorter than the response time of the device (around 20 minutes for the relative humidity). The second reason could be that leaf transpiration can be suppressed due to water scarcity in the soil (Vico et al., 2014), increased air temperature, and/or photoprotection of the photosystem from excess of light (Galmés et al., 2012). During the measurement campaign, there were extremely dry conditions in the city, and

it was combined with high solar exposition of the vegetation. This drought situation is combined with the high imperviousness of urban surface covers, which increase the water runoff and decrease the accumulation of water in inner soil layers. The net result is that street trees lack water at the root levels to perform the leaf transpiration, deriving in stomatal closure and producing similar specific humidity in the two streets. The third reason is that neighborhood scale advection may have caused sufficient mixing to suppress humidity differences between the streets.

Contrasting with the results, BEP-Tree simulations present a difference in specific humidity between the two streets that can be appreciated better during the daytime. This discrepancy with the observations can be produced due to the long response time of the meteorological device used in the campaign or because BEP-Tree model is not including ecophysiological responses of the vegetation to soil hydrology. In the current version of BEP-Tree there is no soil water dynamics and in the current application the term that controls the stomatal opening related with soil moisture is set to 1.0 (see equation 14 in Krayenhoff et al. (2020)), such that trees do not experience water scarcity. This simplification of soil hydrology can affect estimation of the effects of trees on street microclimate in periods of severe drought, as in the one studied.

Model vs observations discrepancies

The observational campaign described in this study has been designed to evaluate the BEP-Tree model for the highly-compact city of Barcelona. Due to the considerable limitations of performing a micrometeorological campaign in a highly dense city, vehicle transects were conducted inside one of the densest and most urbanized neighborhoods of Barcelona. Although this methodology allows sampling of the variability of building and tree shading along the street's direction, this strategy limits sampling to the traffic lanes, and it is not able to capture the microclimatic conditions in the sidewalks, where pedestrians circulate. This contrasts with the street-average microclimate simulated with BEP-Tree, which represents the average climate over the full canyon width. This difference in spatial representation/sampling generates minor discrepancies between observed and modelled downwelling shortwave radiation (Section 2.3.2) and road surface temperature (Section 2.3.3), and larger discrepancies between observed and modelled downwelling longwave radiation (Section 2.3.2).

Moreover, street trees are usually placed near the sidewalks, in order to maximize the shading to the pedestrians. This affects principally the comparison of the measurements and BEP-Tree simulations in the Sparsely_treed street, where trees are covering principally the sidewalks, while for Densely_treed they cover fully the canyon width, including the traffic lanes. While vehicle radiation measurements were not able to capture the shading from Sparsely_treed trees, BEP-Tree simulations considered tree shading because trees are randomly distributed over the street canyon in the model. Future observational micrometeorological studies may combine the vehicle measurements in the central portion of the street with a mobile human-biometeorological station such in Middel and Krayenhoff (2019) for the sidewalks, so as to determine the average effect of street trees in the whole canyon.

Overall, there is a good agreement in the comparison between the microclimatic effect of street trees observed in the campaign and modelled with BEP-Tree, considering the limitations associated with simulating the complex microclimate observed inside deep urban canyons with street trees; and the spatial discrepancies between point measurements and spatially-averaged model output. Moreover, while BEP-Tree effectively assumes the whole neighbourhood has the characteristics of the single canyon modelled here (or of two canyons of different orientation in its typical implementation), in reality the air temperature and humidity are determined by the characteristics beyond the individual canyon. BEP-Tree is designed to be coupled with a mesoscale model which in turn provides horizontal advection above and within the urban canyon. In standalone (offline) mode, as it is used in this study, BEP-Tree cannot capture horizontal temperature and humidity advection which may play a role in the discrepancies observed in this study, i.e. the underestimation of nighttime air temperatures or the discrepancy observed in the specific humidity. Even though, the regular building pattern and similar building height of the study area along to the identical morphology conditions in the entire neighborhood facilitates the representation of the actual conditions inside the canyons by the model, and probably explains the good performance of the model representing the daytime air temperatures or the specific humidity in the Sparsely_treed street. Further studies can be centred on the evaluation of BEP-Tree coupled with a mesoscale model in order to consider the possible impacts of horizontal advection of air temperature and humidity, along to study the impacts of street trees in other regions of the city, i.e. regions with more complex street patterns and even higher packing densities such as those observed in the second most dominant geometry of the city (see Section 2.2.2).

Larger differences between simulated and observed air and surface temperature are seen at night, which can be attributed to the lack of representation of anthropogenic heat source in the model or due to potential inaccuracies in the representation of the heat storage in street surfaces. Highly-compact areas such the studied area in Barcelona have high emissions of anthropogenic heat from vehicles and residual heat from building air conditioning systems (Gilabert et al., 2021b), which can be an important component in the overall energy balance of the urban canopy layer (Oke et al., 2017). Future evaluations of BEP-Tree model in high-dense cities must consider the contribution of anthropogenic heat sources in the local climate of the street's canyons, such as including a building energy model as the Building Effect Parameterization and the Building Energy Model (BEP-BEM) (Salamanca and Martilli, 2010) and including additional inventoried traffic emissions in the lowest vertical levels.

2.5 Summary and Conclusions

In this study, a neighborhood-scale urban canopy model that integrates the effects of street trees on the street microclimate is evaluated and improved for the highly-compact city of Barcelona, Spain. BEP-Tree model simulations of two parallel streets with high and low tree cover densities are compared against observations of a micrometeorological measurement campaign performed in the area for two summer days. During the campaign, hourly vehicle transects were performed in the two streets measuring vertically-oriented shortwave and longwave radiation fluxes, air

temperature and humidity. The measurement period spanned from before sunrise to long after sunset to capture the evolution of the street microclimate along the diurnal cycle. The regular building pattern and the identical urban morphology along the entire neighborhood of the study area, allowed a better representation of the observed canyon-averaged climate and radiation fluxes by the BEP-Tree model.

We have presented a new turbulent wind speed parameterization included in the BEP-Tree model to solve the inefficient modelled heat exchange between urban surfaces and the air in the lowest levels of the deep street canyons. We have defined a new buoyancy driven turbulent vertical wind velocity w^* (see Equation 2.3) to consider non-negligible buoyancy production of turbulence inside the canyon for unstable conditions. BEP-Tree simulations with the new parameterization show a higher aerodynamic heat conductance between ground surface and air, improving the simulation of surface temperatures. Moreover, the new parameterization also reduces pedestrian-level air temperatures during daytime from the enhancement of the turbulent kinetic energy inside the canyon, improving the representation of air temperatures and buoyancy mixing in the urban canopy layer.

The observations evidenced that street trees contribute to the regulation of the climate inside the canyons through shading of urban surfaces. BEP-Tree simulations were able to reproduce the observed reduction of shortwave radiation through leaf interception and the reduced road temperature derived from the lower irradiance reaching the street surface. Moreover, an increment of the downwelling longwave radiation is observed (modelled) at pedestrian-level (ground level) explained by the higher canopy temperature compared to the relative cool sky that the leaves obscure. Based on the differences observed in air temperatures between the two days of the campaign we can conclude that the effect of street trees in air temperatures is highly dependent on the local meteorological conditions, such as the wind direction above the urban canopy layer. During the first day of campaign, we observed similar daytime air temperatures between the two streets, coinciding with the above roof wind blowing in the same direction as the orientation of the streets being measured and modelled. Wind blew perpendicular to the direction of the streets of interest on the second day of the campaign, and the air temperature in the street with lower tree cover density was 1.3 ºC higher on average compared with the street with higher tree cover density. BEP-Tree simulations were able to closely capture the daily evolution of air temperatures with a modest negative bias during nighttime. However, BEP-Tree was not able to capture the differences in the effects of street trees with the above wind direction because it does not capture the effects of sub-neighborhood scale horizontal heterogeneity.

Finally, based on the modelled and observed effects of street trees on the street microclimate we discuss the possible impacts of street trees on the thermal comfort during hot, dry conditions in a highly-compact urban neighborhood. Street trees are expected to improve the thermal comfort during daytime, due to the reduction of the mean radiant temperature through shortwave radiation interception and reduced emission of longwave radiation from the canyon surfaces due to the lower surface temperatures. On the contrary, at night the higher presence of street trees is expected to create minor thermal discomfort due to higher emission of longwave radiation

downwards.
BEP-Tree arises as an adequate tool to perform studies on the impact of street trees on the human thermal comfort during hot, dry conditions in highly-compact neigbhourhoods, since this model incorporates a reliable representation of the effect of street trees on the street climate and radiation. Further implementations in BEP-Tree should focus in integrating the mean radiant temperature calculation in the model, in order to assess all the meteorological forcings that drive influence in the thermal comfort during hot and dry periods.

Chapter 3

The impacts of street trees on outdoor thermal stress during a heat wave in a highly-compact city

Abstract: Street trees are contemplated as a potential solution for mitigating heat in highly-compact cities due to their capacity to provide shading and transpirative cooling, key mechanisms in the cooling of air and the reduction of the human thermal stress. However, the meteorological conditions found during strong heat stress events as heat waves, such as the high temperatures and water stress can compromise the capacity of street trees to provide these thermal benefits. In this study, we determine the capacity of street trees in mitigating urban heat and reducing human thermal stress during heat wave events in highly-compact cities under moist and dry soil conditions. Using a modified version of the Building Effect Parameterization with Trees (BEP-Tree) model, we conduct a case study in Barcelona (Spain), comparing two neighbourhoods with different tree densities during a summer month encompassing a heat wave. We include a mean radiant temperature (T_{MRT}) calculation and a vertical soil moisture model in BEP-tree, allowing the study of thermo-physiological heat stress indices like the Universal Thermal Climate Index (UTCI) during water stress episodes. The results highlight the substantial impact of street trees in reducing near-surface air temperatures and T_{MRT}, particularly under moist soils. On average, street trees lowered midday/mid-afternoon air temperatures by 0.7 ± 0.4 ºC and T_{MRT} by 4.9 ± 2.8 ºC in hotter areas, leading to UTCI reductions up to 0.9 – 1.2 ºC. However, accounting for the dry soil conditions found during the heat wave event, the cooling effect of street trees on air temperatures was notably diminished, and in some periods even presenting higher air temperatures (0.2 ± 0.3 ºC higher) compared to neighbourhoods with sparser tree cover. Nevertheless, minimal impacts on the T_{MRT} effect from preserved tree shading and a reduction of transpiration-related humidity, still enabled street trees to reduce the UTCI, up to 0.5 – 0.8 ºC. This research emphasizes on the critical role of soil moisture in maximizing the cooling capabilities of street trees during extreme heat events. Effective street trees management in highly-compact cities should prioritize maintaining optimal soil water conditions to ensure tree health and that street trees consistently provide their microclimatic benefits, particularly during periods of strong heat stress.

3.1 Introduction

Street trees are a potential solution for mitigating heat in highly-compact cities characterized by limited areal coverage but high building density. They can be integrated seamlessly into urban planning (Baró et al., 2019) compared to larger urban green infrastructures. Street trees contribute to reducing urban air temperatures through transpiration and shading, thereby decreasing radiation absorption by surfaces such as the ground and building walls (Bowler et al., 2010). Several studies explore the impact of street trees on the urban heat island effect (UHI) at the local scale (Loughner et al., 2012) and human thermal stress at the microscale (Shashua-Bar and Hoffman, 2000; Coutts et al., 2016; Huang et al., 2020; Jia and Wang, 2021; Miao et al., 2023). The magnitude of daytime cooling by street trees depend on shading amount, street canyon geometry, and local meteorological conditions (Coutts et al., 2016). Street trees in low-rise neighbourhoods were highly effective in reducing daytime thermo-physiological heat stress indices in the city of Melbourne (Australia) (Coutts et al., 2016), such as the Universal Thermal Climate Index (UTCI) (Jendritzky et al., 2012), due to the reduction of mean radiant temperature (T_{MRT}) from shading. T_{MRT} is a crucial factor in thermo-physiological heat stress (Middel and Krayenhoff, 2019), because it determines the effect of shortwave and longwave radiation exposure on the human body (Jia and Wang, 2021). Huang et al. (2020) reported air temperature reductions of up to 3.3 ºC and T_{MRT} reductions of up to 13.9 ºC when comparing microclimatic measurements inside a tree-covered street in Wuhan, China, with a similar street lacking tree shade. Jia and Wang (2021) studied thermal stress variability in a high-density urban area in Hong Kong under various heat mitigation strategies using a micro-scale computation fluid dynamics model. They found that the largest reductions in T_{MRT} and UTCI were achieved with the street trees strategy, with peak reductions of 4.23 ºC and 0.88 ºC during daytime, respectively.

However, uncertainty surrounds the capacity of street trees to cool air and reduce human thermal stress during extreme heat events, which can impact physiological processes and structural components of trees (Qu et al., 2024). The warmer urban temperatures, compared to their rural surroundings, intensify during heat waves due to non-linear interactions (Li and Bou-Zeid, 2013), heightening heat stress on urban vegetation and citizens.While heat stress may increase water evapotranspiration from tree leaves and soil when water is not limited (Drake et al., 2018), heat events are often accompanied by droughts. Droughts restrict soil water availability, limiting transpiration and prompting the closure of the stomata on the surfaces of leaves to prevent further soil water depletion and reduce the risk of "hydraulic failure" in plants (McDowell et al., 2008). Soil water availability can be a crucial factor in the capacity of trees to mitigate thermal stress, though other factors such as drought occurrence, irrigation restrictions, and high urban surface impermeability can compromise the retention of water in the soil, and consequently, affecting tree transpiration (Coutts et al., 2016). Understanding the complex interactions of street trees during heatwaves is crucial for supporting their management and implementation in highly-compact cities, particularly in regions where heat waves are projected to increase due to climate change, such as the Mediterranean region (Giorgi and Lionello, 2008).

In order to understand the complexities of urban geometry and urban vegetation on the human thermal stress inside street canyons, diverse microscale computational fluid dynamic models (Perini et al., 2017; Jia and Wang, 2021) have integrated the estimation of several meteorological variables that affect thermal stress. These models represent the motion of air around explicitly resolved buildings and trees with three spatial dimensions, along to the energy balance of multiple surfaces, and the spatial variability of wind speed and longwave and shortwave radiation. These models are very expensive computationally and are limited spatially to represent one urban block or a small neighbourhood during short periods of time (Martilli et al., 2023). By contrast, urban canopy models (UCMs) simulate the interactions between buildings and the urban canopy layer atmosphere at a neighbourhood scale, and are suitably efficient for the coupling with mesoscale atmosphere models to study the effects of urban areas and urban heat mitigation strategies at larger scales (Chen et al., 2011). Recently, Martilli et al. (2023) developed a methodology to quantify the spatial variability of wind speed and T_{MRT} within the UCM Building Effect Parameterization and Building Energy Model (BEP-BEM) (Martilli et al., 2002; Salamanca and Martilli, 2010), to provide a range of variability of thermal exposure in urban grids of mesoscale atmosphere models. Although, this BEP-BEM version can represent the impact of street trees on the thermal exposure and shading, based on a simple approach proposed by Stone et al. (2021), BEP-BEM does not consider the impact of street trees on the wind flow and longwave radiation exchange and oversimplifies the estimation of the tree's transpiration.

Alternatively, BEP-Tree model (Krayenhoff et al., 2020) is a multi-layer UCM that accounts for the integrated effects of streets trees on the neighbourhood-scale climate, in terms of radiation exchange, energy balance, wind drag, turbulence and pedestrian level climate. BEP-Tree has been evaluated and improved for the representation of the meteorology during summer days in highly-compact cities, specifically the Mediterranean coastal city of Barcelona (Spain) (Segura et al., 2022). However, BEP-Tree model in its standard version, does not estimate T_{MRT}, impeding on its application for the derivation of comprehensive thermo-physiological heat stress indices to analyse the impact of street trees on the human thermal stress. Moreover, BEP-Tree does not include the hydrology of permeable urban soil and omits the impacts of soil water availability on tree transpiration, limiting the ability of the model to study the impacts of heat waves on the cooling capacity of street trees. The assessment of the cooling capacity and the reduction of the human thermal stress of street trees during extreme heat events requires an UCM that properly integrates the effects of street trees at the pedestrian level climate, considering soil water availability impacts on the tree transpiration, and that computes the T_{MRT}, to derive heat stress indices.

This study aims to determine how street trees impact air cooling and human thermal stress during a heat wave event in a highly compact city. To achieve this aim, we simulate, using a modified version of BEP-Tree, the evolution of local and microclimatic conditions inside two neighbourhood configurations with different tree densities but similar geometry in the Mediterranean coastal city of Barcelona (Spain). The simulations encompass a hot summer month between 25th June 2015 and 25th July 2015, containing a heat wave event (4 to 7 July 2015).

To allow the analysis of thermal stress with BEP-Tree, a mean radiant temperature calculation is implemented in the model, allowing an assessment of the spatial variability of the T_{MRT} and UTCI, while a vertical soil moisture model is also implemented to evaluate tree-soil moisture interactions. First, we evaluate the impacts of heat only, and subsequently compound heat and water stress, on the individual climatic factors affecting thermal stress (i.e., air temperature, specific and relative humidity and T_{MRT}). Second, we evaluate the impacts on human thermal stress using UTCI. This study aims to support the management and implementation of street trees in highly-compact cities addressing the abatement of heat during summer.

3.2 Methodology

3.2.1 BEP-Tree model

In this study, the BEP-Tree model with the new turbulent wind speed parameterization described in Section 2.2.1 is used.

Mean radiant temperature and UTCI variability in urban canyons

This study implements a method for computation of the mean radiant temperature in the BEP-Tree model, following a methodology similar to that described in Martilli et al. (2023). The T_{MRT} quantifies the radiation flux absorbed by human bodies, encompassing both shortwave and longwave radiation. Calculating the T_{MRT} experienced by a pedestrian within a street involves consideration of several factors. These include whether the pedestrian is in direct sunlight, shadowed by a building or tree, and the distance from warm surfaces emitting longwave radiation and reflecting incident solar radiation. Consequently, T_{MRT} within streets canyons exhibit significant spatial variability, influenced by the distance from building walls and the presence of shadows from trees or buildings. To capture this variability within each neighbourhood, the updated version of BEP-Tree computes T_{MRT} at 12 different positions within simulated canyons. Initially, T_{MRT} is computed separately for the case of locations directly under tree crowns and the case of those locations that are not under tree crowns. For each case, T_{MRT} is assessed at the street centre and at a distance of 1.5 m from each building wall on each street side, representing the sidewalks. This results in six T_{MRT} values for each street orientation (three for each case). Additionally, BEP-Tree represents two street canyon orientations (i.e. North-South and East-West) with similar building height distributions and identical street widths, doubling the number of positions to 12 (six for each canyon orientation).

For locations not beneath the tree crowns, the computation involves estimating direct shortwave radiation from the sun and the reflection from walls and ground, along with the emitted and reflected longwave radiation from canyon surfaces that reaches the pedestrian. This is achieved using the view factors and shading routines outlined in Martilli et al. (2023). The methodology is applied to determine the total shortwave and longwave radiation reaching a vertical segment, 1.80 m tall, representing a person, at the six designated locations within the two streets, as in

Martilli et al. (2023). The pedestrian is modelled as a transparent surface for radiation, implying that its presence has no impact on the radiation incident to the walls and ground. In locations directly under the tree canopy, view factors and shading routines are similarly computed, but assuming that trees completely cover the sky and the wall above a specified height ($z_{midtree}$) where the middle of the tree foliage is located (i.e., trees are assumed to have relatively high leaf area density). The longwave radiation reaching the vertical segment (i.e. pedestrian) originates from trees, walls below $z_{midtree}$, and the ground. While the direct and diffuse shortwave radiation incident on the segment resembles the previous case, it is attenuated using the Beer-Lambert-Bouguer law in Equation 2.1. T_{MRT} is derived using a six-directional weighting method (Middel and Krayenhoff, 2019). Radiation from four horizontal directions is weighted at 0.22 each, and two vertical directions (upward and downward) at 0.06 each, assuming that lateral radiation has a greater influence on a standing person. Considering BEP-Tree as a two-dimensional model representing streets with infinite length, the lateral weightings are aggregated into two lateral weightings of 0.44, each from a different side of the vertical segment facing each side of the street. Thus, T_{MRT} for each of the 12 locations is derived as follows:

$$T_{MRT} = \sqrt[4]{\frac{\sum_{i=1,4} W_i(a_k K_i + a_L L_i)}{a_L \sigma}} \tag{3.1}$$

where, for a street oriented in the East-West direction, i=1,2 are for the vertical sides of the pedestrian looking at North and South, respectively, and i=3,4, are for the upward and downward directions. Then, $W_{1,2}$ = 0.44, $W_{3,4}$ = 0.06, a_K = 0.7 being the coefficient of absorption of shortwave radiant flux densities, a_L = 0.97 being the coefficient of absorption of longwave radiant flux densities, $K_{1,2}$ and $L_{1,2}$ are the shortwave and longwave radiation fluxes reaching the vertical segment laterally, $K_{3,4}$ and $L_{3,4}$ are the shortwave and longwave radiation fluxes reaching the top and bottom of the segment, respectively, and σ is the Stefan-Boltzmann constant.

To depict the variability in the UTCI, computations are performed separately for locations under tree crowns and those outside, involving six T_{MRT} values (as detailed earlier), three air temperature values, and three wind speed values. The wind speed values are derived from BEP-Tree and undergo the methodology outlined in Martilli et al. (2023), incorporating parameterizations obtained from computational fluid dynamic models to represent airflow variability. For air temperature, a variation of plus/minus 1 ºC is applied to values obtained from the BEP-Tree model, as computational fluid dynamic simulations lack microscale representation of temperature variability. This value aligns with a realistic estimate of the variability observed in urban neighbourhoods.

While no variability is considered for absolute humidity, variation in relative humidity is incorporated via the three air temperature values. This results in 54 possible combinations of T_{MRT}, wind speed and air temperatures, each combination producing a unique UTCI value. Both scenarios, under tree crowns and outside tree crowns, share identical air temperature and wind speed values but differ in T_{MRT} values, yielding two sets of 54 UTCI estimates.

To combine these UTCI values, the variable $\lambda_{v,can}$, representing the fraction of plan area cover-

age of tree crowns inside the street canyon is used. The two distributions of UTCI values are combined by selecting $\lambda_{v,can}$*100 percentiles (rounded to the nearest integer) from the distribution obtained under tree crowns and 100-$\lambda_{v,can}$*100 percentiles from the distribution obtained outside tree crowns (see Figure 3.1). The selected percentiles are centred around the 50th percentile. This approach results in a combination of 100 UTCI values maintaining the distributions of each set, while simultaneously distributing them within tree-shaded and non-tree-shaded areas using the $\lambda_{v,can}$ variable. From this resulting distribution, the percentiles 10th, 50th, and 90th are estimated to represent the cold, median and hot spots for thermal stress within each neighbourhood.

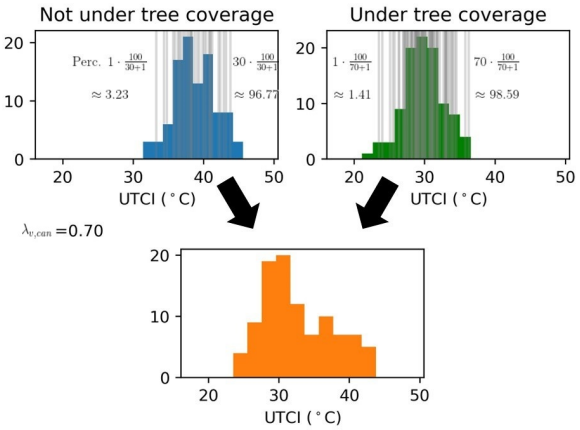


Figure 3.1: Schematic diagram of the methodology used for the creation of the UTCI distribution, based on the combination of the distributions of UTCI values estimated in the locations under tree coverage and not under tree coverage. In this example, $\lambda_{v,can}$ = 0.70, implying that 70 values are selected from the distribution under tree coverage, and 30 from the other. The values are selected according to the percentiles (grey vertical lines), $i \cdot 100/(n+1)$, where i ranges between 1 to n=70 for the distribution under tree coverage, and between 1 to n=30 for the other. In the plots, the value of the first and last percentiles used for each distribution is marked.

Soil moisture vertical diffusion model

In order to derive the temporal evolution of soil moisture and temperature in the permeable soil inside the street bottom, a prognostic multi-layer soil model is implemented in BEP-Tree based on the bare soil scheme used in the Regional Atmospheric Modeling System (RAMS) described by Tremback and Kessler (1985). This model assumes a finite depth soil/atmosphere interface layer to derive the prognostic equations for soil temperature and moisture. The soil model implemented presents 13 vertical layers from 1 cm depth down to 2 m in depth. The soil moisture diffusivity (D_η) ($m^2\,s^{-1}(m^3m^{-3})^{-1}$), hydraulic conductivity (K_η) ($m\,s^{-1}$), and moisture potential (Ψ_η) (m), are formulated by:

$$D_\eta = \frac{-bK_f\Psi_f}{\eta}\left[\frac{\eta}{\eta_f}\right]^{b+3}$$

$$K_\eta = K_f\left[\frac{\eta}{\eta_f}\right]^{2b+3} \tag{3.2}$$

$$\Psi_\eta = \Psi_f\left[\frac{\eta_f}{\eta}\right]^{b}$$

where η is the soil moisture content with units of volume of water per volume of soil (m^3m^{-3}), K_f ($m\,s^{-1}$), Ψ_f (m), and η_f (m^3m^{-3}) are the hydraulic conductivity, moisture potential and soil moisture content at saturation which depend on the soil texture class. The constant b also depends on the soil texture.

The volumetric specific heat (C_s) ($J\,m^{-3}K^{-1}$) and the thermal diffusivity (λ_s) ($m^2\,s^{-1}$) define the thermal properties of the soil and depend on the soil moisture, and the previous properties, being derived for each soil layer as follows:

$$C_s = (1-\eta)C_d + \eta C_w$$

$$\lambda_s = \frac{e^{-[log_{10}|\Psi|+2.7]}}{C_s} * 4.186 * 10^7,\ log_{10}|\Psi| \leq 5.1 \tag{3.3}$$

$$\lambda_s = \frac{0.00041}{C_s} * 4.186 * 10^7,\ log_{10}|\Psi| > 5.1$$

where C_d and C_w are the specific heat of dry soil and water, respectively. The heat in soil is diffused as follows:

$$\frac{\partial\theta_s}{\partial t} = \frac{\partial}{\partial z}\left[\lambda_s\frac{\partial\theta_s}{\partial z}\right] \tag{3.4}$$

where θ_s is the potential temperature of the soil (K). The boundary conditions for this model are that the potential temperature in the lower layer is held constant at the initial value, while the potential temperature in the ground surface layer varies with the following prognostic equation:

$$D_s\Delta z_g\frac{\partial\theta_g}{\partial t} = \alpha_g K\downarrow + L\downarrow - \sigma\theta_g^4 + \rho_a C_p u_\star\theta_\star + \rho_a C_p u_\star r_\star - C_s\lambda_s\frac{\partial\theta_s}{\partial z}\,|_g \tag{3.5}$$

where $K\downarrow$ and $L\downarrow$ are the downward shortwave and longwave radiation fluxes in the ground surface, α_g is the soil albedo, $\rho_a C_p u_*\theta_*$ is the sensible heat flux to the atmosphere, $\rho_a C_p u_* r_*$ is the latent heat flux resulting from direct soil evaporation, Δz_g is the depth of the top soil layer.

The soil moisture diffusion is computed in all the soil layers using the following equation:

$$\frac{\partial\eta_s}{\partial t} = \frac{\partial}{\partial z}\left[D_\eta\frac{\partial\eta}{\partial z} + K_\eta\right] \tag{3.6}$$

The soil moisture in the ground surface and bottom layers are derived using the following prognostic equations:

$$\frac{\partial \eta_g}{\partial t} = \frac{(\rho_a u_* r_* / \rho_w) - D_\eta \frac{\partial \eta}{\partial z} - K_\eta}{\Delta z_g}$$
$$\frac{\partial \eta_b}{\partial t} = \frac{(nf/\rho_w) + D_\eta \frac{\partial \eta}{\partial z} + K_\eta}{\Delta z_b} \quad (3.7)$$

where nf is the latent heat flux resulting from the transpiration from trees, ρ_w is the water density, and Δz_b is the depth of the bottom soil layer. In this methodology, evaporation is taken from the topsoil layer, while tree's transpiration is extracted from the bottom layer, simulating the long roots of urban trees, which can reach water from deep water tables, especially in high compact cities with limited tree pits. This model does not include rain as this parameterization would require of more complex assumptions than just rather increasing the soil moisture in the top layer. This scheme is suitable for studying episodes with no precipitation. The sensible heat and latent heat fluxes from the street ground, and the street ground surface temperature are averaged between the impervious and pervious fractions of the soil using the variable *a_perv*, defined as the street width section covered by pervious soil.

To represent the impact of soil moisture depletion on tree transpiration we apply a new factor (F_4) in the leaf stomatal conductance (g_{vs}) to determine the effect of soil moisture based on Chen and Dudhia (2001).

$$g_{vs} = g_{vs,max} F_1 F_2 F_3 F_4$$
$$F_4 = \sum_{i=1}^{13} \frac{(\eta_i - \eta_w)\Delta z_i}{(\eta_{ref} - \eta_w)\sum_{i=1}^{13} \Delta z_i} \quad (3.8)$$

where $g_{vs,max}$ is species-dependent maximum stomatal conductance, and F_1, F_2, and F_3 are coefficients between 0 and 1 that represent the effect of photosynthetically-active radiation, vapour pressure deficit and air temperature on the opening of stomata (Chen and Dudhia, 2001). η_w and η_{ref} are the field capacity and wilting point of the soil and depend on the soil texture class.

3.2.2 Study area and period of study

The area of study is the Eixample district of the city of Barcelona, as it is described in Section 2.2.2, using the same two streets. To extend the results from the street scale to the neighbourhood scale, avoiding possible effects of wind direction with respect to the streets orientation (Segura et al., 2022), the two street orientations predominant in the Eixample district are used in BEP-Tree model, despite the two streets are oriented from Southeast to Northwest. We assume that the building height distribution and tree properties and densities in the perpendicular streets to the Aribau and Balmes streets are equal to the measured ones in those streets. Then, from now on, the Sparse trees and Dense trees terms refer to the small neighbourhoods or urban blocks from the combination of two perpendicular street orientations with the same building heights and tree properties as the Balmes and Aribau streets. In both cases, the pervious section of the street ground is limited only to the tree pits, covering only a 1 % of the street surface (*a_perv*=0.01).

The study period spans from the 25th June 2015 to the 25th July 2015, although the BEP-Tree simulations start 5 days before (00 UTC 20 June 2015) for model spin-up. This period is characterized by persistent high temperatures in the city of Barcelona. According to the observations from the nearest meteorological station from the Meteorological Service of Catalonia, in the Raval neighbourhood, the maximum daily temperatures were not lower than 27 ºC for all the days in the study period except the first one, and the mean daily temperatures were well above 25 ºC during the whole month. Air temperatures reach a maximum of 35 ºC during a heatwave that spanned from the 4 July 2015 to 7 July 2015. Night-time temperatures were also considerably high with minimum temperatures above 24 ºC over almost the entire period, and some nights with temperatures higher than 27 ºC. No precipitation was observed during the entire period.

3.2.3 Model simulations

In order to study the impacts of street trees on air-cooling and human thermal stress during a heat wave event, four simulations are conducted with BEP-Tree. First, two simulations are conducted for Sparse trees and Dense trees neighbourhood without the soil moisture model implemented in BEP-Tree, assuming an infinite availability of moisture in the soil and the trees evapotranspiring the maximum they can. We refer to these simulations as the moist soil case. Moreover, two additional simulations are conducted including the soil moisture and temperature vertical diffusion model with BEP-Tree and the interactions between soil moisture and trees representing a realistic value of soil moisture, with initial conditions obtained from Weather Research and Forecasting (WRF) model simulations for the same study period (Segura et al., 2021). We refer to these simulations as the dry soil case. Based on the differences of the four simulations, the decoupled impacts of heat and water stress from the heat wave event on the street trees can be analysed, evidencing the relative contribution of the different tree mechanisms for air-cooling and thermal stress reduction.

The vertical resolution of the model is 1 m, while the maximum vertical level with buildings is 35 m for Sparse trees and 30 for Dense trees, and the model upper boundary is at 70 m from the ground, approximately two times the height of the highest buildings. The initialization of the urban surface thermal properties has been based on the properties of the most common construction materials of the study area, while the leaf area density and tree crown and height have been computed from LiDAR data and airborne photos of the canyon, as are detailed in (Segura et al., 2022).

The meteorological forcing at the top boundary is obtained from the meteorological observations in the Raval station, at 2.0 km from the study area (see Figure 2.1). This station, placed over a building rooftop at 21 m over the street ground level, records 10 m (above roof top) wind speed and direction, 2 m (above roof top) air temperature, relative humidity, air pressure and solar irradiance. Wind speed, air temperature and air pressure are corrected to estimate the value at 70 m using the methods described in Section 2.2.4.

3.3 Results

3.3.1 Road surface and air temperatures

The modelled surface temperatures and pedestrian-level air temperatures illustrate the pronounced impact of street trees on air and surface cooling in this dense neighbourhood, particularly during the periods of heightened heat stress when the soil moisture effects are not considered (i.e., soil moisture maintained at constant field capacity). In Figure 3.2a, we compare the diurnal cycle of road surface temperatures between Dense trees and Sparse trees neighbourhoods, both with and without soil moisture effects (i.e., dry and moist soils). When soil moisture effects are not considered, this analysis reveals that denser trees lead to a reduction in daytime road surface temperatures by up to 3.0 ºC at 11 UTC (13 local time). The average reduction is 2.6 ± 0.7 ºC (the error corresponds to the standard deviation in the study period) during midday/mid-afternoon (between 9-15 UTC, for Barcelona, UTC equals the local solar time). The differences in midday/mid-afternoon road surface temperatures between the two neighbourhood configurations exhibit slight variations over the study period, as depicted in Figure 3.1b, with a maximum difference of 3.2 ºC during the heat wave. However, with dry soil, both neighbourhood configurations experience increased daytime and night-time road surface temperatures relative to the cases with ample soil moisture, with higher increases noted in Dense trees during midday/mid-afternoon. Consequently, the maximum reductions in road surface temperatures by the denser trees during the day reaches only 2.4 ºC.

Street trees exert a minor influence on the diurnal cycle of air temperatures compared to road surface temperatures, as shown in Figure 3.2c. With moist soils, they reduce air temperatures by up to 1.1 ºC at 8 UTC, and Dense trees neighbourhoods consistently exhibit significantly lower temperatures, averaging 0.7 ± 0.4 °C lower during midday/mid-afternoon (see Figure B.1 in the Appendix B). Street trees display a heightened capacity to lower pedestrian-level air temperatures during heatwave episode with moist soils (Figure 3.2d), with greater reductions found at midday/mid-afternoon (1.2 ± 0.4 ºC) compared to non-heat wave days (0.6 ± 0.4 ºC). On day 5 July (see Figure 3.2d and Figure B.1), the maximum air temperature modelled in Dense trees (35.3 ºC) is 1.4 ºC lower than the maximum temperature in Sparse trees (36.7 ºC). The air-cooling effect of street trees persists even during nighttime (20-5 UTC), presenting temperature reductions of 0.5 ± 0.1 ºC throughout the study period. However, the impact of soil moisture on the air-cooling capacity of street trees is more pronounced than on the surface temperature cooling. With dry soils, midday/mid-afternoon air temperatures increase compared to moist conditions by 1.2 ± 0.3 ºC in Dense trees, and by 0.4 ± 0.1 ºC in Sparse trees, resulting in a slightly higher air temperature of 0.2 ± 0.3 ºC in Dense trees compared to Sparse trees (Figure B.1).

Over the heat wave episode (Figure 3.2d), neighbourhoods with dry soils present higher average temperatures during the midday/mid-afternoon (up to 35.3 ºC Sparse trees, and 35.1 ºC Dense trees), compared to the neighbourhoods with moist soils (up to 34.8 ºC Sparse trees, and 33.2 ºC Dense trees). The higher increase in air temperature during midday/mid-afternoon in the Dense trees neighbourhood, as a consequence of dry soils, is attributed to a reduction in tree evapotranspiration (Figure 3.3a), where latent heat fluxes decrease by more than half due to a

reduction in stomatal conductance by soil moisture effects (Figure 3.3b). This findings accords with recent modelling demonstrating that non-transpiring leaves, which have little heat capacity, would warm the air (Meili et al., 2021), primarily because they shed most of the heat they absorb from shortwave radiation via sensible heat. Critically, this finding will depend on the height of the leaves absorbing shortwave radiation relative to the pedestrian layer, and the turbulent transport of heat between these layers. Unlike Meili et al. (2021), the current modelling resolves all of these air layers and associated turbulent transport, and thus supports the finding that for the moderate-height trees simulated here, non-transpiring leaves can warm the pedestrian air layer during daytime.

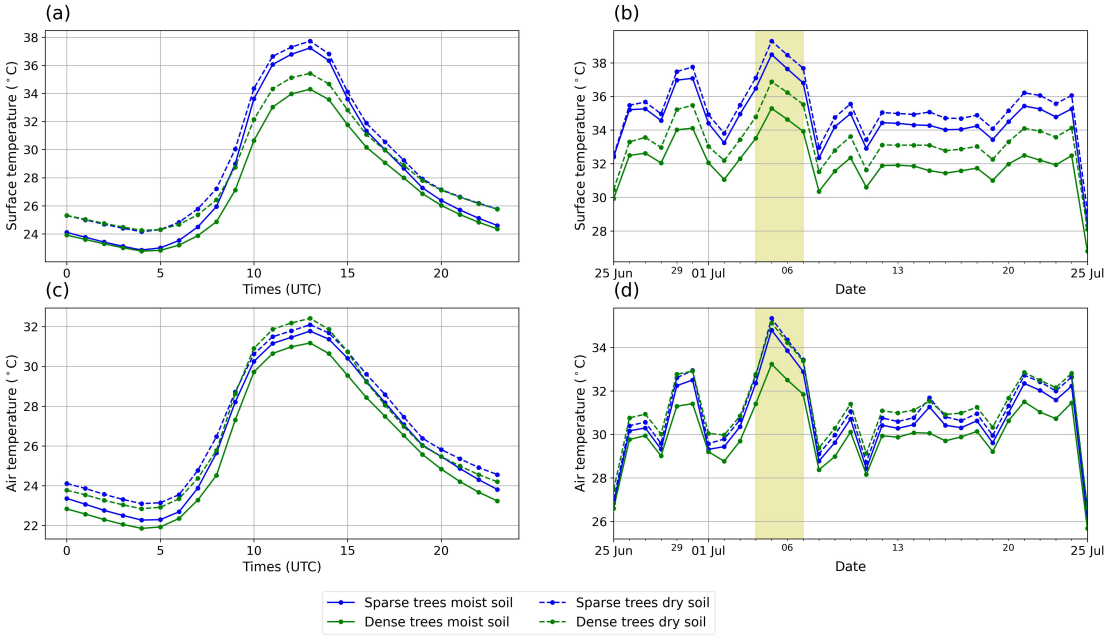


Figure 3.2: BEP-Tree modelled diurnal cycles (left) and midday/mid-afternoon (between 9-15 UTC, 11-17 LT) averages in the study period of the canyon-averaged road surface temperatures (upper row), and air temperatures (at 1.5 m height from the ground) (lower row) for the Sparse trees (blue) and Dense trees (green) neighborhoods with moist soil, and dry soil. The yellow rectangles in subplots (b) and (d) indicate the heat wave period (4-7 July).

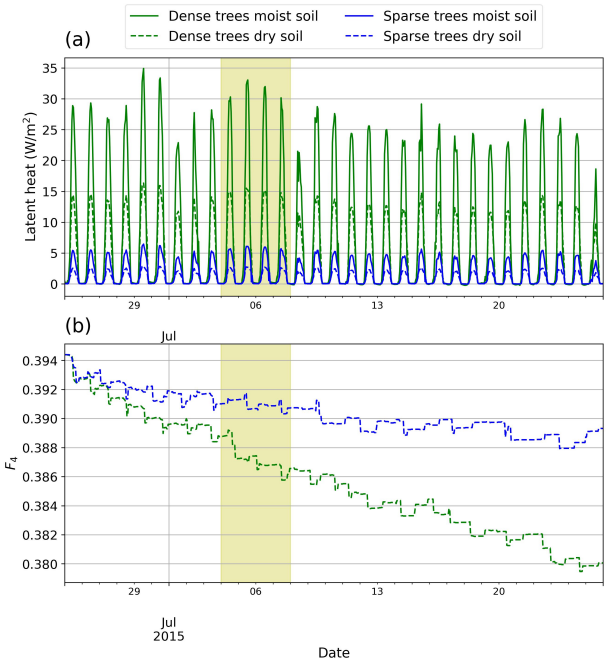


Figure 3.3: BEP-Tree modelled vertically averaged tree latent heat flux (a) for the Sparse trees (blue) and Dense trees (green) neighborhoods with moist soil and dry soil, and (b) F_4 coefficient of the soil moisture impact on stomatal conductance.

3.3.2 Relative humidity and specific humidity

The evapotranspiration mechanism of street trees increases the specific humidity of air during the daytime for Dense trees in comparison to Sparse trees (Figure 3.4a). This increase reaches up to 2.4 $g\,kg^{-1}$ for moist soils (at 17 UTC), and up to 1.4 $g\,kg^{-1}$ for dry soils (at 8 UTC). The larger differences in midday/mid-afternoon specific humidity during the study period are found during the heat wave episode, when Dense trees presents up to 3.5 $g\,kg^{-1}$ higher specific humidity than Sparse trees with moist soil, and only 1.2 $g\,kg^{-1}$ with dry soil (Figure 3.3b). The combined impact of increased specific humidity and reduced temperature in near-surface air for denser street trees results in higher relative humidity, reaching up to 13.2 % higher in Dense trees (at 8 UCT) and averaging 7.8 ± 3.8 % higher during midday/mid-afternoon with moist soils (Figure 3.4c). During the night, street trees increase relative humidity by 5.3 ± 4.0 % on average. In the case of dry soils, the reduction in differences in air temperature and specific humidity narrows the relative humidity gap between the two neighbourhoods during midday/mid-afternoon to an average of 1.5 ± 1.1 %. Throughout the study period (Figure 3.4d), under moist soil conditions, the relative humidity differences between the two neighbourhoods present higher differences during midday/mid-afternoon on heat wave days (11.6 ± 5.7 %) than on non-heat wave days (7.2 ± 3.1 %). Conversely, when dry soils are considered, the differences in relative humidity between heat wave (3.3 ± 4.2 %) and non-heat wave days (1.2 ± 1.7 %) are less pronounced. Even though, street trees still increase nighttime relative humidities by 2.5 ± 1.5 % on average.

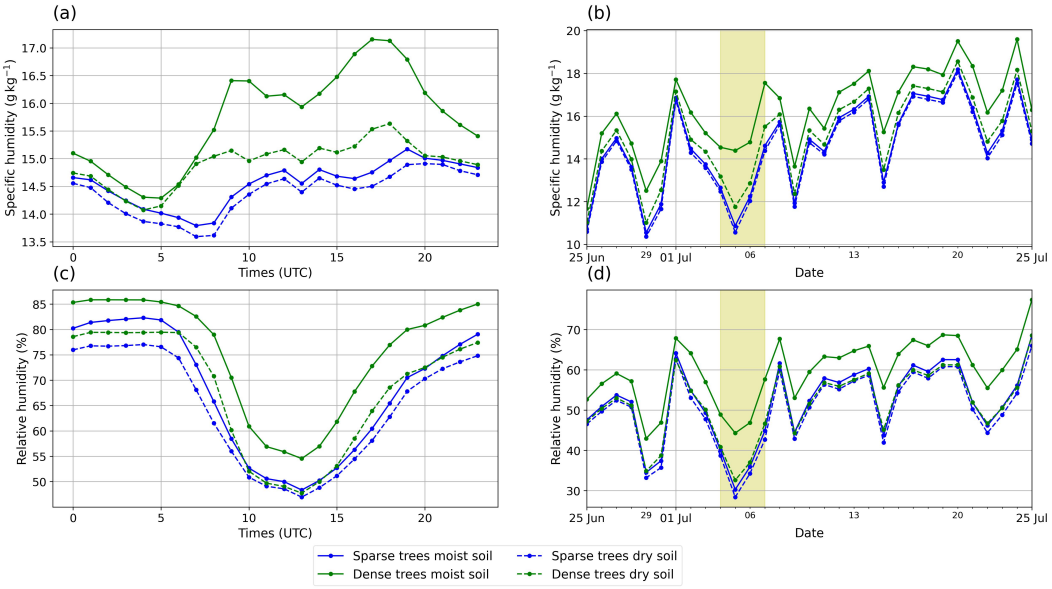


Figure 3.4: BEP-Tree modelled diurnal cycles (left) and midday/mid-afternoon (between 9-15 UTC, 11-17 LT) averages in the study period of the air specific humidity (at 1.5 m height from the ground) (upper row), and relative humidity (lower row) for the Sparse trees (blue) and Dense trees (green) neighborhoods with moist soil and dry soil. The yellow rectangles in subplots (b) and (d) indicate the heat wave period (4-7 July).

3.3.3 Mean radiant temperature

Street trees have an impact on T_{MRT} by two different mechanisms. Firstly, they decrease canyon surface temperatures beneath the tree crown during the day by providing shade. This reduction is attributed to decreased longwave radiation emissions from building walls and ground surfaces, as well as diminished absorption by pedestrians. Figure 3.5a illustrates this cooling effect by comparing T_{MRT} variability in two neighbourhood configurations with moist soils, computed in locations that are outside tree coverage. It is essential to note that although these locations are not under tree coverage, this only influences the amount of total shortwave radiation reaching the transparent segment, while the surface temperatures of walls and ground reflect the average effects of tree shading. This mechanism results in a decrease in T_{MRT} in the hotspot (street location with highest T_{MRT}) by up to 2.9 ºC (at 11 UTC) and a reduction in the cold spot (street location with lowest T_{MRT}) by up to 3.9 ºC (at 12 UTC) (see Figure B.2). Notably, this cooling mechanism remains largely unaffected by soil moisture effects on trees (Figure 3.5b). Despite an increase in T_{MRT} with dry soils, the impact is consistent across locations and neighbourhoods, maintaining a maximum difference in T_{MRT} of 2.6 ºC in the hotspot and 3.4 ºC in the cold spot.

Secondly, street trees reduce solar radiation reaching pedestrians by providing shade and minimizing reflected shortwave radiation from walls and ground. The combined impact of these

mechanisms is evident in Figure 3.5c, showing spatial variability in T_{MRT} just under tree crowns. This results in a decrease in T_{MRT} in the hotspot and cold spot by up to 5.2 ºC (at 12 UTC) (Figure B.2). On average during midday/mid-afternoon, street trees decrease T_{MRT} experienced by pedestrians by 4.9 ± 2.8 ºC in the hotspot and by 3.1 ± 1.5 ºC in the cold spot.

Similar to the first mechanism, shading is not significantly affected by soil moisture (assuming no variations in tree phenology), maintaining differences in T_{MRT} in hotspots and cold spots of the two neighbourhoods during midday/mid-afternoon, of 4.4 ± 2.8 ºC in the hotspot, and by 2.6 ± 1.4 ºC in the cold spot of the locations under trees (see Figure 3.5d). During nighttime, the T_{MRT} increases in the location under trees compared to outside trees for Sparse trees (0.9 ± 0.2 ºC) and for Dense trees (0.2 ± 0.2 ºC), implying a warming effect of street trees during night, although the comparison between the two streets during night under trees yields lower T_{MRT} in Dense trees (0.8 ± 0.2 ºC lower) in Dense trees.

It is noteworthy that the peak in T_{MRT} coincides with the peak in solar radiation, occurring at 10 UTC (12 LT). The cold spot peak is reached at 12 UTC (14 LT) with high temperatures and sustained solar radiation. Analysing the spatial distribution of hotspots and cold spots (Figure B.3 in Appendix B, see Figure B.4 for locations), we observe that hotspots are primarily situated in the centre of the Northwest-Southeast oriented street and secondarily on the northern sidewalk of the same street in the morning before noon. After noon until sunset, the hotspot is located on mainly in the centre of the Northeast-Southwest oriented street and secondarily on the northern sidewalk. In contrast, cold spots exhibit higher dispersion, primarily on the northern and southern sidewalks of the Northeast-Southwest oriented street from dawn until noon and on the southern and northern sidewalks of the Northwest-Southeast oriented street from noon until sunset.

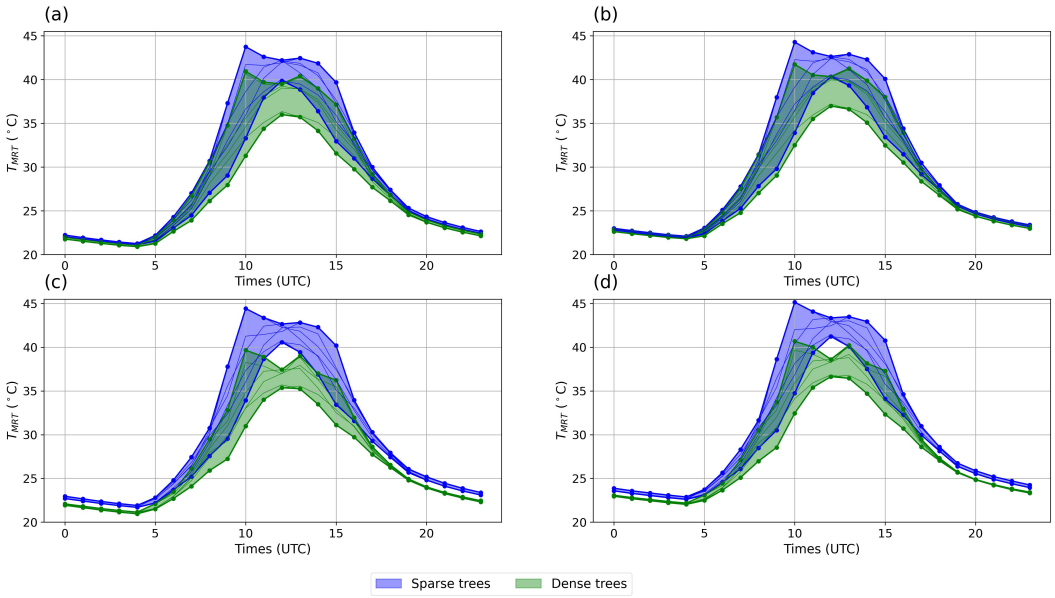


Figure 3.5: BEP-Tree modelled diurnal cycles of the mean radiant temperature (a) in the locations outside tree crown projections and moist soil, (b) the locations outside tree crown projections and dry soils, (c) the locations under tree crowns and moist soils, and (d) the locations under tree crowns and dry soils for the Sparse trees (blue) and Dense trees (green) neighborhoods. The shaded areas represent the range of variability of the T_{MRT} inside the neighborhoods.

The evolution of the midday/mid-afternoon T_{MRT} during the study period (Figure 3.6) highlights that the peak modelled T_{MRT} does not coincide with the heat wave event. Instead, it occurs on July 17, registering values of 47.3 ºC and 46.0 ºC for Sparse trees and Dense trees with moist soil, respectively, and 47.7 ºC and 46.7 ºC with dry soil. T_{MRT} in the hotspot during midday/mid-afternoon is predominantly influenced by solar radiation, azimuthal and zenith angles. Conversely, maximum values in the cold spot are observed during the heat wave (July 4 for moist soil and July 5 for dry soil), with average values of 39.8 ºC and 36.6 ºC for Sparse trees and Dense trees with moist soil, respectively, and 40.4 ºC and 37.6 ºC with dry soil. Furthermore, the disparity between the two streets in the cold spot is most pronounced during the heat wave with moist soils, reaching 3.5 ºC and 4.8 ºC outside the coverage of street trees and beneath the street trees, respectively (Figure B.5).

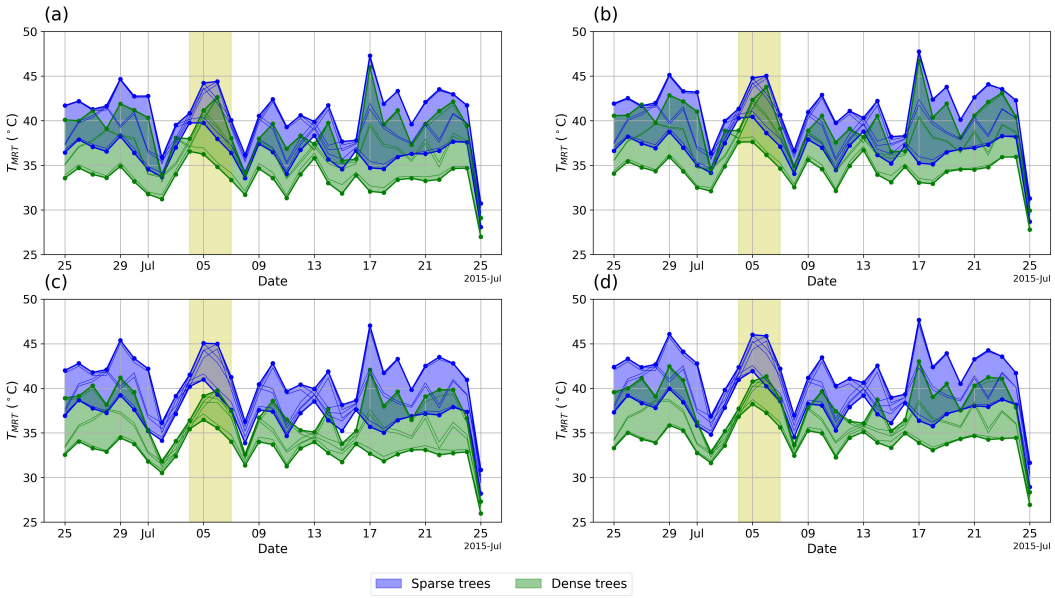


Figure 3.6: BEP-Tree modelled midday/mid-afternoon (between 9-15 UTC, 11-17 LT) averages in the study period of the mean radiant temperature (a) in the locations outside tree crown projections and moist soil, (b) the locations outside tree crown projections and dry soils, (c) the locations under tree crowns and moist soils, and (d) the locations under tree crowns and dry soils for the Sparse trees (blue) and Dense trees (green) neighborhoods. The shaded areas represent the range of variability of the T_{MRT} inside the neighborhoods.

3.3.4 Universal Thermal Climate Index

Human heat stress, as represented by the UTCI, relies on the interplay of various climate conditions — specifically, air temperature, T_{MRT}, wind speed and air humidity. These meteorological factors are influenced by street trees, which have both positive and negative effects on human thermal stress. Figure 3.7 shows diurnal profiles for the 10^{th} (cold spot), 50^{th} (median), and 90^{th} (hotspot) percentiles of the UTCI distribution within Sparse trees and Dense trees neighbourhoods, modelled by BEP-Tree.

Under moist soils (Figure 3.7a), the maximum UTCI for the 10^{th}, 50^{th}, and 90^{th} percentiles are observed at 33.8 ºC (at 12 UTC), 34.8 ºC (at 12 UTC) and 35.8 ºC (at 13 UTC) for Sparse trees, and 32.9 ºC (at 13 UTC), 33.9 ºC (at 13 UTC) and 34.9 ºC (at 13 UTC) for Dense trees. This results in a street tree effect, reducing UTCI by a maximum of 0.9 ºC (at 12 UTC), 1.1 ºC (at 12 UTC), and 1.2 ºC (at 14 UTC), for the 10^{th}, 50^{th}, and 90^{th} percentiles, respectively. During nighttime, street trees have a minimal effect, only being appreciable a non-significant decrease for the hotspot of 0.1 ± 0.2 ºC.

However, considering the effects of soil moisture on street trees, thermal stress increases in both neighbourhoods, minimizing the impact of street trees (Figure 3.7b). Under dry soil conditions, a maximum reduction of thermal stress between the two neighbourhoods is found to be of 0.5 ºC

(at 12 UTC), 0.6 ºC (at 12 UTC), and 0.8 ºC (at 14 UTC) for the 10th, 50th, and 90th percentiles, respectively. This implies that the impact of street trees reducing the thermal stress is only a 50-60 % during dry soil conditions, compared to the capacity under moist soil conditions.

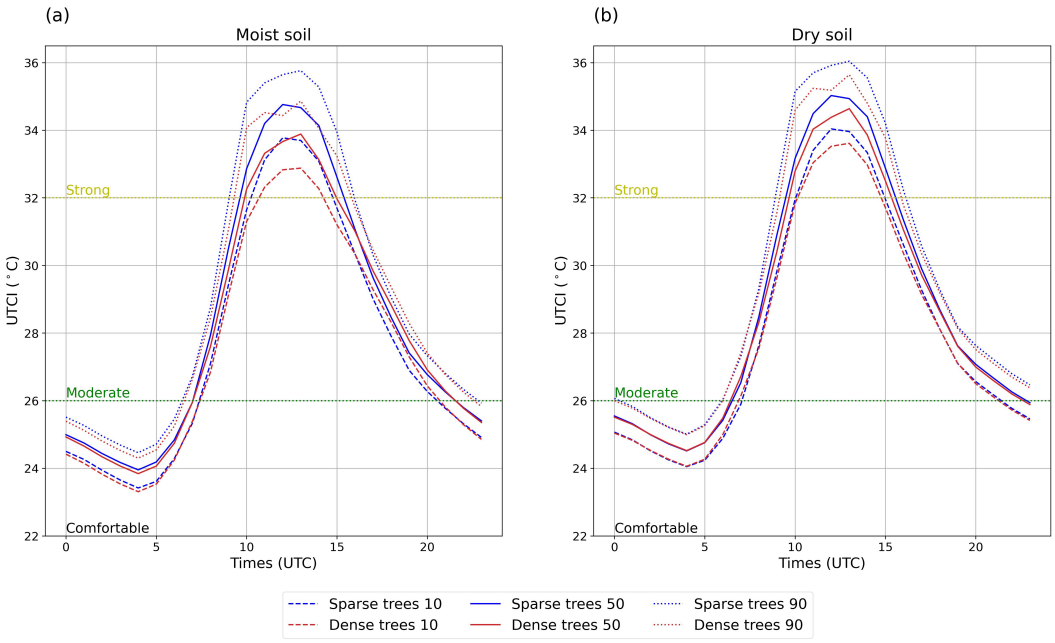


Figure 3.7: Average diurnal cycles for the UTCI for the comparison between Sparse trees (blue) and Dense trees (red) neighbourhoods (a) under moist soil, (b) under dry soils, for the 10th, 50th, and 90th percentiles. The horizontal lines represent the levels of thermal stress for the UTCI.

Concerning the effectiveness of street trees in alleviating thermal stress during a heat wave event (Figure 3.8), this depends on the percentile in the distribution of the UTCI, and the availability of water in the soil. The highest reductions in the cold spot (1.1 ºC) are observed at the beginning of the heat wave (July 4) and decrease constantly until the last day of heat wave (0.2 ºC). In the case of the median spot, the highest reductions (1.4 ºC) are seen during the day of highest air temperatures (July 5), decreasing also along the heat wave episode until reaching (0.3 ºC). For the hotspot, the highest reductions (1.7 ºC) are not seen during the heat wave episode, but rather on day July 1, although strong reductions are also seen during the first three days of the heat wave event (1.2-1.5ºC).

When considering the compounded effects of soil moisture and heat stress during the heat wave (Figure 3.8b), the maximum UTCI reductions from the street trees are reduced for the 10th (0.7 ºC), 50th (0.9 ºC) and 90th (0.9 ºC) percentiles. Even though, Dense trees generally exhibits lower thermal stress throughout the study period. Similar to the case of the whole study period, the impact of street trees reducing the thermal stress during the heat wave is only a 50-60 % during dry soil conditions, compared to the capacity under moist soil conditions.

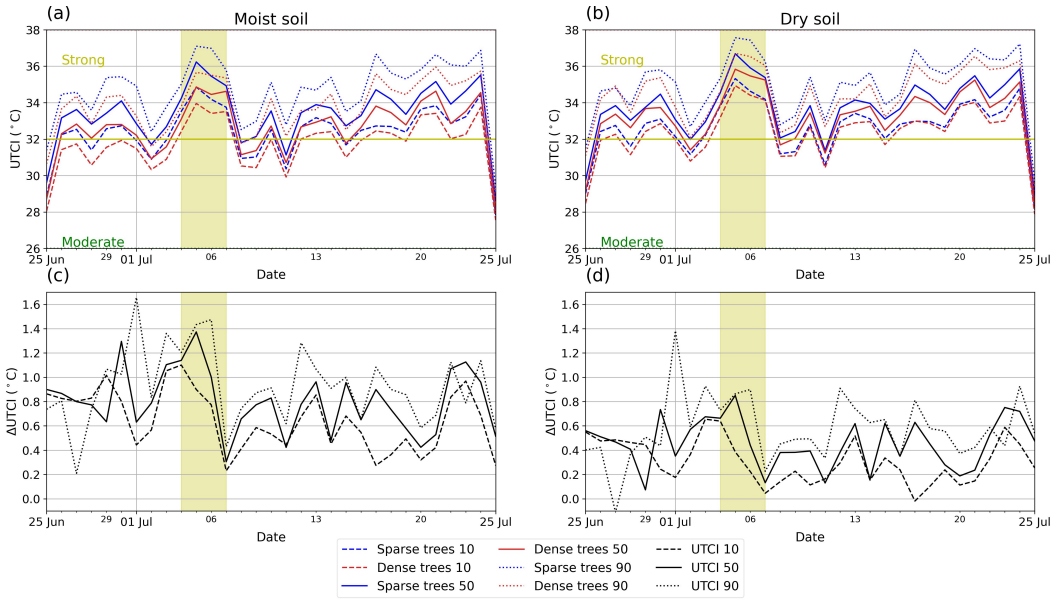


Figure 3.8: Average midday/mid-afternoon (between 9-15 UTC, 11-17 LT) UTCI for the comparison between Sparse trees (blue) and Dense trees (red) neighbourhoods (a) under moist soil, (b) under dry soils, (c) difference between Sparse trees and Dense trees with moist soil, (d) difference with dry soil, for the 10th, 50th, and 90th percentiles. The horizontal lines represent the levels of thermal stress for the UTCI.

3.4 Discussion

3.4.1 The impact of street trees on human thermal stress

The evaluation of street trees' impact on human thermal stress in densely populated Mediterranean climate cities during typical summer conditions reveals varied effects on climatic variables influencing thermal stress. In conditions of moist soil, dense trees exhibit an average reduction of near-surface air temperature by 0.7 ± 0.4 ºC during midday/mid-afternoon compared to sparser trees. These differences align with those reported in other studies focusing on the air-cooling effects of street trees in Mediterranean climates. For instance, Shashua-Bar and Hoffman (2000) observed cooling effects ranging from 1.3 to 3.3 ºC in Tel-Aviv (Israel), while Coutts et al. (2016) reported morning air temperature reductions of 0.9 ºC in Melbourne (Australia). Segura et al. (2022) found average temperature reductions during midday and afternoon of 1.3 ºC in the Dense trees street compared to the Sparse trees street of this study in Barcelona. When soil moisture conditions are considered, the air temperature inside the neighbourhood with denser trees increases non-significantly compared to sparser trees, by 0.2 ± 0.3 ºC, possibly as a consequence of an increase in the leaves temperature (Gräf et al., 2021), likely as a results of intercepted shortwave radiation by leaves being shed as sensible heat, due to the reduced evapotranspiration and the little capacity of leaves to store heat. In contrasts with

the results of other observational studies which observe an increase in nighttime temperatures due to the presence of street trees (Taha et al., 1991; Bowler et al., 2010), in our case there is no increase in night air temperatures due to the increased tree cover, which implies that there is no worsening of the thermal stress associated to the effect of street trees on the air temperature.

Moreover, we identified an average reduction of road surface temperatures by 2.6 ± 0.7 ºC during midday/mid-afternoon. The combined impacts of street trees on built surface temperatures and shortwave radiation exposure on pedestrians result in an average reduction of T_{MRT} experienced by pedestrians of 4.9 ± 2.8 ºC in the hotspot and 3.1 ± 1.5 ºC in the cold spot during midday/mid-afternoon under tree coverage. These reductions persist even when accounting for the impact of low soil moisture availability, suggesting average reductions of 4.4 ± 2.8 ºC in the hotspot and 2.6 ± 1.4 ºC in the cold spot.

The model depicts a higher T_{MRT} in locations under street trees compared to those outside during nighttime (0.9 ± 0.2 ºC for Sparse trees and 0.2 ± 0.2 ºC for Dense trees). This aligns with multiple studies (Coutts et al., 2016; Lee et al., 2016; Middel and Krayenhoff, 2019; Huang et al., 2020) that have observed that increase, attributed to an increase in downwelling longwave radiation from street tree leaves rather than from the cool sky, during the night. However, in the comparison between the two neighbourhoods, T_{MRT} remains lower in Dense trees than in Sparse trees during the night. This is attributed to the lower surface temperatures of walls and roads earlier in the night prevailing over the higher downwelling longwave radiation from trees. The mechanism used to compute longwave radiation impacts on T_{MRT} assumes that tree leaves absorb all incoming longwave radiation from above and emit their own downward longwave radiation to pedestrians. In reality, there are gaps between tree leaves for low-moderate density tree canopies, which partially absorb radiation from the sky and upper wall levels, allowing a fraction to pass through and reach pedestrians (Krayenhoff et al., 2014). A future improved longwave radiation model for T_{MRT} estimation in BEP-Tree could consider these nuances.

Despite the modelled benefits of street trees on air temperature and T_{MRT} during high thermal stress hours, we observed that street trees can elevate air humidity (Figure 3.4), potentially compromising thermal stress (Gilabert et al., 2015). Relative humidity is higher in neighbourhoods with denser trees under moist soil conditions, peaking at 13.2 % higher (at 8 UCT) and averaging 7.8 ± 3.8 % higher during midday/mid-afternoon. This humidity increase generates a UTCI increase of 0.6 ºC, under the meteorological conditions of the study period. However, this effect is minimized during dry soil conditions, with humidity differences reduced to 1.5 ± 1.1 % during midday/mid-afternoon, as a consequence of the reduction in the daily tree transpiration (Figure 3.3). Additionally, although street trees can impact wind speed through wind drag (Krayenhoff et al., 2020), the observed effect in this study is minimal (below 0.1 m s-1), due to the low average wind speed modelled in deep street canyons (see Figure B.6 in Appendix B).

Overall, the positive impacts of street trees on human thermal stress during hot summer episodes (lower air temperatures and T_{MRT}) outweigh the negative impacts (increased air humidity and reduced wind speed), resulting in a net reduction of UTCI during periods of strong heat stress.

However, this impact is highly dependent on meteorological and soil conditions, with street trees potentially experiencing a 40-50 % reduction in their capacity to reduce thermal stress during dry soil conditions. Street trees in compact areas can reduce UTCI by up to 0.9 – 1.2 ºC under wet soil conditions and up to 0.5 – 0.8 ºC under dry soil conditions. This remainder effect is principally caused by the reduction of T_{MRT}, as the effects on the air temperature and relative humidity are minimized under dry conditions.

Few observational studies have compared the human thermal stress conditions inside deep street canyons to detect the impact of street trees (Coutts et al., 2016; Middel and Krayenhoff, 2019), and they find high diversity of results. Middel and Krayenhoff (2019) found high reductions in the UTCI observed under two locations over concrete (one under street trees and other outside) with daily average reductions of 4 ºC during an extreme heat episode in the city of Tempe (Arizona). However, their study compared point locations, rather than canyon averages. Coutts et al. (2016) found that street trees were able to reduce the thermal stress from very strong stress (UTCI > 38 ºC) to strong stress (UTCI > 32 ºC) under severe heat wave episodes in Melbourne (Australia). Jia and Wang (2021) modelled UTCI reductions of 0.88 ºC using the computational fluid dynamics model ENVI-met for studying street trees implementation in the city of Hong Kong. However, the comparison between studies is difficult due to the differences in many factors, such as vegetation leaf area density, clumping factors, climate, building height-to-street width ratios, tree species, building material properties, street orientation and local meteorological conditions. For this reason, the evaluation of the modelled results presented in this study requires of comprehensive observational results that consider all the meteorological aspects affecting thermal stress, as the UTCI, as well as the aspects related to the health of the vegetation as the leaf area density and soil moisture.

3.4.2 The impact of heat waves on human thermal stress reduction from street trees

During the heat wave event, the impact of street trees on the meteorological conditions affecting thermal stress undergoes temporal variations in response to fluctuations in heat and drought stress. Notably, we observed an augmented air-cooling capacity of street trees during heat stress under moist soil conditions, evident in Figure 3.2b and Figure B.4 in Appendix B. The period of extreme heat results in an intensified reduction of air temperature from trees, presenting a disparity between non-heat wave days (0.6 ± 0.4 ºC lower in Dense during midday/mid-afternoon) and heat wave days (1.2 ± 0.4 ºC lower). This is attributed to an increase in tree transpiration (Figure 3.3a), stimulated by the rise in vapor pressure deficit or air dryness. It is noteworthy that higher air temperatures might potentially lead to stomatal closure (Marchin et al., 2022). The response of tree transpiration to heat waves under moist soils varies among tree species. Some species exhibit increased transpiration rates as an adaptative trait to extreme heat (Barriopedro et al., 2023), while others close their stomata during heat waves to prevent soil moisture depletion (Marchin et al., 2022). The observed variations between and within tree species to temperature sensitivity contribute to inconsistencies in the observed responses of leaf stomas to high heat

stress (Marchin et al., 2022). Although this study focused on a single tree species (Krayenhoff et al., 2020), overlooking the potential impacts of different species on temperature cooling Gillner et al. (2015a). The most common tree species found in Barcelona streets, Platanus X Hispanica, is considered a tolerant species to the stressful urban conditions and maintains higher transpiration and conductance under high atmospheric dryness and low soil moisture (Gillner et al., 2015a).

Under compounded dry soil conditions and heat stress, the air-cooling capacity of street trees is significantly reduced due to decreased tree transpiration (Figure 3.3a). Despite this, a non-significant increase in air temperature cooling is observed between heat wave days 0.1 ± 0.4 ºC lower for Dense trees) and non-heat wave days (0.3 ± 0.3 ºC higher for Dense trees). This increase results from elevated vapor pressure deficit during heat wave days, although the term regulating stomatal conductance with soil moisture (F_4) reduces to 0.38 – 0.40 under dry soil conditions (Figure 3.2b). While both mechanisms influence stomatal conductance, they are independent of each other, highlighting an inaccuracy in the plant physiology model of Noilhan and Planton (1989) (via Chen and Dudhia (2001)) adopted in this version of BEP-Tree. Despite this, certain plant species have been identified to open stomata under compounded heat and drought conditions, potentially leading to increased mortality rates (Marchin et al., 2022). The study's exclusive focus on one tree species and oversights in model assumptions necessitate a comprehensive understanding of various plant responses in future investigations.

Concerning the role of street trees in reducing human thermal stress through shading, the impact of heat waves on the reduction of T_{MRT} by street trees remains unclear (Figure 3.6 and Figure B.5). The T_{MRT} reductions found between the two neighbourhoods do not present significant differences between heat wave and non-heat wave days. Soil moisture conditions have a limited impact on T_{MRT} reduction by street trees in this study, assuming a constant leaf area density. Yet, prolonged drought or heat waves could induce various effects on tree structural systems, depending on species, health, and location, potentially undermining the effectiveness of street trees in T_{MRT} reductions through shade (Qu et al., 2024). Therefore, the study's assumptions might not hold during extended drought conditions or late-summer heat waves when deciduous trees undergo leaf senescence (Stratópoulos et al., 2019).

Despite the increased air-cooling of street trees during the heat wave, the concurrent rise in tree transpiration also leads to a notable elevation in air humidity. The street with denser trees presents an average relative humidity 11.6 ± 5.7 % higher than the street with sparser trees during midday/mid-afternoon on heat wave days with moist soil conditions. This heightened increase in relatively humidity adversely impacts human thermal stress, resulting in a direct increase of 0.8 – 1.4 ºC in the UTCI. This increase is compensated by higher reductions in air temperature and T_{MRT}. The retention of air humidity along the heat wave episode can be caused by street trees compromising ventilation in deep canyons, disconnecting the wind flow above the canyon from that under the tree canopy (Oke et al., 2017). This effect can potentially affect not only the dispersion and dissipation of air humidity, but also air pollutants concentrations from traffic within streets, supposing on an indirect detrimental effect on human health (Janhäll, 2015; Jin

et al., 2014). This effect necessitates a comprehensive understanding of the interplay between street trees, air quality, and thermal stress in compact cities.

Regarding the impact of heat waves on the thermal stress effect of street trees, a high variability in response is observed, dependent on location within neighbourhoods, soil moisture conditions, and the evolution of the heat wave. The cold spot exhibits the highest reductions in UTCI during midday/mid-afternoon on July 4, gradually decreasing until the last day of the heat wave. This location is strongly influenced by the evolution of T_{MRT} under tree crowns. The median spot presents the highest reductions in UTCI on July 5 (Figure 3.8c and 3.8d), coinciding with the day of highest air temperatures, while experiencing minimal reductions in the last day of the heat wave. This location, under tree cover for Dense trees and outside for Sparse trees, presents the maximum differences altogether with the maximum air temperature and T_{MRT} reductions. Conversely, the hotspot does not exhibit maximum reductions during the heat wave. This location is probably situated outside the coverage of trees for both neighbourhoods, being influenced by the changes in T_{MRT} in the hotspot outside the tree coverage, the air temperature, relative humidity, and solar radiation changes over the heat wave episode. Across all locations, the last day of the heat wave shows the lowest reductions in UTCI, suggesting a potential decline in thermal stress reduction from trees as heat waves persist. This trend is also appreciated under dry soil conditions although with a lower effect. This raises concern for compact city adaptability to climate change in regions where more prolonged, intense, and frequent heat waves and droughts are expected, as the Mediterranean region (Giorgi and Lionello, 2008).

Cities facing challenges related to soil moisture availability for street trees can potentially address this issue through the application of irrigation water. This approach aims to sustain adequate soil moisture levels, ensuring that street trees effectively contribute to air-cooling and reduce thermal stress. The necessity of this maintenance practice becomes apparent during heat episodes, coinciding with periods of limited water availability for trees. During hydrological droughts, where water resources are scarce, local administrations constrain water accessibility for irrigation practices related to green infrastructure, with other sectors having more priority to access water resources. Despite these challenges, our study emphasizes the importance of prioritizing the health and maintenance of street trees in these conditions. Doing so ensures their continued capacity to reduce thermal stress and provides additional ecosystem services not contemplated in this study, such as runoff control, air purification, noise reduction and habitat for biodiversity (Baró et al., 2019). Implementing a system to monitor the water requirements of street trees emerges as a potential solution, aiding in the identification of areas with insufficient water availability and facilitating resource conservation.

3.5 Conclusions

In response to the escalating challenges posed by rising temperatures in urban environments, local governments in highly compact cities are increasingly compelled to address the urgent need for heat mitigation measures, particularly in the face of more frequent and intense heat events.

Recognizing their potential, street trees are commonly considered an optimal nature-based solution to counter these climatic impacts. Their microclimatic benefits, manifested through the regulation of air temperature and the provision of shade to pedestrians and built surfaces, position them as valuable assets. In this study we evaluated the impact of street trees on the meteorological factors influencing human thermal stress, to determine the main mechanism of cooling from street trees under common summertime conditions in a Mediterranean climate city and to explore how their effectiveness in reducing thermal stress may be influenced by heat wave events and low soil water availability.

The evaluation has been performed using a modified version of the BEP-Tree model adapted for use in compact cities and applied to two neighbourhoods in the city of Barcelona that present contrasting street trees densities. The modifications to BEP-Tree account for an implementation of the mean radiant temperature estimation and the coupling of a vertical soil moisture diffusion model to represent the impact of soil perviousness with the street canyons and estimate the impact of soil water availability on street tree transpiration. These modifications have yielded on a neighbourhood scale meteorological model able to represent the effects of street trees on the thermal stress, as well was being able to study the spatial variability of the thermal stress in urban areas, which is found necessary to investigate the efficiency of street trees implementations in compact cities.

The results of this study reveal that street trees have a considerable impact on air-cooling and reducing the human thermal stress. A neighbourhood with denser street trees (65 % of street plan area covered by trees and a tree crown-average leaf area index of 4.0 $m^2\,m^{-2}$) presents lower air temperatures during midday/mid-afternoon, by 0.7 ± 0.4 ºC on average under soil moist conditions compared to a similar neighbourhood with sparser street trees (16 % of street plan area covered by trees and a tree crown-average leaf area index of 2.7 $m^2\,m^{-2}$). Street trees reduce the perceived mean radiant temperature from pedestrians by 4.9 ± 2.8 ºC in the hotspot (location with highest mean radiant temperature) and 3.1 ± 1.5 ºC in the cold spot (location with lowest mean radiant temperature) under trees. Despite the finding that street trees increase the air relative humidity by 7.8 ± 3.8 %, the combined impacts on air temperature and mean radiant temperature still yield a net reduction of the UTCI up to 0.9 – 1.2 ºC under wet soil conditions. However, we found that tree transpiration and the provision of air-cooling is highly controlled by the availability of soil moisture. Under dry conditions, such as those experienced during the heat wave episode studied, the impact of street trees on air temperatures is highly reduced, even presenting slightly higher midday/mid-afternoon temperatures with dense trees (0.2 ± 0.3 ºC higher) than sparse trees neighbourhoods. Nevertheless, the mean radiant temperature effect from tree shade is largely preserved and the warming effect of enhanced air humidity is reduced due to lower transpiration, such that street trees still yield UTCI reductions, of up to 0.5 – 0.8 ºC, a 50-60 % of the total UTCI reduction under moist soil conditions.

During the heat wave event, we found that the air-cooling capacity of street trees increased with the air temperatures for moist soil conditions, with dense trees neighbourhoods exhibiting maximum air temperatures up to 1.4 ºC lower than in sparse trees neighbourhoods at 13 UTC. Con-

cerning the effectiveness of street trees in alleviating thermal stress during a heat wave event, a high variability in response is observed, dependent on location within neighbourhoods, soil moisture conditions, and the evolution of the heat wave. The highest reductions in the UTCI (1.2 – 1.5 ºC) were observed in the hotspot locations of the neighbourhoods, with moist soil conditions. Nevertheless, the thermal stress reduction diminished during the course of the heat wave, suggesting a potential decline in thermal stress reduction from trees as heat waves persist. The availability of water in the soil arises as an important factor in the capacity of street trees to mitigate thermal stress, as important as the tree shade. Protecting and maintaining adequate soil water conditions for urban street trees is crucial for their health and the provision of microclimate benefits, especially in Mediterranean climate cities under warm temperatures.

Chapter 4

Sensitivity study of PBL schemes and soil initialization using the WRF-BEP-BEM model over a Mediterranean coastal city

The work of this chapter has been published in:

Segura, R., Badia, A., Ventura, S., Gilabert, J., Martilli, A., & Villalba, G. (2021). Sensitivity study of PBL schemes and soil initialization using the WRF-BEP-BEM model over a Mediterranean coastal city. Urban Climate, 39, 100982. (doi.org/10.1016/j.uclim.2021.100982)

Abstract: Due to increased urbanization and global warming, cities are experiencing more heat wave (HW) events that cause extreme heat stress. To mitigate such effects, better understanding the impact of urban morphology on the boundary layer development is needed. This study investigates the sensitivity of high-resolution mesoscale simulations to 1) soil moisture initializations; 2) the inclusion of site-specific urban morphology parameters; and 3) the planetary boundary layer (PBL) scheme. Using the WRF model coupled with the building effect parameterization and the building energy model (BEP-BEM) at a 1-km resolution to simulate a HW that occurred in the metropolitan area of Barcelona. We find that the use of a high-resolution land data assimilation system (HRLDAS) to initialize soil properties results in larger temperature diurnal range, but it did not improve the performance of simulated temperatures compared to using low-resolution ERA5 data. The inclusion of site-specific urban parameters improved the representation of urban fractions, reducing the night-time overprediction of 2-m temperatures compared to using default urban parameters. Overall, the Bougeault-Lacarrere (BouLac) scheme represents the PBL-height noontime observations better than the Mellor-Yamada-Janjic (MYJ) scheme. This was related to a better representation of daytime near-surface temperatures by the BouLac scheme compared to the MYJ scheme.

4.1 Introduction

More than half of the world's population is currently living in urban areas, and this demographic trend is expected to increase up to 68 % in 2050 (83.7 % in the case of Europe), according to the United Nations (United Nations, 2019). With the dramatic global rise in urbanization, the impacts of climate change on urban areas have become a major worldwide concern. Some of these impacts that have already been observed or estimated include increasing temperatures (Hunt et al., 2013;IPCC, 2014), changing precipitation dynamics (IPCC, 2014), increasing frequencies and intensities of extreme events such as heat waves (HWs) (Stott et al., 2004; Hunt and Watkiss, 2011), worsening air quality (Jacob and Winner, 2009), and accelerating sea-level rise (Hunt and Watkiss, 2011;IPCC, 2014). The Mediterranean region has been identified as a highly vulnerable area to the effects of climate change (Giorgi, 2006) and is expected to see an increase in the frequency of longer-lasting and more severe HWs (Meehl and Tebaldi, 2004; Ballester et al., 2009).

Historically, the most-studied urban micro-climatic feature is the urban heat island (UHI) phenomenon (Oke, 1982; Moreno-garcia, 1994; Arnfield, 2003), which refers to the tendency of urban areas to be warmer than their peri-urban and rural surroundings, particularly at night. This effect arises due to multiple causes, such as the excessive absorption of heat by building materials, the geometries of urban canopies, the decreased evapotranspiration owing to the lack of vegetation, and the heat released from anthropogenic emissions (Oke, 1982; Grimmond, 2007). Moreover, global warming is expected to exacerbate the differences between urban and rural temperatures (McCarthy et al., 2010), making urban dwellers more vulnerable to heat stress and other heat-related pathologies (Ingole et al., 2020). Li and Bou-Zeid (2013) revealed that HWs interact non-linearly with UHIs to produce extremely high heat stress on urban citizens. The combined effect of UHIs and climate change also implies a significant challenge for the sustainability of energy and water systems in urban environments and the integrity of urban infrastructures and ecosystems (Hunt and Watkiss, 2011). Responding with urgency to these challenges requires a deep understanding of the behaviour of the urban boundary layer (UBL), particularly during extreme heat events.

In this context, numerical models play a key role, both as scientific tools to help researchers understand how different physical mechanisms shape UBL evolution, and as practical tools to aid scientists in evaluating the efficiencies of different mitigation strategies in the context of a changing climate (Chen et al., 2011). However, today's atmospheric models have a range of different options in terms of their physical parameterizations, initializations, etc., that often need to be adapted to each case study. The aim of this study is to test the sensitivity of the mesoscale meteorological Weather Research and Forecasting (WRF) model (Skamarock et al., 2021) with the multilayer urban canopy model (UCM) Building Effect Parameterization and the Building Energy Model (BEP-BEM) (Salamanca and Martilli, 2010) to three configurations that we identified as the most relevant, using the coastal Mediterranean city of Barcelona and its metropolitan area as a case of study. These configurations are described as follows:

1) Soil moisture and temperature initialization. Soil moisture is a key parameter that affects

both the heat capacity of the ground and the partitioning between the sensible and latent heat fluxes, while soil temperature affects the amount of heat transferred between the surface and inner soil layers. The initialization of these variables in land surface models (LSMs) represents a challenge in atmospheric modelling due to sparse available measurements (Best and Grimmond, 2014). Global reanalysis datasets, such as ERA5 (C3S, 2017), derive these variables at low resolutions (31 km x 31 km) that cannot resolve the complex heterogeneities of land cover types and soil textures at the urban scale. To minimize the uncertainties related to the initial conditions in WRF simulations, spin-up strategies have been developed, such as the uncoupled LSM high-resolution land data assimilation system (HRLDAS) (Chen et al., 2007), which can be used to simulate seasonal variability in soil properties at a high resolution. The HRLDAS system provides high-resolution soil moisture and temperature fields for WRF initialization, as was reported in Lakshmi et al. (2011) for the simulation of three regions in the United States.

2) Urban morphology parameters. WRF-BEP-BEM requires the initialization of multiple urban canopy parameters that define the geometrical, radiative, energetic, and metabolic properties of urban areas. In this sense, the World Urban Database and Access Portal Tools (WUDAPT) project focused on creating a detailed database of urban description land-use/land-cover (LULC) maps for each city using the local climate zones (LCZ) classification (Stewart and Oke, 2012; Brousse et al., 2016). The LCZ establishes a framework for classifying neighbourhoods within the same city with similar urban cover types, structures, materials, and human activities, thus showing similar tendencies regarding UHI effects and establishing a range of values for the urban parameters of each LCZ that can serve as inputs for the UCM (Stewart and Oke, 2012). Alternatively, the WRF-BEP-BEM system has also incorporated the option to directly initialize urban canopy parameters into WRF grids in a point-by-point based approach (Chen et al., 2011). In this way, each grid has its own unique set of urban morphological parameters, such as canopy geometry and urban fraction (λ_u, defined as the fraction of the impervious surface area to the total plan area). Hammerberg et al. (2018) compared the WUDAPT methodology with the LCZ-averaged urban morphology to initialize WRF BEP-BEM over the city of Vienna (Austria). Their results showed that using LCZ-averaged urban morphology from specific data of the city of Vienna only provided marginal improvements compared to the WUDAPT methodology due to the high homogeneity of the city and the high horizontal resolution of their WRF simulations (500 m). Additionally, Wong et al. (2019) compared the WUDAPT and the point-by-point methodologies for defining UCM datasets for the city of Hong Kong. Their main findings were that the use of tables with default values instead of local specific data, such as those used in Stewart and Oke (2012), can add a large source of uncertainty in urban WRF-BEP-BEM simulations.

3) Planetary Boundary Layer schemes. In the WRF model, PBL schemes represent the turbulent sub-grid-scale processes by computing the boundary layer fluxes of heat, moisture, and momentum in the lowest part of the troposphere along with resolving vertical diffusion due to turbulence for the entire vertical column. Two available PBL schemes are available in WRF that can be coupled with the BEP-BEM urban canopy model: the Bougeault-Lacarrere (BouLac) (Bougeault and Lacarrere, 1989) and the Mellor-Yamada-Janjic (MYJ) (Janjić, 2001) schemes.

Other studies have analysed the performance of the WRF model using these PBL schemes for the city of Barcelona, such as Banks et al. (2015) and Banks and Baldasano (2016). Banks et al. (2015), showed that the MYJ scheme was the least correlated to LiDAR estimates of the PBL height. Banks and Baldasano (2016) showed that the BouLac scheme estimated air and dew point temperature better than MYJ for the cities of Barcelona, Girona and Reus. However, these studies did not use urban canopy parametrization to represent urban atmospheric processes, and they relied on the BULK scheme (Liu et al., 2006), which does not consider urban heterogeneity.

Recent studies have used numerical modelling approaches to investigate the UHI phenomenon of different cities (Arnfield, 2003; Salamanca et al., 2012; Li and Bou-Zeid, 2013; Sharma et al., 2014, 2016; Li et al., 2019). Some observational studies have found a spatial correlation between near-surface temperatures and λ_u (Kottmeier et al., 2007; Ryu and Baik, 2012; Schatz and Kucharik, 2014; Li et al., 2019). Usually, near-surface temperatures increase with λ_u, presenting a linear trend (Schatz and Kucharik, 2014, 2015; Li et al., 2019). Li et al. (2019), used a linear regression between simulated two-meter temperatures (T_{2m}) and λ_u using WRF coupled to an UCM for the city of Berlin, and a method for determining the UHI intensity of Berlin based on a set of validated λ_u linear functions.

This comprehensive sensitivity analysis can constitute a reference for future urban modelling exercises by providing the most suitable WRF-BEP-BEM model configuration for a coastal Mediterranean city during a HW event. Moreover, this analysis constitutes a basis to improve our scientific understanding of the physical mechanism responsible for the development of the UBLs of these types of cities, as well as to derive information that can be used to design mitigation strategies. As an example, in the second part of this study, the reference model configuration is used to investigate the impact of the studied urban area on UBL development and the impact of vegetation on the urban air temperature.

4.2 Methodology

4.2.1 Region of interest and case study

In this study, we analyse urban atmospheric simulations of the metropolitan area of Barcelona (AMB) and its surrounding areas. The AMB is situated in the northwest region of the Mediterranean basin and in the northeast region of the Iberian Peninsula (Fig. 4.1a). The AMB coast is oriented from southwest to northeast, and the AMB is surrounded by the Mediterranean Sea, the Catalan Coastal Range (near 500 m in altitude) at the NW and two rivers, the Llobregat River (South) and the Besòs River (North) (Fig. 4.1b). The AMB covers an area of 636 km^2 with a population of more than 3 million inhabitants (the 6^{th} largest metropolitan area in Europe). The city of Barcelona has 1.6 million inhabitants and covers a total area of 101 km^2, with a population density of 160 individuals ha^{-1}.

The Mediterranean climate is made up of dry summers with a regime of local breezes and warm

temperatures (25-27 ºC) influenced by the thermoregulatory effect of the sea, which in turn creates an increasing heat sensation effect due to humidity (Lionello et al., 2006). During the summer months, stagnant synoptic patterns and the absence of synoptic events make mesoscale convective processes predominate, especially on the coast, which is influenced by sea/land breezes (Pérez et al., 2006). The day and night transitions of the sea/land breezes together with the UHI effect cause a complex structure in the atmospheric boundary layer, modifying the temperature and the dispersion of contaminants (Soler et al., 2011). Sea breezes start between 8 – 9 UTC (Barcelona's longitude is 2º E, therefore UTC can be considered equivalent to Local Solar Time), reaching their maximum strength at approximately 12 – 14 UTC, with higher values recorded near the coast but spanning hundreds of kilometres of the land surface until 18 – 20 UTC when they gradually disappear (Soler et al., 2011). At night, the coastal regions are characterized by land-to-sea breezes, which have much lower forces than those of the sea breezes, increasing the influence of the possible effects of topography on the winds (Soler et al., 2011).

Our study case corresponds to a HW episode that occurred between 4 and 6 July 2015 in southern and central Europe. The maximum daily temperatures surpassed the 98^{th} percentile for three or more consecutive days at numerous meteorological stations, meeting the definition of a HW episode established by the Catalan Meteorological Service (SMC). During this period, the maximum daily temperatures reached 40 ºC in the interior of the AMB and 35 ºC on the coast (SMC, 2015). The night-time temperatures were also considerably high during the entire HW, exceeding 25 ºC for several consecutive days in some neighbourhoods (SMC, 2015). Maximum daily temperatures were considerably high during the previous weeks over the entire Iberian Peninsula and extended for almost a whole month (27 June 2015 to 22 July 2015) with no precipitation. Most of the days during the HW are classified with the Shallow cyclone or Undetermined pressure gradient and Anticyclonic western advection synoptic types according to the synoptic classification methodology described in Miró et al. (2020). These two circulation patterns are the most common types of situations for the summer days in the Iberian Peninsula, making this HW an excellent case study representative of the most frequent synoptic events leading to HWs. Further details of the synoptic situation during the HW can be seen in C.1 and in Section 2 of the Supplementary material of Gilabert et al. (2021b).

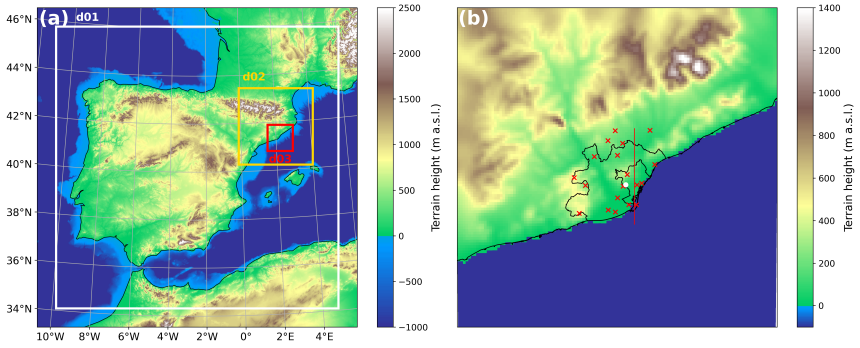


Figure 4.1: (a) Domains of the WRF model for this study with 9, 3 and 1km grid size for d01, d02 and d03, respectively. (b) Detail of the domain 3 with a terrain height map and the political boundaries of the AMB and Barcelona city (black contours). The red line represents the cross-section shown in Section 4.3.5. The red crosses show the position of the meteorological stations used in this study for the performance evaluation of the WRF simulations. The white dot shows the radiosonde launching position.

4.2.2 WRF implementation

Model set-up

The Weather Research and Forecasting (WRF) v4.0 model (Skamarock et al., 2021) is used to study the urban boundary layer evolution over the AMB. The WRF model is a mesoscale numerical weather prediction system that allows atmospheric simulations to be performed across a wide range of spatial scales (from regional to urban) due to its nesting capabilities and its potential to be coupled to a UCM (Chen et al., 2011). In this study, WRF is coupled with the BEP-BEM scheme (Martilli et al., 2002; Salamanca and Martilli, 2010) to better represent the physical surface energy exchanges inside the urban canopy, the drag effect on the wind and the urban spatial heterogeneities. The WRF configuration used for this study consists of 3 two-way nested domains with horizontal resolutions of 9 km, 3 km, and 1 km (Figure 4.1a). The domains were selected to include all geographical features that have synoptic or regional influences on the meteorology of the AMB. The large domain covers the entire Iberian Peninsula and Northern Africa. The middle domain contains the entire Catalan territory and extends in the north above the eastern Pyrenees. The small domain covers Barcelona Province, which contains the AMB on its eastern coast (Figure 4.1b).

All simulations cover the period from 00 UTC on 24 June 2015 to 00 UTC on 10 July 2015, using the first 24 hours as the spin-up period and covering the three days considered to be the HW (July 4, 5 and 6, 2015). Only the innermost domain is evaluated against the observed data. The model characteristics and experimental configurations, such as the domain resolution and physical parameterizations, are shown in Table 4.1, which have been derived from previous sensitivity studies based on a model performance evaluation in comparison with meteorological

observations (Gilabert et al., 2021b; Ribeiro et al., 2021).

Table 4.1: Model characteristics and experiment configurations.

Resolution and initial conditions	
Horizontal resolution	9 km x 9 km; 3 km x 3 km; 1 km x 1 km
Domain dimesions	150 x 145; 118 x 118; 121 x 121
Vertical layers	57 (16 between the surface and 100 m)
Top of the atmosphere	50 hPa
Initial conditions	ERA5 (C3S, 2017) with 31 km horizontal resolution, 137 vertical levels and 6-hour separation
Physical parameterizations	
Microphysics	WRF Single-Moment 6-class scheme (Hong et al., 2006a)
Shortwave and longwave radiation	RRTMG scheme (Iacono et al., 2008)
Cumulus	Kain-Fritsch scheme (Kain, 2004) (only the outermost domain)
Surface/UCM	Noah Land Surface Model (pervious areas) (Chen and Dudhia, 2001) / BEP-BEM (impervious areas) (Martilli et al., 2002; Salamanca and Martilli, 2010)
Surface layer	Monin-Obukhov Eta similarity scheme with Zilitinkevich thermal roughness length

Land-use classification

For the LULC classification, the WRF model was adapted following the indications of Martilli et al. (2016) and the WUDAPT project to use the detailed urban descriptions of urban LCZs (Brousse et al., 2016; Gilabert et al., 2021a). The LCZ map of the AMB and adjoining areas was created following the WUDAPT classification (Bechtel et al., 2015) at a 100-m resolution. Then, it was improved through the reclassification and integration of high-resolution LULC maps such as Urban Atlas 2012, the LULC AMB 2015 and LiDAR data (Gilabert et al., 2021a). The LCZ map for the AMB region and adjoining areas covers a rectangular extension (ROI, Figure 4.2a), which was used as the region of study. For this study, 10 urban LCZs and the LCZ E (reformulated as asphalt) are used in combination with the Corine Land Cover 2018 classification (CLC) (Büttner et al., 2017 https://land.copernicus.eu/pan-european/corine-land-cover/clc2018) at a 100-m resolution for the other areas as the background land-use types. The CLC is remapped from its original 44 classes into 16 classes using the MODIS IGBP land classification and four urban LCZs following the method of (Pineda et al., 2004); these maps are then used by the WRF model. Both LULC classifications are interpolated at each model domain resolution using the most common land-use class in each cell. Additionally, the green vegetation fraction (GREENFRAC) was updated using the fraction of green vegetation cover (FCOVER) product of the Copernicus Global Land Service (Smets et al., 2019) with a 1-km resolution. The default FPAR MODIS data did not represent well the vegetation of the highly urbanized coast of the AMB due to the low resolution.

After interpolation to the resolution of the innermost domain, the most common LULC class inside the ROI (without considering water) is the evergreen needleleaf forest class (23.2 %) (Figure 4.2b), representing the natural regions of Collserola (512 m a.s.l) north of Barcelona city and the Garraf Massif (657 m a.s.l.) to the west of the AMB, both of which are located in the Catalan Coastal Range. Urban areas represent 47 % of the non-maritime area of the ROI.

The largest LCZ is the large low-rise zone (19.6 %), followed by the open low-rise zone (12.7 %) and the compact mid-rise zone (9.6 %), while the other urban LCZs constitute minorities (5.3 % combined).

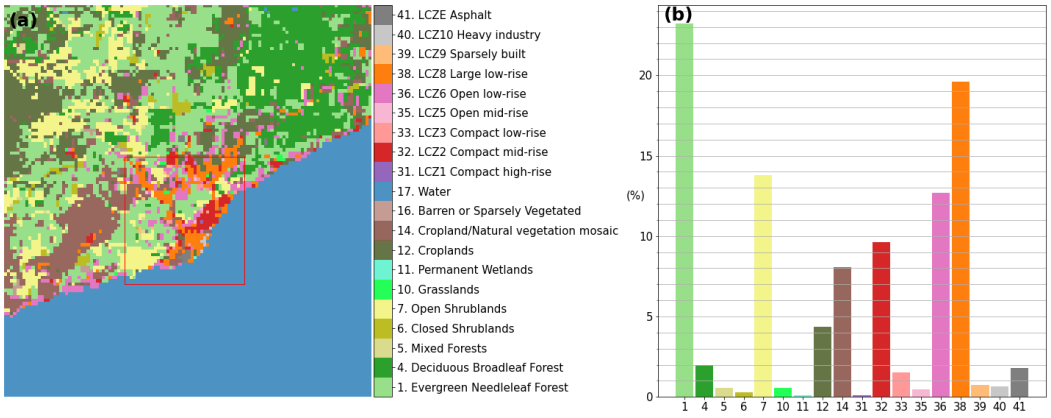


Figure 4.2: a) Land-use classification for the innermost domain d03, from the interpolation of LCZ and CLC with the red box defining the borders of the ROI; b) Histogram of land-use classes inside the ROI (without considering water).

Urban canopy parameters

Different approaches are used to define the WRF-BEP-BEM urban parameters. The radiative and thermal properties must be specified for each surface type in the urban canopy (roofs, building walls and ground/roads). The radiative properties of building roofs (albedo and emissivity) were computed using Landsat 5 TM images with 30 m resolution (USGS, 2019) containing roof and ground albedos following the methods of Liang (2001) and Landsat 8 OLI/TIRS images (Vermote et al., 2016) containing roof and ground emissivity values following the methods of Ndossi and Avdan (2016); then, both properties were averaged for each urban LCZ. Geometric and surface cover parameters such as the urban fraction, street width, building width and height distribution were established using the two methodologies described in Section 4.2.3

The rest of the urban parameters (thermal properties, surface roughness, room occupancy and A/C systems specifications) were adjusted using different assumptions to be as representative as possible for each urban LCZ and can be seen in Section 3 of the Supplementary material of Gilabert et al. (2021b). The anthropogenic heat released by buildings due to A/C systems can have an important contribution to the surface energy balance, especially during HW events. For this reason, the A/C option of the BEP-BEM scheme is activated for all urban LCZs (except LCZ E Asphalt) during the daytime hours (6-18 UTC or 8-20 local time, LT), with a target indoor temperature of 24.0 ºC and a comfort range of 1.5 ºC, based on the recommendations of Burroughs and Hansen (2011).

4.2.3 Sensitivity studies

Various simulations were conducted, as summarized in Table 4.2, to perform the various sensitivity studies that are described in the next three sections.

Table 4.2: Simulations design for the different WRF-BEP-BEM model sensitivities performed in this study. The reference simulation (BL-UM) is highlighted in bold.

Simulation	Soil initialization	PBL Scheme	Specific urban morphology	Comment
BL-UM	**ERA5**	**BouLac**	**Yes**	**-**
BL-UM-HRL	HRLDAS	BouLac	Yes	-
BL-noUM	ERA5	BouLac	No	-
MYJ-UM	ERA5	MYJ	Yes	-
BL-crop	ERA5	BouLac	No	Urban modified to cropland/natural vegetation mosaic

High-resolution land data assimilation system implementation

To properly initialize the soil temperature and moisture variables in rural grid cells and the pervious part of urban grid cells, LCZ-adapted HRLDAS v3.7.1 (Chen et al., 2007) was used. These variables were input to the Noah LSM in the WRF system. In this study, a comparison between a simulation initialized with low-resolution 1-day spin-up soil variables from the ERA5 reanalysis (BL-UM) data and a simulation initialized with high-resolution long spin-up soil variables obtained from HRLDAS outputs (BL-UM-HRL) is presented. The BL-UM simulation was chosen as the reference simulation in this study because it displays the best performance for near-surface temperatures in comparison with the observations (see Section 4.3.2).

HRLDAS was run independently for each nested domain using analysed meteorological forcing data and high-resolution static data. ERA5 reanalysis hourly 0.25º x 0.25º data were used to drive HRLDAS during a period of almost one year (1 July 2014 -24 June 2015). According to (Chen et al., 2007), soil properties require approximately 1 year to reach a quasi-equilibrium state using the HRLDAS model. Since soil variables are only used in the WRF model by the land surface model and not by the UCM, HRLDAS is used without coupling any urban scheme. In this way, HRLDAS considers only the pervious fraction of each grid cell (the vegetated and bare soil surfaces inside the grid cell), and the impervious fraction (all built surfaces including buildings) is ignored.

Figure 4.3 shows a comparison in the WRF model initialization of the temperature and moisture conditions of first soil layer (0 to 0.1 m depths) using ERA5 data and the HRLDAS outputs (after running the HRLDAS model for one year). These data were used to initialize the WRF model at 00 UTC on 24 June 2015; therefore, we compared the input files for the WRF model after running the pre-processor tool (real.exe). In the first soil layer, the ERA5 data had slightly

warmer soil temperatures (up to 0.4 ºC warmer) than the HRLDAS data in low-altitude regions (Figure 4.3c), while colder temperatures were seen in the ERA5 data in mountainous regions (down to -1.3 ºC lower). In the case of the HRLDAS data, the soil temperature values showed high spatial uniformity, with first-layer temperatures ranging between 21.2 and 24.0 ºC. The fact that HRLDAS only considers the vegetated and bare soil surfaces of each grid cell reduces the spatial heterogeneity resulting from the LULC variability; thus, the spatial differences depend more on other factors such as the vegetation type and fraction and orography. In Figure C.2 in Appendix C.2, the temporal series of the HRLDAS output for the soil temperature variables show that the soil temperature difference between rural and urban areas barely changes over the one-year simulation.

Figure 4.4 shows the WRF model soil initialization variables of the second soil layer (0.1 to 0.4 m depths), which, together with the first soil layer, constitute the layers that have the greatest influence on the temporal evolution of near-surface variables in short simulations. For the second soil layer, the HRLDAS data generally had much higher soil temperatures (up to 4.6 ºC higher for the second layer) and higher spatial variability than the ERA5 data (see Figure 4.4c).

Comparing soil moisture, the WRF pre-processor only applies a simple bilinear interpolation for this variable in the case of the low-resolution ERA5 data, with low moisture values ranging from 0.17 $m^3\,m^{-3}$ (0.18 $m^3\,m^{-3}$) in inland areas to 0.04 $m^3\,m^{-3}$ (0.04 $m^3\,m^{-3}$) in coastal areas for the first (second) soil layer (Figure 4.3e and 4.4e). In contrast, HRLDAS generally showed higher soil moisture (0.19 $m^3\,m^{-3}$ and 0.21 $m^3\,m^{-3}$ on average for the first and second layers, respectively) than the ERA5 data, and the model was able to represent spatial heterogeneities in the studied domain. Higher differences between the two initialization methods are seen near the southwest coast of the AMB (Figure 4.3f and 4.4f). Minimum differences between urban and rural areas can be seen in the temporal series of soil moisture from the HRLDAS output (Figure C.3).

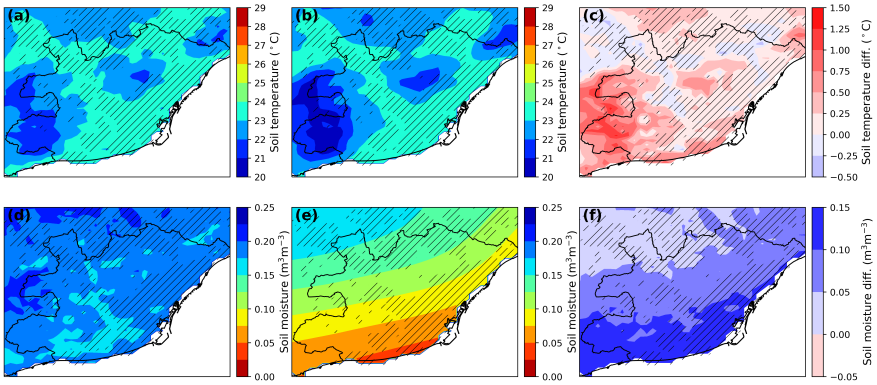


Figure 4.3: Comparison of WRF model initialization at 00 UTC on 24 June 2015 in the first soil layer (0-0.1m depth) for a) soil temperature with HRLDAS; b) soil temperature with ERA5; c) difference in soil temperature (HRLDAS – ERA5); d) soil moisture with HRLDAS; e) soil moisture with ERA5; f) difference in soil moisture (HRLDAS – ERA5). The black hatched lines represent the urban areas classified with an urban LCZ.

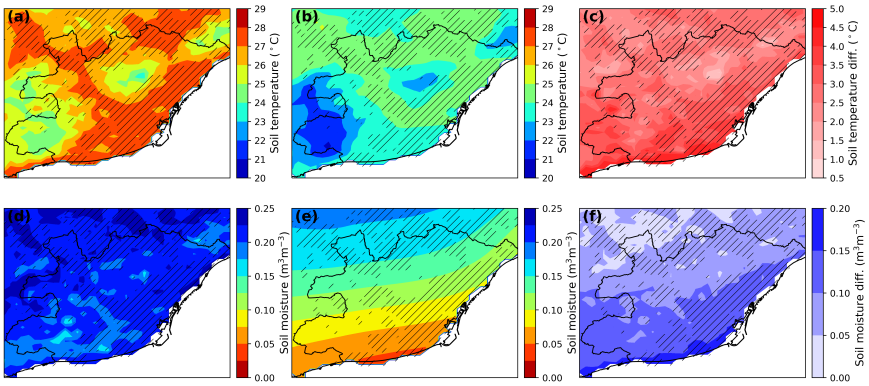


Figure 4.4: Comparison of WRF model initialization at 00 UTC on 24 June 2015 in the second soil layer (0.1 – 0.4 m depth) for the a) soil temperature with HRLDAS; b) soil temperature with ERA5; c) difference in soil temperature (HRLDAS – ERA5); d) soil moisture with HRLDAS; e) soil moisture with ERA5; f) difference in soil moisture (HRLDAS – ERA5). The black hatched lines represent the urban areas classified with an urban LCZ.

Sensitivity to urban morphology parameters

In this study, we evaluated the capability of LCZs to represent the urban morphology of the AMB compared to using specific urban morphology for the region. In the case of the WUDAPT methodology, the default urban morphology parameters typical for each urban LCZ class suggested by Stewart and Oke (2012) and Stewart et al. (2014) were used to set the parameters in the URBPARM.TBL file of the WRF-BEP-BEM model (see Table C.3). The building heights distribution is obtained from Brousse et al. (2016), based on the Stewart et al. (2014) tables but slightly adapted to the city of Madrid (Spain).

In contrast, for the point-by-point approach, the buildings heights were extracted from LiDAR captures of the ROI and a digital surface model with a resolution of 2 m (ICGC, 2019). Then, the Urban Multiscale Environmental Predictor (Lindberg et al., 2018) was used to generate the walls height. The histogram of building heights was generated following the methodology described by Pappaccogli et al. (2017). In the case of urban fractions, yearly maximum NDVI maps derived from Landsat 8 OLI/TIRS images at a 30 m resolution (USGS, 2019) were reclassified to differentiate urban areas from vegetated areas, as is explained in Gilabert et al. (2021b). Then, these data were interpolated specifically for each urban classified grid cell at a 1-km resolution by the WRF pre-processing tool (Chen et al., 2011).

In this work, both methodologies were compared to evaluate the model improvement in the refinement of the urban morphology description and the capability of the WUDAPT methodology to represent the heterogeneities in the climate of the city (see Appendix C.3). To do this, one simulation where BEP-BEM used the default morphological urban parameters derived by the WUDAPT methodology and based on the ranges proposed by Stewart and Oke (2012) (BL-noUM) was conducted, and another simulation where BEP-BEM used the grid-cell-specific morphological urban parameters extracted with GIS on a point-by-point-based approach was performed (BL-UM).

We studied how the simulations BL-noUM and BL-UM differed depending on which urban morphology parameter were used. In the case of BL-noUM, urban morphology parameters were defined using the default values for each LCZ at a 100-m resolution, with a relatively high homogeneity of building morphology and low fraction of pervious areas. Therefore, when the land-use classification was extrapolated from the LCZ resolution to the WRF grid cells at a 1-km resolution, the model overestimated the λ_u values, since coarser resolutions tend to contain rural areas inside the grid cell apart from urban areas. This is reflected in Figure C.4, were a comparison of urban morphology parameters between BL-noUM and BL-UM simulations can be seen. BL-noUM showed higher average values for urban grid cells (0.82) than BL-UM (0.42) (see Figure C.4c), especially for LCZ 6 (open low-rise) areas. The difference between the urban fractions used in the two simulations was lower in the city centre, where denser urban areas are located.

In contrast, the mean street widths for the WUDAPT methodology are calculated for each LCZ from the mean building height and the mean canyon aspect ratio described in the look-up ta-

bles, obtaining much lower values than the ones extracted from the point-by-point methodology. BL-UM showed higher mean street widths (39.1 m) than BL-noUM (24.3 m) (Figure C.4l), especially for LCZ 10 (heavy industry, +64.2 m), LCZ 3 (compact low-rise, +19.3 m) and LCZ 8 (large low-rise, +16.8 m) areas.

The area-weighted mean building heights comparison show similar values between the two simulations (Figure C.4f), with an average of 9.3 m for BL-noUM and 10.0 m for BL-UM, respectively. This is related to the similarity of the average values for the 3 more frequent LCZ in the AMB (LCZ 2, 6 and 8) between the city of Barcelona and the values obtained from Brousse et al. (2016), adapted to the city of Madrid, which has a similar building height distribution than Barcelona. This is also seen on the mean building width (Figure C.4i), for which both simulations show similar average values of 19.6 m for BL-noUM and 19.6 m for BL-UM.

Sensitivity to the PBL scheme

In this study, the sensitivity of the model to the PBL scheme was analysed by comparing the BouLac (Bougeault and Lacarrere, 1989) and MYJ (Janjić, 2001) schemes. For this study, two WRF-BEP-BEM simulations were compared using these two PBL schemes: MYJ-UM for the MYJ scheme and BL-UM for the BouLac scheme. Both schemes are one-and-a-half-order prognostic turbulent kinetic energy (TKE) schemes with local closure, although the BouLac scheme has a non-local counter gradient term for convective conditions. The MYJ scheme, which is more widely used than the BouLac scheme in atmospheric models (Banks et al., 2015), is a modified version of the old ETA scheme from the MM5 model. The BouLac scheme has been designed for use with the BEP multi-layer model and has been tested most extensively with BEP and BEP-BEM (Salamanca et al., 2012; Sharma et al., 2014; Huang et al., 2019; Teixeira et al., 2019; Ribeiro et al., 2021).

Sensitivity of the UBL to urbanization

To determine the impacts of the city of Barcelona and the surrounding metropolitan areas on the UBL and near-surface temperatures, along with sea and land breezes, an additional simulation (BL-crop) was performed and compared with the BL-UM simulation. For BL-crop, the same configuration as that of the BL-UM was used, but the land-use of the urban areas inside the ROI was changed to the cropland/natural vegetation mosaic class of the modified MODIS IGBP classification.

In this way, we changed the AMB landscape into a mix of croplands, shrublands and grasslands, without any type of vegetation occupying more than 60 % of the total landscape, such as the current cropland areas near the Llobregat River in the south of the city. This class is used in the WRF-BEP-BEM model to define the characteristics of the natural pervious areas inside an urban classified grid cell. The vegetation fraction variable (SHDFAC in VEGPARM.TBL of the WRF model) and the leaf area index (LAI), were kept constant between the two simulations,

with the only difference being that the λ_u value was decreased to 0 in each grid cell. For all the simulations in this study, the vegetation fraction and the LAI of the pervious urban grid cell components are established with the definitions of the cropland/natural vegetation mosaic class of the VEGPARM.TBL: 0.80 and 4.29 m^2m^{-2}, respectively, which are values that do not coincide with the real values in the AMB for this period (SHDFAC$\sim$0.26 and LAI$\sim$0.67 m^2m^{-2}, respectively) but are used to not tune the model with data that are not replicable for other study cases.

4.2.4 Observed data

Near-surface datasets

The WRF simulations were evaluated using observational data from the SMC and the Spanish Meteorological Agency (AEMET). Urban and rural stations were used for this evaluation with a total of 19 stations (Figure 4.1b), 14 of which are located inside the AMB and 5 of which are located outside. The characteristics of these stations are provided in Appendix C.4. The stations were classified into 5 groups according to their LULC at a 100-m resolution: 1) urban fabric and non-vegetated urban areas (UF&NVUA); 2) non-agricultural vegetated urban areas (NAVUA); 3) agricultural areas (AA); 4) forest and seminatural areas (F&SNA); and 5) water bodies (WB).

The stations provide hourly point measurements that are compared with spatially averaged 1 km x 1 km hourly model output data, so we should expect more spatial variability in the observations than in the model outputs (Sharma et al., 2016). Moreover, a coarse 1 km x 1 km grid cell can contain multiple LULC types in the region it covers; therefore, misclassifications could occur between the LULC class of a given grid cell and the local surroundings of a station. For example, several stations from the NAVUA and AA groups (urban parks and agricultural lands) were placed on grid cell that were classified as urban LCZs at a 1 km x 1 km resolution due to the proximity of larger industrial and residential areas nearby. It is expected that for these stations, discrepancies would be found between the observations and model outputs due to the significant differences between the characteristics of the areas. These discrepancies are discussed during the model evaluation (Section 4.3.1). In the case of three stations, where the measurement equipment is placed on rooftops at 40-50 m above ground, the temperature and wind speed observations were compared with the outputs of the nearest vertical level in the WRF simulation, while for the other stations, the observations were compared with diagnostic 2-m temperature (T_{2m}) and 10-m wind speed (WS_{10m}) from the model outputs.

Vertical profiles

The surface evaluation was complemented with an assessment of the vertical structure of potential temperature and wind speed using radio-sounding measurements from radiosonde launches performed by the SMC. The launches were made in the city of Barcelona (41.384495N, 2.117497E, 98 m a.s.l.) every day at 12 UTC. The radiosonde equipment measured temperature (ºC), relative humidity (%), wind speed ($m\,s^{-1}$) and direction (º), barometric pressure (hPa), and height

(m). From these radio-soundings, the planetary boundary layer height (PBLH) could be inferred for comparison with the simulated values. To estimate the PBLH from the radio-soundings, we use the definition of Stull (2000) and Seibert (2000), which defines the top of the PBL as the minimum height where the virtual potential temperature (θ_v) is equal to that of the surface. This methodology is also used in the BouLac scheme to diagnose the PBLH. Note that the lowest height measured by the radiosonde is at the rooftop of a building (33 m from the ground), while the first level measured by the WRF model is around 2.5 m above the ground.

4.3 Results and discussion

Statistical analyses of the root-mean-square error (RMSE), mean bias (MB) and correlation factor (R) were used to compare the model simulations with the observations. The equations used for computing these indicators and the methodology to average them between stations is included in Appendix C.4.The standard deviation is included when the differences between averaged fields or averages of the statistical indexes are presented.

The simulations of each sensitivity test (BL-UM-HRL, BL-noUM and MYJ-UM), further described in the following subsections, are tested against the reference simulation (BL-UM) with a two-tailed Welch's t-test for each variable, statistical index and LULC group. The differences between modelled results and observation data are assessed through two-sample t-tests with two-tailed distribution for each pair of simulations, where we reject the null hypothesis with a 95 % confidence interval if the p-value is lower than 0.05 (see Appendix C.4 for a more detailed description). We only remark in the next sections the differences between statistical indexes of each simulation that are statistically significant.

4.3.1 Evaluation of the reference simulation

The near-surface temperature analysis is displayed in Figure 4.5 for each LULC group for the period of study (25 June to 10 July 2015) over the daytime (6-18 UTC) and night-time (19-5 UTC) periods.

During the daytime, BL-UM showed an average RMSE of 1.61 ± 0.39 ºC. The lowest RMSE for this period was obtained for the AA stations (1.38 ± 0.29 ºC) corresponding to overpredictions of near-surface temperatures. The highest RMSE was seen for the F&SNA stations (1.79 ± 0.56 ºC). Some reasons for this underestimation of T_{2m} in F&SNA stations could be: 1) an overestimation of the Bowen ratio, defined as the ratio between the sensible and latent heat fluxes, and 2) an overestimation of wind speed, that causes the reduction of air temperatures due the advection of cooler air from sea-breezes. The BL-UM simulation shows a high correlation with the average daytime temperature observations (0.91 ± 0.03), with higher correlations observed for AA stations (0.93 ± 0.02).

At night, BL-UM showed a reduction in the average RMSE (1.43 ± 0.56 ºC) with respect to the daytime period, although the error increased considerably for the AA (2.31 ± 0.71 ºC) stations, corresponding to overestimations of T_{2m}. The model also overestimated night-time T_{2m} for NAVUA stations (MB=1.03 ºC) and the other stations in lower measure (MB < 0.4 ºC). The overpredictions of the NAVUA and AA stations could be explained since most of these stations were classified as urban LCZs (see Table C.4), although other rural stations also showed positive MBs. Stations with higher night-time RMSEs corresponded to stations that are located on agricultural lands or in urban parks but are classified as urban LCZs. LULC misclassifications can have a considerable impact on the statistical analysis of results when compared to observations (Ribeiro et al., 2021). Overall, the simulated night-time temperatures were less correlated with the observations (0.86 ± 0.06) than the simulated daytime temperatures, except for at the F&SNA stations (R=0.90 ± 0.02).

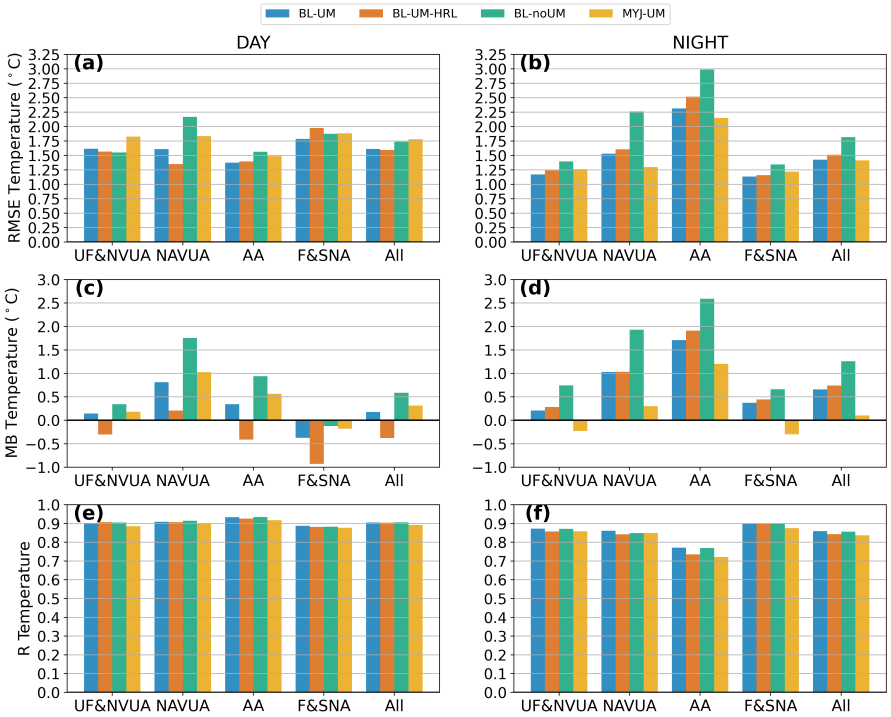


Figure 4.5: Temperature analysis for the performance of WRF simulations. Root mean square error (RMSE) (top), Mean bias (MB) (middle) and correlation coefficient (R) (bottom) at daytime (left) and night-time (right) for each simulation and LULC group of stations.

Similar to Figure 4.5, Figure 4.6 displays a statistical analysis of the modelled near-surface wind speed compared with the observed data. The statistical analysis of the wind speed showed an

average RMSE value of 1.67 ± 0.54 $m s^{-1}$ and 1.21 ± 0.48 $m s^{-1}$ for daytime and night-time, respectively, with lower RMSE values obtained for the NAVUA stations (0.82 ± 0.02 $m s^{-1}$, 0.65 ± 0.02 $m s^{-1}$). The analysis revealed a significant variability of the MB (-0.21 ± 1.34 $m s^{-1}$, -0.39 ± 1.36 $m s^{-1}$ and 0.45 ± 1.18 $m s^{-1}$ at daytime; -0.10 ± 0.75 $m s^{-1}$, 0.10 ± 0.60 $m s^{-1}$ and -0.08 ± 1.35 $m s^{-1}$ at night-time for UF&NVUA, AA and F&SNA stations, respectively), which we mostly attribute to poor simulation of wind flow over these stations. For some stations, the wind speed was clearly underestimated because the model considered higher building density than the actual local surrounding of these stations. The presence of dense building exerts a high drag effect on the wind which reduces its strength near the surface. For other stations placed on rooftops and two rural stations that measure 2-m wind speed, wind speed was overestimated because the model was not able to reproduce the increased surface drag of building rooftops or the ground.

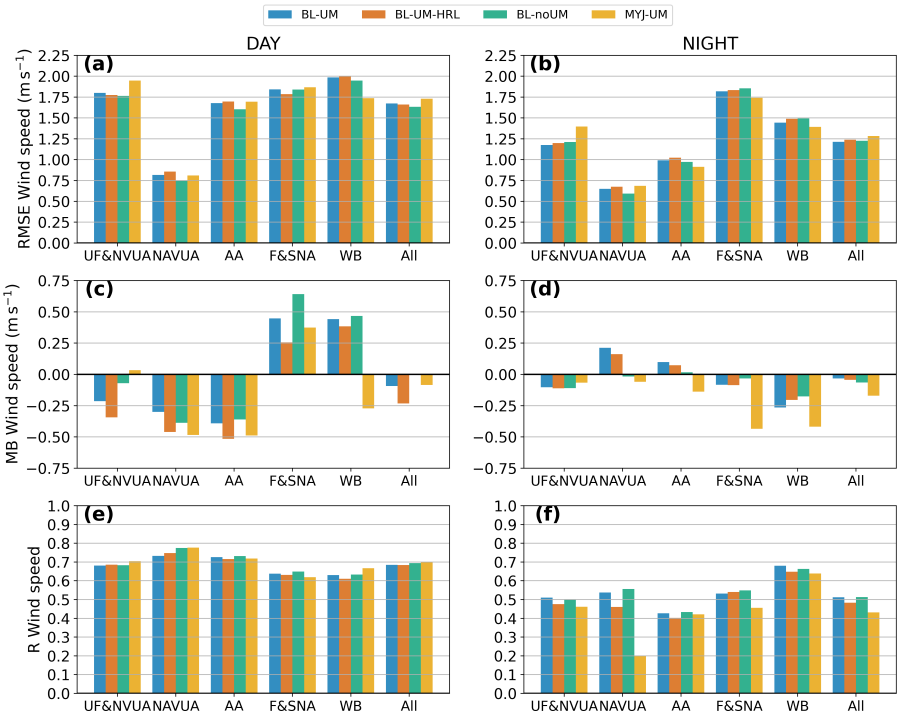


Figure 4.6: Wind speed analysis for the performance of WRF simulations. Root mean square error (RMSE) (top), Mean bias (MB) (middle) and correlation coefficient (R) (bottom) at daytime (left) and night-time (right) for each simulation and LULC group of stations.

Our RMSE results (1.57 ± 0.38 ºC and 1.49 ± 0.49 $m s^{-1}$) for temperature and wind speed,

respectively) and correlation factors (0.94 ± 0.03 and 0.73 ± 0.10) for the entire study period agree with the results of the study of Ribeiro et al. (2021), who also analysed meteorology in the AMB. Their study also uses the WRF-BEP-BEM model, with no specific urban morphology, to study the weather of the AMB for an entire summer month (July 2016). We obtain similar RMSE values and correlation factors for near-surface temperatures and wind speed than those obtained in their study (1.9 ºC and 0.91 for temperature and 1.5 $m\,s^{-1}$ and 0.73 for wind speed), despite the differences between the two studies. However, they observed an underprediction of daytime near-surface temperatures, while in our case, we observed an overprediction of night-time temperatures. These differences may be related to the differences between the two case studies and to the definitions of the urban canopy parameters.

Figure C.6 shows a comparison of the time series of simulated near-surface temperatures by the BL-UM simulation and the observed measurements averaged among all the stations. In general, the model can capture the temporal evolution of near-surface temperatures. The BL-UM simulation underpredicts maximum daytime near-surface temperatures for the 1 and 4 of July and overpredicts the temperatures considerably the day after the HW (July 7), considering this day to be the warmest day of the period of study. Day 7^{th} of July was the hottest day of the HW for some inland stations, although temperatures decreased during this day in coastal areas with respect to the previous 3 days. Moreover, as seen in the analysis (Figure 4.5d), the model accounts for an overestimation of night-time temperatures during the study period. The model simulates the evolution of the near-surface wind speed reasonably well during the study case (Figure C.7), except for underpredicting the maximum sea breeze speed for 26 June and 5 and 9 July and overestimating the sea-breeze speed for 7 July.

4.3.2 Sensitivity to the initialization of soil properties

Figure 4.7 presents a model comparison of T_{2m} and 10-m wind fields temporally averaged for the period of study over daytime and night-time between the simulation using HRLDAS soil data (BL-UM-HRL) and the reference using the ERA5 soil data (BL-UM). The spatial distribution of the standard deviation of the differences in T_{2m} between the two simulations over all the time steps available at daytime and night-time can be seen in Figure C.8.

From comparison in Figure 4.7, we can see that BL-UM-HRL accounts for lower daily temperature variability, with lower (higher) daytime (night-time) temperatures than those obtained from BL-UM, especially in the south and west rural regions of the AMB (Figure 4.7c and 4.7f). These temperature differences are significant in rural areas where BL-UM-HRL considers higher soil moisture values than BL-UM (see Figure 4.3f and 4.4f), such as in the west region of the AMB and the south coast. These differences between the two simulations can be seen during the entire simulation period for the T_{2m} time series of the rural station Viladecans (see Figure C.9c). Higher soil moisture values enhance evapotranspiration from pervious areas during the daytime, altering the surface energy balance that increases latent heat fluxes in detriment of lower sensible heat fluxes.

High night-time temperatures seen for BL-UM-HRL can be explained by two different reasons: 1) the HRLDAS data accounts for higher inner soil temperatures than ERA5, which implies high ground heat fluxes from the inner soil layers to the surface, and 2) moist soils have increased thermal properties (heat capacity and thermal conductivity) which implies higher heat retention in inner soil layers compared to dry soils during the day (Vahmani and Hogue, 2014). Both implies higher retention of the heat or an accumulated heat in inner soil layers which is released at night from the surface, compared to BL-UM.

During the daytime, the temperature differences between the two simulations led to enhanced sea breezes in the BL-UM simulation (differences up to 0.5 ± 0.9 $\mathrm{m\,s^{-1}}$) compared to those in BL-UM-HRL, although the maximum differences are below the standard deviation of wind speed. Moreover, at night, similar results were obtained by the two simulations, although the simulation without HRLDAS data accounted for slightly higher land breezes on the south-west coast of the AMB, where the temperature differences between the simulations were higher.

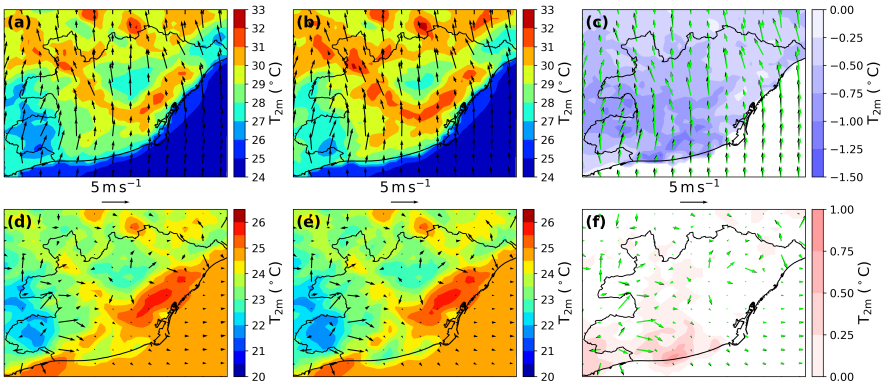


Figure 4.7: Model comparison of T_{2m} and 10 m wind vectors averaged at daytime (top row) and night-time (bottom row), for (a, d) BL-UM-HRL; (b, e) BL-UM; (c, f) difference BL-UM-HRL – BL-UM. The white colour in difference plots stands for temperature differences lower than 0.1 ºC in absolute value. In plots c and f, green vectors stand for the time-averaged wind vectors for BL-UM-HRL and black vectors for BL-UM.

The comparison between soil property initializations revealed different model performances for near-surface temperatures at daytime and night-time. During the daytime, the BL-UM-HRL simulation did not show a statistical improvement of the RMSE (1.60 ± 0.57 ºC) compared to the BL-UM simulation (1.61 ± 0.39 ºC) (Figure 4.5a). However, the RMSE differences were significant for NAVUA (BL-UM: 1.61 ± 0.21 ºC, BL-UM-HRL: 1.35 ± 0.07 ºC) stations due to reductions in the hot bias values. Urban irrigation is a common practice in the urban parks of the AMB in summer (Ajuntament de Barcelona, 2013), which enhances the evapotranspiration

while reduces the vegetation water stress. The increased soil moisture of the HRLDAS data compared to the ERA5 dataset can resemble the effect of irrigation on these areas and can explain the improvement of the BL-UM-HRL simulation in front of the BL-UM. Even though, the BL-UM-HRL showed higher RMSE in F&SNA areas (1.98 ± 0.85 ºC) than BL-UM at daytime, corresponding to an increase in the temperatures underpredictions.

During night-time, the model showed higher RMSEs with BL-UM-HRL (1.51 ± 0.59 ºC) than with BL-UM (1.43 ± 0.56 ºC) due to an increase in the overprediction of night-time temperatures for all the stations (Figure 4.5d). This increment in night-time overestimations with HRLDAS data was especially seen for AA stations, which are rural stations nearer to the south-west coast of the AMB, where higher night-time temperature differences are observed between the two simulations compared with other stations. This is related to a higher overestimation of night-time ground heat fluxes by the BL-UM-HRL simulation, due to an overestimation of inner soil temperatures by the HRLDAS data compared to the ERA5 data (see Figure 4.4c), or to an overestimation of the thermal capacity and thermal conductivity of the soil (functions of the soil moisture) by the BL-UM-HRL simulation. Overall, BL-UM shows better performance in the representation of night-time temperatures, with lower RMSE and higher correlation values than those obtained for BL-UM-HRL.

The statistics of WS_{10m} for all LULC groups of stations were all comparable between the two simulations and are shown in Figure 4.6.

In contrast with our results, other studies have obtained improvements in near-surface variables when HRLDAS data were used for different regions (Lakshmi et al., 2011; Rajesh et al., 2016; Sharma et al., 2017). Lakshmi et al. (2011) obtained a relative improvement in simulations of surface energy fluxes and soil moisture, including simulations using HRLDAS data, when simulating three regions with different climatic characteristics in the United States. However, they did not see a significant effect on the simulations of surface temperatures. Additionally, Rajesh et al. (2016) simulated a heavy rainfall event in northern India, comparing a mesoscale simulation initialized with HRLDAS data and one initialized with low-resolution reanalysis data. Using HRLDAS data, they obtained better representations of soil moisture when validated with station observations, along with more accurate evolutions of the PBL characteristics. Sharma et al. (2017) obtained clear improvements in simulations of T_{2m} and WS_{10m} when soil state variables were initialized with HRLDAS data for the simulation of a HW over the Chicago Metropolitan Area. Best and Grimmond (2014) remarked on the substantial impact of initial soil moisture on the performance of urban LSMs.

To our knowledge, this is the first study of this kind for a Mediterranean climate city. Overall, the statistical analysis done in this study has revealed that the inclusion of high-resolved long spin-up soil variables in the WRF-BEP-BEM model do not imply in a significant improvement of the model performance when a HW episode in the AMB is considered. The only significant improvement is seen for stations in urban parks at daytime, due to a better representation of urban soil conditions. Alternatively, the inclusion of HRLDAS data in the WRF model has

increased the RMSE of daytime temperatures in natural regions stations and night-time temperatures for all the stations.

4.3.3 Senstivity to urban morphology parameters

From Figure 4.8 and Figure C.10, we see that BL-noUM shows higher daytime and night-time temperatures than the BL-UM simulation in the urban areas in the northern region of the AMB (up to 2.2 ± 0.7 ºC higher during the daytime and 2.1 ± 0.4 ºC at night), while lower temperatures are seen in the south during the day (up to 0.8 ± 0.5 ºC), corresponding to industrial areas (LCZ 10) (Figure 4.8c). This difference is related to the changes in λ_u between the two model configurations, as mentioned in Section 4.2.3. Comparing Figure 4.8c and 4.8f with Figure C.4c, a correlation between daytime temperatures and λ_u can be observed. This correlation can be explained by an overestimation of urban fractions that increase heat absorption and sensible to latent heat ratios, producing higher near-surface temperatures in both daytime and night-time (Nemunaitis-Berry et al., 2017).

Both simulations presented similar wind fields during the daytime (Figure 4.8c), although BL-noUM presented slightly higher wind speeds in rural areas (differences up to 1.0 ± 0.4 $m s^{-1}$). This can be related to the increased temperature difference between sea and land, which causes an increased pressure difference between land and sea, enhancing the development of the sea breezes in this simulation. Considering that urban areas imply higher wind drag due to the presence of buildings (Barlow, 2014), this effect on wind speed is higher in rural areas. Moreover, at night, BL-UM presented considerably stronger wind speeds than BL-noUM (up to 1.1 ± 0.9 $m s^{-1}$). Unlike during the daytime, the increased night-time temperatures in urban areas due to λ_u overestimations by the BL-noUM simulation oppose the formation of a temperature gradient between land and sea, offsetting the formation of land breezes and mountain-to-valley breezes.

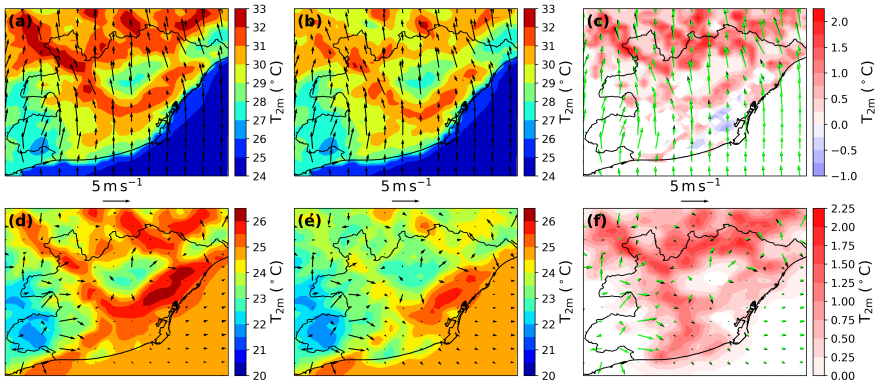


Figure 4.8: Model comparison of T_{2m} and 10 m wind vectors averaged at daytime (top row) and night-time (bottom row), for (a, d) BL-noUM; (b, e) BL-UM; (c, f) difference BL-noUM – BL-UM. The white colour in difference plots stands for temperature differences lower than 0.1 ºC in absolute value. In plots c and f, green vectors stand for the time-averaged wind vectors for BL-noUM and black vectors for BL-UM.

Overall, the inclusion of specific urban morphology (BL-UM) implies a slight reduction in the RMSEs of daytime near-surface temperatures compared to BL-noUM (1.74 ± 0.43 ºC), especially for NAVUA stations (BL-UM: 1.61 ± 0.21 ºC; BL-noUM: 2.17 ± 0.23 ºC) where daytime overpredictions were considerably decreased (Figure 4.5a). However, at night, the inclusion of specific morphology significantly improved the modelled near-surface temperatures in terms of RMSEs for all LULC groups (BL-UM: 1.43 ± 0.56 ºC, BL-noUM: 1.82 ± 0.78 ºC) (Figure 4.5b). The overestimation of λ_u by the default morphological parameters used in the WUDAPT methodology produced an increase in night-time temperature overpredictions in urban areas (Figure 4.5d). This overestimation especially affected the NAVUA and AA stations that were classified with a LCZ, increasing the RMSE of night-time near-surface temperatures.

In the case of near-surface wind speed, the model did not show a better performance when specific urban morphology parameters were used (BL-UM), showing that the WUDAPT methodology is capable of representing the effect of buildings on wind effectively. However, BL-UM obtained considerably higher RMSEs than BL-noUM did at two stations classified as urban LCZs where wind speed was significantly underestimated. These two stations are located in open spaces without the presence of buildings in their surroundings, so wind is not obstructed by the presence of buildings at these locations. Therefore, BL-noUM showed better agreement with the observations for these two stations since it considered higher wind speeds during the daytime (see Figure 4.8). However, the statistical analysis shows that the two simulations are similarly correlated to the near-surface wind speed observations, for all the LULC groups during the day and night.

This contrasts with the results obtained by Hammerberg et al. (2018), who found only marginal improvements using the LCZ-averaged site-specific urban morphology parameters in comparison with the WUDAPT methodology for the city of Vienna, Austria. However, significant differences arise between their study and our study. The city of Vienna is characteristic of the central European cities with uniform neighbourhoods, while the AMB is a highly heterogenous region characteristic of the Mediterranean coastal cities. Moreover, Hammerberg et al. (2018), compared the average the WUDAPT method with a gridded mean value calculation of the detailed site-specific Vienna GIS data set, not the point-by-point methodology used in our study. Therefore, their simulations were not able to represent properly any variation of morphology within grid cells of the same LCZ. Additionally, the differences seen in urban fractions between the Vienna urban morphology database and the WUDAPT database was minimal and compared to the differences seen in our study, evidencing that the WUDAPT database was more fitted for the city of Vienna than for our domain. Wong et al. (2019) also pointed out that the use of tables, such as those used in Stewart and Oke (2012), instead of using local specific data for each LCZ can add a large source of uncertainty in urban simulations. Therefore, as derived from the results of our study, we conclude that it is important to use site-specific urban morphology parameters in simulations of urban climates.

4.3.4 Sensitivity to PBL scheme

The sensitivity analysis (Figure 4.9 and Figure C.11) shows that MYJ-UM outputs higher daytime rural temperatures than BL-UM (up to 1.1 ± 0.9 ºC) (Figure 4.9c). In contrast, different results are seen over urban areas depending on the urban density. In open built areas (LCZ 6, open low-rise), MYJ-UM outputs higher near-surface temperatures than BL-UM, while in high-density built areas (LCZ 2, compact mid-rise), higher near-surface temperatures were obtained with the BouLac scheme (differences up to 1.3 ± 1.0 ºC). During night-time, BL-UM presented higher T_{2m} values (differences up to 1.2 ± 0.7 ºC) than MYJ-UM in all the domain. Therefore, MYJ-UM showed a higher daily temperature variability than BL-UM in rural areas.

From Figure 4.9, we can see that the model shows considerable sensitivity to the PBL scheme in its representation of near-surface winds, especially in the sea and rural areas. Interestingly, although the temperature differences between land and sea were lower for the BL-UM simulation during the daytime, BL-UM presented greater magnitudes of sea breezes in rural areas (especially in mountain ranges, with differences up to 1.3 ± 1.2 $m s^{-1}$) and sea areas, where changes in wind direction were identified (Figure 4.9c). However, MYJ-UM showed considerable sea-breeze strengths at higher levels inside the UBL (see Figure 4.11e). Over urban areas, we did not observe a significant difference in wind speed since wind speed was considerably low over these areas. In the case of night-time winds, MYJ-UM represented larger wind speeds than BL-UM in rural areas due to enhanced mountain-to-valley breezes.

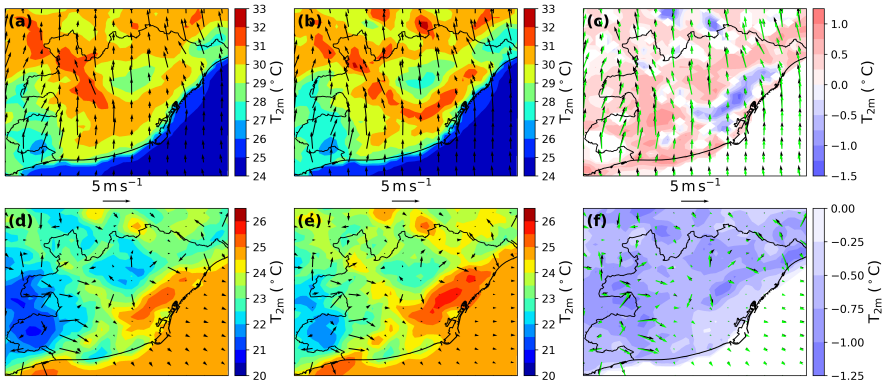


Figure 4.9: Model comparison of T_{2m} and 10 m wind vectors averaged at daytime (top row) and night-time (bottom row), for (a, d) MYJ-UM; (b, e) BL-UM; (c, f) difference MYJ-UM – BL-UM. The white colour in difference plots stands for temperature differences lower than 0.1 °C in absolute value. In plots c and f, green vectors stand for the time-averaged wind vectors for MYJ-UM and black vectors for BL-UM.

The modelled near-surface temperatures showed clear differences between the BL-UM and MYJ-UM simulations (Figure 4.5). The simulation conducted with BouLac scheme showed lower daytime RMSE values at all stations compared to those output by the MYJ-UM (1.78 ± 0.34 ºC). In especial, MYJ-UM showed higher errors for UF&NVUA (1.83 ± 0.30 ºC) and NAVUA (1.84 ± 0.21 ºC) stations compared to BL-UM (1.61 ± 0.30 ºC and 1.61 ± 0.21 ºC, respectively). In the case of night-time temperatures, different performances were obtained depending on the LULC group. From Figure 4.5b, we can see that BL-UM had lower night-time RMSEs for the UF&NVUA and F&SNA stations because MYJ-UM underpredicted T_{2m} for these regions. In contrast, for the NAVUA and AA stations, higher RMSEs were seen for BL-UM than for MYJ-UM; this difference is related to the larger overprediction of night-time temperatures by BL-UM (Figure 4.5d).

Therefore, there is a relation between the MB observed at night-time temperatures and the PBL scheme, considering the night-time differences between the two simulations (see Figure 4.9f). Even though, the MB is still high for AA (1.2 ± 0.85 ºC) stations, evidencing that there are other systematic errors related to different aspects of the WRF-BEP-BEM model.

The choice of the PBL scheme did not significantly impact the performance of the model in the case of the wind speed. The BL-UM simulation showed lower RMSEs for UF&NVUA stations at day (BL-UM: 1.80 ± 0.54 m s-1m s^{-1}; MYJ-UM: 1.95 ± 0.59 m s^{-1}) and night (BL-UM: 1.18 ± 0.37 m s^{-1}; MYJ-UM: 1.40 ± 0.61 m s^{-1}). These reduction in the RMSE is seen in the stations placed over rooftops where BL-UM considered a lower overprediction of the wind speed compared to MYJ-UM. The wind speed at these stations is taken from the closest vertical level

to the height of the meteorological station from the ground. Therefore, we can point out that the differences seen in the performance analysis of the wind speed between the two PBL schemes are related principally to the vertical distribution of the wind speed. Moreover, a difference in the performance of the two simulations is seen at daytime for the station placed over the sea, where MYJ-UM showed closer values to the observed ones than BL-UM. Overall, the BL-UM near-surface wind speeds showed higher correlations (0.51 ± 0.12) to the observed values at night-time than the simulated by MYJ-UM (0.43 ± 0.15), although similar correlations are obtained at daytime (BL-UM: 0.68 ± 0.09; MYJ-UM: 0.70 ± 0.10).

Figure 4.10 shows the time series of the modelled diagnosed PBL heights (PBLH) at the radiosonde launching location (nearest grid cell values to the radiosonde launching location) for the BL-UM and MYJ-UM simulations and the PBLH computed from the radio-sounding observations. Generally, both simulations reflected a rapid growth of the PBLH during the morning, reaching a maximum at midday, followed by the sinking of the inversion cape during the afternoon (Sicard et al., 2006). We observed that BL-UM considered higher diurnal PBLHs than MYJ-UM, except for on 9 July, when MYJ predicted a PBLH maximum. This difference between schemes was mostly produced by the discrepancies in the methodology used to determine the PBLH by each PBL scheme. These PBL schemes define the PBLH in different ways: MYJ defines the PBLH as the level at which the turbulent kinetic energy (TKE) decreases under a certain threshold, while BouLac defines the PBLH as the level where θ_v reaches the same value as that at the surface; the latter is the same method used for the observations.

If we derive the PBLH in the MYJ-UM simulation using the same method as that used in the BL-UM simulation (MYJ-UM_θ_v), we can see that the differences between the two simulations are not as high as before. Both simulations considered similar PBLH maxima except for days 25 and 26 of June and 1 and 3 of July when BL-UM show much higher PBLH; and on 5, 6 and 7 July, when MYJ-UM_θ_v provided higher mixing layer tops. The differences in PBLH between BL-UM and MYJ-UM_θ_v can be related to the differences seen in daytime near-surface temperatures between the two simulations for these days. As it can be seen in the temporal series of T_{2m} for the Zona Univ. station (Figure C.9b), at 1.2 km distance to the radiosonde launching location, BL-UM showed higher maximum T_{2m} than MYJ-UM days 25 and 26 of June and 1 and 3 of July. As for days 5, 6 and 7 of July; MYJ-UM presents higher midday T_{2m} than BL-UM.

Compared to the observations, BL-UM overpredicted the PBLH for all the simulated days except for 28 June, 4, 7 and 9 July. On the other hand, MYJ-UM underpredicted the PBLH at midday for all the measurements using the TKE profile method for the diagnosis, while it overestimated all the measurements using the virtual potential temperature method (MYJ-UM_θ_v), except for on 28 June, 1, 2, 4 and 9 July. The overestimations of the PBLH by the BL-UM and MYJ-UM_θ_v can be related to the overestimations of daytime near-surface temperatures by these two simulations as it can be seen on Figure C.9b. The day with the highest underestimation of the PBLH is the 4^{th} July, which corresponds to the only day that both simulations underpredict midday temperatures at the radiosonde launching location (Figure C.9b). Overall, the BL-UM simulations represented PBLHs close to the observations than the MYJ-UM simu-

lation. However, when the PBLHs of the MYJ-UM simulation are computed using the virtual potential method (MYJ-UM_θ_v), both simulations show similar performance in the prediction of the PBL height.

Banks et al. (2015) found similar results, where the BouLac represents closest PBLH at 12 UTC over the city of Barcelona for the main synoptic event of this HW (Shallow cyclone or Undetermined pressure gradient, regional recirculations). Banks et al. (2015) also used the WRF model, although without the coupling with a UCM for the urban areas. The inclusion of the BEP-BEM model and site-specific urban parameters in the PBL comparison has not implied in a modification of the results obtained by Banks et al. (2015).

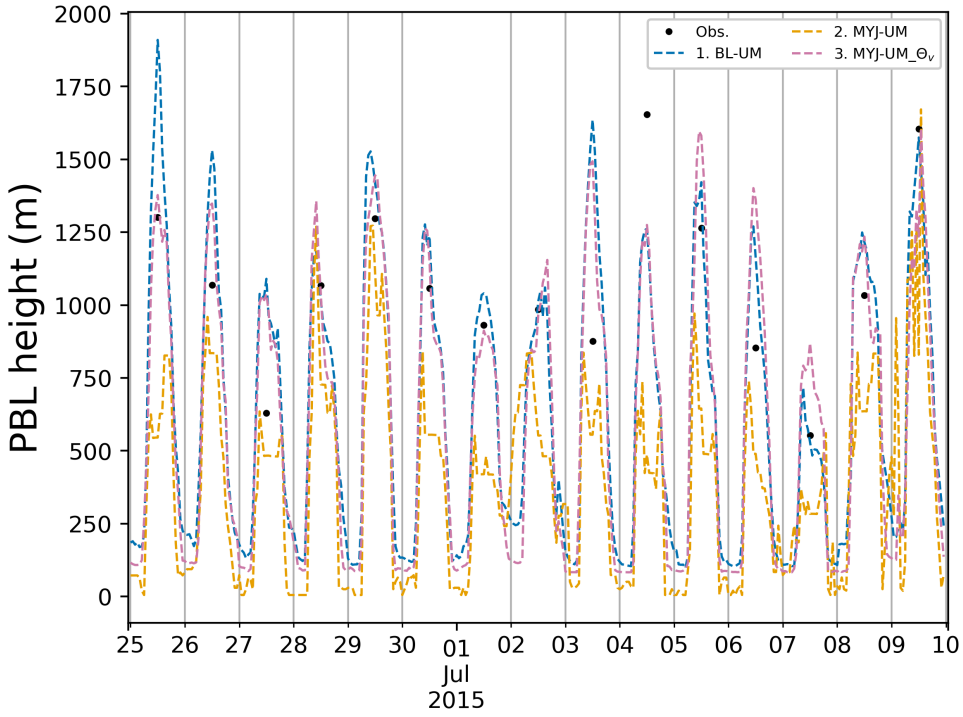


Figure 4.10: Time series of diagnosed PBL height at the radiosounding site by BL-UM and MYJ-UM simulations and the computed PBL height from radiosounding observations (Obs.) represented with black dots.

However, more observations recorded at different times of the day (the only available data for use in this study were recorded in the early morning or late evening) could help in the evaluation of the PBL schemes by increasing the reliability of the analysis. In this sense, different studies have used LiDAR measurements (Banks et al., 2015) to infer the mixing layer height at high temporal resolutions and almost continuously. Unfortunately, there were no available LiDAR

measurements for our period of study.

To analyse the differences in the representation of the vertical structure of the PBL seen in Figure 4.10, the vertical profiles of θ_v (K) and wind speed ($m\,s^{-1}$) derived from the simulations along with available radiosonde observations are displayed in Figure 11 for the three days that were considered the HW period (4, 5 and 6 July 2015) at 12 UTC.

For the first day of the HW (4 July 2015), both simulations showed considerably shallow PBLHs compared with the radiosonde observations (Figure 4.11a). We can see that both simulations underpredicted θ_v below 500 - 600 m, although MYJ-UM had a lower output (Figure 4.11a). From 600 m to 2000 m, the model overpredicted θ_v. In general, MYJ-UM showed the closest simulated values to the observations. In the case of wind speed, all the simulations showed underestimations above the PBL (Figure 4.11d), which was also seen in the other days of study (Figure 4.11e and 4.11f). The underestimations seen for the wind speeds at higher altitudes were produced by underestimations of the boundary conditions from the ERA5 wind fields (see Figure C.12 for the comparison of the ERA5 wind speed vertical profiles). At lower altitudes, BL-UM showed better results inside the PBL than MYJ-UM for the first day of the HW.

For 5 July 2015, the PBL seemed to be more stratified than that in the previous day, possibly due to the increase in the sea breeze force on this day (see Figure 4.11e). The WRF model-simulated θ_v values were slightly overestimated throughout the PBL (up to 1400 m), with the BL-UM simulation showing the closest values to the observations (Figure 4.11b). In the case of wind speed, the MYJ scheme showed better results than the BouLac scheme compared to the radio-sounding data inside the PBL.

The third day of the HW period (6 July 2015) showed the lowest observed PBLH, with a value of 850 m (Figure 4.11c). This low PBLH under unstable conditions was produced by large mesoscale compensatory subsidence over the sea and the formation along the coast of a thermal internal boundary layer, as reported by Sicard et al. (2006), which is typical for the city of Barcelona in summer months and weak pressure gradients with dominating mesoscale forcing conditions (e.g. sea and land breezes). Both simulations presented vertical profiles similar to that of the observations, although with overestimations of θ_v below 1400 m, which cause the model to overestimate the PBLH (Figure 4.11c). For the wind speed, no large difference was observed between the two simulations with underestimations inside the PBL. In general, the WRF simulations showed a cold bias tendency on the first day of the HW (4 July 2015), which changed throughout the simulation period to a warm bias towards the last day of the HW (6 July 2015).

When we compare these two schemes for the entire simulation period, we see that the vertical profile of θ_v using the MYJ scheme showed closer agreement with the observations for the firsts days of the simulation (25 – 28 June) (see Figure C.13). This is most likely due to a higher overestimation by the BL-UM simulation of the θ_v inside the PBL, especially near the surface. Between the 5^{th} and 7^{th} of July, the MYJ-UM overpredicted the virtual potential temperature

near the surface, so the BL-UM simulation showed closer vertical profiles to the radio-sounding. For the rest of the days, except days 29 and 30 June and 4 July, both simulations show similar profiles. Therefore, we can conclude that the vertical profiles are closely related to the bias in the near-surface, and that this bias can extend to the entire PBL. We can not identify a better PBL scheme for the representation of the vertical structure of the PBL due to the high variability of the results obtained and the different performance depending on the near-surface bias.

Additionally, we have found that BL-UM-HRL simulation has a better agreement than BL-UM for the vertical profile of the virtual potential temperature for almost all the studied days, due to the lower overestimation of UBL virtual potential temperatures (not shown). This agrees with the better performance of the BL-UM-HRL simulation representing midday near-surface temperatures for the Zona Univ. station (see Figure C.9b).

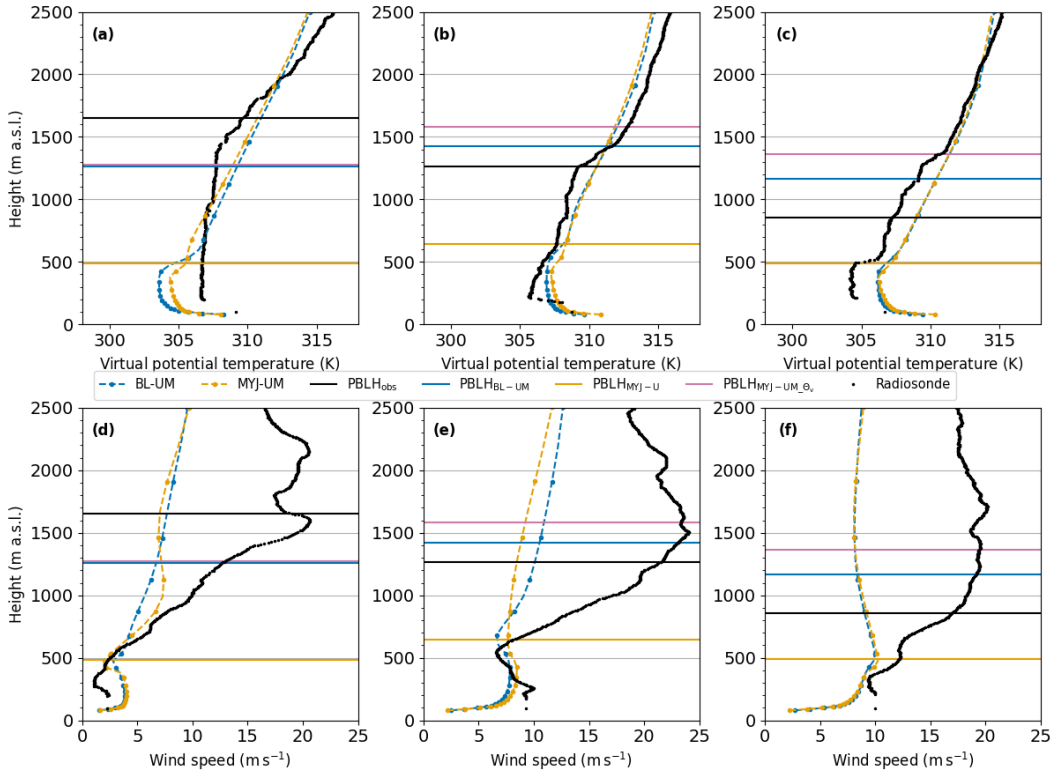


Figure 4.11: Comparison of vertical profiles of WRF model simulated potential temperature (K) (top) and wind speed ($m s^{-1}$) (bottom) and radiosonde observations from the launches at 12 UTC at the days 4 July 2015 (a, d), 5 July 2015 (b, e) and 6 July 2015 (c, f).

4.3.5 Sensitivity of the UBL to urbanization

Figure 4.12 shows a vertical cross-section of the potential temperature overlaid by wind vectors for the reference simulation (BL-UM) and the urban-to-croplands/natural vegetation mosaic-

modified simulation (BL-crop) on 4 July 2015 at 14 UTC (Figure 4.12a and 4.12b) and 22 UTC (4.12c and 4.12d), the representative moments of the maximum sea breeze periods over the city (daytime) and the period of maximum UHI intensity (night-time), respectively. Overlaid in the black dashed line is the PBLH diagnosed by the BouLac scheme. During the day, the BL-UM simulation showed higher near-surface temperatures than the BL-crop simulation (up to 3.4 ± 1.1 ºC, see Figure C.14). Urban areas also modified the potential temperature inside the UBL, increasing the temperatures of the overlying air by convection and, consequently, increasing the mixing height (Stull, 1988). Interestingly, we can also see that the sea breeze front penetrated further inland in the BL-crop simulation than in BL-UM, even though the temperature differences between land and sea were smaller. Similar results were obtained by Sharma et al. (2017), who compared two similar scenarios but for the Metropolitan Area of Chicago and the interaction between the UHI of the city and the Lake Michigan breeze. They suggested that the reduced surface roughness length of cropland fields compared to buildings exerted a lower drag on the wind, implying higher near-surface wind speeds, as can also be seen in our case (see Figure C.14c). Moreover, Barlow (2014) reviewed different studies relating sea breezes and the UBL. They concluded that UHIs delay the passage of sea breeze fronts when passing through urban areas due to the effect of building drag on wind flow. In the BL-UM simulation, the presence of the city near the coast modified the UBL; therefore, sea breezes advected warmer temperatures inland, forming a heat plume that crossed Collserola Mountain and extended to the Vallès region (Valley). Therefore, we can observe that the spatial extent of the sea breeze thermoregulatory effect is influenced not only by the temperature difference between the land and sea but also by the surface friction of the land-use type (Martilli, 2003; Barlow, 2014; Sharma et al., 2017).

At night, the release of the heat accumulated during the day by urban fabric materials caused the intensification of the UHI effect, increasing temperatures inside the UBL and especially near the surface (up to 4.3 ± 1.1 ºC; Figure 4.12c, 4.12d and C.14f). This impact was higher at night than in the daytime, as would be expected due to the properties of the UHI in Barcelona city (Moreno-garcia, 1994; Martin-Vide and Moreno-Garcia, 2020). From Figure 4.12c, we can see that in the BL-UM simulation, a well-formed mixing layer above the city (PBLH $\sim$ 500 m a.s.l) was sustained even after sunset. The release of sensible heat from urban areas can maintain the structure of the mixing layer due to the rise of thermals from the surface (Stull, 1988). Moreover, the presence of the UHI above the city prevented the development of land breezes. When urban areas were modified to cropland fields, the UHI effect did not develop, and a weak land breeze could be seen (Figure 4.12d and Figure C.14e).

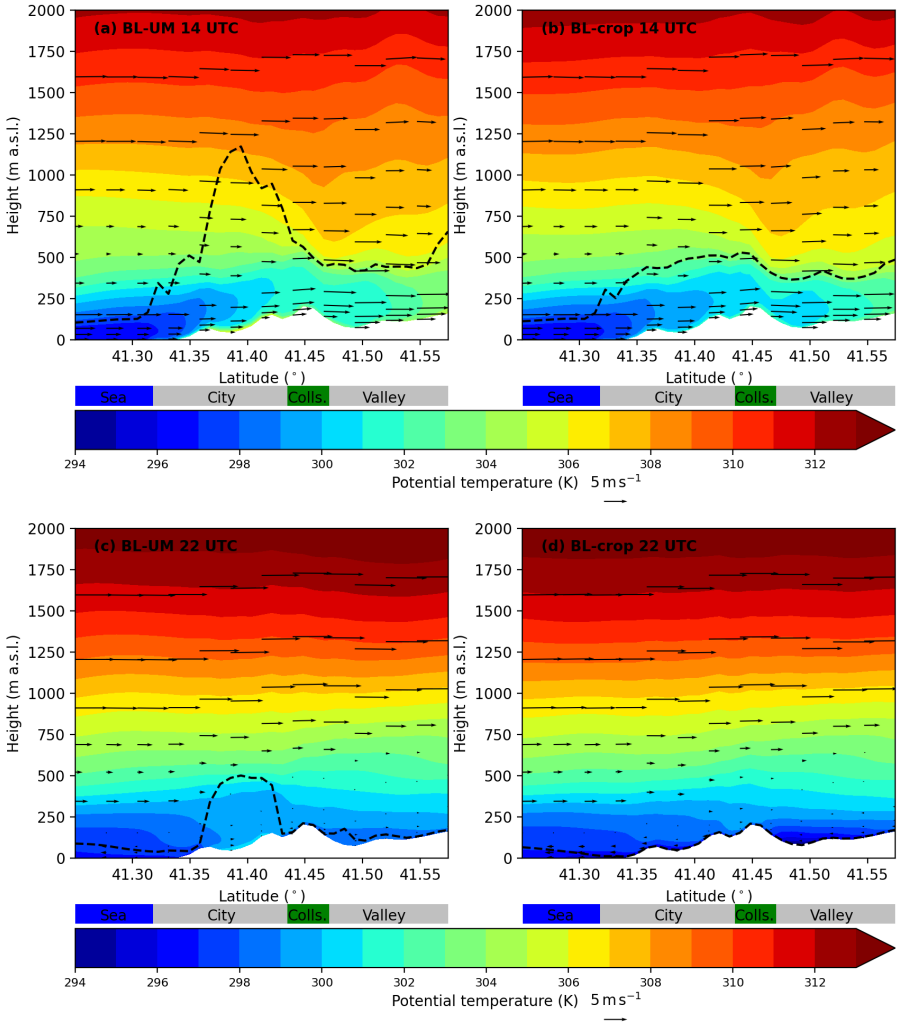


Figure 4.12: Vertical cross-section of potential temperature (K) (as shown in Figure 4.1 as a red line) overlaid by wind vectors on 4 July 2015, for (a) BL-UM during day (14:00 UTC), (b) BL-crop during day (14:00 UTC), (c) BL-UM during night (22 UTC), (d) BL-crop during night (22 UTC). Overlaid in dashed black line is the PBLH diagnosed by the BouLac PBL scheme. Colls. refers to Collserola Mountain.

4.3.6 Relation between near-surface temperatures and urban fraction

To study the relation between near-surface temperatures in urban areas of the AMB and λ_u, an analysis similar to the one used in Li et al. (2019) was performed. We used simulated T_{2m} values obtained from the BL-UM simulation for the analysis, as BL-UM accounted for the specific λ_u of each urban grid cell in its initialization of the urban morphology. To compare different urban areas with heterogeneous LULCs, surface properties, building morphologies and terrain heights, a zonal statistical analysis was used. All the urban classified grids in the ROI were divided into 20 groups with a constant λ_u interval of 0.05. The first group contained grids with λ_u values higher than 0 and lower or equal to 0.05; the second group contained grids with λ_u values higher than 0.05 and lower or equal to 0.10; and this pattern continued until the last group contained grids with λ_u values between 0.95 and 1.00. The average number of grids per bin is 26.6 ± 12.4; and the maximum and minimum values are 55 and 3 grids for the 0.00-0.05 and the 0.95-1.00 bins, respectively. The mean simulated T_{2m} and λ_u were computed within each group. Then, a linear regression was performed to obtain the λ_u-linear function for T_{2m}. The coefficient of determination (R^2) of the linear regression was used to evaluate the accuracy of the linear functions.

Figure 4.13 shows the relation between the simulated daytime and night-time T_{2m} and λ_u by computing the mean values for each 0.05-λ_u interval for the reference simulation (BL-UM). T_{2m} increased with increasing λ_u, with a higher correlation at night (R^2=0.96, p< 0.01) than in the daytime (R^2 = 0.88, p<0.01). The near-surface temperatures showed higher sensitivity to urban fractions during daytime, with a slope of 1.95 ºC than during the night-time, when the slope was 1.78 ºC. The intercept value should be similar to the mean of the rural T_{2m} since it corresponds to the case where λ_u is 0. During the daytime, the intercept was 29.3 ºC, which coincided with the average simulated T_{2m} over rural areas in the ROI for the BL-UM simulation (28.5 ± 2.2 ºC). The night-time interception parameter obtained from the linear regression with a value of 23.4 ºC also coincided with the average rural T_{2m} obtained for the BL-UM during the whole period of study (23.9 ± 0.9 ºC).

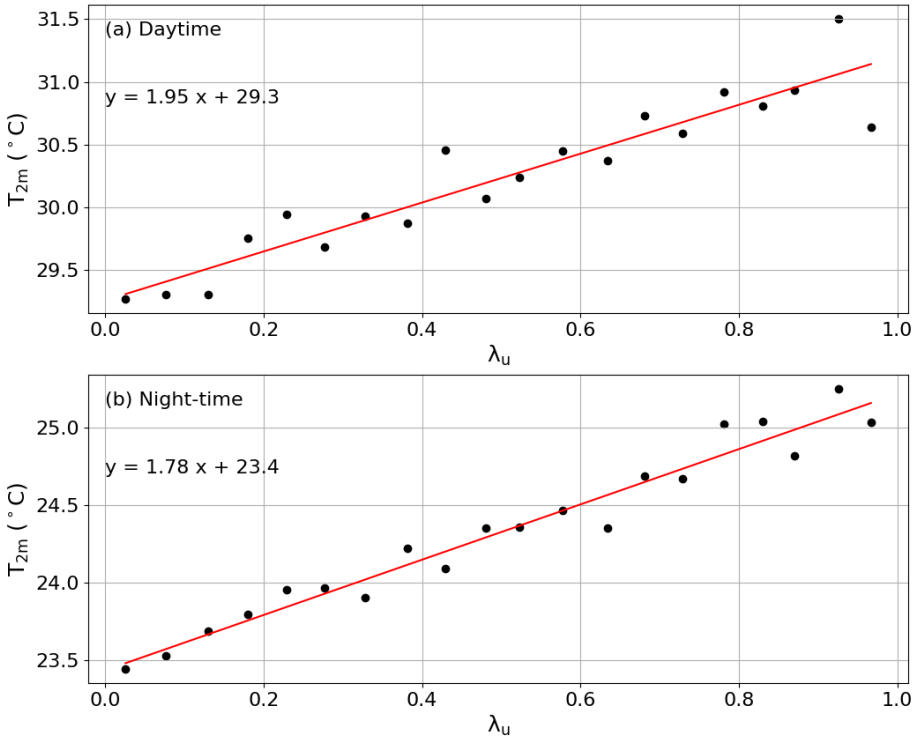


Figure 4.13: Relation between urban fractions (λ_u) and the simulated mean 2 m temperatures (T_{2m}) in the daytime (a) and night-time (b) during the period of study. The black dots show the mean values of the simulated T_{2m} and λ_u within all the 0.05 intervals of the λ_u in the urban areas inside the ROI.

The differences between the surface energy budgets of urban and vegetated areas caused this observed increase in T_{2m} with urbanization (Oke, 1982; Li et al., 2019). The WRF-BEP-BEM computed the T_{2m} for each grid cell from the first-level potential temperature, which is strongly influenced by the sensible heat flux. Furthermore, the sensible heat flux (SH) was computed using the linear relation between the sensible heat flux from the urban part (SH_{urb}) and the term from the rural part (SH_{rural}), averaged by the urban fraction as shown below:

$$SH = \lambda_u \cdot SH_{urb} + (1 - \lambda_u) \cdot SH_{rural} \tag{4.1}$$

To investigate the physical mechanism that controls the relation between T_{2m} and λ_u, the same methodology was used to reflect the relation between SH and λ_u. We obtained a linear relation with a determination coefficient of 0.96 ($p<0.01$) during the daytime and 0.99 ($p<0.01$) at night (Figure C.15). Therefore, even though SH_{urb} may vary among different urban areas depending on the urban morphology parameters, the linear relation was strong since SH_{rural} was

practically constant for all the urban grid cells because the model used the same land-use class (cropland/natural vegetation mosaics) for all the pervious areas inside any urban grid cell, with the same SHDFAC and LAI values applied to all these grid cells. This influences the strong linear relation of the sensible heat flux with λ_u, and a linear relation was also derived for T_{2m}; although this variable is not only dependent on the sensible heat flux, it is strongly affected by it. Additionally, the overprediction of the SHDFAC and LAI of the pervious areas in urban grid cells could explain the strong relation between λ_u and *SH* at daytime seen in this study during the daytime, which was not seen in the study of Li et al. (2019).

However, the evaluation of the model performance in this study revealed that the WRF-BEP-BEM simulations showed a considerable positive bias for night-time near-surface temperatures in urban grid cells with considerable vegetated areas such as urban parks and peri-urban agricultural areas (λ_u ranging from 0.21 to 0.65). Therefore, we can expect that the actual linear relation is not as correlated as the one that we obtained in our results, because, in reality, heavily vegetated urban areas are likely cooler than what simulated. The higher sensitivity of T_{2m} with the λ_u function during the day compared to the night reveal an inefficiency of the model as we could expect a higher UHI effect over the urban areas of the AMB during the night, as it is shown in Section 4.3.5. This study is repeated with the WRF-BEP-BEM simulations detailed in Chapter 5, which include a higher spatial horizontal resolution (333 m), a newer version of WRF (version 4.3.3), the inclusion of a methodology to represent different land-cover types in the pervious areas of urban grid cells (varying SHDFAC and LAI in urban grid cells), and the simulation of a longer period (1 month). The replication of these results for the new simulations is shown in Appendix C.6.

4.4 Conclusions

In this study, we analysed a high-resolution simulation of a heat wave (HW) event in the metropolitan area of Barcelona using the WRF model coupled to the BEP-BEM urban canopy parameterization at a 1-km resolution. The overall aim was to investigate the sensitivity of high-resolution mesoscale simulations to the 1) soil moisture initialization; 2) inclusion of site-specific urban morphology parameters; and 3) planetary boundary layer (PBL) scheme. The initialization of soil properties using HRLDAS data, in comparison with low-resolution ERA5 data, significantly changed the simulations of the near-surface temperatures, decreasing the diurnal temperature range. Although the HRLDAS data showed a qualitatively better representation of the heterogeneity of soil properties with land-use in the ROI, the results of this study showed that the performance of the model only significantly improved for stations situated in urban green areas at daytime due to a better representation of soil moisture. For all the stations, the inclusion of HRLDAS data supposed in an increase in the overestimation of night-time near-surface temperatures. Unfortunately, there are currently no soil moisture measurements available to quantitatively evaluate these soil initialization datasets. More evaluation studies are required for Mediterranean coastal cities to understand the impact of different initializations of soil properties.

As we expected, including site-specific urban morphology data in the BEP-BEM model instead of default urban parameters derived based on the WUDAPT methodology significantly improved the modelled near-surface temperatures during the day and night-time, especially in urban green areas. The usage of the urban morphology parameters, as detailed in the tables of Stewart and Oke (2012) for each LCZ, overestimated urban fractions when the LCZ map, originally at a 100-m resolution, was resampled to the coarser WRF model resolution (1 km), losing important sub-grid-scale variability. Therefore, we can conclude that it is important to use site-specific urban morphology parameters of the studied region.

The larger biases seen in this study correspond to stations placed in urban green areas with considerable vegetation surrounded by large urban landscapes, and the model classified the nearest grid cell to the station as an urban LCZ. Because of this, a considerable discrepancy existed between the local surroundings of these stations and the conditions that the model represented. This aspect can reflect an additional source of uncertainty and can interfere in the comparison of different sensitivity runs. Running the model at a higher resolution to fully capture urban green areas should improve the model performance, especially in green urban areas and agricultural lands close to urbanized areas. Future urban studies should be run with higher horizontal resolutions (below 1 km) to increase their representation of urban heterogeneity in the utilized models.

The sensitivity study of the WRF model to the PBL scheme had a significant impact on the modelled state variables inside the PBL. The BouLac PBL scheme performed better than the MYJ scheme for near-surface temperatures for all stations during the daytime and for urban stations and forest regions at night-time. Nevertheless, MYJ showed lower overestimation of night-time temperatures in high vegetated urban stations due to a reduction of temperature overestimations. Similar performances were obtained for the modelled wind speed. Additionally, the vertical profile of the simulated virtual potential temperature was used to derive the PBLH for both simulations at midday. BouLac scheme considered much higher PBLH than MYJ, although the differences were reduced when a similar method for deriving the PBLH was used for the two simulations. Overall, BouLac scheme overestimated PBLH for midday radiosounding measurements of the PBL top, while MYJ underestimated all the mixing layer heights. Using the BouLac scheme provided better agreement with the PBLH observations, in line with other studies for the city of Barcelona (Banks et al., 2015; Banks and Baldasano, 2016). We also found that the vertical profiles are closely related to the bias in the near-surface temperatures, and that this bias can extend to the entire PBL.

In addition to the above-mentioned sensitivity studies, we also investigated a theoretical scenario without urban areas in the AMB with the aim of studying the impact of urbanization on the UBL temperature and wind speed with a special focus on T_{2m}. Increasing the vegetation in urban areas revealed the considerable impact of a decrease in T_{2m} since the UHI effect does not develop under these conditions, which consequently reduces the PBLH in this scenario. Moreover, the strength of sea-land breezes in the daytime and at night was higher in the scenario without urbanization. Even though daytime UHIs favour the temperature gradient between land and sea

that forms sea breezes, the surface roughness induced by urban buildings has a greater impact on wind speed, inducing a drag effect on wind flows. During night-time, the UHI of the city prevents the formation of land breezes, which can be seen in the scenario without urbanization. Moreover, in this study, we observed that urban areas also reduced the penetration distance of sea breezes in the land interior throughout the entire height of the UBL, in accordance with other studies (Barlow, 2014).

Finally, we showed that the T_{2m} field followed a linear relation with urban fractions for the urban areas inside the ROI, which is more evident at night than in the daytime. This linear relation arises from the difference in temperature between vegetated and urban areas due to the differences in their surface energy balances. However, this relation was unrealistically intensified in our study by the homogeneity of the pervious areas in the urban grid cells. Adapting the WRF-BEP-BEM model to account for sub-grid-scale LULC variability, such as integrating different vegetation land cover types for the pervious part of urban areas, or increasing the horizontal resolution in the model, could lead to improved simulations of urban areas. Overall, more studies are needed to determine the relation between near-surface urban temperatures and urban fractions accounting for specific urban morphology, sub-grid-scale variability in LULC and increased horizontal resolutions to achieve an optimal representation of landscape heterogeneity within the simulations. Understanding this relation will provide an important tool in studies of future heat-abatement urban planning strategies.

Chapter 5

The food-water-climate nexus of green infrastructure: Examining ecosystem services trade-offs of peri-urban agriculture

Abstract: Emission reduction, heat mitigation, and improved access to water and food provision are increasingly critical challenges for urban areas in the context of global climate change adaptation and mitigation. The revival of local agricultural production is often lauded as a potential nature-based solution. However, an expansion of peri-urban agriculture (peri-UA) may entail significant trade-offs in the ecosystem services it provides. This study explores the impacts on the food-water-climate nexus of different scenarios of peri-urban agricultural expansion in a semi-arid, Mediterranean climate city, addressing local food provision, freshwater use, local temperature regulation, global climate change mitigation, and the trade-offs thereof. Examining four theoretical land-use scenarios in the Metropolitan Area of Barcelona, the study integrates estimates of food provision and irrigation water requirements based on georeferenced urban metabolism approach with the local atmosphere and biogenic carbon balance estimates produced through the combination of an atmospheric model with a satellite and meteorological-driven biosphere model. Our study reveals that a 31.12 % (+17.27 km^2) and 115.08 % (+64.25 km^2) increase in the current peri-UA in the AMB, achieved by replacing natural non-forested and forest areas, results in an increase in local food production of 24.0 % (+16503 tons $year^{-1}$) and 85.8 % (+58940 tons $year^{-1}$), respectively. However, it would also increase the irrigation water requirements by 10.0 % (+3.2 hm^3) and 43.5 % (+14.1 hm^3), respectively. The analysis of the midday/mid-afternoon temperatures during a summer hot month reveals that peri-UA especially when it is irrigated can potentially reduce near-surface temperatures up to 0.7 ºC with respect to a current scenario, however the air cooling affects principally located in rural regions with lower population density, while temperature reductions in the densest urban areas are minimal. If an expansion of peri-UA goes at the expense of natural non-forested and forests areas, as in the scenarios we used, it has further the potential to disrupt the regional carbon balance, impacting

the net ecosystem productivity of the AMB green infrastructure and overall carbon stocks with reductions in the net ecosystem productivity of up to 18.5 % and reduce total carbon stocks by 3.3 %. These findings, derived from an innovative and combined modelling approach, reveal significant trade-offs in ecosystem services associated with an expansion of peri-urban agriculture. It is likely that similar trade-offs would be observed with other nature-based solutions strategies. An integrated understanding of these trade-offs, facilitated by nexus approaches that combine different models, appears to be a promising direction for informing land-use decision-making in the context of urban climate adaptation and mitigation.

5.1 Introduction

Cities are challenged with providing food security and access to water amid climate changes that are provoking droughts and dwindling crop yields (Kang et al., 2009; Beillouin et al., 2020). Densely populated urban areas are particularly vulnerable to these combined threats, yet they also hold great potential for solutions to environmental challenges (Elmqvist et al., 2013). Lately, Nature-based solutions (NBS) have gained strong attention in this context (Debele et al., 2023; Zhu et al., 2023). NBS refers to actions that protect, conserve, restore, sustainably use, and manage natural or modified ecosystems to tackle social, economic, and environmental issues (United Nations Environment Programme, 2022). Within these actions, green infrastructure (GI), as natural and semi-natural areas, are designed and managed to enhance biodiversity and to provide a wide range of ecosystem services (European Commission, 2013; Langemeyer and Baró, 2021), including: urban parks, forests shrublands, street trees, green roofs, gardens, urban agriculture, green corridors, and wetlands (Naumann et al., 2011). Among others, ecosystem services sustained by GI include local temperatures regulation (Bowler et al., 2010; Marando et al., 2022), and global climate mitigation by atmospheric carbon sequestration through photosynthesis and storage in soil and vegetation biomass (Jo and McPherson, 1995; Nowak and Crane, 2002; Zhao et al., 2010). However, these NBS also require resources such as irrigation water. Understanding such trade-offs regarding the costs and benefits of ecosystem services broadens the evaluative space for planning NBS within wider GI strategies (Chan et al., 2011; Howe et al., 2014; Turkelboom et al., 2018).

Peri-urban agriculture (peri-UA) is a critical GI strategy that aims to provide locally grown crops, offering a multifunctional NBS to promote circular economies, social cohesion, biodiversity preservation, and reduced environmental impacts within the food supply chain (Langemeyer et al., 2021; Piorr et al., 2018). Notably, at regional scales, irrigated agriculture has been found to reduce regional temperatures during the dry season by 4-8 ºC compared to urban environments and natural dry vegetation, effectively creating a cooling effect for urban areas (Kueppers and Snyder, 2012). However, there are also trade-offs associated with peri-UA: these agricultural areas often displace other natural land uses that provide crucial ecosystem service such as biodiversity conservation and carbon sequestration (Tilman, 1999). While the methane (CH_4), carbon dioxide (CO_2), and ammonia (NH_3) emissions resulting from the use of mineral fertilizers and biomass burning are avoiding those same emissions somewhere else in the world, conventional

agricultural practices applied in peri-UA reduce soil organic carbon in agricultural land (Aguilera et al., 2018). Peri-UA can lead to significant water usage, potentially impacting the water balance in dry regions, especially under future drier climates such as the Mediterranean region (Giorgi and Lionello, 2008).

To help policymakers in the recognition of potential synergies and trade-offs in urban planning and resource management, integrated nexus approaches have been well employed at national and regional scales (Laspidou et al., 2020; Lee et al., 2020). The most studied nexus in the literature so far is the water-energy-food nexus (Bazilian et al., 2011; Albrecht et al., 2018; Dargin et al., 2019; Endo et al., 2020), offering a promising conceptual approach in the complex task of resource management. Yet, this approach has not been fully applied to the study of NBS (Carvalho et al., 2022), especially in terms of the ecosystem services and requirements of GI at the metropolitan scale. Carvalho et al. (2022) identified that NBS are commonly assessed for tackling one of the elements of the nexus unidimensionally, and that ecosystem service's nexus assessments are rarely quantified using metrics. For instance, Mendonça et al. (2023) have addressed the water-food-environment nexus on a qualitative analysis, exploring integrative management solutions to reduce environmental impacts in the water and food resources, but not quantifying the interlinkages with climate. In this study, we propose the implementation of the food-water-climate nexus in the context of the assessment of peri-UA, as an exemplary NBS, at the metropolitan scale, considering the increasing efforts in urban planning to mitigate and adapt to climate change and to increase water and food security in urban areas, while proposing sustainable solutions to diverse environmental impacts.

The trade-offs between agriculture provisioning services and other ecosystem services and environmental impacts might emerge both at spatial and temporal scales (Power, 2010). Especially relevant is the temporal variability of the provision of ecosystem services during extreme heat events, as this not only threatens public health (Li and Bou-Zeid, 2013; Iungman et al., 2023), but also suppose a problem for food (Beillouin et al., 2020) and water security (Belleza et al., 2023), and the integrity of ecosystems conforming the GI (Qu et al., 2024). The provision of ecosystem services is highly dependent on the health of the ecosystems and the resistance and resilience of the vegetation to different climatic disturbances as it can be heat waves and droughts (Qu et al., 2024), which are projected to be more frequent and intense in the future over dry regions as the Mediterranean region (Giorgi and Lionello, 2008). The resilience of the ecosystems to heat and drought events depend on the vegetation and local climate. Natural ecosystems can be more adapted to the impacts of extreme climate events as droughts and water scarcity (Bastos et al., 2020; Ermitão et al., 2021). Over the Mediterranean basin, forested areas present higher resistance to droughts and heat events than croplands, being affected with a smaller decrease in vegetation productivity (Ermitão et al., 2021). Therefore, peri-UA strategies can displace the natural vegetation, reducing the resilience and resistance of the GI of a city to heat and drought events, and compromising the provision of ecosystem services.

We would like to contribute further to the quantification of potential synergies and trade-offs between ecosystem services and costs in NBS implementations, systemically exploring the impacts

of land use changes resulting from expanding peri-UA and analysing the trade-offs involved in the food-water-climate nexus such as: (a) local food provision, (b) freshwater use (irrigation requirements), (c) local temperature regulation (heat mitigation), and (d) global climate change mitigation (biogenic carbon balance). We also study the impact of a heat wave event on the air-cooling and atmospheric carbon capture capacities of the GI to identify different responses between natural and agricultural vegetation. Ultimately, our study aims to support the design of effective NBS-GI strategies framed within the urban challenges of the food-water-climate nexus. We illustrate our approach by examining four theoretical land use scenarios proposed by the Urban Master Plan in the Metropolitan Area of Barcelona (AMB), encompassing different degrees of urban and agricultural development. In this study, we combine the estimation of agricultural food provision and irrigation water requirements using a georeferenced urban metabolism approach, while the local atmosphere and biogenic carbon balance are simulated using regional atmospheric and biosphere models.

5.2 Case Study

The AMB, with 36 municipalities and 3.3 million people, is situated in the Catalonia region, in north-west of the Mediterranean basin and in the north-east of the Iberian Peninsula. The AMB is characterized by a land cover distribution where 45 % is dedicated to built-up spaces, including urban areas, roads, and urban parks, while 42 % is occupied by forests and shrublands (CREAF, 2015). After a strong decline over the past 70 years, agricultural land covers currently only 8 % of the area (Rufí-Salís et al., 2019). The newly developed Metropolitan Urban Master Plan (Barcelona Regional and AMB P.D.U., 2019) aims to inverse this trend. While most agricultural land has been converted into new urban areas, a large fraction has also been abandoned and taken over by natural vegetation. The recovery of these abandoned agroforestry spaces for agricultural purposes could enhance local food production, but it could also have a disadvantage in terms of reducing the carbon sequestration capacity of the GI in the AMB and enhancing water demands. This strategy thus raises questions about synergies and trade-offs between local food production and global and local climate regulation and irrigation water requirements.

5.2.1 Peri-UA scenario development

To explore these issues, four land use scenarios have been developed: the Current scenario (S0), the Trending scenario with increased urbanization and reduced agriculture based on current urban planning (S1), an Alternative scenario involving the recovery of open spaces for agricultural purposes (S2), and a Potential scenario building upon S2 by further reclaiming abandoned agricultural fields for agriculture (S3). Each scenario has a different impact on the peri-UA surface extension and proportion inside the AMB, as it is seen in Figure 5.1.

The scenario S1 entails in an increase of urban parks and urban built-up areas of 18.56 km^2 and 16.54 km^2, respectively, in detriment of a decrease in the croplands, forests and natural non-

forested areas of 10.93 km^2, 12.31 km^2 and 11.82 km^2, respectively (Figure 5.1c). In the case of S2, the peri-UA in this scenario increases in 17.37 km^2, especially in the form of irrigated agriculture, in detriment of forests and natural non-forested areas which decreases in 8.48 km^2 and 9.47 km^2, respectively. Finally, in the scenario S3, the peri-UA increases by 64.25 km^2 in the AMB, at an expense of natural non-forested areas (-26.20 km^2), forests (-26.08 km^2) and urban areas (-12.32 km^2). More details about the land-use and land-cover (LULC) classification used and its creation are detailed in Appendix D.1.

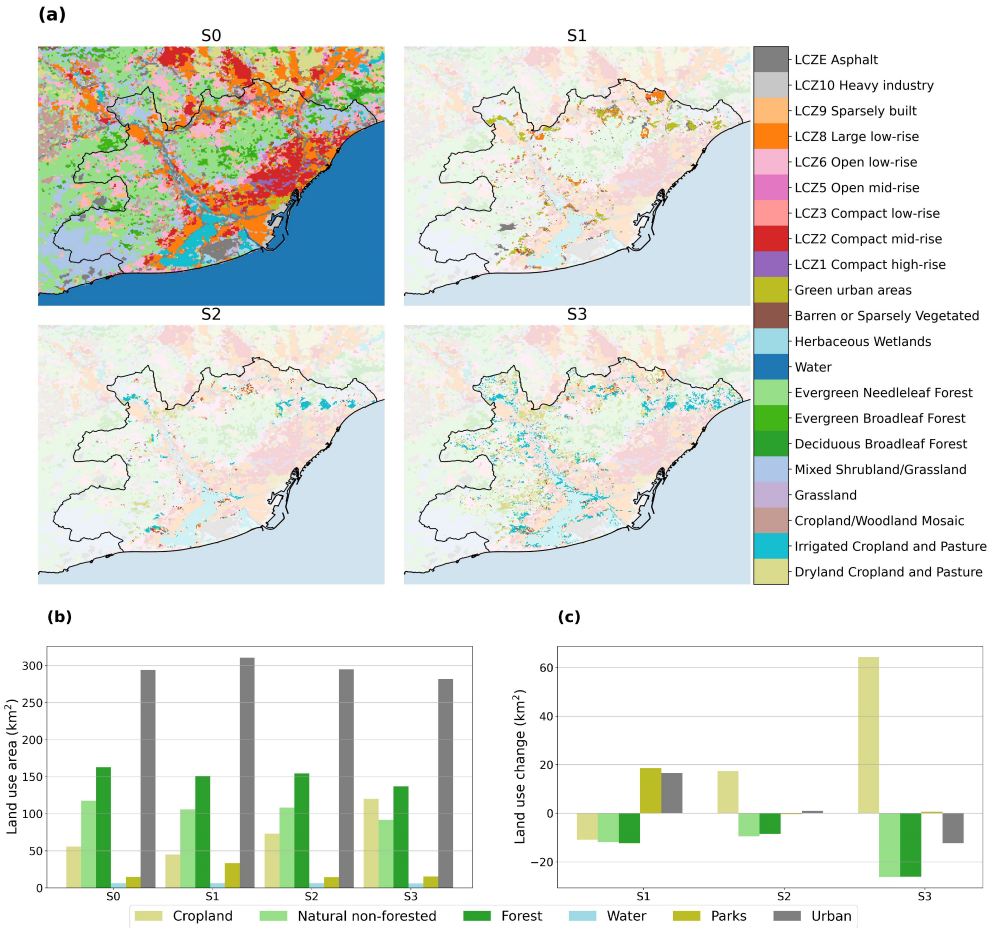


Figure 5.1: (a) LULC maps at 100 m resolution within the D04 domain for scenarios S0, S1, S2 and S3, highlighting areas of land-use change in S1, S2 and S3, compared to S0. (b) Histogram showing the total land-use extent in the AMB land-cover type. (c) Changes in land-cover extent compared to S0.

5.3 Methodology

5.3.1 Local food provision

A high level of crop disaggregation to calculate crop yields for 2015 is obtained from the URBAG map provided by Beltran et al. (2022, 2023) which combines data for individual crops from the Department of Agriculture, Livestock, Fisheries and Food from the Generalitat de Catalunya (DARPA, 2015) and its annual declaration of crops (Declaració agrària, DUN for its acronym in Catalan) made by farmers in Catalonia, the Spanish land registry (Dirección General del Catastro, 2022), and the Land Cover Map of Catalonia (CREAF, 2015).

The crop production of each crop parcel is calculated based on the crop yields reported by the Catalan Department of Agriculture, Livestock, Fisheries and Food from the Generalitat de Catalunya (Generalitat de Catalunya, 2016), reported by crop, county and considering irrigated and non-irrigated. The potential agricultural fields envisioned by the future LULC scenarios are assigned the same crop and irrigation method as the nearest field of the current scenario S0. This assumption overlooks whether these crops are optimally chosen for cultivation in the new crop parcels or if they are selected to maximise crop yields, total food production, or market profits. It relies predominantly on crop parcel proximity to establish similar conditions for the cultivation of the same crop types. Parcel crop production is obtained by multiplying the crop parcel area by its crop yield.

5.3.2 Irrigation water use

Monthly irrigation water use estimates for 2015 are considered for the freshwater ecosystem services demand indicator distinguishing between agriculture and urban parks and gardens, implying different estimation methods.

In agriculture, monthly water requirements at parcel level are determined using a water metabolism approach. Using the URBAG map, each crop is assigned a monthly crop coefficient (K_c) based on the local farmer's calendar and literature. The crop water requirement in mm per month is obtained from an adaptation of the FAO method (Pereira et al., 2015). Monthly raster maps of irrigation water use are obtained from the crop's coefficients, observed evapotranspiration and precipitation interpolated maps and irrigation efficiencies reported in Agència Catalana de l'aigua (2010). Additional details on the agriculture irrigation water estimates can be found in Appendix D.2.

For urban parks and gardens, AMB reports a maximum application of 2.5 L $m^{-2}\,day^{-1}$ in summer over the irrigated surfaces representing a 13 % of the park extension (AMB, 2021). Irrigation decreases in other months according to the reported schedules by the Ajuntament de Barcelona (2013)). Vegetated areas in built-up areas and urban park regions define the regions where irrigation is applied. The two irrigation datasets are combined and resampled at 100 m resolution.

5.3.3 Temperature regulation

Midday air temperatures at 2 m height and daily evapotranspiration serve as indicators for the temperature regulation ecosystem service. Hourly estimates are obtained using the Weather Research and Forecasting model (WRF) v4.3.3 (Skamarock et al., 2021) coupled with the the Building Effect Parameterization and the Building Energy Model (BEP-BEM) (Salamanca and Martilli, 2010) as it is detailed in Section 4.2.2 of this thesis. The WRF model setup involves four domains with resolutions of 9 km (D01), 3 km (D02), 1 km (D03), and 333.3 m (D04), covering from the entire Iberian Peninsula to the entire AMB limits (see Figure 5.2).

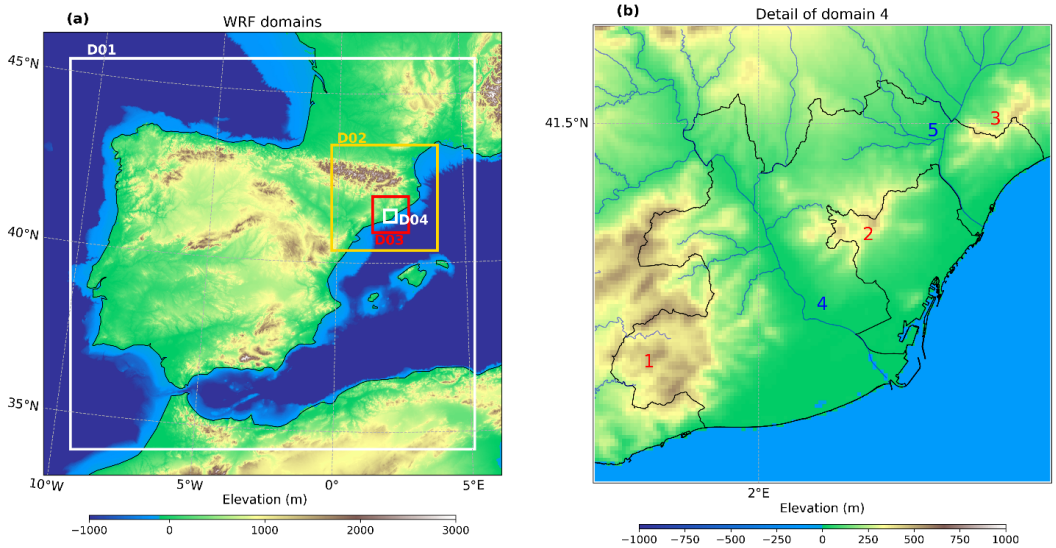


Figure 5.2: (a) Domains of the WRF model for this study with 9 km, 3 km, 1 km and 333.3 m grid size for D01, D02, D03 and D04, respectively. (b) Detail of the domain 4 with an elevation map and the political boundaries of the AMB and the city of Barcelona (black contour). The most important features in the AMB orography are marked in the map: 1) Garraf Massif; 2) Collserola range; 3) Marina range; 4) Llobregat river; and 5) Besòs river.

Simulations span from 00 UTC on 20 June 2015 to 00 UTC 25 July 2015, with the initial five days as a spin-up period. The period features persistent high temperatures in the AMB, with a daily average temperature consistently above 25 ºC and maximum temperatures peaking (40 ºC inland and 35 ºC on the coast) during a heat wave episode from 4 to 7 July 2015 (SMC, 2015). Model characteristics and experimental configuration, extensively tested in previous AMB sensitivity studies (Ribeiro et al., 2021; Gilabert et al., 2021b; Segura et al., 2021), are outlined in Table 4.1. The addition of a 333.3 m resolution domain, compared to the prior studies, enables addressing the impact of small (< 100 ha) land-use changes on the regional meteorology. LULC maps are interpolated from 100 m resolution to the domain resolution using the most common

LULC class in each grid cell.

To account for the impact of agricultural and urban irrigation, the Noah Land surface model surface irrigation scheme (Valmassoi et al., 2020) is employed with the channel option, involving direct water application on the soil surface. This method considers only direct evaporation from the soil surface. Irrigation amount maps are directly input to the WRF model, with specific values for each grid cell. Irrigation is set to occur daily between 4-5 UTC (6-7 local time, LT). Additionally, two simulations without irrigation are conducted for scenarios S0 and S3 to assess the impact of land irrigation on temperature regulation in the LULC scenarios.

Additional modifications compared to the previous studies have been applied to the WRF model and configuration to enhance the representation of LULC changes between scenarios. Details of these modifications are provided in Appendix D.3, along with an evaluation of the meteorology modelled in the reference scenario (S0) and a sensitivity study of the impact of the planetary boundary layer scheme in Appendix D.4.

5.3.4 Biogenic carbon balance

The AMB biogenic carbon balance is evaluated through the net ecosystem productivity and the carbon stocks. These components capture different aspects of the climate-carbon relationship in the GI. Net ecosystem productivity reflects intra-annual variability in carbon sequestration and release under diverse climate conditions between scenarios. Total carbon stocks indicate the GI's capacity to retain carbon under equilibrium conditions with current climate and agricultural practices. Additionally, net ecosystem productivity variability reveals the GI's resilience to extreme weather phenomena such as heat and drought events. The goal is to assess how potential land-use scenarios impact net ecosystem productivity and carbon stocks in the AMB, and to evaluate the GI's resilience to extreme heat conditions across different land-use scenarios.

Net ecosystem productivity

The net ecosystem productivity data for 2015 is obtained at hourly frequency using the Vegetation Photosynthesis and Respiration Model (VPRM) (Mahadevan et al., 2008). VPRM estimates CO_2 exchange between the atmosphere and biosphere based on meteorological data and satellite-sensed vegetation indices (Mahadevan et al., 2008). In this study, a modified VPRM version for the Mediterranean region is used, incorporating soil moisture effects on the photosynthesis and ecosystem respiration fluxes as it is described in Section 6.2.1 of this thesis.

Meteorological data for VPRM is derived from yearly WRF-BEP-BEM simulations for each LULC scenario at horizontal resolutions of 1 km. VPRM carbon fluxes resolution is constrained by required vegetation indices, the enhanced vegetation index (EVI) and the land surface water index (LSWI), processed from MODIS Terra satellite data at 500 m resolution. Monthly simulations start five days before each month to ensure soil moisture conditions are adequately

considered.

LULC maps at 100 m resolution are reclassified into the VPRM's plant functional types (PFT) using reclassification rules (Table D.1 in Appendix D). Two additional PFTs are defined: green urban areas representing urban parks and gardens, assumed to consist of 50 % evergreen forest and 50 % grasslands; and low-intensity residential areas representing regions with private gardens and adjacent natural vegetation, assumed similar to evergreen forests. A correction for soil respiration in these areas is applied based on urban fraction reduction, as suggested in other studies (Hardiman et al., 2017; Gourdji et al., 2022). The reclassified maps are resampled to 500 m resolution. More details on the VPRM model and configuration, along to the description of the procedure to derive the model uncertainties are available in Appendix D.5. The evaluation of the WRF twelve months S0 simulation is available in Appendix D.6.

Carbon stocks

The total carbon stocks in open spaces, including agriculture, forests, shrublands, pastures and large urban parks (Marull et al., 2021), are calculated for croplands and non-agricultural natural spaces separately. Four carbon pools are considered: carbon in mineral soil, carbon in the organic soil layer, carbon in plant roots, and carbon in woody aerial structures. Carbon pools of herbaceous crops, trees and shrub leaves, and litter are excluded due to shorter turnover times (Wang et al., 2018). The carbon pools estimate integrate data from multiple regional maps and soil models as it is detailed in Marull et al. (2021).

The result is a 500 m resolution map with aggregated carbon stocks from the four carbon pools, integrating both agricultural and non-agricultural surfaces from the Land-cover map of the AMB (CREAF, 2015). For scenarios S1, S2, and S3, carbon stocks in areas with LULC changes use the stocks in the nearest grid cell with the same LULC in the S0 scenario.

5.4 Results

The results are organized as follows: in Section 5.4.1, we evaluate the indicators of the ecosystem services related to the food-water-climate nexus for the current scenario (S0) and the relative change of the indicators with respect to the other scenarios. In Section 5.4.2, we study the seasonal variability of these ecosystem services, and in section 5.4.3, we explore the resistance and recovery capacity to heat of the GI under the various scenarios.

5.4.1 Spatial comparison of the food-water-climate nexus ecosystem services

The ecosystem services analysis in the current scenario (S0) reveal different spatial distributions. For instance, the most food productive agricultural areas in the AMB are situated in the southern basin of the Llobregat river. Here, irrigated croplands yield between 3.7 and 51.2 tons of

food per hectare per year (Figure 5.3a). The total food provision in the S0 scenario is estimated at 68,665 tons per year (Table 5.1, Figure 5.4a). Of this total, 87.4 % corresponds to irrigated agriculture, with the remaining 12.6 % being dedicated to non-irrigated agriculture. Intensive irrigated agriculture in the dry Mediterranean leads to high irrigation water requirements (Figure 5.3b), especially in the irrigated cropland areas in the southern Llobregat basin, where irrigation water usage reaches up to 840 mm per year. The overall irrigation water consumption in the AMB is estimated at 32.4 hm^3 (Figure 5.4b), with 78.4 % (25.4 hm^3) allocated to irrigated agriculture and 21.6 % (7.0 hm^3) designated to urban parks and gardens.

Table 5.1: Peri-UA surface and food provision in the land-use planning scenarios in the AMB.

Scenario	**peri-UA surface** (km^2)	**peri-UA surface (% AMB)**	**Food provision (tons** $year^{-1}$)	**Fruit provision (% AMB demand)**	**Vegetable provision (% AMB demand)**
Current (S0)	55.83	8.6	68665	2.67	11.60
Trending (S1)	44.90	6.9	52158	2.23	10.19
Alternative (S2)	73.21	11.2	85168	3.49	14.53
Potential (S3)	120.08	18.4	127605	6.65	19.26

Regarding temperature regulation, GI effectively lowers air temperatures through mechanisms of evapotranspiration and shade provision. In this assessment, we focus on cooling from the evapotranspiration. Notably, areas with the highest cooling potential in summer include natural forests, such as in the Garraf Massif and Collserola, and agricultural areas in the southern Llobregat river basin (Figure 5.3c), with daily evapotranspiration rates reach up to 3.9 mm. In Barcelona city, daily evapotranspiration ranges from 0.0 to 1.7 mm, with higher rates in larger urban parks. Midday to afternoon temperatures (11-17 local time, LT) vary from 24.9 to 33.3 ºC with the highest temperatures in the northern Llobregat river basin, in the North of the AMB, as well as in densely populated neighbourhoods in the city of Barcelona. Inland regions experience reduced cooling effects from sea-breezes, typically occurring between 10-11 LT and ending between 20-22 LT (Soler et al., 2011). The lowest temperatures occur in high-altitude areas of the south-western Garraf Massif and the Marina Mountain range due to strong sea-breeze effects.

As regards the biogenic carbon balance, evergreen forests in the Garraf Massif and the Collserola Mountain range exhibit the highest annual net ecosystem productivity (Figure 5.3e), ranging from 3 to 10 tons of carbon uptake $ha^{-1}\,year^{-1}$ (positive implies captured carbon from the atmosphere, negative implies a net release) and the highest carbon stocks (up to 286.4 tons of carbon ha^{-1}). Agricultural areas show a more neutral carbon balance, ranging from -4 to 4 tons of carbon $ha^{-1}\,year^{-1}$ with an average exchange of -1 tons of carbon $ha^{-1}\,year^{-1}$. The total net ecosystem production by the AMB's GI in 2015 is estimated at 104.7 ± 1.5 kilotons of carbon (Figure 5.4d) and the carbon stocks amount to 3,747.5 kilotons of carbon (Figure 5.4e).

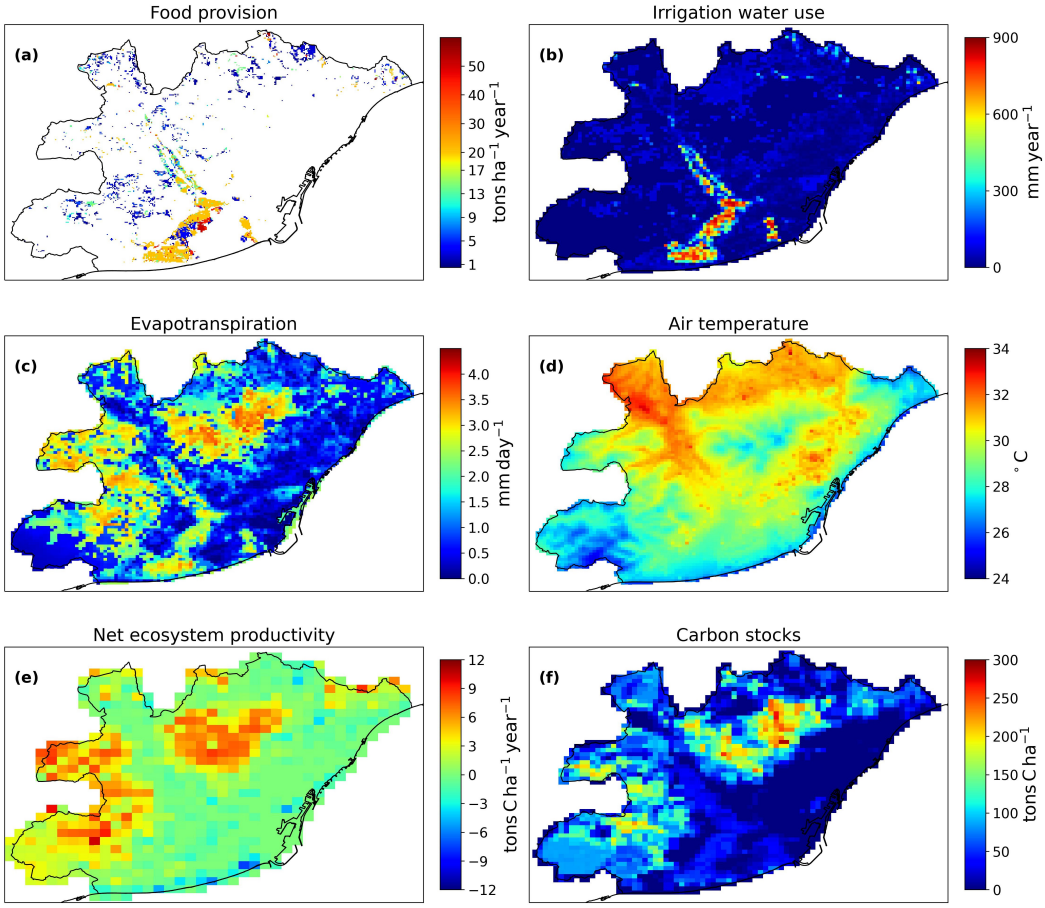


Figure 5.3: Comparison of the ecosystem services indicators for the current scenario (S0) for the year 2015. (a) Food provision; (b) Irrigation water use; (c) Summer daily evapotranspiration; (d) Summer midday/afternoon air temperature; (e) Net ecosystem productivity; and (f) Carbon stocks.

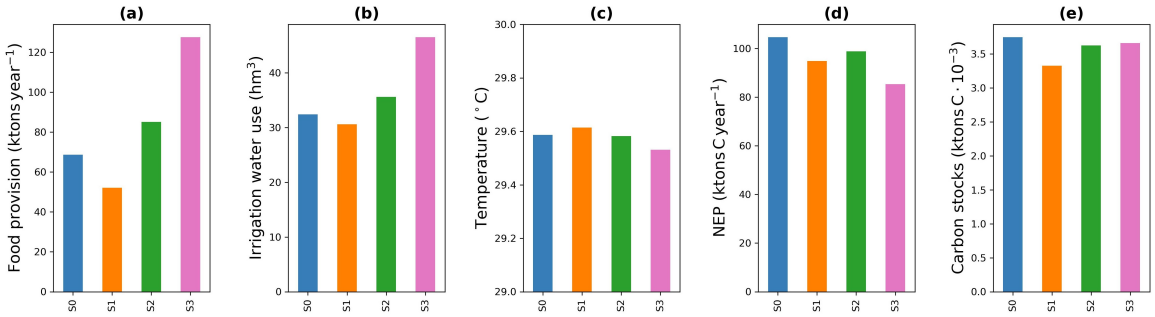


Figure 5.4: Comparison between the four LULC scenarios for (a) total food provision in 2015; (b) total irrigation water use in 2015; (c) median summer midday/afternoon air temperature; (d) Net ecosystem productivity in 2015; and (e) Carbon stocks for the AMB.

The spatial analysis of the indicator variations between LULC scenarios reveals multiple synergies and trade-offs. For instance, in scenario S1 with reduced peri-UA, a clear trade-off emerges between food provision and water irrigation (Figure 5.5a and 5.5d). The decrease in peri-UA in irrigated areas leads to a reduction in total food provision (-16507 tons year^{-1}, a 24.0 % decrease compared to S0) and a decrease in total water irrigation (-1.8 hm^3, a 5.6 % decrease). Scenarios S2 and S3 reverse this trend with increased annual food provision by +16,503 tons year^{-1} (+24.0 %) and +58940 tons year^{-1} (+85.8 %), respectively (Figure 5.4a). Additionally, annual irrigation demands increase by +3.2 hm^3 (+10.0 %) and +14.1 hm^3 (+43.5 %) despite of a higher share of non-irrigated agriculture (21.6 % and 25.7 % of the total food production, respectively).

Depending on the type of GI introduced or replaced with respect to S0, the LULC changes result in a relative cooling or warming effect. Based on differences in daily evapotranspiration between S1 and S0 (as depicted in Figure 5.5g), the cooling effect of the GI diminishes when natural or agricultural areas are transformed into urban areas, with an average reduction of -0.6 mm day^{-1}. The increase of irrigated urban parks only leads to higher daily evapotranspiration when replaces dryland croplands or shrublands, while it decreases when they replace forests or irrigated agriculture. The expansion of urban developments in S1 results in local increases in air temperature of up to 0.9 ºC, especially in the North of the AMB and the Garraf Massif (Figure 5.5j). The local increases in air temperature are transported inland to downwind areas to the new urban areas, by the effect of the sea-breezes, causing increases of air temperature below 0.2 ºC. Despite the local increases of temperature in S1, the average temperature at the AMB scale increases by less than 0.1 ºC with respect to S0 (Figure 5.4c).

For scenarios S2 and S3, the increase in water irrigation and the replacement of shrublands by croplands lead to an increase in the evapotranspiration by up to 2.5 mm day^{-1} (Figures 5.5h and 5.5i). However, the replacement of forests with dryland croplands reduces the cooling effect of GI down to -2.1 mm day^{-1}. These changes in daily evapotranspiration are reflected in near-surface air temperatures (Figures 5.5k and 5.5l). In the case of S3, air cooling reaches 0.7

ºC with respect to S0, resulting in generally lower air temperatures throughout the AMB, especially over the Llobregat river basin. Nonetheless, the median temperature reduction in the AMB between S3 and S0 remains below 0.1 ºC (Figure 5.4c), primarily affecting rural areas and having minimal impact on the densely populated city of Barcelona. Scenario S2 displays the most similar temperatures to S0, with only local temperature reductions of -0.3 ºC. Therefore, the analysis suggests a potential synergy between the food provisioning ecosystem service and the local temperature regulation during summer.

However, we highlight a significant spatial correlation between changes in daily evapotranspiration and irrigation amounts during June-July 2015 in S2 and S3 (Pearson correlation coefficient = 0.60). This suggests that the observed cooling capacity of LULC changes, as shown in Figure 5.5k and 5.5l, may be more attributed to irrigation implementation than the land-cover transformation. The impact of irrigation on near-surface temperatures is demonstrated in WRF simulations of S0 with and without irrigation (Figure D.4 in Appendix D), revealing reductions up to 0.6 ºC over highly irrigated agriculture areas. Conversely, irrigation may slightly increase night time air temperatures by up to 0.2 ºC due to the enhanced heat retention properties of moist soil. The comparison between scenarios S0 and S3 with and without irrigation (Figure D.5 and D.6), emphasizes the importance of irrigation in achieving temperature reductions, producing that almost the 10 % of the AMB surface presents a temperature reduction higher than 0.1 ºC. Conversely, in the case without irrigation, only the 2 % of the territory perceives a 0.1 ºC temperature reduction. This suggests that non-irrigated agriculture may not yield the same cooling effects for this case study.

Regarding the biogenic carbon balance, the three hypothetical scenarios exhibit similar changes compared to S0. In scenario S1, net ecosystem productivity is reduced when urban areas or parks replace natural evergreen forests (as seen in Figure 5.5m), resulting in reductions of up to 4.6 tons C $ha^{-1}\,year^{-1}$. In contrast, productivity increases in areas where urban areas or parks replace dryland or irrigated croplands, with an increase of 2.0 tons C $ha^{-1}\,year^{-1}$. The net productivity is more similar between S0 and S2 (Figure 5.5n), due to fewer LULC changes, although reductions of up to 3.7 tons C $ha^{-1}\,year^{-1}$ compared to S0 occur due to the conversion of natural forest areas into croplands. In the case of S3 (Figure 5.5o), the most substantial reductions in net ecosystem productivity with respect to S0 (-7.0 tons C $ha^{-1}\,year^{-1}$) affect a larger portion of the AMB, with 11 % of the grid cells in the AMB experiencing reductions of more than 1.0 tons C $ha^{-1}\,year^{-1}$. The total net ecosystem production in the AMB reduces to 94.9 ± 1.4 kilotons C (-9.4 %), 98.9 ± 1.4 kilotons C (-5.5 %), and 85.3 ± 1.6 kilotons C (-18.5 %), for scenarios S1, S2 and S3, respectively (Figure 5.4d).

In terms of carbon stocks, the analysis principally estimates reductions between the hypothetical scenarios and S0, resulting from the reduction of natural forested areas transformed into urban areas, parks, or croplands. In contrast to the carbon exchanges, the most significant reductions are observed in S1, with reductions in carbon capture of up to 153 tons C ha^{-1}. The total carbon stocks in S1, S2 and S3 decrease to 3327.0 (-11.2 %), 3624.1 (-3.3 %), and 3661.1 kilotons C (-2.3 %), respectively (Figure 5.4e).

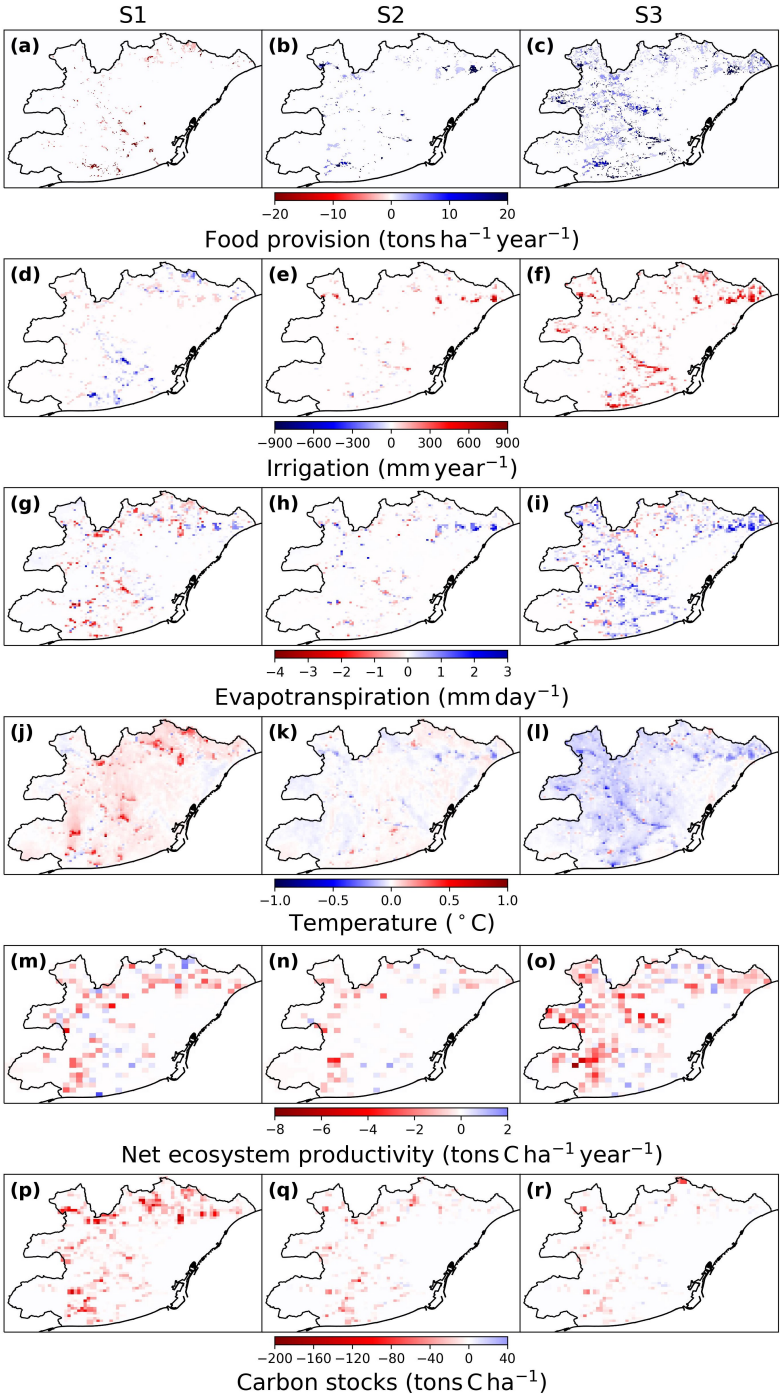


Figure 5.5: Comparison of the ecosystem services indicators differences between the LULC scenarios S1 (left column), S2 (middle column) and S3 (right column) and the current scenario (S0) for the year 2015. (a,b,c) Food provision; (d,e,f) Irrigation water use; (g,h,i) Daily evapotranspiration; (j,k,l) Midday air temperature; (m,n,o) Annual carbon capture; and (p,q,r) Carbon stocks.

5.4.2 Seasonal variability in ecosystem services

Irrigation consumption is highest during the typical growing season months of natural and agricultural vegetation, spanning from April to August (Figure 5.6a). This increased irrigation demand in April to July is influenced by the scant precipitation and the higher air temperatures compared to the climatic mean during these months (Figure 5.6b). July stands out as the peak month for irrigation requirements, with volumes ranging from 5.5 hm^3 to 8.9 hm^3. Notably, this coincides with the period of highest monthly temperatures (Figure 5.6b). Additionally, the low precipitation, averaging less than 2 mm $month^{-1}$, recorded between June 25 and July 24, 2015, during the peak of the year's high temperatures, exacerbated the need for irrigation.

Comparing scenarios, S3 presents the highest proportion of irrigation water for agriculture respect to the total, ranging from 50.7 % to 91.8 %, whereas S1 presents the lowest, from 39.4 % to 84.0 %. These findings highlight the temporal trade-offs associated with agricultural irrigation demands. Water requirements for agriculture surge during periods of heightened water scarcity and atmospheric evaporative demand throughout the year, potentially contributing to river basin water depletion.

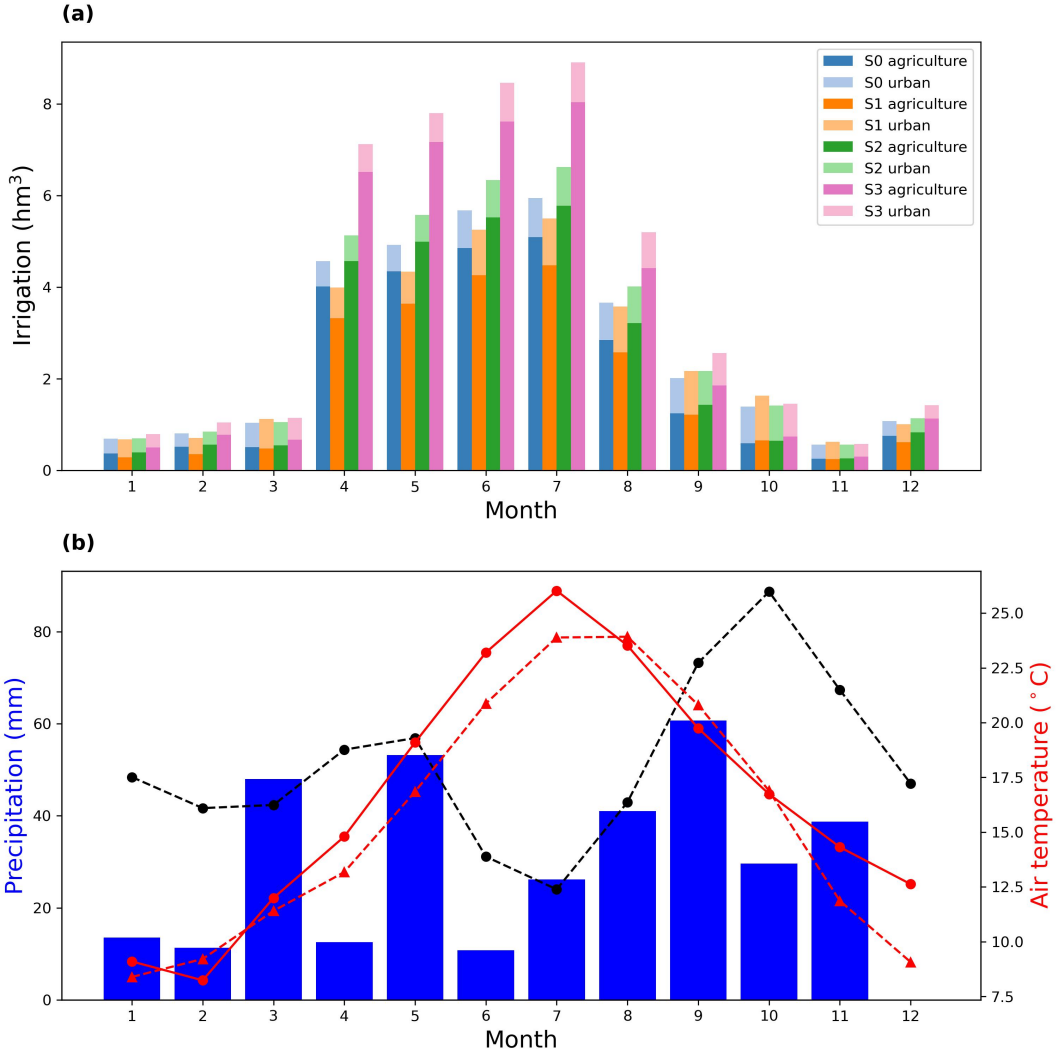


Figure 5.6: (a) Monthly irrigation amounts over the Metropolitan Area of Barcelona over the year 2015 for the four LULC scenarios; (b) Average monthly temperatures (red dots) and monthly precipitation (blue bars) for the city of Barcelona over the year 2015, and the climatic mean (1980-2010) for the monthly temperatures (red discontinuous line) and precipitation (black discontinuous line).

The monthly variation of the average midday air temperatures at the AMB scale reveals small temperature variations between LULC scenarios (see Figure D.7), finding the larger reductions with respect to S0 during the summer months of June and July for S3 (-0.09 ºC and -0.06 ºC, respectively) and S2 (-0.06 ºC and -0.03 ºC). This result evidences potential trade-offs between the capacity of the GI to reduce midday air temperatures and the water requirements of these GI, as the higher provision of air-cooling arises during the periods of higher heat stress, higher irrigation requirements and lower water availability.

The net ecosystem productivity by GI, exhibits seasonal variations linked to vegetation cycles (Figure 5.7). In all LULC scenarios, maximum net sequestration occurs in April (27.3 to 28.9 kilotons of carbon per month), coinciding with peak greenness in natural vegetation (see Figure D.8). During July and August, AMB's GI becomes a carbon source to the atmosphere (release to the atmosphere of 7.3 and 9.1 kilotons C month^{-1}) due to increased respiration and reduced photosynthesis caused by higher summer temperatures, lower precipitation, and soil moisture which hamper vegetation photosynthesis. After August, it resumes being a net carbon sink, influenced by increased land surface water index (Figure D.8), higher autumn precipitation and lower temperatures.

Scenario comparisons show variations, with S1 consistently differing by -0.5 to -0.7 kilotons C month^{-1}, over winter and autumn, except between April and June when the difference increases to 1.5 kilotons C month^{-1}, primarily due to reduced natural vegetation during the growing season peak.

S2 closely follows the seasonal cycle of S0, with the lowest differences (-0.1 to -0.8 kilotons C month^{-1}), particularly between March and July, corresponding to the crops growing season peak. In contrast, S3 exhibits the lowest net ecosystem productivity, especially from January to March and September to December, with differences compared to S0 reaching -2.5 kilotons C month^{-1}.

These results indicate that the net ecosystem productivity of the GI is influenced by both land cover characteristics and land management. Poor management, especially of croplands, can lead to LULC-related CO_2 emissions during off-season, limiting the net ecosystem productivity of the GI over the year.

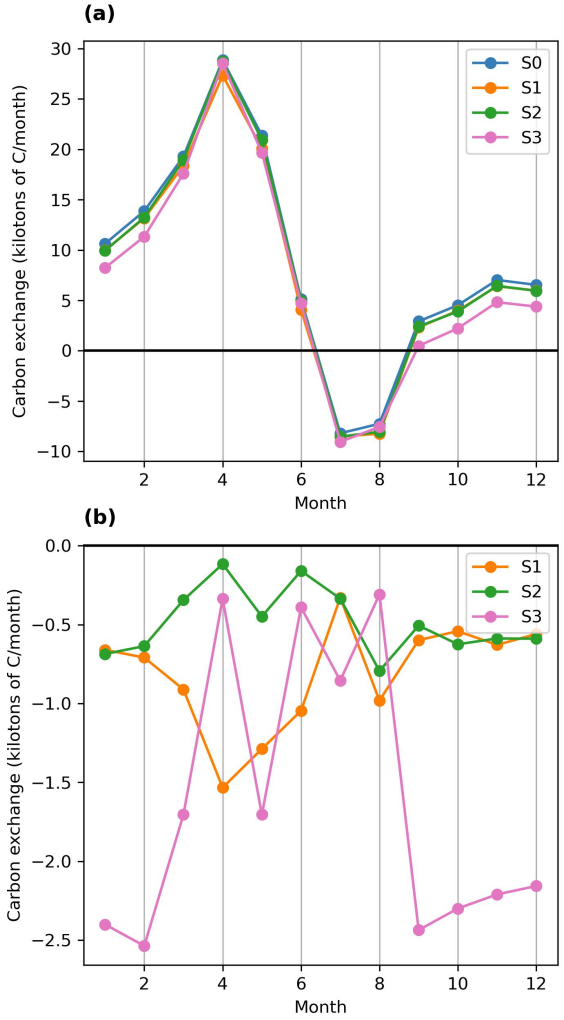


Figure 5.7: (a) Monthly total net ecosystem productivity by the AMB GI for the four LULC scenarios in the year 2015. (b) Difference of the net ecosystem productivity with respect to the scenario S0.

5.4.3 Temporal variability within a hot summer month

During the summer heat wave, we observe varying responses in temperature regulation and carbon capture indicators among the four LULC scenarios. In Figure 5.8, average indicators are calculated within the model grid cells where LULC changes occur in at least one of the hypothet-

ical scenarios. Daily evapotranspiration (Figure 5.8a) does not appear to be significantly affected by the heat wave event that occurred from July 4 to July 7, 2015. Instead, it follows a general decreasing trend throughout the study period. This decline may be attributed to water depletion in the natural areas of the AMB due to low precipitation, resulting in reduced soil water availability for evaporation. Among the three scenarios, S3 exhibits the highest daily evapotranspiration, with differences from S0 ranging from 0.27 to 0.49 mm day^{-1}. Analysing the time-series for each land-cover (Figure D.9), we observe that irrigated croplands have a high evapotranspiration (1.9-2.9 mm day^{-1}) similar to forests (1.9-3.5 mm day^{-1}), even higher during the last days of the period. Meanwhile, dryland croplands (0.9-1.8 mm day^{-1}) and wooded crops (1.2-2.5 mm day^{-1}) present considerable higher evapotranspiration than natural non-forested vegetation (0.4-0.8 mm day^{-1}), explaining the higher evapotranspiration rates for the S3 scenario.

Regarding midday and mid-afternoon air temperatures, Figure 5.8c illustrates that during the heat wave period, there is an increase in air temperatures compared to previous days, with temperatures exceeding 32 ºC. In comparison to S0, S1 generally presents higher air temperatures (over 0.12 ºC higher than S0), while S3 displays generally lower air temperatures (-0.10 °C lower than S0). However, the daily temperature differences show a day-to-day variability. This variability is attributed to the changing wind direction of sea-breezes during the simulation days, which dictates the areas where air-cooling or heating is transported. On some days, the wind direction carries temperature differences outside the AMB, reducing temperature increases/decreases between scenarios. This means that even though S3 (S1) has higher (lower) daily evapotranspiration, it can still exhibit higher (lower) temperatures than S0, depending on the prevailing wind patterns. This suggests that the regional cooling effect of different GI strategies depends not only on the cooling effect of vegetation but also on regional wind patterns that transport these cooling effects to downwind areas, thereby impacting local air temperatures in areas affected by LULC changes.

In the terms of net ecosystem productivity, as shown in Figure 8e, the heat wave affects the LULC scenarios differently. In all scenarios, net carbon capture decreases from the start of the heat wave event until the hottest day by 0.53 to 0.74 kg C ha^{-1} day^{-1}. After the heat wave, carbon capture increases by 0.97 to 1.10 kg C ha^{-1} day^{-1}. S3 experiences the most significant decrease in net ecosystem productivity during the heat wave, followed by S2. Furthermore, S3 exhibits the least recovery after the heat wave episode (Figure 5.8f), maintaining a lower net ecosystem productivity from the heat wave until the study period end. These results suggest that cropland areas are more vulnerable to the impacts of heat waves compared to natural vegetation, even when they are irrigated.

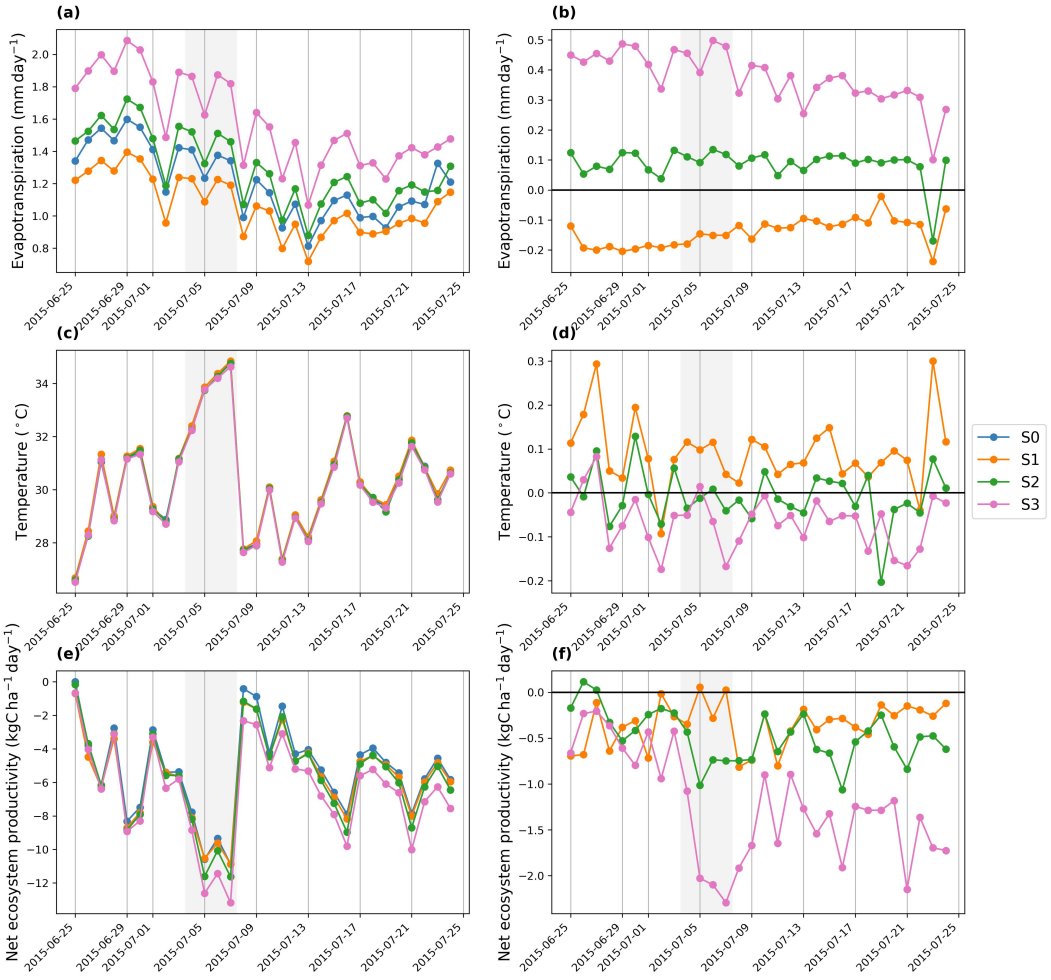


Figure 5.8: Time-series of the ecosystem services indicators simulated during the study period between June 25 and July 24, 2015 for the four LULC scenarios (a, c, e) and the difference with respect to S0 (b, d, f), for: (a,b) Daily evapotranspiration; (c, d) midday and mid-afternoon average temperature; (e, f) net ecosystem productivity. The indicators have been averaged over the grid cells where there occurs a LULC change. The grey interval corresponds to the heat wave event.

5.5 Discussion

In this study, we evaluated the ecosystem service provision in the context of the food-water-climate nexus across four land-use scenarios in the AMB. The aim was to identify and quantify synergies and trade-offs in ecosystem services when implementing peri-UA strategies. Estimations of ecosystem services and requirements from GI were based on official reports from local and regional governments or on well-validated metabolism and numerical models. These models have been optimized and improved to study the impact of GI on the water balance, urban climate (Gilabert et al., 2021b; Segura et al., 2021), and biogenic carbon balance in a

Mediterranean climate city. In the following, we will discuss a) methodological considerations, including the limitation of our study, b) ecosystem services trade-offs in the food-water-climate nexus, and c) policy and planning implications of our study, in the context of urban resilience and environmental justice.

5.5.1 Methodological considerations

This study provides an innovative combination of models which allows for the study of the ecosystem services in a nexus approach under current climate conditions and agricultural practices. Other studies mapping multiple ecosystem services (Baró et al., 2016; Nelson et al., 2009; Zulian et al., 2018) have relied on integrated ecosystem service models that perform integrated assessments of the capacity of ecosystems to provide ecosystem services as the ESTIMAP tool (Zulian et al., 2014) or the Integrated Valuation of Ecosystem Services and Tradeoffs (InVEST) model (Natural Capital Project, 2024). These models are examples of practical tools that spatially resolve the provision of ecosystem services to support decision-makers in the implementation and designing of land-use strategies. Although, these models integrate numerous ecosystem services, they do not usually work on a food-water-climate nexus approach at an urban scale, overlooking interlinkages in the nexus. Moreover, they tend to ignore or oversimplify the estimations of air-cooling and carbon storage and sequestration from the GI (Aznarez et al., 2024).

For local temperature regulation ecosystem services, the prevailing approaches (Zardo et al., 2017; Koc et al., 2018) rely on satellite imagery of land surface temperatures (García-Haro et al., 2023), on-site observations of green areas (Ng et al., 2012), monthly evapotranspiration from climatic observations (Basnou et al., 2020) or process-based tree models (i.e., i-Tree Eco Model) (Baró et al., 2019). While these techniques may deliver precise evapotranspiration and land surface temperatures, they disregard crucial sub-daily processes (e.g., sea-breezes), since their estimates range from daily to monthly basis, and they do not consider air temperature. These challenges have recently been overcome using regional atmospheric models coupled with urban canopy parameterisations, such as WRF-BEP-BEM, which have been employed in studying greening strategies within urban areas (Li et al., 2014; Li and Norford, 2016; Sharma et al., 2016; Imran et al., 2018; de la Paz et al., 2022; Gilabert et al., 2021b). WRF-BEP-BEM simulations not only record near-surface temperature changes from greening, but also from irrigation (Valmassoi et al., 2020) and their combined impact on the surface energy balance. The novelty of this study arises from downscaling the model implementation to 333.3 m, allowing a better representation of LULC variations in modelled near-surface temperatures.

The most used methods to quantify carbon storage and sequestration involve using tree biomass and growth equations (i.e., i-Tree) (Baró et al., 2019), statistical models which combine field survey data and LIDAR data (Basnou et al., 2020), and land-use regression modelling (Baró and Gómez-Baggethun, 2017).These methods yield precise estimates regarding the carbon stored in trees and the corresponding annual increase in biomass. They employ field measurement data retrieved from national forest inventories or allometric equations, categorised according to specific trees species. Nevertheless, they do not have the ability to assess the impact of LULC changes

associated with agriculture as these models usually exclude low vegetation and soil carbon.

Data-driven biosphere models can depict the exchange of CO_2 between the atmosphere and ecosystems for various land cover types (Mahadevan et al., 2008), whilst also considering the net ecosystem productivity. This method considers the summed carbon exchanges from the significant carbon pools in the ecosystem, making it a more comprehensive gauge of ecosystem carbon capture. Our research utilizes an improved version of VPRM, tailored for the Mediterranean area and fine-tuned with observational data from south-western Europe's flux tower stations. This model enables the examination of climate impacts on the net ecosystem productivity at differing spatio-temporal scales, which could be better represented in the future with the assimilation and integration of more novel and diverse observations. The increasing availability of eddy-covariance flux towers, such as the global FLUXNET network (Pastorello et al., 2020) or the Integrated Carbon Observatory System (ICOS), and atmospheric CO_2 concentrations observations facilitate the optimization and validation of the estimated biogenic carbon fluxes, providing a better understanding of regional biogenic carbon balance. Moreover, the implementation of finer-resolved satellite vegetation indices such as those from the satellite Sentinel-2 at 10 m resolution within biosphere models (Bazzi et al., 2024), could enhance the spatio-temporal modelling of the carbon fluxes.

To conduct an integrated, quantitative food-water-climater nexus assessment, several assumptions were made that impose constraints on the analysis and application of our results, particularly for the estimation of ecosystem services in hypothetical scenarios.

Firstly, we assume vegetation conditions (greenness and composition) and soil conditions (carbon storage, fertility, and quality) to mirror those in the corresponding LULC class in the current scenario. This analysis excludes the impact of land-use changes during the transition between scenarios, considering potential differences in recovery time for soil carbon content (Lal, 2008), maturation time for the new vegetation's air-cooling efficiency (Rahman et al., 2020), and its evolution into a more effective carbon sink (Stephenson et al., 2014). Investigating evolving ecosystem services supplies during dynamic LULC transitions necessitates downscaling the output of dynamic global vegetation models to the urban scale. These models simulate vegetation growth in relation to land carbon cycles and near-surface climate over extended periods, accounting for climate changes (Yue et al., 2018, 2020).

Secondly, this study assumes agricultural management in hypothetical scenarios to exclusively adhere to conventional peri-UA practices, thereby aligning with the status-quo of peri-UA in the AMB represented in the current scenario. Conventional farming techniques, including mineral fertilisation, tillage, grazing, and soil cover removal, can harm soil organic carbon content (Lal, 2008; Aguilera et al., 2018)), undermining efforts to reduce greenhouse gas emissions in agriculture (Drinkwater and Snapp, 2007; Smith et al., 2008; Power, 2010). Alternative organic practices, which might reduce these impacts, and which might gain relevance in the future, have not been considered in the scenario development (Padró et al., 2020). To investigate diverse LULC scenarios under different agricultural practices, a comprehensive understanding of the

effect of these practices on the net carbon balance of various crops would be essential (Smith et al., 2008; Eugster et al., 2010), requiring an integration of impacts into data-driven or process-based biogeochemical models (Bazzi et al., 2024) and spatially and temporally resolved surveys of these agricultural practices (Goldstein et al., 2017).

Thirdly, in this study, we have estimated the food provision and irrigation water requirements based on a georeferenced urban metabolism approach, producing ecosystem services and requirements with a very detailed and consistent crop types map (Beltran et al., 2022, 2023). Yet, estimating metropolitan irrigation water use is a highly uncertain process, where the inclusion of detailed irrigation databases and the methodology employed to derive irrigation requirements can significantly influence the final estimation. In this context it is important to note that for the irrigation water demand, the irrigation totals calculated for agriculture (25.4 hm^3) and urban parks (7.0 hm^3) contrast with those estimated by Serrano-Tovar et al. (2022), who estimated 34 hm^3 and 14 hm^3 for agriculture and urban parks, respectively. Their estimation of irrigation requirements for agriculture took a similar approach to ours, but they used generic crop typologies and did not consider actual crop types and their respective crop coefficients and irrigation methods, similarly they might overestimate irrigation needs for parks.

5.5.2 Ecosystem services trade-offs in the food-water-climate nexus

The examination of the impacts on the food-water-climate nexus of various peri-urban agricultural expansion scenarios in the Metropolitan Area of Barcelona underpins previous findings that indicate for the implementation of NBS to produce synergies, but also trade-offs between costs and benefits of different ecosystem services (Chan et al., 2011). In the following, we will highlight the key insights from our case study regarding ecosystem service's trade-offs across the food-water-climate nexus.

First, the food-water-climate nexus approach has shown to be a helpful tool that allows for the evaluation of NBS and GI strategies at metropolitan scale, and the identification of synergies and trade-offs between ecosystem services in metropolitan regions. Particularly, this nexus allows for the integration of trade-offs and feedbacks between the regional meteorology on the food and water systems, as well as between the food and water systems on the regional and global climates. Such feedbacks are rarely quantified on other nexus approaches, especially when it comes to the representation of interlinkages between land and atmosphere (cf. Laspidou et al. (2020)). In order to evaluate NBS and GI strategies in the context of climate change adaptation and mitigation, the food-water-climate nexus approach applied here provides important novelty.

Second, the analysis of the impacts of NBS should consider the interlinkages between the elements of the food-water-climate nexus to reach sustainable solutions (Carvalho et al., 2022). Past research has highlighted interlinkages between the expansion of irrigated agriculture and increased demand for irrigation water (Mueller et al., 2012; Mendonça et al., 2023). This study expands on these findings by incorporating the irrigation of urban parks. Understanding irrigation needs is a critical, yet often under-considered aspect in the creation of NBS and GI (Li

et al., 2021). In a period of drought in Catalonia, our study has shown for an eventual expansion of peri-UA to exert important additional pressure on the hydric resources of the AMB. Climate change is projected to further stress the food-water-climate nexus, with higher global temperatures increasing water demand from agriculture due to elevated evapotranspiration rates (Power, 2010) and changing precipitation regimes intensifying drought occurrences, limiting water availability, making crops more dependent on irrigation (Mendonça et al., 2023).

Third, while trade-offs between food and water ecosystem services are already well understood, less evidence is given regarding how food and water system interactions may modify local and global climates. This study suggests that peri-UA expansion can impact the reduction of summertime air temperatures in Mediterranean climate regions (Figure 5.5l). A deeper analysis reveals that the main mechanism of air temperature cooling arises from water irrigation (Figure D.5), although results indicate lower temperature reductions compared to previous studies (Kueppers and Snyder, 2012; Valmassoi et al., 2020). We assume the irrigation-temperature relationship of peri-UA to be altered by a combination of factors, including seasonal variations, climatic differences of the region, extension of irrigated areas, and irrigation magnitude. In line with studies by Gilabert et al. (2021b), we encourage future research to further explore the trade-off relationship between urban temperatures and irrigation.

Fourth, the implementation of peri-UA can also influence the global climate by altering the regional carbon balance. The replacement of natural vegetation, mainly forested areas, by agriculture or urban areas reduces the capture of atmospheric carbon by the metropolitan GI by 18.5 % and 9.4 % respectively. This aligns with a global trend. For instance, Gitz and Ciais (2004) estimated that the global expansion of crop and pastures in detriment of forests lead to an increase in atmospheric CO_2 of 61 ppm by the year 2100. The increase is related to the loss of forests biomass and organic carbon in the soil on the one hand, and the reduction of the residence time of carbon in croplands compared to natural vegetation, on the other. In our study, where we have found that cropland areas present lower net ecosystem productivity, which might even become negative over the course of the year. Hence, implying a reduction of the regional ecosystem productivity when forests or natural vegetation are transformed to agriculture.

The spatial analysis of the trade-offs and synergies allows for the identification of efficient heat and climate change mitigation strategies, while also identifying highly efficient water productivity areas. This analysis allows identifying areas where the GI has a high contribution in temperature regulation or carbon capture retention and capture, allowing for their preservation and conservation, as these areas also have a high contribution on other ecological benefits, such as biodiversity (Basnou et al., 2020). Moreover, the spatial analysis is useful to evaluate the effectiveness of the NBS in the provision of temperature reduction in areas of high vulnerability to summer heat (Camacho-Caballero et al., 2024). In this sense, temperature reductions are not only affected by local land use changes and their spatial distribution, but also on the regional climate dynamics which define the most prevalent wind regimes, implying on a deep understanding of the regional atmospheric dynamics for effective GI design and implementation.

In this study we found that the implementation of peri-UA in the AMB can potentially contribute to air temperature reduction during the periods of higher heat stress, generating a modest cooling effect in downwind areas to the regions with LULC changes. The cooling impact, particularly evident in the northern Llobregat river basin, could benefit nearby urban populations, representing one of the hottest areas during summer (refer to Figure 5.3d). However, only a small percentage (3.56 %) of the AMB population would experience a cooling of at least 0.1 ºC in the potential scenario (refer to Table D.2 in Appendix D), with the majority residing in Barcelona and surrounding urban areas (almost 70 % of the AMB population). In that sense, sea-breezes have a high influence on the determination of the areas affected by the temperature cooling. For the city of Barcelona, other GI strategies within city limits, such as green roofs, cool roofs, or increased urban parks, may be more effective in targeting local temperature reductions (Gilabert et al., 2021b).

The temporal analysis of the ecosystem services and requirements using the food-water-climate nexus allows for the evaluation of the temporal evolution of trade-offs between ecosystem services and requirements, identifying the periods when the conflicts between the elements of the nexus are more prone to happen. This analysis is required for the correct management of these trade-offs, avoiding undesired environmental impacts. For instance, for the case study, we found that the irrigation demand is heightened during the summer months (Figure 5.6a), coinciding with the periods of higher air temperatures (Figure 5.6b), and altogether the months when the irrigated agriculture produce a higher air-cooling effect (Figure D.7b). The reduction of the irrigation practices in high irrigation intensity agricultural areas following water-saving strategies can derive on an increase in air temperatures (up to 0.6 ºC) over nearby urban populations increasing the vulnerability of these urban areas to heat stress. Additionally, the temporal analysis allows to identify periods when the management of the GI have a higher effect on the net atmospheric carbon exchange. For instance, we found that the LULC scenario with the higher expansion of peri-UA has the lowest net ecosystem productivity compared to the other scenarios, especially during the autumn and winter months (Figure 7b). These differences are probably attributed to reduced photosynthetic activity of the crops outside the growing season, and multiple management practices promoting the release of CO_2 from the soil respiration as tillage and residue management (Smith et al., 2008; Eugster et al., 2010). The temporal identification of these events can allow to identify the practices with a higher impact on the regional carbon balance and to target more sustainable practices under agriculture expansion strategies.

In summary, analysing the food-water-climate nexus of NBS under consideration of spatial and temporal trade-offs across ecosystem services is a challenging endeavour, requiring high data input and modelling capacities. We still believe this effort to be worth it, if not necessary in order to properly plan and manage NBS and GI in the context of global climate change and its local adaptation requirements.

5.5.3 Policy and planning NBS in the context of resilience and environmental justice

Global climate change increases the occurrence and intensity of extreme climate events (IPCC, 2014). To properly inform policy and planning in the design of NBS, the assessment of the impacts of NBS should not only consider climatological normal conditions, but also extreme climate events as these are the periods during which the provision of ecosystem services can be most compromised (Reichstein et al., 2013; Hatfield and Prueger, 2015; Zhao et al., 2023), while at the same time most needed. For instance, extreme heat events such as heat waves can lead to reduced yields in crops, affecting plant growth, pollination, and reproductive stages (Hatfield and Prueger, 2015). Selecting heat resistant crops in urban regions prone for the occurrence of summer heat episode seems necessary for minimizing the impact of heat events on the plant production. In the case of the impact of heat wave events on the air-cooling capacity of urban vegetation, Zhao et al. (2023) found that the responses vary significantly over the geographical regions and climates, as well as on the climate forcing (e.g. the intensity of the heat wave) and the human management (e.g. irrigation). For instance, in Mediterranean climate cities, natural rainfed vegetation is shown to experience high suppressed air-cooling potentials due to a decrease in the transpiration, while irrigated vegetation can enhance transpiration. The vegetation species also affect the response to heat. Teuling et al. (2010) found that some tree species may pre-emptively limit transpiration to avoid soil water depletion, in contrast to grasses that continue transpiring until all available water is used. In our study, we found that evapotranspiration slightly increases across all scenarios during the heat wave (Figure 5.8a), driven by soil moisture availability and heightened evaporative demand.

Even though, the net ecosystem productivity experiences a decline at the heat wave onset until the peak day, ranging from 0.53 to 0.74 kg C $ha^{-1}\,day^{-1}$. Photosynthetic activity and gross ecosystem production decline as trees close stomata beyond an optimum air temperature, particularly in conjunction with drought conditions (Ciais et al., 2005; Teskey et al., 2015). High-temperature episodes elevate ecosystem respiration (von Buttlar et al., 2018) due to increased microbial biomass degradation (Mahecha et al., 2010), leading to reduced net ecosystem productivity. We found a more intense decline in net ecosystem productivity in the scenario with higher expansion of peri-UA (Figure 5.8f). Despite agriculture potentially cooling the air more than natural non-forest vegetation under high heat stress, especially with irrigation (Figure D.9), crop carbon sink capacity proves more vulnerability to heat stress than natural vegetation. These results align with Ermitão et al. (2021) findings, highlighting that forested regions exhibit greater resistance to droughts and heat events compared to croplands in the Iberian Peninsula. This kind of analysis help in the comprehension of the impacts of heat waves on the urban and peri-urban GI and their capacity to provide ecosystem services, in order to design more climate resilient NBS.

Urban planning of GI strategies should not only contemplate the implications on the food-water-climate nexus, as other ecosystem services beyond the nexus are also important and should be considered as biodiversity, water purification, soil conservation and fertility, air quality improvement, pollination, nutrient recycling, ecological connectivity, flood mitigation, and the creation

of job and recreational opportunities (Power, 2010). The multifunctionality concept of the GI and NBS highlights this capacity to provide multiple ecosystem services simultaneously. Even though, these systems are principally managed and planned to optimise a single ecosystem service, leading to conflicts in the overall set of services provided. This results in trade-offs, when the enhancement of one desired ecosystem service comes at the cost of diminishing others, or even increasing the risk of environmental impacts. These trade-offs are commonly found in urban areas, as the limited space and the presence of various stakeholders compete to secure benefits as food production, heat mitigation, carbon storage, or recreational spaces (Turkelboom et al., 2018).

In order to mitigate these trade-offs in land-use planning, increasing efforts are made from the urban planning research to explore more equitable forms of ecosystem services distribution. First, these trade-offs must be analysed in front of a local context, contextualizing the variations in the ecosystem services in terms of urban vulnerabilities (Camacho-Caballero et al., 2024) or ecosystem services demands (Baró et al., 2016). Framing the studies of the impact of NBS under these concepts can help relativizing the impact of different strategies under the local objectives. Second, multiple frameworks as the participation of stakeholders in decision-making and multi-criteria decision-making frameworks have been developed to ensure fair outcomes in the distributions of ecosystem services (Langemeyer et al., 2020). Recent analytical approaches are combining the estimation of ecosystem services with metabolic and life-cycle assessments to determine the resources consumption and environmental impacts they entail (Camacho-Caballero et al., 2024). As for instance, an ongoing research area has centred on expanding the analysis of ecosystem services trade-offs from a local context to a global scope, analysing the dependencies of local impacts within the global context, as it could be the impacts of the expansion of local food production on food imports and their relative water and carbon footprints (Boillat et al., 2020; Corbera et al., 2019). This approach allows for the identification of indirect environmental impacts and entails a more holistic understanding of the impacts of NBS.

5.6 Conclusions

The implementation of GI in urban areas has been suggested as a NBS for tackling multiple environmental, societal, and economic problems. Although these strategies are usually planned for tackling one ecosystem service or multiple ecosystem services in a multifunctional approach, their implementation can arise trade-offs between these ecosystem services and others or suppose an increase in ecosystem requirements or environmental impacts. In this study we have identified significant trade-offs in the expansion of peri-urban agriculture in the Metropolitan Area of Barcelona. The research revealed that peri-urban agriculture expansion can increase local food production by 85.8 %, and reduce local summer temperature by 0.7 ºC, while also presenting challenges, including an elevated irrigation demand (increased by 43.5 %), and reducing carbon capture capacity of the regional GI by 18.5 %. It is likely that these trade-offs are observed with other NBS strategies, as it can be the case of recreational urban parks in detriment of natural areas.

We advocate for an integrated assessment of these trade-offs, using a food-water-climate nexus approach to consider the interlinkages between the elements of the nexus. As for instance, this study found that irrigated agriculture expansion can be detrimental for the hydric resources, while altogether land irrigation takes a fundamental role in the abatement of regional temperatures in areas of highly thermal regulation demand in the AMB. Other relevant factors when analysing the impact of NBS on the food-water-climate nexus are the spatial and temporal variabilities of these trade-offs, the resilience of the GI to extreme climate events and the local context, represented as posing the trade-offs in terms of changes in urban vulnerabilities or ecosystem services demands. Moreover, we highlight the importance of evaluating the impacts of the NBS on a relevant spatial scale to the ecosystem service, for instance considering a global scale in the global climate regulation, due to the interconnectedness of local actions with broader environmental consequences.

An innovative combination of ecosystem services models, considering the interlinkages between food-water-climate systems, has been used for the quantification of potential trade-offs between the food provision, irrigation water requirements, local temperature regulation and regional carbon balance of potential peri-urban agriculture expansion scenarios in the Metropolitan Area of Barcelona. These model configurations could be similarly applied for the assessment of peri-urban agriculture or alternative NBS strategies in other Mediterranean climate cities. This holistic approach appears to be a promising direction for informing land-use decision-making in the context of urban climate adaptation and mitigation.

Chapter 6

Improving the Vegetation Photosynthesis and Respiration Model for the South-western European ecosystems

Abstract: Terrestrial ecosystems in south-western Europe face increased heat and drought events due to climate change, while the understanding of these climatic impacts on the ecosystems carbon balance remains incomplete. Accurately estimating carbon fluxes at an ecosystem and regional scale, particularly during extreme climatic events, is crucial for assessing the carbon balance under current and future climates. This chapter focuses on improving the Vegetation Photosynthesis and Respiration Model (VPRM) to better represent biogenic carbon fluxes during heat and drought events. The modified VPRM incorporates a soil moisture stress function for the gross ecosystem exchange and an improved ecosystem respiration with abiotic and biotic factors. The modelled fluxes are evaluated with eddy-covariance flux tower data, and atmospheric CO_2 observations using an atmospheric transport model in a passive tracer approach. The modified VPRM outperforms the default VPRM in estimating the net ecosystem exchange (NEE), the gross ecosystem exchange (GEE), and the ecosystem respiration (R_{ECO}) at the ecosystem scale, improving the seasonality, and reducing the error on the carbon fluxes estimations for most of the land-covers types. At larger scales, the inclusion of biotic factors in the parameterization of the ecosystem respiration enhances the spatial representation of the impacts of heat events on the modelled biogenic carbon signal in the atmosphere. The inclusion of the soil moisture stress factor improves the timing and magnitude of the drought effects on GEE, especially in temperate evergreen forest ecosystems. These findings highlight the importance of including soil moisture impacts on the GEE and R_{ECO} fluxes, contributing to a better understanding of the regional carbon balance in south-western Europe terrestrial ecosystems

6.1 Introduction

The climate change projections for south-western Europe indicate a larger increase in air temperatures and precipitation variability compared to other global regions (Giorgi, 2006), resulting in elevated frequency and intensity of heat and drought events (Giorgi and Lionello, 2008). However, the impacts of these extreme climatic events on the carbon fluxes from the ecosystems in the region remain incompletely understood. The carbon balance of terrestrial ecosystems is governed by these fluxes, which quantify the impacts of regional extreme climate on the global carbon budget (Reichstein et al., 2013). The carbon fluxes consist of the net ecosystem exchange (NEE), and its two components, the gross ecosystem exchange (GEE), and the total ecosystem respiration (R_{ECO}). Accurately estimating carbon fluxes at a regional scale, particularly during extreme climatic events, is crucial for enhancing our comprehension of the carbon balance in south-western Europe and its evolution in response to changing climates (Friedlingstein et al., 2020).

Various terrestrial ecosystem models have been used to estimate carbon fluxes at regional scales. These range from mechanistic process-driven models (Sellers et al., 1986; Jung et al., 2007; Kuppel et al., 2012; Santaren et al., 2014) to data-driven models (Mahadevan et al., 2008; Maselli et al., 2009; Gilabert et al., 2015). The former ones are more complex, as they represent a higher number of biogeochemical processes in the ecosystems, as the carbon dynamics between the atmosphere, and different carbon pools (soil, aboveground and belowground biomass, dead biomass). Even though, the calibration of these models for regional applications poses significant challenges due to the multitude of parameters involved (Santaren et al., 2014). Additionally, these models often fail to capture the ecosystem's response to extreme variation in soil moisture, such as droughts, which are a key variable in vegetation photosynthesis and soil respiration (Stocker et al., 2018, 2019).

In contrast, data-driven models such as the Vegetation Photosynthesis and Respiration Model (VPRM) require fewer parameters to estimate carbon fluxes (Mahadevan et al., 2008). VPRM is driven by meteorological data and remotely-sensed vegetation indices. The model uses a light-use efficiency approach for ecosystem photosynthesis and a simple function based on air temperature for ecosystem respiration. The model has been shown to be highly applicable to various regions and land covers (Lin et al., 2011; Yuan et al., 2014; Kountouris et al., 2015; Dayalu et al., 2018). The limited number of VPRM parameters can be optimised using eddy-covariance flux tower data (Kountouris et al., 2018). Recently, VPRM was calibrated for use over the European continent using data from 46 eddy-covariance flux towers (Kountouris et al., 2018). However, the use of VPRM is limited over the south-western European region due to multiple restrictions. Firstly, the model does not account for the effect of soil moisture on carbon fluxes, which restricts its applicability in studying the impact of drought events on carbon fluxes (Mahadevan et al., 2008). Secondly, the default version of VPRM, which was applied over the USA, considers all croplands as a single vegetation class, regardless of the crop type (Bazzi et al., 2024). Therefore, VPRM does not differentiate between winter crops (e.g. wheat and rapeseed), which require lower temperatures to grow, and summer crops (e.g. maize and

rice), which thrive in higher temperatures (above 35 ºC) (Fatima et al., 2020). Nevertheless, different studies have shown the potential of customizing VPRM to a specific domain through model parameters optimisation and the inclusion of additional land-cover types (Dayalu et al., 2018; Gourdji et al., 2022) or modifying the flux equations (Gourdji et al., 2022), presenting similar or even better performance than more complex biosphere models.

Carbon fluxes estimates can be evaluated at ecosystem scale using eddy-covariance flux tower data from national and international networks of flux towers such as the global FLUXNET (Pastorello et al., 2020) or the Integrated Carbon Observatory System (ICOS) in Europe (Warm Winter 2020 Team and ICOS Ecosystem Thematic Centre, 2022). However, flux towers have a limited footprint area of approximately 1 km^2, which lacks spatial representativeness to evaluate larger-scale estimates of the fluxes (Feng et al., 2021). Recently, the evaluation of regional carbon flux estimates from ecosystems using atmospheric CO_2 observations has been addressed as a complementary method (Feng et al., 2021; Gourdji et al., 2022). Unlike CO_2 flux measurements, atmospheric CO_2 towers have footprints of hundreds of kilometres, integrating biosphere signals from day and night (Feng et al., 2021). This evaluation involves combining CO_2 mole fraction observations from dense ground-based networks with atmospheric transport and biosphere models (Pillai et al., 2012; Feng et al., 2021; Hu et al., 2021). Among the different methodologies available, the Eulerian approach uses atmospheric transport model to represent CO_2 transport as a passive tracer (Pillai et al., 2012; Feng et al., 2021; Hu et al., 2021). The total modelled atmospheric CO_2 concentrations are the sum of the different components, including biogenic, anthropogenic, oceanic, and large-scale background concentrations. Model errors can arise from each one of the CO_2 components, as well as from model transport errors (Feng et al., 2021). However, Feng et al. (2019) found that the biogenic component is the largest contributor to the total error of the atmospheric CO_2 concentrations over North America.

This study aims to evaluate and improve VPRM to represent the impact of heat and drought events on the biogenic carbon fluxes of south-western European ecosystems. Here, two versions of VPRM are compared, the default version described in Mahadevan et al. (2008) and a modified version with an additional stress function of soil moisture for the GEE and a new R_{ECO} parameterization. The model parameters are optimised using flux tower data from south-western Europe stations from the FLUXNET and ICOS networks. The models are evaluated by comparing them with eddy-covariance flux tower data, and atmospheric CO_2 observations using a Eulerian approach. The atmospheric transport simulations are conducted using the Weather Research and Forecasting with Chemistry (WRF-Chem) model (Skamarock et al., 2021). Finally, the modified and default VPRM versions are evaluated at two selected flux tower sites over the summer 2017 to determine the ability of the models to represent the impacts drought and heat waves on the carbon fluxes.

6.2 Methodology

6.2.1 VPRM parameterization

The default VPRM

VPRM is a diagnostic light-use-efficiency model that estimates the CO_2 exchange between the atmosphere and biosphere (Mahadevan et al., 2008). VPRM estimates the NEE as the difference between R_{ECO} and GEE, following a negative sign convention where negative fluxes represent CO_2 uptake by ecosystems. VPRM computes the biosphere fluxes for 8 different plant functional types (PFT), representing different vegetation land covers. The PFT in the default VPRM are evergreen, deciduous and mixed forests, shrublands, Mediterranean savannas, croplands, grasslands, and other non-vegetated areas. The different PFT parameters have been optimised using data from flux tower observations. VPRM combines the fluxes derived for each PFT weighted by a fractional coverage in a tile approach to derive the ecosystem fluxes of a land region.

The GEE parameterization of VPRM consists of a light-use-efficiency approach that relates the GEE to the fraction of photosynthetically active radiation that is absorbed by the vegetation:

$$GEE = \lambda \cdot T_{scale} \cdot W_{scale} \cdot P_{scale} \cdot \frac{1}{(1 + PAR/PAR_0)} \cdot PAR \cdot EVI \tag{6.1}$$

Where λ is the potential light-use efficiency factor, T_{scale}, W_{scale}, and P_{scale}, are stress scaling factors that reduce the light-use efficiencies depending on temperature, soil water and phenology (Mahadevan et al., 2008). PAR is the Photosynthetically Active Radiation, PAR_0 is the half-saturation constant of PAR and EVI is the Enhanced Vegetation Index processed from the Moderate Resolution Imaging Spectroradiometer (MODIS) surface reflectance data (product MOD09A1 v006). In this equation, $PAR \cdot EVI$ represents the amount of active radiation absorbed by the vegetation, and $\lambda \cdot PAR \cdot EVI$ is the potential GEE, that is regulated by the different scaling factors. PAR is usually changed by the downwelling shortwave radiation (SW) since these two variables are closely related ($PAR \approx 0.505 \cdot SW$) and the shortwave radiation is usually available between the variables of meteorological products. In that case, λ and PAR_0 are substituted by λ_{SW} and SW_0.

The temperature scaling factor defines the sensitivity of photosynthesis to the air temperature, and it is defined as:

$$T_{scale} = \frac{(T - T_{min}) \cdot (T - T_{max})}{(T - T_{min}) \cdot (T - T_{max}) - (T - T_{opt})^2} \tag{6.2}$$

where T is the air temperature and T_{min}, T_{max} and T_{opt} are minimum, maximum, and optimum temperatures for each PFT and are derived from literature values.

The water scaling factor accounts for the effect of water stress on the photosynthesis, and is defined as:

$$W_{scale} = \frac{1 + LSWI}{1 + LSWI_{max}} \tag{6.3}$$

where $LSWI$ is the Land Surface Water Index (Xiao et al., 2005) derived from MODIS surface reflectance, and $LSWI_{max}$ is the site-specific maximum daily $LSWI$ in the growing season.

The phenology scale factor accounts for the effect of leaf age on the canopy photosynthesis. It relies on the vegetation indices (EVI and $LSWI$) to capture the different stages of the leaf in the growing and decay seasons. For evergreen vegetation during all the year and deciduous and grassland vegetation in the growing season peak-greenness, P_{scale} is set to 1. Otherwise, P_{scale} is defined as:

$$P_{scale} = \frac{1 + LSWI}{2} \tag{6.4}$$

The R_{ECO} parameterization of the VPRM model consists of a simple linear function with the air temperature:

$$R_{ECO} = \alpha \cdot T + \beta \tag{6.5}$$

where α and β are model parameters representing the linear sensitivity of respiration to air temperature and the baseline respiration, respectively. Air temperature is set to a PFT specific low threshold (T_{low}), when the air temperatures are lower than T_{low}, to account for the persistent soil respiration during winter.

The parameters λ_{SW} (μmol CO_2 $m^{-2}\,s^{-1}\,(Wm^{-2})^{-1}$), SW_0 ($W\,m^{-2}$), α (μmol CO_2 $m^{-2}\,s^{-1}\,(^{\circ}C)^{-1}$) and β (μmol CO_2 $m^{-2}\,s^{-1}$) are model constants with specific values for each PFT and are estimated by calibrating the model to represent flux tower data. The NEE for a land region is obtained from the area-weighted sum of the components derived for each PFT:

$$NEE = \sum_{i=1}^{n} \left(-GEE_i + R_{ECO,i}\right) \cdot \varphi_i \tag{6.6}$$

where n is the number of PFT in the model, φ_i is the plan area fraction for the PFT i in the land region, and it is computed from land cover vegetation maps.

The modified VPRM

To account for the impact of soil moisture on GEE and CO_2, modifications were made in the VPRM equations, with an R_{ECO} parameterization based on (Migliavacca et al., 2011). We introduce a new scaling factor, SM_{scale}, to better represent soil moisture stress on GEE, distinguishing between energy-limited (adequate soil water) and water-limited regimes (insufficient soil water), according to Stocker et al. (2019). The GEE parameterization is defined as:

$$GEE = \lambda_{SW} \cdot T_{scale} \cdot W_{scale} \cdot P_{scale} \cdot SM_{scale} \cdot \frac{SW}{1 + SW/SW_0} \cdot EVI \tag{6.7}$$

The function SM_{scale} is defined to be 1 when the soil moisture (η) is above a critical soil moisture threshold (η^*) and decreases linearly below this threshold (Fu et al., 2022). Soil moisture in the uppermost soil level (0-15 cm depth), is normalized between the permanent wilting point and the field capacity of the soil. The form of the SM_{scale} function is:

$$SM_{scale} = \begin{cases} q \cdot (\eta - \eta^*), & \eta < \eta^* \\ 1, & \eta \geq \eta^* \end{cases} \tag{6.8}$$

where q and η^* are optimised parameters. With this modification, we increase the number of parameters in the GEE parameterization from two (λ_{SW}, SW_0) to four (adding q and η^*).

The default VPRM employs a linear function of air temperature to determine R_{ECO}. In this study, we use an equation proposed in Reichstein et al. (2003) and Migliavacca et al. (2011). In our approach, we employ soil moisture, represented by a hyperbolic tangent function, to depict water stress on R_{ECO}, rather than precipitation. This choice is due to soil moisture's superior role in influencing both autotrophic and heterotrophic respirations, driving soil microbial processes and plant stress (Liu et al., 2009). The R_{ECO} equation in the modified VPRM relies on air temperature, soil moisture and short-term vegetation productivity (daily GEE) as follows:

$$R_{ECO} = (R_0 + k_1 \cdot GEE) \cdot tanh(k_2 \cdot \eta + \gamma) \cdot e^{E_0 \cdot \left(\frac{1}{T_{ref} - T_0} - \frac{1}{T - T_0}\right)} \tag{6.9}$$

GEE represents the average GEE over the previous 24 hours. T_{ref} and T_0 are fixed temperatures at 288.15 K (15 ºC) and 227.13 K (-46.02 ºC), respectively. Model-specific constants, R_0, k_1, k_2, γ and E_0 vary for each PFT and refer to reference abiotic ecosystem respiration, sensitivity of ecosystem respiration to GEE, sensitivity of the ecosystem to soil moisture, a constant indicating how R_{ECO} responds to null η, and the activation energy parameter for the sensitivity of R_{ECO} to air temperature, respectively. Including vegetation productivity in the respiration parameterization enhances the spatial and temporal dynamics of R_{ECO}, preventing a bias in seasonal amplitude (Migliavacca et al., 2011). Air temperature influences R_{ECO} with non-linear dependencies (Reichstein et al., 2003; Jolly et al., 2005), which can be represented using an Arrhenius type equation, as employed in this parameterization.

6.2.2 Eddy-Covariance flux tower data

Land-atmosphere CO_2 biosphere fluxes were obtained from 33 flux tower stations over south-western Europe and nearby regions (from 11º W to 19º E and 35º N to 50º N), characterizing the different biomes and climates present in the region of study (Figure 6.1). The fluxes at half-hourly frequency are from the FLUXNET 2015 dataset (Pastorello et al., 2020) (https://fluxnet.org) and the Warm Winter 2020 product from ICOS (Warm Winter 2020 Team and ICOS Ecosystem Thematic Centre, 2022) (https://doi.org/10.18160/2G60-ZHAK). The data have been selected to

cover the period from 2010 to 2020 to maximize the availability of the data for all the different PFT. These datasets have been processed with a common standard processing methodology which harmonizes and ensures the high quality of the data, along to estimate the corresponding fluxes uncertainties (Pastorello et al., 2020). Apart from the fluxes, the data contains ancillary meteorological measurements (air temperature and shortwave radiation) and volumetric soil water content measurements from the topsoil layer (from 5 to 15 cm depth) at the same temporal frequency as the fluxes. Tables E.1 and E.2 summarize the stations information needed in this study.

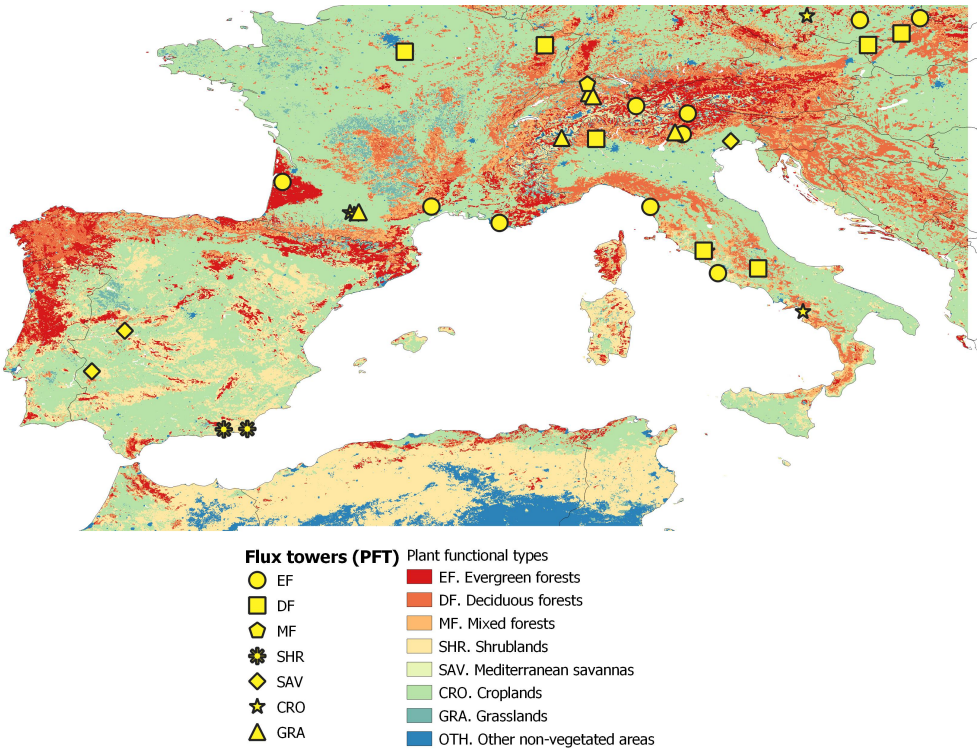


Figure 6.1: Map of land cover classification from the VPRM PFT map and the location of the 33 flux towers included in the VPRM parameter optimisation and evaluation. EF: evergreen forest; DF: deciduous forest; MF: mixed forest; SHR: shrublands; SAV: Mediterranean savanna; CRO: croplands; GRA: grasslands.

In this study, GEE and R_{ECO}, are estimated from the observed NEE using the night-time partitioning method (Pastorello et al., 2020). This method consists of using the night-time fluxes to parameterize a respiration model that it is applied then to the rest of the data to determine the R_{ECO} of the daytime period. GEE is obtained subtracting R_{ECO} to the NEE. A variable Ustar ($u^{\star}$) threshold for each year was applied for filtering low turbulence periods, which can bias the data. The data was gap-filled and classified according to some quality control (QC) flags (Reichstein et al., 2005). Half-hours where the quality control flag was poor (QC=3) were discarded. In the case of GEE values greater than 0, which can be produced by an slight underestimation of the

temperature response partitioned R_{ECO}, are set manually to 0 and the R_{ECO} is set to equal the observed NEE just in the cases when there is an adequate friction velocity ($u^{\star} > 0.1$) and the QC flag of the measurement is either measured (0) or very good gap filling (1). Otherwise, the half hourly measurements with positive GEE where discarded, along to the corresponding NEE and R_{ECO} values.

The permanent wilting point and field capacity of the soil must be estimated for each station for normalizing the soil water content measurements. The permanent wilting point is assumed as the minimum recorded soil moisture. The field capacity is taken from the station PI reported value if it is available, otherwise, it is computed from the reported soil texture by the station PI and the Saxton equations (Saxton and Rawls, 2006). In the case that there is no information, the soil texture is obtained from the Topsoil physical properties map for Europe at 500 m resolution of the European Soil Data Center (ESDAC) (Ballabio et al., 2016). This soil field capacity is visually checked for each station from the time-series of the volumetric soil water content.

Additional information on the crop types, agricultural management and crop calendars was provided by the ICOS site investigators of the cropland flux stations. Moreover, due to the lack of representation of stations located in Mediterranean evergreen broadleaf forests with complete measurements in the two datasets, data for the French station Puechabon (FR-Pue) and the Italian station Castelporziano (IT-Cp2), were obtained from ICOS level 2 Ecosystem data for 2022 (RI., 2022).

6.2.3 Optimisation of the VPRM parameters

The parameters of the default and modified VPRM are optimised for the major characterizing ecosystem types in the south-western European region. The VPRM parameters are optimised separately for each PFT using the half-hourly observed fluxes from the flux towers. For each PFT, we have selected a subset of the data for the optimisation, containing two years for each different flux tower (note that depending on data availability we selected only one year of data). These two years have been selected from the total data record of the flux tower based on two criteria: 1) more than 70 % available data; and 2) a representation of the highest and lowest annual precipitation anomalies during the growing seasons. In this way, we provide wet and dry climatic conditions for each station. A separate evaluation subset of siteyears is built from the stations that do not fit the first criteria, and the other years remaining for the other stations that satisfy the first criteria. The siteyears used for these subsets can be seen in Table E.2.

In the case of croplands stations, we distinguish between years when winter crops (CRO_W) are mainly cultivated from those with summer crops (CRO_S). To account for these two crop typologies in the optimisation and evaluation processes for the cropland PFT, we differentiate the interannual crop rotation of the stations in order that a station with winter crops is different than the same station with summer crops. For instance, a cropland station can provide with 4 siteyears for the optimisation and evaluation subsets (two years with winter crops and two with

summer crops).

The parameters for the GEE and R_{ECO} are optimised separately, for the default VPRM parameters and the modified VPRM parameters. Firstly, the GEE parameters are optimised by minimizing the least squares between modelled GEE and the flux tower estimation of the GEE derived from the NEE observations. We use non-linear least squares minimization, from the Trust Region Reflective algorithm of the Python's Scipy library (Virtanen et al., 2020). Afterwards, the R_{ECO} parameters are optimised by minimizing the least-squares between the modelled NEE (using the previous optimised parameters for the GEE) and the observed NEE by the flux towers. The separate optimisation of the GEE and R_{ECO} parameters is needed due to their related dependence on the R_{ECO} parameterization (Equation 6.9) and for properly capturing the diurnal cycle amplitude of both ecosystem fluxes, rather than just reducing the bias on the NEE on a 24-h basis (Gourdji et al., 2022). The prior estimates of the parameters are obtained from previous studies of the European ecosystem fluxes (Migliavacca et al., 2011; Kountouris et al., 2018) and expert knowledge (see Table E.3 in Appendix E).

The performance of the modified VPRM ($VPRM_{MOD}$ from now on) to represent the observed fluxes is compared with the performance of the default VPRM with the prior parameter estimates ($VPRM_{DEF}$) and the default VPRM with the optimised parameters ($VPRM_{DEF_OPT}$). The value of the optimized parameters for the default and modified VPRM are shown in Tables E.4 and E.5 in the Appendix E.The statistical metrics used for the evaluation of the model-data fitting are the Pearson correlation coefficient (r, Equation C.3), the Root Mean Squared Error (RMSE, Equation C.3) and the Mean Squared Deviation ($MSD = RMSE^2$). The Mean Squared Deviation is presented decomposed as the sum of three components: the squared bias (SB), the squared difference between measured and simulated standard deviation (SDSD) and the lack of correlation weighted by the standard deviation (LCS). Further details of the MSD decomposition are explained in (Kobayashi and Salam, 2000). The equations for the SB, SDSD and LCS are detailed in Appendix E.

In the optimisation and evaluation at the flux tower scale, the VPRM model is driven with the meteorological measurements of the sites. For forest, savanna and shrubland stations, the vegetation indices (EVI and LSWI) are derived from the product MOD09A1 of MODIS at 500 m resolution and 8-daily frequency using a Google Earth Engine script. The indices are averaged over the MODIS grid cells interceding a circular buffer zone of 500 m radius. In the case of the grasslands and croplands, a higher spatial resolution is needed to determine the seasonality of small crop fields and grass patches, considering that cropland areas in Europe tend to contain small field patches (< 25 ha) in a mosaic of cultivated crops with different growing seasons. For these stations, the EVI product MOD13Q1 of MODIS at 250 m resolution and 16-daily frequency is used, while the MOD09A1 product is used for the LSWI due to unavailability of higher resolution products. For grasslands and croplands, the indices are extracted from the nearest MODIS grid cell to the station. The MODIS indices are linearly interpolated to half-hourly scale, and then, a locally weighted least square algorithm (LOWESS) is applied to smooth the data and clear possible noise produced by the satellite sensing. During the calibration of the

VPRM parameters for each PFT, we assume that the footprint areas of the stations are represented by only one PFT, the one that is defining the PFT of each station.

6.2.4 VPRM at regional scale

To perform the large-scale spatial evaluation of the carbon fluxes using the atmospheric CO_2 observations, $VPRM_{DEF}$, $VPRM_{DEF_OPT}$ and $VPRM_{MOD}$ are used to estimate biogenic carbon fluxes (NEE, GEE and R_{ECO}) at an hourly resolution spanning from the 1st of March 2017 to the 1st of November 2018 at a spatial resolution of 9 km. This study period encompass two summers (2017 and 2018) with contrasting climatic conditions. The year 2017 was one of the warmest and driest years on the record for the south-western European region, with high positive anomalies in temperature for the spring and summer and a prolonged drought during summer that affected most of Italy, the Balkans, southern France and north-eastern Iberian Peninsula (Rita et al., 2020). In the case of the year 2018, very wet conditions happened in the region due to higher precipitation amounts during the spring, being the wettest spring in the last 70 years, while wetter conditions were also seen in summer and autumn (Copernicus Climate Change Service and Copernicus Atmosphere Monitoring Service, 2018).

The model uses meteorological drivers from the ERA5-Land dataset (Muñoz-Sabater et al., 2021) with hourly frequency and 0.1º resolution. The key variables used include 2m temperature for air temperature, surface solar radiation downwards for shortwave radiation, and volumetric soil water of the second layer (7 to 28 cm depth) for soil moisture. This specific soil layer is chosen due to its higher correlation with observed soil water content from flux tower stations, compared to other layers. Satellite vegetation indices are processed from MODIS surface reflectances (Vermote, 2015). The model computes fluxes individually for each PFT and results were subsequently aggregated based on VPRM PFT map. The VPRM model uses the Synergetic Land Cover Product (SYNMAP) (Jung et al., 2006) for the vegetation classification map. SYNMAP is a 1-km global land cover product built from remote sensing observations and its classes are defined based on PFT mixtures with explicit leaf type and longevity definitions, ideal for carbon cycle modelling applications. The 48 land classes of the SYNMAP map were reclassified in the VPRM preprocessor to the 8 VPRM PFT. Given the minimal temporal overlap in growing seasons for summer and winter crops, VPRM employs parameters for summer crops from June to August and parameters for winter crops from September to May. While this approach may introduce errors in June and September due to overlapping seasons, it was chosen for practicality over the complex task of spatially and temporally classifying crop types at the regional scale.

6.2.5 WRF-Chem model

Chemical transport simulations are performed with the meteorological model WRF-Chem version 4.3.3 (Grell et al., 2005; Skamarock et al., 2021). The model is run with a modification that allows to include multiple passive tracers in one unique transport simulation (Lauvaux et al.,

2012), that we use to transport an ensemble of tracers for biogenic CO_2 fluxes, anthropogenic fluxes, biomass burning fluxes, oceanic fluxes, and boundaries concentrations. The modelled CO_2 concentration is the sum of one of each of these tracers (Feng et al., 2019, 2021). The WRF-Chem configuration used for this study consists of a single domain (Figure 6.2) with horizontal resolution of 9 km (165 x 227). WRF-Chem has 45 vertical levels from surface to 50 hPa, with 21 levels in the lowest 1 km. The meteorological initial and boundary conditions have been obtained from the ERA5 reanalysis product at 3 hourly temporal resolution, which is also used to perform model nudging above the PBL for all the variables, and over all the vertical layers for the wind. The model physical parameterizations are shown in Table 6.1, which have been derived from previous sensitivity studies (Gilabert et al., 2021b; Segura et al., 2021).

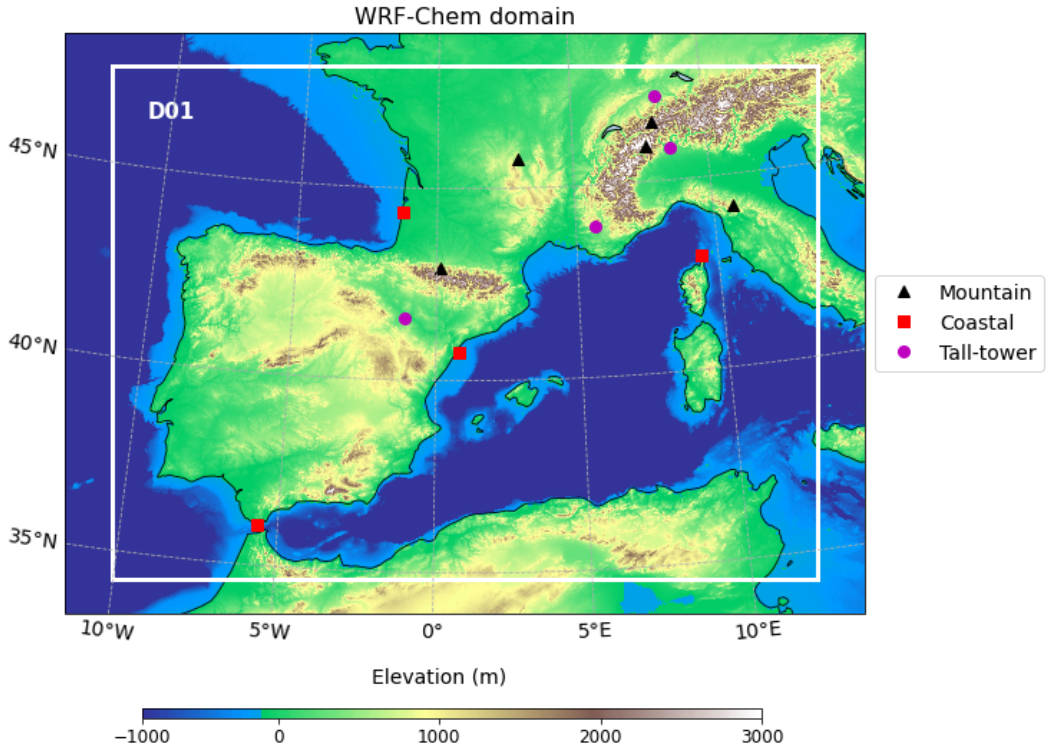


Figure 6.2: WRF-Chem domain and the location of the Drought 2018 dataset atmospheric CO_2 stations.

Table 6.1: WRF-Chem model physics parameterizations schemes.

Parameterization	**Scheme**
Microphysics	WRF Single-Moment 6-class scheme (Hong et al., 2006a)
Shortwave radiation	RRTMG (Iacono et al., 2008)
Longwave radiation	RRTMG (Iacono et al., 2008)
Cumulus	Grell 3D (Grell and Dévényi, 2002)
Planetary Boundary Layer	Mellor-Yamada-Janjic (Janjić, 2001)
Surface and Urban scheme	Unified Noah LSM (Chen and Dudhia, 2001) / BEP-BEM (Salamanca and Martilli, 2010)
Surface Layer	Eta similarity scheme

One 20-month simulation is performed between 1st of March 2017 (00 UTC) and end the 1st of November 2018 (00 UTC). The simulations restart the meteorology fields every 10 days, with 24 hours of meteorological spin-up, while conserving the tracers' concentrations along the entire simulation.

$VPRM_{DEF}$, $VPRM_{DEF_OPT}$ and $VPRM_{MOD}$ fluxes are included as tracers in the WRF-Chem simulations. The boundary and initial CO_2 concentrations are provided by the Copernicus Atmosphere Monitoring Service (CAMS) Global atmospheric inversion CO_2 concentrations at 3-hourly frequency and 1.9º x 3.75º spatial resolution, which is optimised using surface air samples (Chevallier et al., 2010). The anthropogenic CO_2 fluxes are derived from the Emissions Database for Global Atmospheric Research (EDGAR) version 6.0 monthly emissions grid maps (Crippa et al., 2021) (downloaded from https://edgar.jrc.ec.europa.eu/index.php/dataset_ghg60). This emissions inventory is based on international statistics and emission factors, that are built for different sectors at 0.1º spatial resolution. The biomass burning emissions are obtained from the CAMS Global Fire Assimilation System (GFAS) (Kaiser et al., 2012), which derives emissions from assimilation of MODIS satellite observations of the fire radiative power at daily frequency and 0.1º spatial resolution. Both anthropogenic and biomass burning emissions are preprocessed with the HERMESv3 preprocessor tool (Guevara et al., 2019), which temporally and spatially downscales the data to hourly frequency and the domain resolution. In the case of the ocean fluxes, the hourly ocean fluxes from the European CarbonTracker High-resolution system (van der Woude et al., 2023a) are used at 0.1º x 0.2º. The ocean fluxes are reprojected to 9 km resolution using a conservative spatial interpolation.

6.2.6 CO_2 atmospheric observations

The observed atmospheric concentrations are provided by the compilation of historical tower-based in situ CO_2 concentration observations in Europe collected by the Drought-2018 analysis team and available in the ICOS Data Portal (Drought 2018 Team and ICOS Atmosphere Thematic Centre, 2020; Ramonet et al., 2020) containing data from 48 atmosphere stations, covering the period 1979-2018. From this dataset, 14 atmospheric stations (Table 6.2 and Figure 6.2) inside the WRF-Chem domain are selected and classified for its type of location (coastal, tall-tower

in a rural area or a mountain site). In the case of tall-towers, the highest sampling level is selected for the study. The model-observation comparison is obtained by extracting the modelled concentrations in the nearest grid cell to the station location and the nearest vertical level to the station elevation with respect to sea level.

Table 6.2: Atmospheric stations selected in this study.

ID	Station	Country	Type	Lat [°]	Lon [°]	Altitude [m.a.s.l]	Inlet [m.a.g.l]
BIS	Biscarrosse	France	Coastal	44.3781	-1.2311	73	47
BRM	Beromünster	Switzerland	Tall-tower	47.1896	8.1755	797	212
CMN	Monte Cimone	Italy	Mountain	44.1667	10.6833	2165	12
DEC	Delta de l'Ebre	Spain	Coastal	40.7439	0.7867	1	10
EEC	El Estrecho	Spain	Coastal	36.0586	-5.6640	20	20
ERS	Ersa	France	Coastal	42.9692	9.3801	533	40
IPR	Ispra	Italy	Tall-tower	45.8147	8.6360	210	100
JFJ	Jungfraujoch	Switzerland	Mountain	46.5500	7.9879	3570	10
LHW	Laegern-Hochwacht	Switzerland	Mountain	47.4822	8.3973	840	32
LMU	La Muela	Spain	Tall-tower	41.5941	-1.1003	571	80
OHP	Obs. De Haute Provence	France	Tall-tower	43.9310	5.7120	650	100
PDM	Pic du Midi	France	Mountain	42.9372	0.1411	2877	28
PRS	Plateau Rosa	Italy	Mountain	45.9300	7.700	3480	10
PUY	Puy de Dôme	France	Mountain	45.7719	2.9658	1465	10

6.3 Results

6.3.1 VPRM Performance in front of flux tower data

In this section, we compare the performances of $VPRM_{DEF}$, $VPRM_{DEF_OPT}$ and $VPRM_{MOD}$ for simulating the CO_2 fluxes over eddy-covariance flux towers in south-western Europe, using half-hourly observed fluxes (NEE, GEE and R_{ECO}) from the evaluation dataset for model-data comparison.

Figure 6.3 displays heatmaps illustrating RMSE variation for the three fluxes. $VPRM_{MOD}$ exhibits lower NEE RMSE values across most PFTs, except for mixed forest. Optimising VPRM parameters achieves significant RMSE reductions (exceeding 0.55 μmol CO_2 $m^{-2}\,s^{-1}$) for evergreen forests, summer crops and grasslands. $VPRM_{MOD}$ outperforms $VPRM_{DEF}$ in RMSE, particularly for evergreen forests, savannas, winter and summer crops, and grasslands, with reductions from 0.52 to 1.22 μmol CO_2 $m^{-2}\,s^{-1}$. For GEE, $VPRM_{MOD}$ presents the lowest RMSE for several PFTs (EF, DF, SHR, CRO, CRO_W, CRO_S), with notable reductions achieved through parameter optimisation. However, $VPRM_{DEF_OPT}$ exhibits the lowest GEE RMSE for grasslands and savannas. In terms of R_{ECO}, $VPRM_{MOD}$ generally has lower RMSE, except for mixed forests and shrublands where $VPRM_{DEF_OPT}$ performs better. $VPRM_{MOD}$ significantly improves model data-fitting for savannas, croplands (in all aggregations) and grasslands.

Figure 6.4 shows determination coefficient heatmaps for the three fluxes. Correlations between simulated GEE, NEE fluxes, and observed data are similar among the three VPRM versions.

However, NEE from the $VPRM_{MOD}$ has a slightly higher correlation with observations for shrublands, savannas, and winter crops. Regarding R_{ECO}, correlations are similar for evergreen, deciduous, mixed forests, shrublands, and grasslands across all VPRM version. $VPRM_{MOD}$ exhibits a better fit for savannas (0.8), croplands (0.83), winter crops (0.81), and summer crops (0.91) compared to default VPRM (SAV: 0.32; CRO:0.54; CRO_W:0.54; CRO_S:0.75).

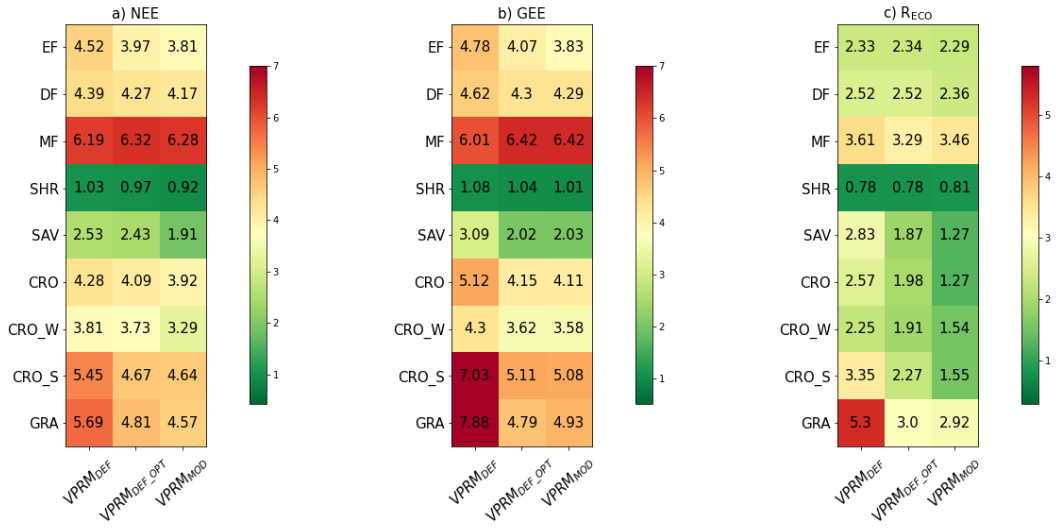


Figure 6.3: Heatmap of the variation of the root mean squared error (RMSE, μmol CO_2 m^{-2} s^{-1}) for the three VPRM versions.

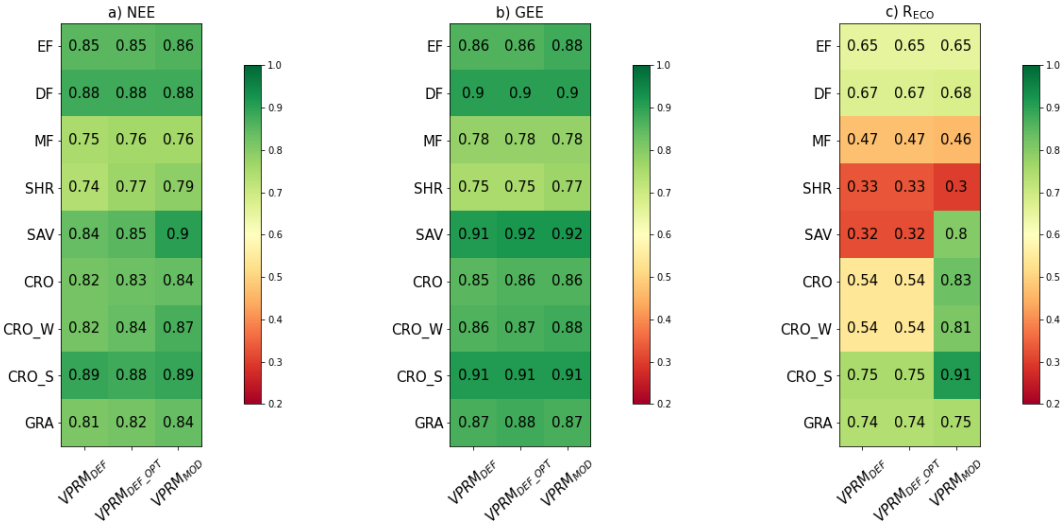


Figure 6.4: Heatmap of the variation of the determination coefficient (r^2) for the three VPRM versions.

Figure 6.5 presents the Mean squared deviation (MSD = $RMSE^2$) decomposed into three components: SB, SDSD and LCS. For NEE, $VPRM_{DEF}$'s main components are SDSD and LCS, while $VPRM_{DEF_OPT}$ and $VPRM_{MOD}$ show reduced SDSD, while LCS becomes the dominant component. This indicates that the improved performance of $VPRM_{DEF_OPT}$ and $VPRM_{MOD}$, across all PFTs except MF, results from a closer match in standard deviation to the observed values compared to $VPRM_{DEF}$. $VPRM_{MOD}$ slightly improves MSD over $VPRM_{DEF_OPT}$ by reducing LCS, suggesting enhanced pattern alignment in NEE fluctuations.

Regarding GEE and R_{ECO}, optimising VPRM parameters with the new cost function decreases SB and SDSD across all PFTs except mixed forests, while increasing LCS. This implies better estimation of the GEE and R_{ECO} in the magnitudes of the fluctuations, at the expense of lower correlation with observed fluxes, particularly notable for savannas, croplands, and grasslands. Forests and shrublands show no significant improvement in R_{ECO} MSD with the modified VPRM. The modifications in VPRM seem to have a more pronounced impact on R_{ECO} than on GEE.

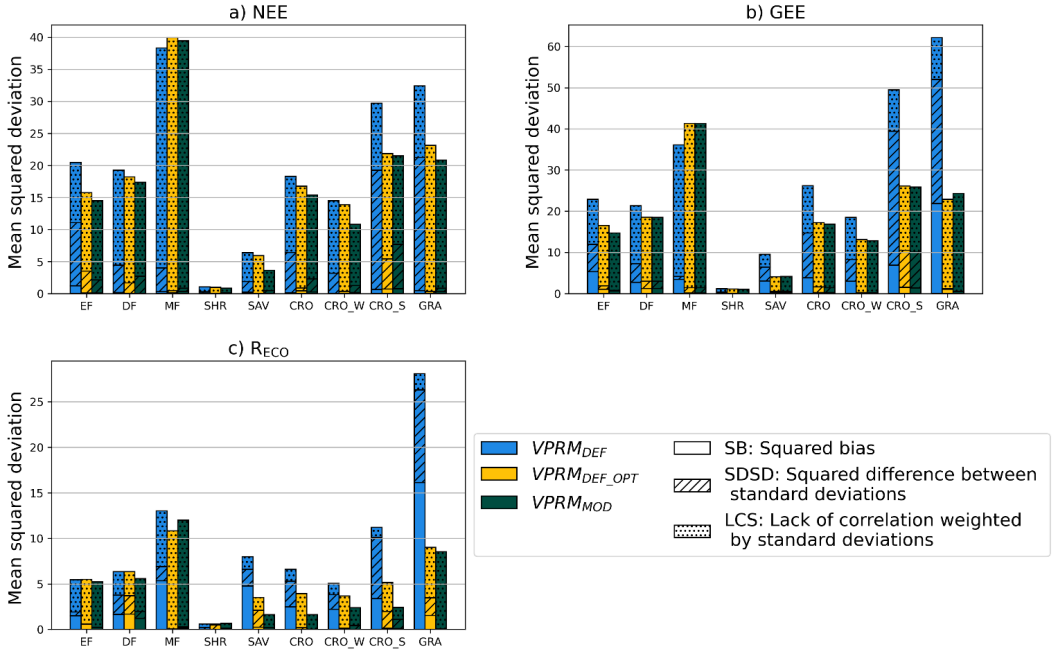


Figure 6.5: Mean squared deviation (MSD) and its components squared bias (SB), squared difference between measured and modelled standard deviations (SDSD) and lack of correlation weighted by standard deviation (LCS) for the three VPRM versions calculated using half hourly data and the different PFTs. a) NEE, b) GEE and c) R_{ECO}.

In the analysis of seasonal cycles in monthly mean fluxes (Figure 6.6), the ability of the three VPRM versions to capture variations depends on the specific flux and PFT. For NEE, all versions closely match the observed negative peak during the growing season for all PFTs, except

savannas, where $VPRM_{MOD}$ aligns more closely with the observations than the default VPRM. Optimising VPRM parameters separately for GEE and R_{ECO}, using the new cost function, improves the representation of the growing season GEE peaks in all PFTs except mixed forests. Mixed forests show overestimation of GEE and R_{ECO} in summer and underestimation in winter for both $VPRM_{DEF_OPT}$ and $VPRM_{MOD}$. The differences in GEE seasonal cycles between $VPRM_{DEF_OPT}$ and $VPRM_{MOD}$ are not significant, indicating minor impact from GEE parameterization modifications at the monthly scale. For R_{ECO}, $VPRM_{MOD}$ better captures peak seasonal cycles for deciduous forest, savanna, croplands, and grasslands compared to compared to $VPRM_{DEF_OPT}$ and $VPRM_{DEF}$. Introducing GEE in the R_{ECO} parameterization corrects the timing of the respiration peak to spring, contrary to $VPRM_{DEF_OPT}$ predicting it in summer. However, for shrublands, there is a clear lack of correlation between VPRM estimates and respiration observations.

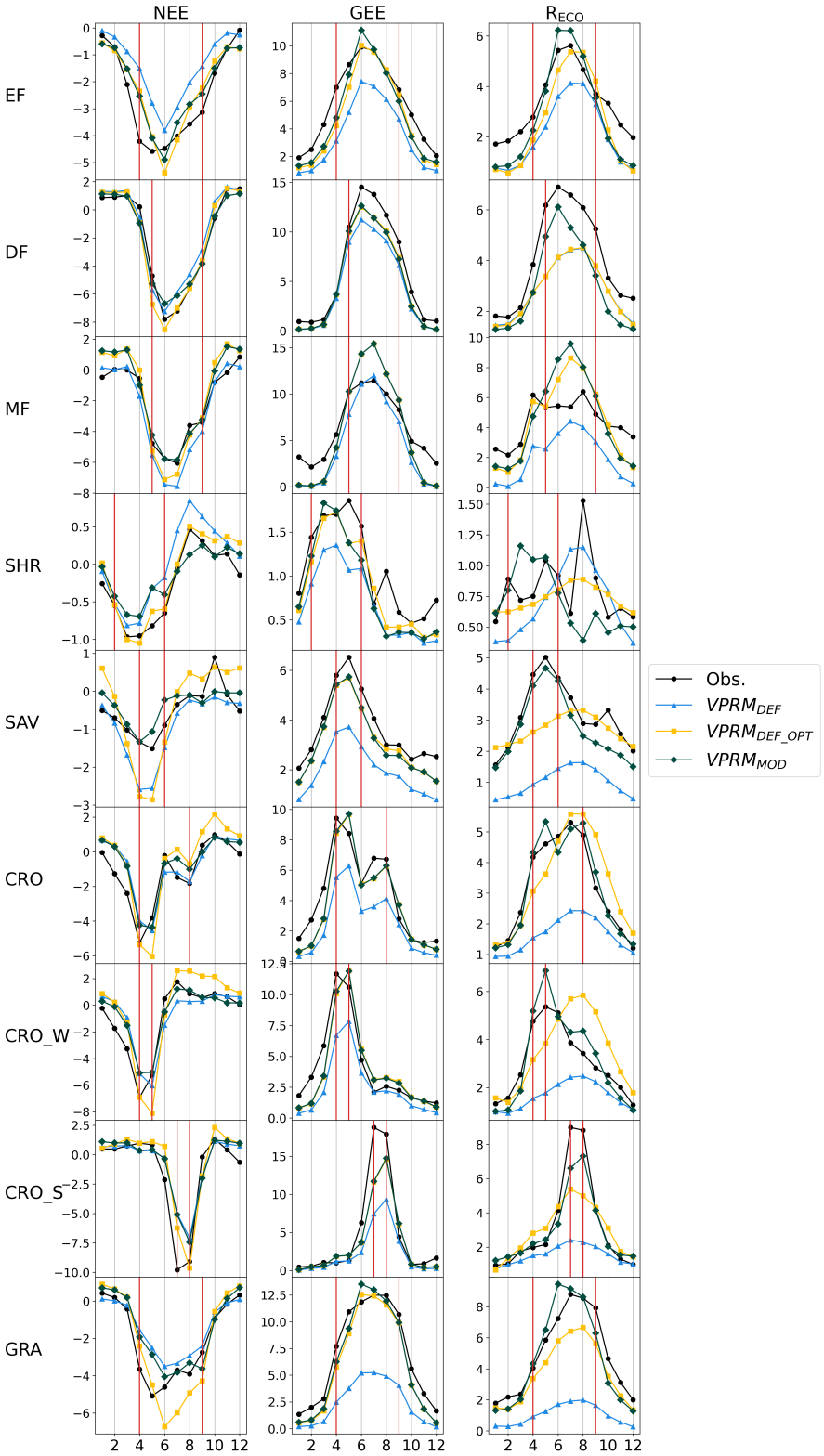


Figure 6.6: Seasonal cycles of monthly mean NEE (left column), GEE (middle column) and R_{ECO} (right column) for the observations (black) and the three VPRM versions using half-hourly data from the evaluation dataset. The vertical red lines mark the beginning and end of the growing seasons defined as the period when the GEE is over the 55 % of the GEE monthly range over the year.

6.3.2 VPRM performance in front of atmospheric CO_2 concentrations observations

In this section, we compare the performances of $VPRM_{DEF}$, $VPRM_{DEF_OPT}$ and $VPRM_{MOD}$ coupled with WRF-Chem for simulating the CO_2 atmospheric concentrations observed in the ground-based stations in south-western Europe. For the comparison, a data filtering scheme is applied to modelled and observed concentrations, consisting in retaining only the hourly data during mid-afternoon (12-17h local winter time) for tall-tower and coastal stations, and nighttime (20-05 h local winter time) data at mountain stations (Ramonet et al., 2020). In this way, the comparison is restricted to periods during the day when the air is well-mixed, providing a high spatial representativeness and minimizing the influence of local sources (Geels et al., 2007; Gerbig et al., 2008; Ramonet et al., 2020). The data is averaged to daily values for the comparison and RMSE and r^2 are estimated.

Figure 6.7 shows the temporal evolution of mid-afternoon daily average CO_2 concentrations, both observed and modelled, for six tower sites. WRF-Chem model with VPRM fluxes is able to represent accurately well the seasonal variations of the CO_2 concentrations for all the tower sites, except for EEC, where a clear overestimation ranging between 0.7 and 7.3 ppm for $VPRM_{DEF}$ and between 1.4 and 6.6 ppm for $VPRM_{MOD}$ is observed. For BIS, OHP, and BRM stations, $VPRM_{MOD}$ presents a lower underestimation of the mid-afternoon concentrations between the months of May and June (BIS: -0.4 – 1.0 ppm; OHP: -0.9 – 0.2 ppm; BRM: -1.4 – 0.1 ppm) than $VPRM_{DEF}$ for the same months (BIS: -2.6 – -0.8 ppm; OHP: -2.3 – -1.4 ppm; BRM: -2.6 – -0.9 ppm). The results of $VPRM_{DEF_OPT}$ (not shown) present even larger underestimations (BIS: -3.1 – -0.4 ppm; OHP: -4.1 – -0.2 ppm; BRM: -4.4 – -2.3 ppm) than $VPRM_{DEF}$.

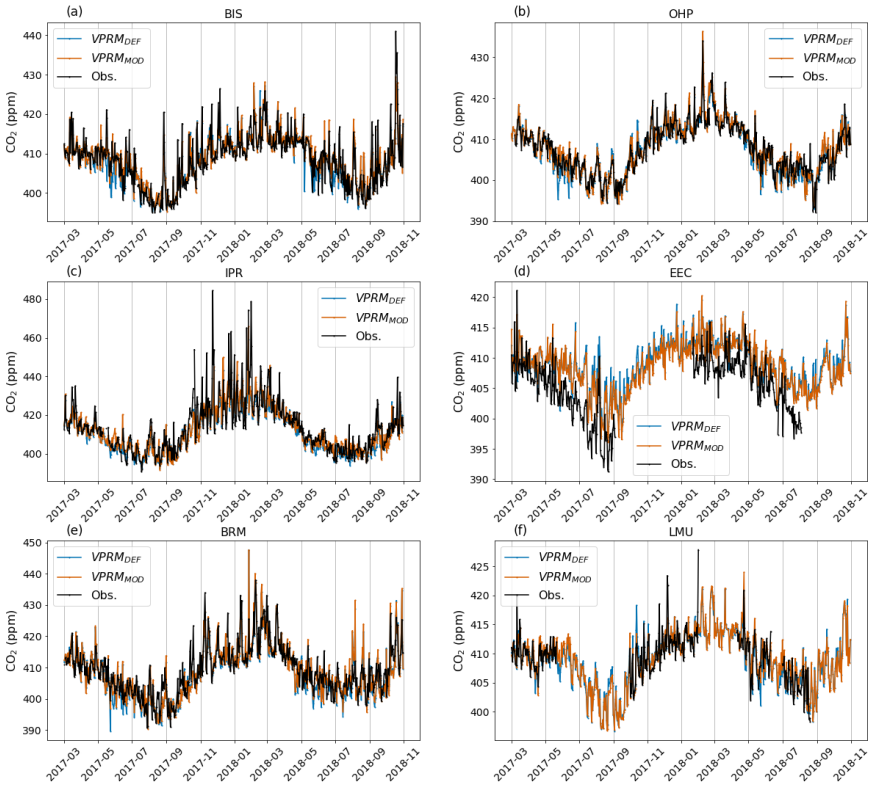


Figure 6.7: Time-series of daily CO_2 concentrations averaged during mid-afternoon (12-17 h local time), observed at six Drought 2018 dataset tower sites (black dots) and simulated by WRF-Chem with $VPRM_{DEF}$ (blue dots) and $VPRM_{MOD}$ (red dots).

We focus on concentrations during May – August 2017, a period marked by notable difference between VPRM versions and increased heat and drought events. Figure 8 represents mid-afternoon daily average CO_2 concentrations decomposed between the different CO_2 tracers (background, biogenic and anthropogenic) at the OHP station in South-east France, surrounded mainly by croplands and evergreen forests. $VPRM_{DEF}$ shows a larger carbon sink in May – June, notably mismatching observations especially between May 23rd and 26th and between June 9th and 14th. During these two periods a similar synoptic event took place in south-western Europe, corresponding with African anticyclonic ridges bringing warmer air from the south, increasing the air temperatures. Warmer temperatures cause divergent responses in GEE and R_{ECO} for $VPRM_{DEF}$ and $VPRM_{MOD}$, producing a larger carbon sink for $VPRM_{DEF}$. During a severe heat wave in late July – August, both VPRM versions capture the shift of ecosystems from carbon sinks to sources. $VPRM_{MOD}$ most accurately represents the peak in CO_2 concentrations with

a lower overestimation of 2.0 ppm, compared to $VPRM_{DEF}$ (3.0 ppm). At the IPR station in northern Italy (Figure E.1), despite a lower correlation between modelled and observations CO_2 concentrations, $VPRM_{MOD}$ improves biogenic signal estimation during the heat wave, with a 3.7 ppm underestimation compared to $VPRM_{DEF}$ (8.1 ppm). These results indicate that VPRM modifications enhance modelled ecosystem flux responses to temperature increases, improving the model's ability to capture weather event impacts on the biogenic carbon signal.

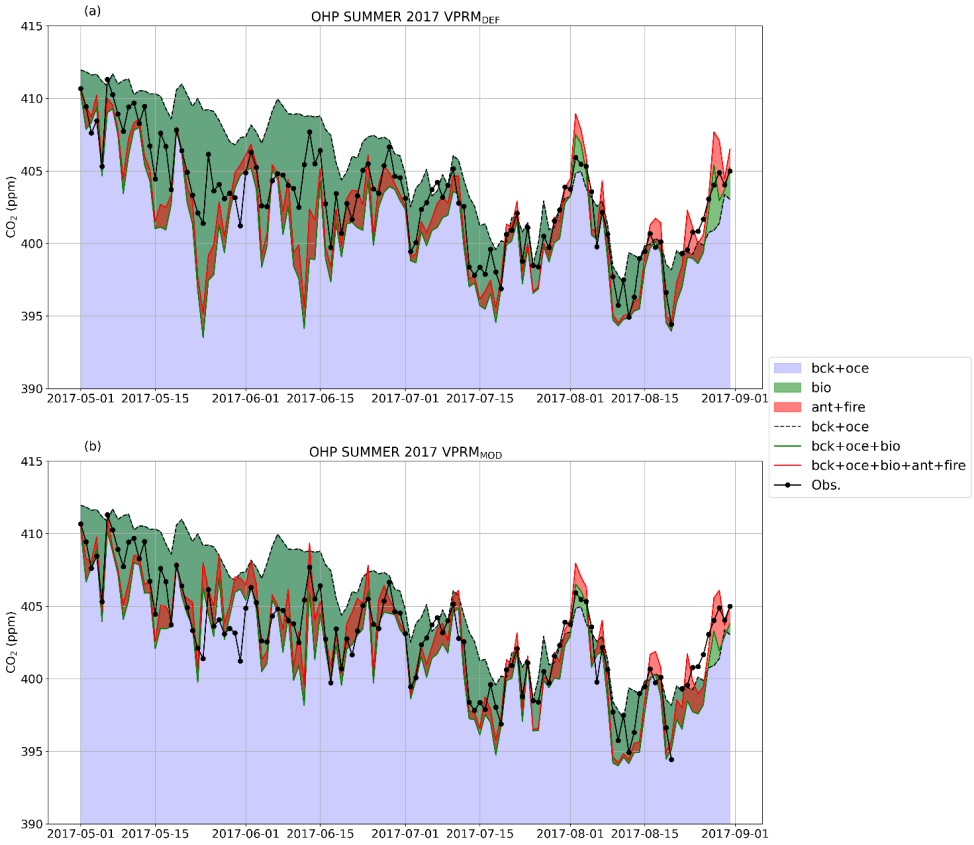


Figure 6.8: Observed (black dots) and WRF-Chem modelled daily mid-afternoon CO_2 concentrations decomposed into the different tracers for the OHP station between May and September 2017 for (a) $VPRM_{DEF}$ and (b) $VPRM_{MOD}$. The shaded blue area until the dotted black line corresponds to background (bck) and oceanic (oce) tracers, the green shaded area is the biogenic (bio) tracer, the red shaded area is the sum of fossil fires (fire) and anthropogenic (ant) tracers. The solid green line is the sum of background, oceanic and biogenic tracers, and the solid red line the total modelled concentration.

The spatial distribution of the monthly aggregate NEE fluxes estimated by the three VPRM versions for these months (Figure 6.9) reveal clear spatial differences. The NEE estimated by $VPRM_{DEF}$ and $VPRM_{DEF_OPT}$ present larger carbon sinks (down to -275 and -326 g C m^{-2}, respectively) compared to $VPRM_{MOD}$, especially during May and over highly productive areas as France, north of the Iberian Peninsula, and the Apennines. These differences are captured in the comparison with the observed CO_2 concentrations in BIS, OHP and BRM, where $VPRM_{MOD}$ presents a lower underestimation than $VPRM_{DEF}$ and $VPRM_{DEF_OPT}$. Over the southern and central Iberian Peninsula, $VPRM_{DEF}$ and $VPRM_{MOD}$ present more similar fluxes, compared to $VPRM_{DEF_OPT}$, which present large carbon sources (up to 300 g C m^{-2}). The results for the LMU station situated in the Iberian Peninsula show a larger overestimation of $VPRM_{DEF_OPT}$ compared to the other versions during the summer months (not shown). In the case of the Po valley, $VPRM_{DEF}$ presents larger carbon sinks in the agricultural areas, varying up to 80 g C m^{-2} in May compared with $VPRM_{MOD}$. These differences could be caused by a higher respiration during the months of May and summer in $VPRM_{MOD}$ compared with $VPRM_{DEF}$ (up to 210 g C m^{-2} higher).

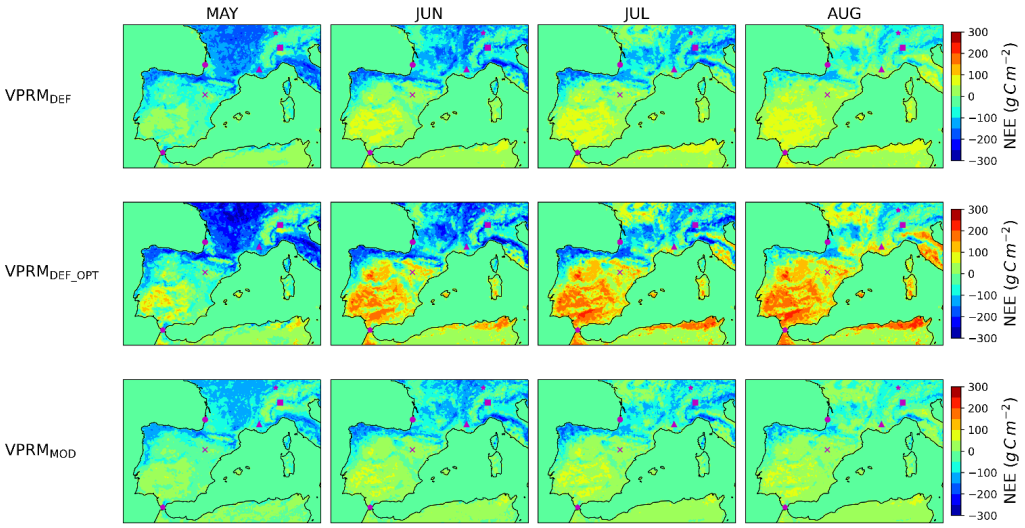


Figure 6.9: Spatial distribution of monthly aggregated NEE simulated by $VPRM_{DEF}$ (top row), $VPRM_{DEF_OPT}$ (middle row), and $VPRM_{MOD}$ (bottom row), for the months of May, June, July, and August 2017. The position of the site towers BIS (circle), OHP (triangle), IPR (square), EEC (pentagon), BRM (star), and LMU (x) are marked in the maps in purple.

Figure 6.10 displays the heatmaps of RMSE and determination coefficient for the modelled CO_2

concentrations using WRF-Chem and $VPRM_{DEF}$, $VPRM_{DEF_OPT}$, and $VPRM_{MOD}$, during mid-afternoon in the tall-tower and coastal stations, and night-time in the mountain stations. The evaluation reveals that $VPRM_{MOD}$ presents a lower RMSE and a higher determination coefficient than $VPRM_{DEF}$ and $VPRM_{DEF_OPT}$ for all the tall-tower and coastal stations, except for the IPR station where the simulation with $VPRM_{DEF}$ presents a slightly higher correlation (0.74) than the simulation with $VPRM_{MOD}$ (0.72). Even though, this station presents the largest RMSE among the site towers, evidencing the challenges for WRF-Chem in resolving the intricate topography and the prominent anthropogenic spikes in CO_2 concentrations during winter (Figure 6.7c). Conversely, the WRF-Chem model with the three VPRM versions presents low RMSE in mountain stations (CMN, JFJ, PDM, PRS and PUY), with RMSE ranging between 2.6 – 1.1 ppm for $VPRM_{DEF}$ and between 2.5 – 1.1 ppm for $VPRM_{MOD}$, and high correlations with r^2 ranging between 0.77 – 0.94 for $VPRM_{DEF}$ and $VPRM_{MOD}$. This indicates a high agreement between the observations and the background concentrations as observed in Geels et al. (2007). The influence of regional fluxes around mountain stations is less pronounced than at low-altitude sites, as well as the vertical heights of the WRF-Chem used for the comparison are principally influenced by the background concentrations.

In summary, WRF-Chem model has a higher performance in estimating mid-afternoon CO_2 concentrations in south-western Europe when it is coupled with $VPRM_{MOD}$, as this model improves the biogenic signal over periods with higher air temperatures, as heat waves events.

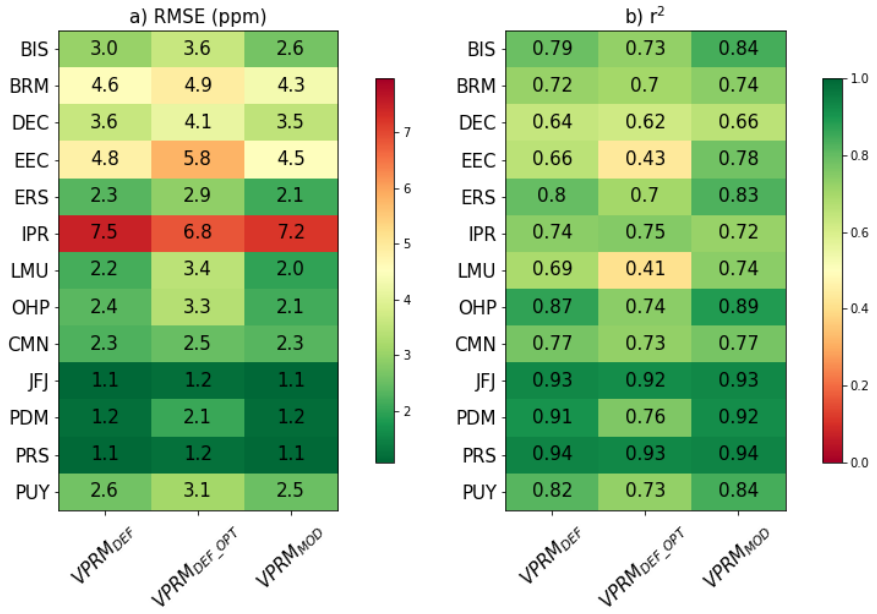


Figure 6.10: Heatmap of the variation of (a) root mean square error (RMSE) and (b) determination coefficient (r^2) for modelled CO_2 concentrations using WRF-Chem and $VPRM_{DEF}$, $VPRM_{DEF_OPT}$, and $VPRM_{MOD}$, for the mid-afternoon in the tall-tower and coastal stations, and night-time in the mountain stations.

6.3.3 VPRM ability to represent the 2017 Drought Impact

In this subsection, we explore the ability of the three VPRM versions to represent the impact of 2017 drought and heat waves on GEE and CO_2 at two flux tower sites. These sites, selected to represent evergreen forests (FR-Bil) and vineyards with grass-covered soil (englobed within the Mediterranean savannas PFT) (IT-Lsn), experienced distinct impacts during this climatic event. Weekly average modelled carbon fluxes are compared with carbon flux observations, as well as the soil moisture fraction (η) and air temperature measured by the flux towers.

The 2017 drought affected the ecosystems at the two flux tower stations differently. In the evergreen forest station (see Figure 6.11a), η dropped to a minimum of 0.14 in November, falling below the soil moisture threshold for evergreen forests (0.39) for two periods: June 11 to June 25, and July 30 to December 3. All three VPRM versions successfully capture the impact of water stress on GEE during the initial period, coinciding with a heat wave event from June 19 to June 21. The observed decrease in the weekly average GEE of 3.0 μmol CO_2 $m^{-2}\,s^{-1}$ between June 11 and June 18 is more accurately represented by $VPRM_{MOD}$ (2.3 μmol CO_2 $m^{-2}\,s^{-1}$) than by $VPRM_{DEF}$ (1.1 μmol CO_2 $m^{-2}\,s^{-1}$) and $VPRM_{DEF_OPT}$ (1.4 μmol CO_2 $m^{-2}\,s^{-1}$). However, in the second period, $VPRM_{MOD}$ is the only VPRM version that precisely follows the declining GEE trend between July 23 and August 20, with an observed decrease of 5.0 μmol CO_2 $m^{-2}\,s^{-1}$,

similarly captured by $VPRM_{MOD}$ (2.9 μmol CO_2 $m^{-2}\,s^{-1}$ decrease), but not by $VPRM_{DEF}$ and $VPRM_{DEF_OPT}$ (GEE increases of 0.3 and 0.4 μmol CO_2 $m^{-2}\,s^{-1}$, respectively). All three VPRM versions exhibit an underestimation of GEE during autumn, falling to capture the weekly variability.

For respiration (Figure 6.11b), $VPRM_{MOD}$ and $VPRM_{DEF_OPT}$ closely follow the observed summer fluxes, compared to $VPRM_{DEF}$ which underestimates CO_2. However, $VPRM_{MOD}$ shows a higher underestimation between September and November, probably produced by an underestimation in GEE and/or low values of η.

In the vineyard flux tower (Figure 6.11c), the minimum η during the drought is 0.20 in July, though this value exceeds the soil moisture threshold established for the Mediterranean savannas PFT (0.08). This results in a similar GEE estimation between $VPRM_{MOD}$ and $VPRM_{DEF_OPT}$. The low soil moisture threshold is attributed to limitations in the VPRM parameters optimisation methodology for determining the soil moisture threshold in ecosystem with drought-deciduous responses. For these PFTs, phenology captured with the EVI and LSWI already provides a sufficient estimation of the drought impact on GEE occurring at the end of June, July and the beginning of August (see Figure E.2 in Appendix E). However, all three VPRM versions present an underestimation during June, up to 4.0 μmol CO_2 $m^{-2}\,s^{-1}$ for $VPRM_{MOD}$ and $VPRM_{DEF_OPT}$, and up to 6.7 μmol CO_2 $m^{-2}\,s^{-1}$ for $VPRM_{DEF}$. Regarding the ecosystem respiration (Figure 6.11d), both $VPRM_{DEF}$ and $VPRM_{DEF_OPT}$ are unable to capture the seasonality of CO_2 or the impact of the drought during July and August, while $VPRM_{MOD}$ closely captures the seasonality and the drought impact.

Overall, this study reveals valuable insights about the ability of the different VPRM versions in capturing the impact of drought and heat wave events on the carbon fluxes, while presenting some limitations during some seasons of the year and for some PFTs.

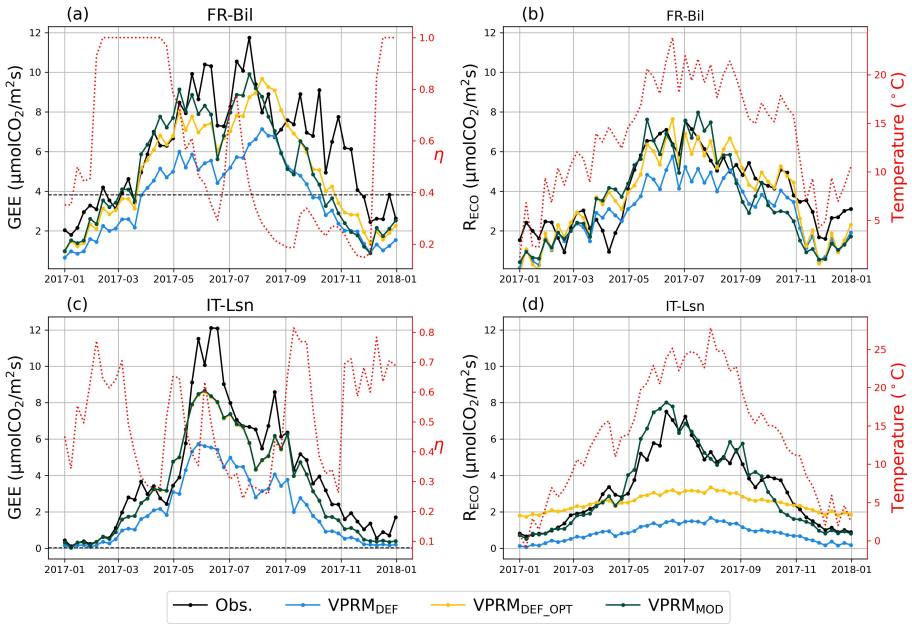


Figure 6.11: Time-series of weekly ecosystem carbon fluxes during the year 2017 for (a) GEE for FR-Bil; (b) CO_2 for FR-Bil; (c) GEE for IT-Lsn; (d) CO_2 for IT-Lsn. Superimposed in the GEE subplots is the soil moisture fraction (red discontinuous line) and the soil moisture fraction threshold (η^*, discontinuous black line) indicating the periods with a water stress. Superimposed in the CO_2 subplots is the air temperature measured by the flux tower station (red discontinuous line).

6.4 Discussion

6.4.1 Evaluation using flux tower data

The evaluation of the performance of the three VPRM versions to estimate the biogenic fluxes compared to eddy-covariance flux tower data shows that the improvement of the VPRM modifications vary with respect to the PFTs. The modified VPRM presents a clear reduction in the NEE RMSE with respect to the default VPRM with prior parameters for evergreen forests, summer crops and grasslands, while there is an improvement in the correlation of the simulated NEE for shrublands and savannas. The modified VPRM also represents a closer standard deviation of the NEE to the observed standard deviation, improving in the representation of the magnitude of the NEE fluctuations compared to the default VPRM. Moreover, unlike in other VPRM parameters optimisations, the improvement in the NEE is accompanied by an improvement in the estimation of the GEE and the CO_2, especially for savannas, croplands, and grasslands ecosystems. The improvement in the model-data fitting is obtained by a reduction of the RMSE, an increase in the determination coefficient and the closely fitting of the seasonal cycles of the GEE and respiration, especially better capturing the magnitude of the peaks during the growing season.

In the case of the GEE, the evaluation shows a similar performance between the modified VPRM and the default VPRM with optimised parameters, indicating that the improvement of the $VPRM_{MOD}$ comes from the separate optimisation of the GEE parameters, which allows to adjust better the magnitude of the GEE fluxes. The modifications made in the GEE parameterization have a minor impact in the performance of the model evaluated using half-hourly data and monthly aggregates. These modifications consist of the inclusion of a soil moisture stress factor, which allows the model to distinguish when the ecosystems are in an energy-limited regime from a water limited regime (Stocker et al., 2019). This soil moisture stress factor has the function to complement and solve the shortcomings of the water stress factor in the default VPRM, derived from the 8-daily LSWI. LSWI provides an estimate of the total liquid water in the vegetation and the background soil (Mahadevan et al., 2008). Therefore, the LSWI varies with the leaf phenology at seasonal timescales, and it is more sensitive to droughts in ecosystems that senesce as a water response such as grasslands, shrublands and Mediterranean savannas (Mahadevan et al., 2008). Then, this modification in the GEE parameterization is especially relevant in ecosystems that have a permanent canopy along the year and are placed in arid and semi-arid climates, such as the Mediterranean evergreen forests.

When the three VPRM versions are compared with simulated fluxes aggregated at weekly basis and compared to the observed data, the GEE from the $VPRM_{MOD}$ is higher correlated to the observed GEE for evergreen forests (r^2=0.89) than $VPRM_{DEF_OPT}$ (0.85) and $VPRM_{DEF}$ (0.84). If we consider only the evergreen forest stations that are placed in temperate climates (altitude below 800 m above sea level), the difference in the determination coefficient is even higher for the $VPRM_{MOD}$ (r^2=0.89) compared to $VPRM_{DEF_OPT}$ (0.75) and $VPRM_{DEF}$F (0.75), implying that the modifications in the GEE parameterization improve the model response of photosynthesis to short-term droughts in temperate Mediterranean forests.

However, these improvements are not seen for other PFTs at weekly aggregates, which points out to multiple reasons. Firstly, the response of non-forested ecosystems seems to be sufficiently captured with the water stress factor of the default VPRM as it is seen in section 3.3, considering that these ecosystems tend to have a drought-deciduous behaviour (Mahadevan et al., 2008; Smith et al., 2024). Moreover, croplands are extremely managed ecosystems, and its exposure to the low soil moisture events are usually reduced by different practices, such as irrigation interventions, drought resistant crop selections (Chaves, 2004) and growing season timing and duration (Porter and Semenov, 2005). Secondly, forests in montane regions tend to have a much lower exposure to low soil moisture than temperate Mediterranean forests (Jolly et al., 2005), which minimizes the impact of low soil moisture parameterization in the GEE equations compared to other responses such as the phenology and temperature response. This points out that the performance of the model is dependent on the ecosystem type, and that other factors that have not been accounted for in the model (e.g., altitude and local climate conditions) can have an influence in the variability of ecosystem carbon fluxes between each PFT (Cartwright et al., 2020).

The evaluation shows that the modifications in the CO_2 parameterization have improved the

representation of the fluxes for savannas, croplands, and grasslands, with a more realistic seasonality and a better estimation of the annual peak. Savannas, croplands, and grasslands are more affected than the other PFTs by the inclusion in the CO_2 parameterization of the photosynthetic activity in the recent days, due to the large seasonal changes in GEE. This can be observed by the timing of the peak in the CO_2 during the year, coinciding with the peak in the GEE. However, the low improvements in the RMSE and r^2 with the VPRM modifications in the other PFT can be attributed to multiple causes. For instance, the performance of the CO_2 is directly related to the performance of the GEE, due to the direct relation in the CO_2 parameterization. Using the observed GEE in the optimisation process of the CO_2 parameters could improve in the parameter's estimation (Migliavacca et al., 2011), yielding better CO_2 estimations, although this could also affect analogously in a worse performance in the estimation of the NEE. Overall, the results in the evaluation of the modelled CO_2 evidence the need for further parameterization developments and the consideration of other biophysical and climatic characteristics of the ecosystems.

The low performance in the evaluation of the biogenic fluxes of the $VPRM_{DEF_OPT}$ and $VPRM_{MOD}$ for the mixed forest PFT marks that the optimisation of the VPRM parameters it is not sufficiently robust for this PFT. VPRM performance yields high RMSE and low r^2, implying that the model struggles to represent the ecosystem dynamics for mixed forests. Over the FLUXNET 2015 and the Warm Winter 2020 there is only one station in the study area that is classified as mixed forest, the CH-Lae station in Switzerland. The high presence of noise in the half-hourly NEE data of this station, produced by the complex orography in the region, limits the reliability of the dataset, critically affecting the optimisation of the VPRM parameters. The addition of new reliable observations from novel ground-based flux towers or the usage of other ground-based stations in other regions of Europe can solve the underrepresentation of the mixed forests stations in south-western Europe.

6.4.2 Evaluation using atmospheric CO_2 concentrations observations

The evaluation of the performance of the different VPRM versions at landscape scale using atmospheric CO_2 concentrations observations from ground-based stations reveals that the modifications applied to VPRM improve the ability of the model to represent the seasonality in the biogenic atmospheric CO_2, as well as the representation of the ecosystem's response to heat events in VPRM. This evaluation also helps elucidating between the performance of the modified VPRM and the default VPRM with optimised parameters, which did not reveal significant differences in the evaluation using data from the eddy-covariance flux tower.

At the larger scale, the default VPRM with optimised parameters produces a lower seasonal correlation with the biogenic signal captured in atmospheric CO_2 stations, due to larger decompensations between GEE and CO_2 fluxes, while presenting the lowest performance overall the model versions (Figure 6.10). The inclusion of the biotic factor in the CO_2 parameterization improves the estimation of the seasonality of the respiration, which is translated in a better representation of the spatial distribution of the NEE (Figure 6.9). Gourdji et al. (2022) have also

highlighted the importance of including a biotic factor in the VPRM CO_2 parameterization for realistic seasonality and fine-scale spatial variability in ecosystem respiration fluxes, particularly for crops in eastern North America ecosystems.

The VPRM evaluation conducted in this study employing atmospheric CO_2 observations from a regional network of ground-based stations is novel for the south-western European region, as this methodology has been successfully applied over North-America (Feng et al., 2021; Gourdji et al., 2022), and Central Europe (Kountouris et al., 2018; Munassar et al., 2022). The south-western European region presents a lack of long-term observational atmospheric CO_2 infrastructure which limits the spatio-temporal coverage of the CO_2 observations and yields under-sampled ecosystems, as those in western and central Iberian Peninsula and southern Italic Peninsula, restraining the evaluation of the carbon fluxes in those ecosystems. Moreover, the sparse observational network also affects the error and accuracy of the global coarse-resolution atmospheric transport models that optimise CO_2 spatial distributions based on inversion of atmospheric CO_2 observations as those used in this study for the background concentrations (Chevallier et al., 2010). In this study, large errors are found at the EEC station (Figure 6.7 and 6.10), situated in an isolated area of CO_2 observational network in southern Spain, which may be attributed to large errors in the background concentrations (Geels et al., 2007).

While background concentrations are partially estimated through nighttime evaluation in mountain stations, this is insufficient for the entire domain. An ensemble approach incorporating multiple tracers and anthropogenic datasets may determine associated uncertainties (Gourdji et al., 2022). Regarding the uncertainties derived from the transport model, these are principally associated to regional wind fields and the height of the mixing layer. In the case of the first one, we rely on nudged ERA5 reanalysis product to accurately estimate wind direction within the domain. In the case of the planetary boundary layer height (PBLH), we use the Mellor-Yamada-Janjic PBL scheme after a sensitivity test comparing multiple schemes, presenting this scheme the lowest errors and higher correlations in terms of PBLH in comparison with observations estimated from daily radiosonde measurements conducted inside the study domain (see Figure E.3). These measurements are obtained from the Integrated Global Radiosonde Archive (Durre et al., 2018). The evaluation reveals locations with a low estimation of the PBLH, underestimated by up to 300 m on average, and RMSE up to 560 m. This can derive on an overestimation of the mid-afternoon CO_2 concentrations. In order to quantify the uncertainties related with the transport, Feng et al. (2021) advocate for using WRF-Chem with a combination of multiple land surface models and planetary boundary layer schemes in a transport model ensemble. Future research should be focus on determining the uncertainties associated to the transport model, background concentrations and anthropogenic emissions in WRF-VPRM simulations over the south-western European region.

6.4.3 Heat and drought impact on the VPRM carbon fluxes

The evaluation of atmospheric CO_2 concentrations reveals that the modifications performed in VPRM enhance the model's representation of heat impacts on the carbon fluxes. This is observed

by the better explanation of summer mid-afternoon CO_2 concentrations day-to-day variability in OHP station, as well as for better capturing the impact of the severe heat wave event of July-August 2017 on the biogenic carbon signal of OHP and IPR stations. These modifications are principally affecting the ecosystem respiration parameterization, increasing the response of the ecosystem respiration to heat during the growing season peak due to the non-linear dependencies with air-temperature (Migliavacca et al., 2011) and reducing the response outside the growing season due to the biotic factor linking respiration with recent GEE. This is also accomplished by temporally discerning two crop groups, winter and summer crops, which present significant differences in their response to heat events.

In the case of the impact of droughts, the assessment of the carbon fluxes during the year 2017 at two flux tower stations reveal that the inclusion of a soil moisture parameterization in the GEE ($VPRM_{MOD}$) improve the model response to drought in temperate evergreen forest, where the effect of soil water stress is better captured than relying exclusively on satellite vegetation indices. Even though, for other PFTs, this improvement with respect to the $VPRM_{DEF}$ is not observed for the GEE (Figure 6.4b), resulting in a minimal influence of the inclusion of the soil moisture function. For these PFTs the detection of the drought impact is relying on the LSWI, which has been assessed to produce a positive bias in the GEE during severe drought events (Stocker et al., 2019). The estimation of a PFT-specific soil moisture threshold as a model parameter may present high uncertainties, as this value may depend on ecosystem-dependent characteristics which are not considered in the optimisation process, as the climatic conditions of the ecosystem (Stocker et al., 2019). This could be potentially solved by defining the soil moisture threshold prior to the optimisation of the other parameters based on ecosystem dependent functions (Stocker et al., 2019; Fu et al., 2022), although this could arise on a lower model performance in the estimation of the carbon fluxes. Further model evaluation and modifications are required for improving the representation of extreme drought events on the GEE for the south-western European region.

6.5 Conclusions

In this study, we improved the Vegetation Photosynthesis and Respiration Model for application in south-western European ecosystems. Model modifications included incorporating a soil moisture stress function for gross ecosystem exchange, a new ecosystem respiration parameterization that contains abiotic and biotic dependences, and temporally segregating summer and winter crops through the use of separately optimised model parameters for each crop group. The optimisation process involved utilizing multi-year data from eddy-covariance stations in the region, with separated optimisations performed for the GEE and CO_2 parameters to enhance the optimisation of each carbon flux.

The evaluation of the modelled carbon fluxes was conducted at the ecosystem scale by comparing with eddy-covariance flux tower data not-used in the parameter optimisation, and at the landscape scale using an atmospheric transport model and atmospheric CO_2 concentrations ob-

servations from ground-based stations in south-western Europe. Overall, the evaluation revealed that the VPRM modifications enhance the model performance in estimating NEE, GEE and CO_2 for most plant functional types. They also improve the seasonality and spatial distribution of carbon fluxes by coupling CO_2 and GEE. The interactions between CO_2 and GEE, representing the effects of recently assimilated carbon in photosynthesis on autotrophic respiration, and the inclusion of non-linear air temperature dependencies in the respiration parameterization enhance the spatial representation of the impacts of heat events on the modelled biogenic carbon signal in the atmosphere.

Moreover, the inclusion of an empirically derived soil moisture threshold in the GEE parameterization corrects the timing and magnitude of the drought effects on GEE, especially in temperate evergreen forest ecosystems, although the impact of this modification is less evident in other plant functional types.

These findings highlight positive outcomes from the modification of a simple data-driven ecosystem model, contributing to a better understanding of the regional carbon balance in south-western Europe terrestrial ecosystems, particularly concerning the impacts of heat and drought events. Further research is necessary to explore additional model enhancements, integrate new eddy-covariance datasets and variables, and improve the representation of disparate responses to heat and drought events between and within ecosystems.

Chapter 7

Heat and drought events alter biogenic capacity to balance CO_2 budget in south-western Europe

Abstract: Heat and drought events are increasing in frequency and intensity, posing significant risks to natural and agricultural areas with uncertain effects on the net ecosystem CO_2 exchange (NEE). In this chapter, we determine the temporal variability of NEE over south-western Europe for 2001-2022, using the modified version of the Vegetation Photosynthesis and Respiration Model (VPRM) (described in Chapter 6). Warming temperatures lengthen growing seasons causing an increase in GEE which is mostly compensated by a similar increment in R_{ECO}, resulting in a modest annual increase of net carbon sink of 0.80 R_{ECO} but with high spatial and annual variability. The heatwave of 2022 reduced NEE by 78.5Tg C, a 27% decrease from the mean. The interannual NEE variability is more influenced by drought in temperate humid regions than in Mediterranean semi-arid regions. These results emphasize the vulnerability of the net carbon sink as drying trends could revert the NEE trends, as it is happening for croplands in the French Central Massif.

7.1 Introduction

Global climate change and the increasing occurrence of extreme climate events are profoundly impacting the terrestrial carbon balance, altering vegetation dynamics, and influencing the net carbon uptake from ecosystems (Ciais et al., 2005; Reichstein et al., 2013; Keenan et al., 2016). Climate warming has extended the growing season in Northern ecosystems by producing more favorable conditions for photosynthesis, thereby increasing their terrestrial ecosystem productivity or gross ecosystem exchange (GEE) (Zhu et al., 2016; Ciais et al., 2019). The increased atmospheric carbon dioxide (CO_2) concentrations also have positive fertilization effects on the vegetation productivity (Thornton et al., 2007; Los, 2013; Schimel et al., 2015). However, warming has also stimulated the release of terrestrial carbon to the atmosphere or ecosystem

respiration (R_{ECO}), by enhanced soil organic matter decomposition and vegetation respiration (Keenan et al., 2016). Interannual variations of biogenic carbon fluxes are expected to increase with increasing frequency and intensity of extreme climate events (Zscheischler et al., 2014a,b), potentially destabilizing the long-term carbon cycle (Fernández-Martínez et al., 2023). These trends depend on vegetation and local climate. For example, arid and semi-arid regions, such as the southern Iberian Peninsula and northern Africa, present higher interannual variations of GEE (Zhang et al., 2016). On the other hand, GEE in humid benefit from the CO_2 fertilization and the longer growing seasons in high latitudes responsible for larger GEE trends compared to other regions (Zhang et al., 2016).

There is an urgent need to better understand how warming and drying trends affect the vegetation in transition regions like south-western Europe. Recent studies have focused on southern Europe, one of the key regions impacted by climate change (Giorgi and Lionello, 2008), with an increasing frequency and intensity of heat and drought events (Fischer and Schär, 2010; Molina et al., 2020). Over the last two decades, observable impacts have been observed (Barriopedro et al., 2011; Vicente-Serrano et al., 2014), which pose significant risks to crops and natural ecosystems. Although the Mediterranean climate is typically characterized by long dry summers (Gilabert et al., 2015), the resilience of its forests (Gazol et al., 2018) reaches its limits when long drought episodes combined with heat waves start to affect the vegetation, leading to a reduction of the net atmospheric CO_2 capture by the ecosystems or net ecosystem exchange (NEE). It is crucial to comprehend the impact of heat and drought events on the south-western European carbon balance.

In recent years, the south-western European region has faced a series of droughts and hot episodes. In France and Central Europe, air temperatures during the summer 2003 were the highest in the last 500 years, which caused a reduction of the continental net carbon uptake in the range of 20 – 500 Tg C year^{-1}, and in some regions changing the ecosystems from carbon sinks to carbon sources (Ciais et al., 2005; Reichstein et al., 2007). The Iberian Peninsula experienced droughts in 2004/2005, 2012, 2015, 2017 and 2022, which produced detrimental effects on the ecosystems, and combined with high summer temperatures intensified the occurrence of fires in the territory (Ionita et al., 2017; Sánchez-Benítez et al., 2018; Nunes et al., 2019; Ermitão et al., 2021; Faranda et al., 2023). In Italy, the summers of 2003, 2017 and 2022 with exceptional temperatures which combined with persistent soil water deficits, resulted into extreme impacts on vegetation productivity (Rita et al., 2020; Trucchia et al., 2022; Faranda et al., 2023). The exceptional drought of the summer 2022, affecting central and south-eastern Europe, caused a reduction of the net biosphere uptake in summer between 56 and 62 Tg C over the drought area (van der Woude et al., 2023b). While different studies have investigated the role of water and heat stress on GEE in southern Europe (Gilabert et al., 2015; Gouveia et al., 2017; Ermitão et al., 2021; Rita et al., 2020), changes in the net ecosystem exchange remains highly uncertain due to complex dependencies from heat and drought episodes on ecosystem respiration R_{ECO} (Reichstein et al., 2013; von Buttlar et al., 2018).

While the impact of heat and drought events on the carbon balance has been well studied for

central and northern Europe (Ciais et al., 2005; Bastos et al., 2020; Ramonet et al., 2020), a multi-year analysis for south-western Europe is lacking. South-western Europe has less long-term observational records of CO_2 concentrations and fluxes, which constrains the understanding of regional biogenic carbon dynamics. Additionally, soil water availability and vapor pressure deficit (atmospheric dryness) are the main factors driving interannual variability of photosynthesis (Gilabert et al., 2015), but the timing of drought and heat events are also important factors in the vegetation response (Jin et al., 2023). Moreover, process-based biogeochemical models usually fail at capturing the vegetation carbon response to extreme variations in soil moisture (Stocker et al., 2018, 2019).

Remote sensing data-driven biosphere models, which estimate ecosystem fluxes based on satellite vegetation indices and meteorological drivers, usually estimate the water stress effect on GEE using satellite sensed water indices or the vapor pressure deficit without considering soil moisture as a model input (Stocker et al., 2018, 2019; Fu et al., 2022). Although satellite indices can capture to some extent the effect of droughts on GEE (Maselli et al., 2009), they tend to underestimate the magnitude of GEE reductions under dry conditions (Stocker et al., 2019). For instance, the Vegetation Photosynthesis and Respiration Model (VPRM) (Mahadevan et al., 2008) does not consider soil moisture as a driver (Mahadevan et al., 2008). Different studies have shown the potential of enhancing the VPRM model capabilities by model parameters optimisation (Dayalu et al., 2018) or by modifying the respiration equation (Gourdji et al., 2022), resulting in similar or even better model performances compared to more complex process-based models.

The main objective of this study is to determine the effect of heat and drought events on the temporal variability of the net biogenic carbon fluxes over south-western Europe, including Portugal, Spain, southern France, and Italy. To do so, we modify the VPRM model to represent the impact of soil moisture on the GEE and R_{ECO} for the period 2001-2022. In addition to the analysis of long-term carbon fluxes variability over this whole period we also study the control of climate driver anomalies (temperature, soil moisture and solar radiation) and drought indices as the Standardized Precipitation Evaporation Index (SPEI) (Vicente-Serrano et al., 2010, 2013) on the carbon fluxes interannual anomalies over ten biogeographical regions (Figure 7.1). To complement the analysis of VPRM simulations, we also estimate GEE based on the sun-induced chlorophyll fluorescence (SIF) provided by the Global Orbiting Carbon Observatory-2 (OCO-2) SIF product (GOSIF) (Li and Xiao, 2019). Finally, we also study the intra-annual variations in carbon fluxes during three exceptional heat and drought events: Western Europe region in the year 2003, the Iberian sclerophyllous region in the year 2005, and the Atlantic region in the year 2022.

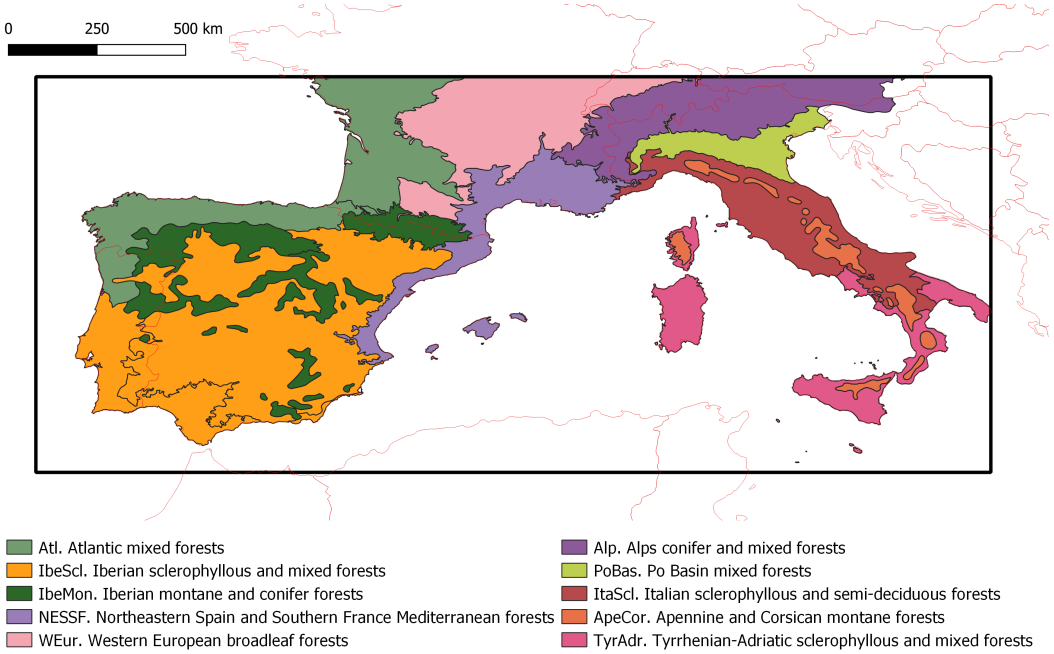


Figure 7.1: Area of study and biogeographical regions of this study.

7.2 Materials and methods

7.2.1 Study area

The study region encompasses south-western Europe from Portugal to Italy, as shown in Figure 7.1. This large area presents a great diversity of ecosystems, topographical features, climates, land-uses, and soil typologies (Gouveia et al., 2017), which we classify into 10 biogeographical regions based on the map of Terrestrial Ecoregions of the World from the World Wildlife Fund (Olson et al., 2001). The prevailing climate is the subtropical Mediterranean climate, with hot and dry summers, although other climates are present such as temperate oceanic (Atlantic part of France, north of Portugal and Spain), mountainous (high-altitude regions of the Alps, Pyrenees, and Dinaric Alps) and humid continental (Central Europe and north-eastern Italy) climates.

7.2.2 VPRM model

VPRM simulates surface CO_2 exchanges between the atmosphere and the biosphere using meteorological data and remote-sensing vegetation indices. NEE is estimated as the difference between R_{ECO} and GEE, following a negative sign convention where negative fluxes represent CO_2

uptake by ecosystems. VPRM parameters are optimised for 8 plant functional types (PFT) representing various land cover types (i.e. evergreen, deciduous, mixed forest, shrubland, Mediterranean savanna, cropland, grassland, and sparsely vegetated), weighted by fractional coverage to calculate the regional ecosystem fluxes. The VPRM model used in this study is the modified VPRM ($VPRM_{MOD}$) described in Chapter 6 (Section 6.2.1) of this thesis that incorporates the impact of soil moisture on GEE and R_{ECO}, and an improved R_{ECO} parameterization with biotic and abiotic factors.

The VPRM model is used to estimate biogenic carbon fluxes (NEE, GEE and R_{ECO}) at an hourly resolution spanning from 2001 to 2022 at a spatial resolution of 9 km. The model uses meteorological drivers from the ERA5-Land dataset (Muñoz-Sabater et al., 2021) and satellite vegetation indices processed from MODIS surface reflectances (Vermote, 2015), as it described in Sections 2.3.1. and 2.3.2. The model computes fluxes individually for each PFT and results were subsequently aggregated based on VPRM PFT map (see Section 2.3.3). Another modification to VPRM includes differentiating between summer and winter crops within the cropland PFT, as it is explained in Section 6.2.1 of this thesis.

7.2.3 Climate and remotely sensed data

Climate drivers

Climatic driver data for the VPRM model are from the European Centre for Medium-Range Weather Forecasts ERA5-Land reanalysis product. These data cover the years 2001 to 2022, with hourly frequency and 0.1° resolution (Muñoz-Sabater et al., 2021). The key variables used include 2m temperature (T2M) for air temperature, surface solar radiation downwards (SSRD) for shortwave radiation, and volumetric soil water of the second layer (7 to 28 cm depth; SM2) for soil moisture. This specific soil layer is chosen due to its higher correlation with observed soil water content from flux tower stations, compared to other layers.

To assess drought episodes across south-western Europe, monthly averaged ERA5-Land variables, including T2M, SSRD and SM2, are employed (Muñoz-Sabater, 2019). Monthly anomalies for these variables are calculated as the difference with monthly mean between 2001 and 2022. Additionally, the Standardized Precipitation Evaporation Index (SPEI) is computed at various months aggregations to assess drought intensity and variability using monthly averaged ERA5-Land data. The SPEI aggregated over 1-, 3-, 6-, 9- and 12-months are named respectively SPEI01, SPEI03, SPEI06, SPEI09 and SPEI12. SPEI is a multi-scalar drought index that considers not only precipitation but also the hydrological balance with atmospheric evaporative demand crucial for studying vegetation impacts in warm regions (Vicente-Serrano et al., 2010, 2013). SPEI is determined based on the difference between precipitation and potential evapotranspiration (PET), with PET calculated using the Food and Agriculture Organization (FAO-56) Penman-Monteith equation, utilizing ERA5-Land monthly averaged variables from 1951 to 2022.

Vegetation indices

The EVI and the land surface water index (LSWI), are processed from the MODIS Terra satellite MOD09A1 v006 product (Vermote, 2015) using the VPRM preprocessor from the Department of Biogeochemical Systems in the Max Planck Institute for Biogeochemistry (https://www.bgc-jena.mpg.de/bgc-systems/pmwiki2/pmwiki.php/Download/VPRMpreproc).

Land cover map

The VPRM model uses the Synergetic Land Cover Product (SYNMAP) (Jung et al., 2006) for the vegetation classification map. SYNMAP is a 1-km global land cover product built from remote sensing observations and its classes are defined based on PFT mixtures with explicit leaf type and longevity definitions, ideal for carbon cycle modelling applications. The 48 land classes of the SYNMAP map were reclassified in the VPRM preprocessor to the 8 VPRM PFT.

Sun-induced fluorescence GEE dataset

To complement the analysis of VPRM simulations, we also estimate GEE based on the sun-induced chlorophyll fluorescence (SIF) provided by the Global Orbiting Carbon Observatory-2 (OCO-2) SIF product (GOSIF), following the methodology outlined by (Li and Xiao, 2019). GOSIF exhibits strong correlations with GEE at hourly, monthly, and annual scales, maintaining a high correlation with GEE even during drought episodes (Qiu et al., 2022; Lv et al., 2023), and offers the advantage of relying solely on satellite SIF observations, eliminating the need for climate data.

7.2.4 Statistical analysis

Monthly anomalies of GEE, R_{ECO}, and NEE are calculated at 9 km resolution, as the difference to monthly means (g C m^{-2} $month^{-1}$) for the entire period 2001-2022. The time series of monthly anomalies are aggregated seasonally for spring, summer, autumn, and winter, as well as for all months, with the mean computed between the monthly anomalies within the selected months of each year. Long-term trends in biogenic carbon fluxes are determined at the grid cell level through linear regression of the time series, and the significance of these trends is assessed using a Pearson correlation test (Equation C.3). The correlation coefficient is called statistically significant if the p value is lower than 0.05. Subsequently, the results are grouped by biogeographical region.

To investigate the influence of SPEI at various timescales on the interannual variability of fluxes, a Pearson correlation analysis is conducted using the time series of detrended flux anomalies. In the case of the climate drivers (T2M, SM2 and SSRD), the partial correlation coefficient is calculated for each variable controlling the interannual variations in the other two driver variables. For this analysis, detrended anomalies are aggregated annually and for growing season

months, identified for each biogeographical region and average seasonal cycles. Growing season months are determined based on when GOSIF GEE exceeds 30 % of the intra-annual GEE range. Although GOSIF GEE and VPRM GEE generally exhibit similar seasonal cycles across all biogeographical regions, discrepancies are observed for the Iberian and Tyrrhenian-Adriatic sclerophyllous regions (Figure F.1 in Appendix F).

Finally, we select three study cases consisting of years with severe heat and drought events affecting largely the NEE of the south-western European ecosystems, to study intra-annual variations in biogenic carbon fluxes in response to these major events. The study cases are the Western Europe region in the year 2003, the Iberian sclerophyllous region in the year 2005, and the Atlantic region in the year 2022. For these three study cases, VPRM-simulated biogenic fluxes are aggregated on an 8-daily basis, along with T2M and SM2. Anomalies relative to the means over the 2001-2022 period are computed for each grid cell and 8-daily period within the year.

7.3 Results

7.3.1 Trends of south-western Europe biogenic carbon fluxes

The long-term analysis of biogenic carbon fluxes from both VPRM and GOSIF shows an overall increase of both GEE and R_{ECO}, with certain regions of flux stability (Figure 7.2). GOSIF presents a positive trend in GEE (spatial median of 5.51 g C m^{-2} $year^{-2}$ and 53.4 % of the vegetated areas in the domain have a significant increase in GEE), while VPRM positive GEE trends are limited to the mountainous regions. Both models are consistent in estimating a non-significant negative trend in the GEE in the Massif Central mountains (south-central France) and the south-west of the Iberian Peninsula. Both models agree that the Apennine and Corsican biogeographical region presents the highest positive trends (spatial medians of 8.97 and 10.25 g C m^{-2} $year^{-2}$ for GOSIF and VPRM, respectively), and Western Europe the lowest trends (2.75 and 1.25 g C m^{-2} $year^{-2}$) (see Figure F.2 in Appendix F).

The long-term trends of the VPRM R_{ECO} present a similar spatial distribution to the trends of GEE, although the magnitude is smaller (spatial median of 3.06 g C m^{-2} $year^{-2}$) than for the GEE (3.75 g C m^{-2} $year^{-2}$). Based on the VPRM, the spatial extent of the areas with significant R_{ECO} trends (37.6 %) extends further than the areas with significant GEE trends (27.2 %), reflecting that the ecosystem respiration has a steadier increase than the gross ecosystem exchange.

This similar spatial distributions of the trends of the GEE and R_{ECO} reflect that long-term variations in released and captured carbon by the ecosystems compensate each other, implying in a trend approaching zero in the NEE (-0.80 g C m^{-2} $year^{-2}$) (Figure 7.2d). VPRM estimates a significant annual increase of net carbon sink over specific regions located in the Alps (-2.35 g C m^{-2} $year^{-2}$), and the Apennines, and Corsican (-3.83 g C m^{-2} $year^{-2}$) mountainous regions (Figure F.2). Only one region shows a decrease in net carbon sink (maximum trends of 11.69

g C m^{-2} $year^{-2}$) over the 2001-2022 period, located in the northern part of the Massif Central, although not statistically significant.

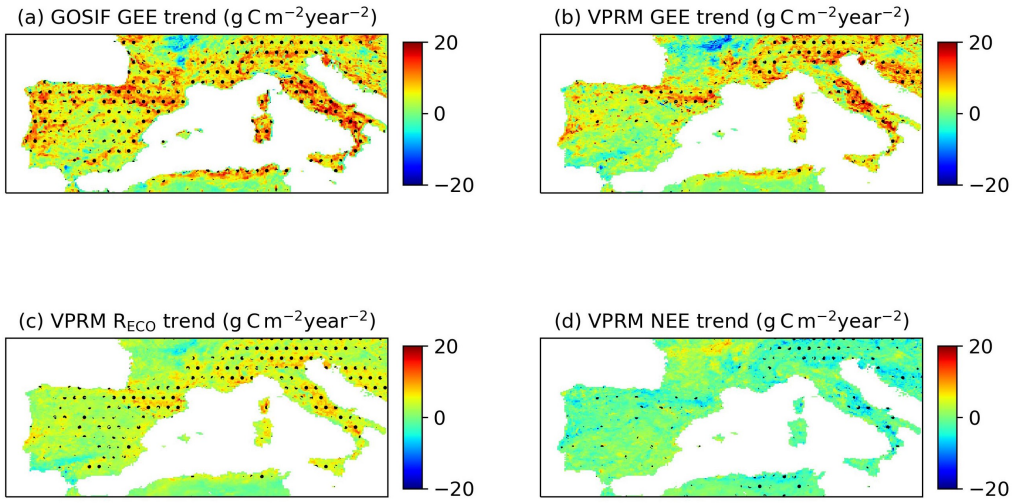


Figure 7.2: Spatial pattern of the long-term trends of annual fluxes for (a) GOSIF GEE; (b) VPRM GEE; (c) VPRM R_{ECO}; (d) VPRM NEE between 2001 and 2022. The black dots correspond to areas where the linear regression is significant ($p < 0.05$).

The seasonal analysis of the biogenic carbon flux trends show that spring is the season when GEE and R_{ECO} (NEE) exhibited higher (lower) values (Figure F.3). During spring, the spatial medians of annual trends are of 0.66, 0.54, 0.31 and -0.24 g C m^{-2} $month^{-1}$ $year^{-1}$ for the GOSIF GEE, VPRM GEE, R_{ECO}, and NEE, respectively. Larger discrepancies between GOSIF and VPRM GEE are present during summer, with 0.43 and 0.08 g C m^{-2} $month^{-1}$ $year^{-1}$, respectively (Figure F.3).

The disaggregation of the fluxes by plant functional types (PFT) reveals that the increase in the long-term trends of the GEE and R_{ECO} in the Po Basin, the Italian sclerophyllous, the Apennine and Corsican montane and the Tyrrhenian-Adratic sclerophyllous regions is mainly located over croplands (Figure 7.3). In other regions such as the Atlantic, the Iberian sclerophyllous and the Western European broadleaf regions, the long-term trends of the respiration are higher than for the GEE in croplands, counteracting the contributions of the natural PFT with stronger sink increases.

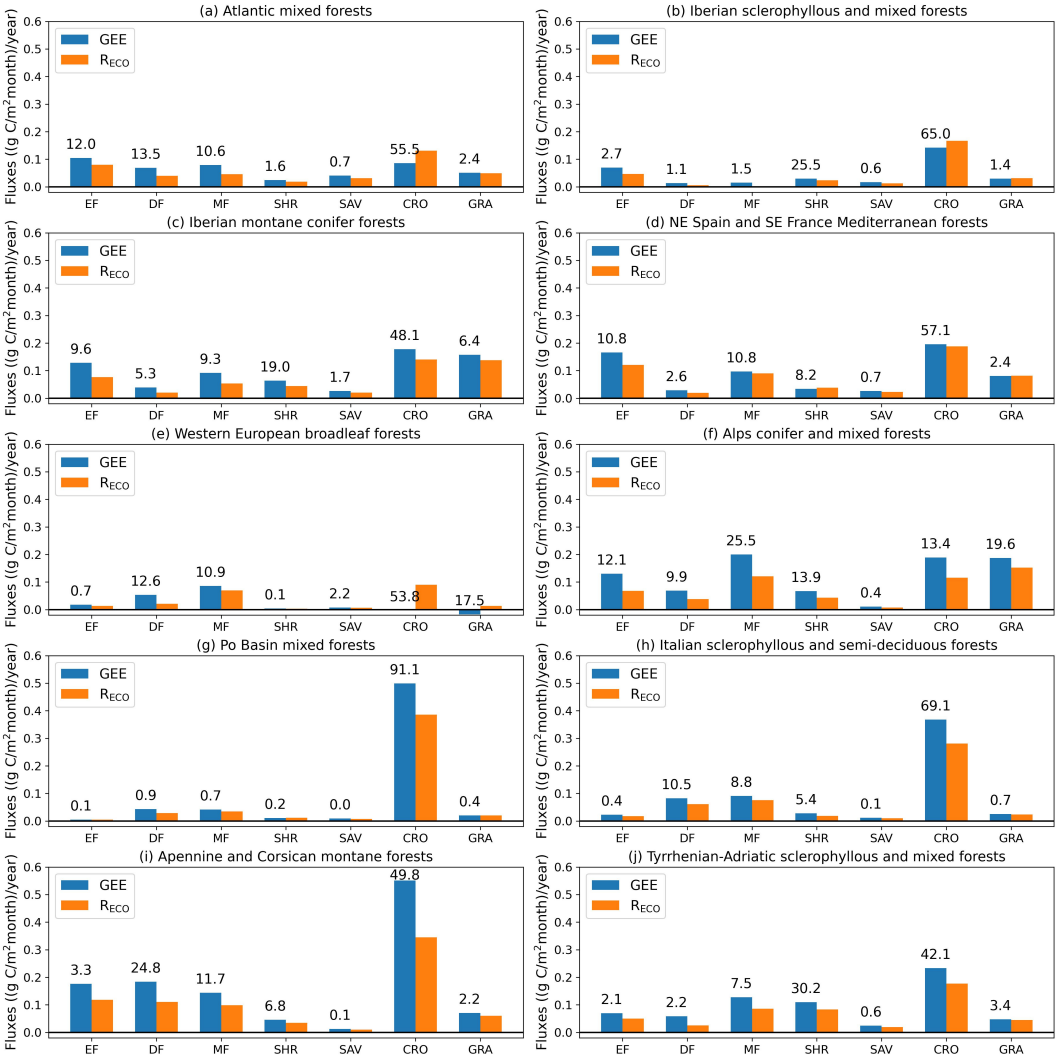


Figure 7.3: Average annual trends of the GEE and R_{ECO} aggregated annually for the different biogeographical regions and integrated for the different plant functional types. The PFT percent coverage in each biogeographical region is marked over each bar. EF: evergreen forest, DF: deciduous forest, MF: mixed forest, SHR: shrubland, SAV: savanna, CRO: cropland, GRA: grassland.

Over the entire study area (Figure 7.4), both VPRM and GOSIF present a significant increase of the annual GEE of 6.5 and 9.4 Tg C year^{-2}, respectively. Both GOSIF and VPRM show a strong agreement on the interannual variability of the GEE. VPRM also presents a significant increase in R_{ECO} of 5.0 Tg C year^{-2}. This occurs in conjunction with a significant warming trend of 0.057 ºC year^{-1} and a non-significant soil drying trend of -0.0003 m^3 m^{-3} year^{-1} over the region. Due to the compensation between GEE and R_{ECO}, the VPRM model shows a non-significant decrease in NEE in the study area of -1.5 Tg C year^{-2}. Moreover, the occurrence of summer heat and drought events increases the interannual variability of NEE, producing the

largest positive NEE anomalies and contributing to destabilize the negative trend in the NEE.

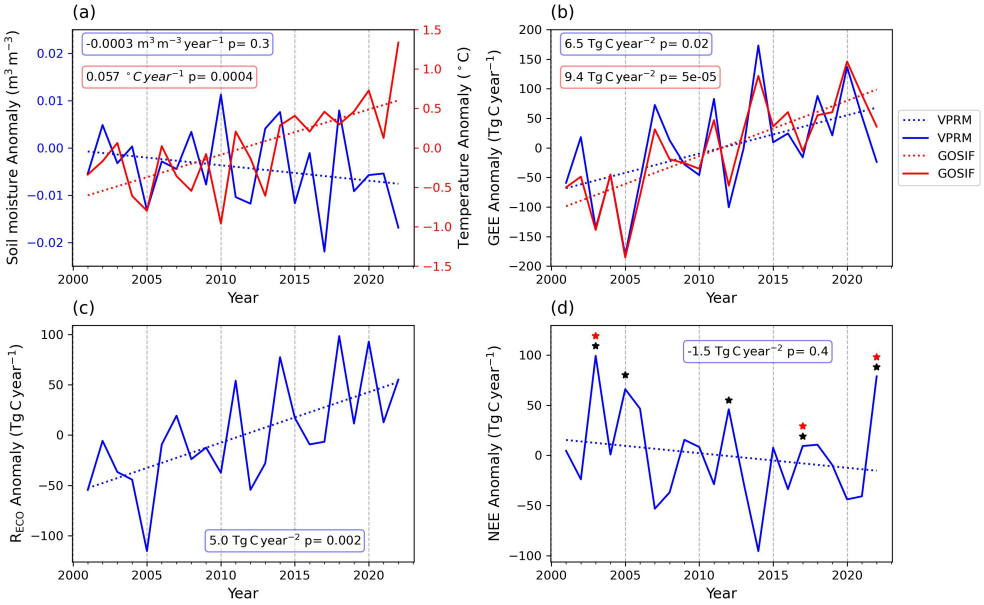


Figure 7.4: Annual anomalies in the climate data and carbon fluxes during 2001-2022. (a) soil moisture and temperature, (b) GEE, (c) R_{ECO} and (d) NEE aggregated annually over the entire study area (black box in Figure 7.1). The dashed lines represent the trends, while in the boxes the trends and the p value are detailed. The black stars in subplot (d) mark the years in which the SPEI aggregated over 1-, 3-, 6-, 9- or 12-months during summer is below -1, indicating a drought affecting most of the study area. The red stars mark the years when the summer temperature anomalies are above 1 ºC, indicating a summer heat event.

7.3.2 Interannual variability of the biogenic carbon fluxes

Figure 7.5 shows the correlation between GEE and R_{ECO} interannual anomalies and the SPEI aggregated over 1, 3, and 6 months (SPEI01, SPEI03 and SPEI06, respectively), and the partial correlation with the climate drivers such as air temperature (T2M), soil moisture and radiation during the growing season months at the ten biogeographical regions. Water availability prevails as the dominant driver of GEE interannual variability. Except for the Alps, the strongest correlations with GEE anomalies are found for SPEI (spatial median ranges between 0.38 and 0.76) and soil moisture (between 0.35 and 0.64). These results suggest that seasonal and extended droughts significantly influence GEE fluctuations. The correlations with SPEI at higher timescale aggregations (9 and 12 months) show lower correlations (between 0.26 and 0.73) than for lower timescale (Figure F.4). Excluding the Alps, soil moisture exhibits generally significant positive partial correlations with GEE anomalies, while air temperature (between -0.28 and 0.21) shows primarily non-significant negative partial correlations. Higher temperatures during

the growing season led to reduced CO_2 capture, while increased precipitation and soil moisture promote the photosynthetic activity. Although radiation presents a positive correlation with GEE, it is generally non-significant. Both GOSIF and VPRM show a good agreement across biogeographical regions and climate drivers (Figure F.4), confirming that both models are able to simulate the observed interannual variability.

In semi-arid regions such as the Iberian sclerophyllous and Tyrrhenian-Adriatic regions, with low annual precipitation (< 800 mm year^{-1}) and early growing seasons (Figure F.1), strong positive correlations are found between SPEI aggregated over 6 months and GEE anomalies (r=0.76 for IbeScl., and r=0.73 for TyrAdr.). During the growing season of low-altitude regions (excluding Alps, Apennine, and Corsican montane forests), GEE exhibits generally negative partial correlations with air temperature (between -0.28 and 0.01), while R_{ECO} shows positive partial correlations (between 0.03 and 0.40). In temperate humid regions like the Atlantic, Western Europe and Po Basin, R_{ECO} displays weaker correlations with SPEI (r= 0.12 to 0.42) compared to GEE (SPEI: r= 0.37 to 0.61), indicating that R_{ECO} is less sensitive to droughts in such regions. Conversely, in south-eastern regions like Tyrrhenian-Adriatic, Apennine and Corsican montane, R_{ECO} exhibits stronger correlations with SPEI and partial correlations with soil moisture (SPEI: r= 0.55 to 0.81; SM2: r= 0.61 to 0.79).

Annually-aggregated GEE anomalies show similar patterns with drought indices and climate drivers (Figure F.5), including SPEI and soil moisture, but weaker absolute values (SPEI: 0.14-0.60; SM2: 0.24-0.52), suggesting that climate driver strength throughout the year has a smaller impact on annual anomalies compared to the growing season. However, excluding Alps, Apennine and Corsican montane forests, annual aggregate GEE anomalies display higher positive correlations with air temperature (between 0.00 and 0.28), indicating that off-season temperature increases enhance gross carbon capture. In high-altitude regions, the partial correlations of annual temperature and GEE anomalies are lower (between 0.09 and 0.40) than during the growing season months (between 0.21 and 0.44).

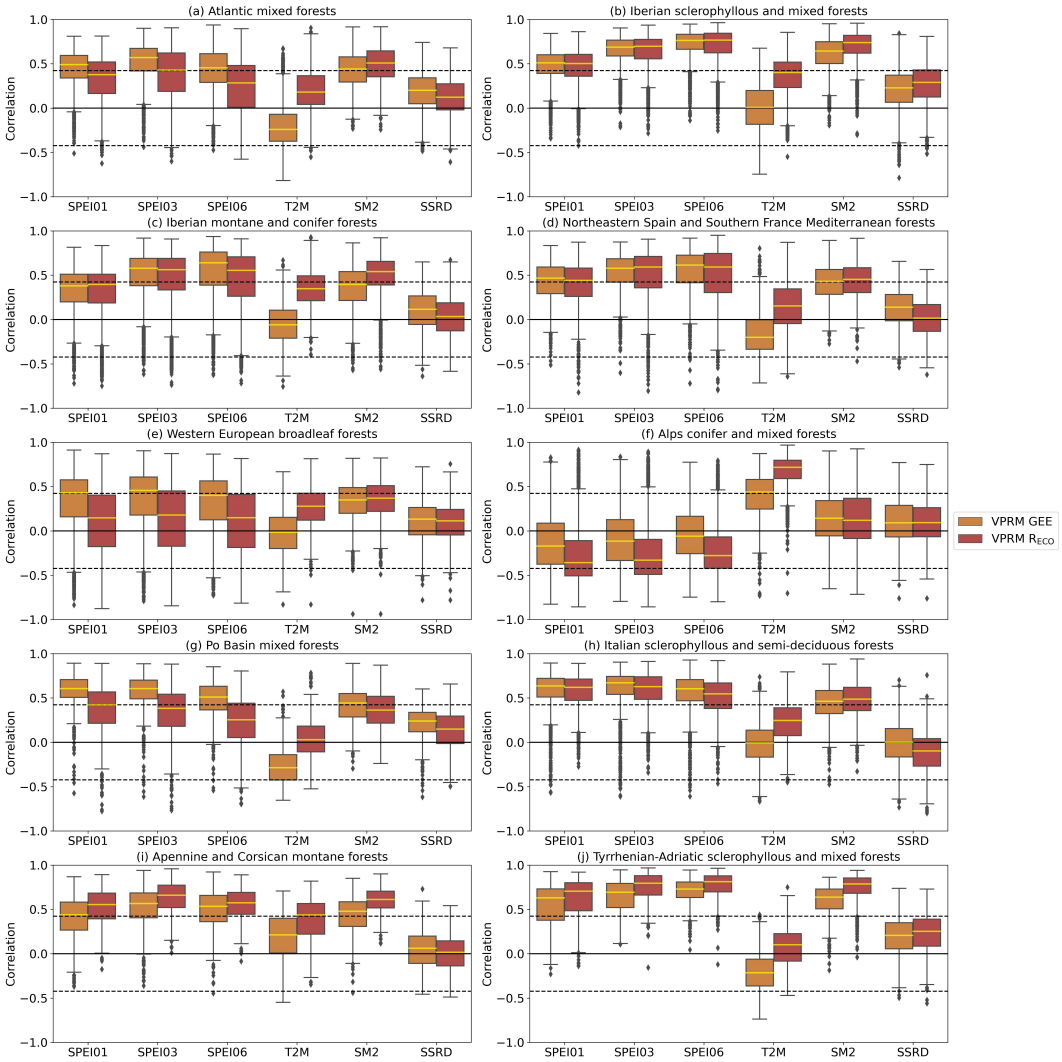


Figure 7.5: Boxplots of correlation values between GEE and R_{ECO} detrended anomalies and the drought indices, and partial correlations with the climate drivers aggregated during the growing season months of each biogeographical region. The median is represented with a yellow line. The discontinuous black lines represent the limit when correlations are significant ($p<0.05$). T2M: 2 m temperature. SM2: soil moisture between 7 and 28 cm depth. SSRD: surface solar radiation downwards.

We analyse the correlation between SPEI and GEE anomalies for the biogeographical regions displaying significant trends (Figure 7.6, see Appendix F, Figure F.6 for the rest). This time-lagged analysis covers the summer season in the same year (0 months), spring in the same year (-3 months), and so forth, up to autumn two years before the growing season (-21 months). Generally, strong, and significant correlations exist between SPEI and GEE anomalies during the growing season in the same year, gradually decreasing with earlier seasons. An exception occurs in the Alps (Figure 7.6f), where SPEI displays a negative non-significant correlation in

the same year's summer and spring, with the correlation increasing in the preceding seasons until the previous autumn. In humid temperate regions like the Atlantic and Western Europe, correlations decrease faster over time, becoming non-significant before the summer season. We observe in these humid regions that correlations decrease much faster over the previous seasons for R_{ECO} than for GEE (Figure F.7). This is different from the Mediterranean climate regions, such as Iberian and Tyrrhenian-Adriatic sclerophyllous, where significant correlations persist even for the previous spring (-3 months) or winter (-6 months), both for GEE and R_{ECO}. In these two regions, GEE anomalies exhibit a stronger correlation with short-time scale droughts (SPEI01 and SPEI03) occurring during the spring than during the summer.

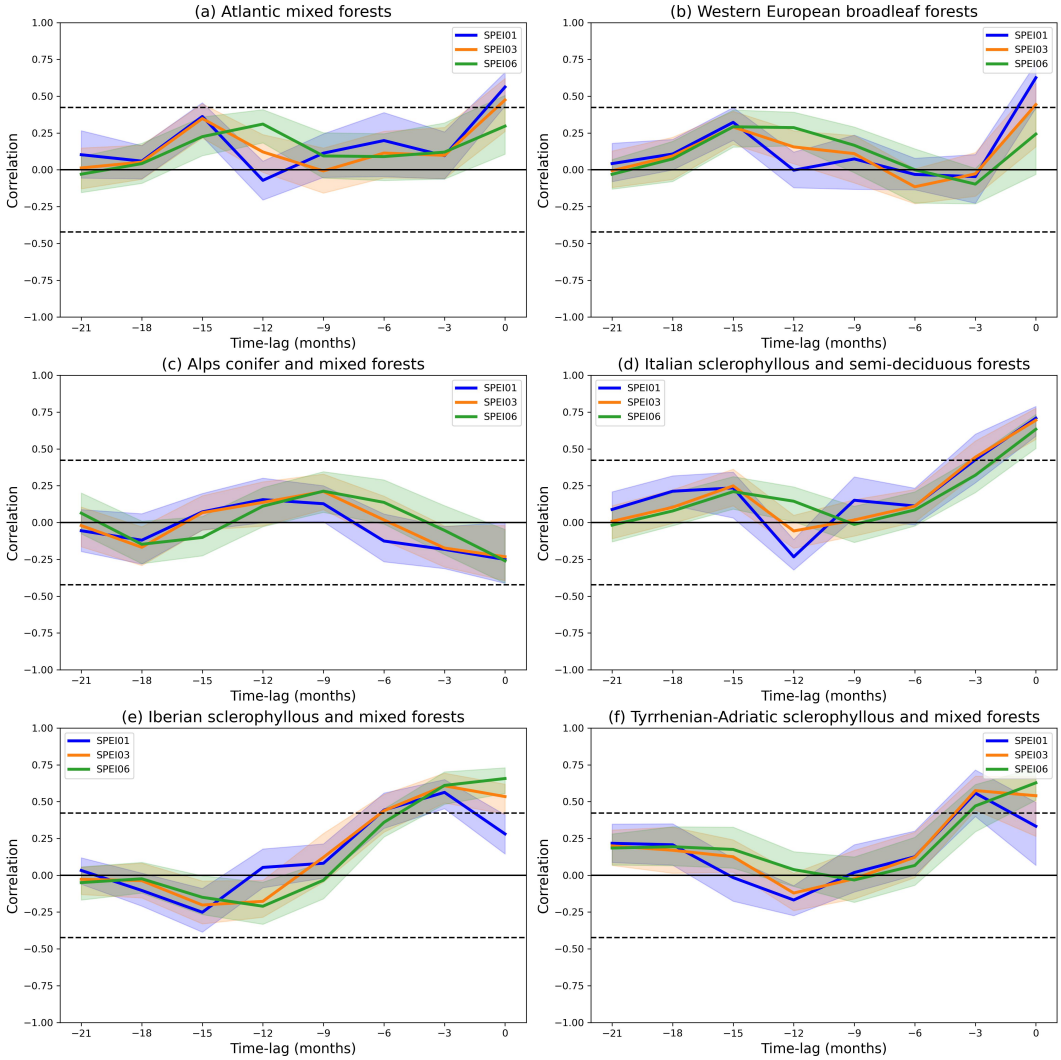


Figure 7.6: Correlogram between the growing season anomaly in the GEE and the SPEI aggregated at 1 month (blue), 3 months (orange) and 6 months (green) averaged over the time-lagged previous seasons. 0 months represent the SPEI between June to August of the same year, -3 months the SPEI between March to May of the same year, and so on, until -21 months represent the SPEI between September to November of two years before the growing season. The bold lines represent the median correlation between all the grid cells inside the biogeographical region, and the shaded areas represent the interquartile range.

In the case of the NEE (Figure 7.7), we observe that for humid regions like the Atlantic and Western Europe, the correlation pattern is similar to the GEE but in opposite sign. However, in Mediterranean climate regions, such as Iberian and Tyrrhenian-Adriatic sclerophyllous, the correlations between NEE anomalies and droughts during summer, spring and winter are much lower in absolute value than for the GEE.

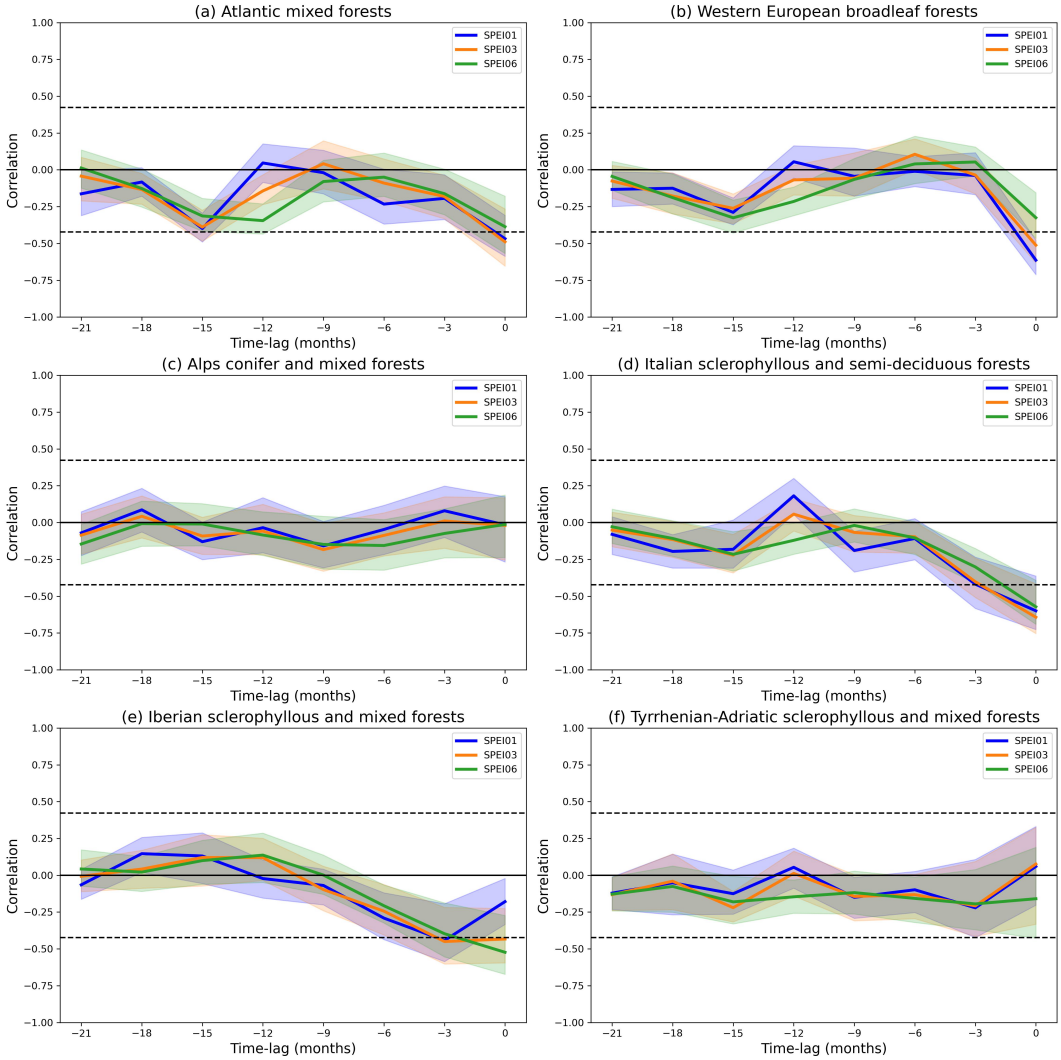


Figure 7.7: As Figure 7.6 but for NEE anomalies.

7.3.3 Intra-annual variability of the biogenic carbon fluxes

In the following section we study the intra-annual variability of the biogenic carbon fluxes for three study cases. Figure 7.8a presents the temporal evolution of the biogenic flux anomalies inside the Western Europe region in 2003. The model indicates reduced GEE from June to September, reaching a minimum of -3.2 ± 1.7 g C m^{-2} day^{-1} (the error corresponds to spatial standard deviation) in early August. R_{ECO} also shows a negative anomaly during summer, albeit smaller than GEE, reaching only -1.3 ± 0.8 g C m^{-2} day^{-1}. The region experienced low soil moisture from March to September, exacerbated by high summer temperatures, especially during a heat wave in August (+8 ºC). This affected considerably the GEE and the NEE, presenting the lowest values in the moment of maximum soil moisture anomaly, and turning the ecosystems

in the region from net carbon sinks into net carbon sources (Figure F.8). The negative anomalies during summer were partially offset by an increase in April, May, and June, linked to positive air temperature anomalies (Figure 7.8d). The drought event of 2003 caused a 20.4 Tg C $year^{-1}$ (-38.8 %) reduction in net carbon capture in Western Europe region. The Atlantic, Po Basin, and Italian sclerophyllous regions were also severely affected (Figure F.9), with respective annual NEE reductions of 11.5 Tg C $year^{-1}$ (-15.9 %), 7.8 Tg C $year^{-1}$ (-85.4 %) and 10.2 Tg C $year^{-1}$ (-40.8 %). Across the entire domain (Figure 7.1), the year 2003 had a net carbon loss of 99.6 Tg C $year^{-1}$ (-34.1 %).

Figure 7.8b depicts the impact of the 2005 drought on biogenic carbon fluxes in the Iberian sclerophyllous region. VPRM indicates reduced GEE and R_{ECO} from late January to October. Higher GEE reductions appear in late April and May (-1.9 ± 1.0 g C $m^{-2} day^{-1}$). GEE and R_{ECO} anomalies evolve similarly, although the impact on the R_{ECO} is lower (-1.6 ± 0.7 g C $m^{-2} day^{-1}$). Climate driver anomalies (Figure 7.8e) reveal persistent negative soil moisture anomalies, dipping to -0.08 $m^3 m^{-3}$ from the start of the year to October, particularly during spring when fluxes are lowest. Negative temperature anomalies (below -5 ºC) were observed during winter, delaying the beginning of the growing season, while May-July featured positive temperature anomalies (> 3 ºC), further depleting soil moisture. The event led to a 64.9 Tg C $year^{-1}$ (-25.0 %) reduction in annual GEE, and 47.1 Tg C $year^{-1}$ (-18.6 %) decrease in annual R_{ECO}, resulting in a 17.8 Tg C $year^{-1}$ (-281.4 %) NEE decrease. The Atlantic, Iberian montane, north-eastern Spain and southern France regions also experienced NEE reductions (Figure F.10) of 11.0 Tg C $year^{-1}$ (-15.2 %), 6.5 Tg C $year^{-1}$ (-35.4 %) and 3.2 Tg C $year^{-1}$ (-17.9 %), respectively. In the south-western European region, the 2005 drought caused a total reduction of 66.5 Tg C $year^{-1}$ (-22.8 %).

In 2022, south-western Europe experienced its hottest recorded summer, coupled with an extended drought event extending from winter until November (C3S, 2023). Winter and spring precipitation and soil moisture deficits further increased during summer due to the unusual warmer temperatures and multiple heat wave episodes (C3S, 2023). Figure 7.8c shows the 2022 spatial mean GEE and R_{ECO} anomalies in the Atlantic region. GEE remains persistently low from June to August, except for early July. R_{ECO} also showed negative summer anomalies, although for a shorter period and with smaller reductions than GEE. During spring, GEE and R_{ECO} experienced positive anomalies (over 2.1 ± 0.9 g C $m^{-2} day^{-1}$), driven by the exceptionally high temperatures during May (over +4 ºC) (Figure 7.8f). The VPRM model estimates an annual decrease of the net carbon capture of 13.8 Tg C $year^{-1}$ (-19.1 %) in the region and 78.5 Tg C $year^{-1}$ (-26.9 %) in the south-western European domain.

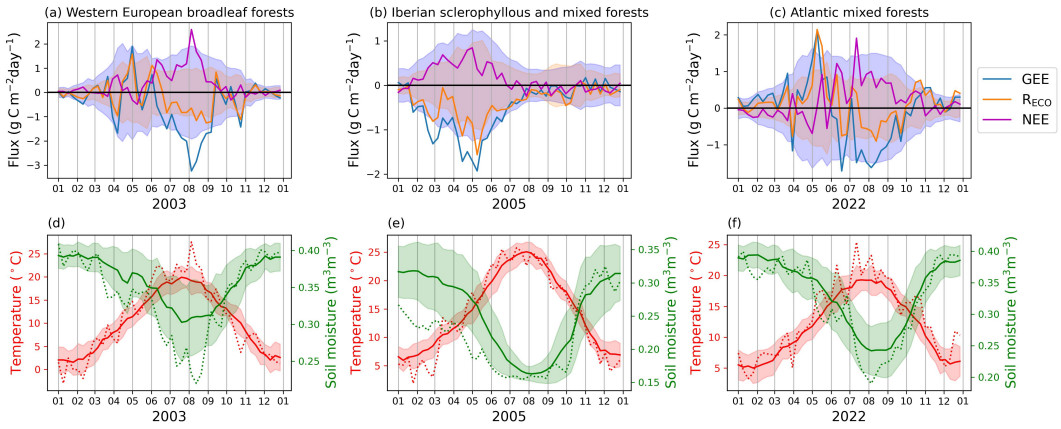


Figure 7.8: Time series of the spatially average anomalies for the Western European in 2003 (a,d), Iberian sclerophyllous in 2005 (b,e), and Atlantic mixed forest in 2022 (c,f) for (a,b,c) 8-daily GEE (blue), R_{ECO} (orange) and NEE (pink). (d,e,f) spatially averaged 8-daily 2 m temperature (red) and soil moisture in the 7-28 cm depth layer (green) for the study year (dotted line) and the climatic mean for the 2001 to 2022 period (solid line). The shaded areas correspond to the temporal standard deviation for each 8-daily period.

7.4 Discussion

7.4.1 Long-term trends of the biogenic carbon fluxes

In this study, we analysed the long-term trends and interannual variability of biogenic carbon fluxes in the south-western European region from 2001 to 2022, to understand the response of these fluxes to heat and drought events. The statistical analysis of the biogenic carbon fluxes reveals an overall increase or stability of GEE (spatial median of 5.51 g C m^{-2} year^{-2} for GOSIF and 3.75 g C m^{-2} year^{-2} for VPRM) and R_{ECO} (3.06 g C m^{-2} year^{-2} for VPRM). These trends are particularly prominent in spring and in montane regions like the Alps, Apennines, Pyrenees, and Dinaric Alps. We identify a positive trend of the enhanced vegetation index (EVI) derived from MODIS surface reflectances over the Mediterranean region (trends up to 0.0014 EVI year^{-1}) which is more evident during the spring and winter months (Figure F.11). Additionally, when examining long-term trends in the air temperatures using ERA5-Land data (Figure F.12), a more substantial winter warming (up to 0.2 ºC year^{-1}) is observed over these same regions. The temperature rise during the colder season contributes to the increase in GEE and R_{ECO} values by alleviating growth limitations and extending the growing season (Keenan et al., 2016). This is supported by similar increases in the GOSIF dataset, which relies solely on SIF satellite data (Li and Xiao, 2019), reinforcing the notion of elevated carbon capture in high-altitude regions of the south-western European region.

However, differences between GOSIF and VPRM are observed in other biogeographical regions, possibly due to differences in model parameterization and input data. The discrepancies between the two models impairs our ability to conclude about the long-term trends in NEE. GOSIF exhibits overall a higher spatial median compared to VPRM. GOSIF solely relies on SIF data and

an ensemble of SIF-GEE linear relationships computed from global flux tower data, whereas VPRM combines remotely sensed vegetation indices, meteorological data, and region-specific model parameters. Consequently, the long-term increase in GOSIF is directly linked to SIF data, whereas VPRM's response is influenced by both vegetation indices and climate drivers. The higher sensitivity of VPRM to interannual climate variations explains the lower extension of areas with a significant long-term trend. Additionally, VPRM is more responsive to higher temperatures during the growing season (Figure F.12), particularly in summer and autumn, and the decrease in the soil moisture (Figure F.13), over the south-western Iberian Peninsula and the Central Massif of France.

According to VPRM simulations, long-term trends indicate that R_{ECO} has also increased in the past two decades, at a slower rate than GEE but affecting a larger area (see Figure 7.2). The increase in R_{ECO}, especially in high-altitude regions, partially offsets the increase in GEE, resulting in only a modest increase in the NEE carbon sink (0.80 g C m^{-2} $year^{-2}$). This balance suggests that the south-western Europe ecosystems maintain equilibrium between increased carbon uptake through photosynthesis and carbon released through respiration. Unlike temperate and boreal forests, which are experiencing a long-term increase of their carbon sink potential (Yu et al., 2022; Yang et al., 2023), the Mediterranean regions exhibits balanced long-term carbon cycle trends. Ongoing warming and drying trends in the region may lead to uncompensated responses in GEE and R_{ECO}, causing variations in the NEE trends. For instance, we have identified a positive trend in NEE of croplands in the Central Massif of France (Figure 7.3e) coinciding spatially with a drying trend in the region (Figure F.13) (Liu et al., 2021). These prospects could further compromise the net carbon sink capacity of other agricultural ecosystems in south-western Europe as the ongoing drying trend (Figure 7.4a) continues and affects other regions in the domain. These findings highlight the vulnerability of the south-western European region's carbon sink capacity to potential shifts in carbon flux trends, especially under the influence of more frequent and intense droughts.

7.4.2 Heat and drought events control the interannual variability of the fluxes

The analysis of the interannual variability in biogenic carbon fluxes emphasizes the significant influence of climatic drivers on the detrended anomalies of these fluxes. Across all the biogeographical regions, except for the Alps ecosystems, water availability emerges as the dominant climatic driver for interannual variabilities (see Figure 7.5). This is evident through the strong correlation observed between these fluxes and both soil moisture and the SPEI. The close agreement between VPRM and GOSIF correlations further supports the influence of soil moisture and SPEI on GEE variability. This alignment is notable, considering that initially, one might attribute this relationship to soil moisture as a driver of the VPRM model.

Analysing the influence of climate drivers on GEE reveals a direct link between climate dryness and the extent to which droughts influence the interannual variabilities of GEE. The regions where the water balance plays a more important role on the interannual anomalies of the GEE during the growing season are the semi-arid regions of the Iberian and Tyrrhenian-Adriatic scle-

rophyllous and mixed forests (see Figure 7.5). In these regions, GEE is strongly correlated with the occurrence of droughts during the growing season and in the previous six months (from the previous autumn forward). These findings align with previous research by (Gouveia et al., 2017), who noted that, during the month of May, Mediterranean dry vegetation communities present the highest correlations between the vegetation activity and the SPEI aggregated at time scales between 3 and 9 months, which are associated with croplands. These regions have a high extension of non-forest vegetation (more than 85 % of the vegetated areas) and the lowest annual precipitation among the studied biogeographical regions (less than 800 mm), explaining the heightened sensitivity to soil moisture availability during periods of active vegetation growth (50). In contrast, the Alps, characterized by the lowest annual temperatures (3.8 ºC) and the highest precipitation levels (1485 mm) in the study area, exhibit a positive correlation with air temperature and negative correlations with SPEI and soil moisture. This pattern suggests that the Alps' vegetation faces continuous energy limitations. Warmer temperatures and increased solar radiation tend to bring climatic conditions closer to the optimal temperatures for photosynthesis (between 18 and 22 ºC), while regional droughts have a relatively lower impact on the water availability of the region.

While increased air temperatures negatively impact GEE anomalies (except for the Alps), their impact on the R_{ECO} is less pronounced. These differences can be attributed to distinct ecophysiological responses of photosynthesis and respiration to temperature and soil moisture stress. Air temperature impacts the photosynthesis when it surpasses a certain optimum temperature by reducing the chemical reaction kinetics (von Buttlar et al., 2018), whereas soil moisture stress impacts photosynthesis by ecophysiological and structural changes (Bréda et al., 2006). On the other hand, increasing soil temperatures, and hence air temperatures, stimulates heterotrophic respiration by increasing the kinetics of soil microbial decomposition, root respiration and the diffusion of enzymes (von Buttlar et al., 2018), while strong soil moisture deficits produced by droughts affects negatively the soil microbial activity and reduces autotrophic respiration due to the reduction of recently assimilated carbon (Reichstein et al., 2003; Migliavacca et al., 2011). Therefore, while an increase of temperature during the growing season can be negative for the photosynthesis, especially if it is accompanied by a drought, the impact on the ecosystem respiration is reduced by the compensating effects. It is worth noting that these responses vary depending on the ecosystem and vegetation species.

Our analysis reveals a higher influence of droughts on GEE anomalies compared to R_{ECO} anomalies in temperate humid regions like the Atlantic, Western Europe, and the Po Basin regions. In contrast, the impacts of droughts on GEE and R_{ECO} in other Mediterranean climate regions show similar correlations. The different responses of GEE and R_{ECO} to drought occurrences between humid and dry climates may be attributed to various factors, including higher intra-annual compensation effect for R_{ECO} compared to GEE in humid regions, the resistance capacity of Mediterranean vegetation to seasonal droughts (Gazol et al., 2018), and lagged responses of R_{ECO} to drought compared to more immediate effects on GEE (Ryan and Law, 2005). These findings align with previous studies on the 2003 summer drought and heat event in Central Europe (Ciais et al., 2005; Reichstein et al., 2007), which reported a higher impact of drought on

GEE compared to R_{ECO} in temperate ecosystems. We note that temperate humid regions exhibit the highest net carbon sink in the study area (see Figure F.14) but also higher nonlinearities in the response of GEE and R_{ECO} to drought occurrence during the growing season. Consequently, anomalies in NEE are highly influenced by droughts in these regions compared to Mediterranean regions (Figure F.15). These results emphasize the vulnerability of the south-western Europe's net carbon sink to drought occurrences.

7.4.3 Warm spring do not compensate the decreasing effect of droughts on CO_2 fluxes

We find that both GEE and R_{ECO} decrease during the summer for Western European broadleaf forests in 2003 and the Atlantic mixed forests in 2022, revealing similar impact of heat and water stress on the ecosystem carbon fluxes. This can be explained by the heat wave in conjunction with persistent drought conditions (García-Herrera et al., 2010; Bastos et al., 2014) as shown by several studies on the coupled effects of heat and water stress on the photosynthetic capacity of Mediterranean ecosystems (Ciais et al., 2005; Reichstein et al., 2007; Bastos et al., 2014; Ermitão et al., 2021).

However, the impact of heat-drought combined conditions on R_{ECO} is lower than for GEE. Moreover, the impact on the R_{ECO} seems to be lagged with respect to the GEE, starting to stress between 8 and 16 days after the stress is observed in the GEE, while recovering concurrently to the GEE once the heat and water stress subsided. These differential responses between GEE and R_{ECO} resulted in a reduction of the net carbon capture capacity of the ecosystems and turning ecosystems from net carbon sinks to carbon sources (see Figure F.8). These results align with the ones obtained by von Buttlar et al. (2018), who found from eddy-covariance flux measurements that the combination of drought and heat typically led to a strong decrease in GEE, whereas heat and drought impacts on respiration partially offset each other.

For the 2003 and 2022 study cases, we find that the impact of summer heat and drought events are partially compensated by abnormally warm temperatures between April and June, which led to an increase in GEE and R_{ECO}. The impact of the warm spring temperatures produced similar positive anomalies in magnitude on the GEE and R_{ECO}. The high spring R_{ECO} anomaly detected in these two study cases could be attributed to the combination of high spring temperatures and the high GEE anomalies at the peak of the growing season, causing an increment of the recently assimilated carbon to respire. The similar increment of the GEE and R_{ECO} during spring compensates each other, resulting in a minimal NEE anomaly during the spring.

These distinct seasonal compensation effects between spring and summer led to an overall reduction in NEE compared to normal values during the growing season, dominating the anomalies for the entire year. These findings highlight the importance of studying the combined impacts of heat and drought events on both GEE and R_{ECO}, as they can cause non-linear effects on the terrestrial carbon balance. Focusing solely on GEE might underestimate the true impact of heat

and drought events on ecosystems, and the terrestrial carbon balance.

These results suggests that the Mediterranean ecosystems, adapted to recurrent seasonal droughts during the summer (Peñuelas and Sardans, 2021), are more vulnerable to the occurrence of persistent soil moisture deficits at the beginning of the growing season, especially if persistent drought conditions affect the previous humid seasons. The Iberian sclerophyllous region is principally cultivated with winter crops (Gouveia et al., 2017), which can be affected by water deficits at early stages of crop development. Moreover, the cold winter conditions during 2005 in the Iberian Peninsula (anomalies of -5ºC) may have also affected GEE by delaying the beginning of the growing season or with a direct frost damage. These results highlight the potential recurrent stress that will suffer the Iberian ecosystems under future climate scenarios, and the compromised carbon balance from these ecosystems (Moemken et al., 2022).

7.4.4 VPRM modifications improve the response of the fluxes to heat and drought

We modified the data-driven biosphere model VPRM for GEE and R_{ECO} parameterizations, incorporating plant functional type-specific parameters calibrated using data solely from flux tower stations in the southern Europe and neighbouring regions. These modifications include the inclusion of soil moisture-related water stress in the GEE parameterization (Fu et al., 2022), resulting in improved model GEE estimates that better align with changes between energy and water-limited regimes. This modification improves the correlation between modelled-predicted and observed weekly GEE estimates in evergreen-leaf ecosystems, such as Mediterranean evergreen forests (see Chapter 6). Additionally, we implemented a more sophisticated semi-empirical R_{ECO} parameterization that considers vegetation productivity (GEE) and soil moisture, enhancing the predictive capability of the model to analyse seasonal and annual variations of the carbon balance (Migliavacca et al., 2011).

However, several limitations emerge from the VPRM model for long-term biogenic flux studies. For instance, the VPRM model relies on a land cover map based on the Synergetic Land Cover Product (SYNMAP) (Jung et al., 2006), which joins three global land cover products based on satellite observations as recent as 2001, failing to account land-use/land-cover changes during the 2001 to 2022 period. This limitation could be solved by incorporating dynamic land-cover maps as the MODIS MCD12Q1 product (Friedl and Sulla-Menashe, 2019). Moreover, the application of static parameters for each PFT for the 2001 to 2022 period could not properly capture the increase in the light-use-efficiency factor due to the atmospheric CO_2 fertilization effect (Keenan et al., 2016). A dynamic set of VPRM parameters, updated every few years, could address this issue, provided a continuous and standardized dataset of carbon flux tower observations encompassing various biogeographical regions, climates and PFT becomes available. Despite the commendable efforts of organizations like FLUXNET (Pastorello et al., 2020) and the Integrated Carbon Observation System (ICOS), certain biomes and PFT remain underrepresented in observation datasets, as it is the case of the croplands in semi-arid regions of the Iberian, Tyrrhenian, and Adriatic sclerophyllous regions. This underrepresentation contributes to model uncertainties in estimating biogenic fluxes in these regions. The VPRM predicting

capabilities and the analysis of the carbon balance would benefit from the incorporation of novel flux tower sites in these underrepresented biomes and PFT.

Despite the enhancements made to the R_{ECO} parameterization, the model evaluation reveals moderate correlations with R_{ECO} observations, compared to GEE and NEE (Figure 6.4). This discrepancy suggests the existence of unaccounted processes within the model. These processes could relate to carbon pool size (Reichstein et al., 2003), the maximum leaf area index throughout the year, nitrogen deposition, and stand age (Migliavacca et al., 2011) in natural ecosystems. In the case of croplands, factors like management practices and soil carbon pools could potentially influence respiration (Eugster et al., 2010). Addressing these aspects could improve R_{ECO} estimation but may introduce additional sources of model uncertainty due to increased complexity. Overcoming these sources of uncertainty may be possible through regional-scale inverse analysis of the CO_2 budget (Mahadevan et al., 2008), leveraging atmospheric CO_2 concentration observations from towers in south-western Europe (Kountouris et al., 2018; Munassar et al., 2022).

7.5 Conclusions

Using a modified VPRM model with parameters optimised for south-western Europe ecosystems, this study analysed the long-term trends and interannual variability of carbon fluxes in south-western Europe from 2001 to 2022, to understand the response of these fluxes to heat and drought events. Our results revealed high spatial variations of the carbon fluxes trends, being higher over mountainous regions in the Alps, Apennine, and Corsican montane forests. The similar increases of the ecosystem's photosynthesis and respiration compensate each other, resulting in only a modest increase of 0.80 g C m^{-2} $year^{-2}$ (spatial median) in net carbon capture over the region. Ongoing warming and drying trends in the region may lead to uncorrelated responses in gross ecosystem exchange and ecosystem respiration, causing variations in the net ecosystem exchange trends. These findings highlight the vulnerability of the south-western Europe's carbon sink capacity to potential shifts in carbon flux trends, especially under the influence of more frequent and intense droughts.

Analysing the influence of climate drivers on the gross ecosystem exchange and respiration reveals a direct link between climate dryness and the extent to which droughts influence the interannual variabilities of the carbon fluxes. The regions where the water balance plays a more important role on the interannual anomalies of the gross ecosystem exchange and respiration during the growing season are the semi-arid regions of the Iberian and Tyrrhenian-Adriatic sclerophyllous regions. These regions, contrary to the other regions, present a higher influence of droughts on the gross ecosystem exchange variability during the spring, rather than on summer. However, this analysis reveals a higher influence of droughts on gross ecosystem exchange anomalies compared to ecosystem respiration anomalies in temperate humid regions like the Atlantic, Western Europe, and the Po Basin. We show here that temperate humid regions exhibit the highest net carbon sink in our study area but also display highly nonlinear responses of the carbon fluxes to drought occurrence during the growing season. Consequently, anoma-

lies in net ecosystem exchange are highly influenced by droughts in these regions compared to Mediterranean regions. These results emphasize the vulnerability of the south-western Europe's net carbon sink capacity to drought occurrences. Additionally, we observed that the impact of summer heat and drought events reduces the net carbon capture, even turning ecosystems from carbon sinks to carbon sources, while we did not observe intra-annual compensations from the preceding warm spring due to compensating increases in gross ecosystem exchange and respiration. These findings emphasize the importance of studying the combined impacts of heat and drought events on both ecosystem photosynthesis and respiration, as they can cause non-linear impacts on the terrestrial carbon balance.

Chapter 8

Conclusions and further research

8.1 Conclusions

This section provides a summary of the main conclusions of the thesis in response to the research questions formulated in Chapter 1.

RQ1. How do street trees impact microscale air-cooling and radiation exchange within a highly compact city?

Street trees significantly influence street canyon micrometeorology by shading. This shading reduced downwelling shortwave radiation on the road surface by 550 ± 309 W m^{-2} at midday (observations) and nearly 300 W m^{-2} (BEP-Tree model). The disparity between observed and simulated data resulted from different spatial representations of radiations. Trees intercepting shortwave radiation decreased road surface temperatures by up to 10.1 ± 2.9 ºC (observations) and 4.5 ºC (BEP-Tree model) during midday (see **Chapter 2**).

Furthermore, street trees can increase downwelling longwave radiation at pedestrian and ground levels due to higher tree canopy temperatures than the cooler sky above (**Chapter 2**). Observations showed an average increase of 22 ± 6 W m^{-2} during the diurnal cycle, more pronounced in areas shielded from building wall-emitted longwave radiation. BEP-Tree simulations indicated a smaller increase in areas with denser trees, considering the cooling effect of trees on building wall temperatures beneath the canopy, that is more appreciated with canyon-averaged estimates.

Regarding air-cooling, street trees combine built surface shading with transpirative cooling. Air temperature differences between two streets demonstrated dependencies on urban canyon geometry, tree leaf density, and local meteorological conditions, including wind direction and speed above buildings. Higher temperature reductions were observed on a day with above roof wind blowing perpendicular to the direction of the streets. Under these conditions, the street with fewer trees recorded air temperatures 1.3 ºC higher during the midday and afternoon compared to its denser counterpart (**Chapter 2**). Conversely, air temperatures were similar in both streets under parallel wind conditions. Note that, while the BEP-Tree model accurately predicted di-

urnal air temperatures cycles, it struggled to account for the effect of wind direction on street tree's air-cooling due to limitations in capturing sub-neighbourhood scale heterogeneity.

Additionally, we found that denser street trees can decrease midday/mid-afternoon road surface temperatures by an average of 2.6 ± 0.7 ºC, peaking at 3.0 ºC at 11 UTC (13 local time) at the neighbourhood-scale meteorology study (see **Chapter 3**). The extent of these reductions varied within urban canyons, depending on sun exposure, tree leaf density, and building shade. Hence, street trees significantly impact road surface temperatures at the microscale, with diminishing effects at the neighbourhood scale.

At the neighbourhood-scale (**Chapter 3**), the air-cooling effect of street trees during a hot summer month was quantified to reduce 0.7 ± 0.4 ºC midday/mid-afternoon temperatures under moist soil conditions. This effect was dependent on the soil moisture conditions, with trees potentially raising air temperatures slightly (0.2 ± 0.3 ºC) under dry conditions. Thus, the transpiration mechanism from street trees emerged as the primary mechanism for microscale and neighbourhood scale air-cooling, highly influenced by urban soil moisture availability.

RQ2. How do street trees impact outdoor thermal stress during heat waves in a highly-compact city?

The BEP-Tree model (**Chapter 3**) showed that denser street trees generally reduce human thermal stress. Trees lowered air temperature (by an average of 0.7 ± 0.4 ºC during midday/mid-afternoon) and mean radiant temperature (by 4.9 ± 2.8 ºC at the urban canyon's hottest location), under moist soils for average summer conditions. However, they also slightly increased air humidity due to more transpiration, with relative humidity averaging 7.8 ± 3.8 % higher during the same time. This led to a decrease in the Universal Thermal Climate Index (UTCI) by 0.9 – 1.2 ºC under optimal soil conditions. However, the benefit is less pronounced under dry soil conditions, due to reduced effects on air temperature.

This study found that tree shading and transpiration present a similar contribution to the reduction of the thermal stress. Assuming a constant tree foliage, which may not be the case for deciduous species after summer or long droughts, shading alone (from the minimization of the transpiration during dry soils) reduce the UTCI by 0.5 – 0.8 ºC, representing a 50-60 % of the total UTCI reduction under moist soil conditions.

During the heat wave, the impact of street trees on the thermal stress showed significant temporal variations. Under moist conditions, trees double its capacity to cool the air during the heat wave, with air temperatures in areas with denser trees being 1.2 ± 0.4 ºC lower than in areas with sparser trees. This increase in air-cooling was attributed to higher tree transpiration due to increased air dryness, although from the literature review this response could vary between different tree species, an even leading to a reduction of the air-cooling effect during heat waves for some species. However, this increase in transpiration also led to higher air humidity, which somewhat detrimentally diminished the thermal stress reduction from the street trees effect. Un-

der dry soil and heat stress, the tree air-cooling and humidifying effects are greatly reduced, preserving the shading. The study observed the most significant UTCI reductions (1.2 – 1.5 °C) in the neighbourhood's hottest locations with moist soil, while these benefits sharply decreased in dry conditions (0.7 – 0.9 °C). During the first days of the heat wave, denser tree areas showed the highest thermal stress reduction, although this effect severely decreased over the last day of the heat wave indicating a potential decline in the microclimatic benefits from trees as the heat wave continued.

These findings highlight the critical role of soil water availability in maximizing street tree's effectiveness in mitigating thermal stress. Adequate soil moisture is as crucial as tree shade during heat wave events, for maintaining tree health and ensuring their microclimatic benefits, especially in Mediterranean climates with warm temperatures. Therefore, effective tree management should focus on maintaining optimal soil water conditions to preserve tree health and maximize their microclimatic benefits for urban residents.

RQ3. What is the role of urban green infrastructure in local temperature regulation in a coastal Mediterranean city?

A significant reduction in near-surface air temperatures (T_{2m}) is seen when urban areas were replaced with vegetation under a theoretical scenario (**Chapter 4**). This increase in vegetation, led to the suppression of the UHI effect, implying on reduced PBL height and enhancing sea-land breezes for both day and night time due to lower wind drag. Notably, temperature differences were more pronounced at night (4.3 ± 1.1 ºC) than during the day (3.4 ± 1.1 ºC).

Further analysis using zonal statistical methods linked 2 m temperatures to urban fractions, defined as the plan area fraction of impervious surfaces. This analysis highlighted a stronger correlation of R^2 = 0.92 between temperatures and urban fractions at night. Comparisons of the relations between temperatures and urban fractions showed greater temperature sensitivity during the night (1.76 ± 0.12 ºC) compared to the day (0.73 ± 0.13 ºC).

These findings indicate that urban green infrastructure can significantly impact nighttime temperatures in summer months, reducing near-surface temperatures by 0.18 ± 0.01 ºC for every 10 % of the area converted from impervious to pervious surface. During the day, the impact at the metropolitan scale is less, showing only a 0.07 ± 0.01 ºC decrease per 10 % surface conversion. Compared to the microscale or neighbourhood scale, the temperature regulation capacity of green infrastructure during the daytime at the metropolitan scale present a lower potential, being mostly perceptible at higher spatial scales and over highly vegetated areas in dense forests and irrigated agricultural areas (see **Chapter 5**), far away from the urban centres and with a limited capacity to reduce urban heat. Conversely, the study, conducted at a finer spatial resolution (333 m x 333 m), suggests the feasibility of implementing green infrastructure at small scales for nighttime heat abatement, allowing to focus in areas most needed of heat mitigation.

However, this study acknowledges a limitation, as the zonal statistical analysis did not differ-

entiate the effects of various types of urban green infrastructure, such as forests, parks, or agricultural land, nor did it consider their impact on different urban morphologies (such as different urban local climate zones). To address this, this thesis advocates for an ex-ante atmospheric modelling evaluation of green infrastructure implementations at the metropolitan scale. This approach would enable the spatial identification of potential temperature regulation benefits of new green infrastructure, considering the trade-offs and synergies with other ecosystem services within a food-water-climate nexus (discussed in **Chapter 5**).

RQ4. Can the expansion of peri-urban agriculture have measurable effects on local temperature regulation and atmospheric carbon capture?

An alternative and a potential scenarios with 31.12 % (+17.27 km^2) and 115.08 % (+64.25 km^2) increase in the current peri-UA in the AMB, mostly from the recovery of abandoned agricultural areas taken over by natural vegetation, resulted in an increase in local food production of 24.0 % (+16503 tons $year^{-1}$) and 85.8 % (+58940 tons $year^{-1}$), respectively (see **Chapter 5**). However, this increase inn local food was also associated with a detrimental increase of the irrigation water requirements by 10.0 % (+3.2 hm^3) and 43.5 % (+14.1 hm^3), respectively.

The expansion of irrigated agriculture contributed for the local temperature regulation, with reductions up to 0.3 ºC and 0.7 ºC during afternoon over a summer month for the alternative and potential scenarios, respectively. A deeper analysis, identified the water irrigation as the main factor for cooling the near surface air temperature during a dry summer month, presenting irrigated agriculture even higher evapotranspiration than forests after long periods without precipitation. However, although the air-cooling from peri-UA expansion was more evident over the Northern Llobregat basin, where nearby urban areas can be really benefitted as this represents one of the hottest areas during summer in the AMB, these NBS would only benefit a small percentage (3.56 %) of the AMB population with a significant temperature regulation. The majority of the AMB population would not be affected in terms of temperature regulation. In the case of the AMB and other coastal areas during summer, sea-breezes have a high influence on the determination of the areas affected by the temperature cooling as these advect cool air inland. This study suggests that other GI strategies within city limits, such as green roofs, cool roofs, or increased urban parks, may be more effective in targeting local temperature reductions.

If the expansion of peri-UA goes at the expense of natural non-forested and forested areas, as in the alternative and potential scenarios investigated, it has further the potential to disrupt the regional carbon balance. Alternative and potential scenarios reduce the atmospheric carbon capture of the AMB green infrastructure by 5.5 % (-5.8 ± 2.9 kilotons C $year^{-1}$) and 18.5 % (-19.4 ± 3.1 kilotons C $year^{-1}$), respectively, while reduce the carbon stocks by 3.3 % (123.4 kilotons C) and 2.3 % (86.4 kilotons C). These decreases are related to the loss of forests biomass and organic carbon in the soil on the one hand, and the reduction of the residence time of carbon in croplands compared to natural vegetation, on the other hand.

The expansion of peri-UA in the AMB may lead to greenhouse gas emissions from land-use

changes, as this thesis shows. However, the evaluation of the global impacts requires the assessment of these implementations to reach further beyond the AMB limits, including both local and replaced imported crop product's carbon footprints. Additionally, direct agricultural emissions (methane, nitrous oxide) and indirect (upstream and downstream) environmental impacts from the agriculture processes must be considered. This global perspective will help identify indirect environmental impacts, contributing to the design of more equitable nature-based solutions.

RQ5. What is the impact of heat and drought events on the biogenic carbon capture of ecosystems in the south-western European region?

Photosynthesis and respiration increase in the south-western European region, 3.75 g C m^{-2} $year^{-1}$ per year and 3.06 g C m^{-2} $year^{-1}$ per year, respectively, attributed to warming temperatures lengthening growing seasons (see **Chapter 7**). We found an increase of 0.80 g C m^{-2} $year^{-1}$ per year in the net carbon sink (up to 3.83 g C m^{-2} $year^{-1}$ per year in high-altitude forests), due to the compensation between photosynthesis and respiration partially. This balance suggests that the south-western Europe ecosystems maintain equilibrium between increased carbon capture through photosynthesis and carbon released through respiration. However, this equilibrium could be reverted if the ongoing warming and drying trends in the region persists. For instance, a positive trend in net carbon sink was identified in the croplands of the Central Massif of France, coinciding spatially with a drying trend in that region. Moreover, the occurrence of summer heat and drought events increases the interannual variability of net ecosystem exchange, producing the largest positive net ecosystem exchange anomalies and contributing to destabilize the increasing trend in the net carbon sink.

Finally, a more detailed study of the carbon fluxes anomalies during the exceptional summer heat and drought events of the years 2003, 2005 and 2022, revealed that the net carbon capture of south-western European ecosystems was reduced by 99.6 Tg C $year^{-1}$ (-34.1 %), 66.5 Tg C $year^{-1}$ (-22.8 %), and 78.5 Tg C $year^{-1}$ (-26.9 %). This reduction is due to a more severe decrease of photosynthesis than respiration. Contrary to other studies, intra-annual compensations from the preceding warm spring were not observed, due to compensating increases in photosynthesis and respiration fluxes.

In summary, the ecosystems in the south-western European region present a complex response to heat and drought events, which can compromise the biogenic offsetting of anthropogenic CO_2 emissions in the region if the intensity and frequency of heat and drought events persists increasing.

8.2 Future research

The work undergone in this thesis has arisen new lines of research in the main goal of understanding the capacity of green infrastructures to provide temperature regulation and atmospheric carbon capture under the influence of heat and drought at the different spatial scales. These

potential research lines are presented in the following subsections grouped by the spatial scale they are addressed.

8.2.1 Street and neighbourhood scales

The work conducted at the streets and neighbourhood scales has centred on applying the BEP-Tree model over the Eixample District in Barcelona. Although this District represents a common urban morphology in the city, Barcelona features varied urban geometries, each potentially benefitting differently from street trees for climate adaptation. Extending this study to other urban areas within the metropolitan region and other Mediterranean cities with different layouts is essential. Additionally, examining how various tree species contribute to air cooling and thermal stress reduction can aid in selecting the most effective trees for heat mitigation. The BEP-Tree model can easily be adapted to these other case studies.

This study can be expanded to include different urban geometries, tree characteristics (species, height, leaf density), and meteorological conditions, providing valuable data for tree management strategies in Mediterranean cities aimed at creating heat-resilient urban environments. However, the model's accuracy in estimating mean radiant temperature and thermo-physiological indices in compact neighbourhoods needs validation. Therefore, a comprehensive evaluation with micrometeorological observations, including mean radiant temperature and other heat stress factors is essential.

For instance, the URBAG group's recent studies during the summers of 2022 and 2023 on human thermal stress variability in urban parks within the Metropolitan Area of Barcelona have yielded insights into detecting heat vulnerability and designing efficient parks for thermal stress reduction. Extending these observations to compact urban environments can validate urban canopy models such as the BEP-Tree.

Furthermore, integrating BEP-Tree with mesoscale models like WRF can broaden the scope of thermal stress assessments to a metropolitan scale. This integration forms a framework for spatially assessing heat vulnerability and designing effective neighbourhood-scale greening strategies for heat mitigation. Incorporating urban park thermal stress variability into these models will provide a comprehensive tool for evaluating urban vulnerabilities and the heat abatement potential of urban parks and street trees.

Moreover, the development of new ecophysiological tree models (Joshi et al., 2022) has enhanced the prediction of the tree response to climatic stressors, and the evaluation of the air-cooling and atmospheric carbon capture of different tree species under heat and drought events. Although these models have been developed for forest tree individuals, the application to street trees could follow similar considerations but accounting for the urban climate stressors, such as high air temperatures, reduced sun exposure and reduced and more compact soil volume. These models could be integrated in BEP-Tree for more accurate predictions of the effect of street

trees, especially during extreme climate events.

Finally, based on the results of this study, a trade-off could arise between the capacity of the street trees to reduce thermal stress and their potential effect for increasing the concentration of air pollutants and its impact on human health in the streets with dense traffic activity. Further research is required for the study of air quality within deep canyons with street trees and heavy traffic, a common situation in the city of Barcelona, to better comprehend the interplay between street trees, traffic air pollutants, and thermal stress in highly-compact cities.

8.2.2 Metropolitan scale

This study assessed the impacts of nature-based solutions, as the expansion of peri-urban agriculture, on the food-water-climate nexus under current climatic conditions. However, climate change's effects could alter the observed trade-offs and synergies in this study. For example, reduced precipitation and increased evapotranspiration due to global warming may intensify water irrigation needs in agriculture and urban green infrastructure, affecting crop yields and natural vegetation dynamics. To analyse these changing ecosystem service trade-offs, dynamic global vegetation models (DGVM) can be utilized (Yue et al., 2018, 2020). DGVMs simulate vegetation growth, crop yields, and water requirements in relation to land carbon cycles and near-surface climate, factoring in climate changes over time. A limitation of DGVMs is their coarse spatial resolution (approximately from 0.5 to 2º), derived from coupling with global atmosphere models or using data from these models. Downscaling this data to the urban scale and integrating regional climate phenomena remains challenging due to high computational demands.

An emerging alternative is applying pseudo-global warming effects to regional climate models (Gutmann et al., 2018), creating high-resolution climate-change scenarios. This method involves in adopting a simulated global atmospheric flow evolution applying specific thermodynamic changes to a regional model's initial fields and time-dependent lateral boundaries. This approach could be employed to examine green infrastructure's response to future climates.

Additionally, the results in **Chapter 5** are based on the assumption that agricultural management follows conventional urban agriculture practices, reflecting the current state in the Metropolitan Area of Barcelona. These practices, including mineral fertilization, tillage, grazing, and soil cover removal, can reduce soil organic carbon content, contrary to greenhouse gas emission reduction goals. This study does not consider the potential future relevance of alternative organic practices, which might lessen these impacts. To explore diverse land-use and land-cover scenarios under different agricultural practices, understanding the effects of these practices on crop's net carbon balance is crucial. Integrating these impacts into data-driven or process-based biogeochemical models and conducting detailed surveys of agricultural practices are necessary.

A complementary approach is the life-cycle assessment of direct and indirect environmental impacts of conventional and organic agricultural practices. This more comprehensive method can

include the entire carbon footprint of these practices, not just direct on-site emissions. However, it adds uncertainty due to factors like system boundaries definitions and inventory information. Further research is needed to fully understand the impact of urban green infrastructure strategies and agricultural management practices on the global carbon balance. Finally, evaluating the regional carbon balance in the Metropolitan Area of Barcelona requires comprehensive validation for a deeper understanding of biogenic carbon fluxes. The lack of CO_2 flux measurements and long-term atmospheric concentration data in the Metropolitan Area of Barcelona and other Mediterranean cities has been a challenge for optimizing biosphere models parameters for urban applications. Recent efforts to monitor atmospheric CO_2 concentrations in the Metropolitan Area of Barcelona (see https://urbag.eu/ghg/) could enhance future evaluations of VPRM net ecosystem productivity and parameters.

8.2.3 Regional scale

The evaluation of the VPRM using eddy-covariance flux tower observations revealed a need for enhanced parameterization of ecosystem respiration to improve model-observation correlations. This discrepancy suggests the existence of unaccounted processes within the model. In the case of natural ecosystems, factors like carbon pool size, maximum leaf area index, nitrogen deposition, and stand age, likely influence respiration. While for croplands ecosystems, the inclusion of management practices and soil carbon pools could potentially influence respiration. These elements, although enhancing ecosystem respiration estimation, introduce further uncertainty as these aspects are rarely mapped spatially, or they are done at coarse resolutions. Additionally, the link between ecosystem respiration and photosynthesis suggests that refining gross ecosystem exchange estimates will improve respiration predictions. Variations in response to heat and drought within plant functional types, observed in different altitude evergreen forests, highlight the influence of unmodelled factors like altitude and local climate on ecosystem carbon flux variability. Developing new plant functional types, such as evergreen broadleaf and needleleaf forests, could refine the spatial and temporal modelling of ecosystem services. However, progress in model development hinges on access to continuous, standardized carbon flux tower data across diverse biogeographical areas, climates, and plant types.

This study also proposes that independently estimating soil moisture thresholds, separate from VPRM parameter optimization, could more accurately time vegetation water stress. These thresholds, varying spatially and among ecosystems, might be derived from climatic and environmental factors, as proposed by Fu et al. (2022). To better represent extreme drought impacts on gross ecosystem exchange in south-western Europe, further model evaluation and modifications are essential.

Assessing VPRM with atmospheric CO_2 concentration observations lacks a quantification of uncertainties in anthropogenic and background tracer concentrations and atmospheric transport. Employing an ensemble of tracers with varied background and anthropogenic concentrations could quantify these uncertainties. Additionally, integrating WRF-Chem with various land surface models and planetary boundary layer schemes in a transport ensemble could estimate atmo-

spheric transport uncertainties, enhancing our understanding of biogenic carbon flux evaluation using WRF-Chem and CO_2 data.

Finally, while VPRM was initially designed for simplicity in integration with models like WRF-Chem, the good performance of the model compared to more complex models and its ability to detect climate signals in biogenic fluxes broaden its potential applications. This includes assessing regional biogenic carbon fluxes during heat and drought events. Expanding its capacity to represent long-term carbon fluxes necessitates addressing limitations in accounting for land-use/land-cover changes, and changes in vegetation photosynthesis light-use efficiency with rising atmospheric CO_2 levels. Overcoming these challenges could offer a complementary biosphere model for reanalysing regional carbon balances in past episodes.

Bibliography

E. Aguilera, G. I. Guzmán, J. Álvaro Fuentes, J. Infante-Amate, R. García-Ruiz, G. Carranza-Gallego, D. Soto, and M. G. de Molina. A historical perspective on soil organic carbon in mediterranean cropland (spain, 1900–2008). *Science of The Total Environment*, 621:634–648, 4 2018. ISSN 00489697. doi: 10.1016/j.scitotenv.2017.11.243.

Agència Catalana de l'aigua. Estimació i prognosi de la demanda d'aigua a catalunya. bases tècniques., 2010.

Ajuntament de Barcelona. Guidelines for irrigation: A practical guide for the irrigation of green areas of barcelona. medi ambient i serveis urbans. https://ajuntament.barcelona.cat/ecologiaurbana/sites/default/files/manual-reg-parcs-jardins.pdf (last accessed may 2021)., 2013.

H. Akbari, M. Pomerantz, and H. Taha. Cool surfaces and shade trees to reduce energy use and improve air quality in urban areas. *Solar Energy*, 70:295–310, 2001. ISSN 0038092X. doi: 10.1016/S0038-092X(00)00089-X.

T. R. Albrecht, A. Crootof, and C. A. Scott. The water-energy-food nexus: A systematic review of methods for nexus assessment. *Environmental Research Letters*, 13:043002, 4 2018. ISSN 1748-9326. doi: 10.1088/1748-9326/aaa9c6.

A. J. Arnfield. Two decades of urban climate research: A review of turbulence, exchanges of energy and water, and the urban heat island. *International Journal of Climatology*, 2003. ISSN 08998418. doi: 10.1002/joc.859.

C. Aznarez, S. Kumar, A. Marquez-Torres, U. Pascual, and F. Baró. Ecosystem service mismatches evidence inequalities in urban heat vulnerability. *Science of The Total Environment*, 922:171215, 4 2024. ISSN 00489697. doi: 10.1016/j.scitotenv.2024.171215.

D. Baldocchi, Y. Ryu, and T. Keenan. Terrestrial carbon cycle variability. *F1000Research*, 5: 2371, 9 2016. ISSN 2046-1402. doi: 10.12688/f1000research.8962.1.

D. Balk, M. Montgomery, G. McGranahan, D. Kim, V. Mara, M. Todd, T. Buettner, and A. Dorelien. *Mapping Urban Settlements and the Risks of Climate Change in Africa, Asia and South America*. 2013.

C. Ballabio, P. Panagos, and L. Monatanarella. Mapping topsoil physical properties at european scale using the lucas database. *Geoderma*, 261, 2016. ISSN 00167061. doi: 10.1016/j.geoderma.2015.07.006.

J. Ballester, H. Douville, and F. Chauvin. Present-day climatology and projected changes of warm and cold days in the cnrm-cm3 global climate model. *Climate Dynamics*, 32:35–54, 2009. ISSN 09307575. doi: 10.1007/s00382-008-0371-0.

R. Banks and J. Baldasano. Impact of wrf model pbl schemes on air quality simulations over catalonia, spain. *Science of The Total Environment*, 572:98–113, 12 2016. ISSN 00489697. doi: 10.1016/j.scitotenv.2016.07.167.

R. F. Banks, J. Tiana-Alsina, F. Rocadenbosch, and J. M. Baldasano. Performance evaluation of the boundary-layer height from lidar and the weather research and forecasting model at an urban coastal site in the north-east iberian peninsula. *Boundary-Layer Meteorology*, 2015. ISSN 15731472. doi: 10.1007/s10546-015-0056-2.

Barcelona City Council Statistical Yearbook. Department of statistics, barcelona city council, barcelona, spain. retrieved from. http://www.bcn.cat/estadistica, 2021.

Barcelona Regional and AMB P.D.U. Initial strategic document. advance of the urbanistic metropolitan master plan barcelona, spain., 2019.

J. F. Barlow. Progress in observing and modelling the urban boundary layer. *Urban Climate*, 10: 216–240, 2014. ISSN 22120955. doi: 10.1016/j.uclim.2014.03.011. URL `http://dx.doi.org/10.1016/j.uclim.2014.03.011`.

D. Barriopedro, E. M. Fischer, J. Luterbacher, R. M. Trigo, and R. García-Herrera. The hot summer of 2010: Redrawing the temperature record map of europe. *Science*, 332, 2011. ISSN 00368075. doi: 10.1126/science.1201224.

D. Barriopedro, R. García-Herrera, C. Ordóñez, D. G. Miralles, and S. Salcedo-Sanz. Heat waves: Physical understanding and scientific challenges. *Reviews of Geophysics*, 61, 6 2023. ISSN 8755-1209. doi: 10.1029/2022RG000780.

F. Baró and E. Gómez-Baggethun. *Assessing the Potential of Regulating Ecosystem Services as Nature-Based Solutions in Urban Areas*, pages 139–158. 2017. doi: 10.1007/978-3-319-56091-5_9.

F. Baró and S. Maestre-Andrés. El paper de la infraestructura verda metropolitana en relació amb la qualitat de l'aire i la mitigació i adaptació al canvi climàtic. *Papers: Regió Metropolitana de Barcelona: Territori, estratègies, planejament*, 64:118–129, 2022.

F. Baró, I. Palomo, G. Zulian, P. Vizcaino, D. Haase, and E. Gómez-Baggethun. Mapping ecosystem service capacity, flow and demand for landscape and urban planning: A case study in the barcelona metropolitan region. *Land Use Policy*, 57:405–417, 11 2016. ISSN 02648377. doi: 10.1016/j.landusepol.2016.06.006.

F. Baró, A. Calderón-Argelich, J. Langemeyer, and J. J. Connolly. Under one canopy? assessing the distributional environmental justice implications of street tree benefits in barcelona. *Environmental Science & Policy*, 102:54–64, 12 2019. ISSN 14629011. doi: 10.1016/j.envsci.2019.08.016.

C. Basnou, F. Baró, J. Langemeyer, C. Castell, C. Dalmases, and J. Pino. Advancing the green infrastructure approach in the province of barcelona: integrating biodiversity, ecosystem functions and services into landscape planning. *Urban Forestry & Urban Greening*, 55:126797, 11 2020. ISSN 16188667. doi: 10.1016/j.ufug.2020.126797.

A. Bastos, C. M. Gouveia, R. M. Trigo, and S. W. Running. Analysing the spatio-temporal impacts of the 2003 and 2010 extreme heatwaves on plant productivity in europe. *Biogeosciences*, 11:3421–3435, 7 2014. ISSN 1726-4189. doi: 10.5194/bg-11-3421-2014. URL https://bg.copernicus.org/articles/11/3421/2014/.

A. Bastos, P. Ciais, P. Friedlingstein, S. Sitch, J. Pongratz, L. Fan, J. P. Wigneron, U. Weber, M. Reichstein, Z. Fu, P. Anthoni, A. Arneth, V. Haverd, A. K. Jain, E. Joetzjer, J. Knauer, S. Lienert, T. Loughran, P. C. McGuire, H. Tian, N. Viovy, and S. Zaehle. Direct and seasonal legacy effects of the 2018 heat wave and drought on european ecosystem productivity. *Science Advances*, 6, 6 2020. ISSN 2375-2548. doi: 10.1126/sciadv.aba2724. URL https://www.science.org/doi/10.1126/sciadv.aba2724.

M. Bazilian, H. Rogner, M. Howells, S. Hermann, D. Arent, D. Gielen, P. Steduto, A. Mueller, P. Komor, R. S. Tol, and K. K. Yumkella. Considering the energy, water and food nexus: Towards an integrated modelling approach. *Energy Policy*, 39:7896–7906, 12 2011. ISSN 03014215. doi: 10.1016/j.enpol.2011.09.039.

H. Bazzi, P. Ciais, E. Abbessi, D. Makowski, D. Santaren, E. Ceschia, A. Brut, T. Tallec, N. Buchmann, R. Maier, M. Acosta, B. Loubet, P. Buysse, J. Léonard, F. Bornet, I. Fayad, J. Lian, N. Baghdadi, R. S. Barrero, C. Brümmer, M. Schmidt, B. Heinesch, M. Mauder, and T. Gruenwald. Assimilating sentinel-2 data in a modified vegetation photosynthesis and respiration model (vprm) to improve the simulation of croplands co2 fluxes in europe. *International Journal of Applied Earth Observation and Geoinformation*, 127:103666, 3 2024. ISSN 15698432. doi: 10.1016/j.jag.2024.103666.

B. Bechtel, P. J. Alexander, J. Böhner, J. Ching, O. Conrad, J. Feddema, G. Mills, L. See, and I. Stewart. Mapping local climate zones for a worldwide database of the form and function of cities. *ISPRS International Journal of Geo-Information*, 4:199–219, 2015. ISSN 22209964. doi: 10.3390/ijgi4010199.

D. Beillouin, B. Schauberger, A. Bastos, P. Ciais, and D. Makowski. Impact of extreme weather conditions on european crop production in 2018. *Philosophical Transactions of the Royal Society B: Biological Sciences*, 375:20190510, 10 2020. ISSN 0962-8436. doi: 10.1098/rstb.2019.0510. URL https://royalsocietypublishing.org/doi/10.1098/rstb.2019.0510.

G. A. C. Belleza, M. F. P. Bierkens, and M. T. H. van Vliet. Sectoral water use responses to droughts and heatwaves: analyses from local to global scales for 1990–2019. *Environmental Research Letters*, 18:104008, 10 2023. ISSN 1748-9326. doi: 10.1088/1748-9326/acf82e.

A. M. Beltran, K. Jepsen, M. Rufí-Salís, S. Ventura, C. M. Lopez, and G. Villalba. Mapping direct n2o emissions from peri-urban agriculture: The case of the metropolitan area of barcelona. *Science of The Total Environment*, 822:153514, 5 2022. ISSN 00489697. doi: 10.1016/j.scitotenv.2022.153514.

A. M. Beltran, R. Padró, M. J. L. Rota-Aguilera, J. Marull, M. J. Eckelman, J. Cirera, A. Giocoli, and G. Villalba. Displaying geographic variability of peri-urban agriculture environmental impacts in the metropolitan area of barcelona: A regionalized life cycle assessment. *Science of The Total Environment*, 858:159519, 2 2023. ISSN 00489697. doi: 10.1016/j.scitotenv.2022.159519.

M. Best and C. Grimmond. Importance of initial state and atmospheric conditions for urban land surface models' performance. *Urban Climate*, 10:387–406, 12 2014. ISSN 22120955. doi: 10.1016/j.uclim.2013.10.006.

S. Boillat, A. Martin, T. Adams, D. Daniel, J. Llopis, E. Zepharovich, C. Oberlack, G. Sonderegger, P. Bottazzi, E. Corbera, C. I. Speranza, and U. Pascual. Why telecoupling research needs to account for environmental justice. *Journal of Land Use Science*, 15:1–10, 1 2020. ISSN 1747-423X. doi: 10.1080/1747423X.2020.1737257.

P. Bougeault and P. Lacarrere. Parameterization of orography-induced turbulence in a mesobeta–scale model. *Monthly Weather Review*, 117:1872–1890, 8 1989. ISSN 0027-0644. doi: 10.1175/1520-0493(1989)117<1872:POOITI>2.0.CO;2. URL http://journals.ametsoc.org/doi/10.1175/1520-0493(1989)117%3C1872:POOITI%3E2.0.CO;2.

D. E. Bowler, L. Buyung-Ali, T. M. Knight, and A. S. Pullin. Urban greening to cool towns and cities: A systematic review of the empirical evidence, 2010. ISSN 01692046.

O. Brousse, A. Martilli, M. Foley, G. Mills, and B. Bechtel. Wudapt, an efficient land use producing data tool for mesoscale models? integration of urban lcz in wrf over madrid. *Urban Climate*, 17:116–134, 9 2016. ISSN 22120955. doi: 10.1016/j.uclim.2016.04.001.

N. Bréda, R. Huc, A. Granier, and E. Dreyer. Temperate forest trees and stands under severe drought: a review of ecophysiological responses, adaptation processes and long-term consequences. *Annals of Forest Science*, 63:625–644, 9 2006. ISSN 1286-4560. doi: 10.1051/forest:2006042. URL http://www.edpsciences.org/10.1051/forest:2006042.

H. Burroughs and S. Hansen. *Managing indoor air quality*. Fairmont Press, 2011.

G. Büttner, B. Kosztra, T. Soukup, A. Sousa, and T. Langanke. Clc2018 technical guidelines. pages 0–60, 2017.

W. Cai and I. C. Prentice. Recent trends in gross primary production and their drivers: analysis and modelling at flux-site and global scales. *Environmental Research Letters*, 15:124050, 12 2020. ISSN 1748-9326. doi: 10.1088/1748-9326/abc64e.

K. Calvin, D. Dasgupta, G. Krinner, A. Mukherji, P. W. Thorne, C. Trisos, J. Romero, P. Aldunce, K. Barrett, G. Blanco, W. W. Cheung, S. Connors, F. Denton, A. Diongue-Niang, D. Dodman, M. Garschagen, O. Geden, B. Hayward, C. Jones, F. Jotzo, T. Krug, R. Lasco, Y.-Y. Lee, V. Masson-Delmotte, M. Meinshausen, K. Mintenbeck, A. Mokssit, F. E. Otto, M. Pathak, A. Pirani, E. Poloczanska, H.-O. Pörtner, A. Revi, D. C. Roberts, J. Roy, A. C. Ruane, J. Skea, P. R. Shukla, R. Slade, A. Slangen, Y. Sokona, A. A. Sörensson, M. Tignor, D. van Vuuren, Y.-M. Wei, H. Winkler, P. Zhai, Z. Zommers, J.-C. Hourcade, F. X. Johnson, S. Pachauri, N. P. Simpson, C. Singh, A. Thomas, E. Totin, A. Alegría, K. Armour, B. Bednar-Friedl, K. Blok, G. Cissé, F. Dentener, S. Eriksen, E. Fischer, G. Garner, C. Guivarch, M. Haasnoot, G. Hansen, M. Hauser, E. Hawkins, T. Hermans, R. Kopp, N. Leprince-Ringuet, J. Lewis, D. Ley, C. Ludden, L. Niamir, Z. Nicholls, S. Some, S. Szopa, B. Trewin, K.-I. van der Wijst, G. Winter, M. Witting, A. Birt, and M. Ha. Ipcc, 2023: Climate change 2023: Synthesis report. contribution of working groups i, ii and iii to the sixth assessment report of the intergovernmental panel on climate change [core writing team, h. lee and j. romero (eds.)]. ipcc, geneva, switzerland., 7 2023.

D. Camacho-Caballero, J. Langemeyer, R. Segura-Barrero, S. Ventura, A. M. Beltran, and G. Villalba. Assessing nature-based solutions in the face of urban vulnerabilities: a multi-criteria decision approach. *Sustainable Cities and Society*, page 105257, 2 2024. ISSN 22106707. doi: 10.1016/j.scs.2024.105257.

P. Campra. *Global and Local Effect of Increasing Land Surface Albedo as a Geo-Engineering Adaptation/Mitigation Option: A Study Case of Mediterranean Greenhouse Farming*. InTech, 9 2011. doi: 10.5772/23286.

J. M. Cartwright, C. E. Littlefield, J. L. Michalak, J. J. Lawler, and S. Z. Dobrowski. Topographic, soil, and climate drivers of drought sensitivity in forests and shrublands of the pacific northwest, usa. *Scientific Reports*, 10:18486, 10 2020. ISSN 2045-2322. doi: 10.1038/s41598-020-75273-5.

P. N. Carvalho, D. C. Finger, F. Masi, G. Cipolletta, H. V. Oral, A. Tóth, M. Regelsberger, and A. Exposito. Nature-based solutions addressing the water-energy-food nexus: Review of theoretical concepts and urban case studies. *Journal of Cleaner Production*, 338:130652, 3 2022. ISSN 09596526. doi: 10.1016/j.jclepro.2022.130652.

Center for Ecological Research and Forestry Applications – CREAF. Land cover map of the barcelona metropolitan area, 2015.

K. M. A. Chan, L. Hoshizaki, and B. Klinkenberg. Ecosystem services in conservation planning: Targeted benefits vs. co-benefits or costs? *PLoS ONE*, 6:e24378, 9 2011. ISSN 1932-6203. doi: 10.1371/journal.pone.0024378.

M. M. Chaves. Mechanisms underlying plant resilience to water deficits: prospects for water-saving agriculture. *Journal of Experimental Botany*, 55:2365–2384, 9 2004. ISSN 1460-2431. doi: 10.1093/jxb/erh269.

F. Chen and J. Dudhia. Coupling an advanced land surface–hydrology model with the penn state–ncar mm5 modeling system. part i: Model implementation and sensitivity. *Monthly Weather Review*, 129:569–585, 4 2001. ISSN 0027-0644. doi: 10.1175/1520-0493(2001)129<0569:CAALSH>2.0.CO;2. URL http://journals.ametsoc.org/doi/10.1175/1520-0493(2001)129%3C0569:CAALSH%3E2.0.CO;2.

F. Chen, K. W. Manning, M. A. LeMone, S. B. Trier, J. G. Alfieri, R. Roberts, M. Tewari, D. Niyogi, T. W. Horst, S. P. Oncley, J. B. Basara, and P. D. Blanken. Description and evaluation of the characteristics of the ncar high-resolution land data assimilation system. *Journal of Applied Meteorology and Climatology*, 46:694–713, 6 2007. ISSN 1558-8432. doi: 10.1175/JAM2463.1.

F. Chen, H. Kusaka, R. Bornstein, J. Ching, C. S. Grimmond, S. Grossman-Clarke, T. Loridan, K. W. Manning, A. Martilli, S. Miao, D. Sailor, F. P. Salamanca, H. Taha, M. Tewari, X. Wang, A. A. Wyszogrodzki, and C. Zhang. The integrated wrf/urban modelling system: Development, evaluation, and applications to urban environmental problems. *International Journal of Climatology*, 2011. ISSN 08998418. doi: 10.1002/joc.2158.

F. Chevallier, P. Ciais, T. J. Conway, T. Aalto, B. E. Anderson, P. Bousquet, E. G. Brunke, L. Ciattaglia, Y. Esaki, M. Fröhlich, A. Gomez, A. J. Gomez-Pelaez, L. Haszpra, P. B. Krummel, R. L. Langenfelds, M. Leuenberger, T. MacHida, F. Maignan, H. Matsueda, J. A. Morguí, H. Mukai, T. Nakazawa, P. Peylin, M. Ramonet, L. Rivier, Y. Sawa, M. Schmidt, L. P. Steele, S. A. Vay, A. T. Vermeulen, S. Wofsy, and D. Worthy. Co2 surface fluxes at grid point scale estimated from a global 21 year reanalysis of atmospheric measurements. *Journal of Geophysical Research Atmospheres*, 115, 2010. ISSN 01480227. doi: 10.1029/2010JD013887.

P. Ciais, M. Reichstein, N. Viovy, A. Granier, J. Ogée, V. Allard, M. Aubinet, N. Buchmann, C. Bernhofer, A. Carrara, F. Chevallier, N. D. Noblet, A. D. Friend, P. Friedlingstein, T. Grünwald, B. Heinesch, P. Keronen, A. Knohl, G. Krinner, D. Loustau, G. Manca, G. Matteucci, F. Miglietta, J. M. Ourcival, D. Papale, K. Pilegaard, S. Rambal, G. Seufert, J. F. Soussana, M. J. Sanz, E. D. Schulze, T. Vesala, and R. Valentini. Europe-wide reduction in primary productivity caused by the heat and drought in 2003. *Nature*, 437:529–533, 9 2005. ISSN 0028-0836. doi: 10.1038/nature03972. URL http://www.nature.com/articles/nature03972.

P. Ciais, J. Tan, X. Wang, C. Roedenbeck, F. Chevallier, S.-L. Piao, R. Moriarty, G. Broquet, C. L. Quéré, J. G. Canadell, S. Peng, B. Poulter, Z. Liu, and P. Tans. Five decades of northern land carbon uptake revealed by the interhemispheric co2 gradient. *Nature*, 568:221–225, 4 2019. ISSN 0028-0836. doi: 10.1038/s41586-019-1078-6.

B. I. Cook, J. E. Smerdon, E. R. Cook, A. P. Williams, K. J. Anchukaitis, J. S. Mankin, K. Allen, L. Andreu-Hayles, T. R. Ault, S. Belmecheri, S. Coats, B. Coulthard, B. Fosu, P. Grierson, D. Griffin, D. A. Herrera, M. Ionita, F. Lehner, C. Leland, K. Marvel, M. S. Morales,

V. Mishra, J. Ngoma, H. T. T. Nguyen, A. O'Donnell, J. Palmer, M. P. Rao, M. Rodriguez-Caton, R. Seager, D. W. Stahle, S. Stevenson, U. K. Thapa, A. M. Varuolo-Clarke, and E. K. Wise. Megadroughts in the common era and the anthropocene. *Nature Reviews Earth & Environment*, 3:741–757, 10 2022. ISSN 2662-138X. doi: 10.1038/s43017-022-00329-1.

Copernicus Climate Change Service and Copernicus Atmosphere Monitoring Service. European state of the climate 2018, 2018. URL https://climate.copernicus.eu/ESOTC/2018.

Copernicus Climate Change Service (C3S). Era5: Fifth generation of ecmwf atmospheric reanalyses of the global climate. copernicus climate change service climate data store (cds), 13/07/2020. https://cds.climate.copernicus.eu/cdsapp#!/home, 2017.

Copernicus Climate Change Service (C3S). European state of the climate 2022, full report: climate.copernicus.eu/esotc/2022, 2023.

E. Corbera, L. M. Busck-Lumholt, F. Mempel, and B. Rodríguez-Labajos. *Environmental Justice in Telecoupling Research*, pages 213–232. Springer International Publishing, 2019. doi: 10.1007/978-3-030-11105-2_11.

C. Cortinovis and D. Geneletti. Ecosystem services in urban plans: What is there, and what is still needed for better decisions. *Land Use Policy*, 70:298–312, 1 2018. ISSN 02648377. doi: 10.1016/j.landusepol.2017.10.017.

A. M. Coutts, E. C. White, N. J. Tapper, J. Beringer, and S. J. Livesley. Temperature and human thermal comfort effects of street trees across three contrasting street canyon environments. *Theoretical and Applied Climatology*, 124:55–68, 4 2016. ISSN 0177-798X. doi: 10.1007/s00704-015-1409-y.

M. Crippa, D. Guizzardi, E. Schaaf, E. Solazzo, M. Muntean, F. Monforti-Ferrario, J. Olivier, and E. Vignati. Fossil co2 and ghg emissions of all world countries - 2021 report., 2021.

G. Danan, P. Gerland, F. Pelletier, and B. Cohen. Risk of exposure and vulnerability to natural disasters at the city level: A global overview. 2015.

J. Dargin, B. Daher, and R. H. Mohtar. Complexity versus simplicity in water energy food nexus (wef) assessment tools. *Science of The Total Environment*, 650:1566–1575, 2 2019. ISSN 00489697. doi: 10.1016/j.scitotenv.2018.09.080.

DARPA. Mapa de cultius dun-sigpac [www document]. url http://agricultura.gencat.cat/ca/serveis/cartografia-sig/aplicatius-tematics-geoinformacio/sigpac/mapacultius/ (accessed 5.11.21)., 2015.

A. Dayalu, J. W. Munger, S. C. Wofsy, Y. Wang, T. Nehrkorn, Y. Zhao, M. B. McElroy, C. P. Nielsen, and K. Luus. Assessing biotic contributions to co2 fluxes in northern china using the vegetation, photosynthesis and respiration model (vprm-china) and observations from 2005 to 2009. *Biogeosciences*, 15:6713–6729, 11 2018. ISSN 1726-4189. doi: 10.5194/bg-15-6713-2018. URL https://bg.copernicus.org/articles/15/6713/2018/.

D. de la Paz, J. M. de Andrés, A. Narros, C. Silibello, S. Finardi, S. Fares, L. Tejero, R. Borge, and M. Mircea. Assessment of air quality and meteorological changes induced by future vegetation in madrid. *Forests*, 13:690, 4 2022. ISSN 1999-4907. doi: 10.3390/f13050690.

S. E. Debele, L. S. Leo, P. Kumar, J. Sahani, J. Ommer, E. Bucchignani, S. Vranić, M. Kalas, Z. Amirzada, I. Pavlova, M. A. R. Shah, A. Gonzalez-Ollauri, and S. D. Sabatino. Nature-based solutions can help reduce the impact of natural hazards: A global analysis of nbs case studies. *Science of The Total Environment*, 902:165824, 12 2023. ISSN 00489697. doi: 10.1016/j.scitotenv.2023.165824.

M. Demuzere, K. Orru, O. Heidrich, E. Olazabal, D. Geneletti, H. Orru, A. Bhave, N. Mittal, E. Feliu, and M. Faehnle. Mitigating and adapting to climate change: Multi-functional and multi-scale assessment of green urban infrastructure. *Journal of Environmental Management*, 146:107–115, 12 2014. ISSN 03014797. doi: 10.1016/j.jenvman.2014.07.025.

Dirección General del Catastro. Vector mapping data model online: https://www1.sedecatastro.gob.es/cartografia/mapa.aspx?buscar=s., 2022.

J. E. Drake, M. G. Tjoelker, A. Vårhammar, B. Medlyn, P. B. Reich, A. Leigh, S. Pfautsch, C. J. Blackman, R. López, M. J. Aspinwall, K. Y. Crous, R. A. Duursma, D. Kumarathunge, M. G. D. Kauwe, M. Jiang, A. B. Nicotra, D. T. Tissue, B. Choat, O. K. Atkin, and C. V. M. Barton. Trees tolerate an extreme heatwave via sustained transpirational cooling and increased leaf thermal tolerance. *Global Change Biology*, 24:2390–2402, 6 2018. ISSN 1354-1013. doi: 10.1111/gcb.14037.

L. Drinkwater and S. Snapp. *Nutrients in Agroecosystems: Rethinking the Management Paradigm*, pages 163–186. 2007. doi: 10.1016/S0065-2113(04)92003-2.

Drought 2018 Team and ICOS Atmosphere Thematic Centre. Drought-2018 atmospheric co2 mole fraction product for 48 stations (96 sample heights). https://doi.org/10.18160/ere9-9d85, 2020.

I. Durre, X. Yin, R. S. Vose, S. Applequist, and J. Arnfield. Enhancing the data coverage in the integrated global radiosonde archive. *Journal of Atmospheric and Oceanic Technology*, 35: 1753–1770, 9 2018. ISSN 0739-0572. doi: 10.1175/JTECH-D-17-0223.1.

T. Elmqvist, J. Goodness, P. J. Marcotullio, S. Parnell, M. Sendstad, C. Wilkinson, M. Fragkias, B. Güneralp, R. I. McDonald, M. Schewenius, and K. C. Seto. *Urbanization, biodiversity and ecosystem services: Challenges and opportunities: A global assessment*. 2013. doi: 10.1007/978-94-007-7088-1.

A. Endo, M. Yamada, Y. Miyashita, R. Sugimoto, A. Ishii, J. Nishijima, M. Fujii, T. Kato, H. Hamamoto, M. Kimura, T. Kumazawa, and J. Qi. Dynamics of water–energy–food nexus methodology, methods, and tools. *Current Opinion in Environmental Science & Health*, 13: 46–60, 2 2020. ISSN 24685844. doi: 10.1016/j.coesh.2019.10.004.

T. Ermitão, C. M. Gouveia, A. Bastos, and A. C. Russo. Vegetation productivity losses linked to mediterranean hot and dry events. *Remote Sensing*, 13:4010, 10 2021. ISSN 2072-4292. doi: 10.3390/rs13194010. URL https://www.mdpi.com/2072-4292/13/19/4010.

W. Eugster, A. M. Moffat, E. Ceschia, M. Aubinet, C. Ammann, B. Osborne, P. A. Davis, P. Smith, C. Jacobs, E. Moors, V. L. Dantec, P. Béziat, M. Saunders, W. Jans, T. Grünwald, C. Rebmann, W. L. Kutsch, R. Czerný, D. Janouš, C. Moureaux, D. Dufranne, A. Carrara, V. Magliulo, P. D. Tommasi, J. E. Olesen, K. Schelde, A. Olioso, C. Bernhofer, P. Cellier, E. Larmanou, B. Loubet, M. Wattenbach, O. Marloie, M.-J. Sanz, H. Søgaard, and N. Buchmann. Management effects on european cropland respiration. *Agriculture, Ecosystems & Environment*, 139:346–362, 11 2010. ISSN 01678809. doi: 10.1016/j.agee.2010.09.001.

European Commission. Green infrastructure (gi) — enhancing europe's natural capital. communication from the commission to the european parliament, the council, the european economic and social committee and the committee of the regions., 2013.

European Environment Agency (EEA). Green infrastructure and territorial cohesion. the concept of green infrastructure and its integration into policies using monitoring systems. eea technical report n° 18/2011., 2011.

European Environment Agency (EEA). Exploring nature-based solutions. the role of green infrastructure in mitigating the impacts of weather- and climate change-related natural hazards, 2015.

J. Fallmann, S. Emeis, and P. Suppan. Mitigation of urban heat stress -a modelling case study for the area of stuttgart. *Erde*, 144, 2013. doi: https://doi.org/10.12854/erde-144-15.

D. Faranda, S. Pascale, and B. Bulut. Persistent anticyclonic conditions and climate change exacerbated the exceptional 2022 european-mediterranean drought. *Environmental Research Letters*, 2 2023. ISSN 1748-9326. doi: 10.1088/1748-9326/acbc37.

Z. Fatima, M. Ahmed, M. Hussain, G. Abbas, S. Ul-Allah, S. Ahmad, N. Ahmed, M. A. Ali, G. Sarwar, E. ul Haque, P. Iqbal, and S. Hussain. The fingerprints of climate warming on cereal crops phenology and adaptation options. *Scientific Reports*, 10, 2020. ISSN 20452322. doi: 10.1038/s41598-020-74740-3.

S. Feng, T. Lauvaux, K. Keller, K. J. Davis, P. Rayner, T. Oda, and K. R. Gurney. A road map for improving the treatment of uncertainties in high-resolution regional carbon flux inverse estimates. *Geophysical Research Letters*, 46:13461–13469, 11 2019. ISSN 0094-8276. doi: 10.1029/2019GL082987. URL https://onlinelibrary.wiley.com/doi/10.1029/2019GL082987.

S. Feng, T. Lauvaux, C. A. Williams, K. J. Davis, Y. Zhou, I. Baker, Z. R. Barkley, and D. Wesloh. Joint co2 mole fraction and flux analysis confirms missing processes in casa terrestrial carbon uptake over north america. *Global Biogeochemical Cycles*, 35, 7 2021. ISSN 0886-6236. doi: 10.1029/2020GB006914. URL https://onlinelibrary.wiley.com/doi/10.1029/2020GB006914.

M. Fernández-Martínez, J. Peñuelas, F. Chevallier, P. Ciais, M. Obersteiner, C. Rödenbeck, J. Sardans, S. Vicca, H. Yang, S. Sitch, P. Friedlingstein, V. K. Arora, D. S. Goll, A. K. Jain, D. L. Lombardozzi, P. C. McGuire, and I. A. Janssens. Diagnosing destabilization risk in global land carbon sinks. *Nature*, 615:848–853, 3 2023. ISSN 0028-0836. doi: 10.1038/s41586-023-05725-1.

G. L. Feyisa, K. Dons, and H. Meilby. Efficiency of parks in mitigating urban heat island effect: An example from addis ababa. *Landscape and Urban Planning*, 123:87–95, 3 2014. ISSN 01692046. doi: 10.1016/j.landurbplan.2013.12.008.

E. M. Fischer and C. Schär. Consistent geographical patterns of changes in high-impact european heatwaves. *Nature Geoscience*, 3:398–403, 6 2010. ISSN 17520894. doi: 10.1038/ngeo866.

E. M. Fischer, S. I. Seneviratne, D. Lüthi, and C. Schär. Contribution of land-atmosphere coupling to recent european summer heat waves. *Geophysical Research Letters*, 34, 3 2007. ISSN 0094-8276. doi: 10.1029/2006GL029068.

M. Friedl and D. Sulla-Menashe. Mcd12q1 modis/terra+aqua land cover type yearly l3 global 500m sin grid v006 [data set]. nasa eosdis land processes distributed active archive center. accessed 2023-09-18 from https://doi.org/10.5067/modis/mcd12q1.006, 2019.

P. Friedlingstein, M. O'Sullivan, M. W. Jones, R. M. Andrew, J. Hauck, A. Olsen, G. P. Peters, W. Peters, J. Pongratz, S. Sitch, C. L. Quéré, J. G. Canadell, P. Ciais, R. B. Jackson, S. Alin, L. E. O. C. Aragão, A. Arneth, V. Arora, N. R. Bates, M. Becker, A. Benoit-Cattin, H. C. Bittig, L. Bopp, S. Bultan, N. Chandra, F. Chevallier, L. P. Chini, W. Evans, L. Florentie, P. M. Forster, T. Gasser, M. Gehlen, D. Gilfillan, T. Gkritzalis, L. Gregor, N. Gruber, I. Harris, K. Hartung, V. Haverd, R. A. Houghton, T. Ilyina, A. K. Jain, E. Joetzjer, K. Kadono, E. Kato, V. Kitidis, J. I. Korsbakken, P. Landschützer, N. Lefèvre, A. Lenton, S. Lienert, Z. Liu, D. Lombardozzi, G. Marland, N. Metzl, D. R. Munro, J. E. M. S. Nabel, S.-I. Nakaoka, Y. Niwa, K. O'Brien, T. Ono, P. I. Palmer, D. Pierrot, B. Poulter, L. Resplandy, E. Robertson, C. Rödenbeck, J. Schwinger, R. Séférian, I. Skjelvan, A. J. P. Smith, A. J. Sutton, T. Tanhua, P. P. Tans, H. Tian, B. Tilbrook, G. van der Werf, N. Vuichard, A. P. Walker, R. Wanninkhof, A. J. Watson, D. Willis, A. J. Wiltshire, W. Yuan, X. Yue, and S. Zaehle. Global carbon budget 2020. *Earth System Science Data*, 12:3269–3340, 12 2020. ISSN 1866-3516. doi: 10.5194/essd-12-3269-2020. URL https://essd.copernicus.org/articles/12/3269/2020/.

Z. Fu, P. Ciais, D. Makowski, A. Bastos, P. C. Stoy, A. Ibrom, A. Knohl, M. Migliavacca, M. Cuntz, L. Šigut, M. Peichl, D. Loustau, T. S. El-Madany, N. Buchmann, M. Gharun, I. Janssens, C. Markwitz, T. Grünwald, C. Rebmann, M. Mölder, A. Varlagin, I. Mammarella, P. Kolari, C. Bernhofer, M. Heliasz, C. Vincke, A. Pitacco, E. Cremonese, L. Foltýnová, and J. P. Wigneron. Uncovering the critical soil moisture thresholds of plant water stress for european ecosystems. *Global Change Biology*, 28:2111–2123, 3 2022. ISSN 13652486. doi: 10.1111/gcb.16050.

E. Gago, J. Roldan, R. Pacheco-Torres, and J. Ordóñez. The city and urban heat islands: A review of strategies to mitigate adverse effects. *Renewable and Sustainable Energy Reviews*, 25:749–758, 9 2013. ISSN 13640321. doi: 10.1016/j.rser.2013.05.057.

J. Galmés, J. Flexas, H. Medrano, U. Niinemets, and F. Valladares. *Ecophysiology of photosynthesis in semi-arid environments*, pages 448–464. Cambridge University Press, 7 2012. doi: 10.1017/CBO9781139051477.035.

X. Gao and F. Giorgi. Increased aridity in the mediterranean region under greenhouse gas forcing estimated from high resolution simulations with a regional climate model. *Global and Planetary Change*, 62:195–209, 6 2008. ISSN 09218181. doi: 10.1016/j.gloplacha.2008.02.002.

A. M. García, I. Santé, X. Loureiro, and D. Miranda. Green infrastructure spatial planning considering ecosystem services assessment and trade-off analysis. application at landscape scale in galicia region (nw spain). *Ecosystem Services*, 43:101115, 6 2020. ISSN 22120416. doi: 10.1016/j.ecoser.2020.101115.

A. García-Haro, B. Arellano, and J. Roca. Quantifying the influence of design and location on the cool island effect of the urban parks of barcelona. *Journal of Applied Remote Sensing*, 17, 9 2023. ISSN 1931-3195. doi: 10.1117/1.JRS.17.034512.

R. García-Herrera, J. Díaz, R. M. Trigo, J. Luterbacher, and E. M. Fischer. A review of the european summer heat wave of 2003. *Critical Reviews in Environmental Science and Technology*, 40:267–306, 3 2010. ISSN 1064-3389. doi: 10.1080/10643380802238137.

A. Gazol, J. J. Camarero, S. M. Vicente-Serrano, R. Sánchez-Salguero, E. Gutiérrez, M. de Luis, G. Sangüesa-Barreda, K. Novak, V. Rozas, P. A. Tíscar, J. C. Linares, N. Martín-Hernández, E. M. del Castillo, M. Ribas, I. García-González, F. Silla, A. Camisón, M. Génova, J. M. Olano, L. A. Longares, A. Hevia, M. Tomás-Burguera, and J. D. Galván. Forest resilience to drought varies across biomes. *Global Change Biology*, 24:2143–2158, 5 2018. ISSN 13652486. doi: 10.1111/gcb.14082.

C. Geels, M. Gloor, P. Ciais, P. Bousquet, P. Peylin, A. T. Vermeulen, R. Dargaville, T. Aalto, J. Brandt, J. H. Christensen, L. M. Frohn, L. Haszpra, U. Karstens, C. Rödenbeck, M. Ramonet, G. Carboni, and R. Santaguida. Comparing atmospheric transport models for future regional inversions over europe – part 1: mapping the atmospheric co2 signals. *Atmospheric Chemistry and Physics*, 7:3461–3479, 7 2007. ISSN 1680-7324. doi: 10.5194/acp-7-3461-2007.

Generalitat de Catalunya. Superfícies, rendiments i produccions dels conreus agrícoles. [www document]. https://agricultura.gencat.cat/ca/departament/estadistiques/agricultura/estadistiques-definitives-conreus/ (accessed november 2023)., 2016.

C. Gerbig, S. Körner, and J. C. Lin. Vertical mixing in atmospheric tracer transport models: error characterization and propagation. *Atmospheric Chemistry and Physics*, 8:591–602, 2 2008. ISSN 1680-7324. doi: 10.5194/acp-8-591-2008.

J. Gilabert, A. Deluca, D. Lauwaet, J. Ballester, J. Corbera, and M. C. Llasat. Assessing heat exposure to extreme temperatures in urban areas using the local climate zone classification. *Natural Hazards and Earth System Sciences*, 21:375–391, 1 2021a. ISSN 1684-9981. doi: 10.5194/nhess-21-375-2021. URL https://nhess.copernicus.org/articles/21/375/2021/.

J. Gilabert, S. Ventura, R. Segura, A. Martilli, A. Badia, C. Llasat, J. Corbera, and G. Villalba. Abating heat waves in a coastal mediterranean city: What can cool roofs and vegetation contribute? *Urban Climate*, 37, 2021b. ISSN 22120955. doi: 10.1016/j.uclim.2021.100863.

M. Gilabert, A. Moreno, F. Maselli, B. Martínez, M. Chiesi, S. Sánchez-Ruiz, F. García-Haro, A. Pérez-Hoyos, M. Campos-Taberner, O. Pérez-Priego, P. Serrano-Ortiz, and A. Carrara. Daily gpp estimates in mediterranean ecosystems by combining remote sensing and meteorological data. *ISPRS Journal of Photogrammetry and Remote Sensing*, 102:184–197, 4 2015. ISSN 09242716. doi: 10.1016/j.isprsjprs.2015.01.017. URL https://linkinghub.elsevier.com/retrieve/pii/S0924271615000398.

S. Gillner, S. Korn, and A. Roloff. Leaf-gas exchange of five tree species at urban street sites. *Arboriculture & Urban Forestry*, 41, 5 2015a. ISSN 19355297. doi: 10.48044/jauf.2015.012.

S. Gillner, J. Vogt, A. Tharang, S. Dettmann, and A. Roloff. Role of street trees in mitigating effects of heat and drought at highly sealed urban sites. *Landscape and Urban Planning*, 143: 33–42, 11 2015b. ISSN 01692046. doi: 10.1016/j.landurbplan.2015.06.005.

F. Giorgi. Climate change hot-spots. *Geophysical Research Letters*, 33:L08707, 2006. ISSN 0094-8276. doi: 10.1029/2006GL025734. URL http://doi.wiley.com/10.1029/2006GL025734.

F. Giorgi and P. Lionello. Climate change projections for the mediterranean region. *Global and Planetary Change*, 63:90–104, 9 2008. ISSN 09218181. doi: 10.1016/j.gloplacha.2007.09.005. URL https://linkinghub.elsevier.com/retrieve/pii/S0921818107001750.

V. Gitz and P. Ciais. Future expansion of agriculture and pasture acts to amplify atmospheric co2 levels in response to fossil-fuel and land-use change emissions. *Climatic Change*, 67: 161–184, 12 2004. ISSN 0165-0009. doi: 10.1007/s10584-004-0065-5.

B. Goldstein, M. Birkved, J. Fernández, and M. Hauschild. Surveying the environmental footprint of urban food consumption. *Journal of Industrial Ecology*, 21:151–165, 2 2017. ISSN 1088-1980. doi: 10.1111/jiec.12384.

S. N. Gosling, E. K. Bryce, P. G. Dixon, K. M. A. Gabriel, E. Y. Gosling, J. M. Hanes, D. M. Hondula, L. Liang, P. A. B. M. Lean, S. Muthers, S. T. Nascimento, M. Petralli, J. K. Vanos, and E. R. Wanka. A glossary for biometeorology. *International Journal of Biometeorology*, 58:277–308, 3 2014. ISSN 0020-7128. doi: 10.1007/s00484-013-0729-9.

S. M. Gourdji, A. Karion, I. Lopez-Coto, S. Ghosh, K. L. Mueller, Y. Zhou, C. A. Williams, I. T. Baker, K. D. Haynes, and J. R. Whetstone. A modified vegetation photosynthesis and respiration model (vprm) for the eastern usa and canada, evaluated with comparison to atmospheric observations and other biospheric models. *Journal of Geophysical Research: Biogeosciences*, 127, 1 2022. ISSN 2169-8953. doi: 10.1029/2021JG006290. URL https://onlinelibrary.wiley.com/doi/10.1029/2021JG006290.

C. Gouveia, R. Trigo, S. Beguería, and S. Vicente-Serrano. Drought impacts on vegetation activity in the mediterranean region: An assessment using remote sensing data and multi-scale drought indicators. *Global and Planetary Change*, 151:15–27, 4 2017. ISSN 09218181. doi: 10.1016/j.gloplacha.2016.06.011. URL https://linkinghub.elsevier.com/retrieve/pii/S0921818116302363.

G. A. Grell and D. Dévényi. A generalized approach to parameterizing convection combining ensemble and data assimilation techniques. *Geophysical Research Letters*, 29, 7 2002. ISSN 19448007. doi: 10.1029/2002GL015311.

G. A. Grell, S. E. Peckham, R. Schmitz, S. A. McKeen, G. Frost, W. C. Skamarock, and B. Eder. Fully coupled "online" chemistry within the wrf model. *Atmospheric Environment*, 39, 2005. ISSN 13522310. doi: 10.1016/j.atmosenv.2005.04.027.

C. Grimmond, C. Souch, and M. Hubble. Influence of tree cover on summertime surface energy balance fluxes, san gabriel valley, los angeles. *Climate Research*, 6:45–57, 1996. ISSN 0936-577X. doi: 10.3354/cr006045.

C. S. B. Grimmond and T. R. Oke. An evapotranspiration-interception model for urban areas. *Water Resources Research*, 27:1739–1755, 7 1991. ISSN 0043-1397. doi: 10.1029/91WR00557.

C. S. B. Grimmond and T. R. Oke. Aerodynamic properties of urban areas derived from analysis of surface form. *Journal of Applied Meteorology*, 38:1262–1292, 9 1999. ISSN 0894-8763. doi: 10.1175/1520-0450(1999)038<1262:APOUAD>2.0.CO;2.

S. Grimmond. Urbanization and global environmental change: Local effects of urban warming. volume 173, pages 83–88, 3 2007. doi: 10.1111/j.1475-4959.2007.232_3.x.

M. Gräf, M. Immitzer, P. Hietz, and R. Stangl. Water-stressed plants do not cool: Leaf surface temperature of living wall plants under drought stress. *Sustainability*, 13:3910, 4 2021. ISSN 2071-1050. doi: 10.3390/su13073910.

M. Guevara, C. Tena, M. Porquet, O. Jorba, and C. P. García-Pando. Hermesv3, a stand-alone multi-scale atmospheric emission modelling framework-part 1: Global and regional module. *Geoscientific Model Development*, 2019. ISSN 19919603. doi: 10.5194/gmd-12-1885-2019.

E. D. Gutmann, R. M. Rasmussen, C. Liu, K. Ikeda, C. L. Bruyere, J. M. Done, L. Garrè, P. Friis-Hansen, and V. Veldore. Changes in hurricanes from a 13-yr convection-permitting pseudo–global warming simulation. *Journal of Climate*, 31:3643–3657, 5 2018. ISSN 0894-8755. doi: 10.1175/JCLI-D-17-0391.1.

K. Hammerberg, O. Brousse, A. Martilli, and A. Mahdavi. Implications of employing detailed urban canopy parameters for mesoscale climate modelling: a comparison between wudapt and gis databases over vienna, austria. *International Journal of Climatology*, 38:e1241–e1257, 4 2018. ISSN 08998418. doi: 10.1002/joc.5447. URL http://doi.wiley.com/10.1002/joc.5447.

B. S. Hardiman, J. A. Wang, L. R. Hutyra, C. K. Gately, J. M. Getson, and M. A. Friedl. Accounting for urban biogenic fluxes in regional carbon budgets. *Science of The Total Environment*, 592:366–372, 8 2017. ISSN 00489697. doi: 10.1016/j.scitotenv.2017.03.028.

J. L. Hatfield and J. H. Prueger. Temperature extremes: Effect on plant growth and development. *Weather and Climate Extremes*, 10:4–10, 12 2015. ISSN 22120947. doi: 10.1016/j.wace.2015.08.001.

E. A. Hendricks, J. C. Knievel, and Y. Wang. Addition of multilayer urban canopy models to a nonlocal planetary boundary layer parameterization and evaluation using ideal and real cases. *Journal of Applied Meteorology and Climatology*, 59:1369–1392, 8 2020. ISSN 1558-8424. doi: 10.1175/JAMC-D-19-0142.1.

S. Hong, J.-H. Kim, J. Lim, and J. Dudhia. The wrf single moment microphysics scheme (wsm). *Journal of the Korean Meteorological Society*, 42:129–151, 2006a.

S.-Y. Hong, Y. Noh, and J. Dudhia. A new vertical diffusion package with an explicit treatment of entrainment processes. *Monthly Weather Review*, 134:2318–2341, 9 2006b. ISSN 1520-0493. doi: 10.1175/MWR3199.1.

C. Howe, H. Suich, B. Vira, and G. M. Mace. Creating win-wins from trade-offs? ecosystem services for human well-being: A meta-analysis of ecosystem service trade-offs and synergies in the real world. *Global Environmental Change*, 28:263–275, 9 2014. ISSN 09593780. doi: 10.1016/j.gloenvcha.2014.07.005.

X. Hu, S. M. Gourdji, K. J. Davis, Q. Wang, Y. Zhang, M. Xue, S. Feng, B. Moore, and S. M. R. Crowell. Implementation of improved parameterization of terrestrial flux in wrf-vprm improves the simulation of nighttime co 2 peaks and a daytime co 2 band ahead of a cold front. *Journal of Geophysical Research: Atmospheres*, 126, 5 2021. ISSN 2169-897X. doi: 10.1029/2020JD034362.

M. Huang, Z. Gao, S. Miao, and F. Chen. Sensitivity of urban boundary layer simulation to urban canopy models and pbl schemes in beijing. *Meteorology and Atmospheric Physics*, 131:1235–1248, 10 2019. ISSN 0177-7971. doi: 10.1007/s00703-018-0634-1.

Z. Huang, C. Wu, M. Teng, and Y. Lin. Impacts of tree canopy cover on microclimate and human thermal comfort in a shallow street canyon in wuhan, china. *Atmosphere*, 11:588, 6 2020. ISSN 2073-4433. doi: 10.3390/atmos11060588.

A. Hunt and P. Watkiss. Climate change impacts and adaptation in cities: a review of the literature. *Climatic Change*, 104:13–49, 1 2011. ISSN 0165-0009. doi: 10.1007/s10584-010-9975-6. URL http://link.springer.com/10.1007/s10584-010-9975-6.

J. C. Hunt, Y. V. Timoshkina, S. I. Bohnenstengel, and S. Belcher. Implications of climate change for expanding cities worldwide. *Proceedings of the Institution of Civil Engineers: Urban Design and Planning*, 166:241–254, 8 2013. ISSN 17550793. doi: 10.1680/udap.10.00062.

M. J. Iacono, J. S. Delamere, E. J. Mlawer, M. W. Shephard, S. A. Clough, and W. D. Collins. Radiative forcing by long-lived greenhouse gases: Calculations with the aer radiative transfer models. *Journal of Geophysical Research*, 113:D13103, 7 2008. ISSN 0148-0227. doi: 10.1029/2008JD009944. URL http://doi.wiley.com/10.1029/2008JD009944.

H. M. Imran, J. Kala, A. W. Ng, and S. Muthukumaran. Effectiveness of green and cool roofs in mitigating urban heat island effects during a heatwave event in the city of melbourne in southeast australia. *Journal of Cleaner Production*, 2018. ISSN 09596526. doi: 10.1016/j.jclepro.2018.06.179.

V. Ingole, M. Marí-Dell'Olmo, A. Deluca, M. Quijal, C. Borrell, M. Rodríguez-Sanz, H. Achebak, D. Lauwaet, J. Gilabert, P. Murage, S. Hajat, X. Basagaña, and J. Ballester. Spatial variability of heat-related mortality in barcelona from 1992–2015: A case crossover study design. *International Journal of Environmental Research and Public Health*, 17:2553, 4 2020. ISSN 1660-4601. doi: 10.3390/ijerph17072553. URL https://www.mdpi.com/1660-4601/17/7/2553.

Institute Cartographic and Geological of Catalonia (ICGC). Lidar data. https://www.icgc.cat/es/descargas/elevaciones/datos-lidar (accessed 16 july 2019)., 2019.

Intergovernmental Panel on Climate Change. *Climate Change 2014: Synthesis Report. Contribution of Working Groups I, II and III to the Fifth Assessment Report of the Intergovernmental Panel on Climate Change*. 2014.

Intergovernmental Panel on Climate Change. *Human Settlements, Infrastructure, and Spatial Planning*. 2015. doi: 10.1017/cbo9781107415416.018.

M. Ionita, L. M. Tallaksen, D. G. Kingston, J. H. Stagge, G. Laaha, H. A. J. V. Lanen, P. Scholz, S. M. Chelcea, and K. Haslinger. The european 2015 drought from a climatological perspective. *Hydrology and Earth System Sciences*, 21:1397–1419, 3 2017. ISSN 1607-7938. doi: 10.5194/hess-21-1397-2017.

T. Iungman, M. Cirach, F. Marando, E. P. Barboza, S. Khomenko, P. Masselot, M. Quijal-Zamorano, N. Mueller, A. Gasparrini, J. Urquiza, M. Heris, M. Thondoo, and M. Nieuwenhuijsen. Cooling cities through urban green infrastructure: a health impact assessment of european cities. *The Lancet*, 401:577–589, 2 2023. ISSN 01406736. doi: 10.1016/S0140-6736(22)02585-5.

S. J. Jacobs, A. J. E. Gallant, N. J. Tapper, and D. Li. Use of cool roofs and vegetation to mitigate urban heat and improve human thermal stress in melbourne, australia. *Journal of Applied Meteorology and Climatology*, 57:1747–1764, 8 2018. ISSN 1558-8424. doi: 10.1175/JAMC-D-17-0243.1.

S. Janhäll. Review on urban vegetation and particle air pollution – deposition and dispersion. *Atmospheric Environment*, 105:130–137, 3 2015. ISSN 13522310. doi: 10.1016/j.atmosenv.2015.01.052.

Z. I. Janjić. Nonsingular implementation of the mellor-yamada level 2 . 5 scheme in the ncep meso model, national centers for environmental prediction, office note #437. pages 1–61, 2001.

G. Jendritzky, R. de Dear, and G. Havenith. Utci—why another thermal index? *International Journal of Biometeorology*, 56:421–428, 5 2012. ISSN 0020-7128. doi: 10.1007/s00484-011-0513-7.

A. Jenkinson and B. Collison. An initial climatology of gales over the north sea. *Synoptic Climatology Branch Memorandum*, 62:18, 1977.

S. Jia and Y. Wang. Effect of heat mitigation strategies on thermal environment, thermal comfort, and walkability: A case study in hong kong. *Building and Environment*, 201:107988, 8 2021. ISSN 03601323. doi: 10.1016/j.buildenv.2021.107988.

H. Jin, S. M. Vicente-Serrano, F. Tian, Z. Cai, T. Conradt, B. Boincean, C. Murphy, B. A. Farizo, S. Grainger, J. I. López-Moreno, and L. Eklundh. Higher vegetation sensitivity to meteorological drought in autumn than spring across european biomes. *Communications Earth & Environment*, 4:299, 8 2023. ISSN 2662-4435. doi: 10.1038/s43247-023-00960-w.

S. Jin, J. Guo, S. Wheeler, L. Kan, and S. Che. Evaluation of impacts of trees on pm2.5 dispersion in urban streets. *Atmospheric Environment*, 99:277–287, 12 2014. ISSN 13522310. doi: 10.1016/j.atmosenv.2014.10.002.

H.-K. Jo and G. E. McPherson. Carbon storage and flux in urban residential greenspace. *Journal of Environmental Management*, 45:109–133, 10 1995. ISSN 03014797. doi: 10.1006/jema.1995.0062.

E. Johansson and R. Emmanuel. The influence of urban design on outdoor thermal comfort in the hot, humid city of colombo, sri lanka. *International Journal of Biometeorology*, 51:119–133, 10 2006. ISSN 0020-7128. doi: 10.1007/s00484-006-0047-6.

W. M. Jolly, M. Dobbertin, N. E. Zimmermann, and M. Reichstein. Divergent vegetation growth responses to the 2003 heat wave in the swiss alps. *Geophysical Research Letters*, 32:1–4, 9 2005. ISSN 00948276. doi: 10.1029/2005GL023252.

J. Joshi, B. D. Stocker, F. Hofhansl, S. Zhou, U. Dieckmann, and I. C. Prentice. Towards a unified theory of plant photosynthesis and hydraulics. *Nature Plants*, 8:1304–1316, 10 2022. ISSN 2055-0278. doi: 10.1038/s41477-022-01244-5.

M. Jung, K. Henkel, M. Herold, and G. Churkina. Exploiting synergies of global land cover products for carbon cycle modeling. *Remote Sensing of Environment*, 101:534–553, 4 2006. ISSN 00344257. doi: 10.1016/j.rse.2006.01.020. URL https://linkinghub.elsevier.com/retrieve/pii/S0034425706000514.

M. Jung, M. Vetter, M. Herold, G. Churkina, M. Reichstein, S. Zaehle, P. Ciais, N. Viovy, A. Bondeau, Y. Chen, K. Trusilova, F. Feser, and M. Heimann. Uncertainties of modeling gross primary productivity over europe: A systematic study on the effects of using different drivers and terrestrial biosphere models. *Global Biogeochemical Cycles*, 21:n/a–n/a, 12 2007. ISSN 08866236. doi: 10.1029/2006GB002915. URL http://doi.wiley.com/10.1029/2006GB002915.

J. S. Kain. The kain–fritsch convective parameterization: An update. *Journal of Applied Meteorology*, 43:170–181, 1 2004. ISSN 0894-8763. doi: 10.1175/1520-0450(2004)043<0170:TKCPAU>2.0.CO;2.

J. W. Kaiser, A. Heil, M. O. Andreae, A. Benedetti, N. Chubarova, L. Jones, J. J. Morcrette, M. Razinger, M. G. Schultz, M. Suttie, and G. R. V. D. Werf. Biomass burning emissions estimated with a global fire assimilation system based on observed fire radiative power, 2012. ISSN 17264170.

Y. Kang, S. Khan, and X. Ma. Climate change impacts on crop yield, crop water productivity and food security - a review, 2009. ISSN 10020071.

T. F. Keenan, I. C. Prentice, J. G. Canadell, C. A. Williams, H. Wang, M. Raupach, and G. J. Collatz. Recent pause in the growth rate of atmospheric co2 due to enhanced terrestrial carbon uptake. *Nature Communications*, 7:13428, 11 2016. ISSN 2041-1723. doi: 10.1038/ncomms13428.

K. Kobayashi and M. U. Salam. Comparing simulated and measured values using mean squared deviation and its components. *Agronomy Journal*, 92:345, 2000. ISSN 00371912. doi: 10.1007/s100870050043.

C. B. Koc, P. Osmond, and A. Peters. Evaluating the cooling effects of green infrastructure: A systematic review of methods, indicators and data sources. *Solar Energy*, 166:486–508, 5 2018. ISSN 0038092X. doi: 10.1016/j.solener.2018.03.008.

C. Kottmeier, C. Biegert, and U. Corsmeier. Effects of urban land use on surface temperature in berlin: Case study. *Journal of Urban Planning and Development*, 133:128–137, 6 2007. ISSN 0733-9488. doi: 10.1061/(ASCE)0733-9488(2007)133:2(128).

P. Kountouris, C. Gerbig, K.-U. Totsche, A. J. Dolman, A. G. C. A. Meesters, G. Broquet, F. Maignan, B. Gioli, L. Montagnani, and C. Helfter. An objective prior error quantification for regional atmospheric inverse applications. *Biogeosciences*, 12:7403–7421, 12 2015. ISSN 1726-4189. doi: 10.5194/bg-12-7403-2015. URL https://bg.copernicus.org/articles/12/7403/2015/.

P. Kountouris, C. Gerbig, C. Rödenbeck, U. Karstens, T. F. Koch, and M. Heimann. Technical note: Atmospheric co2 inversions on the mesoscale using data-driven prior uncertainties: methodology and system evaluation. *Atmospheric Chemistry and Physics*, 18:3027–3045, 3 2018. ISSN 1680-7324. doi: 10.5194/acp-18-3027-2018.

E. S. Krayenhoff, A. Christen, A. Martilli, and T. R. Oke. A multi-layer radiation model for urban neighbourhoods with trees. *Boundary-Layer Meteorology*, 151:139–178, 4 2014. ISSN 0006-8314. doi: 10.1007/s10546-013-9883-1.

E. S. Krayenhoff, J. L. Santiago, A. Martilli, A. Christen, and T. R. Oke. Parametrization of drag and turbulence for urban neighbourhoods with trees. *Boundary-Layer Meteorology*, 156:157–189, 8 2015. ISSN 15731472. doi: 10.1007/s10546-015-0028-6.

E. S. Krayenhoff, T. Jiang, A. Christen, A. Martilli, T. R. Oke, B. N. Bailey, N. Nazarian, J. A. Voogt, M. G. Giometto, A. Stastny, and B. R. Crawford. A multi-layer urban canopy meteorological model with trees (bep-tree): Street tree impacts on pedestrian-level climate. *Urban Climate*, 32:100590, 2020. ISSN 22120955. doi: 10.1016/j.uclim.2020.100590. URL https://doi.org/10.1016/j.uclim.2020.100590.

E. S. Krayenhoff, A. M. Broadbent, L. Zhao, M. Georgescu, A. Middel, J. A. Voogt, A. Martilli, D. J. Sailor, and E. Erell. Cooling hot cities: a systematic and critical review of the numerical modelling literature. *Environmental Research Letters*, 16:053007, 5 2021. ISSN 1748-9326. doi: 10.1088/1748-9326/abdcf1.

L. M. Kueppers and M. A. Snyder. Influence of irrigated agriculture on diurnal surface energy and water fluxes, surface climate, and atmospheric circulation in california. *Climate Dynamics*, 38:1017–1029, 3 2012. ISSN 0930-7575. doi: 10.1007/s00382-011-1123-0.

S. Kuppel, P. Peylin, F. Chevallier, C. Bacour, F. Maignan, and A. D. Richardson. Constraining a global ecosystem model with multi-site eddy-covariance data. *Biogeosciences*, 9:3757–3776, 10 2012. ISSN 1726-4189. doi: 10.5194/bg-9-3757-2012. URL https://bg.copernicus.org/articles/9/3757/2012/.

H. Kusaka, H. Kondo, Y. Kikegawa, and F. Kimura. A simple single-layer urban canopy model for atmospheric models: Comparison with multi-layer and slab models. *Boundary-Layer Meteorology*, 2001. ISSN 00068314. doi: 10.1023/A:1019207923078.

V. Lakshmi, S. Hong, E. E. Small, and F. Chen. The influence of the land surface on hydrometeorology and ecology: new advances from modeling and satellite remote sensing. *Hydrology Research*, 42:95–112, 4 2011. ISSN 0029-1277. doi: 10.2166/nh.2011.071.

R. Lal. Soil carbon stocks under present and future climate with specific reference to european ecoregions. *Nutrient Cycling in Agroecosystems*, 81:113–127, 6 2008. ISSN 1385-1314. doi: 10.1007/s10705-007-9147-x.

B. Lalic and D. T. Mihailovic. An empirical relation describing leaf-area density inside the forest for environmental modeling. *Journal of Applied Meteorology*, 43:641–645, 4 2004. ISSN 0894-8763. doi: 10.1175/1520-0450(2004)043<0641:AERDLD>2.0.CO;2.

J. Langemeyer and F. Baró. Nature-based solutions as nodes of green-blue infrastructure networks: A cross-scale, co-creation approach. *Nature-Based Solutions*, 1:100006, 12 2021. ISSN 27724115. doi: 10.1016/j.nbsj.2021.100006.

J. Langemeyer, D. Wedgwood, T. McPhearson, F. Baró, A. L. Madsen, and D. N. Barton. Creating urban green infrastructure where it is needed – a spatial ecosystem service-based decision analysis of green roofs in barcelona. *Science of The Total Environment*, 707:135487, 3 2020. ISSN 00489697. doi: 10.1016/j.scitotenv.2019.135487.

J. Langemeyer, C. Madrid-Lopez, A. M. Beltran, and G. V. Mendez. Urban agriculture — a necessary pathway towards urban resilience and global sustainability? *Landscape and Urban Planning*, 210:104055, 6 2021. ISSN 01692046. doi: 10.1016/j.landurbplan.2021.104055.

C. S. Laspidou, N. K. Mellios, A. E. Spyropoulou, D. T. Kofinas, and M. P. Papadopoulou. Systems thinking on the resource nexus: Modeling and visualisation tools to identify critical interlinkages for resilient and sustainable societies and institutions. *Science of The Total Environment*, 717:137264, 5 2020. ISSN 00489697. doi: 10.1016/j.scitotenv.2020.137264.

T. Lauvaux, A. E. Schuh, M. Uliasz, S. Richardson, N. Miles, A. E. Andrews, C. Sweeney, L. I. Diaz, D. Martins, P. B. Shepson, and K. J. Davis. Constraining the co2 budget of the corn belt: exploring uncertainties from the assumptions in a mesoscale inverse system. *Atmospheric Chemistry and Physics*, 12:337–354, 1 2012. ISSN 1680-7324. doi: 10.5194/acp-12-337-2012. URL https://acp.copernicus.org/articles/12/337/2012/.

S.-H. Lee. Further development of the vegetated urban canopy model including a grass-covered surface parametrization and photosynthesis effects. *Boundary-Layer Meteorology*, 140:315–342, 8 2011. ISSN 0006-8314. doi: 10.1007/s10546-011-9603-7.

S.-H. Lee and S.-U. Park. A vegetated urban canopy model for meteorological and environmental modelling. *Boundary-Layer Meteorology*, 126:73–102, 11 2007. ISSN 0006-8314. doi: 10.1007/s10546-007-9221-6.

S. H. Lee, H. Lee, S. B. Park, J. W. Woo, D. I. Lee, and J. J. Baik. Impacts of in-canyon vegetation and canyon aspect ratio on the thermal environment of street canyons: numerical investigation using a coupled wrf-vucm model. *Quarterly Journal of the Royal Meteorological Society*, 142:2562–2578, 7 2016. ISSN 1477870X. doi: 10.1002/qj.2847.

S.-H. Lee, J.-Y. Choi, S.-O. Hur, M. Taniguchi, N. Masuhara, K. S. Kim, S. Hyun, E. Choi, J. hoon Sung, and S.-H. Yoo. Food-centric interlinkages in agricultural food-energy-water nexus under climate change and irrigation management. *Resources, Conservation and Recycling*, 163:105099, 12 2020. ISSN 09213449. doi: 10.1016/j.resconrec.2020.105099.

A. Lemonsu, C. S. B. Grimmond, and V. Masson. Modeling the surface energy balance of the core of an old mediterranean city: Marseille. *Journal of Applied Meteorology*, 43:312–327, 2 2004. ISSN 0894-8763. doi: 10.1175/1520-0450(2004)043<0312:MTSEBO>2.0.CO;2.

Li and Xiao. Mapping photosynthesis solely from solar-induced chlorophyll fluorescence: A global, fine-resolution dataset of gross primary production derived from oco-2. *Remote Sensing*, 11:2563, 10 2019. ISSN 2072-4292. doi: 10.3390/rs11212563. URL https://www.mdpi.com/2072-4292/11/21/2563.

D. Li and E. Bou-Zeid. Synergistic interactions between urban heat islands and heat waves: The impact in cities is larger than the sum of its parts. *Journal of Applied Meteorology and Climatology*, 52:2051–2064, 9 2013. ISSN 1558-8424. doi: 10.1175/JAMC-D-13-02.1. URL https://journals.ametsoc.org/view/journals/apme/52/9/jamc-d-13-02.1.xml.

D. Li, E. Bou-Zeid, and M. Oppenheimer. The effectiveness of cool and green roofs as urban heat island mitigation strategies. *Environmental Research Letters*, 2014. ISSN 17489326. doi: 10.1088/1748-9326/9/5/055002.

H. Li, Y. Zhou, X. Wang, X. Zhou, H. Zhang, and S. Sodoudi. Quantifying urban heat island intensity and its physical mechanism using wrf/ucm. *Science of the Total Environment*, 650: 3110–3119, 2019. ISSN 18791026. doi: 10.1016/j.scitotenv.2018.10.025. URL https://doi.org/10.1016/j.scitotenv.2018.10.025.

M. Li, V. P. Singh, Q. Fu, D. Liu, T. Li, and Y. Zhou. Optimization of agricultural water–food–energy nexus in a random environment: an integrated modelling approach. *Stochastic Environmental Research and Risk Assessment*, 35:3–19, 1 2021. ISSN 1436-3240. doi: 10.1007/s00477-019-01672-4.

X.-X. Li and L. K. Norford. Evaluation of cool roof and vegetations in mitigating urban heat island in a tropical city, singapore. *Urban Climate*, 16:59–74, 6 2016. ISSN 22120955. doi: 10.1016/j.uclim.2015.12.002.

S. Liang. Narrowband to broadband conversions of land surface albedo i. *Remote Sensing of Environment*, 76:213–238, 5 2001. ISSN 00344257. doi: 10.1016/S0034-4257(00)00205-4.

B.-S. Lin and Y.-J. Lin. Cooling effect of shade trees with different characteristics in a subtropical urban park. *HortScience*, 45:83–86, 1 2010. ISSN 0018-5345. doi: 10.21273/HORTSCI.45.1.83.

J. C. Lin, M. R. Pejam, E. Chan, S. C. Wofsy, E. W. Gottlieb, H. A. Margolis, and J. H. McCaughey. Attributing uncertainties in simulated biospheric carbon fluxes to different error sources. *Global Biogeochemical Cycles*, 25:n/a–n/a, 6 2011. ISSN 08866236. doi: 10.1029/2010GB003884.

F. Lindberg, C. Grimmond, A. Gabey, B. Huang, C. W. Kent, T. Sun, N. E. Theeuwes, L. Järvi, H. C. Ward, I. Capel-Timms, Y. Chang, P. Jonsson, N. Krave, D. Liu, D. Meyer, K. F. G. Olofson, J. Tan, D. Wästberg, L. Xue, and Z. Zhang. Urban multi-scale environmental predictor (umep): An integrated tool for city-based climate services. *Environmental Modelling & Software*, 99:70–87, 1 2018. ISSN 13648152. doi: 10.1016/j.envsoft.2017.09.020.

P. Lionello, P. Malanotte-Rizzoli, R. Boscolo, P. Alpert, V. Artale, L. Li, J. Luterbacher, W. May, R. Trigo, M. Tsimplis, U. Ulbrich, and E. Xoplaki. *The Mediterranean climate: An overview of the main characteristics and issues*, pages 1–26. 2006. doi: 10.1016/S1571-9197(06)80003-0. URL https://linkinghub.elsevier.com/retrieve/pii/S1571919706800030.

W. Liu, Z. Zhang, and S. Wan. Predominant role of water in regulating soil and microbial respiration and their responses to climate change in a semiarid grassland. *Global Change Biology*, 15:184–195, 1 2009. ISSN 1354-1013. doi: 10.1111/j.1365-2486.2008.01728.x.

X. Liu, B. He, L. Guo, L. Huang, W. Yuan, X. Chen, X. Hao, X. Xie, Y. Zhang, Z. Zhong, T. Li, and A. Chen. European carbon uptake has not benefited from vegetation greening. *Geophysical Research Letters*, 48, 10 2021. ISSN 0094-8276. doi: 10.1029/2021GL094870.

Y. Liu, F. Chen, T. Warner, and J. Basara. Verification of a mesoscale data-assimilation and forecasting system for the oklahoma city area during the joint urban 2003 field project. *Journal of Applied Meteorology and Climatology*, 45:912–929, 7 2006. ISSN 1558-8432. doi: 10.1175/JAM2383.1.

S. O. Los. Analysis of trends in fused avhrr and modis ndvi data for 1982–2006: Indication for a co2 fertilization effect in global vegetation. *Global Biogeochemical Cycles*, 27:318–330, 6 2013. ISSN 0886-6236. doi: 10.1002/gbc.20027.

C. P. Loughner, D. J. Allen, D.-L. Zhang, K. E. Pickering, R. R. Dickerson, and L. Landry. Roles of urban tree canopy and buildings in urban heat island effects: Parameterization and preliminary results. *Journal of Applied Meteorology and Climatology*, 51:1775–1793, 10 2012. ISSN 1558-8424. doi: 10.1175/JAMC-D-11-0228.1.

X. Luo, P. Vahmani, T. Hong, and A. Jones. City-scale building anthropogenic heating during heat waves. *Atmosphere*, 11:1206, 11 2020. ISSN 2073-4433. doi: 10.3390/atmos11111206.

Y. Lv, J. Liu, W. He, Y. Zhou, N. T. Nguyen, W. Bi, X. Wei, and H. Chen. How well do light-use efficiency models capture large-scale drought impacts on vegetation productivity compared with data-driven estimates? *Ecological Indicators*, 146:109739, 2 2023. ISSN 1470160X. doi: 10.1016/j.ecolind.2022.109739. URL https://linkinghub.elsevier.com/retrieve/pii/S1470160X22012122.

P. Mahadevan, S. C. Wofsy, D. M. Matross, X. Xiao, A. L. Dunn, J. C. Lin, C. Gerbig, J. W. Munger, V. Y. Chow, and E. W. Gottlieb. A satellite-based biosphere parameterization for net ecosystem co2 exchange: Vegetation photosynthesis and respiration model (vprm). *Global Biogeochemical Cycles*, 22, 6 2008. ISSN 08866236. doi: 10.1029/2006GB002735. URL http://doi.wiley.com/10.1029/2006GB002735.

M. D. Mahecha, M. Reichstein, N. Carvalhais, G. Lasslop, H. Lange, S. I. Seneviratne, R. Vargas, C. Ammann, M. A. Arain, A. Cescatti, I. A. Janssens, M. Migliavacca, L. Montagnani, and A. D. Richardson. Global convergence in the temperature sensitivity of respiration at ecosystem level. *Science*, 329:838–840, 8 2010. ISSN 0036-8075. doi: 10.1126/science.1189587.

F. Marando, M. P. Heris, G. Zulian, A. Udías, L. Mentaschi, N. Chrysoulakis, D. Parastatidis, and J. Maes. Urban heat island mitigation by green infrastructure in european functional urban areas. *Sustainable Cities and Society*, 77:103564, 2 2022. ISSN 22106707. doi: 10.1016/j.scs.2021.103564.

R. M. Marchin, D. Backes, A. Ossola, M. R. Leishman, M. G. Tjoelker, and D. S. Ellsworth. Extreme heat increases stomatal conductance and drought-induced mortality risk in vulnerable plant species. *Global Change Biology*, 28:1133–1146, 2 2022. ISSN 1354-1013. doi: 10.1111/gcb.15976.

A. Martilli. A two-dimensional numerical study of the impact of a city on atmospheric circulation and pollutant dispersion in a coastal environment. *Boundary-Layer Meteorology*, 108:91–119, 7 2003. ISSN 0006-8314. doi: 10.1023/A:1023044100064. URL http://link.springer.com/10.1023/A:1023044100064.

A. Martilli, A. Clappier, and M. W. Rotach. An urban surface exchange parameterisation for mesoscale models. *Boundary-Layer Meteorology*, 104:261–304, 8 2002. ISSN 0006-8314. doi: 10.1023/A:1016099921195. URL http://link.springer.com/10.1023/A:1016099921195.

A. Martilli, O. Brousse, and J. Ching. Wudapt to wrf (w2w): Urbanized wrf modeling using wudapt. *ResearchGate*, 3 2016.

A. Martilli, N. Nazarian, E. Krayenhoff, J. Lachapelle, J. Lu, E. Rivas, A. Rodriguez-Sanchez, B. Sanchez, and J. Santiago. Wrf-comfort: Simulating micro-scale variability of outdoor heat stress at the city scale with a mesoscale model. *EGUsphere [preprint]*, 2023. doi: 10.5194/egusphere-2023-1069.

J. Martin-Vide and M. C. Moreno-Garcia. Probability values for the intensity of barcelona's urban heat island (spain). *Atmospheric Research*, 240:104877, 8 2020. ISSN 01698095. doi: 10.1016/j.atmosres.2020.104877.

J. Martín-Vide. Mapas del tiempo: fundamentos, interpretación e imágenes de satélite. oikostau, barcelona (170 pp)., 1991.

B. Martínez, S. Sánchez-Ruiz, M. Campos-Taberner, F. J. García-Haro, and M. A. Gilabert. Exploring ecosystem functioning in spain with gross and net primary production time series. *Remote Sensing*, 14:1310, 3 2022. ISSN 2072-4292. doi: 10.3390/rs14061310.

J. Marull, R. Padró, J. Cirera, A. Giocoli, M. Pons, and E. Tello. A socioecological integrated analysis of the barcelona metropolitan agricultural landscapes. *Ecosystem Services*, 51:101350, 10 2021. ISSN 22120416. doi: 10.1016/j.ecoser.2021.101350.

F. Maselli, D. Papale, N. Puletti, G. Chirici, and P. Corona. Combining remote sensing and ancillary data to monitor the gross productivity of water-limited forest ecosystems. *Remote Sensing of Environment*, 113:657–667, 3 2009. ISSN 00344257. doi: 10.1016/j.rse.2008.11.008. URL https://linkinghub.elsevier.com/retrieve/pii/S003442570800343X.

D. Matsushima. *Thermal Inertia-Based Method for Estimating Soil Moisture*. IntechOpen, 2 2019. doi: 10.5772/intechopen.80252.

A. Matzarakis, F. Rutz, and H. Mayer. Modelling radiation fluxes in simple and complex environments: basics of the rayman model. *International Journal of Biometeorology*, 54:131–139, 3 2010. ISSN 0020-7128. doi: 10.1007/s00484-009-0261-0.

M. P. McCarthy, M. J. Best, and R. A. Betts. Climate change in cities due to global warming and urban effects. *Geophysical Research Letters*, 37:n/a–n/a, 5 2010. ISSN 00948276. doi: 10.1029/2010GL042845. URL http://doi.wiley.com/10.1029/2010GL042845.

N. McDowell, W. T. Pockman, C. D. Allen, D. D. Breshears, N. Cobb, T. Kolb, J. Plaut, J. Sperry, A. West, D. G. Williams, and E. A. Yepez. Mechanisms of plant survival and mortality during drought: why do some plants survive while others succumb to drought? *New Phytologist*, 178:719–739, 6 2008. ISSN 0028-646X. doi: 10.1111/j.1469-8137.2008.02436.x.

G. A. Meehl and C. Tebaldi. More intense, more frequent, and longer lasting heat waves in the 21st century. *Science*, 305:994–997, 8 2004. ISSN 0036-8075. doi: 10.1126/science.1098704.

N. Meili, G. Manoli, P. Burlando, E. Bou-Zeid, W. T. L. Chow, A. M. Coutts, E. Daly, K. A. Nice, M. Roth, N. J. Tapper, E. Velasco, E. R. Vivoni, and S. Fatichi. An urban ecohydrological model to quantify the effect of vegetation on urban climate and hydrology (ut&c v1.0). *Geoscientific Model Development*, 13:335–362, 1 2020. ISSN 1991-9603. doi: 10.5194/gmd-13-335-2020.

N. Meili, G. Manoli, P. Burlando, J. Carmeliet, W. T. Chow, A. M. Coutts, M. Roth, E. Velasco, E. R. Vivoni, and S. Fatichi. Tree effects on urban microclimate: Diurnal, seasonal, and climatic temperature differences explained by separating radiation, evapotranspiration, and roughness effects. *Urban Forestry & Urban Greening*, 58:126970, 3 2021. ISSN 16188667. doi: 10.1016/j.ufug.2020.126970.

L. A. Mendonça, J. J. Loomis, M. Limont, M. L. C. Bartz, and W. B. Rauen. Elements of the water - food - environment nexus for integrated sustainability analysis. *Science of The Total Environment*, 905:166866, 12 2023. ISSN 00489697. doi: 10.1016/j.scitotenv.2023.166866.

C. Miao, P. Li, Y. Huang, Y. Sun, W. Chen, and S. Yu. Coupling outdoor air quality with thermal comfort in the presence of street trees: a pilot investigation in shenyang, northeast china. *Journal of Forestry Research*, 34:831–839, 6 2023. ISSN 1007-662X. doi: 10.1007/s11676-022-01497-y.

A. Middel and E. S. Krayenhoff. Micrometeorological determinants of pedestrian thermal exposure during record-breaking heat in tempe, arizona: Introducing the marty observational platform. *Science of The Total Environment*, 687:137–151, 10 2019. ISSN 00489697. doi: 10.1016/j.scitotenv.2019.06.085.

M. Migliavacca, M. Reichstein, A. D. Richardson, R. Colombo, M. A. Sutton, G. Lasslop, E. Tomelleri, G. Wohlfahrt, N. Carvalhais, A. Cescatti, M. D. Mahecha, L. Montagnani, D. Papale, S. Zaehle, A. Arain, A. Arneth, T. A. Black, A. Carrara, S. Dore, D. Gianelle, C. Helfter, D. Hollinger, W. L. Kutsch, P. M. Lafleur, Y. Nouvellon, C. Rebmann, R. Humberto, M. Rodeghiero, O. Roupsard, M. T. Sebastià, G. Seufert, J. F. Soussana, and M. K.

V. D. Molen. Semiempirical modeling of abiotic and biotic factors controlling ecosystem respiration across eddy covariance sites. *Global Change Biology*, 17:390–409, 2011. ISSN 13652486. doi: 10.1111/j.1365-2486.2010.02243.x.

Millenium Ecosystem Assessment. Ecosystems and human well-being: Current state and trends., 2005.

J. Miró, N. Pepin, J. Peña, and J. Martin-Vide. Daily atmospheric circulation patterns for catalonia (northeast iberian peninsula) using a modified version of jenkinson and collison method. *Atmospheric Research*, 231:104674, 1 2020. ISSN 01698095. doi: 10.1016/j.atmosres.2019.104674.

J. Moemken, B. Koerner, F. Ehmele, H. Feldmann, and J. G. Pinto. Recurrence of drought events over iberia. part ii: Future changes using regional climate projections. *Tellus A: Dynamic Meteorology and Oceanography*, 74:262, 4 2022. ISSN 1600-0870. doi: 10.16993/tellusa.52.

M. O. Molina, E. Sánchez, and C. Gutiérrez. Future heat waves over the mediterranean from an euro-cordex regional climate model ensemble. *Scientific Reports*, 10:8801, 5 2020. ISSN 2045-2322. doi: 10.1038/s41598-020-65663-0. URL https://www.nature.com/articles/s41598-020-65663-0.

M. C. Moreno-garcia. Intensity and form of the urban heat island in barcelona. *International Journal of Climatology*, 14:705–710, 7 1994. ISSN 08998418. doi: 10.1002/joc.3370140609. URL http://doi.wiley.com/10.1002/joc.3370140609.

N. D. Mueller, J. S. Gerber, M. Johnston, D. K. Ray, N. Ramankutty, and J. A. Foley. Closing yield gaps through nutrient and water management. *Nature*, 490:254–257, 10 2012. ISSN 0028-0836. doi: 10.1038/nature11420.

S. Munassar, C. Rödenbeck, F.-T. Koch, K. U. Totsche, M. Gałkowski, S. Walther, and C. Gerbig. Net ecosystem exchange (nee) estimates 2006–2019 over europe from a pre-operational ensemble-inversion system. *Atmospheric Chemistry and Physics*, 22:7875–7892, 6 2022. ISSN 1680-7324. doi: 10.5194/acp-22-7875-2022.

G. Mussetti, D. Brunner, S. Henne, J. Allegrini, E. S. Krayenhoff, S. Schubert, C. Feigenwinter, R. Vogt, A. Wicki, and J. Carmeliet. Cosmo-bep-tree v1.0: a coupled urban climate model with explicit representation of street trees. *Geoscientific Model Development*, 13:1685–1710, 4 2020. ISSN 1991-9603. doi: 10.5194/gmd-13-1685-2020.

J. Muñoz-Sabater. Era5-land monthly averaged data from 1981 to present. copernicus climate change service (c3s) climate data store, 2019. URL https://cds.climate.copernicus.eu/cdsapp#!/dataset/reanalysis-era5-land-monthly-means?tab=overviewhttps://cds.climate.copernicus.eu/cdsapp#!/dataset/10.24381/cds.68d2bb30?tab=overview.

J. Muñoz-Sabater, E. Dutra, A. Agustí-Panareda, C. Albergel, G. Arduini, G. Balsamo, S. Boussetta, M. Choulga, S. Harrigan, H. Hersbach, B. Martens, D. G. Miralles, M. Piles, N. J.

Rodríguez-Fernández, E. Zsoter, C. Buontempo, and J.-N. Thépaut. Era5-land: a state-of-the-art global reanalysis dataset for land applications. *Earth System Science Data*, 13: 4349–4383, 9 2021. ISSN 1866-3516. doi: 10.5194/essd-13-4349-2021. URL https://essd.copernicus.org/articles/13/4349/2021/.

Natural Capital Project. Invest 3.14.1. stanford university, university of minnesota, chinese academy of sciences, the nature conservancy, world wildlife fund, stockholm resilience centre and the royal swedish academy of sciences. https://naturalcapitalproject.stanford.edu/software/invest, 2024.

S. Naumann, D. McKenna, T. Kaphengst, M. Pieterse, M. Rayment, and M. Davis. Design, implementation and cost elements of green infrastructure projects. final report to the european commission, dg environment, 2011.

N. Nazarian, E. S. Krayenhoff, and A. Martilli. A one-dimensional model of turbulent flow through "urban" canopies (mlucm v2.0): updates based on large-eddy simulation. *Geoscientific Model Development*, 13:937–953, 3 2020. ISSN 1991-9603. doi: 10.5194/gmd-13-937-2020.

M. I. Ndossi and U. Avdan. Application of open source coding technologies in the production of land surface temperature (lst) maps from landsat: A pyqgis plugin. *Remote Sensing*, 8: 413, 5 2016. ISSN 2072-4292. doi: 10.3390/rs8050413. URL http://www.mdpi.com/2072-4292/8/5/413.

E. Nelson, G. Mendoza, J. Regetz, S. Polasky, H. Tallis, D. Cameron, K. M. Chan, G. C. Daily, J. Goldstein, P. M. Kareiva, E. Lonsdorf, R. Naidoo, T. H. Ricketts, and M. Shaw. Modeling multiple ecosystem services, biodiversity conservation, commodity production, and tradeoffs at landscape scales. *Frontiers in Ecology and the Environment*, 7:4–11, 2 2009. ISSN 1540-9295. doi: 10.1890/080023.

K. L. Nemunaitis-Berry, P. M. Klein, J. B. Basara, and E. Fedorovich. Sensitivity of predictions of the urban surface energy balance and heat island to variations of urban canopy parameters in simulations with the wrf model. *Journal of Applied Meteorology and Climatology*, 56: 573–595, 2017. ISSN 15588432. doi: 10.1175/JAMC-D-16-0157.1.

E. Ng, L. Chen, Y. Wang, and C. Yuan. A study on the cooling effects of greening in a high-density city: An experience from hong kong. *Building and Environment*, 47:256–271, 1 2012. ISSN 03601323. doi: 10.1016/j.buildenv.2011.07.014.

J. Noilhan and S. Planton. A simple parameterization of land surface processes for meteorological models. *Monthly Weather Review*, 117:536–549, 3 1989. ISSN 0027-0644. doi: 10.1175/1520-0493(1989)117<0536:ASPOLS>2.0.CO;2.

D. J. Nowak. Estimating leaf area and leaf biomass of open-grown deciduous urban trees. *Forest Science*, 42, 1996.

D. J. Nowak and D. E. Crane. Carbon storage and sequestration by urban trees in the usa. *Environmental Pollution*, 116:381–389, 3 2002. ISSN 02697491. doi: 10.1016/S0269-7491(01)00214-7.

L. Nunes, J. Álvarez González, I. Alberdi, V. Silva, M. Rocha, and F. C. Rego. Analysis of the occurrence of wildfires in the iberian peninsula based on harmonised data from national forest inventories. *Annals of Forest Science*, 76:27, 3 2019. ISSN 1286-4560. doi: 10.1007/s13595-019-0811-5.

T. Oke. The micrometeorology of the urban forest. *Philosophical Transactions of the Royal Society of London. B, Biological Sciences*, 324:335–349, 8 1989. ISSN 0080-4622. doi: 10.1098/rstb.1989.0051.

T. R. Oke. The distinction between canopy and boundary-layer urban heat islands. *Atmosphere*, 1976. ISSN 20734433. doi: 10.1080/00046973.1976.9648422.

T. R. Oke. The energetic basis of the urban heat island. *Quarterly Journal of the Royal Meteorological Society*, 108:1–24, 1 1982. ISSN 00359009. doi: 10.1002/qj.49710845502. URL http://doi.wiley.com/10.1002/qj.49710845502.

T. R. Oke, G. Mills, A. Christen, and J. A. Voogt. *Urban Climates*. Cambridge University Press, 9 2017. ISBN 9781139016476. doi: 10.1017/9781139016476.

S. Oliveira, H. Andrade, and T. Vaz. The cooling effect of green spaces as a contribution to the mitigation of urban heat: A case study in lisbon. *Building and Environment*, 2011. ISSN 03601323. doi: 10.1016/j.buildenv.2011.04.034.

D. M. Olson, E. Dinerstein, E. D. Wikramanayake, N. D. Burgess, G. V. N. Powell, E. C. Underwood, J. A. D'amico, I. Itoua, H. E. Strand, J. C. Morrison, C. J. Loucks, T. F. Allnutt, T. H. Ricketts, Y. Kura, J. F. Lamoreux, W. W. Wettengel, P. Hedao, and K. R. Kassem. Terrestrial ecoregions of the world: A new map of life on earth: A new global map of terrestrial ecoregions provides an innovative tool for conserving biodiversity. *BioScience*, 51:933–938, 11 2001. ISSN 0006-3568. doi: 10.1641/0006-3568(2001)051[0933:TEOTWA]2.0.CO;2. URL https://doi.org/10.1641/0006-3568(2001)051[0933:TEOTWA]2.0.CO2.

R. Padró, M. J. L. Rota-Aguilera, A. Giocoli, J. Cirera, F. Coll, M. Pons, J. Pino, S. Pili, T. Serrano, G. Villalba, and J. Marull. Assessing the sustainability of contrasting land use scenarios through the socioecological integrated analysis (sia) of the metropolitan green infrastructure in barcelona. *Landscape and Urban Planning*, 203:103905, 11 2020. ISSN 01692046. doi: 10.1016/j.landurbplan.2020.103905.

G. Papangelis, M. Tombrou, A. Dandou, and T. Kontos. An urban "green planning" approach utilizing the weather research and forecasting (wrf) modeling system. a case study of athens, greece. *Landscape and Urban Planning*, 105:174–183, 3 2012. ISSN 01692046. doi: 10.1016/j.landurbplan.2011.12.014.

G. Pappaccogli, L. Giovannini, F. Cappelletti, and D. Zardi. Sensitivity of wrf/urban simulations to urban morphology parameters: A case study in the city of bolzano. volume 2017-February, 2017.

G. Pastorello, C. Trotta, E. Canfora, H. Chu, D. Christianson, Y.-W. Cheah, C. Poindexter, J. Chen, A. Elbashandy, M. Humphrey, P. Isaac, D. Polidori, M. Reichstein, A. Ribeca, C. van Ingen, N. Vuichard, L. Zhang, B. Amiro, C. Ammann, M. A. Arain, J. Ardö, T. Arkebauer, S. K. Arndt, N. Arriga, M. Aubinet, M. Aurela, D. Baldocchi, A. Barr, E. Beamesderfer, L. B. Marchesini, O. Bergeron, J. Beringer, C. Bernhofer, D. Berveiller, D. Billesbach, T. A. Black, P. D. Blanken, G. Bohrer, J. Boike, P. V. Bolstad, D. Bonal, J.-M. Bonnefond, D. R. Bowling, R. Bracho, J. Brodeur, C. Brümmer, N. Buchmann, B. Burban, S. P. Burns, P. Buysse, P. Cale, M. Cavagna, P. Cellier, S. Chen, I. Chini, T. R. Christensen, J. Cleverly, A. Collalti, C. Consalvo, B. D. Cook, D. Cook, C. Coursolle, E. Cremonese, P. S. Curtis, E. D'Andrea, H. da Rocha, X. Dai, K. J. Davis, B. D. Cinti, A. de Grandcourt, A. D. Ligne, R. C. D. Oliveira, N. Delpierre, A. R. Desai, C. M. D. Bella, P. di Tommasi, H. Dolman, F. Domingo, G. Dong, S. Dore, P. Duce, E. Dufrêne, A. Dunn, J. Dušek, D. Eamus, U. Eichelmann, H. A. M. ElKhidir, W. Eugster, C. M. Ewenz, B. Ewers, D. Famulari, S. Fares, I. Feigenwinter, A. Feitz, R. Fensholt, G. Filippa, M. Fischer, J. Frank, M. Galvagno, M. Gharun, D. Gianelle, B. Gielen, B. Gioli, A. Gitelson, I. Goded, M. Goeckede, A. H. Goldstein, C. M. Gough, M. L. Goulden, A. Graf, A. Griebel, C. Gruening, T. Grünwald, A. Hammerle, S. Han, X. Han, B. U. Hansen, C. Hanson, J. Hatakka, Y. He, M. Hehn, B. Heinesch, N. Hinko-Najera, L. Hörtnagl, L. Hutley, A. Ibrom, H. Ikawa, M. Jackowicz-Korczynski, D. Janouš, W. Jans, R. Jassal, S. Jiang, T. Kato, M. Khomik, J. Klatt, A. Knohl, S. Knox, H. Kobayashi, G. Koerber, O. Kolle, Y. Kosugi, A. Kotani, A. Kowalski, B. Kruijt, J. Kurbatova, W. L. Kutsch, H. Kwon, S. Launiainen, T. Laurila, B. Law, R. Leuning, Y. Li, M. Liddell, J.-M. Limousin, M. Lion, A. J. Liska, A. Lohila, A. López-Ballesteros, E. López-Blanco, B. Loubet, D. Loustau, A. Lucas-Moffat, J. Lüers, S. Ma, C. Macfarlane, V. Magliulo, R. Maier, I. Mammarella, G. Manca, B. Marcolla, H. A. Margolis, S. Marras, W. Massman, M. Mastepanov, R. Matamala, J. H. Matthes, F. Mazzenga, H. McCaughey, I. McHugh, A. M. S. McMillan, L. Merbold, W. Meyer, T. Meyers, S. D. Miller, S. Minerbi, U. Moderow, R. K. Monson, L. Montagnani, C. E. Moore, E. Moors, V. Moreaux, C. Moureaux, J. W. Munger, T. Nakai, J. Neirynck, Z. Nesic, G. Nicolini, A. Noormets, M. Northwood, M. Nosetto, Y. Nouvellon, K. Novick, W. Oechel, J. E. Olesen, J.-M. Ourcival, S. A. Papuga, F.-J. Parmentier, E. Paul-Limoges, M. Pavelka, M. Peichl, E. Pendall, R. P. Phillips, K. Pilegaard, N. Pirk, G. Posse, T. Powell, H. Prasse, S. M. Prober, S. Rambal, Üllar Rannik, N. Raz-Yaseef, C. Rebmann, D. Reed, V. R. de Dios, N. Restrepo-Coupe, B. R. Reverter, M. Roland, S. Sabbatini, T. Sachs, S. R. Saleska, E. P. Sánchez-Cañete, Z. M. Sanchez-Mejia, H. P. Schmid, M. Schmidt, K. Schneider, F. Schrader, I. Schroder, R. L. Scott, P. Sedlák, P. Serrano-Ortíz, C. Shao, P. Shi, I. Shironya, L. Siebicke, L. Šigut, R. Silberstein, C. Sirca, D. Spano, R. Steinbrecher, R. M. Stevens, C. Sturtevant, A. Suyker, T. Tagesson, S. Takanashi, Y. Tang, N. Tapper, J. Thom, M. Tomassucci, J.-P. Tuovinen, S. Urbanski, R. Valentini, M. van der Molen, E. van Gorsel, K. van Huissteden, A. Varlagin, J. Verfaillie, T. Vesala, C. Vincke, D. Vitale, N. Vygodskaya, J. P. Walker, E. Walter-Shea, H. Wang, R. Weber, S. Westermann, C. Wille, S. Wofsy, G. Wohlfahrt, S. Wolf, W. Woodgate, Y. Li,

R. Zampedri, J. Zhang, G. Zhou, D. Zona, D. Agarwal, S. Biraud, M. Torn, and D. Papale. The fluxnet2015 dataset and the oneflux processing pipeline for eddy covariance data. *Scientific Data*, 7:225, 7 2020. ISSN 2052-4463. doi: 10.1038/s41597-020-0534-3. URL https://www.nature.com/articles/s41597-020-0534-3.

S. Pauleit, N. Jones, G. Garcia-Martin, J. L. Garcia-Valdecantos, L. M. Rivière, L. Vidal-Beaudet, M. Bodson, and T. B. Randrup. Tree establishment practice in towns and cities – results from a european survey. *Urban Forestry & Urban Greening*, 1:83–96, 1 2002. ISSN 16188667. doi: 10.1078/1618-8667-00009.

L. S. Pereira, R. G. Allen, M. Smith, and D. Raes. Crop evapotranspiration estimation with fao56: Past and future. *Agricultural Water Management*, 147:4–20, 1 2015. ISSN 03783774. doi: 10.1016/j.agwat.2014.07.031.

K. Perini, A. Chokhachian, S. Dong, and T. Auer. Modeling and simulating urban outdoor comfort: Coupling envi-met and trnsys by grasshopper. *Energy and Buildings*, 152:373–384, 10 2017. ISSN 03787788. doi: 10.1016/j.enbuild.2017.07.061.

J. Peñuelas and J. Sardans. Global change and forest disturbances in the mediterranean basin: Breakthroughs, knowledge gaps, and recommendations. *Forests*, 12:603, 5 2021. ISSN 1999-4907. doi: 10.3390/f12050603.

D. Pillai, C. Gerbig, R. Kretschmer, V. Beck, U. Karstens, B. Neininger, and M. Heimann. Comparing lagrangian and eulerian models for co2 transport – a step towards bayesian inverse modeling using wrf/stilt-vprm. *Atmospheric Chemistry and Physics*, 12:8979–8991, 10 2012. ISSN 1680-7324. doi: 10.5194/acp-12-8979-2012.

N. Pineda, O. Jorba, J. Jorge, and J. M. Baldasano. Using noaa avhrr and spot vgt data to estimate surface parameters: application to a mesoscale meteorological model. *International Journal of Remote Sensing*, 25:129–143, 1 2004. ISSN 0143-1161. doi: 10.1080/0143116031000115201. URL https://www.tandfonline.com/doi/full/10.1080/0143116031000115201.

A. Piorr, I. Zasada, A. Doernberg, F. Zoll, and W. Ramme. *Research for AGRI committee- Urban and Peri-urban agirculture in the EU*. 2018.

J. R. Porter and M. A. Semenov. Crop responses to climatic variation. *Philosophical Transactions of the Royal Society B: Biological Sciences*, 360:2021–2035, 11 2005. ISSN 0962-8436. doi: 10.1098/rstb.2005.1752.

A. G. Power. Ecosystem services and agriculture: tradeoffs and synergies. *Philosophical Transactions of the Royal Society B: Biological Sciences*, 365:2959–2971, 9 2010. ISSN 0962-8436. doi: 10.1098/rstb.2010.0143.

C. Pérez, P. Jiménez, O. Jorba, M. Sicard, and J. M. Baldasano. Influence of the pbl scheme on high-resolution photochemical simulations in an urban coastal area over the western mediterranean. *Atmospheric Environment*, 40:5274–5297, 9 2006. ISSN 13522310. doi:

10.1016/j.atmosenv.2006.04.039. URL https://linkinghub.elsevier.com/retrieve/pii/S1352231006004079.

R. Qiu, X. Li, G. Han, J. Xiao, X. Ma, and W. Gong. Monitoring drought impacts on crop productivity of the u.s. midwest with solar-induced fluorescence: Gosif outperforms gome-2 sif and modis ndvi, evi, and nirv. *Agricultural and Forest Meteorology*, 323, 8 2022. ISSN 01681923. doi: 10.1016/j.agrformet.2022.109038.

L.-P. Qu, J. Chen, J. Xiao, H. J. D. Boeck, G. Dong, S.-C. Jiang, Y.-L. Hu, Y.-X. Wang, and C.-L. Shao. The complexity of heatwaves impact on terrestrial ecosystem carbon fluxes: Factors, mechanisms and a multi-stage analytical approach. *Environmental Research*, 240:117495, 1 2024. ISSN 00139351. doi: 10.1016/j.envres.2023.117495.

M. A. Rahman, C. Hartmann, A. Moser-Reischl, M. F. von Strachwitz, H. Paeth, H. Pretzsch, S. Pauleit, and T. Rötzer. Tree cooling effects and human thermal comfort under contrasting species and sites. *Agricultural and Forest Meteorology*, 287:107947, 6 2020. ISSN 01681923. doi: 10.1016/j.agrformet.2020.107947.

P. V. Rajesh, S. Pattnaik, D. Rai, K. K. Osuri, U. C. Mohanty, and S. Tripathy. Role of land state in a high resolution mesoscale model for simulating the uttarakhand heavy rainfall event over india. *Journal of Earth System Science*, 125:475–498, 4 2016. ISSN 0253-4126. doi: 10.1007/s12040-016-0678-x.

M. Ramonet, P. Ciais, F. Apadula, J. Bartyzel, A. Bastos, P. Bergamaschi, P. E. Blanc, D. Brunner, L. C. di Torchiarolo, F. Calzolari, H. Chen, L. Chmura, A. Colomb, S. Conil, P. Cristofanelli, E. Cuevas, R. Curcoll, M. Delmotte, A. di Sarra, L. Emmenegger, G. Forster, A. Frumau, C. Gerbig, F. Gheusi, S. Hammer, L. Haszpra, J. Hatakka, L. Hazan, M. Heliasz, S. Henne, A. Hensen, O. Hermansen, P. Keronen, R. Kivi, K. Komínková, D. Kubistin, O. Laurent, T. Laurila, J. V. Lavric, I. Lehner, K. E. J. Lehtinen, A. Leskinen, M. Leuenberger, I. Levin, M. Lindauer, M. Lopez, C. L. Myhre, I. Mammarella, G. Manca, A. Manning, M. V. Marek, P. Marklund, D. Martin, F. Meinhardt, N. Mihalopoulos, M. Mölder, J. A. Morgui, J. Necki, S. O'Doherty, C. O'Dowd, M. Ottosson, C. Philippon, S. Piacentino, J. M. Pichon, C. Plass-Duelmer, A. Resovsky, L. Rivier, X. Rodó, M. K. Sha, H. A. Scheeren, D. Sferlazzo, T. G. Spain, K. M. Stanley, M. Steinbacher, P. Trisolino, A. Vermeulen, G. Vítková, D. Weyrauch, I. Xueref-Remy, K. Yala, and C. Y. Kwok. The fingerprint of the summer 2018 drought in europe on ground-based atmospheric co2 measurements. *Philosophical Transactions of the Royal Society B: Biological Sciences*, 375:20190513, 10 2020. ISSN 0962-8436. doi: 10.1098/rstb.2019.0513. URL https://royalsocietypublishing.org/doi/10.1098/rstb.2019.0513.

M. Reichstein, A. Rey, A. Freibauer, J. Tenhunen, R. Valentini, J. Banza, P. Casals, Y. Cheng, J. M. Grünzweig, J. Irvine, R. Joffre, B. E. Law, D. Loustau, F. Miglietta, W. Oechel, J.-M. Ourcival, J. S. Pereira, A. Peressotti, F. Ponti, Y. Qi, S. Rambal, M. Rayment, J. Romanya, F. Rossi, V. Tedeschi, G. Tirone, M. Xu, and D. Yakir. Modeling temporal and large-scale spatial variability of soil respiration from soil water availability, temperature and vegetation

productivity indices. *Global Biogeochemical Cycles*, 17, 12 2003. ISSN 08866236. doi: 10.1029/2003GB002035. URL http://doi.wiley.com/10.1029/2003GB002035.

M. Reichstein, E. Falge, D. Baldocchi, D. Papale, M. Aubinet, P. Berbigier, C. Bernhofer, N. Buchmann, T. Gilmanov, A. Granier, T. Grunwald, K. Havrankova, H. Ilvesniemi, D. Janous, A. Knohl, T. Laurila, A. Lohila, D. Loustau, G. Matteucci, T. Meyers, F. Miglietta, J.-M. Ourcival, J. Pumpanen, S. Rambal, E. Rotenberg, M. Sanz, J. Tenhunen, G. Seufert, F. Vaccari, T. Vesala, D. Yakir, and R. Valentini. On the separation of net ecosystem exchange into assimilation and ecosystem respiration: review and improved algorithm. *Global Change Biology*, 11:1424–1439, 9 2005. ISSN 1354-1013. doi: 10.1111/j.1365-2486.2005.001002.x. URL https://onlinelibrary.wiley.com/doi/10.1111/j.1365-2486.2005.001002.x.

M. Reichstein, P. Ciais, D. Papale, R. Valentini, S. Running, N. Viovy, W. Cramer, A. Granier, J. Ogée, V. Allard, M. Aubinet, C. Bernhofer, N. Buchmann, A. Carrara, T. Grünwald, M. Heimann, B. Heinesch, A. Knohl, W. Kutsch, D. Loustau, G. Manca, G. Matteucci, F. Miglietta, J. M. Ourcival, K. Pilegaard, J. Pumpanen, S. Rambal, S. Schaphoff, G. Seufert, J. F. Soussana, M. J. Sanz, T. Vesala, and M. Zhao. Reduction of ecosystem productivity and respiration during the european summer 2003 climate anomaly: A joint flux tower, remote sensing and modelling analysis. *Global Change Biology*, 13:634–651, 3 2007. ISSN 13541013. doi: 10.1111/j.1365-2486.2006.01224.x.

M. Reichstein, M. Bahn, P. Ciais, D. Frank, M. D. Mahecha, S. I. Seneviratne, J. Zscheischler, C. Beer, N. Buchmann, D. C. Frank, D. Papale, A. Rammig, P. Smith, K. Thonicke, M. van der Velde, S. Vicca, A. Walz, and M. Wattenbach. Climate extremes and the carbon cycle. *Nature*, 500:287–295, 8 2013. ISSN 0028-0836. doi: 10.1038/nature12350. URL http://www.nature.com/articles/nature12350.

D. Reidmiller, C. Avery, D. Easterling, K. Kunkel, K. Lewis, T. Maycock, and B. Stewart. Impacts, risks, and adaptation in the united states: The fourth national climate assessment, volume ii, 2018.

A. Revi, D. Satterthwaite, F. Aragón-Durand, J. Corfee-Morlot, R. Kiunsi, M. Pelling, D. Roberts, and W. Solecki. Urban areas. in: Climate change 2014: Impacts, adaptation, and vulnerability. part a: Global and sectoral aspects. contribution of working group ii to the fifth assessment report of the intergovernmental panel on climate change. e [field, c.b., v.r. barros, d.j. dokken, k.j. mach, m.d. mastrandrea, t.e. bilir, m. chatterjee, k.l. ebi, y.o. estrada, r.c. genova, b. girma, e.s. kissel, a.n. levy, s. maccracken, p.r. mastrandrea, and l.l.white (eds.)]., 2014.

I. RI. Ecosystem final quality (l2) product in etc-archive format - release 2022-1 (version 1.0). icos eric - carbon portal., 2022.

I. Ribeiro, A. Martilli, M. Falls, A. Zonato, and G. Villalba. Highly resolved wrf-bep/bem simulations over barcelona urban area with lcz. *Atmospheric Research*, 248:105220, 1 2021. ISSN

01698095. doi: 10.1016/j.atmosres.2020.105220. URL https://linkinghub.elsevier.com/retrieve/pii/S016980952031156X.

Y. Richard, B. Pohl, M. Rega, J. Pergaud, T. Thevenin, J. Emery, J. Dudek, T. Vairet, S. Zito, and C. Chateau-Smith. Is urban heat island intensity higher during hot spells and heat waves (dijon, france, 2014–2019)? *Urban Climate*, 35:100747, 1 2021. ISSN 22120955. doi: 10.1016/j.uclim.2020.100747.

A. Rita, J. J. Camarero, A. Nolè, M. Borghetti, M. Brunetti, N. Pergola, C. Serio, S. M. Vicente-Serrano, V. Tramutoli, and F. Ripullone. The impact of drought spells on forests depends on site conditions: The case of 2017 summer heat wave in southern europe. *Global Change Biology*, 26:851–863, 2 2020. ISSN 1354-1013. doi: 10.1111/gcb.14825. URL https://onlinelibrary.wiley.com/doi/10.1111/gcb.14825.

M. Rufí-Salís, J. Garcia-Orellana, G. Cantero, J. Castillo, A. Hierro, J. Rieradevall, and J. Bach. Influence of land use changes on submarine groundwater discharge. *Environmental Research Communications*, 1:031005, 4 2019. ISSN 2515-7620. doi: 10.1088/2515-7620/ab1695.

M. G. Ryan and B. E. Law. Interpreting, measuring, and modeling soil respiration. *Biogeochemistry*, 73:3–27, 3 2005. ISSN 0168-2563. doi: 10.1007/s10533-004-5167-7.

Y.-H. Ryu and J.-J. Baik. Quantitative analysis of factors contributing to urban heat island intensity. *Journal of Applied Meteorology and Climatology*, 51:842–854, 5 2012. ISSN 1558-8424. doi: 10.1175/JAMC-D-11-098.1.

Y.-H. Ryu, E. Bou-Zeid, Z.-H. Wang, and J. A. Smith. Realistic representation of trees in an urban canopy model. *Boundary-Layer Meteorology*, 159:193–220, 5 2016. ISSN 0006-8314. doi: 10.1007/s10546-015-0120-y.

W. J. Sacks, B. I. Cook, N. Buenning, S. Levis, and J. H. Helkowski. Effects of global irrigation on the near-surface climate. *Climate Dynamics*, 33, 2009. ISSN 09307575. doi: 10.1007/s00382-008-0445-z.

F. Salamanca and A. Martilli. A new building energy model coupled with an urban canopy parameterization for urban climate simulations-part ii. validation with one dimension off-line simulations. *Theoretical and Applied Climatology*, 2010. ISSN 14344483. doi: 10.1007/s00704-009-0143-8.

F. Salamanca, A. Martilli, and C. Yagüe. A numerical study of the urban heat island over madrid during the desirex (2008) campaign with wrf and an evaluation of simple mitigation strategies. *International Journal of Climatology*, 32:2372–2386, 12 2012. ISSN 08998418. doi: 10.1002/joc.3398. URL http://doi.wiley.com/10.1002/joc.3398.

J. A. Salmond, M. Tadaki, S. Vardoulakis, K. Arbuthnott, A. Coutts, M. Demuzere, K. N. Dirks, C. Heaviside, S. Lim, H. Macintyre, R. N. McInnes, and B. W. Wheeler. Health and climate related ecosystem services provided by street trees in the urban environment. *Environmental Health*, 15:S36, 12 2016. ISSN 1476-069X. doi: 10.1186/s12940-016-0103-6.

D. Santaren, P. Peylin, C. Bacour, P. Ciais, and B. Longdoz. Ecosystem model optimization using in situ flux observations: benefit of monte carlo versus variational schemes and analyses of the year-to-year model performances. *Biogeosciences*, 11:7137–7158, 12 2014. ISSN 1726-4189. doi: 10.5194/bg-11-7137-2014.

J. L. Santiago and A. Martilli. A dynamic urban canopy parameterization for mesoscale models based on computational fluid dynamics reynolds-averaged navier–stokes microscale simulations. *Boundary-Layer Meteorology*, 137:417–439, 12 2010. ISSN 0006-8314. doi: 10.1007/s10546-010-9538-4.

K. E. Saxton and W. J. Rawls. Soil water characteristic estimates by texture and organic matter for hydrologic solutions. *Soil Science Society of America Journal*, 70:1569–1578, 9 2006. ISSN 03615995. doi: 10.2136/sssaj2005.0117. URL http://doi.wiley.com/10.2136/sssaj2005.0117.

J. Schatz and C. J. Kucharik. Seasonality of the urban heat island effect in madison, wisconsin. *Journal of Applied Meteorology and Climatology*, 53:2371–2386, 10 2014. ISSN 1558-8424. doi: 10.1175/JAMC-D-14-0107.1.

J. Schatz and C. J. Kucharik. Urban climate effects on extreme temperatures in madison, wisconsin, usa. *Environmental Research Letters*, 10:094024, 9 2015. ISSN 1748-9326. doi: 10.1088/1748-9326/10/9/094024.

D. Schimel, B. B. Stephens, and J. B. Fisher. Effect of increasing co2 on the terrestrial carbon cycle. *Proceedings of the National Academy of Sciences*, 112:436–441, 1 2015. ISSN 0027-8424. doi: 10.1073/pnas.1407302112.

R. Segura, A. Badia, S. Ventura, J. Gilabert, A. Martilli, and G. Villalba. Sensitivity study of pbl schemes and soil initialization using the wrf-bep-bem model over a mediterranean coastal city. *Urban Climate*, 39, 2021. ISSN 22120955. doi: 10.1016/j.uclim.2021.100982.

R. Segura, E. S. Krayenhoff, A. Martilli, A. Badia, C. Estruch, S. Ventura, and G. Villalba. How do street trees affect urban temperatures and radiation exchange? observations and numerical evaluation in a highly compact city. *Urban Climate*, 46:101288, 12 2022. ISSN 22120955. doi: 10.1016/j.uclim.2022.101288.

P. Seibert. Review and intercomparison of operational methods for the determination of the mixing height. *Atmospheric Environment*, 34:1001–1027, 2000. ISSN 13522310. doi: 10.1016/S1352-2310(99)00349-0.

P. J. Sellers, Y. Mintz, Y. C. Sud, and A. Dalcher. A simple biosphere model (sib) for use within general circulation models. *Journal of the Atmospheric Sciences*, 43:505–531, 3 1986. ISSN 0022-4928. doi: 10.1175/1520-0469(1986)043<0505:ASBMFU>2.0.CO;2.

S. I. Seneviratne, D. Lüthi, M. Litschi, and C. Schär. Land–atmosphere coupling and climate change in europe. *Nature*, 443:205–209, 9 2006. ISSN 0028-0836. doi: 10.1038/nature05095.

T. Serrano-Tovar, R. Padró, M. L. Rota-Aguilera, R. Velasco-Fernández, and J. Marull. Metabolismo hídrico de la infraestructura verde del Área metropolitana de barcelona. *Papers: Regio Metropolitana de Barcelona: Territori, estratègies, plantejament*, 64:130–141, 2022.

Servei Meteorològic de Catalunya (SMC). Butlletí climàtic mensual (juliol del 2015). departament de territori i sostenibilitat. https://static-m.meteo.cat/wordpressweb/wp-ontent/uploads/2015/06/08111706/butllet

A. Sharma, H. J. S. Fernando, J. Hellmann, and F. Chen. Sensitivity of wrf model to urban parameterizations, with applications to chicago metropolitan urban heat island. American Society of Mechanical Engineers, 8 2014. ISBN 978-0-7918-4624-7. doi: 10.1115/FEDSM2014-21292. URL https://asmedigitalcollection.asme.org/FEDSM/proceedings/FEDSM2014/46247/Chicago,Illinois,USA/232506.

A. Sharma, P. Conry, H. J. S. Fernando, A. F. Hamlet, J. J. Hellmann, and F. Chen. Green and cool roofs to mitigate urban heat island effects in the chicago metropolitan area: evaluation with a regional climate model. *Environmental Research Letters*, 11:064004, 6 2016. ISSN 1748-9326. doi: 10.1088/1748-9326/11/6/064004. URL https://iopscience.iop.org/article/10.1088/1748-9326/11/6/064004.

A. Sharma, H. J. Fernando, A. F. Hamlet, J. J. Hellmann, M. Barlage, and F. Chen. Urban meteorological modeling using wrf: a sensitivity study. *International Journal of Climatology*, 37:1885–1900, 3 2017. ISSN 08998418. doi: 10.1002/joc.4819. URL http://doi.wiley.com/10.1002/joc.4819.

L. Shashua-Bar and M. Hoffman. Vegetation as a climatic component in the design of an urban street. *Energy and Buildings*, 31:221–235, 4 2000. ISSN 03787788. doi: 10.1016/S0378-7788(99)00018-3.

S. A. Shiflett, L. L. Liang, S. M. Crum, G. L. Feyisa, J. Wang, and G. D. Jenerette. Variation in the urban vegetation, surface temperature, air temperature nexus. *Science of The Total Environment*, 579:495–505, 2 2017. ISSN 00489697. doi: 10.1016/j.scitotenv.2016.11.069.

M. Sicard, C. Pérez, F. Rocadenbosch, J. M. Baldasano, and D. García-Vizcaino. Mixed-layer depth determination in the barcelona coastal area from regular lidar measurements: Methods, results and limitations. *Boundary-Layer Meteorology*, 119:135–157, 5 2006. ISSN 0006-8314. doi: 10.1007/s10546-005-9005-9. URL http://link.springer.com/10.1007/s10546-005-9005-9.

W. C. Skamarock, J. B. Klemp, J. B. Dudhia, D. O. Gill, D. M. Barker, M. G. Duda, X.-Y. Huang, W. Wang, and J. G. Powers. A description of the advanced research wrf model version 4.3, 2021. ISSN 1477870X.

B. Smets, A. Verger, F. Camacho, R. V. der Goten, and J. Jacobs. Product user manual, vegetation and energy, collection 1km, version 2. copernicus publication – product user manual. retrieved from

https://land.copernicus.eu/global/sites/cgls.vito.be/files/products/cglops1_pum_fcover1km-v2_i1.33.pdf. 2019.

M. D. Smith, K. D. Wilkins, M. C. Holdrege, P. Wilfahrt, S. L. Collins, A. K. Knapp, O. E. Sala, J. S. Dukes, R. P. Phillips, L. Yahdjian, L. A. Gherardi, T. Ohlert, C. Beier, L. H. Fraser, A. Jentsch, M. E. Loik, F. T. Maestre, S. A. Power, Q. Yu, A. J. Felton, S. M. Munson, Y. Luo, H. Abdoli, M. Abedi, C. L. Alados, J. Alberti, M. Alon, H. An, B. Anacker, M. Anderson, H. Auge, S. Bachle, K. Bahalkeh, M. Bahn, A. Batbaatar, T. Bauerle, K. H. Beard, K. Behn, I. Beil, L. Biancari, I. Blindow, V. F. Bondaruk, E. T. Borer, E. W. Bork, C. M. Bruschetti, K. M. Byrne, J. F. C. Jr., D. A. Calvo, M. Carbognani, A. Cardoni, C. N. Carlyle, M. Castillo-Garcia, S. X. Chang, J. Chieppa, M. V. Cianciaruso, O. Cohen, A. L. Cordeiro, D. F. Cusack, S. Dahlke, P. Daleo, C. M. D'Antonio, L. H. Dietterich, T. S. Doherty, M. Dubbert, A. Ebeling, N. Eisenhauer, F. M. Fischer, T. G. W. Forte, T. Gebauer, B. Gozalo, A. C. Greenville, K. G. Guidoni-Martins, H. J. Hannusch, S. V. Haugum, Y. Hautier, M. Hefting, H. A. L. Henry, D. Hoss, J. Ingrisch, O. Iribarne, F. Isbell, Y. Johnson, S. Jordan, E. F. Kelly, K. Kimmel, J. Kreyling, G. Kröel-Dulay, A. Kröpfl, A. Kübert, A. Kulmatiski, E. G. Lamb, K. S. Larsen, J. Larson, J. Lawson, C. V. Leder, A. Linstädter, J. Liu, S. Liu, A. G. Lodge, G. Longo, A. Loydi, J. Luan, F. C. Lubbe, C. Macfarlane, K. Mackie-Haas, A. V. Malyshev, A. Maturano-Ruiz, T. Merchant, D. B. Metcalfe, A. S. Mori, E. Mudongo, G. S. Newman, U. N. Nielsen, D. Nimmo, Y. Niu, P. Nobre, R. C. O'Connor, R. Ogaya, G. R. Oñatibia, I. Orbán, B. Osborne, R. Otfinowski, M. Pärtel, J. Penuelas, P. L. Peri, G. Peter, A. Petraglia, C. Picon-Cochard, V. D. Pillar, J. M. Piñeiro-Guerra, L. W. Ploughe, R. M. Plowes, C. Portales-Reyes, S. M. Prober, Y. Pueyo, S. C. Reed, E. G. Ritchie, D. A. Rodríguez, W. E. Rogers, C. Roscher, A. M. Sánchez, B. A. Santos, M. C. Scarfó, E. W. Seabloom, B. Shi, L. Souza, A. Stampfli, R. J. Standish, M. Sternberg, W. Sun, M. Sünnemann, M. Tedder, P. Thorvaldsen, D. Tian, K. Tielbörger, A. Valdecantos, L. van den Brink, V. Vandvik, M. R. Vankoughnett, L. G. Velle, C. Wang, Y. Wang, G. M. Wardle, C. Werner, C. Wei, G. Wiehl, J. L. Williams, A. A. Wolf, M. Zeiter, F. Zhang, J. Zhu, N. Zong, and X. Zuo. Extreme drought impacts have been underestimated in grasslands and shrublands globally. *Proceedings of the National Academy of Sciences*, 121, 1 2024. ISSN 0027-8424. doi: 10.1073/pnas.2309881120.

P. Smith, D. Martino, Z. Cai, D. Gwary, H. Janzen, P. Kumar, B. McCarl, S. Ogle, F. O'Mara, C. Rice, B. Scholes, O. Sirotenko, M. Howden, T. McAllister, G. Pan, V. Romanenkov, U. Schneider, S. Towprayoon, M. Wattenbach, and J. Smith. Greenhouse gas mitigation in agriculture. *Philosophical Transactions of the Royal Society B: Biological Sciences*, 363: 789–813, 2 2008. ISSN 0962-8436. doi: 10.1098/rstb.2007.2184.

M. R. Soler, R. Arasa, M. Merino, M. Olid, and S. Ortega. Modelling local sea-breeze flow and associated dispersion patterns over a coastal area in north-east spain: A case study. *Boundary-Layer Meteorology*, 140:37–56, 7 2011. ISSN 0006-8314. doi: 10.1007/s10546-011-9599-z. URL `http://link.springer.com/10.1007/s10546-011-9599-z`.

N. L. Stephenson, A. J. Das, R. Condit, S. E. Russo, P. J. Baker, N. G. Beckman, D. A. Coomes, E. R. Lines, W. K. Morris, N. Rüger, E. Álvarez, C. Blundo, S. Bunyavejchewin, G. Chuyong,

S. J. Davies, A. Duque, C. N. Ewango, O. Flores, J. F. Franklin, H. R. Grau, Z. Hao, M. E. Harmon, S. P. Hubbell, D. Kenfack, Y. Lin, J.-R. Makana, A. Malizia, L. R. Malizia, R. J. Pabst, N. Pongpattananurak, S.-H. Su, I.-F. Sun, S. Tan, D. Thomas, P. J. van Mantgem, X. Wang, S. K. Wiser, and M. A. Zavala. Rate of tree carbon accumulation increases continuously with tree size. *Nature*, 507:90–93, 3 2014. ISSN 0028-0836. doi: 10.1038/nature12914.

I. D. Stewart and T. R. Oke. Local climate zones for urban temperature studies. *Bulletin of the American Meteorological Society*, 93:1879–1900, 12 2012. ISSN 00030007. doi: 10.1175/BAMS-D-11-00019.1.

I. D. Stewart, T. R. Oke, and E. S. Krayenhoff. Evaluation of the 'local climate zone' scheme using temperature observations and model simulations. *International Journal of Climatology*, 34:1062–1080, 3 2014. ISSN 08998418. doi: 10.1002/joc.3746. URL http://doi.wiley.com/10.1002/joc.3746.

B. D. Stocker, J. Zscheischler, T. F. Keenan, I. C. Prentice, J. Peñuelas, and S. I. Seneviratne. Quantifying soil moisture impacts on light use efficiency across biomes. *New Phytologist*, 218:1430–1449, 6 2018. ISSN 0028-646X. doi: 10.1111/nph.15123. URL https://onlinelibrary.wiley.com/doi/10.1111/nph.15123.

B. D. Stocker, J. Zscheischler, T. F. Keenan, I. C. Prentice, S. I. Seneviratne, and J. Peñuelas. Drought impacts on terrestrial primary production underestimated by satellite monitoring. *Nature Geoscience*, 12:264–270, 4 2019. ISSN 1752-0894. doi: 10.1038/s41561-019-0318-6. URL http://www.nature.com/articles/s41561-019-0318-6.

B. Stone, E. Mallen, M. Rajput, A. Broadbent, E. S. Krayenhoff, G. Augenbroe, and M. Georgescu. Climate change and infrastructure risk: Indoor heat exposure during a concurrent heat wave and blackout event in phoenix, arizona. *Urban Climate*, 36:100787, 3 2021. ISSN 22120955. doi: 10.1016/j.uclim.2021.100787.

P. A. Stott, D. A. Stone, and M. R. Allen. Human contribution to the european heatwave of 2003. *Nature*, 432:610–614, 12 2004. ISSN 0028-0836. doi: 10.1038/nature03089. URL http://www.nature.com/articles/nature03089.

Stratópoulos, Zhang, Häberle, Pauleit, Duthweiler, Pretzsch, and Rötzer. Effects of drought on the phenology, growth, and morphological development of three urban tree species and cultivars. *Sustainability*, 11:5117, 9 2019. ISSN 2071-1050. doi: 10.3390/su11185117.

R. Stull. *An Introduction to Boundary Layer Meteorology*. Springer Netherlands, 1988. ISBN 978-90-277-2769-5. doi: 10.1007/978-94-009-3027-8.

R. Stull. *Meteorology for Scientists and Engineers.* Brooks/Cole Thomson Learning, Pacific Grove, 2nd edition edition, 2000.

A. Sánchez-Benítez, R. García-Herrera, D. Barriopedro, P. M. Sousa, and R. M. Trigo. June 2017: The earliest european summer mega-heatwave of reanalysis period. *Geophysical Research Letters*, 45:1955–1962, 2 2018. ISSN 00948276. doi: 10.1002/2018GL077253.

H. Taha, H. Akbari, and A. Rosenfeld. Heat island and oasis effects of vegetative canopies: Micro-meteorological field-measurements. *Theoretical and Applied Climatology*, 44:123–138, 1991. ISSN 0177-798X. doi: 10.1007/BF00867999.

J. Tan, Y. Zheng, X. Tang, C. Guo, L. Li, G. Song, X. Zhen, D. Yuan, A. J. Kalkstein, F. Li, and H. Chen. The urban heat island and its impact on heat waves and human health in shanghai. *International Journal of Biometeorology*, 54:75–84, 1 2010. ISSN 0020-7128. doi: 10.1007/s00484-009-0256-x.

TEEB. Teeb manual for cities: Ecosystem services in urban management., 2011.

J. Teixeira, J. Fallmann, A. Carvalho, and A. Rocha. Surface to boundary layer coupling in the urban area of lisbon comparing different urban canopy models in wrf. *Urban Climate*, 28:100454, 6 2019. ISSN 22120955. doi: 10.1016/j.uclim.2019.100454.

R. Teskey, T. Wertin, I. Bauweraerts, M. Ameye, M. A. Mcguire, and K. Steppe. Responses of tree species to heat waves and extreme heat events. *Plant, Cell & Environment*, 38:1699–1712, 9 2015. ISSN 0140-7791. doi: 10.1111/pce.12417.

A. J. Teuling, S. I. Seneviratne, R. Stöckli, M. Reichstein, E. Moors, P. Ciais, S. Luyssaert, B. van den Hurk, C. Ammann, C. Bernhofer, E. Dellwik, D. Gianelle, B. Gielen, T. Grünwald, K. Klumpp, L. Montagnani, C. Moureaux, M. Sottocornola, and G. Wohlfahrt. Contrasting response of european forest and grassland energy exchange to heatwaves. *Nature Geoscience*, 3:722–727, 10 2010. ISSN 1752-0894. doi: 10.1038/ngeo950.

P. E. Thornton, J.-F. Lamarque, N. A. Rosenbloom, and N. M. Mahowald. Influence of carbon-nitrogen cycle coupling on land model response to co 2 fertilization and climate variability. *Global Biogeochemical Cycles*, 21:n/a–n/a, 12 2007. ISSN 08866236. doi: 10.1029/2006GB002868.

D. Tilman. Global environmental impacts of agricultural expansion: The need for sustainable and efficient practices. *Proceedings of the National Academy of Sciences*, 96:5995–6000, 5 1999. ISSN 0027-8424. doi: 10.1073/pnas.96.11.5995.

C. Tremback and R. Kessler. A surface temperature and moisture paramterization for use in mesoscale numerical models. 7th conference on numerical weather prediction, 17-20 june 1985, montreal, canada, ams [preprint]. 1985.

A. Trucchia, G. Meschi, P. Fiorucci, A. Gollini, and D. Negro. Defining wildfire susceptibility maps in italy for understanding seasonal wildfire regimes at the national level. *Fire*, 5:30, 2 2022. ISSN 2571-6255. doi: 10.3390/fire5010030.

F. Turkelboom, M. Leone, S. Jacobs, E. Kelemen, M. García-Llorente, F. Baró, M. Termansen, D. N. Barton, P. Berry, E. Stange, M. Thoonen, Ágnes Kalóczkai, A. Vadineanu, A. J. Castro, B. Czúcz, C. Röckmann, D. Wurbs, D. Odee, E. Preda, E. Gómez-Baggethun, G. M. Rusch, G. M. Pastur, I. Palomo, J. Dick, J. Casaer, J. van Dijk, J. A. Priess, J. Langemeyer, J. Mustajoki, L. Kopperoinen, M. J. Baptist, P. L. Peri, R. Mukhopadhyay, R. Aszalós, S. Roy,

S. Luque, and V. Rusch. When we cannot have it all: Ecosystem services trade-offs in the context of spatial planning. *Ecosystem Services*, 29:566–578, 2 2018. ISSN 22120416. doi: 10.1016/j.ecoser.2017.10.011.

United Nations. *World Urbanization Prospects: The 2018 Revision*. UN, 8 2019. ISBN 9789210043144. doi: 10.18356/b9e995fe-en.

United Nations Environment Programme. Resolution adopted by the united nations environment assembly on 2 march 2022 5/5. nature-based solutions for supporting sustainable development, 2022.

United Nations Framework Convention on Climate Change (UNFCCC). Decision 1/cp.21: Adoption of the paris agreement (no. fccc/cp/2015/l.9/rev.1. 12 dec). unfccc. retrieved from https://unfccc.int/resource/docs/2015/cop21/eng/l09r01.pdf, 2015.

United States Geological Survey (USGS). Earth explorer. https://earthexplorer.usgs.gov/ (accessed 16 july 2019)., 2019.

P. Vahmani and T. S. Hogue. Incorporating an urban irrigation module into the noah land surface model coupled with an urban canopy model. *Journal of Hydrometeorology*, 15:1440–1456, 8 2014. ISSN 1525-755X. doi: 10.1175/JHM-D-13-0121.1.

A. Valmassoi, J. Dudhia, S. D. Sabatino, and F. Pilla. Evaluation of three new surface irrigation parameterizations in the wrf-arw v3.8.1 model: the po valley (italy) case study. *Geoscientific Model Development*, 13:3179–3201, 7 2020. ISSN 1991-9603. doi: 10.5194/gmd-13-3179-2020.

A. van der Woude, R. de Kok, I. Luijkx, W. Peters, and N. Smith. High-resolution, near-real-time fluxes over europe from cte-hr: ocean fluxes 2023-01, icos ri, https://hdl.handle.net/11676/_le7rhnxlmmwsdi3fiysl-8k, 2023a.

A. M. van der Woude, W. Peters, E. Joetzjer, S. Lafont, G. Koren, P. Ciais, M. Ramonet, Y. Xu, A. Bastos, S. Botía, S. Sitch, R. de Kok, T. Kneuer, D. Kubistin, A. Jacotot, B. Loubet, P.-H. Herig-Coimbra, D. Loustau, and I. T. Luijkx. Temperature extremes of 2022 reduced carbon uptake by forests in europe. *Nature Communications*, 14:6218, 10 2023b. ISSN 2041-1723. doi: 10.1038/s41467-023-41851-0.

E. Vermote. Mod09a1 modis/terra surface reflectance 8-day l3 global 500m sin grid v006 [data set]. nasa eosdis land processes daac. accessed 2023-04-12 from https://doi.org/10.5067/modis/mod09a1.006, 2015.

E. Vermote, C. Justice, M. Claverie, and B. Franch. Preliminary analysis of the performance of the landsat 8/oli land surface reflectance product. *Remote Sensing of Environment*, 185: 46–56, 11 2016. ISSN 00344257. doi: 10.1016/j.rse.2016.04.008.

S. M. Vicente-Serrano, S. Beguería, and J. I. López-Moreno. A multiscalar drought index sensitive to global warming: The standardized precipitation evapotranspiration index. *Journal of Climate*, 23:1696–1718, 4 2010. ISSN 1520-0442. doi: 10.1175/2009JCLI2909.1.

S. M. Vicente-Serrano, C. M. Gouveia, J. J. Camarero, S. Beguería, R. Trigo, J. I. López-Moreno, C. Azorín-Molina, E. Pasho, J. Lorenzo-Lacruz, J. Revuelto, E. Morán-Tejeda, and A. Sanchez-Lorenzo. Response of vegetation to drought time-scales across global land biomes. *Proceedings of the National Academy of Sciences*, 110:52–57, 1 2013. ISSN 0027-8424. doi: 10.1073/pnas.1207068110.

S. M. Vicente-Serrano, J.-I. Lopez-Moreno, S. Beguería, J. Lorenzo-Lacruz, A. Sanchez-Lorenzo, J. M. García-Ruiz, C. Azorin-Molina, E. Morán-Tejeda, J. Revuelto, R. Trigo, F. Coelho, and F. Espejo. Evidence of increasing drought severity caused by temperature rise in southern europe. *Environmental Research Letters*, 9:044001, 4 2014. ISSN 1748-9326. doi: 10.1088/1748-9326/9/4/044001. URL https://iopscience.iop.org/article/10.1088/1748-9326/9/4/044001.

G. Vico, R. Revelli, and A. Porporato. Ecohydrology of street trees: design and irrigation requirements for sustainable water use. *Ecohydrology*, 7:508–523, 4 2014. ISSN 1936-0584. doi: 10.1002/eco.1369.

P. Virtanen, R. Gommers, T. E. Oliphant, M. Haberland, T. Reddy, D. Cournapeau, E. Burovski, P. Peterson, W. Weckesser, J. Bright, S. J. van der Walt, M. Brett, J. Wilson, K. J. Millman, N. Mayorov, A. R. J. Nelson, E. Jones, R. Kern, E. Larson, C. J. Carey, İlhan Polat, Y. Feng, E. W. Moore, J. VanderPlas, D. Laxalde, J. Perktold, R. Cimrman, I. Henriksen, E. A. Quintero, C. R. Harris, A. M. Archibald, A. H. Ribeiro, F. Pedregosa, P. van Mulbregt, A. Vijaykumar, A. P. Bardelli, A. Rothberg, A. Hilboll, A. Kloeckner, A. Scopatz, A. Lee, A. Rokem, C. N. Woods, C. Fulton, C. Masson, C. Häggström, C. Fitzgerald, D. A. Nicholson, D. R. Hagen, D. V. Pasechnik, E. Olivetti, E. Martin, E. Wieser, F. Silva, F. Lenders, F. Wilhelm, G. Young, G. A. Price, G.-L. Ingold, G. E. Allen, G. R. Lee, H. Audren, I. Probst, J. P. Dietrich, J. Silterra, J. T. Webber, J. Slavič, J. Nothman, J. Buchner, J. Kulick, J. L. Schönberger, J. V. de Miranda Cardoso, J. Reimer, J. Harrington, J. L. C. Rodríguez, J. Nunez-Iglesias, J. Kuczynski, K. Tritz, M. Thoma, M. Newville, M. Kümmerer, M. Bolingbroke, M. Tartre, M. Pak, N. J. Smith, N. Nowaczyk, N. Shebanov, O. Pavlyk, P. A. Brodtkorb, P. Lee, R. T. McGibbon, R. Feldbauer, S. Lewis, S. Tygier, S. Sievert, S. Vigna, S. Peterson, S. More, T. Pudlik, T. Oshima, T. J. Pingel, T. P. Robitaille, T. Spura, T. R. Jones, T. Cera, T. Leslie, T. Zito, T. Krauss, U. Upadhyay, Y. O. Halchenko, and Y. Vázquez-Baeza. Scipy 1.0: fundamental algorithms for scientific computing in python. *Nature Methods*, 17:261–272, 3 2020. ISSN 1548-7091. doi: 10.1038/s41592-019-0686-2.

J. von Buttlar, J. Zscheischler, A. Rammig, S. Sippel, M. Reichstein, A. Knohl, M. Jung, O. Menzer, M. A. Arain, N. Buchmann, A. Cescatti, D. Gianelle, G. Kiely, B. E. Law, V. Magliulo, H. Margolis, H. McCaughey, L. Merbold, M. Migliavacca, L. Montagnani, W. Oechel, M. Pavelka, M. Peichl, S. Rambal, A. Raschi, R. L. Scott, F. P. Vaccari, E. van Gorsel, A. Varlagin, G. Wohlfahrt, and M. D. Mahecha. Impacts of droughts and extreme-temperature events on gross primary production and ecosystem respiration: a systematic assessment across ecosystems and climate zones. *Biogeosciences*, 15:1293–1318, 3 2018. ISSN 1726-4189. doi: 10.5194/bg-15-1293-2018. URL https://bg.copernicus.org/articles/15/1293/2018/.

J. Wang, J. Sun, J. Xia, N. He, M. Li, and S. Niu. Soil and vegetation carbon turnover times from tropical to boreal forests. *Functional Ecology*, 32:71–82, 1 2018. ISSN 0269-8463. doi: 10.1111/1365-2435.12914.

Warm Winter 2020 Team and ICOS Ecosystem Thematic Centre. Warm winter 2020 ecosystem eddy covariance flux product for 73 stations in fluxnet-archive format—release 2022-1 (version 1.0), 2022. URL https://doi.org/10.18160/2G60-ZHAK.

J. Wieringa. Roughness-dependent geographical interpolation of surface wind speed averages. *Quarterly Journal of the Royal Meteorological Society*, 112:867–889, 7 1986. ISSN 0035-9009. doi: 10.1002/qj.49711247316.

D. Wolfs, A. Verger, R. V. der Goten, and J. Sánchez-Zapatero. Product user manual, vegetation and energy, collection 300m, version 1.1. copernicus publication – product user manual. retrieved from. https://land.copernicus.eu/global/sites/cgls.vito.be/files/products/cglops1_pum_fapar300m-v1.1_i1.20.pdf., 2020.

M. M. F. Wong, J. C. H. Fung, J. Ching, P. P. S. Yeung, J. W. P. Tse, C. Ren, R. Wang, and M. Cai. Evaluation of uwrf performance and modeling guidance based on wudapt and nudapt ucp datasets for hong kong. *Urban Climate*, 28, 6 2019. ISSN 22120955. doi: 10.1016/j.uclim.2019.100460.

X. Xiao, Q. Zhang, D. Hollinger, J. Aber, and M. Berrien. Modeling gross primary production of an evergreen needleleaf forest using modis and climate data. *Ecological Applications*, 15, 2005. ISSN 10510761. doi: 10.1890/04-0470.

X. Xu, F. Chen, S. Shen, S. Miao, M. Barlage, W. Guo, and A. Mahalov. Using wrf-urban to assess summertime air conditioning electric loads and their impacts on urban weather in beijing. *Journal of Geophysical Research: Atmospheres*, 123:2475–2490, 3 2018. ISSN 2169-897X. doi: 10.1002/2017JD028168.

H. Yang, P. Ciais, F. Frappart, X. Li, M. Brandt, R. Fensholt, L. Fan, S. Saatchi, S. Besnard, Z. Deng, S. Bowring, and J.-P. Wigneron. Global increase in biomass carbon stock dominated by growth of northern young forests over past decade. *Nature Geoscience*, 16:886–892, 10 2023. ISSN 1752-0894. doi: 10.1038/s41561-023-01274-4.

J. Yang, Z.-H. Wang, and K. E. Kaloush. Environmental impacts of reflective materials: Is high albedo a 'silver bullet' for mitigating urban heat island? *Renewable and Sustainable Energy Reviews*, 47:830–843, 7 2015. ISSN 13640321. doi: 10.1016/j.rser.2015.03.092.

P. Yu, T. Zhou, H. Luo, X. Liu, P. Shi, Y. Zhang, J. Zhang, P. Zhou, and Y. Xu. Global pattern of ecosystem respiration tendencies and its implications on terrestrial carbon sink potential. *Earth's Future*, 10, 8 2022. ISSN 2328-4277. doi: 10.1029/2022EF002703.

Z. Yu, X. Guo, Y. Zeng, M. Koga, and H. Vejre. Variations in land surface temperature and cooling efficiency of green space in rapid urbanization: The case of fuzhou city, china. *Urban*

Forestry & Urban Greening, 29:113–121, 1 2018. ISSN 16188667. doi: 10.1016/j.ufug.2017.11.008.

W. Yuan, W. Cai, J. Xia, J. Chen, S. Liu, W. Dong, L. Merbold, B. Law, A. Arain, J. Beringer, C. Bernhofer, A. Black, P. D. Blanken, A. Cescatti, Y. Chen, L. Francois, D. Gianelle, I. A. Janssens, M. Jung, T. Kato, G. Kiely, D. Liu, B. Marcolla, L. Montagnani, A. Raschi, O. Roupsard, A. Varlagin, and G. Wohlfahrt. Global comparison of light use efficiency models for simulating terrestrial vegetation gross primary production based on the lathuile database. *Agricultural and Forest Meteorology*, 192-193:108–120, 7 2014. ISSN 01681923. doi: 10.1016/j.agrformet.2014.03.007.

C. Yue, P. Ciais, S. Luyssaert, W. Li, M. J. McGrath, J. Chang, and S. Peng. Representing anthropogenic gross land use change, wood harvest, and forest age dynamics in a global vegetation model orchidee-mict v8.4.2. *Geoscientific Model Development*, 11:409–428, 1 2018. ISSN 1991-9603. doi: 10.5194/gmd-11-409-2018.

C. Yue, P. Ciais, R. A. Houghton, and A. A. Nassikas. Contribution of land use to the interannual variability of the land carbon cycle. *Nature Communications*, 11:3170, 6 2020. ISSN 2041-1723. doi: 10.1038/s41467-020-16953-8.

L. Zardo, D. Geneletti, M. Pérez-Soba, and M. V. Eupen. Estimating the cooling capacity of green infrastructures to support urban planning. *Ecosystem Services*, 26:225–235, 8 2017. ISSN 22120416. doi: 10.1016/j.ecoser.2017.06.016.

Y. Zhang, X. Xiao, L. Guanter, S. Zhou, P. Ciais, J. Joiner, S. Sitch, X. Wu, J. Nabel, J. Dong, E. Kato, A. K. Jain, A. Wiltshire, and B. D. Stocker. Precipitation and carbon-water coupling jointly control the interannual variability of global land gross primary production. *Scientific Reports*, 6:39748, 12 2016. ISSN 2045-2322. doi: 10.1038/srep39748.

Z. Zhang, Y. Lv, and H. Pan. Cooling and humidifying effect of plant communities in subtropical urban parks. *Urban Forestry & Urban Greening*, 12:323–329, 1 2013. ISSN 16188667. doi: 10.1016/j.ufug.2013.03.010.

J. Zhao, N. Meili, X. Zhao, and S. Fatichi. Urban vegetation cooling potential during heatwaves depends on background climate. *Environmental Research Letters*, 18:014035, 1 2023. ISSN 1748-9326. doi: 10.1088/1748-9326/acaf0f.

M. Zhao, Z. hong Kong, F. J. Escobedo, and J. Gao. Impacts of urban forests on offsetting carbon emissions from industrial energy use in hangzhou, china. *Journal of Environmental Management*, 91:807–813, 3 2010. ISSN 03014797. doi: 10.1016/j.jenvman.2009.10.010.

X. Zhou, M. Yamamoto, S. Yan, Y. Ishida, M. Cai, Q. Ji, M. Makvandi, and C. Li. Exploring the impacts of heat release of vehicles on urban heat mitigation in sendai, japan using wrf model integrated with urban lcz. *Sustainable Cities and Society*, 82:103922, 7 2022. ISSN 22106707. doi: 10.1016/j.scs.2022.103922.

Z. Zhu, S. Piao, R. B. Myneni, M. Huang, Z. Zeng, J. G. Canadell, P. Ciais, S. Sitch, P. Friedlingstein, A. Arneth, C. Cao, L. Cheng, E. Kato, C. Koven, Y. Li, X. Lian, Y. Liu, R. Liu, J. Mao, Y. Pan, S. Peng, J. Peñuelas, B. Poulter, T. A. M. Pugh, B. D. Stocker, N. Viovy, X. Wang, Y. Wang, Z. Xiao, H. Yang, S. Zaehle, and N. Zeng. Greening of the earth and its drivers. *Nature Climate Change*, 6:791–795, 8 2016. ISSN 1758-678X. doi: 10.1038/nclimate3004.

Z. Zhu, J. Wang, F. K. S. Chan, Y. Xu, G. Li, M. Xu, W.-Q. Chen, and Y.-G. Zhu. Urban agriculture as nature-based solutions: Three key strategies to tackle emerging issues on food security in chinese cities under climatic and non-climatic challenges. *Frontiers of Engineering Management*, 10:736–741, 12 2023. ISSN 2095-7513. doi: 10.1007/s42524-023-0262-4.

A. Zonato, A. Martilli, S. D. Sabatino, D. Zardi, and L. Giovannini. Evaluating the performance of a novel wudapt averaging technique to define urban morphology with mesoscale models. *Urban Climate*, 31:100584, 3 2020. ISSN 22120955. doi: 10.1016/j.uclim.2020.100584.

A. Zonato, A. Martilli, E. Gutierrez, F. Chen, C. He, M. Barlage, D. Zardi, and L. Giovannini. Exploring the effects of rooftop mitigation strategies on urban temperatures and energy consumption. *Journal of Geophysical Research: Atmospheres*, 126, 11 2021. ISSN 2169-897X. doi: 10.1029/2021JD035002.

J. Zscheischler, M. D. Mahecha, J. von Buttlar, S. Harmeling, M. Jung, A. Rammig, J. T. Randerson, B. Schölkopf, S. I. Seneviratne, E. Tomelleri, S. Zaehle, and M. Reichstein. A few extreme events dominate global interannual variability in gross primary production. *Environmental Research Letters*, 9:035001, 3 2014a. ISSN 1748-9326. doi: 10.1088/1748-9326/9/3/035001.

J. Zscheischler, M. Reichstein, J. von Buttlar, M. Mu, J. T. Randerson, and M. D. Mahecha. Carbon cycle extremes during the 21st century in cmip5 models: Future evolution and attribution to climatic drivers. *Geophysical Research Letters*, 41:8853–8861, 12 2014b. ISSN 00948276. doi: 10.1002/2014GL062409.

G. Zulian, C. Polce, and J. Maes. Estimap: a gis-based model to map ecosystem services in the european union. *Annali di Botanica*, 4:1–7, 2014.

G. Zulian, E. Stange, H. Woods, L. Carvalho, J. Dick, C. Andrews, F. Baró, P. Vizcaino, D. N. Barton, M. Nowel, G. M. Rusch, P. Autunes, J. Fernandes, D. Ferraz, R. F. dos Santos, R. Aszalós, I. Arany, B. Czúcz, J. A. Priess, C. Hoyer, G. Bürger-Patricio, D. Lapola, P. Mederly, A. Halabuk, P. Bezak, L. Kopperoinen, and A. Viinikka. Practical application of spatial ecosystem service models to aid decision support. *Ecosystem Services*, 29:465–480, 2 2018. ISSN 22120416. doi: 10.1016/j.ecoser.2017.11.005.

Àrea Metropolitana de Barcelona (AMB). Indicadors socioambientals de la xarxa de parcs metropolitans. dades 2020., 3 2021.

Appendix

A Supporting information for Chapter 2

A.1 Measurement set up

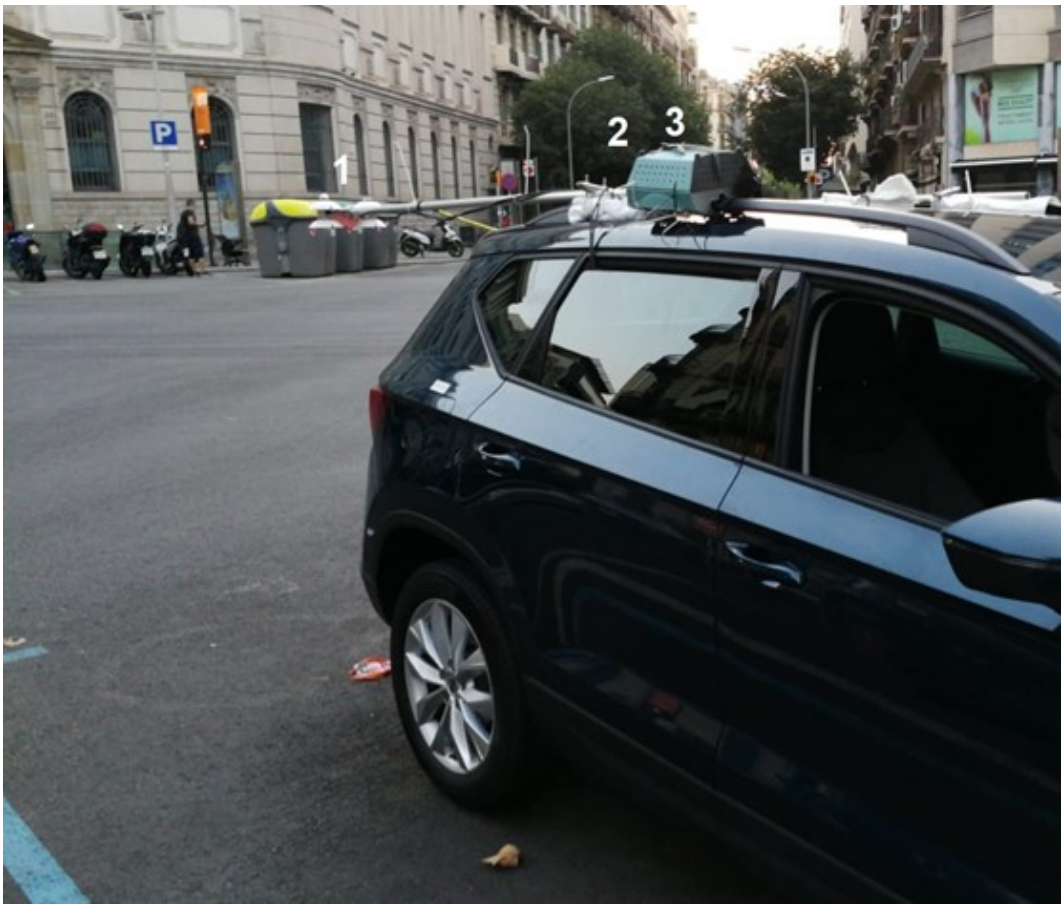


Figure A.1: (a) Schematic set up of the measurement's equipment. 1 Hukseflux NR01 net radiometer; 2 Kestrel 4500 pocket weather tracker (temperature and humidity) under the sun screen; 3 Garmin GPS under the sun screen.

A.2 Manual segmentation of fisheye lens photographs

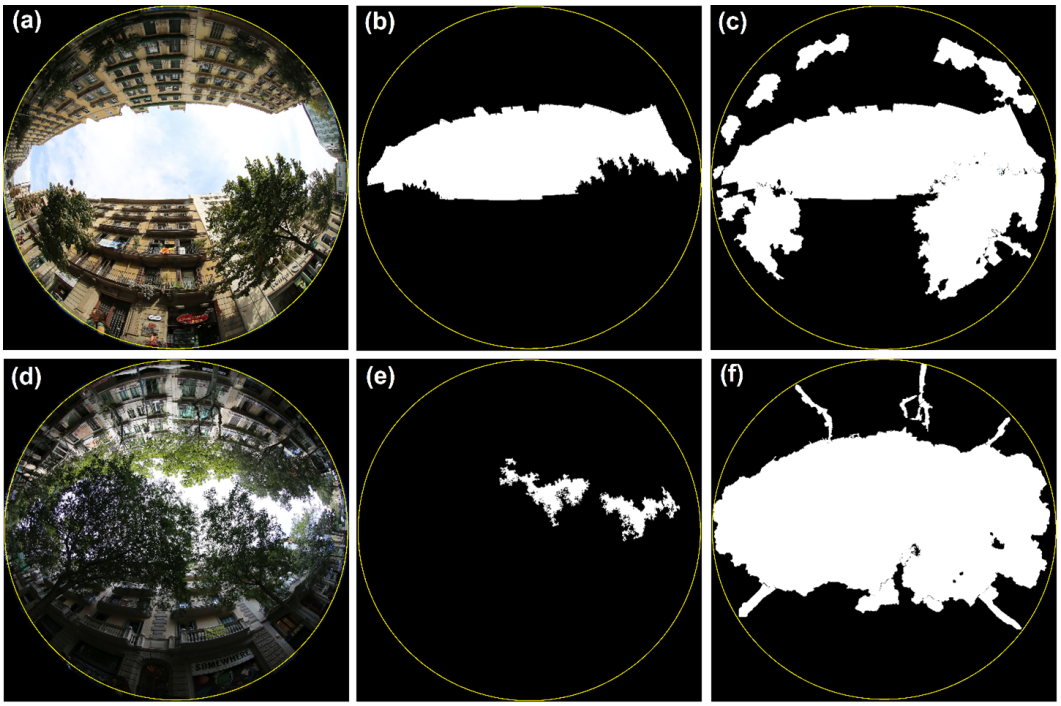


Figure A.2: Example of manual segmentation of upper-hemisphere fisheye photographs taken in the Sparsely_treed (a, b and c) and Densely_treed streets (d, e and f). In the first column (a and d), the original pictures are resized and fitted in a square. In the second column (b and e), the sky pixels are segmented to obtain the SVF. In the third column (c and f), the vegetation and sky pixels are segmented to obtain the VVF from the subtraction of the SVF.

A.3 Urban canopy parameters

Table A.1: Urban canopy parameters and vegetation parameters used in the BEP-Tree simulations for each street.

Parameter		Sparsely_treed	Densely_treed
Urban fraction		0.96	0.98
Building plan area fraction λ_p		0.82	0.83
Vertically-oriented building surface area to plan area fraction λ_f		0.22	0.21
Mean building height (m)		30.6	29.0
Building height probability	20-25 m	7	20
	25-30 m	74	80
	30-35 m	19	0
Heat capacity ($MJm^{-3}K^{-1}$)	Roof	1.77	1.77
	Wall	1.37	1.37
	Ground	1.94	1.94
Thermal conductivity ($Wm^{-1}K^{-1}$)	Roof	0.84	0.84
	Wall	1.31	1.31
	Ground	0.75	0.75
Surface albedo	Roof	0.15	0.15
	Wall	0.30	0.30
	Ground	0.08	0.08
Surface emissivity	Roof	0.89	0.89
	Wall	0.9	0.9
	Ground	0.93	0.93
Roughness length (m)	Roof	0.01	0.01
	Wall	0.0001	0.0001
	Ground	0.01	0.01
Lower temperature (K)	Roof	297.0	297.0
	Wall	297.0	297.0
	Ground	300.5	300.5
Canyon clumping coefficient		0.58	0.63

A.4 Sensitivity analysis to the potential temperature forcing

The methodology used in this study for deriving the potential temperature at the forcing height of the BEP-Tree model can introduce an additional uncertainty in the computation of the air temperature. The adjustment parameter α_k at daytime is seen to vary between the different meteorological conditions represented in the WRF simulation and the urban area considered. For the urban grid cell that contains the Raval station, the α_k is seen to vary between 0.60 and 1.0 at daytime, being 0.8 the average value. In order to determine the uncertainty introduced in the model due to the adjustment parameter, two additional simulations are performed with BEP-Tree using different forcing conditions, varying the parameter α_k between 0.6 and 1.0 at daytime (during nighttime the α_k parameter is 1.0). In the case of the simulation with α_k= 0.6,

the values of α_k at 5 and 20 UTC (the transition hours) are set to 0.8 to minimize the discontinuity in the potential temperature observed between the daytime and the nighttime hours. This range of variation of the parameter α_k coincide with the intended usage of the forcing conditions, representing the meteorological conditions of the study area and period. The period of study corresponds to two summer days with no clouds, where high solar irradiance in the canyon surfaces is expected to generate high sensible heat fluxes to the atmosphere, provoking the generation of free convection and turbulent mixing over the urban canopy layer. From this, we would expect that the potential temperature presents an unstable profile over the building rooftops during the day. This situation is contemplated with the value of α_k= 0.6, presenting the highest differences seen for the Raval area in the WRF simulations of summer days between the roof temperature and the forcing height. This can turn into a neutral profile during the early morning and evening, when the solar radiation is minimum. In this case, the potential temperatures at the forcing height would be similar to the observed at the rooftop (α_k = 1.0).

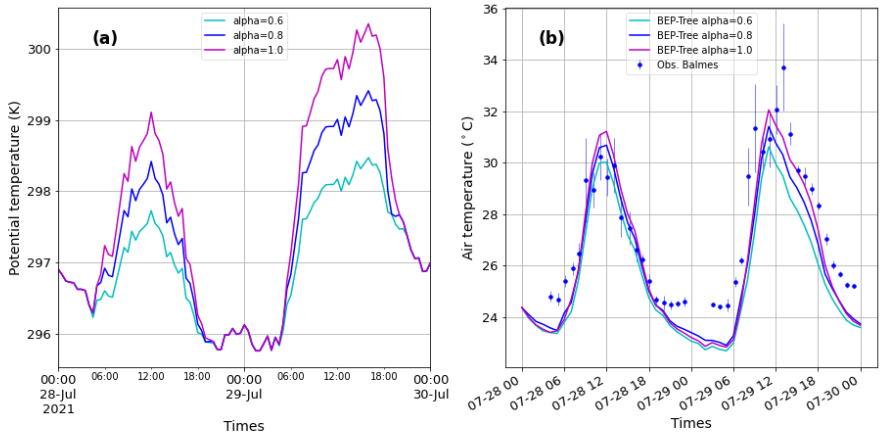


Figure A.3: Temporal profile of the input potential temperature at the forcing level (z=70m) (a) and modelled air temperature at (1.5 m above ground).

The potential temperature at the forcing height variates with α_k presenting a maximum range of 1.9 K between α_k= 0.6 and α_k = 1.0 (Figure A.3a), which corresponds to the potential temperature observed by the meteorological station on the building roof top. This uncertainty is propagated in the model affecting the vertical diffusion equation of potential temperature in the whole canyon, representing a maximum modelled variation of 1.6 ºC between the air temperature at 1.5 m over the ground level at noon using α_k = 0.6 and α_k = 1.0 (Figure A.3b). This difference is principally seen at noon, although it is extended to mid-afternoon for the day 29 of July, coinciding with the large observed temperatures by the Raval station during the whole afternoon of this day. Therefore, we can attribute a maximum uncertainty of 0.8 ºC for the estimation of the air temperatures by BEP-Tree related to the parameterization of the forcing

potential temperatures based on the expression in Equation 2.5. Although this uncertainty is lower than the observed and modelled range of diurnal variation of the air temperature inside the canyon, this uncertainty is comparable to the modelled effect of trees to air temperatures at noon, of about 1.0 ºC. Therefore, this methodology to derive forcing height potential conditions, can introduce uncertainties in the air temperature estimation of the same magnitude as the expected effect of street trees, when it is used for forcing an urban canopy model such as BEP-Tree.

A.5 Comparison of the surface energy fluxes between the default and the new turbulent wind speed parameterization

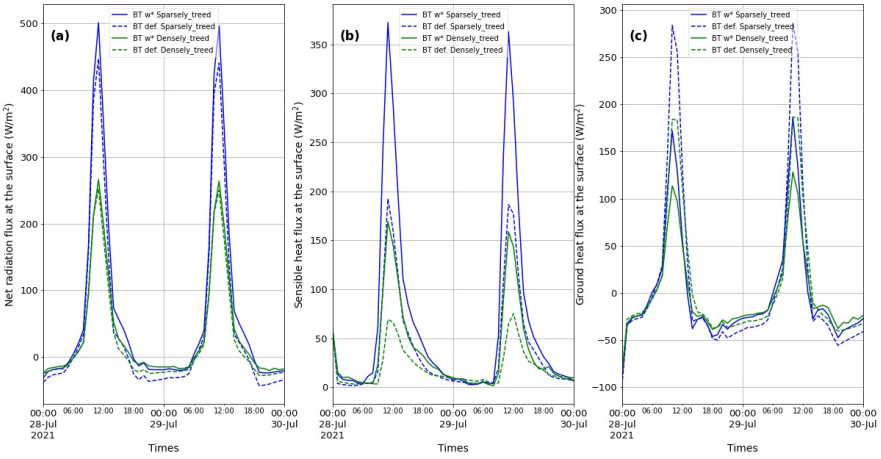


Figure A.4: Modelled with the default BEP-Tree model (BT def., dashed lines) and the BEP-Tree with the buoyancy driven wind speed (BT w^*, straight lines) canyon averaged road surface net radiation flux (a) road surface sensible heat flux (b), and road surface ground heat flux (c) for Sparsely_treed (blue) and Densely_treed (green) streets in Barcelona.

As seen in Figure A.4, the new wind parameterization affects the net radiation at the road surface, due to the reduction of the surface temperature and therefore, decreasing the upwelling longwave radiation from the surface. This can be seen by an increase of the net radiation during the whole day. In the case of the sensible heat flux, the new parameterization increases the sensible flux from the surface to the atmosphere. This change is more remarkable during the day, while during the night there is no difference as it is expected, because the wind parameterization is only activated during unstable conditions. In the case of the ground heat flux, we see that there is a reduction of the ground heat fluxes during the day that can explain the increase in the sensible heat flux. During the night there is a small decrease of the absolute value of the ground heat flux between BEP-Tree w* and BEP-Tree def. that can explain the differences in the surface temperatures at nighttime.

A.6 Comparison of specific humidity between BEP-Tree and observations

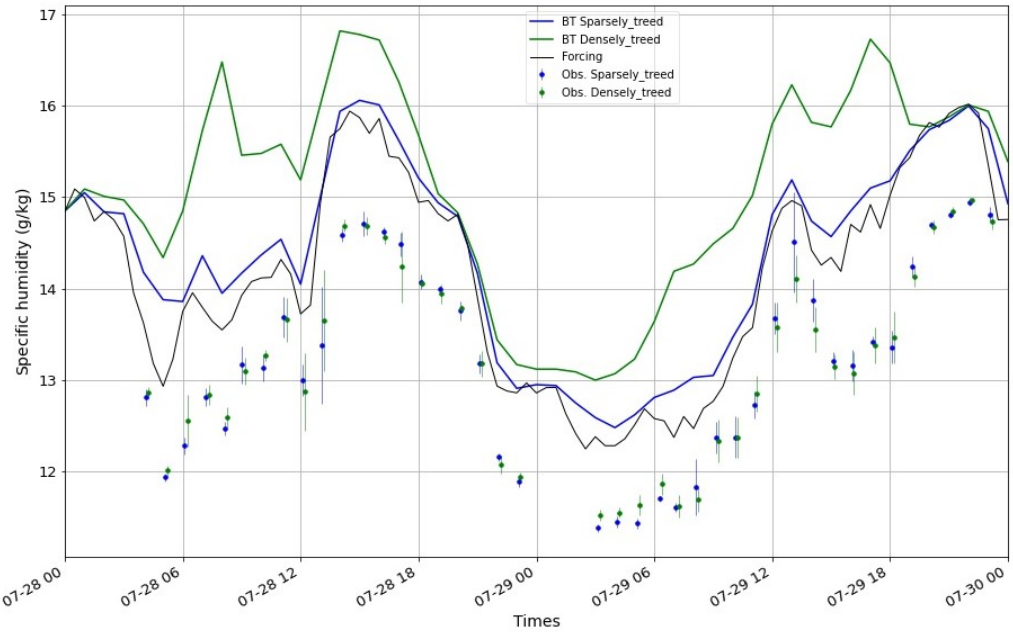


Figure A.5: Modelled by BEP-Tree (BT, lines) and observed (Obs., circles) canyon averaged 1.5 m above ground specific humidity for Sparsely_treed (blue) and Densely_treed (green) streets in Barcelona. Measurement error bars correspond to the standard deviation between all the track stops. Black line corresponds to the forcing conditions at the forcing level.

B Supporting information for Chapter 3

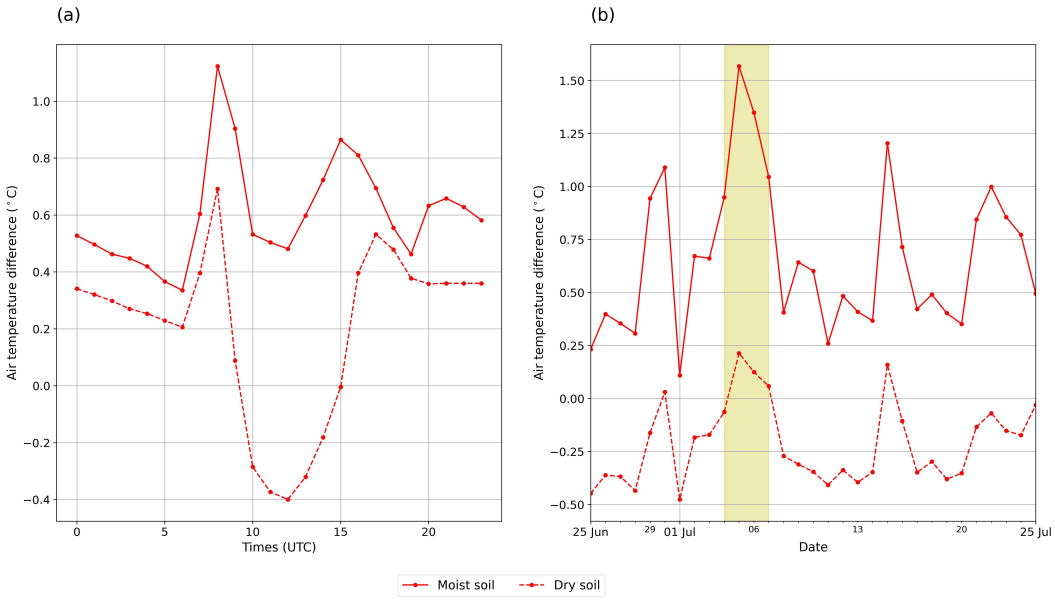


Figure B.1: BEP-Tree modelled diurnal cycles (left) and midday/midafternoon (between 9-15 UTC, 11-17 LT) averages in the study period of the canyon-averaged air temperatures (at 1.5 m height from the ground) for the differences between Sparse trees and Dense trees neighborhoods without coupling the soil moisture model (moist soil), and coupling the soil moisture model (dry soil) . The yellow rectangles in subplot (b) indicate the heat wave period (4-7 July).

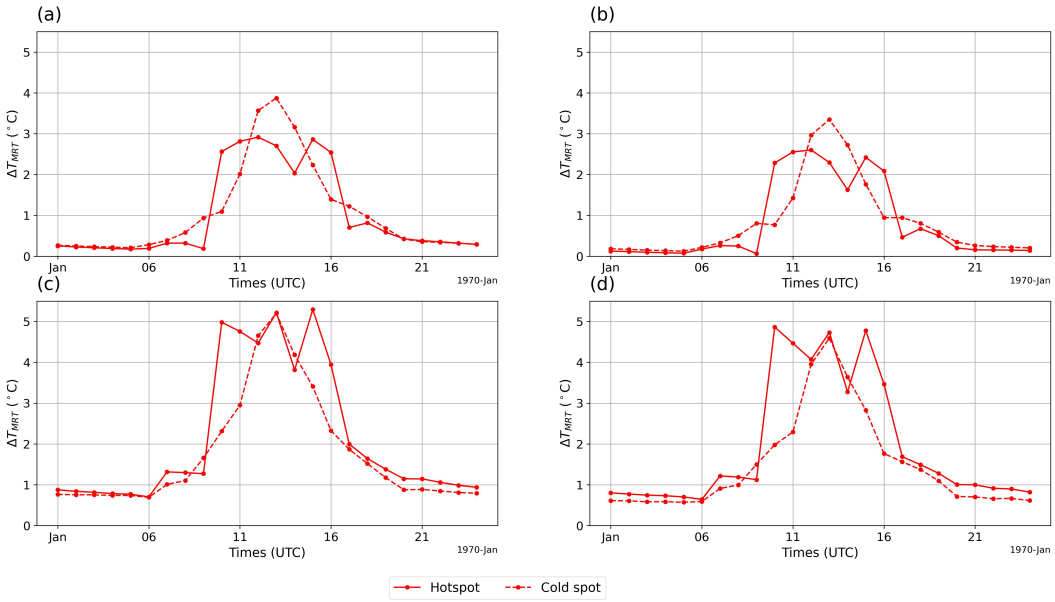


Figure B.2: BEP-Tree modelled diurnal cycles of the mean radiant temperature difference between Sparse trees and Dense trees (a) in the locations outside tree crown projections and moist soil, (b) the locations outside tree crown projections and dry soils, (c) the locations under tree crowns and moist soils, and (d) the locations under tree crowns and dry soils.

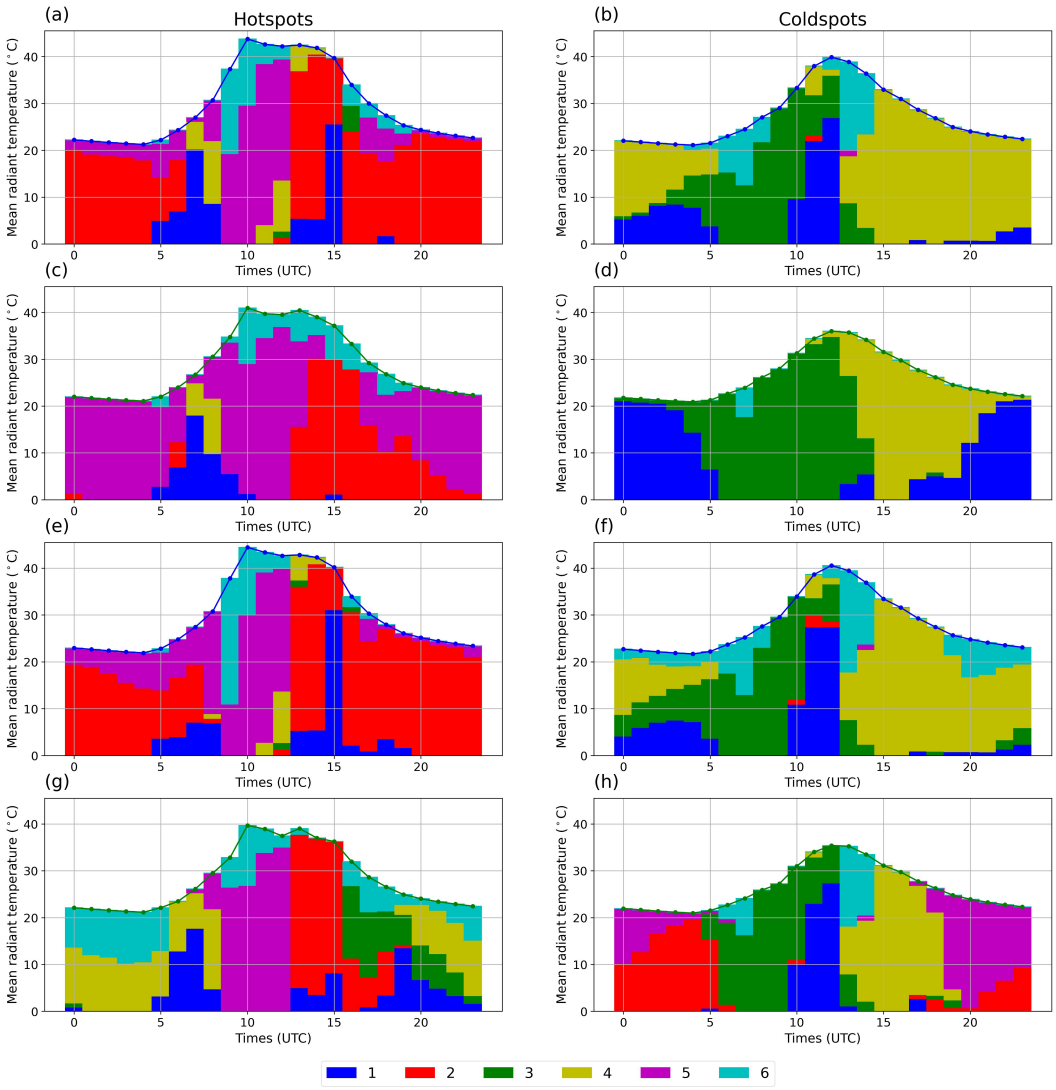


Figure B.3: BEP-Tree modelled diurnal cycles of the T_{MRT} in the hotspots (left column) and the coldspots (right column) with the distribution of most frequent hotspots between the six locations where the T_{MRT} is computed in each neighbourhood for (a, b) in Sparse trees outside tree crown projections, (c, d) in Dense trees outside tree crown projections, (c) in Sparse trees under tree crowns, (d) in Dense trees under tree crowns. These correspond to the simulations with moist soil. The locations are depicted in Figure B.4.

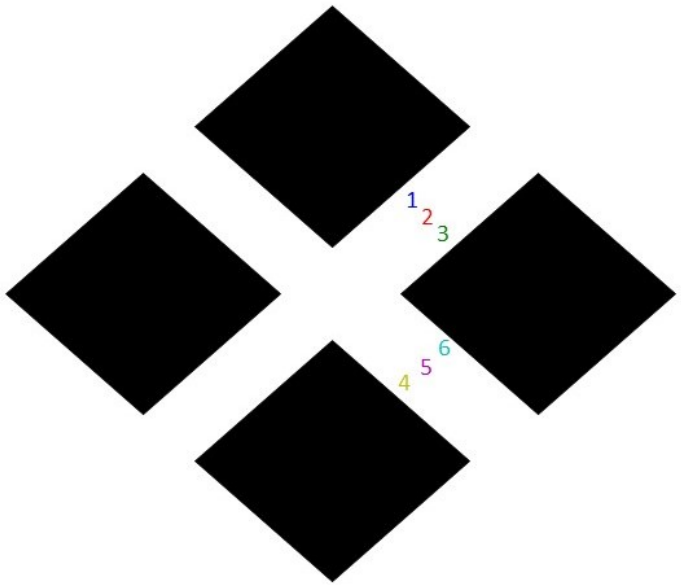


Figure B.4: Locations inside the neighbourhoods where the mean radiant temperature has been calculated.

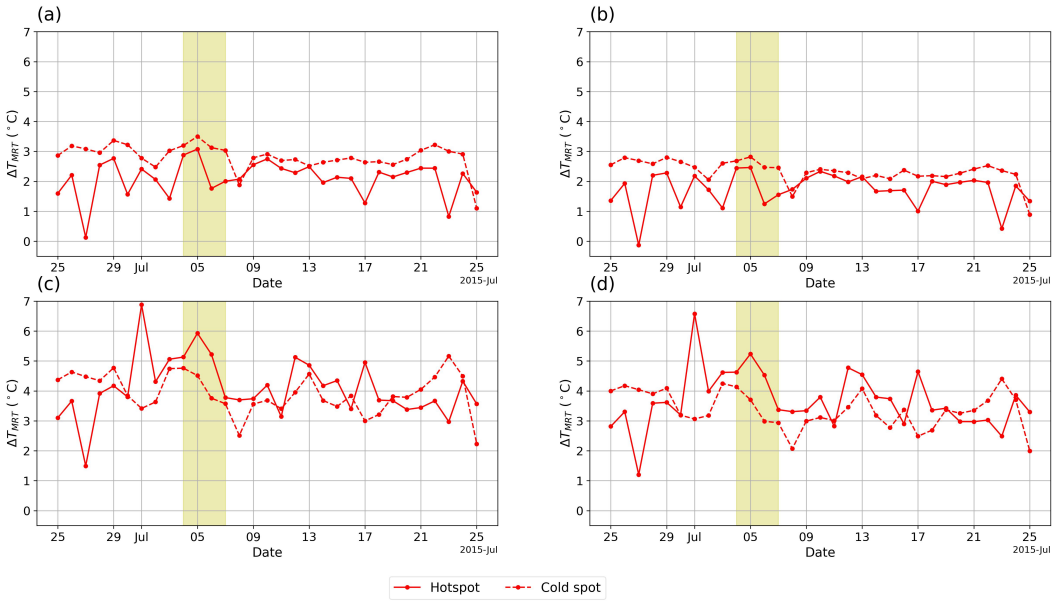


Figure B.5: BEP-Tree modelled midday/midafternoon (between 9-15 UTC, 11-17 LT) averages in the study period of the mean radiant temperature (a) in the locations outside tree crown projections and moist soil, (b) the locations outside tree crown projections and dry soils, (c) the locations under tree crowns and moist soils, and (d) the locations under tree crowns and dry soils for difference between Sparse trees and Dense trees neighborhoods in the hot spots and cold spots locations.

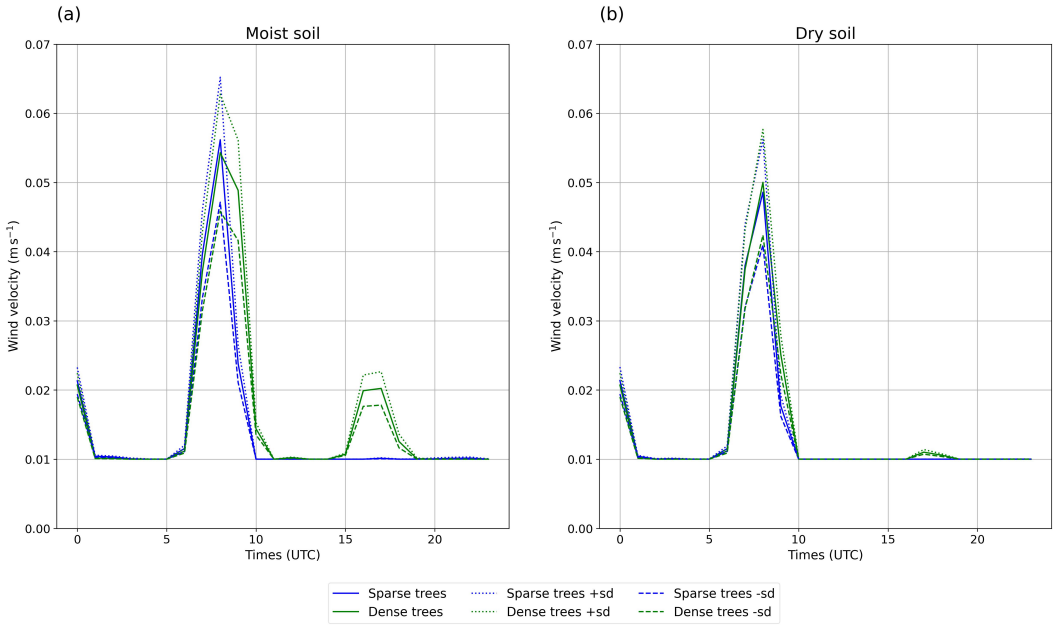


Figure B.6: Comparison of the diurnal profile of wind velocity for Sparse trees and Dense trees, for canyon average, and the spatial variability (± the standard deviation) (a) under moist soils, (b) and dry soils.

C Supporting information for Chapter 4

C.1 Synoptic analysis and the study case: heat wave July 2015

In order to study the frequency and relation of the HW events for the city of Barcelona with their synoptic situation, a brief retrospective study has been done. A meteorological station capturing the rural background meteorology of the city of Barcelona (Observatori Fabra) was selected for the analysis. This station is located at an altitude of 411 m, inside the Collserola Mountain, which measures the rural background atmosphere outside the city.

According to the definition of the Catalan Meteorological Service (SMC), a HW event is considered when maximum daily temperatures recorded by a meteorological station surpass for three or more consecutive days the 98th percentile of the climatological series recorded during the summer months (June, July and August). In the case of the Observatori Fabra station, the established threshold based on the climatology of the last 30 years (1991-2020) is 34.174 ºC (obtained from the SMC Xarxa d'Estacions Meteorològiques Automàtiques open data www.meteo.cat/wpweb/serveis/cataleg-de-serveis/serveis-oberts/dades-obertes/). Since 1991, 55 summer days surpassed the 98th percentile threshold. Notice that these days are not necessarily considered HW events since it could happen that there was just one isolated hot day, and therefore it is not defined as HW day based on the SMC definition. However, for this study all the days surpassing the 98th percentile were used independently if they belong to a HW event or not, in order to increase the representativity of the sample.

Then, once these 55 days are selected, a synoptic classification is applied to each one of these days based on the Miró et al. (2020) methodology. Synoptic classifications are a common practice for weather forecasting since it allows to consider the synoptic influence when downscalling predictions. Miró et al. (2020), described a synoptic classification for the Western Mediterranean area centred over Catalan territory based on a sea-level pressure pattern classification such as Jenkinson and Collison classification (Jenkinson and Collison, 1977) but incorporating the 500 hPa geopotential height pattern. In this way, they pass from the 27 synoptic types of Jenkinson-Collinson to 27*27 with the combination of surface and height. Therefore, the synoptic classification is more complete in the sense that it considers the stability of the atmosphere, especially for synoptic surface types with airflow coming from the Mediterranean Sea. To combine the two classifications (surface and 500 hPa) and reduce the number of categories, the Martin Vide's manual classification method (Martín-Vide, 1991) using 16 circulation patterns was used to provide an objective method.

The classification is based on approximations of the circulation of some atmospheric parameters over a simplified grid of 9 x 9 points centred on the eastern coast of the Iberian Peninsula and a horizontal resolution of 5º x 5º (35º N- 45º N and 10º W-10º E). The data used for the classification is obtained from the European Centre for Medium Range Weather Forecasts (ECMWF) ERA5 daily reanalysis sea-level pressure and 500 hPa geopotential height. The surface category is based on the calculation of three values from the sea-level pressure: wind force, wind direction and vorticity. Applying some classification rules on these three values, advections, cyclones, anticyclones and hybrid types are obtained. To classify the values at the 500 hPa height, the same methodology is applied although only 5 types are obtained: cyclone, trough (merging all cyclonic hybrids), anticyclone, ridge (merging all anticyclonic hybrids) and pure advective types.

Finally, after merging surface and 500 hPa types using the manual Martin-Vide classification and merging some rare categories, every day is classified according to a synoptic type described in Table C.1.

Table C.1: Simplified synoptic classification of Miró et al. (2020) with a brief description and number of days with maximum daily temperature exceeding the 98th percentile recorded at the Observatori Fabra station.

Type number	Description	Number of days	Percentage (%)
1	West advection	1	1.82
2	Anticyclonic western advection	12	21.82
3	Northwest advection	1	1.82
4	North advection	0	0.00
5	Northeast advection	1	1.82
6	East advection	1	1.82
7	East advection with cut-off low above	1	1.82
8	South advection	0	0.00
9	Southwest advection	2	3.64
10	Trough	2	3.64
11	Low or Cyclone	5	9.09
12	Shallow cyclone or Undetermined pressure gradient	27	49.09
13	Anticyclone	2	3.64

As we can see from Table C.1, the most frequent synoptic type for the hottest summer days in Barcelona corresponds to Shallow cyclone or Undetermined pressure gradient with the 49.09 % of the days. This situation is the most typical in the summer days of the Iberian Peninsula when there are no centres of high or low pressure nearby, therefore the pressure gradient is small. This situation generates weak general flow without a dominant synoptic wind direction, in this case local winds (such as breezes) take centre stage. The second most frequent synoptic type is Anticyclonic western advection with the 21.82 % of the days. This situation causes a flow from the west that, after crossing the Iberian Peninsula, arrives to the Catalan territory reheated and dry. This type is potentially dangerous for summer fires.

The two synoptic types that dominate the 2015 HW episode and the previous days are type 12 and type 2 (see Table C.2), therefore, it is a common HW according to the synoptic analysis. This period stands out for its duration. Since middle June, a low-pressure centre located in southern Iceland blocked the Azores Anticyclone at the same latitude as the Iberian Peninsula. This block caused a stable situation (with little or no cloudiness) that, added to the incident solar radiation (maximum in these days of the year) and the advection of the south from North Africa in our study area, generated a potentially dangerous situation of extreme temperatures. The southern advection reached central Europe due to the duration of the atmospheric block.

Table C.2: Synoptic pattern for the period of 25 of June to 9 of July 2015. The bolded lines correspond to the HW period.

Day	Synoptic pattern
2015-06-25	10
2015-06-26	2
2015-06-27	12
2015-06-28	12
2015-06-29	12
2015-06-30	12
2015-07-01	12
2015-07-02	2
2015-07-03	12
2015-07-04	2
2015-07-05	12
2015-07-06	12
2015-07-07	12
2015-07-08	11
2015-07-09	5

The temperature at 850 hPa (approximately 1500 m) was 6 ºC higher than climatic average in the study area (Fig. C.1a) reaching 8 ºC positive in some parts of Europe (20^{th} Century Reanalysis). On the other hand, the geopotential height at 850 hPa (Fig. C.1b) shows two centres of high pressures, the first one over the western Mediterranean Sea and the other one over the Azores, favouring the warm and dry flow from SW. This caused that maximum daily temperatures reached 40 ºC in the interior of the AMB and 35 ºC on the coast (Servei Meteorològic de Catalunya (SMC), 2015). The night-time temperatures were also considerably high during the entire HW, exceeding 25 ºC for several consecutive days in some neighbourhoods (Servei Meteorològic de Catalunya (SMC), 2015).

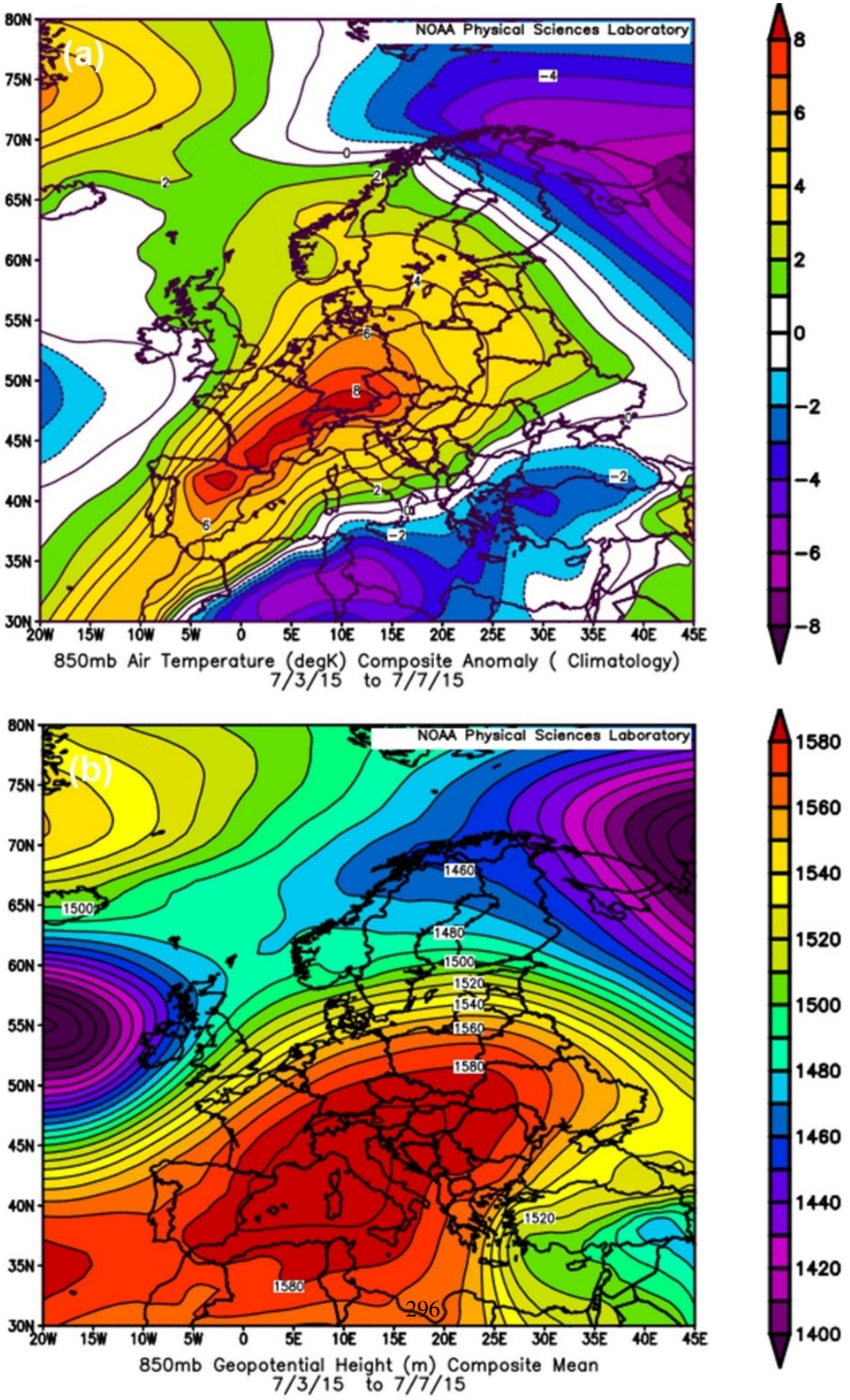


Figure C.1: Composite from 3 to 7 July 2015 for (a) temperature anomaly over the climatic average at 850 hPa and (b) geopotential height at 850 hPa. Source: Project 20th Century Reanalysis.

C.2 High Resolution Land Data Assimilation System simulations

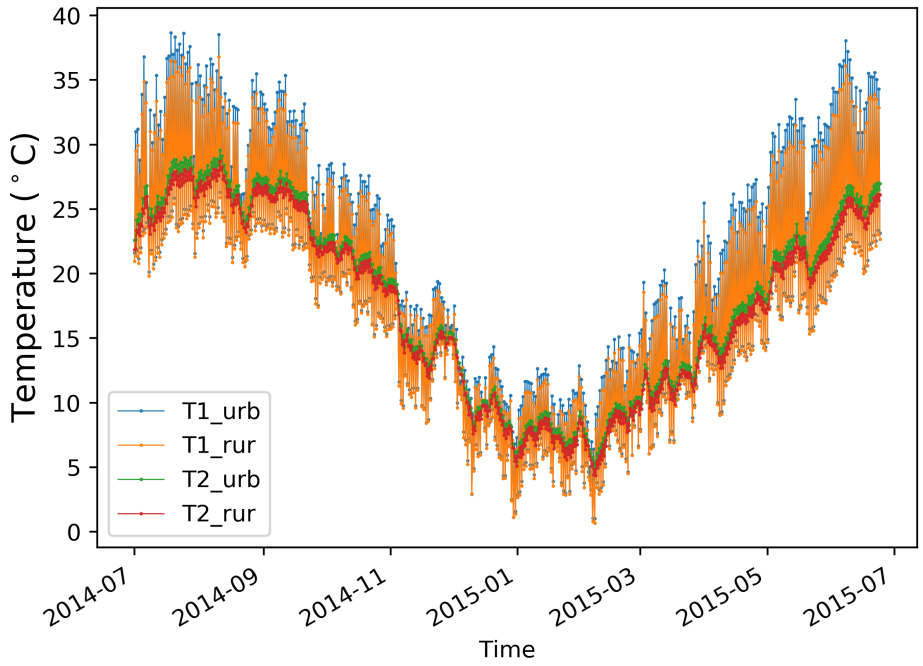


Figure C.2: Temporal series of the soil temperature obtained by the HRLDAS simulation with 12 hour temporal frequency for: first soil layer (0-0.1 m depth) averaged over all urban areas (T1_urb); first soil layer averaged over all rural areas (T1_rur); second soil layer (0.1-0.4 m depth) averaged over all urban areas (T2_urb); second soil layer averaged over all rural areas (T2_rur).

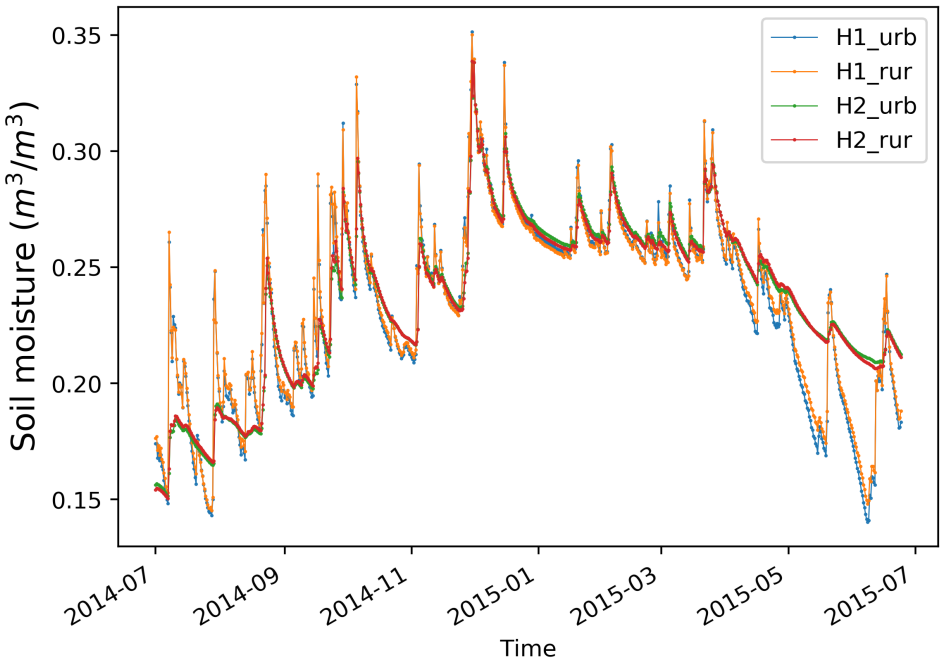


Figure C.3: Temporal series of the soil moisture obtained by the HRLDAS simulation with 12 hour temporal frequency for: first soil layer (0-0.1 m depth) averaged over all urban areas (T1_urb); first soil layer averaged over all rural areas (T1_rur); second soil layer (0.1-0.4 m depth) averaged over all urban areas (T2_urb); second soil layer averaged over all rural areas (T2_rur).

C.3 Urban canopy parameters

Table C.3: Building height (m) and density (%) and width (m), street width (m) and urban fraction (λ_u).

LCZ classes	Building height (m)	Density (%)	Building width (m)	Street width (m)	λ_u
1. Compact high-rise	25	10	15.0	15.0	1.00
	30	25			
	35	30			
	40	25			
	45	10			
2.Compact middle-rise	10	25	17.5	12.7	0.95
	15	45			
	20	20			
	25	10			
3.Compact low-rise	5	55	9.0	5.7	0.90
	10	45			
4.Open high-rise	25	10	32.0	37.5	0.65
	30	25			
	35	50			
	40	15			
5.Open middle-rise	10	10	25.0	33.3	0.70
	15	25			
	20	40			
	25	25			
6.Open low-rise	5	65	10.5	12.4	0.65
	10	35			
7.Lightweight low-rise	5	100	7.0	2.0	0.85
8.Large low-rise	5	35	28.8	32.5	0.85
	10	65			
9.Sparsely built	5	75	10.0	10.0	0.30
	10	25			
10.Heavy industry	5	10	23.8	28.5	0.55
	10	60			
	15	30			
E.Bare rock or paved	5	100	5.0	100.0	1.00

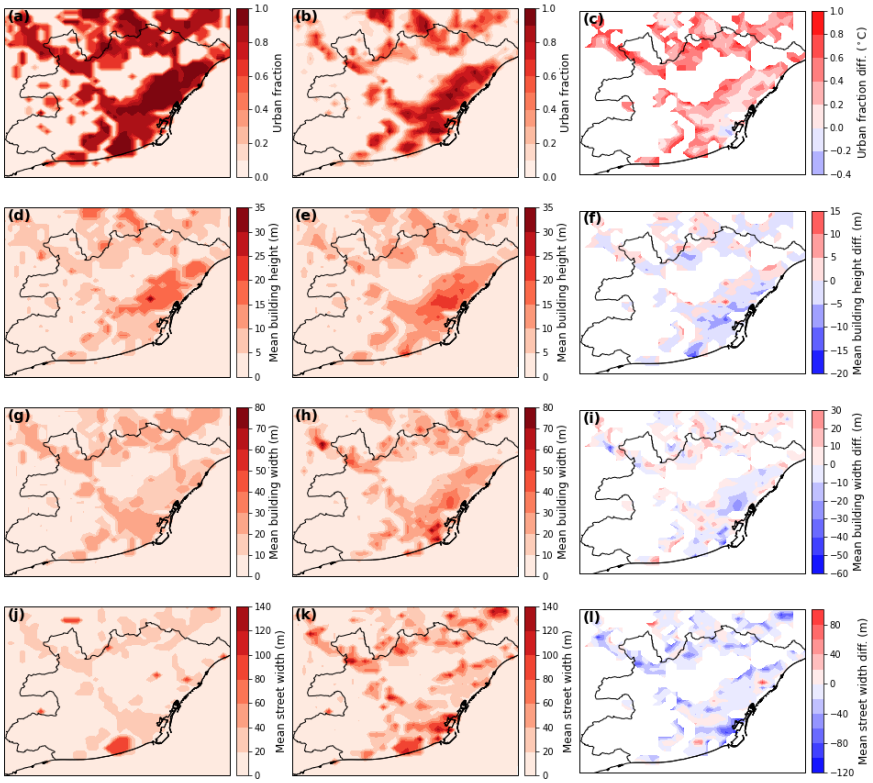


Figure C.4: Comparison between urban morphology parameters for BL-noUM (left column), BL-UM (middle column) and their difference (BL-noUM – BL-UM) (right column) for: (a, b and c) urban fraction, (d, e and f) Area weighted mean building width, (g, h and i) mean building width, (j, k and l) mean street width. The white colour in difference plot refers to difference equal to 0.

C.4 Metadata of weather stations and validation statistics

Table C.4: Meteorological stations used in our model evaluation coordinates, altitude above sea level (m), land-use/land-cover for the CLC classification for non-urban areas and LCZ for urban areas (at 100 m x 100 m resolution), land-use/land-cover reclassified to MODIS IGBP classification and 11 urban LCZ (at 1 km x 1 km model's resolution), availability of temperature and wind observations. (* Urban areas are classified with a LCZ)

Station name	Latitude	Longitude	Altitude a.s.l. (m)	LULC class (100m)	LULC class (1km)	Temp.	Wind.
1. Urban Fabric and non-vegetated urban areas							
Badalona	41.45215	2.24757	42	Compact mid-rise*	Large low-rise*	yes	yes
Raval	41.3839	2.16775	33	Compact mid-rise*	Compact mid-rise*	yes	yes
Terrassa	41.53254	2.03696	198	Open mid-rise*	Open low-rise*	yes	no
Parets	41.56734	2.22619	123	Open mid-rise*	Large low-rise*	yes	yes
Vallirana	41.38197	1.93564	252	Open low-rise*	Open low-rise*	yes	yes
ZAL Prat	41.31723	2.13091	4	Large low-rise*	Large low-rise*	yes	yes
Barcelona airport	41.29285	2.07001	4	Asphalt*	Asphalt*	yes	yes
Sabadell airport	41.52366	2.10307	146	Asphalt*	Compact mid-rise*	no	yes
2. Non-agricultural vegetated urban areas							
Zona Univ.	41.37919	2.1054	79	Sport and leisure facilites	Large low-rise*	yes	yes
Sant Cugat	41.48311	2.07956	158	Sport and leisure facilites	Large low-rise*	yes	yes
Zoo	41.38943	2.18847	7	Green urban areas	Compact mid-rise*	yes	no
3. Agricultural areas							
Prat	41.34045	2.08022	8	Complex cultivation patterns	Large low-rise*	yes	yes
Viladecans	41.29928	2.03787	3	Complex cultivation patterns	Cropland/Natural vegetation mosaics	yes	yes
Sabadell-crop	41.56568	2.06952	258	Non-irrigated arable land	Open low-rise*	yes	yes
4. Forest and seminatural areas							
Castellbisbal	41.47892	1.97546	147	Transitional woodland shrub	Cropland/Natural vegetation mosaics	yes	yes
Obs. Fabra	41.41843	2.12388	411	Coniferous forest	Open low-rise*	yes	yes
PN Garraf	41.28832	1.90775	573	Sclerophyllous vegetation	Open shrublands	yes	yes
Corbera	41.40809	1.88501	647	Sclerophyllous vegetation	Evergreen needleleaf forest	yes	no
5. Water bodies							
Bocana sud	41.31725	2.16537	3	Sea and ocean	Water	no	yes

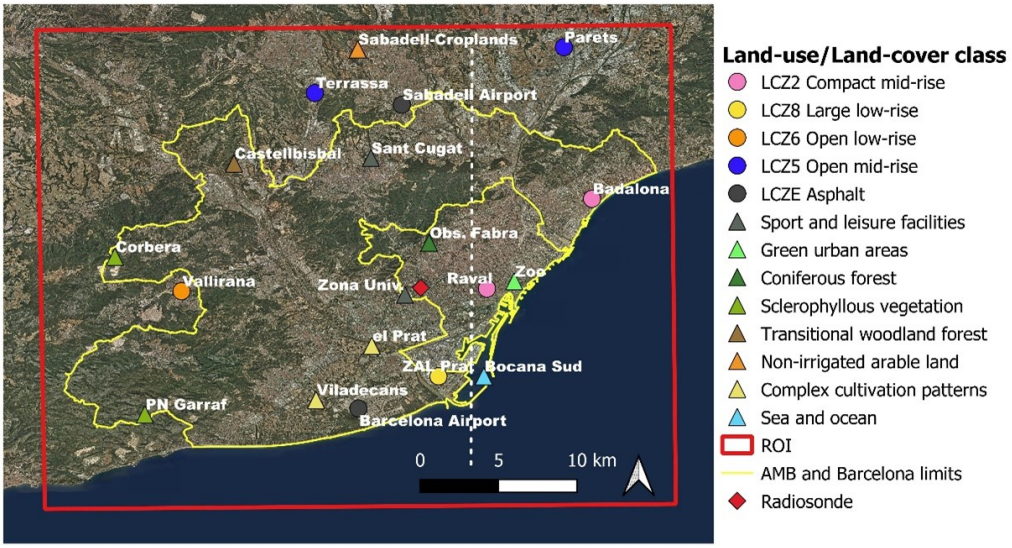


Figure C.5: Detail of the ROI area with the locations and land-use classes (from the 100 m LULC classification) of the meteorological stations used in this study for the performance evaluation of the WRF simulations; the radiosonde launching position; and the AMB and Barcelona city borders. The white dashed line represents the cross-section shown in Section 4.3.5.

Statistical analyses of the root-mean-square error (RMSE), mean bias (MB) and correlation factor (R) were used to compare the model simulations with the observations:

$$RMSE = \left(\frac{1}{N} \sum_{i=1}^{N} (M_i - O_i)^2 \right)^{1/2} \tag{C.1}$$

$$MB = \frac{1}{N} \sum_{i=1}^{N} (M_i - O_i) \tag{C.2}$$

$$R = \frac{\sum_{i=1}^{N} (M_i - \bar{M})(O_i - \bar{O})}{\left(\sum_{i=1}^{N} (M_i - \bar{M})\right)^{1/2} \left(\sum_{i=1}^{N} (O_i - \bar{O})\right)^{1/2}} \tag{C.3}$$

where M_i represents the modelled value at each time step and O_i is the observed value. The overbar represents the mean among all the available time steps (N) for a given meteorological station. Then, the average values and standard deviations of these metrics calculated among all the stations and among the stations in the same LULC groups are presented in this analysis.

To assess the significance of the differences between pairs of statistical indexes, a two-sample t-tests comparing the differences between modelled and observed for different pairs of simulations is done. The different simulations of each sensitivity test (BL-UM-HRL, BL-noUM and MYJ-UM) are tested in front of the reference simulation (BL-UM) with a two-tailed Welch's t-test for each variable, statistical index and LULC group. We assume that data is approximately Gaussian, with the test using a two-tailed distribution. The significance in the difference of a

pair of statistical metrics is determined from the p-value resulted from the test, which is the two-tailed decimal probability of the hypothesis being false. Low p-values indicates high confidence in rejecting the null hypothesis, which here is hypothesized that 2 independent groups of differences (simulated minus observed for all available time steps and stations in the LULC) have identical average values. In this statistical analysis, we reject the null hypothesis with a 95 % confidence interval if the p-value is lower than 0.05.

C.5 Additional Results

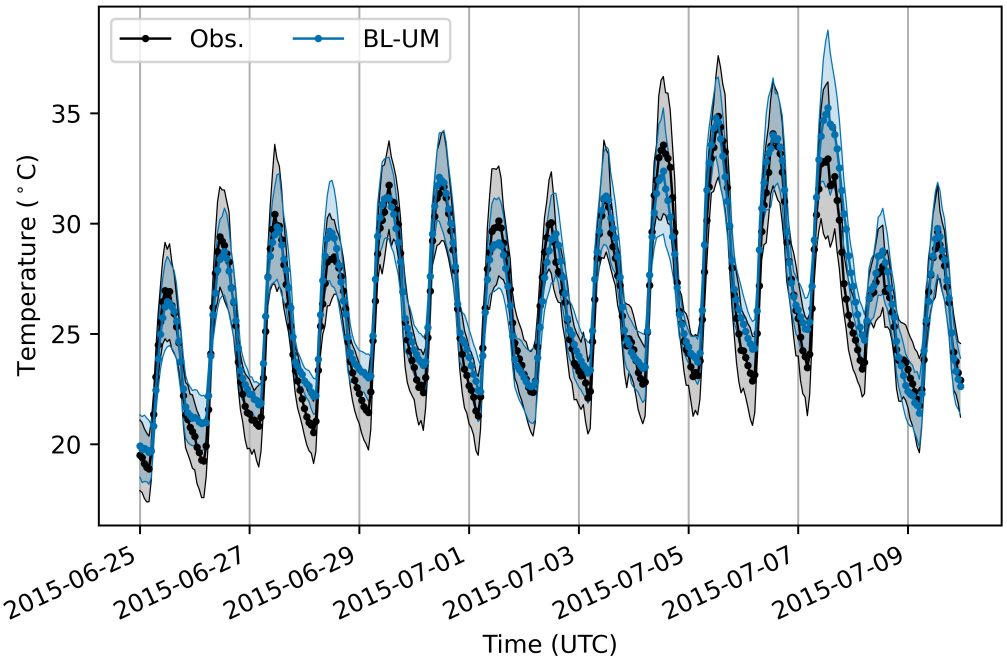


Figure C.6: Time series of observed near-surface temperature averaged between all the meteorological stations compared to averaged simulated near-surface temperatures by the model in the reference simulation during the study period. The black and blue shaded areas correspond to the standard deviation between all the meteorological stations for the observations and BL-UM simulation, respectively.

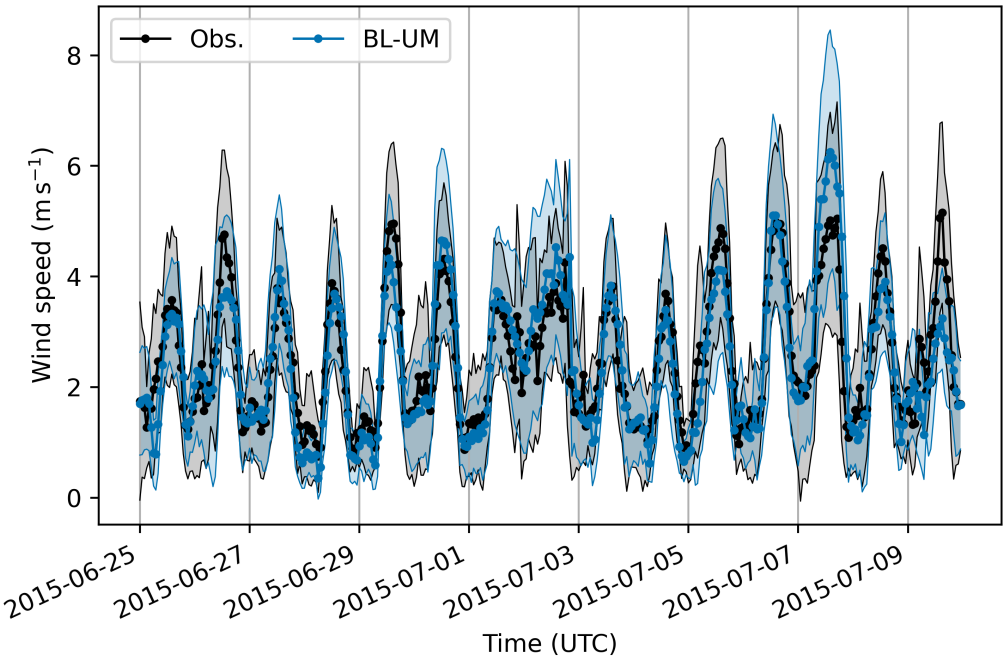


Figure C.7: Time series of observed near-surface wind speed averaged between all the meteorological stations compared to averaged simulated near-surface wind speed by the model in the reference simulation during the study period. The black and blue shaded areas correspond to the standard deviation between all the meteorological stations for the observations and BL-UM simulation, respectively.

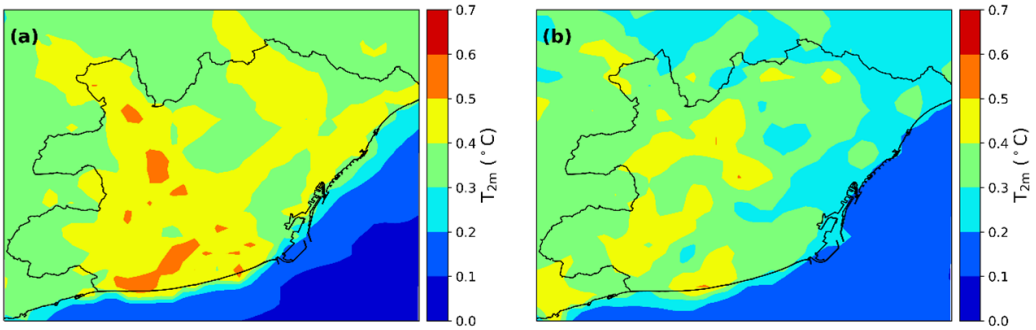


Figure C.8: Standard deviation of the differences between simulated T_{2m} by BL-UM-HRL and BL-UM simulation between all the time-steps at daytime (a) and night-time (b).

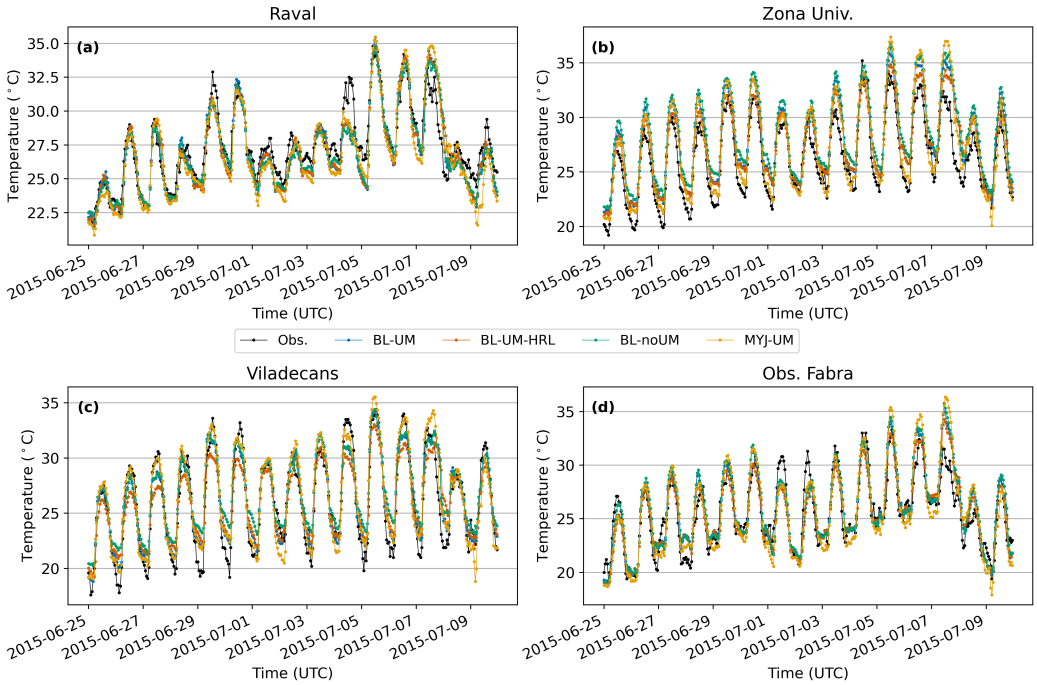


Figure C.9: Time series of observed and simulated T_{2m} for all the simulations and the meteorological stations Raval (UF&NVUA), Zona Univ. (NAVUA), Viladecans (AA) and Obs. Fabra (F&SNA).

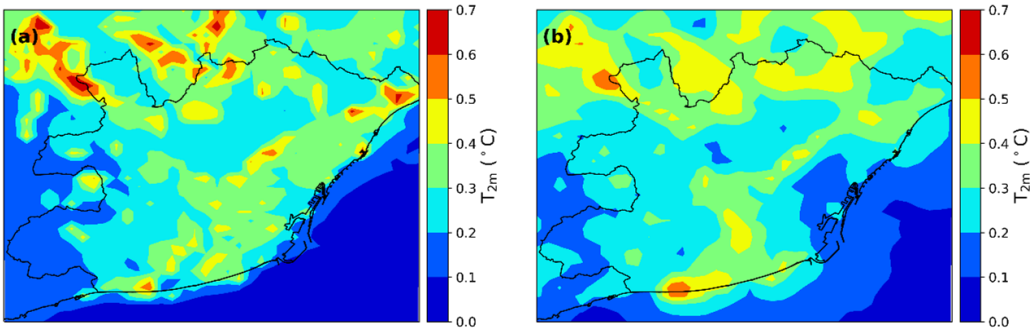


Figure C.10: Standard deviation of the differences between simulated T_{2m} by BL-noUM and BL-UM simulation between all the time-steps at daytime (a) and night-time (b).

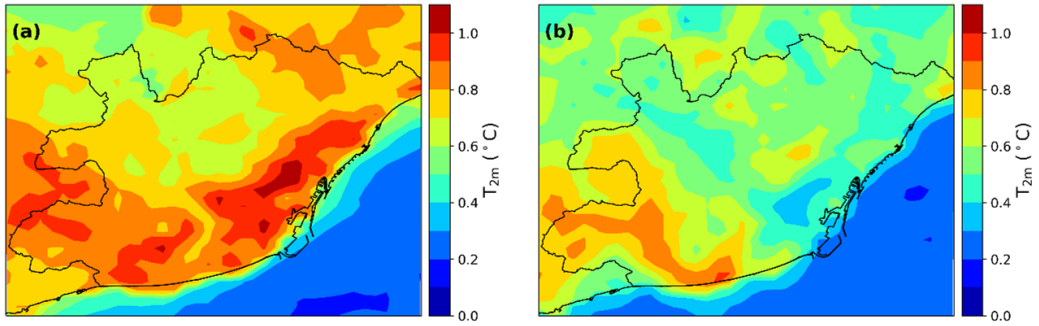


Figure C.11: Standard deviation of the differences between simulated T_{2m} by MYJ-UM and BL-UM simulation between all the time-steps at daytime (a) and night-time (b).

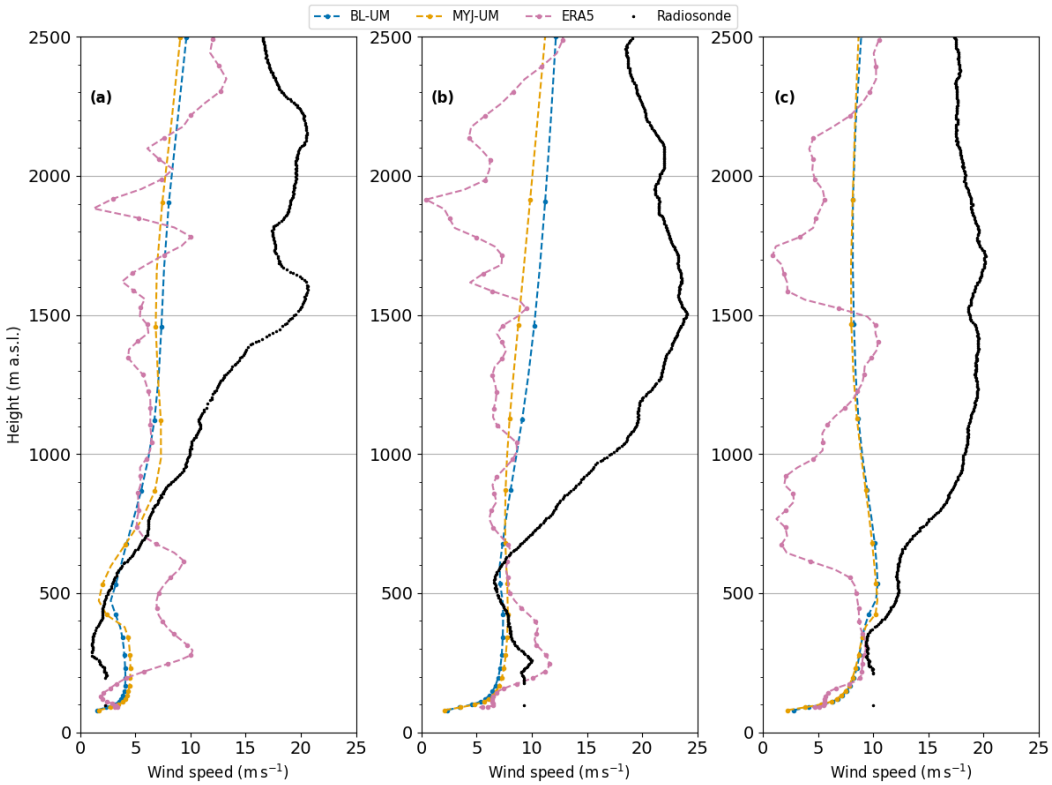


Figure C.12: Comparison of vertical profiles of WRF model simulated wind speed (m s^{-1}), ERA5 wind speed and radiosonde observations from the launches at 12 UTC at the days 4 July 2015 (a), 5 July 2015 (b) and 6 July 2015 (c).

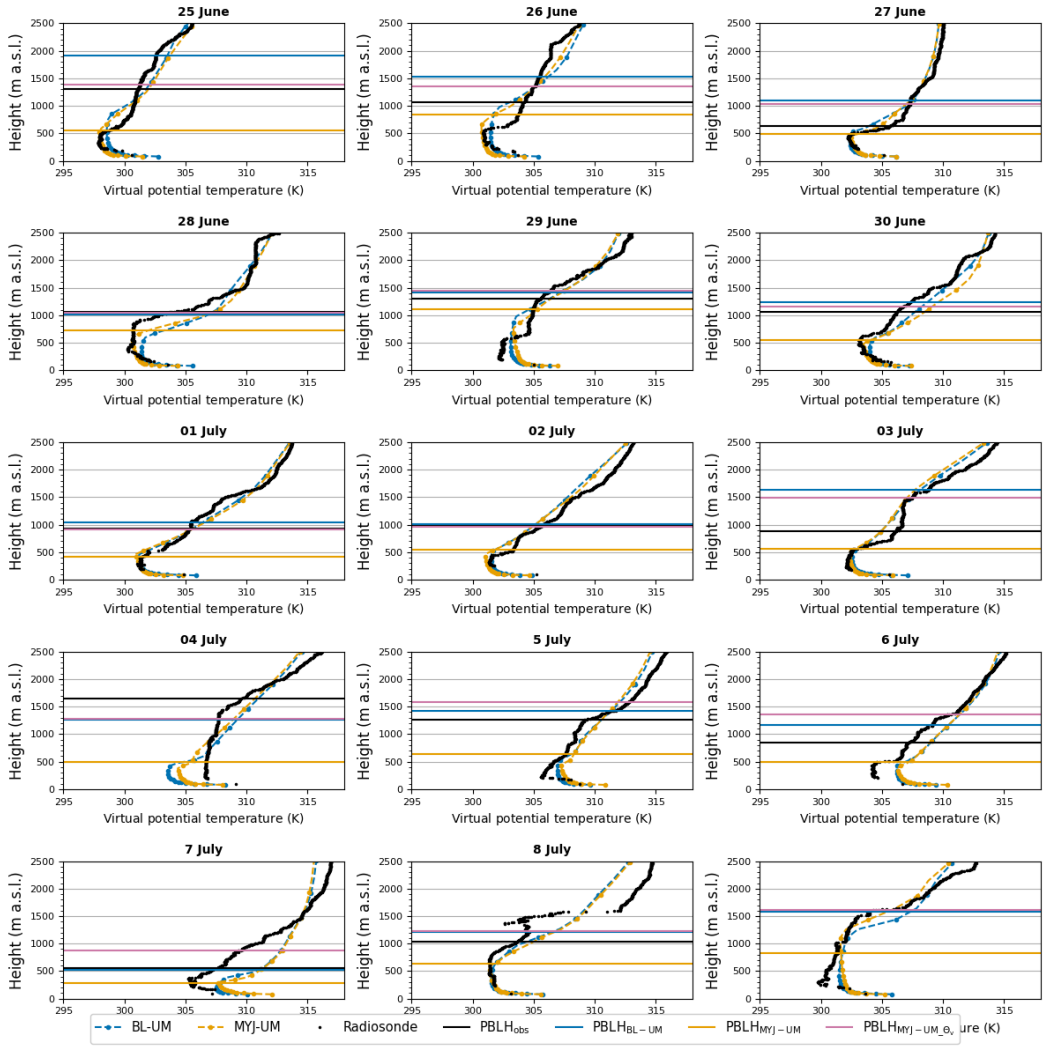


Figure C.13: Vertical profiles of virtual potential temperature measured by the radio-sounding and modelled by the WRF model for every day of the study period at 12 UTC.

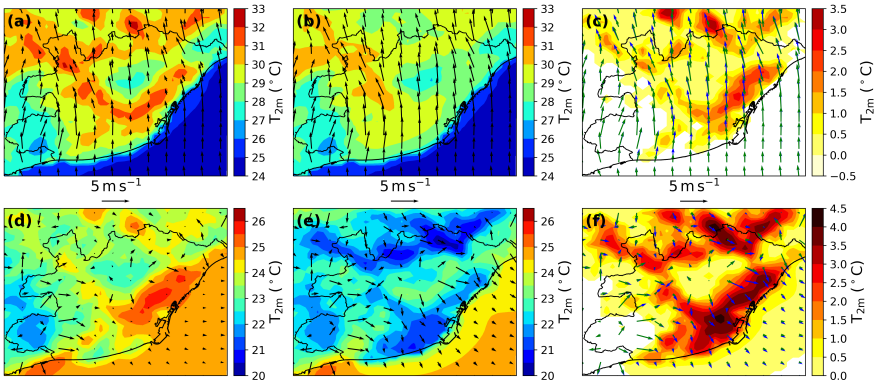


Figure C.14: Model comparison of T_{2m} and 10 m wind vectors averaged at daytime (top row) and night-time (bottom row), for (a, d) BL-UM; (b, e) BL-crop; (c, f) difference BL-UM – BL-crop. The white colour in difference plots stands for temperature differences lower than 0.1 ºC in absolute value. In plots c and f, green vectors stand for the time-averaged wind vectors for BL-UM and blue vectors for BL-crop.

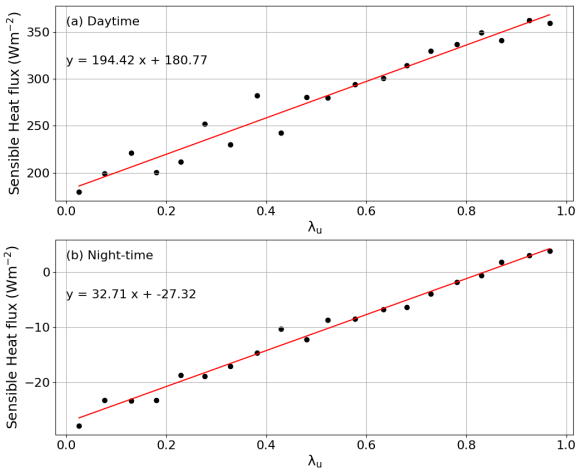


Figure C.15: Relation between urban fractions (λ_u) and the simulated sensible heat flux (SH) in the daytime (a) and night-time (b) during the period of study. The black dots show the mean values of the simulated SH and λ_u within all the 0.05 intervals of the λ_u in the urban areas inside the ROI.

C.6 Relation between near-surface temperatures and urban fraction

This section replicates the results presented in Section 4.3.6 of Chapter 4, but for the WRF-BEP-BEM simulation of the current scenario (S0) described in Chapter 5. The main differences between the two simulations are that these new simulations have a higher spatial resolution (333 m), covering a longer study period (between 25 June 2015 to 00 UTC 25 July 2015), using a more recent version of WRF-BEP-BEM (version 4.3.3), which has been modified to represent a greater spatial variability of land-covers and values for variables SHDFAC and LAI in the pervious areas of urban classified grid cells as it is described in Appendix D.3. Moreover, this simulation employs the Yonsei University PBL scheme, instead of the BouLac PBL scheme. The simulation without irrigation has been used for the study of the relations between λ_u and T_{2m} inside the entire domain of 333 m (d04) represented in Figure 5.2.

Figure C.16 shows the relation between the simulated daytime and night-time T_{2m} and λ_u by the new simulation. In this case, and contrary to the results observed in Figure 4.13, the modelled T_{2m} present a much lower sensitivity to the λ_u, with a slope of 0.73 ± 0.13 ºC, and a lower determination coefficient (R^2) of 0.63. The slope of the λ_u-function is slightly higher during the HW days (0.87 ± 0.13 ºC) evidencing an enhanced capacity of the urban green infrastructure to regulate near-surface temperatures during the periods of higher heat stress. This effect could also be attributed to a higher increase of urban temperatures, as urban areas lack of soil moisture for evapotranspiration, increasing the sensible heat flux during episodes of higher temperatures (Li and Bou-Zeid, 2013), as well as emitting a higher proportion of air-conditioning heat emissions (Luo et al., 2020). However, contrary to the results shown in Figure 4.13, the urban green infrastructure is more efficient reducing the T_{2m} during the nighttime, presenting a higher slope of 1.76 ± 0.12 ºC, an a R^2 of 0.92, although the relation between T_{2m} and λ_u decreases over the HW episode, with a lower slope of 1.36 ± 0.07 ºC. These results agree with the studied and reported characteristics of the UHI effect in the city of Barcelona (Moreno-garcia, 1994; Martin-Vide and Moreno-Garcia, 2020), presenting a higher strength during the calm wind and clear-sky nights. The representation of unrealistically high values for the SHDFAC and LAI variables (0.80 and 4.29 m^2m^{-2}, respectively) of the vegetation in pervious areas in urban grid cells of the previous simulations, could explain the higher sensitivity of T_{2m} with λ_u observed in Figure 4.13, that is corrected in the new simulations with the representation of more realistic and spatially-resolved parameters. The decrease in the slope during the HW nights, evidences a slight homogenization of the air temperatures between urban and rural areas, which can be attributed to disphase between UHIs and HWs. Maximum UHI intensity is been observed to occur before the onset of the HWs, and decrease during the HWs, because nocturnal urban temperatures generally remain stationary, while rural temperatures tend to increase at night (Richard et al., 2021).

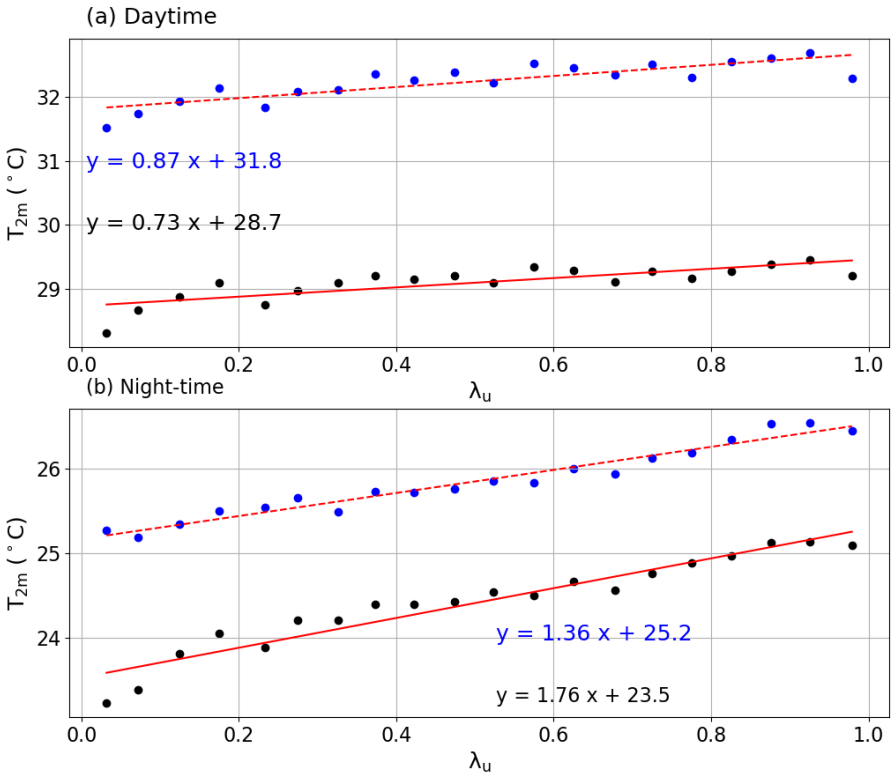


Figure C.16: Relation between urban fractions (λ_u) and the simulated mean 2 m temperatures (T_{2m}) in the daytime (a) and night-time (b) during the period of study (black dots) and during the heat wave event (4 July to 7 July 2015, blue dots). The black and blue dots show the mean values of the simulated T_{2m} and λ_u within all the 0.05 intervals of the λ_u in the urban areas inside domain 4.The continuous red line represent the lineal regression for the black dots, while the discontinuous red line is for the blue dots.

D Supporting information for Chapter 5

D.1 Land-use/Land-cover maps development

For the land-use and land-cover (LULC) classification, the four land-use maps provided by the PDU for each scenario are reclassified into two different LULC classifications depending if the LULC is urban or rural. Initially, for the S0, the Local Climate Zones (LCZ) map of the AMB (Gilabert et al., 2021a) is used to better describe the urban areas as it is explained in Segura et al. (2021). The LCZ establishes a framework for the definition of neighbourhoods within a city with similar urban cover types, structures, materials, and human activities. For this study, 10 urban LCZs and the LCZ E (reformulated as asphalt) are used in combination with the Corine Land Cover 2018 classification Büttner et al., 2017 (Büttner et al., 2017;

https://land.copernicus.eu/pan-european/corine-land-cover/ clc2018) at a 100-m resolution for the rural areas as the background land-use types. The Corine Land Cover 2018 is remapped from its original 44 classes into 27 classes using the United States Geological Survey (USGS) land classification following the method of Pineda et al. (2004), with the exception that we define a new land-cover class in the USGS as green urban areas (we keep it from the class 1.4.1 in the Corine Land Cover classification). This results in a map of 100 m horizontal resolution with 28 rural classes (USGS + green urban areas) and 11 urban classes (10 urban LCZ and asphalt). For the scenarios S1, S2 and S3, we identify the regions where the land-use changes with respect to the S0, and we mask the nearest grid cells to these regions on the S0 map with the new land-use class reclassified to the USGS classification. In case that the new areas are urban, the nearest urban LCZ in the S0 map is selected to define the urban cover type.

D.2 Agriculture irrigation water use estimation

The irrigation water demand is obtained at the crop parcel level using a water metabolism approach that computes the monthly crop water demands, as there are no available reports of the UPUA irrigation water use spatially resolved. Based on the crop map described in Appendix D.1, each crop is assigned a monthly crop coefficient (K_c) from literature using the local farmer's calendar. The crop water requirement in mm per month is obtained from an adaptation of the FAO method (Pereira et al., 2015). Monthly raster maps of potential evapotranspiration (ET_o) and precipitation (PPT) were developed using spatial kriging of monthly accumulated ET_o and PPT observations from the Catalan Meteorological service station network. We simplify the future LULC scenario analysis by assuming that the same precipitation and potential evapotranspiration affect the future scenarios, considering the given uncertainty in the temporal scale of the implementation of the scenarios and that the uncertainties in the water irrigation demand and efficiency are higher than the uncertainties in the meteorology estimation. The crop evapotranspiration (ET_c) is obtained as the product of ET_o and K_c. While the irrigation requirements are calculated as the difference between the crop evapotranspiration and the precipitation.

The irrigation water use is obtained by considering the water losses in the irrigation application process from direct evaporation. Considering that flooding is the most common method in the AMB agriculture (Dirección General del Catastro, 2022), a 65 % efficiency is adopted considering the reported values of efficiencies for each irrigation method in Catalonia (Agència Catalana de l'aigua, 2010).

D.3 Additional WRF modifications

The green vegetation fraction (GREENFRAC) was updated using the fraction of absorbed photosynthetically active radiation (FAPAR) product of the Copernicus Global Land Service with a 300-m resolution (Wolfs et al., 2020), which describes the amount of green and alive elements of the canopy.

In the case of urban morphology parameters needed by WRF-BEP-BEM, they are included as it is detailed in Sections 4.2.2 and 4.2.3 of this thesis for the reference scenario. For the rest of the scenarios, we mask on the S0 urban fraction map the regions where a land-use change occurs with respect to the S0 scenario. In the case that the new land-use is rural or an urban park, it is masked to 0; while if the new land-use is urban, the mean urban fraction for the selected LCZ is used for the urban fraction mask. The building height distribution, building widths and street widths are preserved for each pixel with respect to the S0 map. In the case of the new urban areas, the mean canopy geometries of the LCZ are used.

Additional modifications compared to the previous studies have been applied to the WRF model and configuration to improve the representation of land-use changes between scenarios. Firstly, the land surface model used (Noah LSM) has been modified to represent a more realistic vegetation fraction in urban areas. In the default Noah LSM, the vegetation fraction in urban grid cells uses a fixed percentage of vegetation cover for the pervious part of the grid cell (1- λ_u). In the current application of the model, the input variable GREENFRAC, obtained from the observed FAPAR product, is divided by (1- λ_u) in the urban grid cells in order to calculate the vegetation fraction in the pervious surface of the grid cell. Moreover, in the default Noah LSM, all the urban grid cells have a common natural LULC class that defines the vegetation properties of the pervious surface of the grid cell, which in previous studies is the cropland/grassland mosaic. In the current application of the WRF model, we have defined a new variable that is initialized in the model with the most dominant natural vegetation class in the grid cell (the natural LULC with a higher land fraction). When the most dominant natural land-cover type is an urban park or there is not a fraction for any natural land-cover, then the vegetation properties of these grid cells are defined with the cropland/grassland mosaic category.

In this study, contrary to the previous studies, we use the Yonsei University planetary boundary layer (PBL) scheme (Hong et al., 2006b; Hendricks et al., 2020), as it has provided a better performance in terms of air temperature prediction compared to other schemes. The PBL scheme have a significant impact on the modelled air temperature inside the PBL as it controls the vertical turbulent sub-grid scale processes inside the lowest part of the atmosphere. In Appendix D.4, we present a sensitivity study of the PBL scheme and the evaluation of the reference scenario S0 is shown comparing the hourly modelled 2-m air temperature with observational data from the Catalan Meteorological Service and the Spanish Meteorological Agency.

D.4 Evaluation of the reference scenario and sensitivity to the PBL scheme

The modelled temperatures over the 333.3 m resolution WRF domain are evaluated using observational data from the Catalan Meteorological Service (SMC) and the Spanish Meteorological Agency (AEMET). Urban and rural stations are used for this evaluation with a total of 17 stations (Figure D.1), 13 of which are located inside the AMB and 4 of which are located outside. The characteristics of these stations is provided in Table C.4. The stations are classified into 4 groups according to their LULC at a 100-m resolution: 1) urban fabric and non-vegetated urban areas (UF&NVUA); 2) non-agricultural vegetated urban areas (NAVUA); 3) agricultural areas

(AA); and 4) forest and seminatural areas (F&SNA).

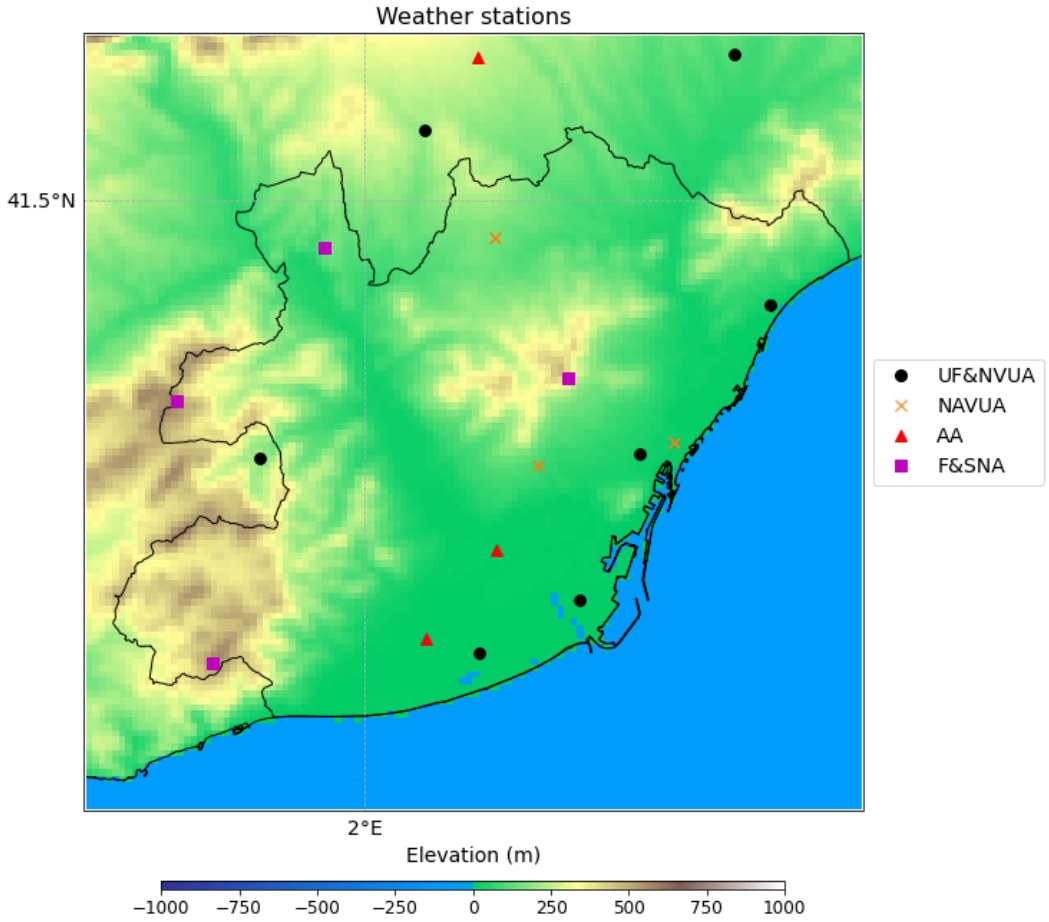


Figure D.1: Location of the observational weather stations.

The three WRF simulations are conducted using the Yonsei University (YSU), the Bougeault-Lacarrere (BouLac) and the Mellor-Yamada-Janjic (MYJ) PBL schemes. The simulation with the YSU PBL scheme is the reference scenario, as it is the PBL scheme employed for the land-use scenario analysis. Statistical analyses of the RMSE, MB and R were used to compare the model simulations with the observations. The near-surface temperature analysis is displayed in Figure D.2 for each LULC group for the period of study (25 June to 24 July 2015) over the daytime (6-18 UTC) and night-time (19-5 UTC). During the daytime, YSU shows an average RMSE of 1.74 ºC. The lowest RMSE for this period is obtained for the NAVUA stations (1.22 ºC), related to an overprediction of daytime temperatures (0.19 ºC). While the highest RMSE was seen for the F&SNA stations (2.36 ºC), related to an underprediction of the daytime temperatures (-1.69 ºC). This underestimation is also seen in UF&SNA (-0.43 ºC) and AA (-1.22

ºC) stations. This underestimation could be attributed to the underestimation of the Bowen ratio, defined as the ratio between sensible heat fluxes and latent heat fluxes, implying on a higher modelled evapotranspiration than what actually is happening. The reference simulation (YSU) presents a high correlation with the daytime temperature observations (0.88), finding the highest correlations with the AA stations (0.90).

During the night-time, the average RMSE is lower (1.32 ºC) with respect to the daytime, being lower for all the LULC groups. The reference simulation accounts for an overestimation of night-time temperatures for NAVUA (0.49 ºC), AA (0.96 ºC) and F&SNA (0.40 ºC) stations. This overestimation could be attributed to an overestimation of the soil moisture in rural areas, as wet soils present a higher thermal inertia than dry soils, presenting higher minimum temperatures during the night and lower maximum temperatures during the day (Matsushima, 2019). The simulated night-time temperatures are less correlated with the observations (0.88) than the simulated daytime temperatures, in all the LULC groups.

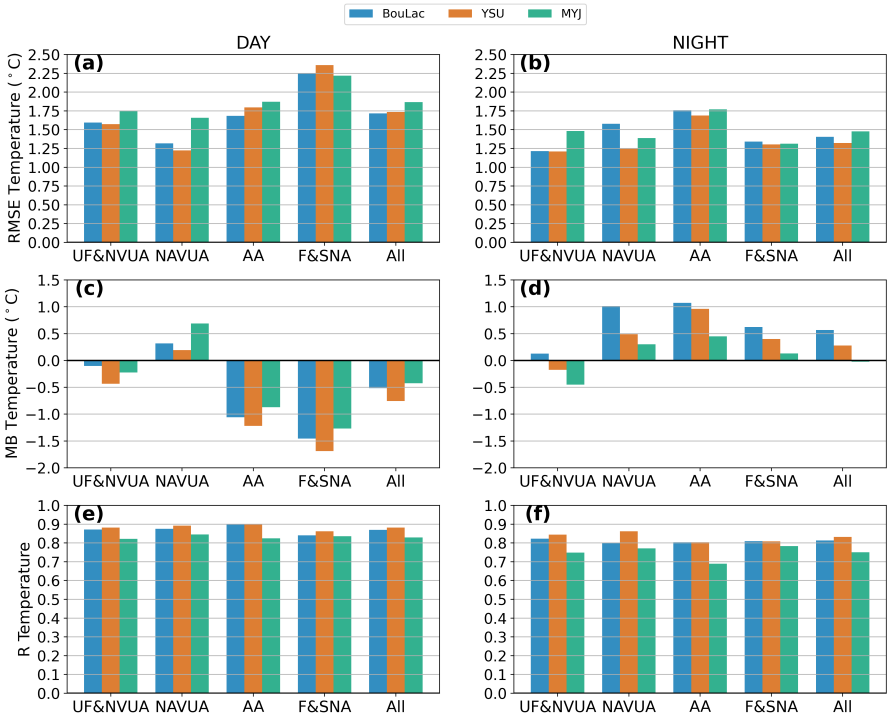


Figure D.2: Temperature analysis for the performance of WRF simulations. Root mean square error (RMSE) (top), Mean bias (MB) (middle) and correlation coefficient (R) (bottom) at daytime (left) and night-time (right) for each simulation and LULC group of stations. UF&NVUA: Urban fabric and non-vegetated urban areas; NAVUA: non-agricultural vegetated urban areas; AA: agricultural areas; F&SNA: forests and semi-natural areas.

The sensitivity analysis of the PBL schemes shows that the BouLac scheme displays lower average daytime RMSE (1.72 ºC) compared to YSU (1.74 ºC) and MYJ (1.87 ºC), although YSU presents lower RMSE in urban stations (UF&SNA and NAVUA). MYJ presents higher errors in UF&NVUA (1.75 ºC), NAVUA (1.65 ºC) and AA (1.87 ºC) stations, while it presents the lowest in F&SNA (2.22 ºC), due to considering the lowest daytime underestimation of temperatures (-1.27 ºC). YSU is the PBL scheme with a higher underestimation of daytime temperatures on average (-0.76 ºC), except for the NAVUA stations. However, the YSU is the highest correlated to the daytime temperature observations, between the three PBL schemes for all the LULC groups.

In the case of the night-time temperatures, YSU presents on average lower RMSE and higher correlations with observed temperatures than BouLac and MYJ. However, overall, MYJ presents the lowest night-time overpredictions in the NAVUA (0.30 ºC), AA (0.45 ºC) and F&SNA (0.13 ºC) stations, despite presenting the lowest correlations with observed night-time temperatures

overall.

This sensitivity analysis yields that the YSU PBL scheme presents the highest correlations with the observations both during the daytime and night-time and for all the LULC groups, compared to the other PBL schemes. Moreover, YSU presents the lowest RMSE of night-time temperatures, while during the daytime the average RMSE obtained by YSU is similar to the lowest one obtained by the BouLac scheme. However, YSU PBL presents the largest underestimations of daytime temperatures, which is partially attributed to the PBL scheme, but also could be attributed to an overestimation of the soil moisture in rural areas, which causes the reduction of the diurnal temperature range. This daytime temperature underestimation should not affect the assessment of the land-use scenarios impacts on the near-surface temperatures, as we are evaluating the temperature change with respect to the S0 scenario.

D.5 Additional VPRM modifications

VPRM calculates net CO_2 capture by taking the difference between ecosystem sequestration due to vegetation photosynthesis and CO_2 release from vegetation and soil respiration. VPRM models 8 plant-functional types (PFT) representing various land cover types: evergreen, deciduous, and mixed forest, shrubland, Mediterranean savanna, cropland, grassland, and sparsely vegetated areas. These PFT are combined, weighted by fractional land coverage, to derive the regional ecosystem fluxes. Table D.1 shows the reclassification rules to reclassify between WRF LULC classes and the VPRM plant functional types.

Table D.1: USGS and LCZ land-use/land-cover classes present in the D03 domain and their corresponding VPRM plant functional types.

USGS class or LCZ	**VPRM PFT**	**PFT name**
2. Dryland cropland and pasture	6	Croplands
3. Irrigated cropland and pasture	6	Croplands
6. Cropland/woodland mosaic	5	Mediterranean savanna
7. Grassland	7	Grassland
9. Mixed shrubland/gassland	4	Shrubland
11. Deciduous broadleaf forest	2	Deciduous forest
13. Evergreen broadleaf forest	1	Evergreen forest
14. Evegreen needleleaf forest	1	Evergreen forest
15. Mixed forest	3	Mixed forest
16. Water bodies	10	Non-vegetated
17. Herbaceous wetland	7	Grassland
19. Barren or sparsely vegetated	4	Shrubland
28. Green urban areas	8	Green urban areas
LCZ 1, 2, 3, 4, 8, 10, and E	10	Non-vegetated
LCZ 5, 6, and 9	9	Low-intensity residential areas

The EVI and LSWI of the reference scenario (S0) are processed using the VPRM Preprocessor developed by the Department of Biogeochemical Systems in the Max Planck Institute for Biogechemistry (https://www.bgc-jena.mpg.de/bgc-systems/pmwiki2/pmwiki.php/Download/VPRMpreproc). In scenarios S1, S2 and S3, vegetation indices of a grid cell are retained if there are no changes in the PFT composition or if new PFTs not present in scenario S0 do not emerge. To address the presence of new PFTs, two methodologies are employed: first, the time-series of vegetation indices are determined using the median within the grid cells in the D03 domain corresponding to the specific PFT, and second, vegetation indices are adopted from the nearest grid cell with the corresponding PFT. These approaches generate two cases used to estimate uncertainty in net carbon sequestration in future LULC scenarios.

Additionally, we have conducted an evaluation of modelled temperatures for scenario S0 during the one-year simulation, comparing them with observational data from the Catalan Meteorological Service and the Spanish Meteorological Agency. Statistical indicators for the model evaluation are computed separately for urban and rural stations and aggregated monthly. The evaluation of the reference scenario is available in Appendix D.6. To assess the bias in carbon fluxes resulting from near-surface temperature discrepancies, we perform separate set of VPRM simulations for each scenario. These simulations involve correcting the air temperature bias in urban (parks and built-up areas) and rural areas for the input temperature variable of the VPRM. The bias correction is applied based on monthly evaluations, distinguishing between day and night and urban and rural grid cells. In total, we obtain two carbon flux datasets for S0 (with and without temperature bias correction) and four carbon flux datasets for other scenarios (utilizing both vegetation index estimation approaches and temperature correction options). From these datasets for each scenario, we calculate the median as the best-case estimate and the standard deviation as the associated uncertainty.

D.6 Evaluation of the reference scenario for the year-long WRF simulation

The modelled temperatures over the 1 km resolution WRF domain over the entire year 2015 are evaluated using the same stations depicted in Appendix D.4. The evaluations are done monthly with the same statistical indicators as in the previous section. In this evaluation, the stations are classified into urban (UF&NVUA and NAVUA stations) and rural areas (AA and F&SNA) to facilitate the posterior implementation of the temperature bias correction in the VPRM simulations.

The evaluation of the near-surface temperature analysis is displayed in Figure D.3 for each month in the year 2015 and for urban and rural stations separated over the daytime and nighttime. The RMSE in daytime temperatures presents a minimum in December for urban (1.27 ºC) and rural (1.29 ºC) stations, while the maximum is observed in March for urban areas (1.72 ºC), and in June for rural areas (1.94 ºC). Over the entire year, the model presents a lower RMSE in urban stations (1.48 ºC) compared to rural stations (1.66 ºC). Between March and August, WRF simulations accounts for an underestimation of the daytime near-surface temperatures between -0.43 ºC and -0.98 ºC, both for urban and rural stations, being the underestimation and the RMSE

larger in the summer months for the rural stations. The model shows similar correlations with the air temperature along the year varying between 0.86 and 0.95.

In the case of the night-time temperatures, the RMSE varies considerably between the different seasons and land-use. The higher RMSE is observed during the winter months (except February), especially during January, with 2.29 ºC for urban stations and 1.88 ºC for rural stations. The model presents the lowest RMSE for night-time temperatures during the month of July, with 1.09 ºC for urban stations and 1.27 ºC for rural stations. However, while on the winter months the urban stations account for a higher RMSE than rural stations, the inverse happens during summer. Overall, the model presents a slightly lower RMSE in rural stations (1.50 ºC) compared to rural stations (1.53 ºC). The model principally overestimates night-time temperatures for urban (+0.55 ºC) and rural stations (+0.46 ºC), especially during the autumn and winter months of January, and between September and December. The maximum overestimations of the night-time temperatures are seen over November (+1.22 ºC) for urban stations and October for rural stations (+ 0.86 ºC). The model correlations with observed night-time temperatures range between 0.83 and 0.92, except for the months of January (urban: 0.74; rural:0.78), July (urban: 0.80; rural:0.78) and December (urban: 0.79; rural:0.79), where the correlations are significantly lower than for the rest of the year.

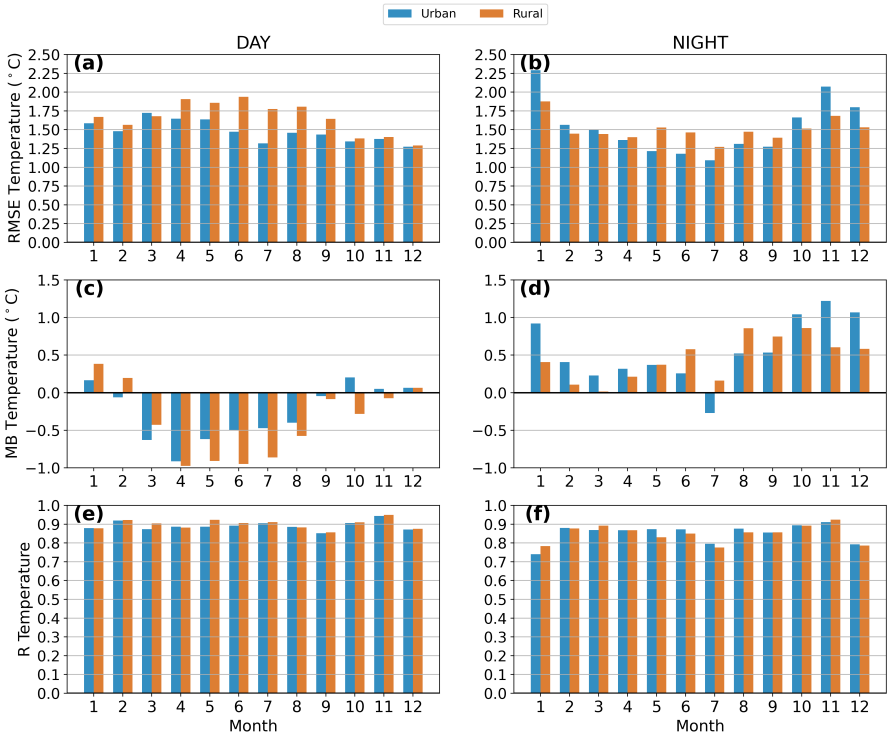


Figure D.3: Temperature analysis for the performance of WRF simulations at 1 km resolution over the months in 2015. Root mean square error (RMSE) (top), Mean bias (MB) (middle) and correlation coefficient (R) (bottom) at daytime (left) and night-time (right) for each simulation and LULC group of stations.

The evaluation has shown that the model has a better performance during the daytime for the autumn and winter months with a lower RMSE and lower underprediction of the daytime temperatures, while it performs better during the summer months for the night-time temperatures. During the growing season months (March to August) the model presents an underestimation of the daytime temperatures, which can affect the carbon capture estimations by the Vegetation Photosynthesis model (VPRM). The daytime temperature underestimations during the spring can reduce the photosynthetic activity, reducing the net carbon capture, while during summer, the thermal stress can be ameliorated by the lower daytime temperatures, enhancing the carbon capture. However, during autumn and winter, the night-time temperature overestimations can enhance the ecosystem respiration, reducing the net carbon sequestration. Applying the temperature bias correction on the temperature input variables of VPRM can lead to more realistic estimation of the biogenic carbon balance in the current and future scenarios.

D.7 Additional results

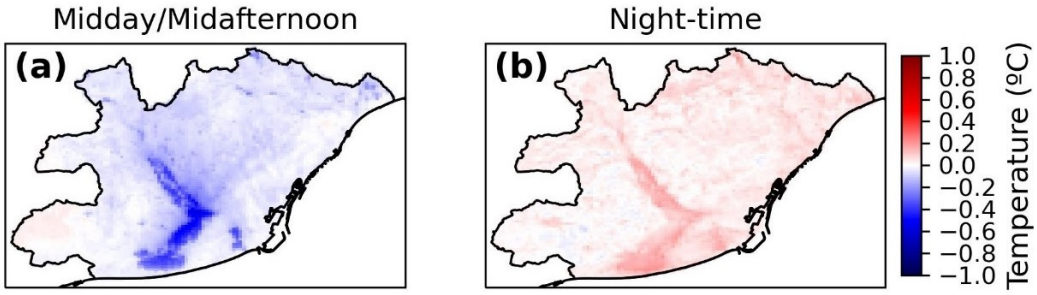


Figure D.4: Comparison of the temperature difference between the current scenario (S0) with irrigation and S0 without irrigation for (a) midday/midafternoon (9-15 UTC); and (b) night-time (19-5 UTC). The average period is between June 25 and July 24, 2015.

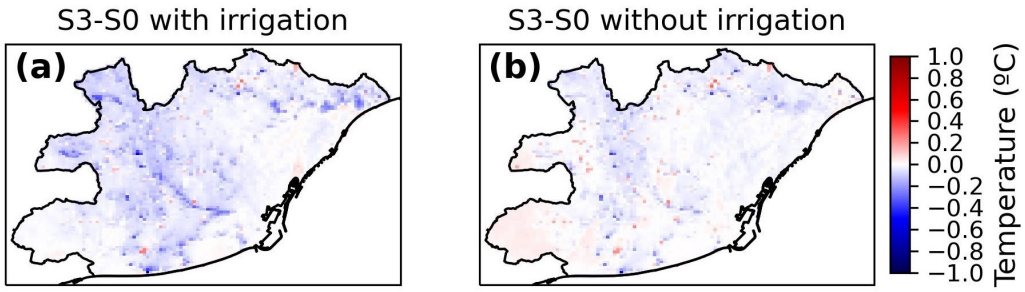


Figure D.5: Comparison of the temperature difference between scenarios S3 and S0 during midday/midafternoon (a) with irrigation; and (b) without irrigation. The average period is between June 25 and July 24, 2015.

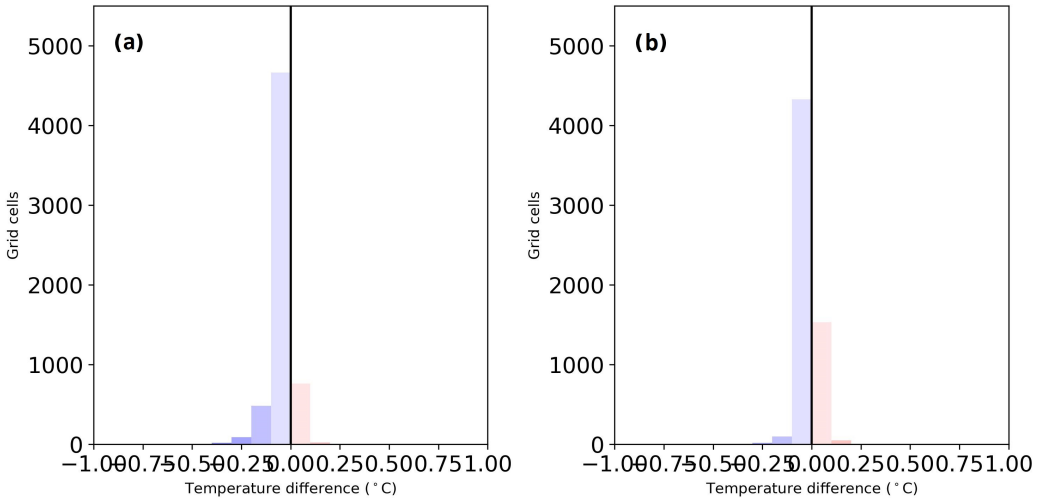


Figure D.6: Comparison of histograms of temperature differences inside the AMB between S3 and S0 (a) with irrigation; and (b) without irrigation. The average period is between June 25 and July 24, 2015.

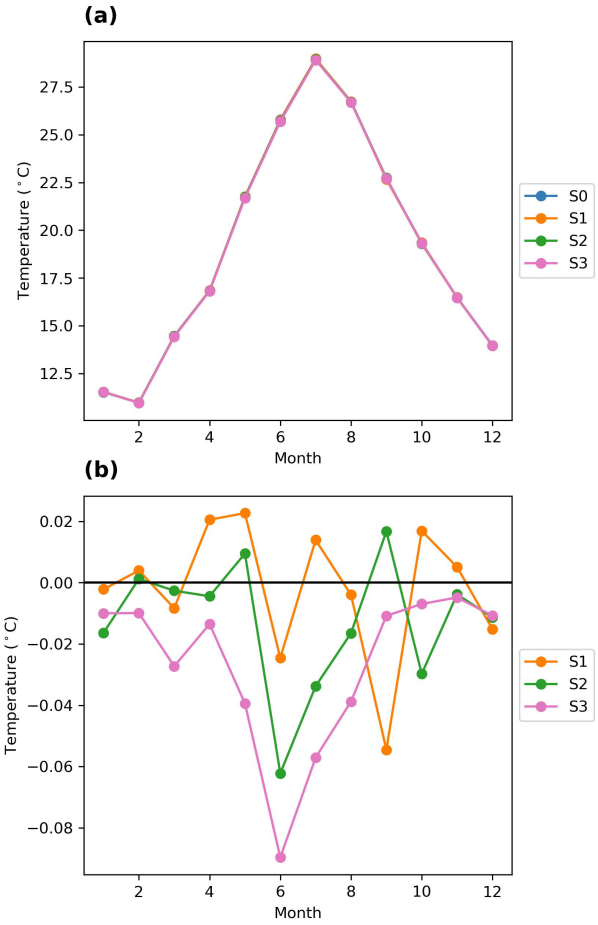


Figure D.7: (a) Monthly average midday and midafternoon (9-15 UTC) near-surface temperatures in the AMB over the year 2015 for the four scenarios. (b) Difference of near-surface air temperatures with respect to the scenario S0.

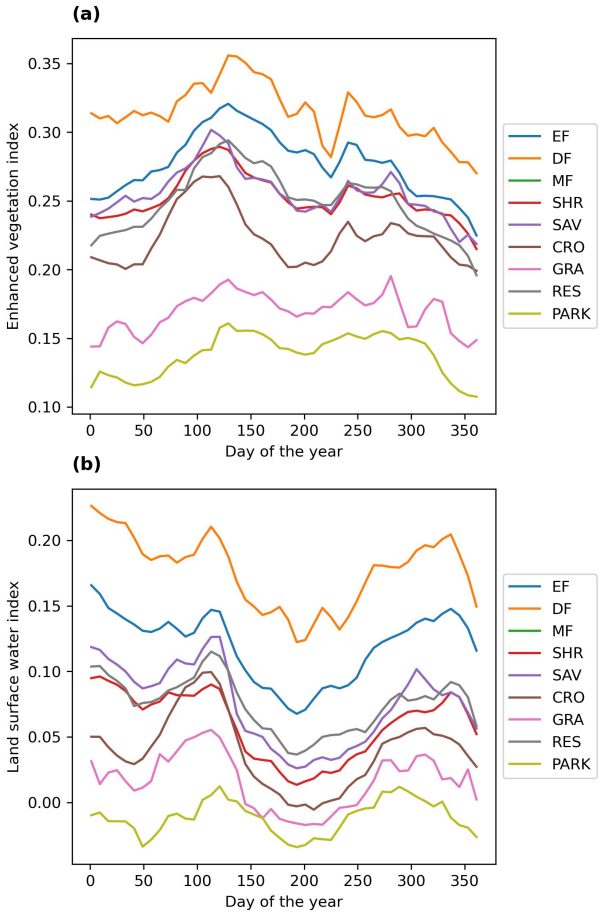


Figure D.8: Time variability of the (a) Enhanced vegetation index (EVI), and (b) Land surface water index (LSWI), over the different plant functional types in the AMB over the year 2015. EF: evergreen forest; DF: deciduous forest; MF: mixed forest; SHR: shrubland; SAV: Mediterranean savanna; CRO: cropland; GRA: grassland; RES: low-intensity residential areas; PARK: urban parks.

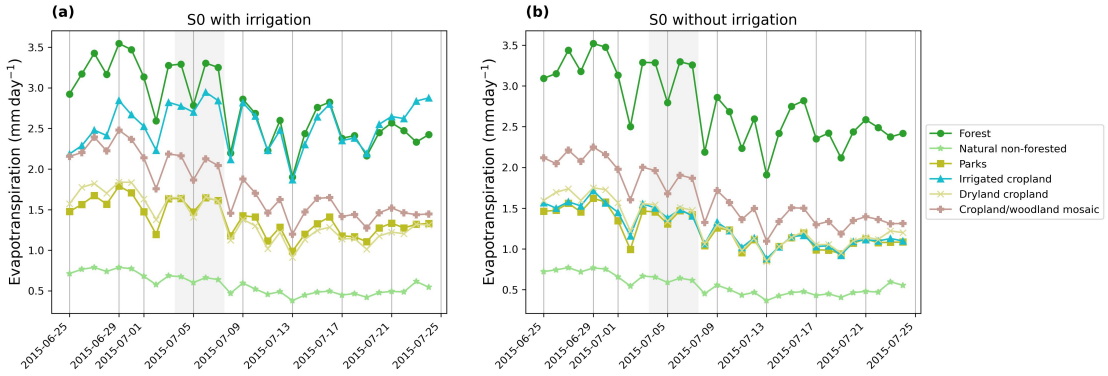


Figure D.9: Time-series of the daily evapotranspiration simulated during the study period between June 25 and July 24, 2015, for 6 different land-cover types (a) for the simulation of the current scenario with irrigation; (b) the current scenario without irrigation. The daily evapotranspiration has been averaged over the grid cells with the same land-cover type. The grey interval corresponds to the heat wave event.

Table D.2: Percentage of the AMB population in the year 2015 that will perceive the midday/midafternoon (9-15 UTC) temperature reductions in each LULC scenario with respect to the current scenario.

Temperature difference with respect to S0 (ºC)	AMB population percentage (%)		
	S1	S2	S3
<-0.5	0.00	0.00	0.01
<-0.4	0.00	0.00	0.03
<-0.3	0.00	0.02	0.13
<-0.2	0.06	0.08	0.60
<-0.1	0.12	0.30	3.56
<0.0	32.44	45.23	84.87
<0.1	97.82	99.79	99.80
<0.2	99.40	99.93	99.95
<0.3	99.67	99.98	100
<0.4	99.84	99.99	100
<0.5	99.90	99.99	100
<0.6	99.94	99.99	100
<0.7	99.94	100	100
<0.8	99.99	100	100
<0.9	99.99	100	100
<1.0	100	100	100

E Supporting information for Chapter 6

Table E.1: Eddy covariance stations information. FLUXNET 2015, Warm Winter 2020 and ICOS level 2 release 2022-1 ecosystem data sites used in this study. The Land cover classification corresponds to the land-cover class reported by the site PI (International Geosphere-Biosphere Programme (IGBP) classes), and the PFT correspond to the Plant Functional Type (PFT) of the VPRM model.

Site Code	Name	Land cover classification	Latitude	Longitude	PFT
CH-Cha	Chamau	GRA	47.21	8.41	GRA
CH-Dav	Davos	ENF	46.82	9.86	EF
CH-Fru	Fruebel	GRA	47.12	8.54	GRA
CH-Lae	Laegern	MF	47.48	8.36	MF
CZ-BK1	Bily Kriz forest	ENF	49.50	18.54	EF
CZ-KrP	Kresin u Pacova	CRO	49.57	15.08	CRO
CZ-Lnz	Lanzhot	DBF	48.68	16.95	DF
CZ-RAJ	Rajec	ENF	49.44	16.70	EF
CZ-Stn	Stitna	DBF	49.04	17.97	DF
ES-Abr	Albuera	SAV	38.70	-6.79	SAV
ES-Agu	Aguamarga	OSH	36.94	-2.03	SHR
ES-LJu	Llano de los Juanes	OSH	36.93	-2.75	SHR
ES-LM1	Majadas del Tietar North	SAV	39.94	-5.78	SAV
FR-Aur	Aurade	CRO	43.55	1.11	CRO
FR-Bil	Bilos	ENF	44.49	-0.96	EF
FR-FBn	Font-Blanche	MF	43.24	5.68	EF
FR-Fon	Fontainebleau	DBF	48.48	2.78	DF
FR-Hes	Hesse	DBF	48.67	7.06	DF
FR-Lam	Lamasquere	CRO	43.50	1.24	CRO
FR-Pue	Puechabon	EBF	43.74	3.60	EF
FR-Tou	Toulouse	GRA	43.57	1.37	GRA
IT-BCi	Borgo Cioffi	CRO	40.52	14.96	CRO
IT-CA2	Castel d'Asso 2	CRO	42.38	12.03	CRO
IT-Col	Collelongo	DBF	41.85	13.59	DF
IT-Cp2	Castelporziano 2	EBF	41.70	12.36	EF
IT-Isp	Ispra	DBF	45.81	8.63	DF
IT-Lav	Lavarone	ENF	45.96	11.28	EF
IT-Lsn	Lison	OSH	45.74	12.75	SAV
IT-MBo	Monte Bondone	GRA	46.01	11.05	GRA
IT-Ren	Renon	ENF	46.59	11.43	EF
IT-Ro2	Roccarespampani 2	DBF	42.39	11.92	DF
IT-SR2	San Rossore 2	ENF	43.73	10.29	EF
IT-Tor	Torgnon	GRA	45.84	7.58	GRA

Table E.2: Additional eddy covariance stations information. Additional information of the sites used in this study. In bold letters are marked the siteyears with summer crops.

Site Code	Soil permanent wilting point	Soil field capacity	Years used for optimisation (crop type)	Years used for evaluation (crop type)
CH-Cha	24.5	57.0	2017, 2018	2015, 2016
CH-Dav	6.6	16.9	2015, 2016	2014, 2017
CH-Fru	17.0	51.0	2013, 2018	2011, 2016
CH-Lae	7.7	27.1	2016, 2017	2010, 2018
CZ-BK1	5.6	17.9	2018, 2019	2011, 2016
CZ-KrP	5.8	25.9	2018 (Oat-pea mixture), 2019 (clover-grass), **2017 (silage maize)**	
CZ-Lnz	17.8	36.0	2017, 2018	2016, 2020
CZ-RAJ	7.8	17.9	2018, 2019	2016, 2017
CZ-Stn	7.1	45.0	2010, 2018	2011, 2015
ES-Abr	6.6	30.0	2016, 2019	2017, 2018
ES-Agu	3.1	21.8	2010, 2012	2011, 2013
ES-LJu	9.0	33.0	2010, 2012	2013, 2015
ES-LM1	5.3	31.3	2017, 2018	2015, 2016
FR-Aur	7.0	37.4	2013 (rapeseed), 2014 (winter wheat), **2016 (sunflower)**	2011 (rapeseed), 2018 (rapeseed)
FR-Bil	1.0	13.2	2017, 2020	2016, 2019
FR-FBn	4.8	27.2	2014, 2017	2016, 2018
FR-Fon	2.2	18.0	2013, 2015	2016, 2018
FR-Hes	7.4	26.5	2015, 2016	2017, 2018
FR-Lam	9.6	37.0	2011 (winter wheat), **2012 (maize)**, 2013 (winter wheat), **2014 (maize)**	**2010 (maize)**, 2016 (winter wheat), 2018 (winter wheat), **2019 (maize)**
FR-Pue	4.2	23.8	2022	
FR-Tou	6.9	32.6	2018, 2019	
IT-BCi	6.1	36.0	2019 (ryegrass and clover), 2020 (ryegrass and clover)	2018 (ryegrass, clover, **sorghum**)
IT-CA2	9.0	30.2		2013 (winter wheat/ryegrass and clover), 2014 (winter wheat/ryegrass and clover)
IT-Col	17.0	35.0		2011, 2014
IT-Cp2	4.5	14.7	2022	
IT-Isp	18.7	26.0		2013, 2014
IT-Lav	21.1	27.1	2014, 2015	2013, 2016
IT-Lsn	22.2	53.0	2017, 2019	2016, 2018
IT-MBo	4.9	45.0	2010, 2017	2011, 2016
IT-Ren	11.0	17.9	2012, 2013	2010, 2011
IT-Ro2	13.1	29.5	2010, 2012	
IT-SR2	3.8	9.6	2014, 2017	2016, 2018
IT-Tor	15.4	38.4	2017, 2018	2011, 2014

Table E.3: VPRM prior parameters: λ_{SW} (μmol CO_2 $m^{-2}\,s^{-1}\,(Wm^{-2})^{-1}$), SW_0 ($W\,m^{-2}$), α (μmol CO_2 $m^{-2}\,s^{-1}\,(°C)^{-1}$), β (μmol CO_2 $m^{-2}\,s^{-1}$), q (unitless), η^* (unitless), R_0 (μmol CO_2 $m^{-2}\,s^{-1}$), k_1 (unitless), k_2 (unitless), γ (unitless), E_0 (K).

PFT	Default VPRM				Modified VPRM						
	λ_{SW}	SW_0	α	β	q	η^*	R_0	k_1	k_2	γ	E_0
EF	0.226	275	0.288	-1.09	1.0	0.2	2.87	0.478	6.28	0.604	125
DF	0.215	254	0.181	0.84	1.0	0.2	2.55	0.247	6.28	0.796	88
MF	0.163	446	0.244	-0.49	1.0	0.2	2.89	0.391	6.28	0.703	177
SHR	0.293	70	0.055	-0.12	1.0	0.2	1.60	0.354	6.28	0.850	157
SAV	0.114	1297	0.060	0.00	1.0	0.2	1.49	0.654	6.28	0.474	82
CRO	0.086	1132	0.092	0.29	1.0	0.2	2.31	0.244	6.28	0.934	129
CRO_W	0.086	1132	0.092	0.29	1.0	0.2	2.31	0.244	6.28	0.934	129
CRO_S	0.086	1132	0.092	0.29	1.0	0.2	2.31	0.244	6.28	0.934	129
GRA	0.119	528	0.125	0.02	1.0	0.2	2.27	0.578	6.28	0.670	101

Table E.4: Default VPRM optimized parameters: λ_{SW} (μmol CO_2 $m^{-2}\,s^{-1}\,(Wm^{-2})^{-1}$), SW_0 ($W\,m^{-2}$), α (μmol CO_2 $m^{-2}\,s^{-1}\,(°C)^{-1}$), β (μmol CO_2 $m^{-2}\,s^{-1}$).

PFT	λ_{SW}	SW_0	α	β
EF	0.416	171	0.399	-1.87
DF	0.256	228	0.184	0.78
MF	0.347	196	0.429	0.02
SHR	0.325	84	0.019	0.45
SAV	0.386	244	0.060	1.68
CRO	0.275	250	0.262	-0.50
CRO_W	0.322	193	0.266	-0.48
CRO_S	0.196	466	0.259	-0.59
GRA	0.539	177	0.385	0.574

Table E.5: Modified VPRM optimized parameters: λ_{SW} (μmol CO_2 $m^{-2}\,s^{-1}\,(Wm^{-2})^{-1}$), SW_0 ($W\,m^{-2}$), q (unitless), η^* (unitless), R_0 (μmol CO_2 $m^{-2}\,s^{-1}$), k_1 (unitless), k_2 (unitless), γ (unitless), E_0 (K).

PFT	λ_{SW}	SW_0	q	η^*	R_0	k_1	k_2	γ	E_0
EF	0.446	186	1.84	0.39	1.44	0.391	3.63	0.420	294
DF	0.258	229	1.05	0.17	2.10	0.346	1.43	0.504	112
MF	0.347	196	0.15	0.05	3.08	0.363	8.47	0.00	147
SHR	0.300	107	1.00	0.49	0.77	0.679	1.42	0.119	233
SAV	0.386	246	7.89	0.08	1.20	0.631	2.85	0.442	126
CRO	0.280	250	2.71	0.20	1.71	0.389	9.14	0.771	190
CRO_W	0.329	195	1.98	0.25	1.43	0.459	6.86	0.564	254
CRO_S	0.199	462	1.17	0.21	1.78	0.349	18.84	0.73	121
GRA	0.586	187	0.29	0.99	3.06	0.732	0.80	0.531	163

The equations for the standard deviation of the measured fluxes (SD_{meas}) and the modelled fluxes (SD_{mod}), the squared bias (SB), the squared difference between measured and simulated standard deviation (SDSD) and the lack of correlation weighted by standard deviations (LCS) are as follows:

$$SD_{meas} = \sqrt{\frac{\sum_{i=1}^{n} \left(y_{meas,i} - \bar{y}_{meas}\right)^2}{n}} \tag{D.1}$$

$$SD_{mod} = \sqrt{\frac{\sum_{i=1}^{n} \left(y_{mod,i} - \bar{y}_{mod}\right)^2}{n}} \tag{D.2}$$

$$SB = (\bar{y}_{mod} - \bar{y}_{meas})^2 \tag{D.3}$$

$$SDSD = (SD_{mod} - SD_{meas})^2 \tag{D.4}$$

$$LCS = 2SD_{mod}SD_{meas}(1 - r) \tag{D.5}$$

where y_{meas} is the observed flux, y_{mod} is the modelled flux with VPRM, $\bar{y}_{meas}$ is the mean of the observed fluxes, $\bar{y}_{mod}$ is the mean of the modelled fluxes and n is the number of observations.

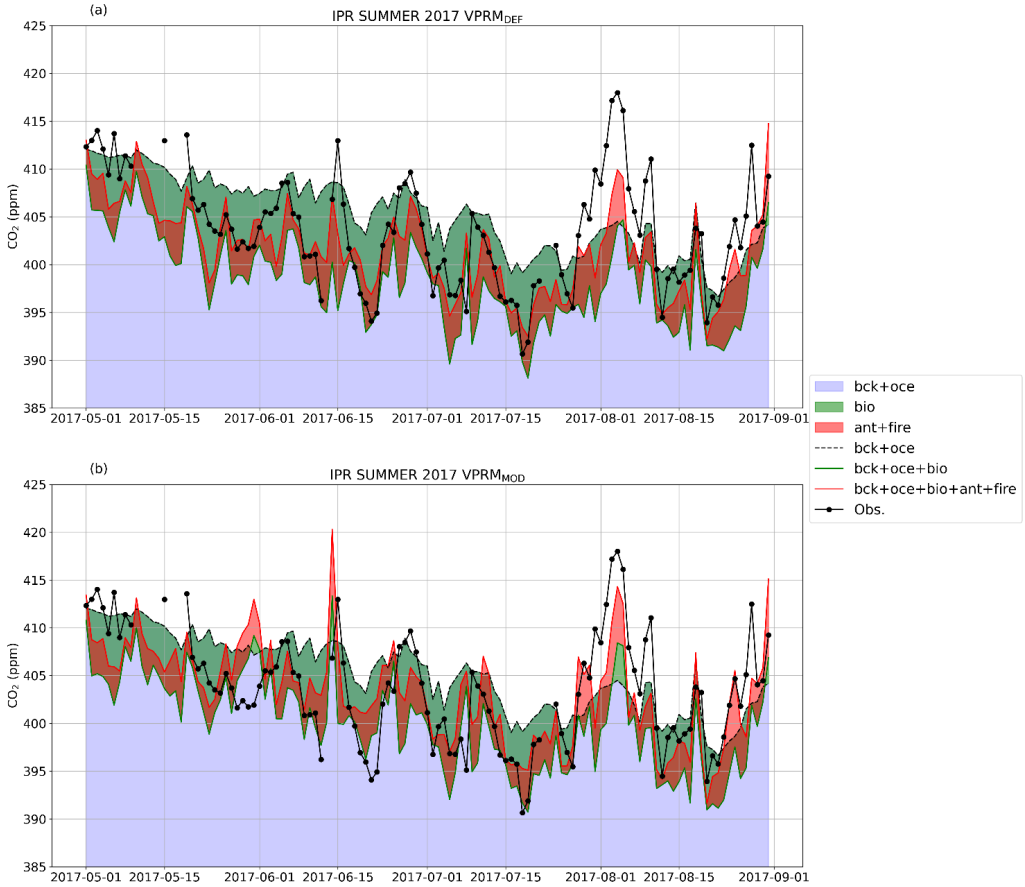


Figure E.1: Time-series of mid-afternoon decomposed CO_2 concentrations for IPR. Observed (black dots) and WRF-Chem modelled daily mid-afternoon CO_2 concentrations decomposed into the different tracers for the IPR station between May and September 2017 for (a) $VPRM_{DEF}$ and (b) $VPRM_{MOD}$. The shaded blue area until the dotted black line corresponds to background (bck) and oceanic (oce) tracers, the green shaded area is the biogenic (bio) tracer, the red shaded area is the sum of fossil fires (fire) and anthropogenic (ant) tracers. The solid green line is the sum of background, oceanic and biogenic tracers, and the solid red line the total modelled concentration.

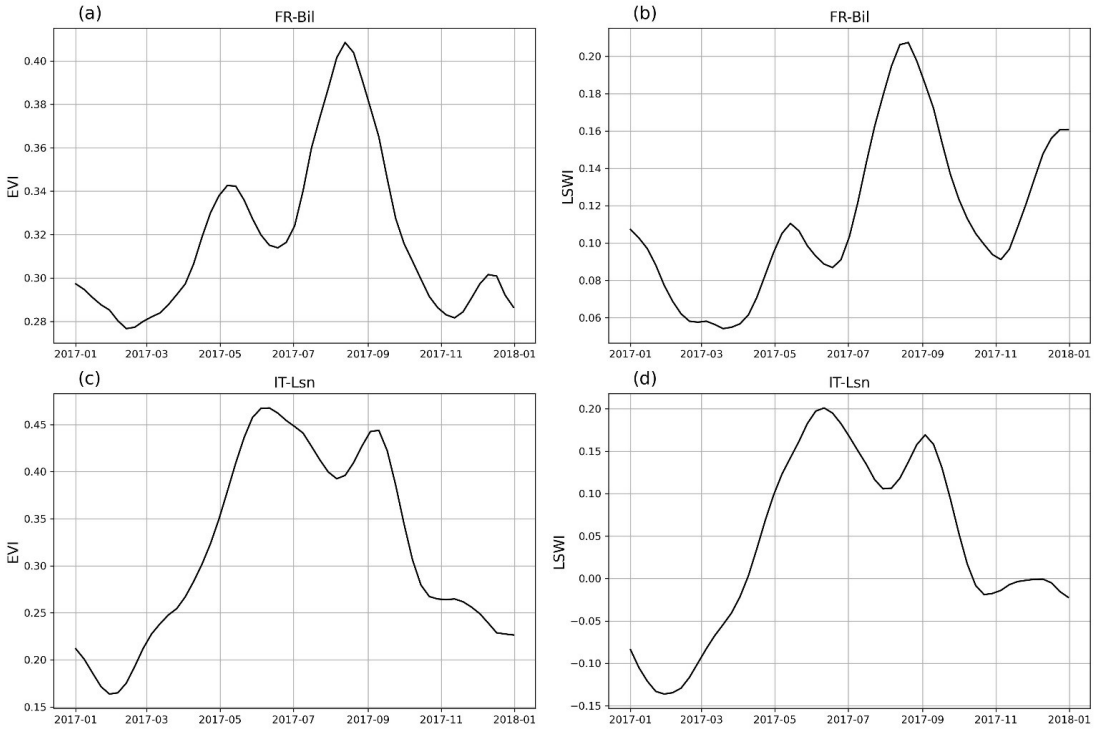


Figure E.2: Weekly EVI and LSWI during the year 2017. Time-series of weekly ecosystem vegetation indices during the year 2017 for (a) EVI for FR-Bil; (b) LSWI for FR-Bil; (c) EVI for IT-Lsn; (d) LSWI for IT-Lsn.

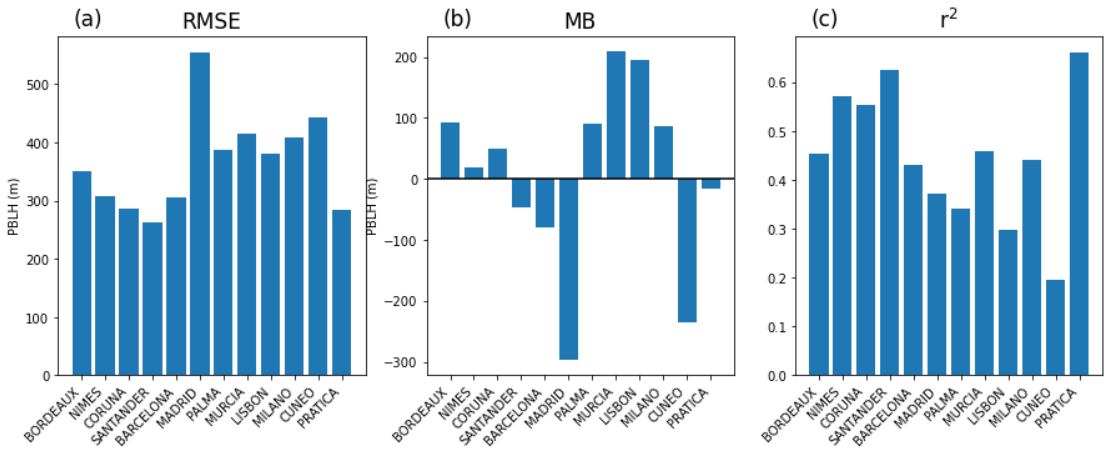


Figure E.3: Evaluation of the PBLH. Performance evaluation of the mid-afternoon planetary boundary layer height for the WRF-Chem simulations during the period March 1 to December 1 2017 for (a) RMSE; (b) Mean bias (MB); and (c) r^2 at different radiosonde launch locations inside the study domain.

F Supporting information for Chapter 7

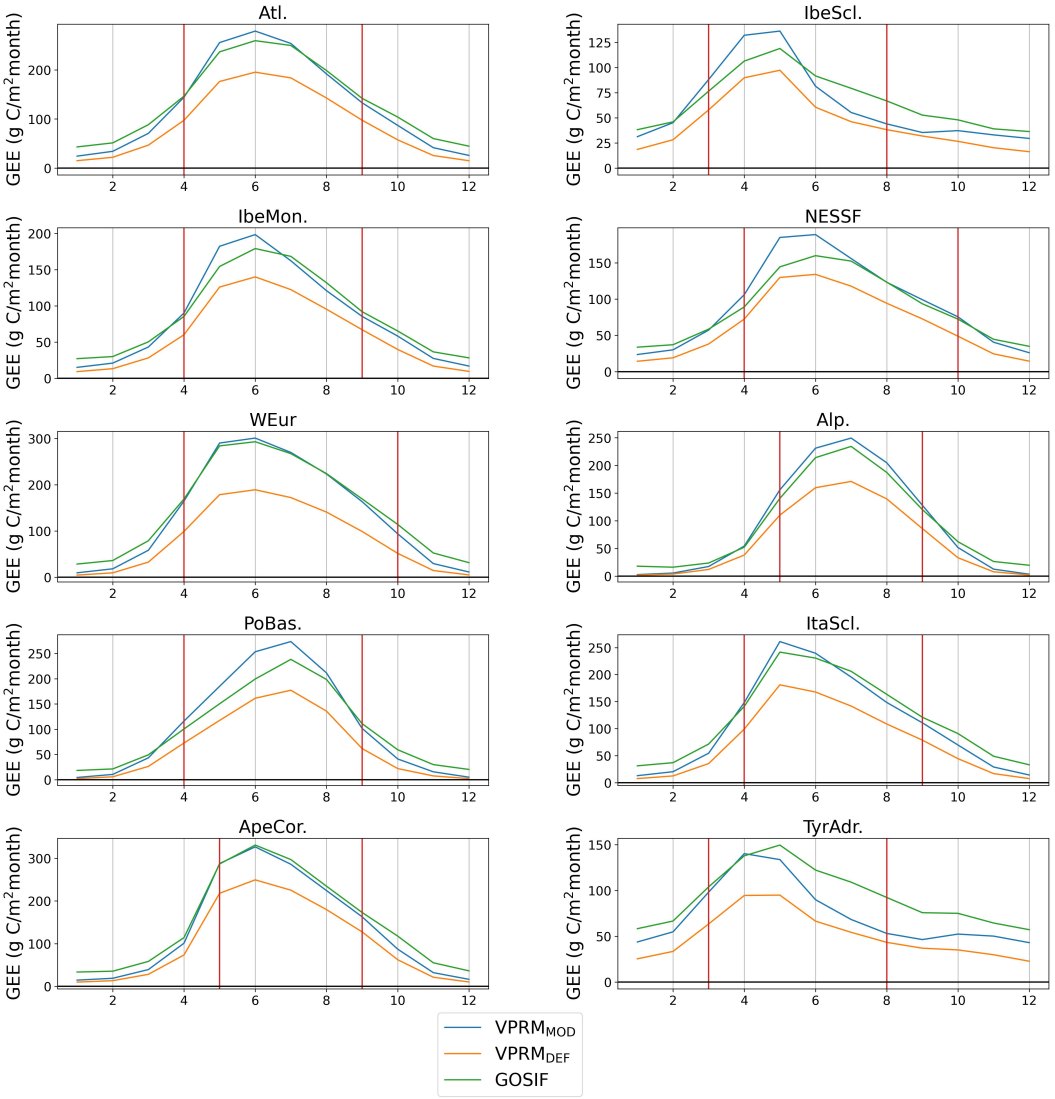


Figure F.1: Seasonal cycles of the GEE for each biogeographical region, for the modified VPRM used in this study ($VPRM_{MOD}$) (blue line), the default VPRM ($VPRM_{DEF}$) orange line, and GOSIF (green line). The red vertical lines indicate the months of beginning and ending of the growing season (both included).

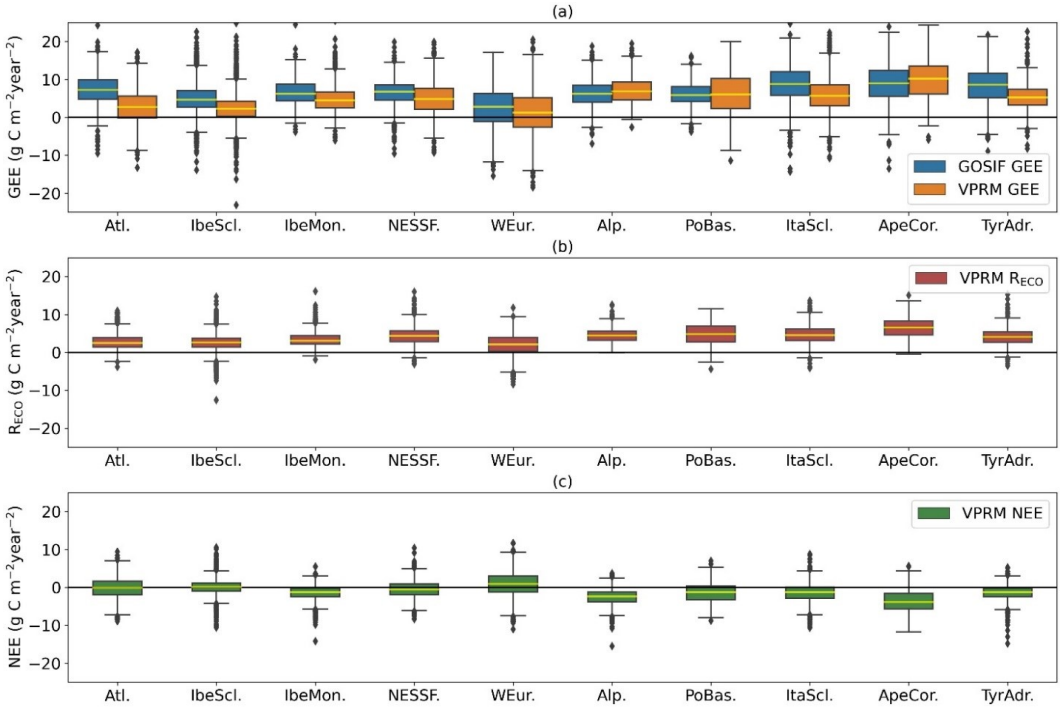


Figure F.2: Boxplot of the fluxes annual trends aggregated annually and for the different biogeographical regions for the (a) GEE; (b) R_{ECO}; (c) NEE. The white point defines the spatial median inside the biogeographical region, and the thick black line corresponds to the interquartile range. The definitions of the biogeographical region acronyms are marked in Figure 7.1 in the Chapter 7.

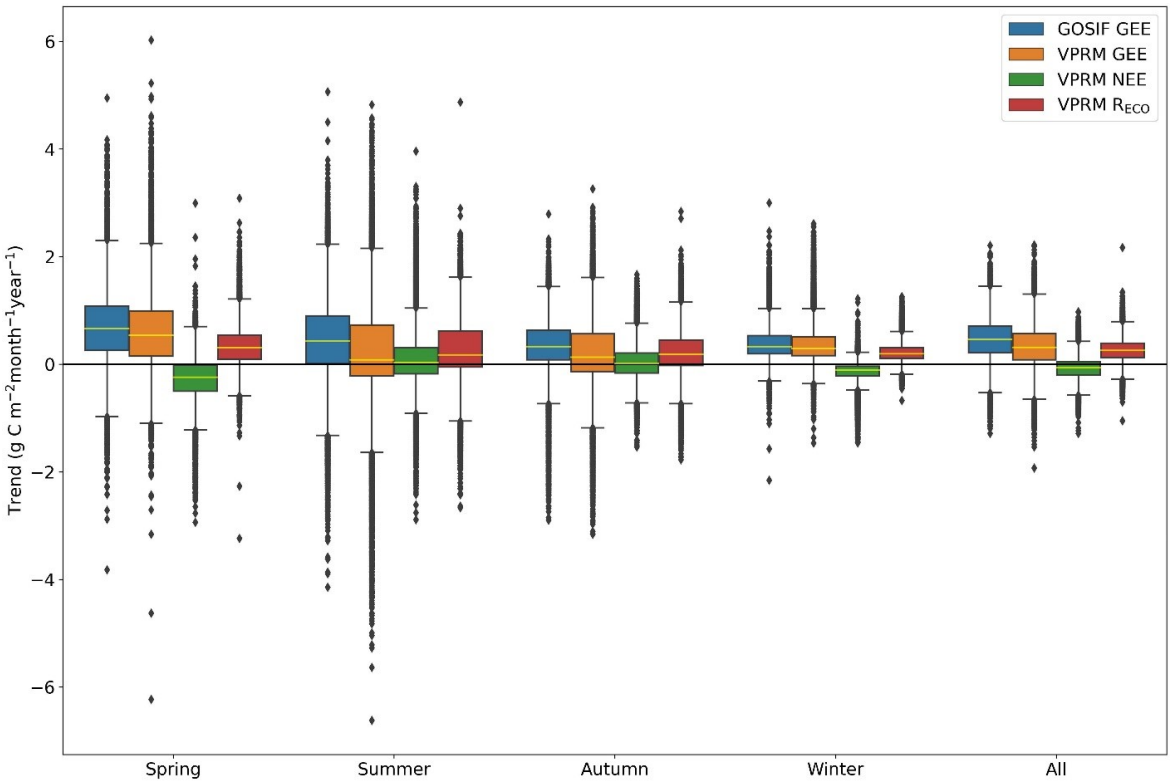


Figure F.3: Boxplot of the fluxes annual trends aggregated by season and all the year. The yellow line defines the spatial median inside the study area, and the box to the interquartile range.

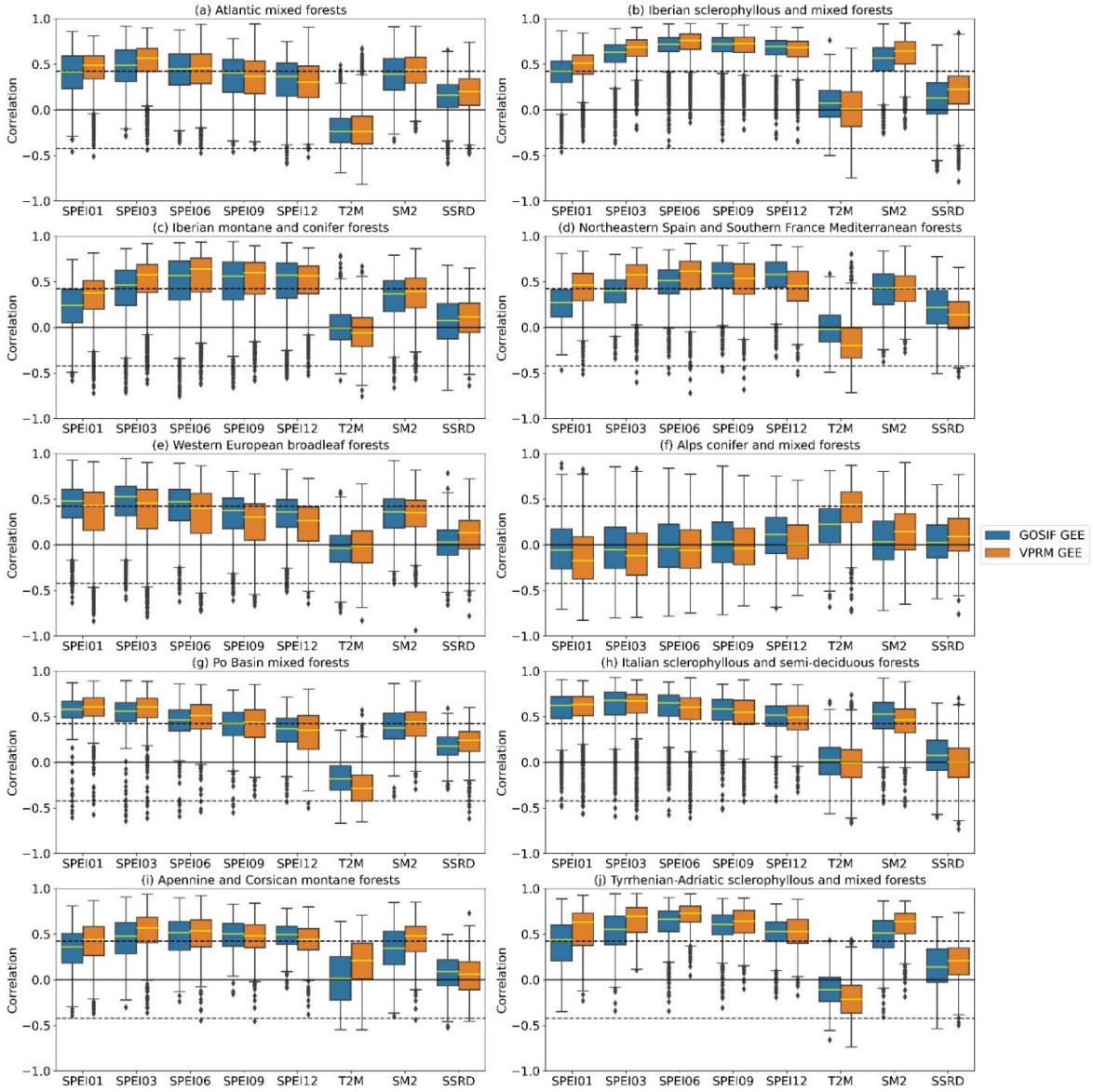


Figure F.4: Boxplots of correlation values between GEE detrended anomalies for GOSIF (blue) and VPRM (orange) and the drought indices, and partial correlations with the climate drivers aggregated during the growing season months of each biogeographical region. The median is represented with a yellow line. The discontinuous black lines represent the limit when correlations are significant ($p<0.05$). T2M: 2 m temperature. SM2: soil moisture between 7 and 28 cm depth. SSRD: surface solar radiation downwards.

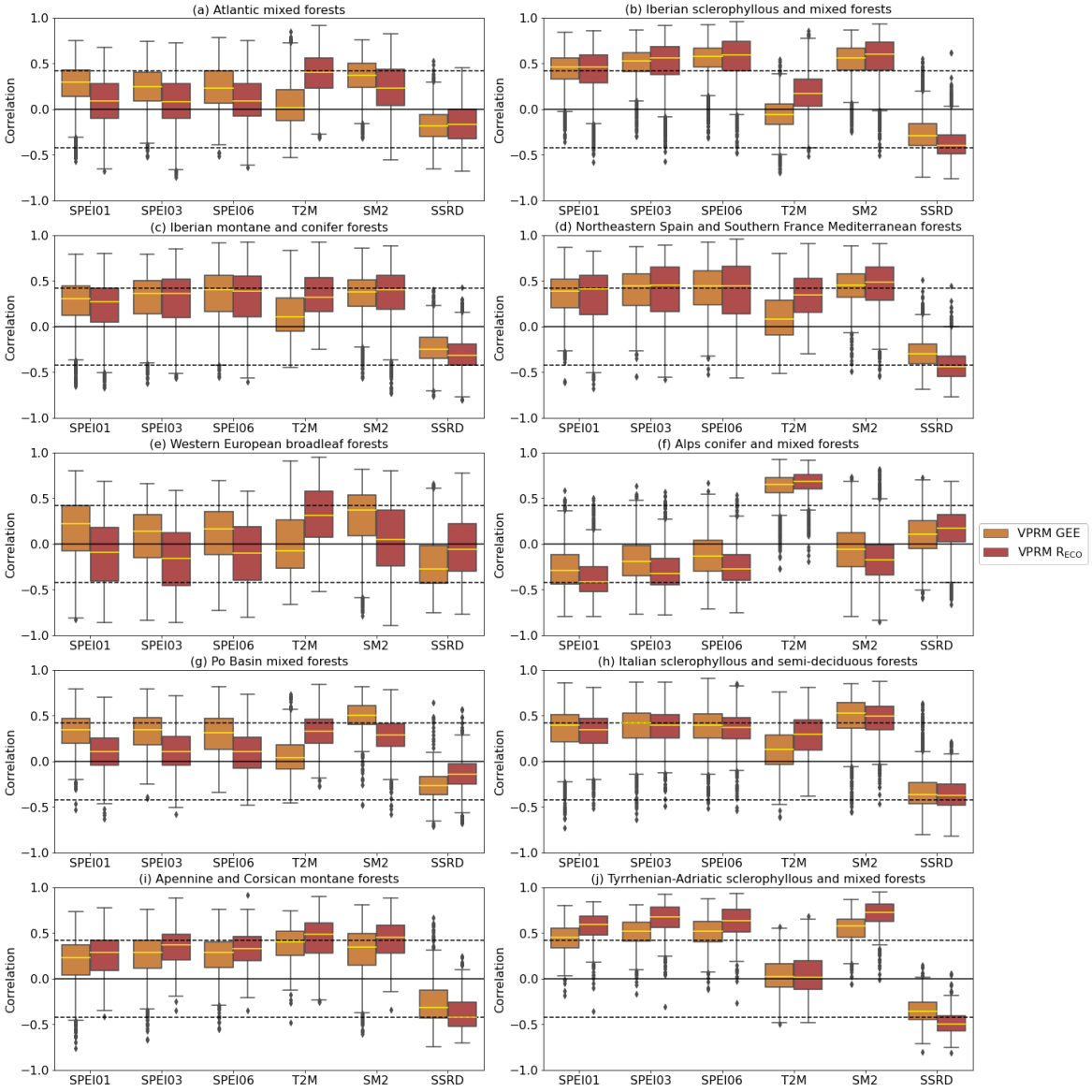


Figure F.5: Boxplots of correlation values between GEE and R_{ECO} detrended anomalies and the different climate drivers and drought indices aggregated over all the year for each biogeographical region. The median is represented with a yellow line. The discontinuous black lines represent the limit when correlations are significant ($p<0.05$). T2M: 2 m temperature. SM2: soil moisture between 7 and 28 cm depth. SSRD: surface solar radiation downwards.

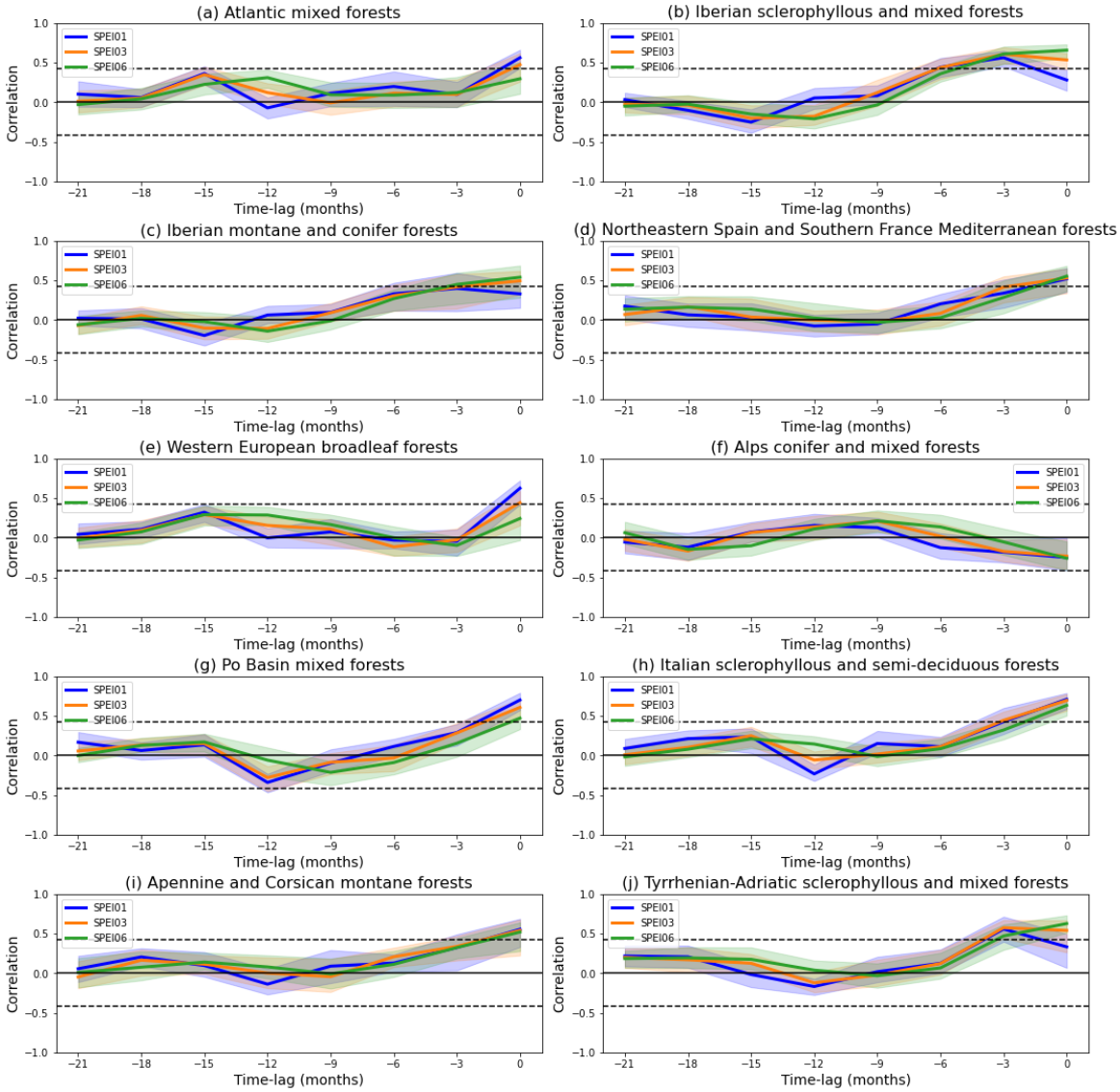


Figure F.6: Correlogram between the growing season anomaly in the GEE and the SPEI aggregated at 1 month (blue), 3 months (orange) and 6 months (green) averaged over the time-lagged previous season, being 0 months the summer season of the current year, 3 months the spring of the current year, and so on. The bold lines represent the median correlation between all the grid cells inside the biogeographical region, and the shaded areas represent the interquartile range.

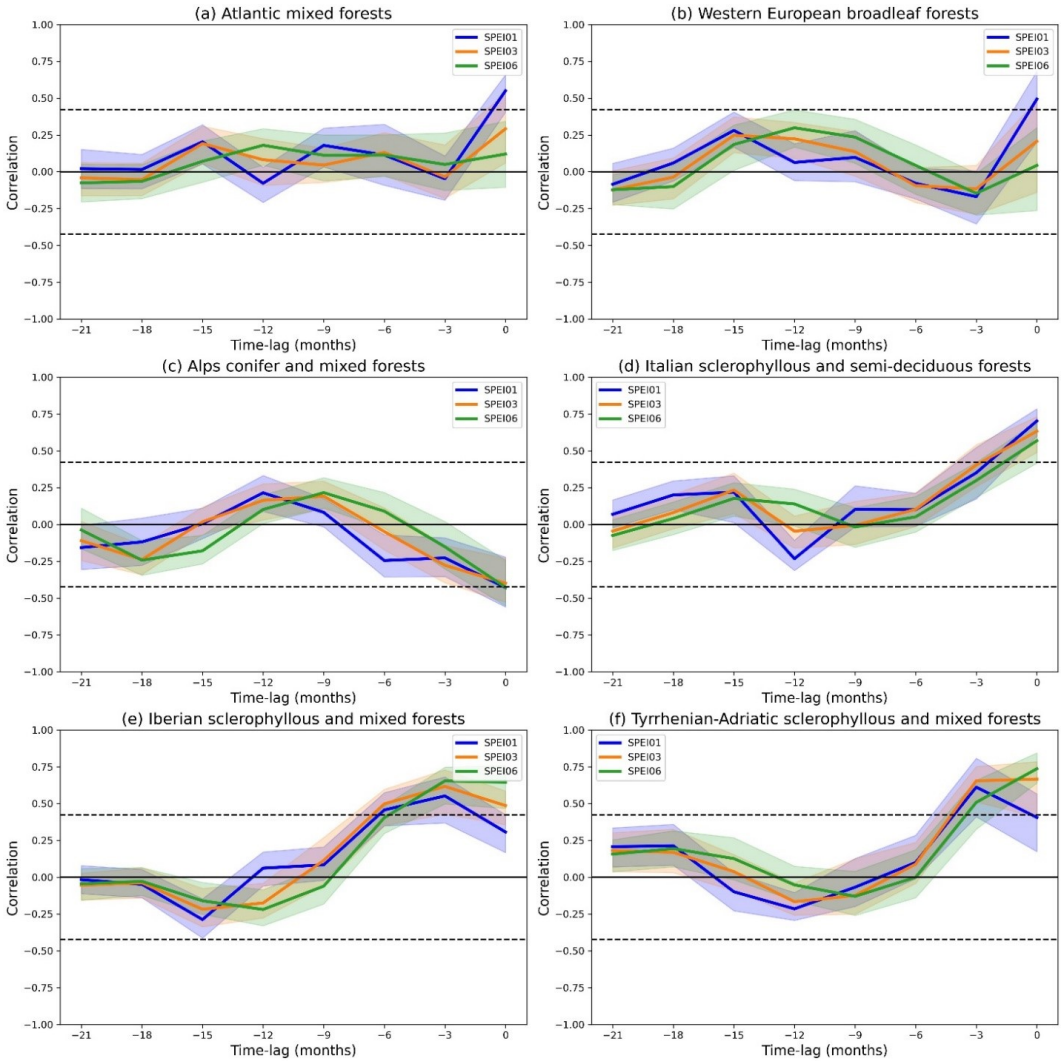


Figure F.7: Correlogram between the growing season anomaly in the R_{ECO} and the SPEI aggregated at 1 month (blue), 3 months (orange) and 6 months (green) averaged over the time-lagged previous season, being 0 months the summer season of the current year, 3 months the spring of the current year, and so on. The bold lines represent the median correlation between all the grid cells inside the biogeographical region, and the shaded areas represent the interquartile range.

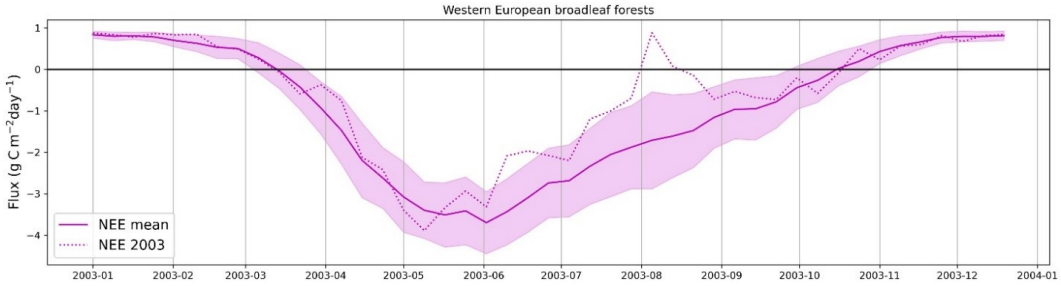


Figure F.8: Time series of the spatially average NEE for the Western European broadleaf forest region in the year 2003 (dotted line) and the climatic mean for the 2001 to 2022 period (solid line). The shaded areas correspond to the temporal standard deviation for each 8-daily period.

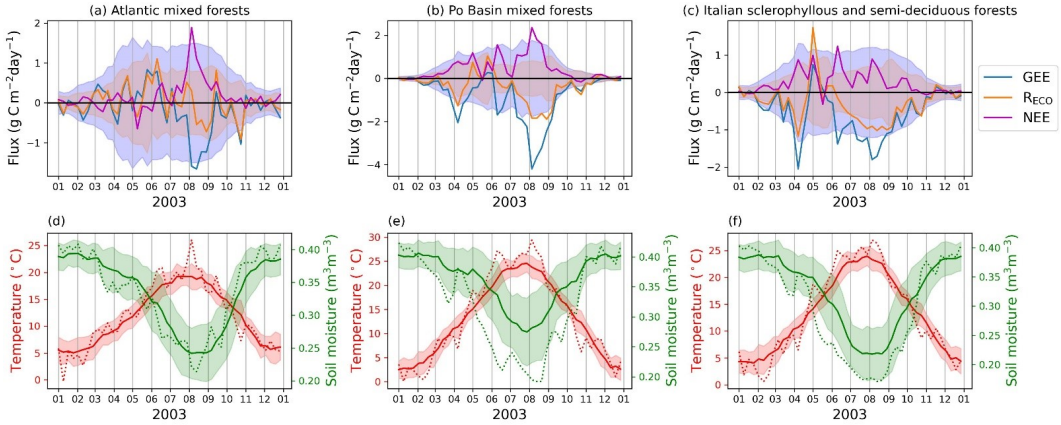


Figure F.9: Time series of the spatially average anomalies for the Atlantic mixed forest (a,d), Po Basin mixed forests (b,e), and Italian sclerophyllous and semi-deciduous forests (c,f) for (a,b,c) 8-daily GEE (blue), R_{ECO} (orange) and NEE (pink) in 2003. (d,e,f) spatially averaged 8-daily 2 m temperature (red) and soil moisture in the 7-28 cm depth layer (green) for the study year (dotted line) and the climatic mean for the 2001 to 2022 period (solid line). The shaded areas correspond to the temporal standard deviation for each 8-daily period.

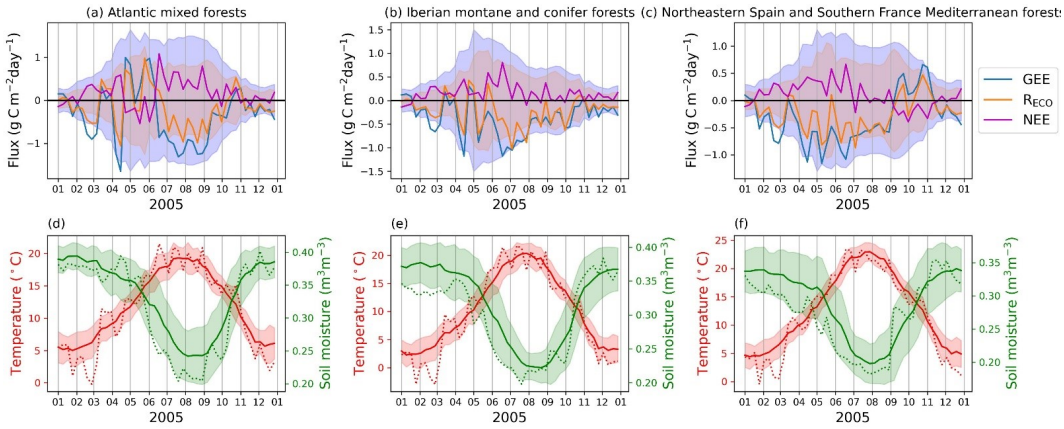


Figure F.10: Time series of the spatially average anomalies for the Atlantic mixed forest (a,d), Iberian montane and conifer forests (b,e), and North-eastern Spain and Southern France Mediterranean forests (c,f) for (a,b,c) 8-daily GEE (blue), R_{ECO} (orange) and NEE (pink) in 2005. (d,e,f) spatially averaged 8-daily 2 m temperature (red) and soil moisture in the 7-28 cm depth layer (green) for the study year (dotted line) and the climatic mean for the 2001 to 2022 period (solid line). The shaded areas correspond to the temporal standard deviation for each 8-daily period.

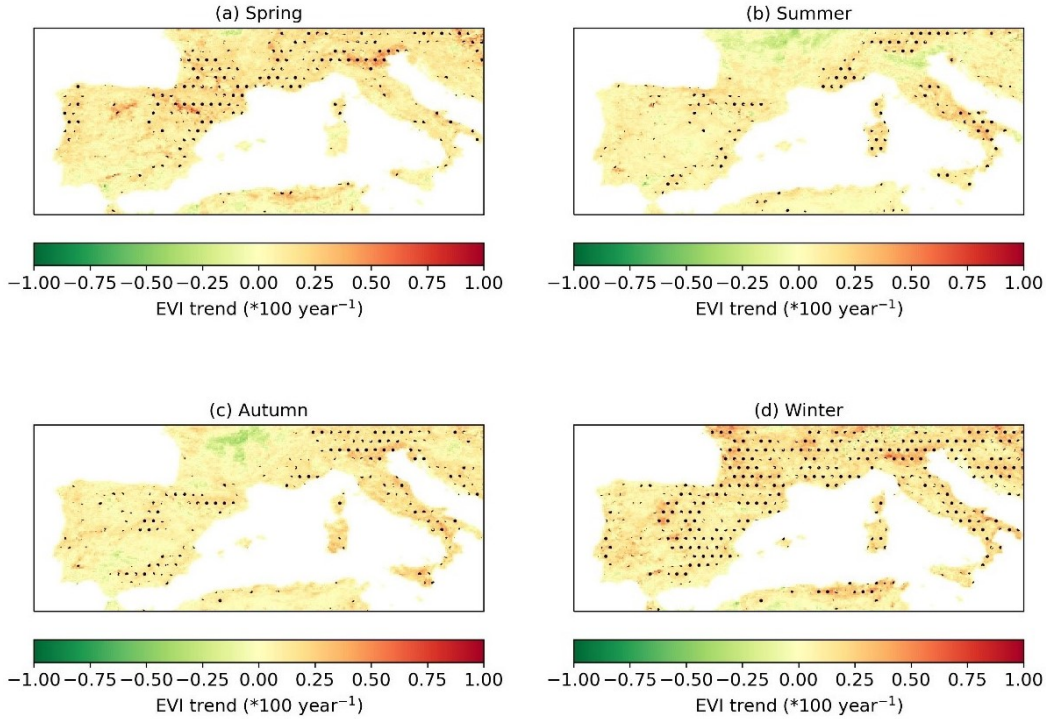


Figure F.11: Spatial pattern of the long-term trends of seasonal enhanced vegetation index (EVI). (a) Spring; (b) Summer; (c) Autumn; and (d) Winter between 2001 and 2022. The black dots correspond to areas where the linear regression is significant ($p < 0.05$).

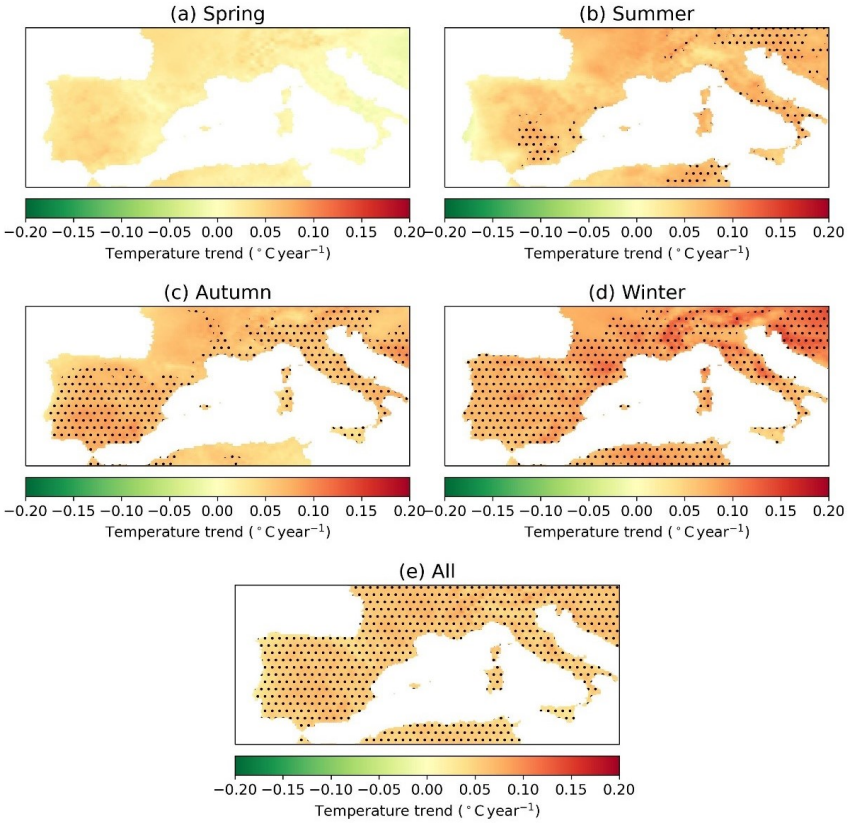


Figure F.12: Spatial pattern of the long-term trends of seasonal and annual 2 m temperatures from ERA5-Land. (a) Spring; (b) Summer; (c) Autumn; (d) Winter; (e) Yearly between 2001 and 2022. The black dots correspond to areas where the linear regression is significant ($p < 0.05$).

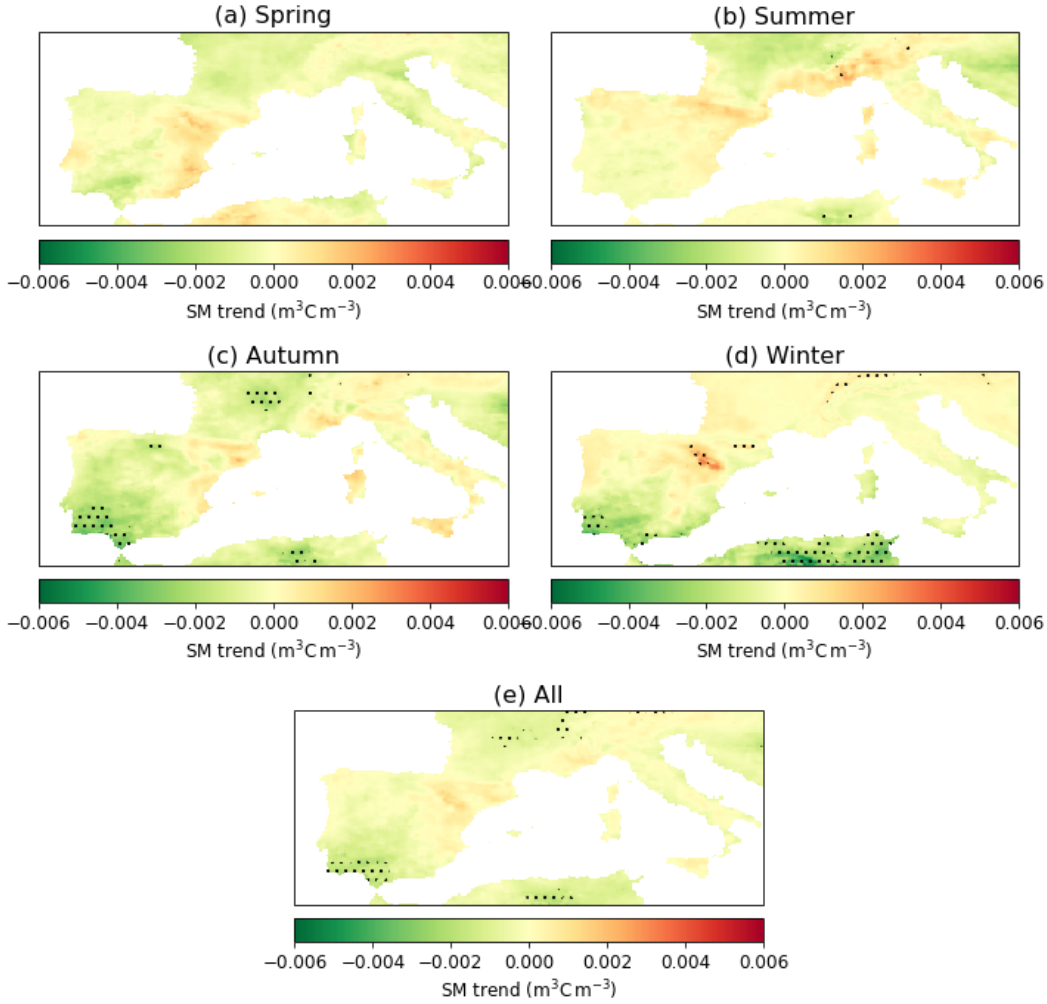


Figure F.13: Spatial pattern of the long-term trends of seasonal and annual soil moisture (7-28 cm depth)from ERA5-Land. (a) Spring; (b) Summer; (c) Autumn; (d) Winter; (e) Yearly between 2001 and 2022. The black dots correspond to areas where the linear regression is significant ($p < 0.05$).

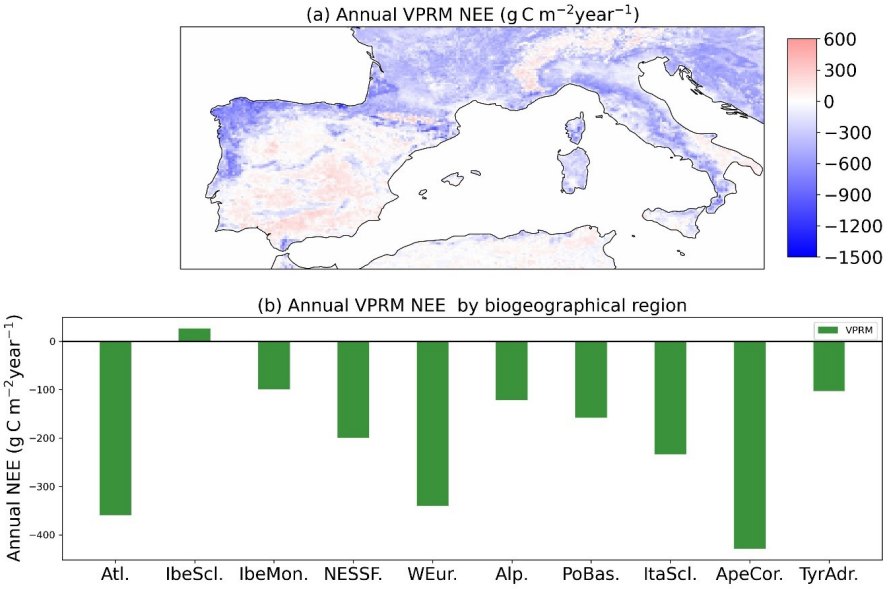


Figure F.14: (a) Spatial patterns of annual mean between 2001-2022 for VPRM NEE. (b) Spatial median of annual mean between 2001-2022 VPRM NEE for each biogeographical region.

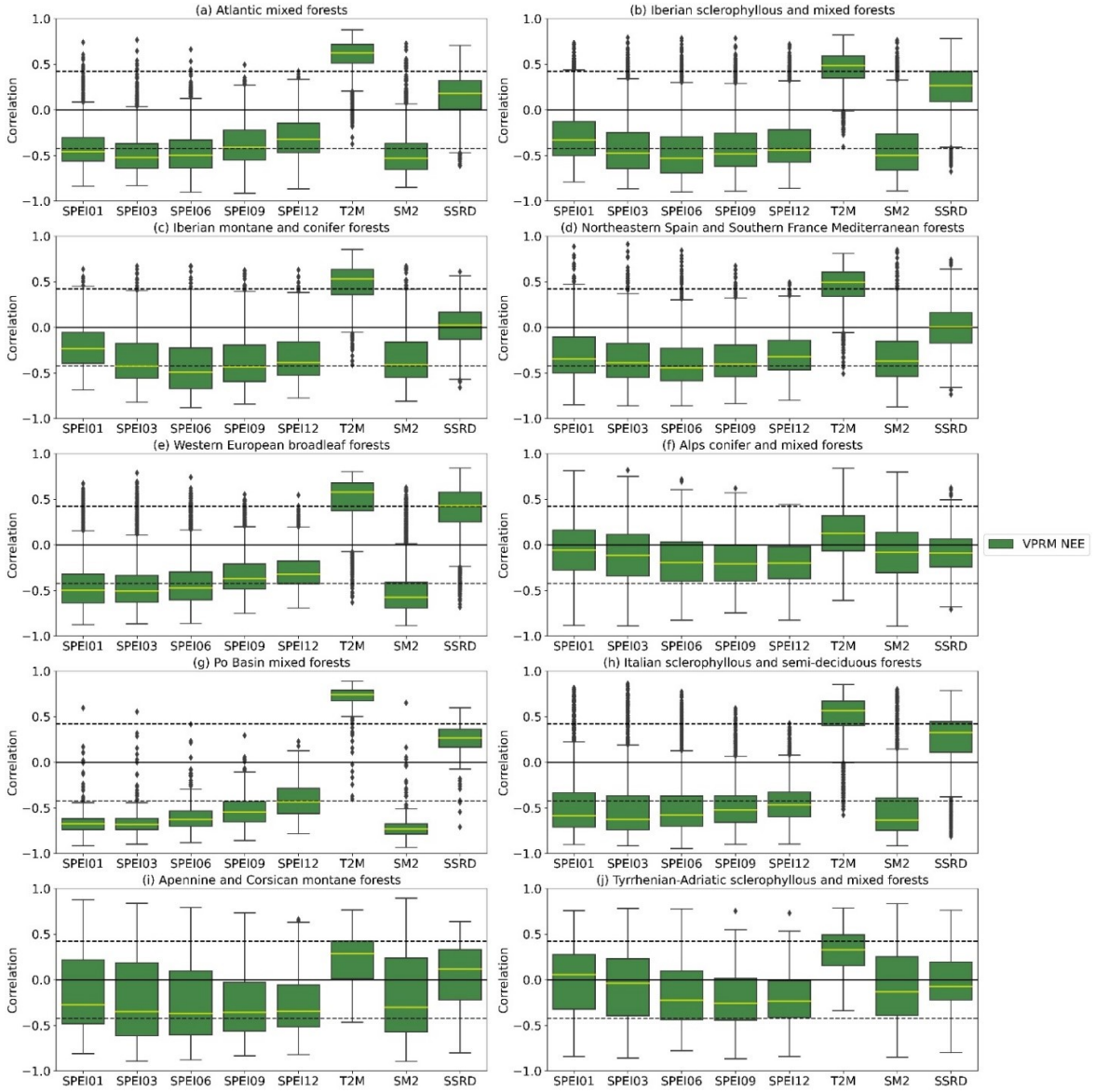


Figure F.15: Boxplots of correlation values between NEE detrended anomalies and the different climate drivers and drought indices aggregated during the growing season months of each biogeographical regions. The median for each climate driver is represented by the yellow line in the boxes. The discontinuous black lines represent the limit when the correlations are significant at $p<0.05$.